ΠΑΝΕΠΙΣΤΗΜΙΟ ΚΡΗΤΗΣ
ΤΜΗΜΑ ΧΗΜΕΙΑΣ

Εργαστήριο Περιβαλλοντικών Χημικών Διεργασιών

ΔΙΔΑΚΤΟΡΙΚΗ ΔΙΑΤΡΙΒΗ

Μέτρηση, σε σχεδόν πραγματικό χρόνο, της χημικής σύστασης των αιωρούμενων σωματιδίων με διάμετρο κάτω του ενός μικρομέτρου, στην ατμόσφαιρα της Ανατολικής Μεσογείου

Ιάσων Σταυρούλας

Υπεύθυνος Καθηγητής: Νικόλαος Μιχαλόπουλος

ΗΡΑΚΛΕΙΟ 2023

UNIVERSITY OF CRETE
DEPARTMENT OF CHEMISTRY

Environmental Chemical Processes Laboratory

Doctoral Thesis

Near real time measurements of chemical composition of fine aerosols (<1μm) in the Eastern Mediterranean

Iason Stavroulas

Thesis Supervisor: Nikolaos Mihalopoulos

HERAKLION 2023

Στον Αλέξη και την Αθηνά

Εξεταστική Επιτροπή

Νικόλαος Μιχαλόπουλος

Καθηγητής, Τμήμα Χημείας, Πανεπιστήμιο Κρήτης

(Επιβλέπων)

Μαρία Κανακίδου

Καθηγήτρια, Τμήμα Χημείας, Πανεπιστήμιο Κρήτης

Ευριπίδης Στεφάνου

Ομότιμος Καθηγητής, Τμήμα Χημείας, Πανεπιστήμιο Κρήτης

Σπυρίδων Περγαντής

Καθηγητής, Τμήμα Χημείας, Πανεπιστήμιο Κρήτης

Jean Sciare

Καθηγητής, Climate and Atmosphere Research Center, The Cyprus Institute

Ευάγγελος Γερασόπουλος

Διευθυντής Ερευνών, Εθνικό Αστεροσκοπείο Αθηνών

Αικατερίνη Μπουγιατώτη

Κύρια Ερευνήτρια, Εθνικό Αστεροσκοπείο Αθηνών

Examination Committee

Nikolaos Mihalopoulos

Professor, Department of Chemistry, University of Crete

(Supervisor)

Maria Kanakidou

Professor, Department of Chemistry, University of Crete

Euripides Stefanou

Professor Emeritus, Department of Chemistry, University of Crete

Spiros Pergantis

Professor, Department of Chemistry, University of Crete

Jean Sciare

Professor, Climate and Atmosphere Research Center, The Cyprus Institute

Evangelos Gerasopoulos

Research Director, National Observatory of Athens

Aikaterini Bougiatioti

Senior Researcher, National Observatory of Athens

Ευχαριστήριο Σημείωμα

Με το παρών σημείωμα, θα ήθελα να ευχαριστήσω όλους όσους συνέβαλαν στην εκπόνηση της παρούσας διατριβής.

Ιδιαίτερες ευχαριστίες οφείλω στον επιβλέποντα καθηγητή Νικόλαο Μιχαλόπουλο, για την υπομονή, την πολύτιμη καθοδήγησή του στο ευρύ πεδίο της ατμοσφαιρικής φυσικής και χημείας αλλά και την ουσιαστική ηθική υποστήριξή του κατά την τελευταία δεκαετία. Τον ευχαριστώ για την αεικίνητη προσήλωσή του στη διάνοιξη νέων ερευνητικών διαδρομών και την ευκαιρία που μου παρείχε να συνεργαστώ με πληθώρα εξαιρετικών επιστημόνων στην Ελλάδα και το εξωτερικό.

Ευχαριστώ επίσης την Καθηγήτρια Μαρία Κανακίδου και τον Ομότιμο Καθηγητή Ευριπίδη Στεφάνου, για τις χρήσιμες παρατηρήσεις τους και τη συμμετοχή τους στην τριμελή συμβουλευτική επιτροπή της παρούσας διατριβής.

Θα ήθελα επιπλέον να αναγνωρίσω τη συμβολή όλων των συναδέλφων στο Εργαστήριο Περιβαλλοντικών Χημικών Διεργασιών του Τμήματος Χημείας του ΠΚ, στο Ινστιτούτο Ερευνών Περιβάλλοντος και Βιώσιμης Ανάπτυξης του Εθνικού Αστεροσκοπείου Αθηνών αλλά και στο Climate and Atmosphere Research Center του Ινστιτούτου Κύπρου. Ονομαστικά θα ήθελα να αναφέρω τους Αικατερίνη Μπουγιατιώτη, Γεώργιο Γρίβα, Νικόλαο Καλιβίτη, Ελένη Λιακάκου, Γεώργιο Κουβαράκη, Δέσποινα Παρασκευοπούλου, Παναγιώτη Καλκαβούρα, Ευάγγελο Γερασόπουλο και Jean Sciare.

Τέλος θα ήθελα να ευχαριστήσω την οικογένεια μου για τη διαρκή συμπαράσταση και υποστήριξή τους.

Acknowledgements

With this note, I would like to thank everyone who contributed to the preparation of this thesis.

I owe special thanks to my supervisor, professor Nikolaos Mihalopoulos, for his patience, his valuable guidance in the wide field of atmospheric chemistry and physics and his essential moral support during the last decade. I thank him for his steadfast commitment to opening new research pathways and the opportunity he gave me to collaborate with a great number of exquisite scientists in Greece and abroad.

I also thank Professor Maria Kanakidou and Professor Emeritus Evripides Stefanou, for their helpful input and their participation in the advisory committee of this dissertation.

I would also like to acknowledge the contribution of all colleagues at the Environmental Chemical Processes Laboratory of the Department of Chemistry at the University of Crete, at the Institute for Environmental Research and Sustainable Development of the National Observatory of Athens and at the Climate and Atmosphere Research Center of the Cyprus Institute. I would like to specifically mention Aikaterini Bougiatioti, Georgios Grivas, Nikolaos Kalivitis, Eleni Liakakou, George Kouvarakis, Despina Paraskevopoulou, Panagiotis Kalkavouras, Evangelos Gerasopoulos and Jean Sciare.

Finally, I would like to thank my family for their continuous support and encouragement.

Περίληψη

Υγρά και στερεά σωματίδια με διαφορετικές διαμέτρους και χημικές συνθέσεις που αιωρούνται στον αέρα μπορεί να αποτελούν απειλή για την ανθρώπινη υγεία και το προσδόκιμο ζωής. Τα αιωρούμενα σωματίδια (ΑΣ; Particulate matter - PM) επηρεάζουν επίσης άμεσα και έμμεσα το κλίμα και διάφορα οικοσυστήματα. Η κατανόηση και ο λεπτομερής χαρακτηρισμός των πηγών τους, των χημικών διεργασιών και των μηχανισμών ατμοσφαιρικής μεταφοράς που διέπουν την εξαιρετικά ευμετάβλητη χωρική και χρονική διακύμανση τους είναι καίριας σημασίας για την περαιτέρω διευκόλυνση των ρυθμιστικών στρατηγικών και νομοθεσίας για τον έλεγχο των εκπομπών τους.

Η παρούσα διατριβή επικεντρώνεται στον χημικό χαρακτηρισμό του υπομικρομετρικού (PM_1) αερολύματος, με μετρήσεις υψηλής χρονικής ανάλυσης μέσω φασματομετρίας μάζας αερολυμάτων, χρησιμοποιώντας τον Χημικό Ειδοταυτοποιητή Αιωρούμενων Σωματιδίων (Aerosol Chemical Speciation Monitor; ACSM) σε απομακρυσμένα και αστικά περιβάλλοντα στην Ανατολική Μεσόγειο. Τα δεδομένα που συλλέχθηκαν επιτρέπουν τον προσδιορισμό των πηγών οργανικού αερολύματος (OA) μέσω της εφαρμογής κατάλληλων τεχνικών μοντελοποίησης (Positive Matrix Factorization; PMF). Στην παρούσα μελέτη παρουσιάζονται αποτελέσματα από μετρήσεις που πραγματοποιήθηκαν για περίπου 3 έτη στη Φινοκαλιά, μια περίοδο ενός έτους στον αστικό σταθμό υποβάθρου Θησείο στην Αθήνα καθώς και δύο προηγούμενες εντατικές εκστρατείες, η μελέτη της παρουσίας συγκεκριμένων πηγών σε μακροπρόθεσμη βάση, και τέλος τα αποτελέσματα από δύο εποχικές εντατικές εκστρατείες στον Πειραιά. Με στόχο τον χωρικό χαρακτηρισμό των πηγών, στο πλαίσιο της παρούσας διατριβής επιδιώχθηκε επίσης η βαθμονόμηση και η υλοποίηση ενός χαμηλού κόστους πυκνού δικτύου παρακολούθησης των ΑΣ.

Στη Φινοκαλία, οι μέσες συγκεντρώσεις PM_1 (σωματίδια με διαμέτρους μικρότερες του 1μm) ήταν $6,4 \pm 4,6$ μg m^{-3} με κυρίαρχο συστατικό καθ' όλη τη διάρκεια της περιόδου τα θειικά, τα οποία συνεισέφεραν κατά μέσο όρο 42,6%. Ακολούθησε το οργανικό αερόλυμα με ποσοστό 36,5%, και το αμμώνιο με 12,6%. Τα νιτρικά και ο Μαύρος Άνθρακας (Black Carbon; BC) συνεισέφεραν 4,4% και 3,8% αντίστοιχα. Οι συγκεντρώσεις ήταν γενικά υψηλότερες κατά τους θερμότερους μήνες του έτους. Καταγράφηκε αντίθεση μεταξύ ψυχρής και θερμής περιόδου όσον αφορά τη συνεισφορά των ειδών. Για την ψυχρή περίοδο, το OA και τα θειικά συνεισέφεραν εξίσου με 39% το καθένα, ενώ κατά τους θερμούς μήνες τα θειικά κυριαρχούσαν σαφώς στο PM_1 αερόλυμα

συνεισφέροντας 44% σε αντίθεση με τη συνεισφορά των οργανικών που ήταν 36%. Όλα τα είδη παρουσίασαν περιορισμένη ημερήσια μεταβλητότητα, ελλείψει σημαντικών τοπικών πηγών, με διακυμάνσεις της τάξης του ± 12% γύρω από τους αντίστοιχους εποχικούς μέσους όρους. Η απομακρυσμένη μεταφορά ρύπων βρέθηκε να κυριαρχεί με κύριες πηγές τη βιομηχανική δραστηριότητα, τη ναυτιλία και την καύση βιομάζας σε περιοχές της Νοτιοδυτικής Ευρώπης, της περιοχής της Μαύρης Θάλασσας, της Τουρκίας και του Αιγαίου Πελάγους. Καταγράφηκε επίσης αξιοσημείωτη συμβολή από το έντονα ρυπασμένο Δέλτα του ποταμού Νείλου και τη Μέση Ανατολή.

Στην Αθήνα, σε ετήσια βάση, το πιο άφθονο συστατικό ήταν το OA (44,5%), ακολουθούμενο από τα θειικά (27,8%), το BC (15,1%), το αμμώνιο (7,9%) και τα νιτρικά (4,3%). Κατά τη διάρκεια της ψυχρής περιόδου, εντοπίστηκαν τρεις κύριες πηγές, και συγκεκριμένα ένας παράγοντας οργανικού αερολύματος που μοιάζει με υδρογονάνθρακες (Hydrocarbon-like Organic Aerosol, HOA; 13%), ο οποίος αντιπροσωπεύει κυρίως την καύση υγρών καυσίμων (κυκλοφορία και θέρμανση κατοικιών), ένας παράγοντας οργανικού αερολύματος που σχετίζεται με το μαγείρεμα (Cooking Organic Aerosol, COA; 10%) και ένας παράγοντας καύσης βιομάζας (Biomass Burning Organic Aerosol, BBOA; 10). Δύο δευτερογενείς παράγοντες μοντελοποιήθηκαν επιπλέον, ένας παράγοντας ημιπτητικού οξειδωμένου OA (Semivolatile Oxygenated Organic Aerosol, SV-OOA; 22%), που συνδέεται με την ταχεία ατμοσφαιρική επεξεργασία των εκπομπών καύσης βιομάζας και ένας παράγοντας χαμηλής πτητικότητας οξειδωμένου OA (Low Volatility Oxygenated Organic Aerosol, LV-OOA; 45%), που συνδέεται με μηχανισμούς μεταφοράς ρύπων από μεγάλες αποστάσεις. Καταγράφηκαν αρκετά γεγονότα σοβαρής επιδείνωσης της ποιότητας του αέρα, γεγονός που υποδεικνύει τις δυσμενείς επιπτώσεις της οικιακής καύσης ξύλου στην ατμόσφαιρα της πόλης. Κατά τη διάρκεια της θερμής περιόδου, ελλείψει ενεργού πηγής καύσης βιομάζας, επιλύθηκαν τέσσερις παράγοντες, και συγκεκριμένα ένας παράγοντας HOA (5%) και ένας παράγοντας COA (11%) με τα ίδια χαρακτηριστικά που βρέθηκαν για την ψυχρή περίοδο, ένας παράγοντας SV-OOA (33%) που σχετίζεται τόσο με την επεξεργασία πρωτογενούς αερολύματος όσο και με δευτερογενή σχηματισμό, και ένας παράγοντας LV-OOA (51%) που αντιπροσωπεύει τη διασυνοριακή ρύπανση.

Στον Πειραιά, οι συνδυασμένες εκπομπές της κυκλοφορίας, της ναυτιλίας και, κυρίως, της θέρμανσης κατοικιών οδήγησαν σε σημαντικά αυξημένα επίπεδα υπομικρομετρικού αερολύματος

(22,8 μg m^{-3}) το χειμώνα, επεισοδικού χαρακτήρα αργά τη νύχτα υπό στάσιμες συνθήκες. Οι ανθρακούχες ενώσεις αποτελούσαν το μεγαλύτερο μέρος του PM_1 αερολύματος το χειμώνα, με μέση συνεισφορά OA και BC στα 61% (13,9 μg m^{-3}) και 16% (3,7 μg m^{-3}), αντίστοιχα. Η συμβολή της καύσης βιομάζας στις συγκεντρώσεις BC ήταν σημαντική και χωρικά ομοιόμορφη. Το OA που σχετίζεται με τις εκπομπές καύσης βιομάζας (πρωτογενείς και επεξεργασμένες) και το OA που σχετίζεται με υδρογονάνθρακες (από την κυκλοφορία οχημάτων και τις εκπομπές ορυκτών καυσίμων που σχετίζονται με τη λιμενική δραστηριότητα και τη ναυτιλία) αντιπροσωπεύουν το 37% και 30% του OA, αντίστοιχα. Το καλοκαίρι, η μέση συγκέντρωση PM_1 ήταν σημαντικά χαμηλότερη (14,8 μg m^{-3}) και λιγότερο μεταβλητή, ιδίως για τα συστατικά που σχετίζονται με τα δευτερογενή αερολύματα (όπως το OA και τα θειικά). Η επίδραση της λιμενικής δραστηριότητας ήταν εμφανής το καλοκαίρι και διατήρησε τις συγκεντρώσεις BC σε υψηλά επίπεδα (2,8 μg m^{-3}), παρά την απουσία καύση βιομάζας και τη βελτιωμένη ατμοσφαιρική διασπορά. Τα οξυγονωμένα συστατικά απέδωσαν πάνω από το 70% του OA το καλοκαίρι, με το πιο οξειδωμένο δευτερογενές περιοχικής προέλευσης OA να είναι κυρίαρχο (41%) παρά την ένταση των τοπικών πηγών, στο περιβάλλον του Πειραιά.

Για την επιτόπια αξιολόγηση των συσκευών Purple Air PA-II (αισθητήρες PM χαμηλού κόστους), πραγματοποιήθηκαν μετρήσεις στην Αθήνα για πέντε μήνες και στα Ιωάννινα, μια μεσαίου μεγέθους πόλη στη βορειοδυτική Ελλάδα, για περίοδο έξι μηνών. Οι μετρήσεις του αισθητήρα συσχετίζεται σε μεγάλο βαθμό με μετρήσεις αναφοράς (R^2 = 0,87 συγκρινόμενες με beta attenuation monitor αναφοράς και R^2 = 0,98 συγκρινόμενες με optical particle counter αναφοράς). Οι αποκλίσεις στη συμφωνία αισθητήρα-οργάνων αναφοράς σχετίζονται κυρίως με τις αυξημένες συγκεντρώσεις αδρών σωματιδίων και την υψηλή σχετική υγρασία του περιβάλλοντος. Δοκιμάσθηκαν μοντέλα απλής και πολλαπλής παλινδρόμησης για την αντιστάθμιση του συστηματικού αυτού σφάλματος, βελτιώνοντας δραστικά την απόκριση του αισθητήρα. Μετά την εφαρμογή τέτοιων μοντέλων παρατηρούνται μεγάλες μειώσεις στο σφάλμα του αισθητήρα, με αποτέλεσμα τα μέσα απόλυτα ποσοστιαία σφάλματα να είναι 0,18 και 0,12 για τα σύνολα δεδομένων της Αθήνας και των Ιωαννίνων, αντίστοιχα. Συνολικά, ένα δίκτυο χαμηλού κόστους με ελεγχόμενη ποιότητα και ισχυρή αξιολόγηση μπορεί να αποτελέσει αναπόσπαστο στοιχείο για την παρακολούθηση της ποιότητας του αέρα σε μια έξυπνη πόλη. Παρουσιάζονται μελέτες περίπτωσης προς αυτή την κατεύθυνση, όπου ένα δίκτυο συσκευών PA-II χρησιμοποιείται για την παρακολούθηση της επιδείνωσης της ποιότητας του αέρα κατά τη διάρκεια ενός περιστατικού

περιαστικής δασικής πυρκαγιάς που επηρέασε την περιοχή της Αθήνας και κατά τη διάρκεια ακραίων φαινομένων αιθαλομίχλης κατά τη διάρκεια του χειμώνα στα Ιωάννινα, που σχετίζονται με την καύση ξύλου για θέρμανση κατοικιών.

Εστιάζοντας στην πηγή ΟΑ σχετιζόμενων με το μαγείρεμα στο αστικό περιβάλλον, σε εορταστικές εκδηλώσεις που περιλαμβάνουν ψήσιμο κρέατος, όπως η Τσικνοπέμπτη και η Κυριακή του Πάσχα στην Αθήνα αλλά και οι Γιορτές Παλιάς Πόλης στην πόλη της Ξάνθης στη Βόρεια Ελλάδα, εξετάστηκαν μέσω ενός συνδυασμού φασματομετρίας μάζας αερολυμάτων και χωρικά πυκνών δεδομένων $PM_{2.5}$ που προέρχονται από ένα δίκτυο αισθητήρων χαμηλού κόστους. Στην Ξάνθη, κατά τη διάρκεια των εορταστικών εκδηλώσεων οι συγκεντρώσεις των $PM_{2.5}$ κατέγραψαν αύξηση κατά 170% σε σύγκριση με το υπόβαθρο της περιοχής. Στην Αθήνα, κατά τη διάρκεια της Τσικνοπέμπτης, οι συγκεντρώσεις $PM_{2.5}$ αυξήθηκαν σημαντικά το βράδυ σε όλο το λεκανοπέδιο καταγράφοντας ένα σαφές μοτίβο αυξημένων συγκεντρώσεων $PM_{2.5}$, οι οποίες στις περισσότερες περιπτώσεις ήταν σχεδόν διπλάσιες και σε συγκεκριμένες περιοχές έως και υπερτριπλάσιες κατά τη διάρκεια της συγκεκριμένης μέρας, σε σχέση με μια περίοδο ελέγχου διάρκειας 2 εβδομάδων πριν και μετά την Τσικνοπέμπτη. Παρόμοια χωρική τάση αλλά και ενίσχυση των συγκεντρώσεων διαπιστώθηκε κατά την εξέταση των εκδηλώσεων της Κυριακής του Πάσχα. Οι μέγιστες τιμές COA τις νυχτερινές ώρες έφτασαν τα 23,3 μg m^{-3} στο Θησείο κατά τη διάρκεια της Τσικνοπέμπτης, όντας περισσότερο από 5 φορές υψηλότερες από τις μέγιστες τιμές κατά την περίοδο ελέγχου. Την Κυριακή του Πάσχα, οι μέγιστες συγκεντρώσεις μετατοπίστηκαν χαρακτηριστικά προς τις πρώτες απογευματινές ώρες ενώ οι συγκεντρώσεις COA παρουσίασαν μέγιστη τιμή στα 27,4 μg m^{-3} στις 15:00 ώρα Ελλάδος, μια εντυπωσιακή αύξηση κατά 50 φορές σε σύγκριση με τη μέση συγκέντρωση COA (0,5 μg m^{-3}) για την ίδια ώρα κατά την περίοδο ελέγχου. Και στις δύο περιπτώσεις καταγράφηκε κυριαρχία των οργανικών αερολυμάτων COA, με τη συνεισφορά του ΟΑ στα PM_1 να αυξάνεται σε περίπου 70%, ενώ ήταν κοντά στο 50% κατά την περίοδο ελέγχου. Από την άλλη, εξετάζοντας το σύνολο δεδομένων ενός ολόκληρου έτους και όχι πια συγκεκριμένες περιπτώσεις, διαπιστώθηκε πως η παρατηρούμενη μεταβλητότητα συνδέεται με δραστηριότητες αναψυχής, με την εβδομαδιαία διακύμανση του COA να δείχνει αυξημένες συγκεντρώσεις και συνεισφορές προς το Σαββατοκύριακο.

Συνολικά, καταδεικνύεται με έμφαση η σημασία των μετρήσεων σε σχεδόν πραγματικό χρόνο σε μακροπρόθεσμη βάση για την καταγραφή της μεταβαλλόμενης φύσης της χημικής σύνθεσης και

των πηγών των αιωρούμενων σωματιδίων, της ποικιλομορφίας τους ανάλογα με τα διαφορετικά περιβάλλοντα από την απομακρυσμένη έως την αστική κλίμακα - ακόμη και εντός του ίδιου οικισμού - και των παραγόντων που ελέγχουν τα επίπεδα και τις συνεισφορές τους. Το ACSM, ειδικά σχεδιασμένο για εφαρμογές μη επιτηρούμενης μακροχρόνιας παρακολούθησης, σε συνδυασμό με την εφαρμογή της προσέγγισης κατανομής των πηγών PMF επιτρέπει τη βαθύτερη κατανόηση των πηγών ατμοσφαιρικής ρύπανσης, βοηθώντας τις τοπικές αρχές και τους υπεύθυνους χάραξης πολιτικής στο σχεδιασμό περαιτέρω δράσεων για τον επιτυχή έλεγχο ενός εγγενώς πολύπλοκου προβλήματος.

Λέξεις Κλειδιά: Οργανικό Αερόλυμα, Ταυτοποίηση Πηγών, ACSM, Αιθαλόμετρο, Μαύρος Άνθρακας, PMF, Χημική Ειδοταυτοποίηση

Abstract

Liquid and solid particles with different diameters and chemical compositions suspended in the air may pose a threat to human health and life expectancy. Particulate matter (PM) also affects the climate and various ecosystems directly and indirectly. Understanding and obtaining a detailed characterization of their sources, chemical processes and atmospheric transportation mechanisms governing their highly variable spatial and temporal variability is of pivotal importance to further facilitate regulative strategies and abatement legislation.

This dissertation focuses on the chemical characterization of submicron (PM_1) aerosol using high temporal resolution measurements via aerosol mass spectrometry, using the Aerosol Chemical Speciation Monitor (ACSM) in the remote and urban environments in the Eastern Mediterranean. Collected data allow for the determination of organic aerosol (OA) sources via the application of appropriate receptor modeling techniques (Positive Matrix Factorization). Results from measurements conducted for approximately 3 years in Finokalia, a one-year period at the urban background Thissio station in Athens plus two preceding intensive campaigns, followed by the analysis of source specific case studies in the long-term, and finally two season specific intensive campaigns in Piraeus, are herein presented. Aiming at the spatial characterization of delineated sources, the calibration and implementation of a dense low-cost PM monitoring network was also pursued in the context of this thesis.

In Finokalia, average PM_1 concentrations were 6.4 ± 4.6 μg m^{-3} with sulfate being the dominant component throughout the period, contributing on average 42.6%. Organic aerosol followed, contributing 36.5%, while ammonium contributed 12.6%. Nitrate and BC contributed 4.4% and 3.8% respectively. Concentrations in general, were higher during the warmer months of the year. A contrast was recorded among the two periods in terms of species contributions. For the cold period, OA and sulfate contributed equally at 39% each, while during the warm months sulfate clearly dominated ambient PM_1 aerosol contributing 44% as opposed to a 36% contribution from organics. All species exhibited limited diurnal variability, in the absence of important local sources, varying by as much as ± 12% around their respective seasonal averages. Long range transport was mainly driving measured concentrations with main sources including industrial activity, shipping and biomass burning in areas of South Western Europe, the Black Sea region, Turkey and the

Aegean Sea. A noteworthy contribution from the heavily polluted Nile river Delta and the Middle East was also documented.

In Athens, on an annual basis, the most abundant component was OA (44.5%), followed by sulfate (27.8%), BC (15.1 %), ammonium (7.9 %), and nitrate (4.3 %). During the cold season, three primary sources were identified, namely a hydrocarbon-like organic aerosol factor (HOA; 13%) mainly representing liquid fuel combustion (traffic and residential heating), a cooking organic aerosol factor (COA; 10%) and a biomass burning factor (BBOA; 10). Two secondary factors were additionally modeled, a semi volatile oxygenated organic aerosol factor (SV-OOA; 22%), linked to the fast atmospheric processing of biomass burning plumes and a low volatility OOA factor (LV-OOA; 45%), linked to long range transporting mechanisms. Several severe air quality deterioration events were recorded, pointing to the adverse effects of residential wood burning to the atmosphere over the city. During the warm period, in the absence of an active biomass burning source, four factors were resolved, namely an HOA (5%) and a COA (11%) factor with the same characteristics found for the cold period, an SV-OOA (33%) factor related to both primary aerosol processing and secondary formation, and an LV-OOA (51%) factor representing transboundary pollution.

In Piraeus, the combined traffic, shipping and, especially, residential emissions led to considerably elevated submicron aerosol levels (22.8 μg m^{-3}) in winter, which frequently became episodic late at night under stagnant conditions. Carbonaceous compounds comprised the major portion of this submicron aerosol in winter, with mean OA and BC contributions of 61% (13.9 μg m^{-3}) and 16% (3.7 μg m^{-3}), respectively. The contribution of BB to BC concentrations was considerable and spatially uniform. OA related to BB emissions (fresh and processed) and hydrocarbon-like OA (from vehicular traffic and port-related fossil fuel emissions including shipping) accounted for 37% and 30% of OA, respectively. In summer, the average PM1 concentration was significantly lower (14.8 μg m^{-3}) and less variable, especially for the components associated with secondary aerosols (such as OA and sulfate). The effect of the port sector was evident in summer and maintained BC concentrations at high levels (2.8 μg m^{-3}), despite the absence of BB and improved atmospheric dispersion. Oxygenated components yielded over 70% of OA in summer, with the more oxidized secondary component of regional origin being dominant (41%) despite the intensity of local sources, in the Piraeus environment.

For the field evaluation of Purple Air PA-II devices (low-cost PM sensors), measurements were conducted in Athens for five months and in Ioannina, a medium-sized city in northwestern Greece for a six-month period. The sensor output correlates strongly with reference measurements (R^2 = 0.87 against a beta attenuation monitor and R^2 = 0.98 against an optical reference-grade monitor). Deviations in the sensor-reference agreement are identified as mainly related to elevated coarse particle concentrations and high ambient relative humidity. Simple and multiple regression models are tested to compensate for these biases, drastically improving the sensor's response. Large decreases in sensor error are observed after implementation of models, leading to mean absolute percentage errors of 0.18 and 0.12 for the Athens and Ioannina datasets, respectively. Overall, a quality-controlled and robustly evaluated low-cost network can be an integral component for air quality monitoring in a smart city. Case studies are presented along this line, where a network of PA-II devices is used to monitor the air quality deterioration during a peri-urban forest fire event affecting the area of Athens and during extreme wintertime smog events in Ioannina, related to wood burning for residential heating.

Focusing on the cooking source in the urban environment, festive celebrations involving meat grilling i.e., Fat Thursday and Easter Sunday in Athens and the Old Town Festival in the town of Xanthi in northern Greece were examined via a combination of aerosol mass spectrometry and spatially dense $PM_{2.5}$ data coming from a low-cost sensor network. In Xanthi, during festivities $PM_{2.5}$ concentrations recorded a 170% increment when compared to the rural background in the area. In Athens, during Fat Thursday $PM_{2.5}$ concentrations rose significantly in the evening throughout the basin recording a clear pattern of elevated $PM_{2.5}$ concentrations, being in most cases close to double and in specific sites up to more than triple during Fat Thursday, with respect to a 2-week long control period around the event. A similar trend spatially and concentration-wise was established when examining the Easter Sunday events. COA night-time maxima were up to 23.3 $\mu g\ m^{-3}$ at Thissio during fat Thursday, being more than 5 times higher than the maxima during the control period. On Easter Sunday, the peaks were characteristically shifted to the early afternoon, and COA concentrations exhibited an extreme average value of 27.4 $\mu g\ m^{-3}$ at 15:00 LST signifying a staggering 50-fold increase compared to the average COA concentration of 0.5 $\mu g\ m^{-3}$ for the same hour in the control period. A COA driven organic aerosol dominance was recorded for both cases with OA contributions to PM_1 increasing to about 70% while being close to 50% during the control period. Moving away from the event-based analysis, revisiting the full-year dataset, a

pattern linked to leisure activities was established, with the weekly variability of COA pointing to increased concentrations and contributions towards the weekend.

Overall, these studies clearly show the importance of near-real-time and long-term measurements in capturing the changing nature of chemical composition and sources, their diversity according to different environments moving from the remote to the urban scale – even within the same agglomeration – and the diurnal factors controlling their levels and contributions. The ACSM, specifically designed for such unattended long-term monitoring applications, along with the application of the PMF source apportionment approach allows for a deeper understanding of air pollution sources, assisting local authorities and policymakers in designing further actions in order to successfully control an inherently complex problem.

Keywords: Organic Aerosol, Source Apportionment, ACSM, aethalometer, Black Carbon, PMF, Chemical Speciation

Contents

1 Introduction

1.1 The Atmospheric Aerosol

Atmospheric aerosol is defined as the ensemble of solid and / or liquid particles that are suspended in ambient air. Their presence in the lower part of the atmosphere is ubiquitous, while their concentrations, physical and chemical properties are highly variable, depending on the specific environment under study. Their origin can be either natural or anthropogenic i.e., related to human activity. Anthropogenic aerosol are mainly derivatives of activities linked to combustion processes, such as vehicular traffic, industrial production, power generation, shipping, aviation and biomass burning for various purposes. Natural aerosol may be attributed to sources such as vegetation, ocean spray, volcanoes and deserts.

On top of the above, aerosol are classified on one hand as primary, meaning that they are directly emitted in the atmosphere in the particulate phase, and on the other hand as secondary, where gas to particle conversion mechanisms such as nucleation, condensation of gas precursors on already formed particles and coagulation, play an important role. Their atmospheric lifetime may vary from a few hours to even some weeks, depending on their physical properties, especially their size, and the prevailing removal mechanisms (Seinfeld and Pandis, 2016).

According to their size and assuming spherical particles, aerosol are classified initially as coarse, having diameters (d_p) above 2.5 μm and as fine, when their diameters are below 2.5 μm. Submicron aerosol i.e., particles with diameters less than 1 μm are further classified as nucleation mode particles (d_p < 25 nm), Aitken mode particles (25 nm < d_p < 100 nm) with these two modes cumulatively known as ultrafine particles, and accumulation mode (100 nm < d_p < 1 μm) particles. A schematic of the aerosol size distribution in the atmosphere also incorporating the prevailing formation and removal mechanisms (Seinfeld and Pandis, 2016) is depicted in **Figure 1.1**. Categorizing particles by particulate mass present in different size fractions is another straightforward classification scheme and are often referred to as PM_x. In this sense submicron particles (d_p < 1μm) are called PM_1, fine particles (d_p < 2.5 μm) are known as $PM_{2.5}$ while particles well into the coarse mode (d_p < 10 μm) are referred to as PM_{10}.

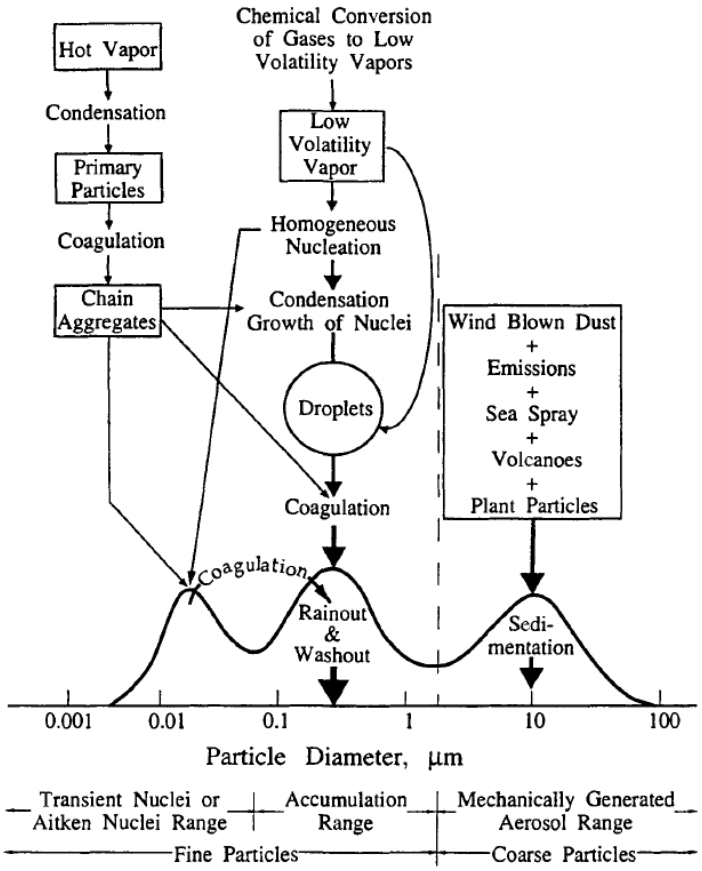

Figure 1.1. Schematic figure of the ambient aerosol size distribution, depicting most common formation and removal mechanisms (Seinfeld and Pandis, 2016).

Ultrafine particles are the most abundant in numbers, but play a rather limited role in total particulate matter mass, due to their small size. They are formed via gas – to – particle phase transition processes as well the condensation of hot vapors from various combustion processes. Accumulation mode particles are directly emitted through incomplete combustion (solid or liquid fuel, wildfires etc) directly in the particulate phase, with particles growing through condensation or coagulation of preexisting smaller diameter particles. Coarse mode particles are mostly mechanically generated, i.e., ocean spray, suspension of desert dust by blowing wind or road dust resuspension via vehicular traffic. Ultrafine particles are mainly removed from the atmosphere via diffusion or coagulation to larger particles, accumulation mode particles are effectively washed out through precipitation while coarse particles can be quickly removed by sedimentation, precipitation and scavenging.

1.2 Aerosol Impacts on Human Health and the Earth's Climate

1.2.1 Health Impacts

Exposure to atmospheric aerosol, among other prominent atmospheric pollutants, is considered to be linked with millions of premature deaths annually in a global scale (Lelieveld et al., 2015). It is considered as one among five greatest health risks, alongside high blood pressure, smoking, diabetes and obesity (Cohen et al., 2017). The World Health Organization (WHO) reported 3.7 million deaths in 2012 that were associated to atmospheric pollution. Recent epidemiological and human exposure studies in the US show that short- and long-term exposure to PM has been found to correlate with cardiovascular diseases and cardiopulmonary morbidity and mortality (Pope and Dockery, 2006). An analysis of several European cohorts has pointed to increased lung cancer risk with increasing PM concentrations (Raaschou-Nielsen et al., 2013) and increased impact on natural cause mortality (Beelen et al., 2014a). Such risks are further corroborated in developing countries suffering of poor ambient as well as indoor air quality (Ezzati, 2005; Mannucci and Franchini, 2017).

Several outstanding pollution events, in the second half of the previous century, especially the lethal 1952 smog over London (Bell and Davis, 2001) have led countries around the world to gradually adopt legislature aiming at cleaner air, along with the establishment of relevant regulatory governmental bodies (e.g the US EPA was founded in 1970). In line with this, intergovernmental agencies, such as the European Commission, have imposed stern emission restrictions to the EU member states as well as air quality guidelines. The imminent EU air quality directive revision, while propose more specific guidelines related to particulate mass, introducing ultrafine particles and BC as important pollutants. On the other hand, the WHO has recently updated its PM exposure guidelines, proposing a target level of 5 $\mu g\ m^{-3}$ and 15 $\mu\ gm^{-3}$ on an annual and daily basis respectively. Adopting such guidelines and eventually meeting the proposed thresholds, may prove crucial in decreasing the health burden owing to exposure to air pollution worldwide and possibly avoid as much as 80% of mortality induced by exposure to poor air quality.

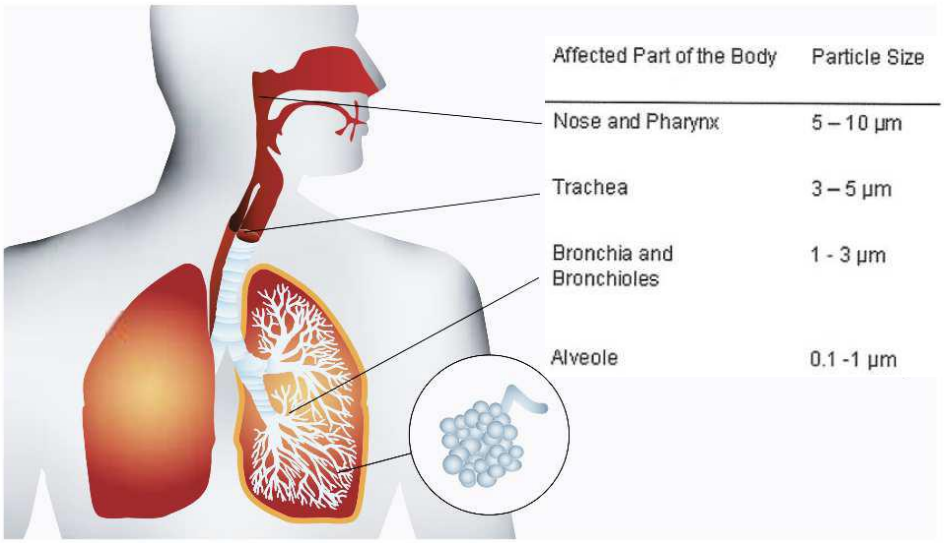

Figure 1.2. A schematic of the human respiratory tract with information on the size resolved deposition of particles in each section adopted from Canonaco (2015).

Aerosols enter the human body through the respiratory system, and depending on their size, may penetrate and deposit deep in the respiratory tract. In **Figure 1.2** the areas where particles can be deposited depending on their size, is depicted. Particles larger than 5 µm efficiently deposit in the upper respiratory tract, the nose and pharynx while smaller particles in the 3 – 5 µm range can reach the trachea. Particles with diameters ranging from 1 to 3 µm can be deposited in the bronchia while particles smaller than 1 µm can reach the alveolar region. Deposition of particles in the alveolar region induces a risk of particle absorption by cells. Ultrafine particles can translocate into the blood stream, or the lymphatic system (Maynard and Kuempel, 2005) and be accumulated in various organs (Kreyling et al., 2002). The resulting health effects depend on the physiochemical characteristics of the PM, such as mass, size, number, surface area, composition, concentration and source (Tomasi et al., 2017). Other than size, aerosol sources are particularly important when considering induced inflammation by oxidative stress via assessing aerosol oxidative potential (Daellenbach et al., 2020).

1.2.2 Climate Impacts

During the past years it has been thoroughly stressed that human activity is heavily impacting the Earth's climate (Intergovernmental Panel On Climate Change, 2023). The planet's surface energy balance, driving temperatures worldwide, is controlled by the amount of absorbed or scattered solar radiation. Any changes in the Earth's solar radiation budget, due to changes in solar input

and / or the atmosphere and the resulting feedbacks between the atmosphere and the Earth's surface, so-called radiative forcing (RF) affects the Earth's surface air temperature. A bar chart depicting RF values for the period 1750 – 2011, ascribed to specific gaseous and particulate components is illustrated in **Figure 1.3**. Positive RF points to a warming effect while negative RF values imply a cooling effect.

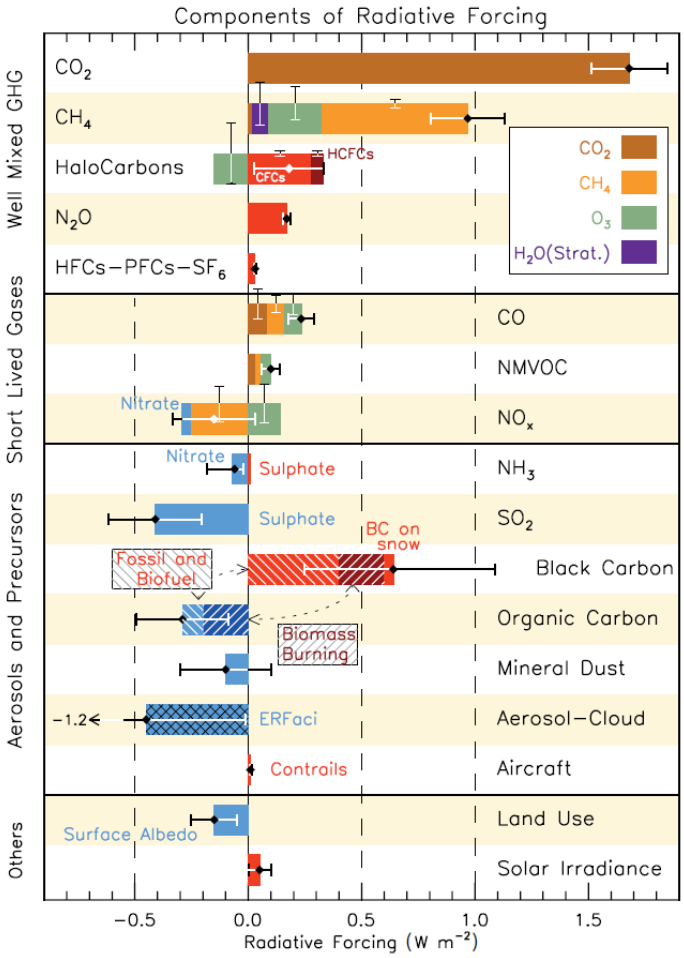

Figure 1.3. Estimated radiative forcing of different gaseous and particulate components as depicted in the Working Group I contribution to the Fifth Assessment Report of the Intergovernmental Panel on Climate Change (IPCC) (Stocker and Qin, 2013).

Major greenhouse gases (CO_2, CH_4 etc) exert a significant warming effect, while particles, either through direct scattering of short- and long- wave solar radiation or through indirect effects, i.e., by actively participating in cloud formation acting as cloud condensation nuclei (CCN), seem to be linked to overall cooling the atmosphere. Aerosol ability to act as CCN is highly dependent on

their chemical composition, that is linked to their hygroscopicity (Vu et al., 2015) meaning that knowledge of particle sources can provide insights on the overall cooling exerted. Overall higher aerosol concentration often leads to higher CCN concentration, which increases the abundance of cloud droplets. This could increase cloud albedo which in turn enhances the scattering efficiency of solar radiation by clouds.

While most aerosol seem to record negative RF values, BC is the exception, associated with a warming effect through light absorption, exerting a net positive RF. Yet, other aerosol components, especially organic aerosol can also have positive RF effects, through direct light absorption by the so called Brown Carbon (BrC) component (Gustafsson and Ramanathan, 2016). Furthermore, positive RF values can be linked with absorption enhancement, induced by internal mixing Black Carbon (BC) with coating material either of organic or inorganic nature, effectively focusing more photons onto the particle's absorbing core (Bond and Bergstrom, 2006).

1.3 Submicron aerosol chemical composition and sources

Submicron atmospheric aerosol are a complex mixture of various chemical components. Their chemical composition is highly dependent on their sources and formations processes. Therefore, aerosol chemical composition exhibits a high temporal and spatial variability. They can be roughly classified as organic aerosol (OA) or inorganic aerosol (IA), and in ambient conditions, their population is a mixture of the two. The aerosol class including OA along with Elemental or Black Carbon aerosol (EC or BC), effectively graphitic structures emitted through incomplete combustion, is referred to as carbonaceous aerosol.

Inorganic aerosol chemical composition and their formation processes are well understood. In most environments, they mainly consist of inorganic salt bound species such as ammonium, sulfate, nitrate and chloride (Putaud et al., 2004). Sulfate is mostly present in the form of $(NH_4)_2SO_4$ and it can be traced back to the oxidation of SO_2 to H_2SO_4. SO_2 can originate from industrial and power generation activities involving combustion, it can be directly emitted through volcanic eruptions, or formed from dimethyl sulfide emitted by marine organisms. In turn H_2SO_4 undergoes reactions with NH_3, mostly emitted in agriculture, forming ammonium sulfate. Ammonia also undergoes neutralization reactions with HNO_3 forming NH_4NO_3, or HCl forming NH_4Cl that are consequently condensing in the particulate phase. HNO_3 is the product of the oxidation of NO_x by OH radicals, or the heterogenous hydrolysis of N_2O_5. HCl can be either emitted directly in biomass

burning plumes, coal combustion or industrial processes. **Figure 1.4** depicts chemical composition of submicron aerosol in a variety of urban and rural locations in Europe (Chen et al., 2022), pointing out its high location dependence. Inorganic components can constitute the majority of PM_1 while in various environments the balance is shifted towards the prevalence of organic material. In this sense a detailed characterization of the submicron aerosol organic fraction is quite important.

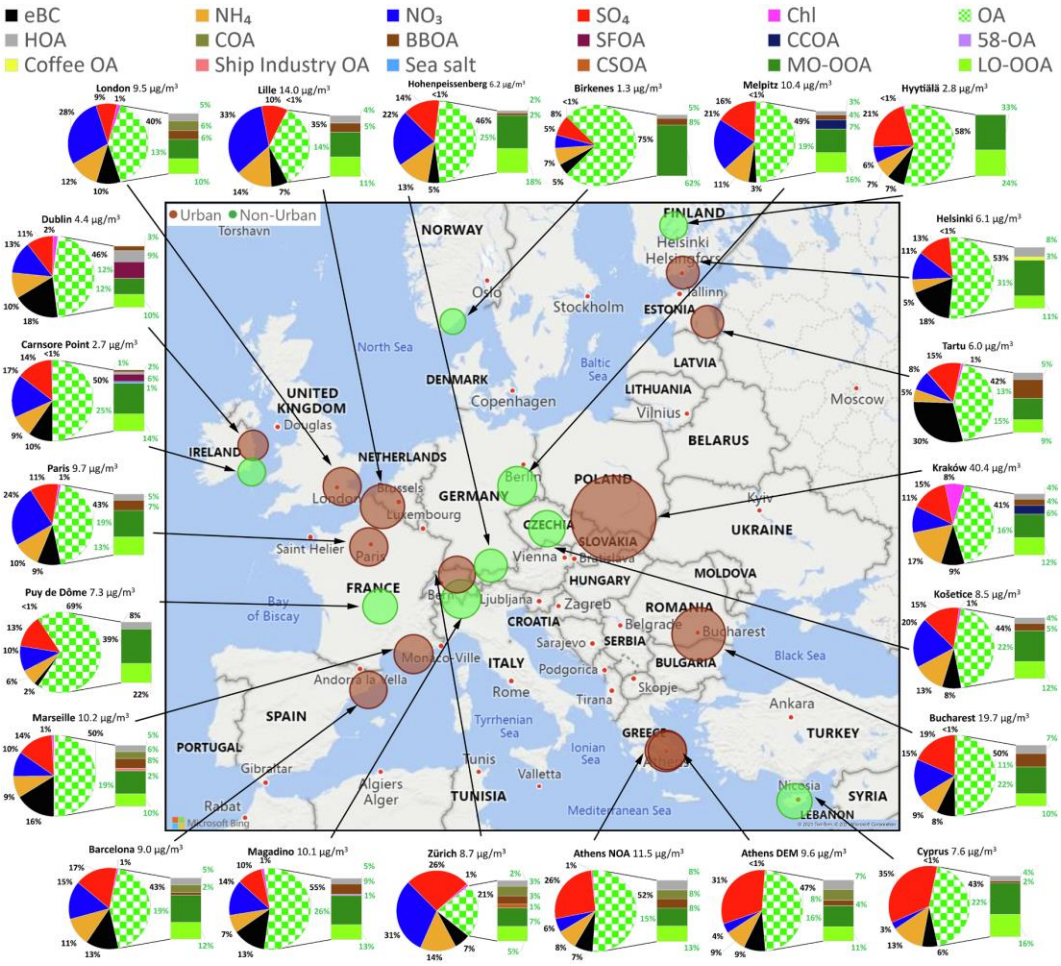

Figure 1.4. Submicron particulate matter (PM_1) mass concentration (in µg m^{-3}) and mass fractions of non-refractory inorganic species, equivalent black carbon (measured by online filter-based methods), and organic aerosol measured with the 22 ACSM/AMS at multiple locations in Europe covering all seasons (Chen et al., 2022).

OA is a highly complex mixture of thousands of different compounds. On top of that they undergo numerous chemical transformations upon being emitted to the atmosphere. They are either primarily emitted, named primary organic aerosol (POA) or the product of secondary processes

(secondary organic aerosol; SOA). POA can be related to fossil fuel combustion (road transport, aviation, shipping, industry and energy production), wildfires, along with prescribed biomass burning and combustion of agricultural waste, as well as domestic burning of both solid and liquid fuel (cooking and heating). SOA are mainly the product of gaseous precursors, namely volatile organic compounds (VOCs), that are oxidized, a process lowering their volatility that eventually leads to transitioning to the particulate phase either by nucleation or gas – to – particle partitioning under favorable chemical and thermodynamic conditions (Hallquist et al., 2009). VOC precursors can be emitted through anthropogenic sources (mainly combustion related) or biogenic processes.

OA can make up as much as 20 – 90 % of the submicron aerosol mass (Jimenez et al., 2009) and their temporal and spatial variability and complexity proves to be a challenge that needs to be addressed in order to reduce uncertainties in the context of predictive models (Kanakidou et al., 2005). Notwithstanding the fact that OA measurement is a challenging task, a significant step towards collecting high quality descriptive datasets in different parts of the world was accomplished through the emergence of aerosol mass spectrometry. The Aerosol Mass Spectrometer (Jayne et al., 2000) and its monitoring oriented counterpart, the Aerosol Chemical Speciation Monitor (Ng et al., 2011b) have been increasingly used in various types of environments during recent years, recording the chemical composition of non-refractory submicron aerosol at high temporal resolution. Finally, application of receptor modeling techniques in obtained OA mass spectra (Paatero, 1999; Paatero and Tapper, 1994) has allowed for the resolving and quantification of different OA sources, both primary – related to various types of human activity – and secondary, by examining OA's degrees of oxidation.

1.4 Thesis Motivation and Outline

The Eastern Mediterranean has been previously characterized as one of the world's most prominent climate change hotspots (Lelieveld et al., 2012). In a recent study, it is suggested that warming in the region is almost twofold faster than the global average warming pace, and is considered as being among the fastest warming inhabited regions in the world (Zittis et al., 2022), with warming being especially pronounced during summer (Zittis et al., 2019). Pollution sources impacting the area are diverse, including the regions' surrounding megacities and fast growing urban centers (Kanakidou et al., 2011), as well as long range transported pollution of either natural or anthropogenic origin (Lelieveld et al., 2002). Given the complex effect of aerosol on the atmosphere's radiative budget, dependent on both its physical and chemical properties, high

temporal resolution measurements, characterizing in detail the sources and mechanisms controlling submicron aerosol in the area's regional background can further contribute in formulating effective mitigation strategies.

Furthermore, from a public health perspective, PM has been characterized as a key air pollution component linked to adverse effects (Brook et al., 2010) as well as premature mortality (Apte et al., 2015). For Athens, the capital city of Greece, home to nearly half of the country's population, an association between fine particulate matter exposure and cerebrovascular disease mortality has been documented in a European wide cohort analysis (Beelen et al., 2014b). It has also been pointed out that toxicity of fine aerosol is correlated to its chemical composition while it can also be linked to submicron organic aerosol sources (Paraskevopoulou et al., 2019). Furthermore, it has been suggested that policies addressing pollution, specifically related to wood burning, can reduce health risks, especially benefiting vulnerable groups of a lower socioeconomic status (Bailey et al., 2019). In view of the above, the long-term characterization of submicron aerosol characteristics as well as their source apportionment in the urban environment, proves to be a task of great significance when attempting to compile effective abatement measures, and is pursued in the framework of this study.

Upon the acquisition of the Aerodyne Aerosol Chemical Speciation Monitor by the Environmental Chemical Processes Laboratory (ECPL), another motivation for this study was to establish the suitability of the instrument for long-term – with limited supervision – monitoring of submicron aerosol chemical composition in the remote environment, at ECPL's well established regional background monitoring station at Finokalia, a task attempted for the first time in the region. Furthermore, knowledge of the diurnal variability of non-refractory components was to be determined, during different seasons, looking for patterns and different sources of long range transported aerosol, as well as the level of processing of organic aerosol arriving at the site, filling some of the current knowledge gaps for regional background conditions in the Eastern Mediterranean. Organic aerosol source apportionment in the long-term would also enrich our – to this time – limited knowledge, mostly obtained through intensive campaigns using aerosol mass spectrometry at the site (Hildebrandt et al., 2010), providing information on potential seasonal contrasts and specific characteristics of organic aerosol atmospheric processing.

After acquiring measurements for roughly 35 months at the Finokalia station, the instrument was moved to Athens. By that time, urban centers in the country were experiencing extended air quality degradation during wintertime, because of the documented shift towards biomass burning as a popular means of space heating, following extraordinary oil price hikes as a consequence of the Greek financial recession in the beginning of the previous decade (Athanasopoulou et al., 2017; Paraskevopoulou et al., 2014). In an effort to characterize the phenomenon through a high temporal resolution perspective, obtaining insights on primary OA sources and secondary OA formation mechanisms, and after having witnessed extremely high OA concentrations, heavily driven by biomass burning during two short-term wintertime intensive campaigns, the instrument was installed for long term observations at the National Observatory of Athens operated Thissio station, in the center of the city.

Previous fine aerosol source apportionment studies in urban background locations in Athens, have identified the existence of a heavy oil combustion factor related to shipping activity (Grivas et al., 2018). The geographical origins of the resolved factor were traced to the port zone of Piraeus lying to the south west of the basin. Given that ships are well known emitters of primary OA and in order to characterize the effect of heavy oil combustion to submicron organic aerosol, especially through its combination with other hydrocarbon-like OA sources such as traffic, two intensive measuring campaigns were held at Piraeus for both the cold and the warm period for the first time, in an attempt to acquire important information on OA sources and local population exposure.

Given the emerging attention that low – cost air quality monitoring solutions have gained during the recent past years, and after establishing important variability of carbonaceous aerosol even among urban background locations in the Greater Athens Area (GAA; Grivas et al., 2019), the opportunity of addressing the spatial variability of PM concentrations throughout the basin, capturing the effect of different site characteristics and area specific sources, was sought through the characterization of a suitable device and the establishment of a low-cost $PM_{2.5}$ monitoring network. Eventually, exploring the potential added value introduced in our understanding of PM source dynamics and impacts via the synthesis of high precision measurements and calibrated low-cost data was one more key motivation for this study.

Finally, after the extensive characterization of the major residential wood burning source in the urban environment in Athens, and given the continuing suppression of the effects of traffic to air

quality through stricter emission regulations imposed, focus was shifted towards the third important primary submicron OA source in Athens, related to cooking activities. The combination of measurements using high – end specialized instrumentation at the Thissio station on one hand and dense spatial information on $PM_{2.5}$ concentrations throughout the basin through the utilization of the established low – cost network on the other, provided the means of a detailed characterization of specific pollution events related to this source.

The current thesis is structured along seven main chapters as follows:

* **Chapter 2** provides a detailed description of the measuring locations, the main instrumentation used during this study, as well as the data processing techniques utilized, allowing for apportionment of sources and pinpointing their geographical origins.
* **Chapter 3** presents results from 35-month long measurements held at the Finokalia station, representing regional background conditions in the Eastern Mediterranean. Sources and chemical composition were assessed form the diurnal to the seasonal scale, while air mass origin affecting pollutant variability was investigated.
* **Chapter 4** discusses the chemical composition and sources of PM_1 aerosol in the urban background in Athens, based on a full 1-year dataset and two complementary intensive wintertime campaigns. A thorough characterization of residential wood burning as a primary and secondary OA source was conducted, while the seasonal variability of concentrations and sources was investigated. The chapter has been published in *Atmospheric Chemistry and Physics* (https://doi.org/10.5194/acp-19-901-2019).
* **Chapter 5** moves the discussion to the urban background of the busy port city of Piraeus, a commercial and transportation hub, addressing PM_1 chemical composition and organic aerosol sources in view of elevated local activity. Results, other than documenting influence by the omnipresent residential wood burning source during wintertime, highlight the importance and seasonal persistence of sources related to fossil fuel combustion (vehicular traffic and shipping), a distinct feature when comparing to urban background locations in Athens. The chapter has been published in *Atmosphere* (https://doi.org/10.3390/atmos12121686).
* **Chapter 6** summarizes results obtained by an extensive intercomparison and calibration exercise, targeting the evaluation of low – cost particulate matter sensors, to be used in

dense networks for the characterization of the spatial variability of concentrations. Upon successfully addressing sensor biases, measurements from the network developed in the framework of the PANACEA[1] national infrastructure were used to assess intense phenomena occurring because of residential wood burning on one hand, or transport of particulate matter from wildfire episodes on the other, in different urban environments. The chapter has been published in *Atmosphere* (https://doi.org/10.3390/atmos11090926).

- **Chapter 7** addresses the importance of cooking related aerosol to air quality in the urban atmosphere through case studies related to large scale festivities involving mostly meat grilling. Two distinct events, namely Fat Thursday and Easter Sunday are placed under scrutiny for several consecutive years. Organic aerosol source apportionment is performed, pointing to dominance of cooking organic aerosol during these events, and providing information on atmospheric processing of primary emitted particles. High performance instrumentation (ACSM + aethalometer measurements) is combined with a dense low – cost sensor network, allowing for assessing the wider impact of such activities to the – densely populated – Athens basin. The chapter is under review for publication in *Science of the Total Environment*.
- **Chapter 8** summarizes the main findings of this work along with their implications and attempts to discuss possible future work, that would further add to the understanding of sources and processes controlling PM_1 aerosol in a variety of environments in the region.

[1] https://air-quality.gr/

2 Materials and Methods

2.1 Sampling Sites and Periods

Measurements, presented in the current study, were held in a variety of environments across Greece, ranging from remote regions to a variety of urban environments spanning in time roughly over the past decade (2012 - 2022) and covering different conditions across distinct environments. A map highlighting the different measuring sites and the different main types of measurements collected and presented in this thesis, is depicted in **Figure 2.1**.

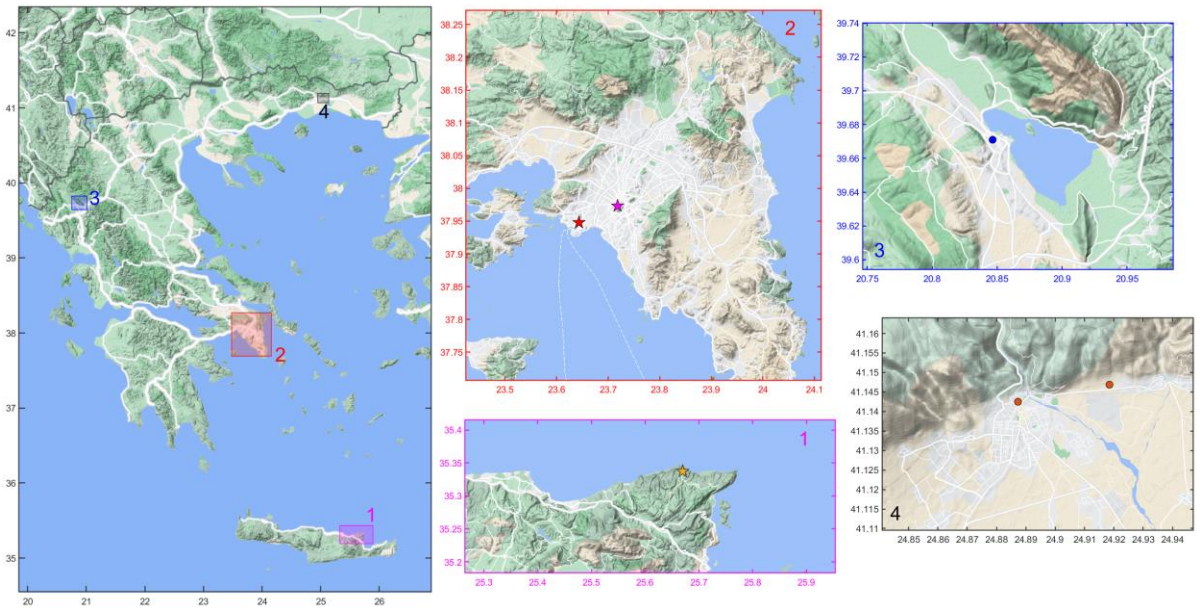

Figure 2.1. A map depicting Greece and the different areas and specific locations where measurements were held in the framework of this dissertation. Stars represent locations where high-resolution chemical composition measurements were collected, while dots represent sites of the PANACEA low-cost $PM_{2.5}$ monitoring network mainly used in the dissertation.

Initially, non-refractory PM_1 chemical composition and BC measurements were held at the Finokalia station (35˚20′ N, 25˚40′ E, 250 m a.s.l.), operated by the Environmental Chemical Processes Laboratory of the University of Crete Chemistry Department (Mihalopoulos et al., 1997). The site is characterized as representative of regional background conditions in the area (Kalivitis et al., 2008; Lelieveld et al., 2002). The site lies on top of a hill on the northern shore of the island of Crete (**Fig. 2.1**), south of mainland Greece, with the largest city in proximity being Heraklion with a population of about 140000 inhabitants, lying approximately 70 km to the south-

west. No major human activity is recorded in the vicinity of the station, while long range transport of pollutants from the Balkans, Turkey and Eastern Europe has been suggested to play an important role (Sciare et al., 2003a), especially during summertime. Measurements of non-refractory PM_1 chemical composition were collected for almost three and a half years (22 May 2012 – 03 December 2015).

As a next step instrumentation was installed in Athens. Measurements were conducted at the Thissio Air Monitoring Station (37.97° N, 23.72° E), operated by the National Observatory of Athens, located in the center of the city. The station is situated on top of a hill (105 a.s.l.), in a low built density area, away from major highways and is considered representative of urban background conditions in central Athens (Fourtziou et al., 2017; Grivas et al., 2019). Measurements in Athens presented in this thesis, span over five consecutive years with small breaks when the instrument was under maintenance, or part of intercomparison studies (Freney et al., 2019), or was moved to other location for participating in intensive measuring campaigns. Assessing OA sources and PM_1 chemical composition in the long term focuses on measurements held during two winter-time intensive field campaigns held at Thissio (winter 2013 – 14 & winter 2015 – 16) and a full year of measurements (August 2016 – August 2017). For studying the effects on OA sources and air quality in general, 15 day long windows around "Fat Thursday" and "Easter Sunday" for the years 2016 through 2021 were also investigated, both in terms of PM_1 measurements utilizing high end instrumentation (ACSM, AE33 etc) as well as in a spatial context, delineating the effects through the entire Greater Athens Area (GAA) utilizing $PM_{2.5}$ concentrations coming from several monitoring sites of the PANACEA low cost $PM_{2.5}$ monitoring network operated in the basin (Sections 6 & 7).

Moving away from the urban background setting at Thissio, focusing on urban environments in the GAA with close proximity to pollution hotspots, an intensive PM_1 chemical composition and sources measuring campaign was held for two months – one during wintertime 2018 and another in the summer of 2019 – in the city of Piraeus. Located in the south west part of GAA, Piraeus other than being one of the more densely populated regions in the GAA, is home to one of Europe's largest commercial and passenger ports. Instrumentation was installed at the premises of the city's Athens Metro terminal station (37.9479° N, 23.6429° E, 10 m a.s.l.), on the first floor of the station

building, very close to the passenger port and the busy roads surrounding it. The site, due to its placing in a commuting and commercial hub, is affected by intense human activity.

The presented detailed calibration exercise targeting the PurpleAir PA-II sensors, was held in two different urban environments. Initially co-location of the sensors with reference instrumentation took place at the Thissio Air monitoring Station in Athens described above. Measurements were conducted during three periods, one in 2019 springtime (08 March 2019 – 02 April 2019), the second during the same year in the summertime (03 July 2019 – 03 September 2019) and the last one during late winter and spring in 2020 (26 February 2020 – 02 April 2020). Measurements were also held in the city of Ioannina, at the Vilara Air Quality Station. The site is located in the center of the city (9.67102° N, 20.84648° E, 484 m a.s.l.) close to a moderately busy road. Ioannina is populated by approximately 100000 inhabitants, and is located on a plateau at the foothills of the Pindus Mountain range on the north western part of Greece. Measurements at Ioannina spanned over approximately five months (15 December 2019 – 31 May 2020).

Finally, in the context of monitoring air quality degradation events related to cooking sources during specific celebrations, measurements from the PANACEA low-cost $PM_{2.5}$ monitoring network in Xanthi (41°8′N, 24°53′E), a city in northern Greece, are also presented. Xanthi is located in the region of Thrace, northeastern Greece, on the foot of the Rhodope Mountain range and is populated by approximately 63000 inhabitants. Data from two measuring sites are presented, one located in an urban background location in the city center (Old Town) and the other at the premises of the Democritus University of Thrace, representing rural background conditions.

2.2 Instrumentation

2.2.1 The Aerosol Chemical Speciation Monitor

The Aerosol Chemical Speciation Monitor (ACSM), is largely based on the Aerosol Mass Spectrometer technology (Allan et al., 2004; Jayne et al., 2000), but is mostly oriented to monitoring applications rather than short-term intensive field deployments targeting high resolution outputs. It is thus smaller than the AMS, lighter, more affordable and with reduced operating cost and power requirements, it is more easily transportable and can be operated for large periods of time with minimal user interference (Ng et al., 2011b). Achieving the above, comes at

the expense of sensitivity and temporal resolution, while the ACSM is not equipped with particle sizing capabilities and the lower resolution quadrupole mass analyzer along with slower electronics results in reporting unit mass resolution spectra. The instrument delivers though satisfactory limits of detection for all quantified species and for the majority of sampling environments and monitoring applications at a 30 min temporal resolution. Specifically, limits of detection (3σ) are 0.284 μg m^{-3}, 0.148 μg m^{-3}, 0.024 μg m^{-3}, 0.012 μg m^{-3} and 0.011 μg m^{-3} for ammonium, organics, sulfate, nitrate and chloride respectively.

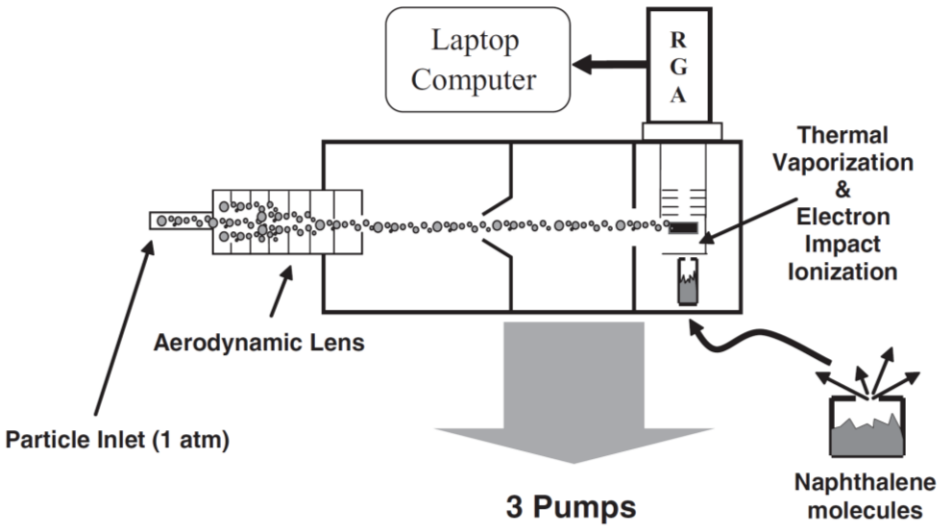

Figure 2.2. Schematic of the Aerosol Chemical Speciation Monitor where the instrument's main components are outlined (Ng et al., 2011b).

A schematic of the instrument is depicted in **Figure 2.2** (Ng et al., 2011b). Sample is drawn in the instrument through a 100 μm diameter orifice, then passes through a PM_1 aerodynamic lens (Liu et al., 2007) that separates particles from the gas phase and then focuses the particles into a narrow beam before entering the instrument chamber, pumped to high vacuum by three turbomolecular pumps. The diameter range where particles are efficiently transmitted through the lens is practically between 75 and 650 nm. After insertion in the vacuum the particles travel and impact on an inverted conically shaped porous tungsten vaporizer, heated at 600 °C where their non-refractory component is flash vaporized (**Fig. 2.3**). The resulting vapors are ionized though electron impact ionization at 70 eV. Flash vaporization and hard electron impact ionization results

in extensive fragmentation of the original molecules. The fragment ions are guided through a quadrupole residual gas analyzer (RGA) where they are separated according to their mass over charge ratio (m/z) and detected by an electron multiplier detector. A source of naphthalene is located inside the detection chamber, below the particle vaporization and vapor ionization assembly, acting as an internal standard. Signal at naphthalene's parent ion at m/z = 128 is continuously monitored providing the means for calibrating the mass-over-charge ratios of the rest of the ions, and monitoring the instrument's ionization efficiency.

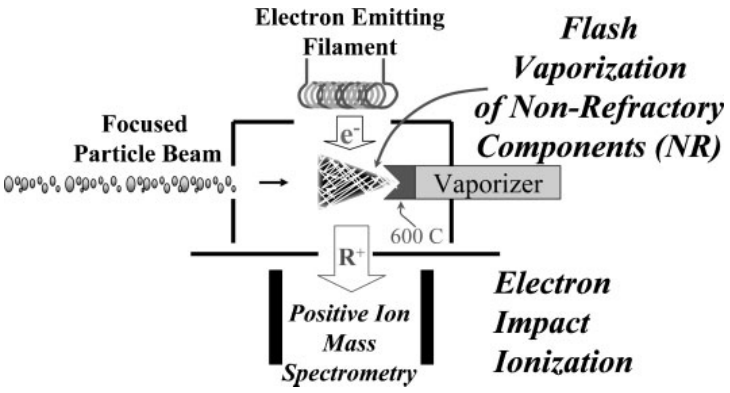

Figure 2.3. Schematic of the vaporizer and ionizer assembly inside an AMS (Canagaratna et al., 2007). An identical apparatus is installed in the ACSM where the focused particle beam impacts the vaporizer and consequently the resulting vapors are ionized via electron impact ionization before being guided to the mass spectrometer.

In order for the ion signal related to the particulate phase, to be separated from the contribution to the signal by atmospheric gaseous species present in the detection chamber, as well as from the signal due to the instrument's internal calibration standard (naphthalene; **Fig. 2.2**), an assembly involving a three-way valve and a particle filter is incorporated in the instrument's sample inlet (**Fig. 2.4**). The valve is automatically switched between two modes of operation: i) sample mode where ambient air is drawn into the instrument and ii) filter mode where ambient air is drawn through a zeroing filter, providing particle free air into the instrument. Subtracting the signal obtained during filter mode from the one obtained in sample mode results to the sampled ambient particulate matter ensemble mass spectrum, i.e., the mass spectrum containing contributions to each m/z by all species.

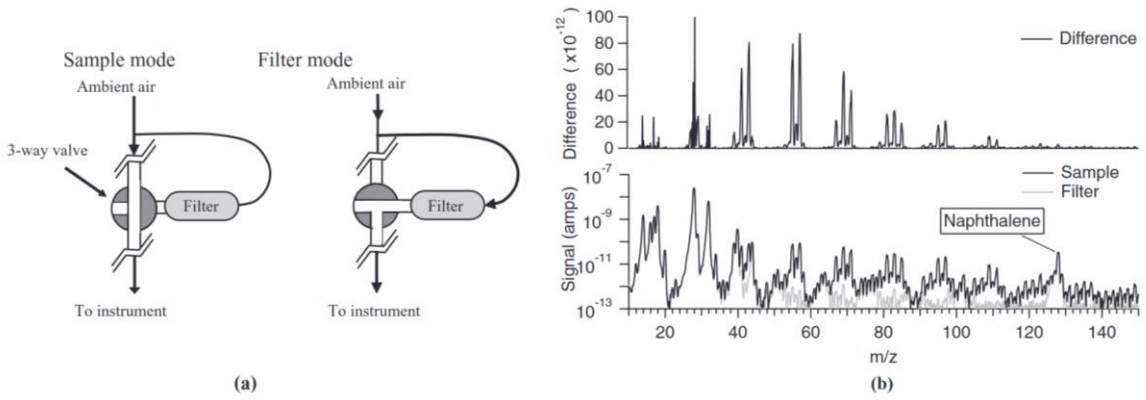

Figure 2.4: (a) The zeroing filter and 3-way valve assembly that is part of the ACSM sampling inlet, were the two modes of operation are depicted and (b) an example of the mass spectrum subtraction process providing the ambient particulate matter mass spectrum (Ng et al., 2011b).

Quantifying is a quite straightforward problem when the partial mass spectrum of the chemical species under scrutiny is characterized by distinct peaks, with minimal contributions by other interfering species. Nitrate as well as sulfate are such examples. For instance, to quantify nitrate, using the ion signals at m/z=30 and m/z = 46 in the quantification equation below (Eq. 2.1) is enough, since these peaks are dominated by nitrate fragments (NO^+ and NO_2^+). This is not the case though for the remaining measured species, were measured peaks in the majority of m/z variables are characterized by cross interferences from different species, ambient gases or water. Such interferences mean that ambient aerosol mass spectra are the superposition of the individual partial mass spectra, that need to be delineated in order for the different species to be quantified. This is achieved via the user definable "fragmentation table" approach developed by Allan et al. (2004), a set of linear dependencies between the contributions of various chemicals to different m/z, that is inferred by knowledge of laboratory based fragmentation ratios of pure chemical species as well as isotopic ratios of the various participating atoms. A simple example of the process pertains to the quantification of ammonium, where linear dependencies derived from empirical observations are used to correct for the interferences in the signal at m/z = 15 (NH^+), m/z = 16 (NH_2^+) and m/z = 17 (NH_3^+) by various fragments such as CH_3^+ (m/z = 15), O^+ from O_2 (m/z = 16) and OH^+ (m/z = 17) from H_2O, thus allowing for constructing ammonium's partial mass spectrum. **Figure 2.5** depicts an ambient ensemble mass spectrum acquired at Thissio, with different colors representing the contribution in each m/z by the different chemicals measured by the ACSM, after implementing the fragmentation table by the instrument's software.

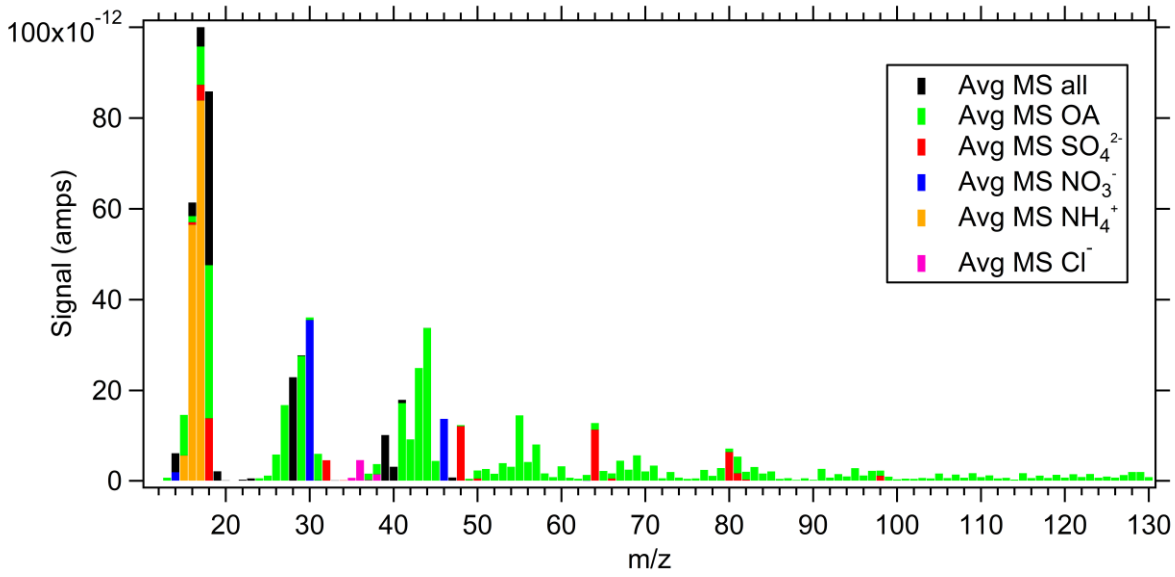

Figure 2.5. An average ensemble mass spectrum, of non-refractory submicron aerosol collected by the ACSM at Thissio (Athens). Different colors represent the contribution of each chemical species to different mass over charge ratios, as calculated by implementing the fragmentation table technique (Allan et al., 2004).

For each one of the detected species, measured ion signals I_s per m/z are consequently quantified to mass concentrations C_s (in μg m^{-3}), by summing the measured signals over all relevant fragments *i* related to the specific chemical species, thus determining each species' partial mass spectrum as discussed above, according to the quantification equation presented in (Canagaratna et al., 2007)

$$C_s = 10^{12} \cdot \frac{1}{IE_s} \cdot \frac{1}{Q} \cdot \frac{MW_s}{N_A} \cdot \sum_{all\ i} I_{s,i} \qquad (2.1)$$

where the factor 10^{12} serves unit conversion purposes, MW_s is the species molecular weight, N_A is Avogadro's number, Q is the volumetric flow rate and IE_s is the ionization efficiency, a quantity describing the number of ions detected per molecule of each species, thus including the probability of a molecule to be ionized, the transmission efficiency of said molecule through the mass spectrometer, as well as the detection efficiency of the electron multiplier.

Given that species specific quantities, such as MW_s and IE_s cannot be determined when measuring the complex ambient aerosol – organic aerosol are composed of numerous different species, making explicit calibration of IE_s impossible – early studies (Jimenez et al., 2003) have shown that

these quantities' ratios can be empirically determined, based on the well characterized ratio for nitrate, the instrument's primary calibrant, as follows

$$\frac{IE_s}{MW_s} = RIE_s \cdot \frac{IE_{NO_3}}{MW_{NO_3}} \tag{2.2}$$

where RIE_s is the relative ionization efficiency of each species s, relative to nitrate. Whilst the above equations stand for the AMS instruments, that are characterized by single particle and single ion measurement capability, allowing for the determination of $I_{s,i}$ and IE_{NO_3}, this does not stand for the ACSM where lower response electronics and the lower resolution residual gas analyzer do not allow for such a task, effectively measuring an ion current ($IC_{s,i}$). To account for that an instrument response factor (RF) is determined as the ratio between aerosol mass concentration and the sum of the signal in relevant m/z variables. This is calculated during standard ammonium nitrate calibrations by taking into account the NO_3 moiety of a known concentration of NH_4NO_3 particles with a determined diameter, measured concurrently by an appropriate setup including a differential mobility analyzer (DMA) and a condensation particle counter (CPC). In this manner RF_{NO_3} is proportional to IE_{NO_3} according to the following:

$$IE_{NO_3} \cdot \frac{N_A}{MW_{NO_3}} = \frac{RF_{NO_3}}{Q_{cal} \cdot G_{cal}} \tag{2.3}$$

where Q_{cal} and G_{cal} is the volumetric flow rate and the electron multiplier gain during the calibration respectively. RIE_s for ammonium and sulfate can be determined by ammonium nitrate and ammonium sulfate calibrations (Freney et al., 2019) while laboratory calibrations have determined that for OA, a value of 1.4 for RIE can be representative for the conditions in most ambient environments (Jimenez et al., 2016). Similarly an RIE of 1.3 is determined for chloride in the literature (Hu et al., 2017). Taking into account the above, the ACSM quantification equation is as follows:

$$C_s = 10^{12} \frac{1}{CE} \frac{1}{RIE_s} \frac{Q_{cal} G_{cal}}{RF_{NO_3}} \frac{1}{QG} \sum_{all\ i} IC_{s,i} \tag{2.4}$$

where CE, the particle collection efficiency, is another parameter that needs to be taken into account when quantifying each species mass concentration. CE is a dimensionless quantity

describing the degree at which particles bounce off the vaporizer surface upon impaction, thus failing to be vaporized (*CE* is 1 for full particle detection). *CE* is generally controlled by the sampling line relative humidity, sampled aerosol acidity and their NH_4NO_3 mass fraction (AMNF; Middlebrook et al., 2012). The relative humidity effect can be tackled by introducing an aerosol dryer before the instrument inlet. While early studies typically report collection efficiencies of 0.5 applied horizontally for the entire timeseries in ambient studies (Canagaratna et al., 2007 and references therein), recently a chemical composition dependent algorithm for dynamically determining CE has been developed (Middlebrook et al., 2012), compensating for the AMNF induced discrepancies.

2.2.2 The Aethalometer

In this study aerosol absorption coefficients and subsequently ambient Black Carbon concentrations were monitored in real time with an AE33 seven wavelength aethalometer (Magee Scientific). The AE33, a filter based absorption photometer (Drinovec et al., 2015), continuously collects particles on a PTFE coated glass fiber filter tape and using a light source in seven different wavelengths (370, 470, 520, 590, 660, 880, 950 nm) and the appropriate detectors, measures light transmission through the particle laden filter tape (Bond et al., 1999; Hansen et al., 1984, 1982). The attenuation of light (ATN) is then calculated in all measured wavelengths:

$$ATN = -\ln\left(\frac{I}{I_0}\right) \tag{2.5}$$

where I is the detector signal below the sample-laden filter spot and I_0 is the detector signal below a reference, clean (with no particles) part of the filter tape (**Fig. 2.6**). As the sample accumulates on the filter tape over time, monitoring the increase in attenuation (ΔATN) for a given time interval (Δt), allows for the calculation of the attenuation coefficient as follows:

$$b_{ATN} = \frac{S}{F}\frac{\Delta ATN}{\Delta t} \tag{2.6}$$

where S is the area of the filter spot and F is the volumetric flow rate through the tape. By calculating the attenuation coefficient (b_{ATN}), the absorption coefficient can also be derived, after dealing with a systematic measurement artefact inherent in the filter-based method. Other than absorbing particles, the attenuation of light is also controlled by a multiple scattering effect, by both the collected particles as well as by the filter medium itself that can be described by an optical

absorption enhancement factor *C* (Weingartner et al., 2003) that is found to be strongly dependent on filter material. The absorption coefficient b_{abs} can be then calculated:

$$b_{abs} = \frac{b_{ATN}}{C} \tag{2.7}$$

while BC concentrations are estimated for the measurements at 880 nm by taking into account a BC mass absorption efficiency σ_{air} that is also wavelength dependent (its value is 7.77 m^2 g^{-1} at 880 nm) as follows

$$BC = \frac{b_{abs}}{\sigma_{air}} \tag{2.8}$$

The mass absorption efficiency parameter σ_{air} can be determined by comparing the absorption coefficient reported by the aethalometer to elemental carbon (EC) obtained by thermal optical determination (Cavalli et al., 2010).

Other than the multiple scattering effect the method suffers from another systematical bias, the so called filter loading effect (Bond et al., 1999; Virkkula, 2010; Virkkula et al., 2007; Weingartner et al., 2003). Even though for small attenuation values an increase in attenuation is linearly linked to an increase in BC concentrations, this is not the case with high attenuation values, making the implementation of correction schemes (Virkkula et al., 2007; Weingartner et al., 2003) and post processing filter absorption photometer data imperative. The AE33 has adopted an approach allowing for correcting such an artefact in real time by collecting particles on two spots on the filter tape simultaneously (**Fig. 2.6**).

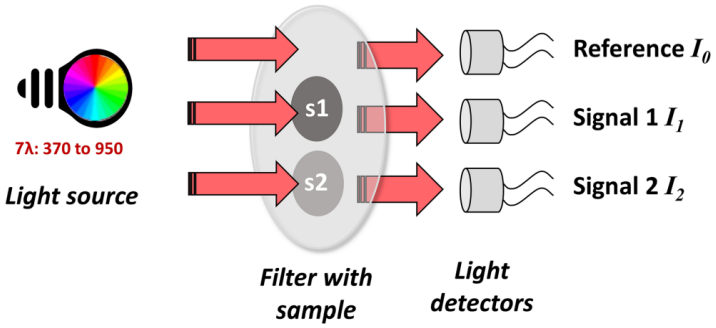

Figure 2.6. Schematic of the AE33 sampling on two different filtered spots allowing for the calculation of a loading effect compensation parameter *k* (Cuesta-Mosquera et al., 2021).

Sampling the same airstream, thus the same BC concentration, at two different flow rates, allows for calculating a filter loading compensation parameter k – essentially representing the loading rate – given that loading B_1 on the spot with the higher flow (F_1) and loading B_2 on the one with the lower flow (F_2) are proportional to the respective flows. The parameter k is calculated by numerically solving the following equation

$$\frac{F_2}{F_1} = \frac{\ln(1 - kATN_2)}{\ln(1 - kATN_1)} \tag{2.9}$$

where ATN_1 and ATN_2 are the calculated attenuations at filter spots 1 (high flow) and 2 (low flow) respectively. Eventually, using attenuation measurements from filter spot 1, after combining all the above, whilst taking into account the lateral leakage (ζ) at the points of contact between the optical measuring chamber and the filter tape, BC concentrations at each wavelength λ are calculated according to the following

$$BC(\lambda) = \frac{b_{ATN}(\lambda)}{(1 - \zeta) \cdot C \cdot \sigma_{air} \cdot \big(1 - kATN_1(\lambda)\big) \cdot 100} \tag{2.10}$$

The wavelength that is traditionally used to report BC concentrations is 880 nm. The instrument is operated at a flow of 5 l min^{-1} and reports concentration values every 1 minute with a sensitivity at this time base in the order of a few ng m^{-3}. Furthermore the instrument implements in real time the so called aethalometer model (Sandradewi et al., 2008) apportioning BC to two fractions, one related to fossil fuel combustion (BC_{ff}) and one related to biomass burning (BC_{bb}). The model assumes that the absorption coefficient at each wavelength is the sum of absorption due to fossil fuel (*ff*) combustion particles and absorption attributed to biomass burning related particles. By applying the Beer – Lambert law governing the wavelength dependency of light absorption by matter, and focusing on measurements at 470 nm and 950 nm the following set of equations can be solved to apportion absorption according to its specific source:

$$\frac{b_{abs}(470\ nm)_{ff}}{b_{abs}(950\ nm)_{ff}} = \left(\frac{470}{950}\right)^{-a_{ff}} \tag{2.11}$$

$$\frac{b_{abs}(470\ nm)_{bb}}{b_{abs}(950\ nm)_{bb}} = \left(\frac{470}{950}\right)^{-a_{bb}} \tag{2.12}$$

$$b_{abs}(\lambda) = b_{abs}(\lambda)_{ff} + b_{abs}(\lambda)_{bb} \tag{2.13}$$

by assuming fixed Angstrom exponent values representing these two sources (a_{ff} = 1 and a_{bb} = 2).

2.2.3 The Purple Air PA-II Monitor

The Purple Air PA-II particulate matter monitor is a low-cost device providing concentrations of PM_1, $PM_{2.5}$ and PM_{10} along with a cumulative particle number size distribution, over six size fractions. The device is built around a pair of Plantower PMS5003 sensors, connected to a control board providing access to the internet over WiFi, also including a low-cost T – RH sensor (BME280, BOSCH Sensortec). The device reports data every two minutes, by uploading to the Purple Air cloud service. Data are visualized in real time on a map on the company's website and can be retrieved through a dedicated application programming interface (API) to an integrated system operated by the user.

The Plantower PMS5003 sensor, described as a low-cost optical particle counter (OPC), measures particles by monitoring light scattered by particles at a 90-degree angle with a photodiode detector. The light source is a laser, operating at a wavelength of approximately 680 nm (Sayahi et al., 2019a). The manufacturer uses a proprietary algorithm to convert the number of pulses to PM concentration. A fan draws air past the laser at a flow rate of approximately 0.1 L/min. The actual cost of the sensor is approximately 20 US dollars. A schematic of the sensor sample flow path, along with its basic components is depicted in **Figure 2.7.**

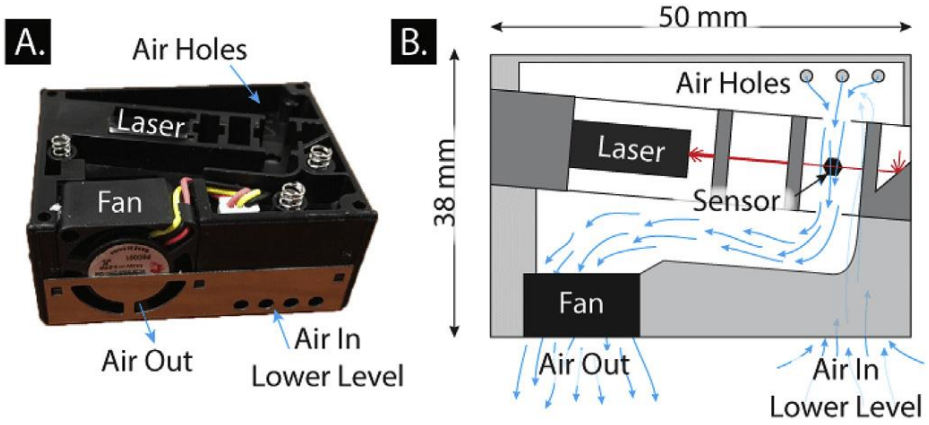

Figure 2.7. (a) The Plantower PMS5003 sensor without it's "top" cover and (b) a schematic of the sample flow path and detection region in the sensor, acquired from Sayahi et al. (2019a).

In terms of PM measurements, the sensor is reporting two different types of data according to the manufacturer, with no detail disclosed on the exact calculations being performed by the devices. One is referred to as incorporating no correction (CF = 1), and one claiming to be corrected appropriately to capture atmospheric conditions (CF = atm). Laboratory studies have pointed out the sensor's poor selectivity for particles in the PM_1 – $PM_{2.5}$ intermodal range and beyond (Kuula et al., 2020), making the addressing of such an inherent behavior a necessary task in order for the sensor to provide meaningful results. On the other hand, more recent studies have reported that the sensors lower size channels seem to excellently corelate with submicrometer aerosol scattering coefficients, thus resembling an imperfect integrating nephelometer, deeming it suitable for use in determining fine aerosol mass concentrations (Ouimette et al., 2022). Furthermore, the PurpleAir PA-II device has been widely used by individuals as well as governmental air quality monitoring services, during the past few years, with the US Environmental Protection Agency, actively pursuing their use, complementing the regulatory network (Barkjohn et al., 2021)

2.3 Data Analysis and Source Apportionment

2.3.1 Source Apportionment through Positive Matrix Factorization

In order to be able to determine different sources of OA, the measurement matrix can be deconvolved in a linear combination of static factor mass spectra (profiles) and factor concentration timeseries via Positive Matrix Factorization (Paatero and Tapper, 1994). In this sense if X is the measured matrix, then:

$$X = GF + E \tag{2.14}$$

where in the measured matrix X columns are OA concentrations at each m/z and rows are OA mass spectra over time. If p is the number of deconvolved OA factors by the PMF model, the matrix G has p columns and the matrix F has p rows. Each column in matrix G is the timeseries of concentrations for each OA factor and the rows in F represent each factor profile. The matrix E contains the model residuals for each time point and m/z. A schematic of the above is presented in Figure 2.8 (Zhang et al., 2011).

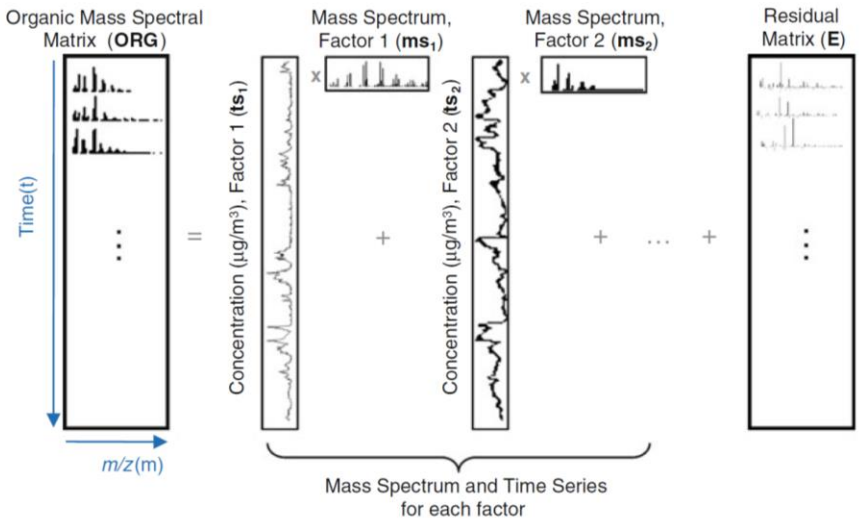

Figure 2.8: Schematic diagram of the deconvolution of measured OA mass spectra time series to different OA factors and their respective concentrations time series via the PMF model (Zhang et al., 2011).

Therefore, if one assumes that k is the index of each factor present, each element of the measurement matrix X is described by the following equation:

$$x_{ij} = \sum_{k=1}^{p} (f_{ik} \cdot g_{kj}) + e_{ij} \tag{2.15}$$

were the subscript i denotes the time point and j stands for the m/z variables present in the matrix X. The number of factors – actually selected by the user – is represented by p. The PMF algorithm assumes that factor profiles are constant through time while each factor's concentration varies. Furthermore, negative values for f_{ik} and g_{kj} are not allowed by the model. To determine the solution, PMF iteratively tries to minimize the model residuals e_{ij} weighted by their corresponding uncertainty $w_{ij,}$ essentially minimizing the quantity Q which is defined by the following equation:

$$Q = \sum_{i} \sum_{j} \left(\frac{e_{ij}}{w_{ij}} \right)^2 \tag{2.16}$$

For the task at hand, solving the PMF algorithm, i.e. minimizing Q, the sophisticated multi – linear engine solver (ME-2) is used (Paatero, 1999) implementing a table driven least square approach.

The PMF solutions are known to suffer from the so-called rotational ambiguity, generally owing to the fact that various *F* and *G* matrices can lead to the same value for *Q*. Thus, the solution space needs to be rigorously explored, even for slightly larger *Q* values, in order to determine solutions that other than being mathematically sound, also exert a certain environmentally coherent physical meaning. An advantage of the ME-2 solver is the fact that a priori information – either in the form of predefined rows of matrix *F* or columns of matrix *G* – can be introduced when calculating the model solution, effectively reducing the rotational ambiguity (Paatero and Hopke, 2009). In this sense factor profiles (*F*) or timeseries (*G*) matrices can be fully or partially constrained to known profiles or contributions. From the available tools described in Paatero and Hopke (2009), e.g., chemical mass balance (CMB; fully constrained *F* matrix), the pulling approach etc, the current thesis specifically exploits the so- called a – value approach within the SoFi 6.1 and SoFi Pro interfaces, developed to implement ME-2 (Canonaco et al., 2013) in the Igor Pro software environment.

Implementing the a – value approach means that factor profiles or factor timeseries can be constrained by importing known mass spectra or timeseries to the solution matrices *F* and *G* according to the following equations:

$$f_{j,solution} = f_j \pm a \cdot f_j \tag{2.17}$$

$$g_{i,solution} = g_i \pm a \cdot g_i \tag{2.18}$$

where the scalar α defining the constrain introduced, can vary between 0 and 1, in the sense that for fully constrained variables i.e., in the CMB approach, α would be set to 0.

2.3.2 Source Region Analysis

A crucial area in understanding air pollution drivers and dynamics is the identification of local versus distant sources. Commonly, such an exercise is performed through receptor modeling techniques followed by coupling of the derived source concentrations with specific geographical origins through combining meteorological and air mass history data.

A standard method is the Conditional Probability Function (Ashbaugh et al., 1985), a simple but effective tool that provides information on the general wind direction sectors associated with each source by combining source concentrations and wind direction:

$$CPF_{\Delta\theta} = \frac{m_{\Delta\theta}}{n_{\Delta\theta}} \quad (2.19)$$

where $m_{\Delta\theta}$ is the number of samples falling within the wind direction sector $\Delta\theta$ recording concentrations above a predefined threshold and $n_{\Delta\theta}$ is the number of all samples associated with the wind sector $\Delta\theta$. Adding wind speed to the mix results in a more detailed characterization of each source, given that different sources can have different wind speed dependencies, i.e., a local source tends to become more important when wind speeds are rather low, inhibiting effective pollutant dispersion. The inclusion of wind velocity results to the conditional bivariate probability function (CBPF) methodology (Uria-Tellaetxe and Carslaw, 2014) where the sources are associated simultaneously to both a certain wind sector as well as a wind velocity range Δu:

$$CBPF_{\Delta\theta,\Delta u} = \frac{m_{\Delta\theta,\Delta u}}{n_{\Delta\theta,\Delta u}} \quad (2.20)$$

where $m_{\Delta\theta,\Delta u}$ and $n_{\Delta\theta,\Delta u}$ are defined in proportion to the definitions above, by including the wind velocity range Δu.

An important tool allowing for the investigation of advected pollution over large geographic areas, effectively coupling air mass history with concentrations measured at the site under investigation, i.e., the receptor site is the Potential Source Contribution Function (PSCF), actually a type of CPF tailored to back-trajectory data. Given that an air parcel back-trajectory endpoint lies within a single cell of a grided map, PSCF is defined as the probability that an air parcel, passing through the ij^{th} grid cell, had a concentration above a user defined threshold (e.g., the 75^{th} or 90^{th} percentile) at the receptor site according to the equation bellow:

$$PSCF_{ij} = \frac{m_{ij}}{n_{ij}} \quad (2.21)$$

where n_{ij} is the total count of trajectory endpoints in cell ij and m_{ij} is the count of trajectory points within the same cell, associated with concentrations above the defined threshold (Fleming et al., 2012). A schematic of the grided cells, including back trajectory paths and the resulting matrices m and n are depicted in Figure 2.9.

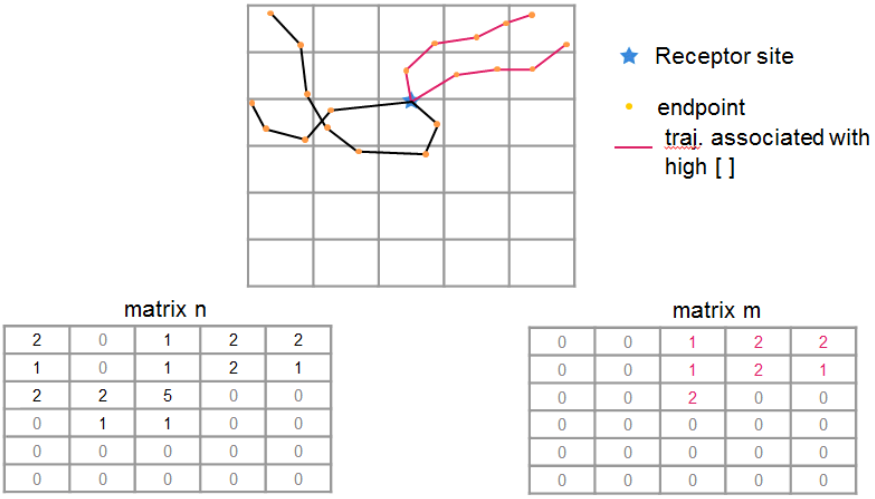

2	0	1	2	2
1	0	1	2	1
2	2	5	0	0
0	1	1	0	0
0	0	0	0	0
0	0	0	0	0

0	0	1	2	2
0	0	1	2	1
0	0	2	0	0
0	0	0	0	0
0	0	0	0	0
0	0	0	0	0

Figure 2.9. Schematic of the matrices *m* and *n*, corresponding to a longitude – latitude gridded map, used to calculate the PSCF value (ZeFir v3.7 Manual).

Air mass back-trajectories were calculated using Weekly Global Data Assimilation System (GDAS) files with a 1° x 1° resolution, implementing the HYSPLIT transport and dispersion model (Stein et al., 2015). Specific settings, such as trajectory frequency, length and arriving altitude, were selected according to each specific application and are provided in detail in the relevant chapters.

3 Long term chemical composition, based on near-real time measurements, at a regional background site over the Eastern Mediterranean

3.1 Introduction

The importance of atmospheric aerosols and the attributes governing their physical and chemical behavior, in both climate and environmental science, as well as in medical science is amply documented. Elevated particulate matter concentrations are shown to have adverse impact on human health (Pope and Dockery, 2006), while much uncertainty still remains in estimating atmospheric aerosol impact on climate (Stocker and Qin, 2013). Since the aerosol distribution is spatially inhomogeneous - either through its direct interaction with radiation or through its ability to act as cloud condensation nuclei, thus significantly affecting the planet's albedo.

The Eastern Mediterranean Basin, as previously established (Gerasopoulos et al., 2006), is highly influenced, in terms of particulate matter, by both natural (e.g. mineral dust coming from Sahara desert) (Kalivitis et al., 2007) and anthropogenic particulate emissions coming from continental Europe (Mihalopoulos et al., 1997; Sciare et al., 2003a), namely combustion of fossil fuel for energy production and pollutants from megacities in the region (Kanakidou et al., 2011). It is shown that the Mediterranean is important in understanding the aerosol-climate interaction since (Vrekoussis et al., 2005) verified a strong cooling effect imposed by the Basin's aerosol population. Furthermore (Lelieveld et al., 2002), characterize the basin as being the receptor of pollutants from different neighboring regions, with intercontinental transport determined by large pollution levels in both the boundary layer and the free troposphere.

Several studies analyzing near-real time datasets acquired using AMS technology have reported PM_1 chemical composition and sources of OA in various urban environments in the Eastern Mediterranean (Florou et al., 2017; Kostenidou et al., 2015; Stavroulas et al., 2021, 2019). Furthermore a recent study has emphasized on the role of long range transported pollution, originating from various hotspots in the area, to urban PM_1 levels (Christodoulou et al., 2023). However, most of the studies exploring chemical composition of ambient aerosol in the regional background setting of the Eastern Mediterranean are based on off line sampling techniques, mainly

focused on the PM_{10} fraction, with the exception of some studies using AMS data but for short-term measuring campaigns (Hildebrandt et al., 2010; Pikridas et al., 2010).

This study aims to present the variability of the submicron aerosol population's chemical composition over a long period of time. Furthermore, within this scope, this work attempts to investigate patterns of differentiation in concentrations over the past years, the diurnal behavior of PM_1 constituents and the dependency upon different aerosol sources identified by means of air mass origin. Especially the PM_1 organic aerosol load is being assessed in terms of source apportionment using Positive Matrix Factorization. In this context an Aerodyne Aerosol Chemical Speciation Monitor (ACSM) was deployed for almost three and a half years at the remote coastal sampling site at Finokalia, within the framework of the Aerosols, Clouds and Trace gases Research InfraStructure (ACTRIS) project.

3.2 Experimental and Methods

3.2.1 Sampling Site

Measurements were held at the remote coastal atmospheric monitoring station of the Environmental Chemical Processes Laboratory (ECPL) at Finokalia (35º 20' N, 25º 40' E) which is a European supersite for aerosol research, part of the ACTRIS network. The station is situated on the north coast of the island of Crete, 70 km to the east of the region's largest city, Heraklion, measuring roughly 170.000 inhabitants. It is located on a hill at 230 m a.s.l. overlooking the Cretan Sea. Very little human activity, mainly agriculture and livestock herding, is observed at a range of approximately 15km (Kouvarakis et al., 2000). Details on the meteorology and prevailing atmospheric conditions of the site can be found in Mihalopoulos et al. (1997). The measuring period spans over roughly 43 months, starting on 18 May 2012 and ending on 31 November 2015, during which a variety of different atmospheric attributes was recorded.

3.2.2 Instrumentation

An Aerodyne Aerosol Chemical Speciation Monitor (ACSM) (Ng et al., 2011b) was deployed in Finokalia in late May 2012. The ACSM provides measurements of aerosol mass and chemical composition at a high temporal resolution making it ideal for atmospheric monitoring purposes. To be more specific, the ACSM, practically an online quadrupole mass spectrometer, built on the same operating principle as the widely acknowledged Aerosol Mass Spectrometer (AMS; Jayne et al., 2000), measures the non-refractory part of the PM_1 ambient aerosol, providing mass

concentrations of Organics, SO_4^{2-}, NO_3^-, NH_4^+ and Cl^-. Temporal resolution of the measurements was set to 30 minutes, thus giving clear information and detail on the temporal variation of these species in the aerosol population over Finokalia.

The instrument sampled through a PM_1 sharp cut cyclone (BGI Inc.) at 3.5 lt/min, yielding a cut-off diameter of approximately 2 μm. The inlet was positioned 3.5 meters above ground level. For a first period, starting on 18 May 2012, when the instrument was deployed and until 1 October 2013, sampled air was not dried before entering the instrument. During this period several cases in which the instrument's 100 μm critical orifice was clogged, were observed. Thereafter a nafion dryer was installed (TROPOS custom built), resulting to the elimination of this kind of behavior. Data were collected using software provided by Aerodyne (DAQ version 1.4.3.8) while data analysis was performed using the ACSM Panel package built for the Wavemetrics Igor Pro software (version 1.6.1.1).

A constant Collection Efficiency (CE) of 0.5 was selected for all measured species. A comparison between data obtained using a constant CE and data obtained using the algorithm to determine the CE proposed by Middlebrook et al. (2012) was performed and similar results were obtained since the ammonium nitrate mass fraction (ANMF) was relatively low throughout the measuring period. Relative Ionization Efficiency (RIE) for NH_4^+ was set to 5.15, derived from the monodisperse ammonium nitrate aerosol calibration process proposed by the instrument's manufacturer. RIE for SO_4^{2-} was set to 0.6, estimated following the fitting approach proposed by Budisulistiorni et al. 2014. The default values of RIE were used for the rest of the species, namely 1.4 for Organics, 1.1 for NO_3^- and 1.3 for Chloride. Due to the sampling site's remote character, calibration processes were not frequent. In order to compensate for this lack of regular calibration, the instruments Response Factor (RF) was adjusted accordingly, during the data analysis procedure, in order to achieve optimum correlation to off line measurements.

From May 2012 until the end of October 2014, Black Carbon (BC) concentrations were measured at a 5-minute temporal resolution using a 7-wavelenght Magee Scientific Aethalometer (AE31). In the AE31, particles are collected on a filter tape and optical attenuation is obtained at seven different wavelengths. The correction proposed by Weingartner et al. (2003) was applied, in order to determine BC concentrations, taking into account the filter loading effect. The multiple scattering effect was assessed by comparing absorption coefficients obtained by the AE31 to those

recorded using a Multi Angle Absorption Photometer (MAAP, Thermo Scientific). The comparison slope was used to obtain an updated, instrument and cite specific correction factor C_{ref}. Moreover, two distinct components of BC particles, attributed to different sources, namely wood burning (BC_{wb}) and fossil fuel combustion (BC_{ff}), were determined, using the model proposed by Sandradewi et al. (2008) and applying a constant Angstrom Exponent value for fossil fuel combustion equal to 1 (a_{ff} = 1), while for wood burning related particles the Angstrom Exponent (a_{wb}) used in the model was 2. For the period after November 2014 and up to the end of the measuring period, BC was monitored using a Magee Scientific AE-33 Aethalometer. The AE33 is equipped with Dual Spot technology (Drinovec et al., 2015), meaning that particles are simultaneously collected on two different spots on the filter tape and an incorporated algorithm compensates in real time for the loading effect.

A TROPOS built, custom made Scanning Mobility Particle Sizer (SMPS) was used to determine aerosol number size distributions in the size range 8 – 850 nm (Kalivitis et al., 2019). Number size distributions were then used to derive surface and volume distributions and concentrations. Using the particle volume concentration, particle mass concentrations were determined, assuming that the PM_1 population is dominated by particles consisting of ammonium sulfate, organics and BC. Thus, the density applied for the calculation is derived from the following equation

$$\rho = \left\{ \frac{x_{as}}{\rho_{as}} + \frac{x_{org}}{\rho_{org}} + \frac{x_{BC}}{\rho_{BC}} \right\}^{-1} \tag{3.1}$$

where x_{as} is the ammonium sulfate mass fraction calculated by the ACSM measurements, ρ_{as} is the ammonium sulfate density, namely 1.77 g cm^{-3}, x_{org} is the organics mass fraction while ρ_{org} is the average 1.35 g cm^{-3} density for organic aerosols determined by Lee et al. 2010, with x_{BC} and ρ_{BC} representing the corresponding values for BC. Given that the ACSM aerodynamic lens transmission efficiency (E_L) is size dependent, and in order to facilitate a direct comparison between the ACSM loadings and SMPS derived mass concentrations, the SMPS volume distribution was treated as follows. After converting electrical mobility diameters (d_m) measured by the SMPS to vacuum aerodynamic diameters d_{va} the experimentally calculated aerodynamic lens transmission efficiency (Liu et al., 2007) was interpolated to match the midpoint diameters of the corresponding size bins of the SMPS (**Fig. 9.1**). An average particle density for the entire measuring period of 1.67 g cm^{-3}, as calculated using the approach described above, was used to

perform the d_m to d_{va} conversion, assuming spherical particles (DeCarlo et al., 2004). Then each bin of the measured particle number distribution was multiplied by the interpolated E_L and the derived total volume concentration was calculated and consequently averaged to daily values.

An automatic aerosol sampler was used to sample PM_{10} aerosol on 48 mm pre combusted quartz fiber filters. Filters were subsequently analyzed for water soluble ions following extraction in an ultrasonic bath with nanopure water. The solutions were subsequently analyzed using ion chromatography in order to determine loadings of several anions (Cl^-, Br^-, NO_3^- , SO_4^{2-}, $C_2O_4^{2-}$) and cations (K^+, Na^+, NH_4^+, Mg^{2+}, Ca^{2+}). Furthermore, the filters were analyzed in order to determine organic (OC) and elemental carbon (EC) by applying the thermal-optical method, using a Sunset OC/EC aerosol analyzer and following the EUSAAR-2 protocol (Cavalli et al., 2010).

In order to determine the origin of air masses arriving at the site the NOAA ARL's HYSPLIT model (Stein et al., 2015) was used. 120-hour backward trajectories of the air masses arriving at Finokalia every 6 hours were calculated for each day of the period. Non parametric wind regression was used to associate pollution with prevailing wind speed and direction patterns, while the Potential Source Contribution Function (PSCF) was utilized to pinpoint long range transported pollution hotspots using the ZeFir package (v. 4.00; Petit et al., 2017) implemented within the Igor Pro software.

3.3 Results and Discussion

3.3.1 Measurement quality control

As a means of quality assurance of the obtained high temporal resolution dataset, measurements from the ACSM were compared to concurrent measurements using both online and offline techniques available at the site. Results from the comparison among the available techniques is illustrated in **Figure 3.1**.

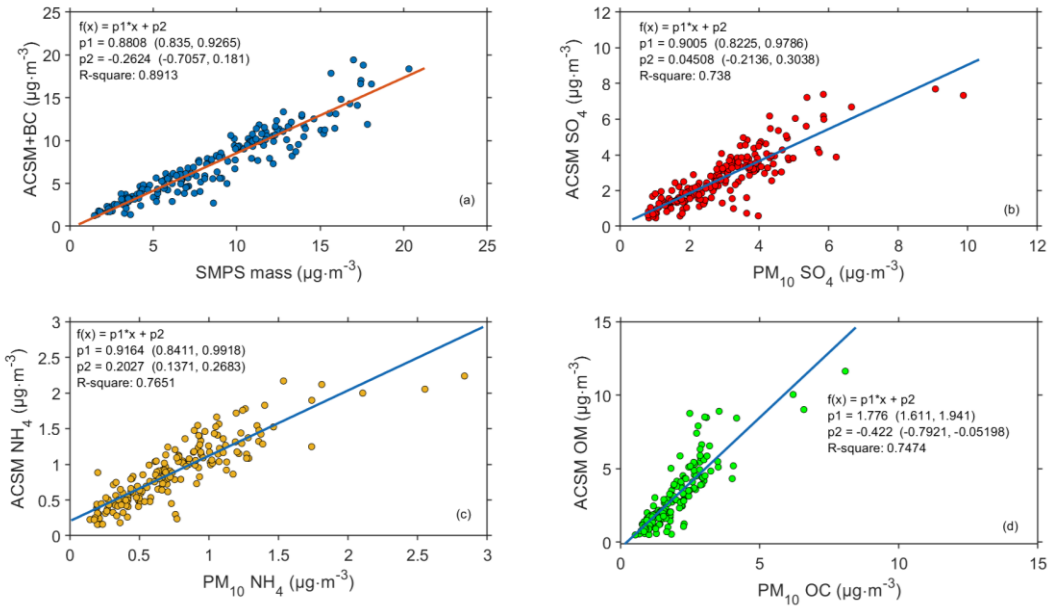

Figure 3.1. Scatter plots and linear regression for (a) PM_1 measured by the ACSM and the aethalometer versus SMPS derived concentrations, (b) ACSM sulfate versus non sea salt sulfate in PM_{10} filters, (c) ACSM ammonium versus PM_{10} filters and (d) ACSM OA versus PM_{10} organic carbon.

Treating the SMPS data as described in Section 3.2.2, effectively removing the influence of dust to the measured size distributions and homogenizing the size range of the instrument to the ACSM, resulted in an excellent correlation (r^2 = 0.89) and a slope close to 0.9, being drastically improve compared to a slope of 0.7 obtained before applying the necessary corrections. Sulfate and ammonium also exhibited good correlations with filter measurements (r^2 = 0.74 and 0.79 respectively) with slopes around 0.9, close to the percentages found in the fine fraction for these two species (Koulouri et al., 2008). For organics correlation was again good (r^2 = 0.75) versus organic carbon (OC) measured on filters, providing the necessary confidence to the near-real time dataset. The slope of 1.8 is lower than the estimated OM – to – OC ratio of 2.1 validated for the site (Sciare et al., 2005). Such a discrepancy can be attributed to the different size fractions compared here, given that OC is known to demonstrate a well-defined mode well within the coarse fraction (Sciare et al., 2003b), with 40% of its concentration being in the $PM_{1\text{-}10}$ range (Koulouri et al., 2008).

3.3.2 Chemical Composition of PM_1 at Finokalia

A timeseries of PM_1 chemical components during the 35-month measuring period, derived from available ACSM and aethalometer measurements, is depicted in **Fig. 3.2**. Average PM_1 concentrations were 6.4 ± 4.6 μg m^{-3} with sulfate being the dominant component throughout the period, contributing on average 42.6% and an average concentration of 3.1 ± 2 μg m^{-3}. Organic aerosol followed, contributing 36.5% and 2.7 ± 1.8 μg m^{-3}, while ammonium contributed 12.6% averaging 0.9 ± 0.6 μg m^{-3}. Nitrate recorded a period average of 0.3 ± 0.2 μg m-3 while levels very close to these values were found for BC. The two species contributed 4.4% and 3.8% respectively. Chloride was mostly close or below the instrument's detection limit, contributing 0.2% to measured concentrations, indicating the lack of non-sea salt sources of chloride that could be detected by the ACSM at the site.

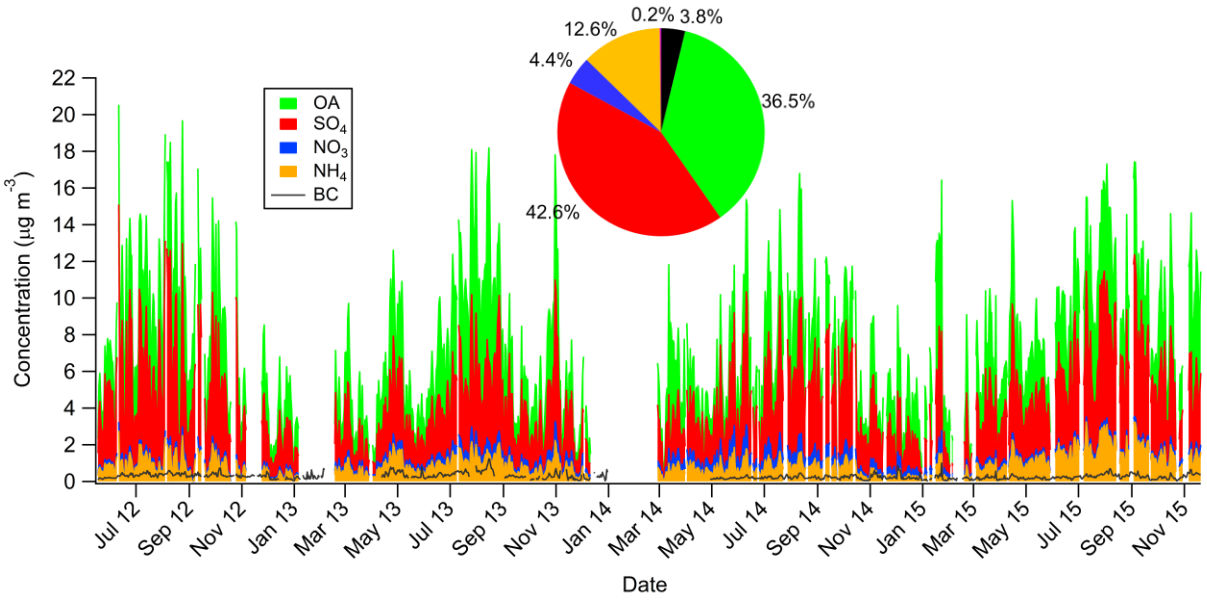

Figure 3.2. Daily timeseries of main non refractory PM_1 chemical components, i.e., OA, SO_4^{2-}, NO_3^- and NH_4^+ plus BC concentrations over the entire measuring period at Finokalia.

Concentrations in general, were higher during the warmer months of the year. Trying to emphasize on this contrast, the year was separated in two periods, a warm and a cold one, by consulting the monthly variability of recorded ambient temperatures and setting as a separation threshold an average of 20 °C as depicted in **Figure 9.3**. The cold period spans over six months, from November to April while the warm period includes May to October. Categorizing the year as such, also

follows precipitation trends in Finokalia, with much less accumulated rainfall during the warm period when compared to the cold period and especially winter and early spring months (December - March).

For the May to October period, PM_1 concentrations averaged 7.6 ± 4.7 μg m^{-3}. For the colder months (November – April), PM_1 concentrations were 72% lower, relative to the warm period, recording an average of 4.4 ± 3.8 μg m^{-3}. A contrast was recorded among the two periods in terms of species contributions. For the cold period, OA and sulfate, the two most abundant species at the site, contributed equally at 39% each, while during the warm months sulfate clearly dominated ambient PM_1 aerosol contributing 44% as opposed to a 36% contribution from organics, underlying the clear regional character of sulfate, driven mostly by general circulation and the absence of removal mechanisms, rather than sources close to the measuring location. Such a pattern could reflect a relative prevalence of sources closer to the site during the warm period, given the fact that cleaner air masses are expected to arrive at the site, effectively hindering long range transport contribution, primarily traced by enhanced sulfate concentrations and favoring the accumulation of OA. Such pronounced contrasts were not observed for the contributions of the rest of the species. Ammonium contributed 13% and 12% for the warm and cold periods respectively, nitrate contribution was calculated at 4% during the warm period and 5% for the cold, while a small increase in contribution was recorded for BC, at 5% during the cold period as opposed to the 3% calculated for the warm period. BC concentrations were rather stable when moving from the warm towards the cold period, even though different mechanisms seem to be in control of levels for these two contrasting scenarios.

When comparing daily concentrations, significant correlations were found between SO_4^{2-} and NH_4^+ (r^2 = 0.75) implying that most probably these two species are detected in the form of ammonium sulfate particles. Furthermore, OA exhibited good correlation with SO_4^{2-} (r^2 = 0.49) and NH_4^+ (r^2 = 0.48), pointing to common variability in the highly homogenous remote environment in the absence of local controlling factors and sources. A higher correlation coefficient was also calculated for OA and BC (r^2 = 0.57), implying common sources and transport mechanisms.

3.3.2.1 Monthly variability of PM_1 chemical composition

When going through each chemical species' monthly variability, the enhancement in summertime levels becomes clearer and can be observed for every constituent. In **Figure 3.3** the monthly variability for OA, sulfate and BC is depicted. For OA, maximum values are observed for August, following an upward trend after May. This trend is in line with the well documented atmospheric circulation patterns in the area, with the Etesian flow of northern origin, carrying pollutants from eastern Europe, the Balkans, Turkey and Greece, enriched by the elevated biomass burning activity in these areas during this particular time of the year (Bougiatioti et al., 2014; Sciare et al., 2003b). A secondary maximum is observed in January, in contrast to the rest of the winter months, that record the lowest concentrations overall, but in line with observations of elevated levoglucosan concentrations at the site during wintertime (Theodosi et al., 2018).

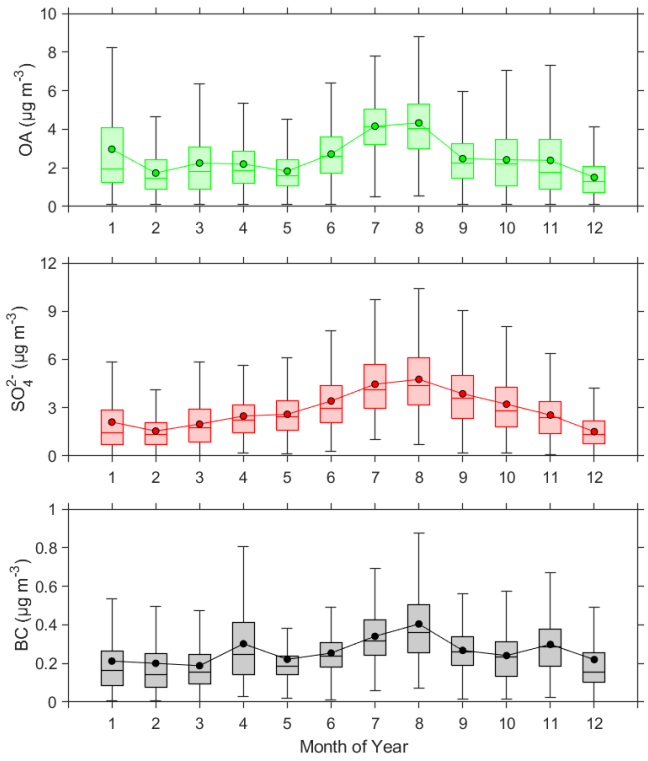

Figure 3.3. Boxplots of monthly variability for OA, sulfate and BC. Boxes represent the lower and upper quartiles, horizontal lines are median values, markers represent averages while the whiskers extend to minimum and maximum values not considered outliers.

3.3.2.2 PM_1 Diurnal Patterns and Associations with Prevailing Winds

Given the location of the measuring site away from primary aerosol sources, diurnal variability of the measured species, seemingly does not seem to include highly pronounced patterns. When plotting the diurnal cycle of each species for both the warm and cold periods (**Fig. 3.3**), a rather uniform behavior seems to appear, in the exception of higher warm season concentrations. In general concentrations seem to be enhanced in the early afternoon, while being lowest early in the morning. In the absence of a sea-land-breeze mechanism in the area (Gerasopoulos et al., 2006) this uniform pattern can be related to the incorporation of long range transported pollutants in a developing boundary layer after sunrise.

For the warm period, variability was rather low for organics, BC and nitrate with concentrations deviating by roughly ± 5% around their daily average. Ammonium was found to vary by approximately ± 10%, while the most pronounced variability was observed for sulfate with its maximum recorded at 16:00, being 12% increased relative to the average sulfate concentration during the warm period, and the minimum, recorded at 08:00 being 11% below average. The enhanced variability of sulfate can be associated with regional photochemical formation, since solar radiation reaches maximum intensity levels during daytime in the warm period.

The picture during the cold season seems to be reversed. BC and organics show the most pronounced variability (± 10%) possibly being enhanced by local sources, nevertheless keeping a similar pattern with morning minima and afternoon maxima, as the one observed in the warm period. The variability of nitrate is also more pronounced during the cold period with a distinct early morning (04:00) secondary maximum, probably favored by the abundance of NO_3 radicals during this timeframe (Vrekoussis et al., 2004) resulting to enhanced HNO_3 concentrations, transitioning to the particulate phase owing to favorable thermodynamic conditions and elevated RH during night-time. Finally sulfate and ammonium show a decreased variability, in line with regional removal mechanisms and minimum photochemistry during this season.

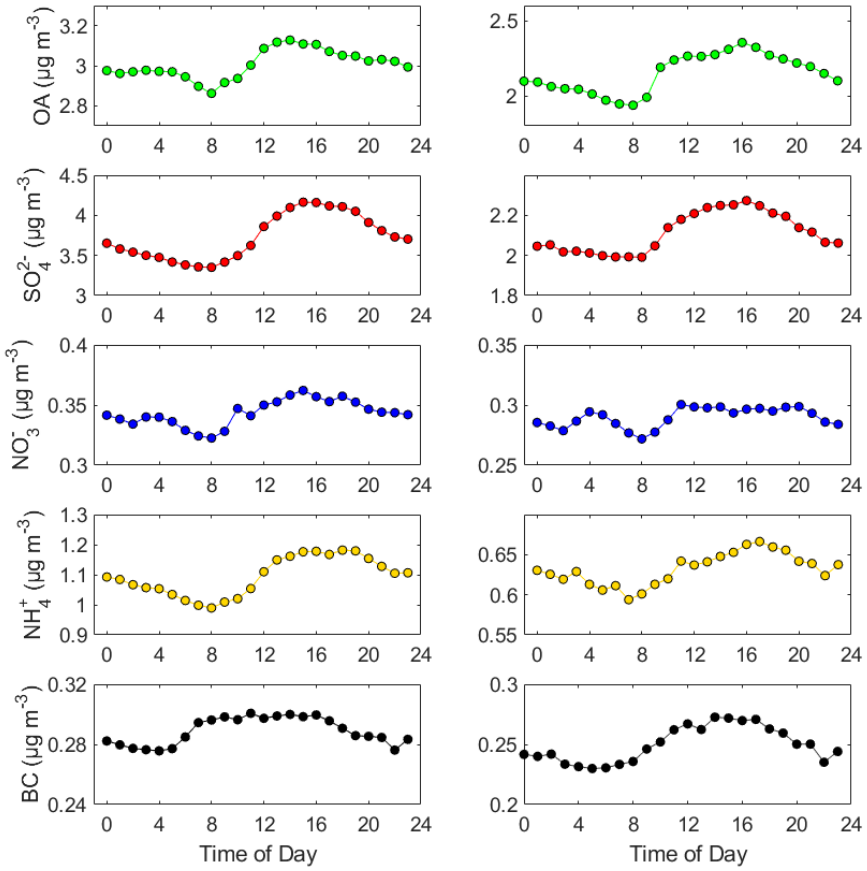

Figure 3.3. Diurnal variability of major monitored chemical components for the warm (left column) and the cold (right column) periods respectively.

Investigating the dependency of measured concentrations to wind speed and direction, provides an important tool in deciphering potential sources and advection mechanisms affecting the site. **Figure 3.4** depicts season-wise non-parametric wind regression polar plots for OA, sulfate and BC. An interesting feature is definitely the important association observed between elevated OA and BC concentrations and higher wind speeds (> 30 km h^{-1}) of a south eastern origin. Such a pattern could imply the effect of air masses passing over the island and carrying pollutants related to local combustion activities. Sulfate is also affected by this pattern, implying regional transported pollution from a southern direction, but some enhanced sulfate concentrations are also found to be linked with the predominant western and northwestern sector carrying long range transported particles.

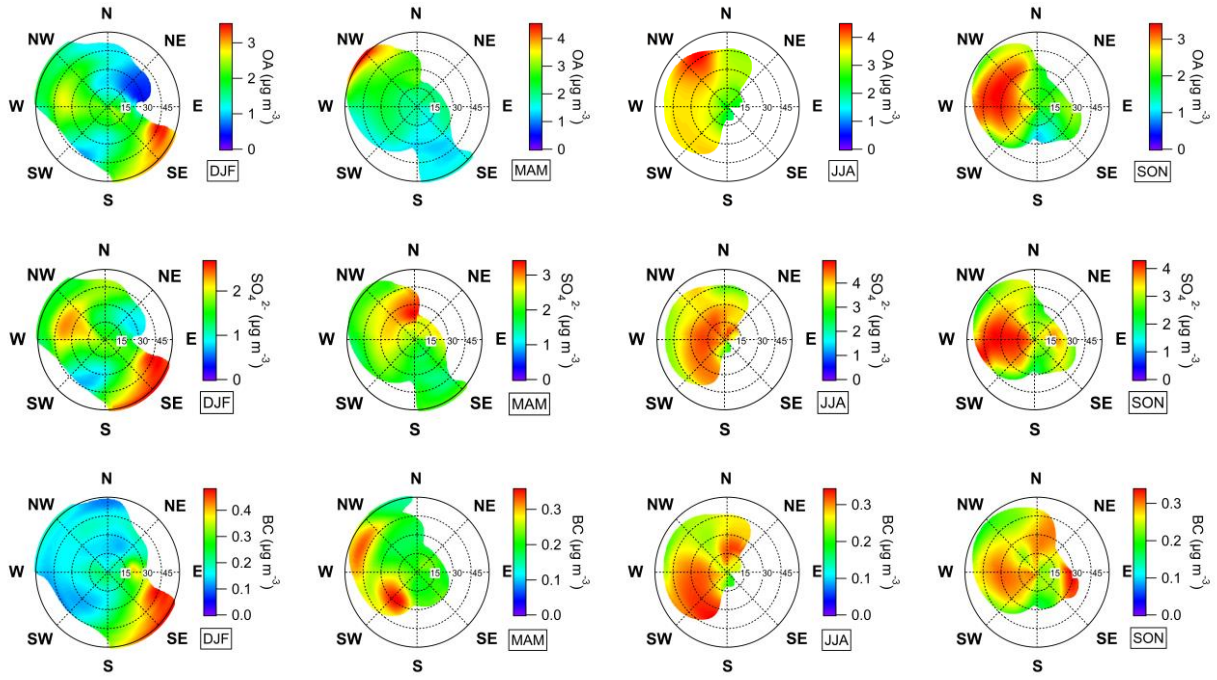

Figure 3.4. Non parametric wind regression polar plots, for concentrations of OA (top row), sulfate (middle row) and BC (bottom row) throughout the four seasons (winter: DJF; spring: MAM; summer: JJA; autumn: SON) during the entire measuring period.

For organics and sulfate during springtime, the wider northern sector contributes the highest concentrations. BC also incorporates a southwest component, further corroborating the assessment of biomass burning activities related to agriculture in the island. During summer the observed patterns are somewhat uniform with the wider western and northern sectors dominating elevated OA, sulfate and BC concentrations, in line with the well documented argument supporting long range transport carried by the predominant Etesian flow (Kalkavouras et al., 2017; Sciare et al., 2003b). During autumn, the east – southeast component for BC and SO_4^{2-} persists, calling for more investigation on the potential contribution of regional pollutants arriving at the site from Africa and the Middle East.

3.3.3 Regional Sources of PM_1 Chemical Components

In an effort to answer the open questions arising from coupling wind speed and direction to measured pollutants and effectively incorporating long range transport through wider geographical scales, examining the region surrounding the basin, the PSCF analysis performed is presented in **Figure 3.5**. This section focuses on winter (December – February) and summer (June – August), essentially, the seasons presenting most contrasting patterns. Sulfate is considered as mostly

deriving from industrial and shipping activity, while organics and BC may incorporate other sources such as biomass burning.

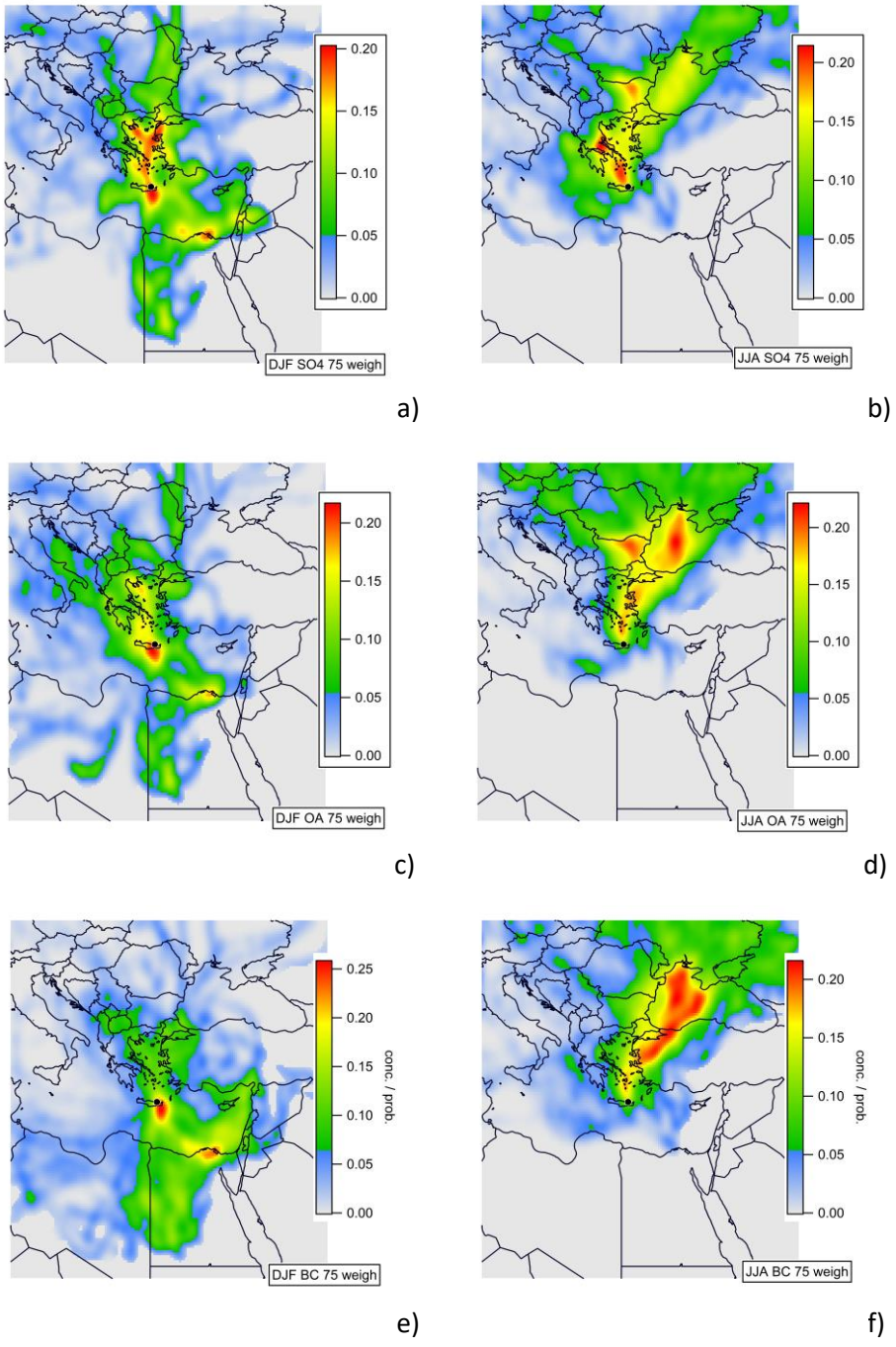

Figure 3.5. PSCF plots for SO_4^{2-} during (a) winter and (b) summer, organics for (c) winter and (d) summer and BC for (e) winter and (f) summer respectively. The colorscale represents the probability of an air parcel to be responsible for measured concentrations at the receptor site above the 75th percentile.

During summertime a clear immage can be seen, verifying results reported for the site in previous studies (Sciare et al., 2003a), with Eastern and South-Eastern Europe along with Turkey, playing an important role. The transport pattern evidently follows the prevailing Etesian flow, dominant in the region during the summer (Tyrlis and Lelieveld, 2013). OA elevated concentrations were identified as being related with the Black Sea region, hosting busssy marine transport routes, while being impacted by wildfires in its surounding countries during this time of the year. Another hotspot can be observed along the Aegean coast of Turkey and the Greek islands where domestic passenger shipping lines are at their peak during the touristic season. Interestingly a well defined hotspot can be observed in eastern Bulgaria. Sulfate seems to share the hotspot in Bulgaria observed for OA. In fact elevated concentrations related to Bulgaria are pinpointed around the Stara Zagora Province, were the largest energy complex in southeastern Europe is installed. It consists of three lignite-fired thermal power stations. The three power plants have a total installed generation capacity of more than 3000 MW. Furthermore, sulfate is associated with central Greece, hosting important industrial activity, while domestic shipping lines connecting the Aegean islands to the mainland seem to play an important role. During the summer higher BC concentrations were found to be linked to the heavily burdened Black Sea region and Turkey, in line with previous observations.

During wintertime an interesting feature seems to emerge. A significant hotspot can be observed for all species on the northern coast of Egypt, in the region of the Nile delta and the mediterranean entrance to the Souez canal. Elevated concentrations for sulfate and OA were linked to a more confined area around the Souez canal, reflecting the elevated amrine traffic density in the region. On the other hand the hotspot associated to BC is a bit wider covering a larger area of the Delta region, incorporating other types of anthropogenic activity in a highly populated area, hostin apporximately 39 million people. A component related to stagnant atmospheric circulation around the island of Crete was identified for OA and BC, further validating our previous assumptions based on temporal variability and the NWR analysis, that local sources are affecting these two species during wintertime. Sulfate seems to be further influenced by sources in the Middle East with a distinct hotspot identified over the area of Israel, Lebanon, Southern Syria and Jordan. Furthermore a local component similar to the one oserved for OA and NC. Nonetheless, a major contribution to SO_4^{2-} elevated levels was still related to the northern sector with hotspots identified in the Aegean sea and the Western coast of Turkey.

3.4 Conclusions

Monitoring of PM_1 chemical composition at high temporal resolution using an Aerosol Chemical Speciation monitor and a 7-wl aethalometer was performed over a period of 3 years in the remote environment of Finokalia in the Eastern Mediterranean. The robustness and suitability of the instrument for long-term monitor applications in harsh environments was ascertained, as exhibited via the excellent results obtained through intercomparison to co-located online and offline techniques.

Sulfate was found to dominate submicron chemical composition, followed by organics, ammonium, BC and nitrate. Chloride recorded concentrations close or below the method detection limit. Concentrations were higher during summertime, owing to long range transported pollutants of a natural or anthropogenic origin from South Eastern Europe, the Black Sea region and Turkey. During wintertime levels were hindered by pronounced removal mechanisms along the predominant transportation path, allowing for a detectable variability owing to sources closer to the receptor site.

On a diurnal scale, all pollutants were found to be enhanced after midday, following the development of the boundary layer. Variability for sulfate and ammonium was pronounced during the warm period, while being quite limited for the rest of the species, pointing to elevated photochemical activity. During the cold period variability was enhanced regarding organics and BC due to more active local sources while a night-time peak was observed for nitrate pointing to the availability of HNO_3 along with favorable thermodynamic conditions allowing for its condensation in the particulate phase.

Analysis of wind speed, wind direction and air mass back-trajectories coupled to measured species' concentrations was performed providing insights on regional and local sources. Sulfate enhanced concentrations were mainly associated with the wider West to North sector, driven by shipping, power generation and industrial activity throughout the year, along a significant medium range southern component and a noteworthy contribution related to the densely populated and marine traffic burdened North Eastern coast of Egypt and middle eastern countries during wintertime. BC during wintertime was mostly linked with air masses originating from the south, with hotspots identified over Egypt and contribution distributed across the Levantine basin. During summertime elevated BC concentrations can be attributed to the well-known pattern involving the

Black Sea and Turkey. For OA a picture combining the assessment for sulfate and BC can be drawn, with observed elevated concentrations being driven by a combination of long range transported biomass burning aerosol and influence from shipping and industrial processes originating from both the northern and southern sectors.

4 Sources and processes that control the submicron organic aerosol composition in an urban Mediterranean environment (Athens): a high temporal-resolution chemical composition measurement study

Iasonas Stavroulas[1,2,3], Aikaterini Bougiatioti[1,3], Georgios Grivas[3], Despina Paraskevopoulou[3,4], Maria Tsagkaraki[1], Pavlos Zarmpas[1], Eleni Liakakou[3], Evangelos Gerasopoulos[3], and Nikolaos Mihalopoulos[1,3]

[1]Environmental Chemical Processes Laboratory, Department of Chemistry, University of Crete, 71003 Crete, Greece

[2]Energy Environment and Water Research Center, The Cyprus Institute, Nicosia 2121, Cyprus

[3]Institute for Environmental Research and Sustainable Development, National Observatory of Athens, Lofos Koufou, P. Penteli, 15236 Athens, Greece

[4]School of Earth and Atmospheric Sciences, Georgia Institute of Technology, Atlanta, GA 30332, USA

Abstract

Submicron aerosol chemical composition was studied during a year-long period (26 July 2016 – 31 July 2017) and two wintertime intensive campaigns (18 December 2013 – 21 February 2014 and 23 December 2015–17 February 2016), at a central site in Athens, Greece, using an Aerosol Chemical Speciation Monitor (ACSM). Concurrent measurements included a particle-into-liquid sampler (PILS-IC), a scanning mobility particle sizer (SMPS), an AE-33 Aethalometer, and ion chromatography analysis on 24 or 12 h filter samples. The aim of the study was to characterize the seasonal variability of the main submicron aerosol constituents and decipher the sources of organic aerosol (OA). Organics were found to contribute almost half of the submicron mass, with 30 min resolution concentrations during wintertime reaching up to 200 μg m^{-3}. During winter (all three campaigns combined), primary sources contributed about 33% of the organic fraction, and comprised biomass burning (10 %), fossil fuel combustion (13 %), and cooking (10 %), while the remaining 67% was attributed to secondary aerosol. The semi-volatile component of the oxidized organic aerosol (SV-OOA; 22 %) was found to be clearly linked to combustion sources, in particular biomass burning; part of the very oxidized, low-volatility component (LV-OOA; 44 %) could also be attributed to the oxidation of emissions from these primary combustion sources.

These results, based on the combined contribution of biomass burning organic aerosol (BBOA) and SV-OOA, indicate the importance of increased biomass burning in the urban environment of Athens as a result of the economic recession. During summer, when concentrations of fine aerosols are considerably lower, more than 80% of the organic fraction is attributed to secondary aerosol (SV-OOA 31% and LV-OOA 53 %). In contrast to winter, SV-OOA appears to result from a well-mixed type of aerosol that is linked to fast photochemical processes and the oxidation of primary traffic and biogenic emissions. Finally, LV-OOA presents a more regional character in summer, owing to the oxidation of OA over the period of a few days.

4.1 Introduction

Exposure to fine particulate matter is recognized as a leading cause of premature mortality in Europe. While the annual concentration limit may not be exceeded at the majority of regulatory monitoring stations in European countries, health effects are also expected to appear at lower concentration levels – even at levels below the WHO guideline values (EEA, 2017). Organic carbon (OC) is among the key PM components that record the strongest associations with short-term mortality (Ito et al., 2011; Klemm et al., 2011).

Moreover, short-term exposure to OC has been linked to respiratory and cardiovascular hospital admissions (Levy et al., 2012; Zanobetti et al., 2009) and pediatric asthma emergency department visits (Strickland et al., 2010). In view of the health significance of fine aerosols, the characterization of their chemical properties and short-term variability is critical, especially at the urban background level which is more relevant for average population exposure. In addition, while the majority of transformations related to particulate sulfate and nitrate have been well described, there is much progress to be made regarding the understanding of mechanisms that govern secondary organic aerosol (SOA) formation from pre- cursors.

Therefore, the development of the aerosol mass spectrometer (AMS) technology has been an important breakthrough, facilitating the study of aerosol chemical composition, at high temporal resolution. The ability to differentiate between primary and secondary components, based on specific markers, introduces an important advancement to organic aerosol (OA) source apportionment (Jimenez et al., 2009), which has otherwise mainly relied on a statistical approach using elemental carbon (EC) and OC thermal–optical data (EC tracer method and variants; Turpin

and Huntzicker, 1995). Capitalizing on abundant spectroscopic data, PMF (Positive Matrix Factorization) source apportionment (SA) is used to discern between various primary sources like traffic and biomass burning, and to categorize secondary aerosols depending on their degree of oxidation. The ACSM (Aerosol Chemical Speciation Monitor) is an instrument that relies on AMS technology and enables long-term routine monitoring (Ng et al., 2011b).

While many relevant studies have focused on regional and rural background areas, long-term ACSM results from large European urban centers are relatively scarce. (Canonaco et al., 2013) performed 1 year of measurements at an urban background site in the center of Zurich. Aurela et al. (2015) deployed an ACSM at residential, traffic, and highway sites within the Helsinki metropolitan area for a total of 5 months. Findings from 10 months of measurements at the North Kensington urban background site in London were reported by Reyes-Villegas et al. (2016). Focusing on southern Euro- pean cities, long-term results are provided by the intensive ACSM campaign of Minguillón et al. (2016), at an urban background site in Barcelona. Shorter – up to 1 month – studies using the AMS have also been conducted in Barcelona (Mohr et al., 2012), Bologna (Gilardoni et al., 2016), and Marseille (El Haddad et al., 2013). In urban Athens, a 1-month AMS campaign during winter 2013 was carried out for chemical composition and OA sources (Florou et al., 2017).

The greater Athens area (GAA) appears as a challenging urban milieu for the study of aerosol dynamics, as it combines a large population (about 4 million) and intense primary emissions, with complex topography and meteorology, which lead to high levels of atmospheric pollutants and significantly deteriorate the air quality (Kanakidou et al., 2011; Pateraki et al., 2014). However, the characteristics and related processes of SOAs, in the long term, have received limited attention up until this point (Grivas et al., 2012; Paraskevopoulou et al., 2014). Moreover, since 2013, due to the economic recession in Greece, primary and secondary precursor emissions have become altered and intensified, as residents have switched from fossil fuel combustion to the uncontrolled burning of wood and biomass for space heating (Fourtziou et al., 2017; Gratsea et al., 2017; Saffari et al., 2013). Existing measurements of aerosol chemical composition in Athens have mainly been performed using filter sampling (Paraskevopoulou et al., 2014; Theodosi et al., 2018, 2011) and have indicated the importance of fine OAs. In this study we present, for the first time, long-term results regarding the sources of submicron OAs in Athens from high temporal resolution

measurements during a year-long period, complemented by two intensive winter campaigns. For the collection of data, we deployed an Aerosol Chemical Speciation Monitor (ACSM) in addition to a particle-into-liquid sampler coupled with ion chromatography (PILS-IC) and an AE-33 Aethalometer, while also conducting auxiliary aerosol (filter-based) and gas phase measurements. The main objectives of this study were (i) to characterize submicron aerosol and its variability using high temporal-resolution measurements, (ii) to quantify the sources of OAs and their seasonal variability (via PMF analysis), and (iii) to study the year-to-year changes of aerosol sources during wintertime.

4.2 Experimental Methods

4.2.1 Sampling site and period

The measurements exploited in this study were conducted, at the urban background site of the National Observatory of Athens (NOA) at Thissio (37.97◦ N, 23.72◦ E), as representative of the mean population exposure over the Athens metropolitan area (Fourtziou et al., 2017). The site is located at an elevation of 105 m a. s. l., in a moderately populated area, where the influence of direct local emissions is limited. The measurement period spanned an entire year, from July 2016 to July 2017. Additionally, two intensive winter campaigns took place at the same site, the first from mid- December 2013 to mid-February 2014 and the second from 23 December 2015 to 17 February 2016. These intensive campaigns aimed at studying the year-to-year variability and impact of biomass burning on the air quality of the city of Athens during wintertime.

4.2.2 Instruments and methods

Measurements were performed with an Aerosol Chemical Speciation Monitor (ACSM) from Aerodyne Research Inc. (Ng et al., 2011b), which measured the non-refractory PM_1 (NR-PM_1) chemical composition in near real-time (30 min temporal resolution). The instrument sampled through a BGI Inc. SCC 1.197 sharp cut cyclone operated at 3 L min^{-1}, yielding a cut-off diameter of approximately 2 μm. Practically, the ACSM operates following a similar principle to the aerosol mass spectrometer (AMS) (Jayne et al., 2000) where ambient air is drawn through a critical orifice to a particle focusing aerodynamic lens; the resulting particle beam is flash-vaporized at 600 ◦C, ionized via electron impact ionization, and guided through a quadrupole mass spectrometer. Ammonium nitrate and ammonium sulfate calibrations were performed prior to the ACSM's deployment at the site for the 2016–2017 period, and the response factor (RF) for nitrate along

with the relative ionization efficiencies (RIEs) for ammonium and sulfate were determined. For the 2013–2014 and 2015–2016 intensive winter campaigns ammonium nitrate calibrations were performed and the RIE for sulfate was determined according to the fitting approach proposed by (Budisulistiorini et al., 2014). Values are presented in **Table 10.1** in the Supplement. The detection limits for the ACSM provided by (Ng et al., 2011b) are as follows: 0.284 μg m^{-3} for ammonium, 0.148 μg m^{-3} for organics, 0.024 μg m^{-3} for sulfate, 0.012 μg m^{-3} for nitrate, and 0.011 μg m^{-3} for chloride. Mass concentrations are calculated using a chemical composition dependent collection efficiency ((Middlebrook et al., 2012); **Fig. 10.1** in the Supplement).

Parallel measurements were performed for biomass burning identification and for quality control purposes. In this context, a Metrohm ADI 2081 particle-into-liquid sampler (PILS; (Orsini et al., 2003) coupled with ion chromatography (Dionex ICS-1500) was used, which sampled ambient air from a different, but adjacent to the ACSM's, PM_1 inlet. Two denuders were placed inline, upstream of the instrument, in order to remove gas phase species (e.g., NH_3, HNO_3, and SO_2). The ion chromatograph was set to measure cations such as ammonium and potassium at a time resolution of 15 min. The resulting concentrations from the ACSM were tested against filter measurements and the concentrations provided by the PILS. For the PILS, the detection limit was calculated at 1 ppb for Na^+ and NH^+ and 2 ppb for K^+. Non-sea-salt K^+ (nss-K^+) concentrations were calculated using the Na^+ concentrations and the Na^+/K^+ ratio in seawater as a reference (Sciare et al., 2005). The concentrations reported were blank corrected.

Furthermore, filter sampling was also conducted in parallel at Thissio station. $PM_{2.5}$ aerosol samples were collected on quartz-fiber filters (Flex Tissuquartz, 2500 QAT-UP 47 mm, Pall), on a daily basis, while during the winter periods the sampling frequency was set to 12 h. A dichotomous Partisol sampler 2025 (Ruprecht & Patashnick) was used at a flow rate of 16.7 L min^{-1}. The samples were analyzed for organic and elemental carbon (OC, EC) with the thermal–optical transmission technique, using a Sunset Laboratories OC/EC analyzer and applying the EUSAAR-2 protocol (Cavalli et al., 2010). Filters where also analyzed for the determination of the main ionic species using ion chromatography as described in (Paraskevopoulou et al., 2014).

Two different absorption photometers were monitoring black carbon (BC) concentrations. A 7-wavelength Magee Scientific AE-42 portable Aethalometer was used for the 2013–2014 and 2015–2016 winter campaigns, which provided 5 min resolution measurements. For the year-long

period a dual spot, 7-wavelength Magee Scientific AE-33 Aethalometer (Drinovec et al., 2015) was used, operating at a 1 min resolution and a 5 L min^{-1} flow rate. Standard gas analyzers for O_3 (Thermo Electron Co., Model 49i), CO, SO_2, and NO_x (HORIBA, 360 series) in addition to a scanning mobility particle sizer for PM_1 size distributions (SMPS 3034, TSI Inc.), measuring in the 10.4–469.8 nm size range, were also operating at the sampling site. Wavelength dependent source apportionment of the BC load was performed by the AE-33 Aethalometer, based on the approach from (Sandradewi et al., 2008), providing a fossil fuel (BC_{ff}) and a wood combustion (BC_{wb}) component. The default absorption Ångström exponents of 1 for fossil fuel combustion and 2 for pure wood burning, as incorporated in the AE-33 software, were used, which were very close to the respective values of 0.9 and 2 used at a suburban site in Athens (Kalogridis et al., 2018). Meteorological parameters for the study were taken from the actinometric meteorological station of NOA, at Thissio (Kazadzis et al., 2018) (**Fig. 10.2**). All measurements were averaged to 1 h intervals in order to synchronize the different datasets.

The bivariate wind speed–direction plotting methodology developed by (Carslaw and Ropkins, 2012) in the "openair" R-package, was used for the identification of source areas, as incorporated in the Zefir Igor Pro-based tool (Petit et al., 2017). Four-day back trajectories were also calculated using the HYbrid Single-Particle Lagrangian Integrated Trajectory (HYSPLIT_4) model (Draxler and Hess, 1998) developed by the Air Resources Laboratory (ARL/NOAA), and 1° GDAS (NCEP) meteorological data. Trajectories were computed every 3 h, for air masses arriving at Athens at a height of 1000 m. The selected height is considered suitable to capture transport at a representative upper limit of the boundary layer in Athens (Markou and Kassomenos, 2010). Trajectory clustering was performed using the TrajStat plug-in (Sirois and Bottenheim, 1995; Wang et al., 2009) of the MeteoInfo GIS software. The change of the total space variance for a decreasing number of clusters was examined as a criterion for cluster number selection. The analysis was performed separately for summer and winter, resulting in five clusters for each period.

4.2.3 Source apportionment of the submicron organic fraction using PMF analysis

4.2.3.1 PMF strategy

Positive matrix factorization (Paatero and Tapper, 1994) was performed on the organic mass spectra obtained from the ACSM. The graphic interface SoFi (Source Finder) version 6.1, developed at the Paul Scherrer Institute (PSI) in Zurich (Canonaco et al., 2013), was used. SoFi

implements the multi-linear engine algorithm ME-2 (Paatero and Hopke, 2003), analyzing the acquired mass spectral time series matrix into a linear combination of factor profiles (FP) and time series submatrices. A detailed description of the method can be found in the studies referenced above.

For our datasets only $m/z \leq 125$ were used in order to avoid interference from the naphthalene signal (m/z 127, 128, and 129). Weak signals, with a signal-to-noise ratio (S/N) below 0.2 were down-weighted by a factor of 10, and those with a S/N between 0.2 and 1 were down-weighted by a factor of 2 (Ulbrich et al., 2009), using the built in utilities of the SoFi toolkit.

The input organics and the organics' error matrices are automatically derived from the ACSM data analysis software. Several model runs were performed, with and without applying constraints to the FPs derived, using the α-value approach (Canonaco et al., 2015, 2013) and following the methodology proposed by (Crippa et al., 2014). The α value ranges between 0 and 1 and is a measure of how much the resulting FPs are allowed to vary from the constraints. Initially, unconstrained PMF runs provided insight into the potential number and type of factors. For the following steps, reference factor profiles (RFPs) were introduced in order to con- strain primary OA factors, (i) first for hydrocarbon-like organic aerosol (HOA), (ii) then for both HOA and BBOA, and (iii) finally for HOA, BBOA, and cooking-like organic aerosol (COA). Potential FPs for SOAs were left unconstrained. A thorough discussion regarding the choice and representativeness of the RFPs used can be found in **Sect. 10.4.1** of the Supplement. Each factor was constrained using different α values within the limits suggested by (Crippa et al., 2014). Next, the model's residuals, for each different model setup, were analyzed in search of structures that could indicate underestimation or overestimation of the number of separated factors. Stability of factors for different model seeds and correlations of the obtained FP spectra with FPs reported in similar environments and conditions were examined (**Sect. 10.4.8**). Finally, correlations of the time series of the selected optimal solutions to both gas phase and particulate independent measurements such as BC, BC_{ff}, BC_{wb}, CO, nss-K^+, NO_3^-, SO_4^{2-}, and NH_4^+ were examined to solidify the selection (**Sect. 10.4.9**).

The year-long data series was divided into a cold period, from November 2016 to March 2017 and a warm period consisting of two sub-periods from August to September 2016 and from May to July 2017 which were treated separately. According to studies on the climatology of southern

Greece, the transient period (spring and fall seasons) in Athens does not exceed 60 days on average (Argiriou et al., 2004), and mainly spans the months of April and October – which were excluded from the seasonal analysis. The two wintertime campaigns of 2013–2014 and 2015–2016 were also treated separately.

The coefficient of determination r^2 for simple linear regression is used as a metric for all comparisons, e.g., both the affinity of the FPs obtained to spectra from the literature and the correlation of the respective factor time series with independent measurements.

4.2.3.2 Choosing the optimal configuration

The presentation of, and discussion of the optimal configuration chosen for the ME-2 model, as well as results from each step of the implemented strategy described above, followed by a sensitivity analysis of the α value influence on the obtained factors, can be found in **Sect. 10.4**. In brief, for the cold period and the two wintertime intensive campaigns, constraining three factors, namely HOA, BBOA, and COA, and leaving two unconstrained SOA factors, produced a solution that is characterized by minimal seed variability and model residual structures, while the FPs, the time series, the relative contribution, and the diurnal variability of the factors appear to be environmentally relevant, resembling previously proposed solutions for the region (Florou et al., 2017; Kostenidou et al., 2015). Leaving factors unconstrained leads to unstable model behavior such as diurnal residual structures for key variables (e.g., alkyl fragments like m/z = 55 or 57) and large FP variability for different model seed runs. Furthermore, deconvolved spectra were missing expected variable contributions in profiles such as BBOA (very low m/z = 41 and 43 relative contributions), while the COA factor was dominated by the CO_2^+ fragment at m/z = 44. Configuring less or more than five factor solutions, either resulted in an even more pronounced residual diurnal cycle, pointing to poor factor separation, or in splitting behavior and resulting factors which were environmentally irrelevant.

Conversely, constraining two factors during the warm period, namely HOA and COA, and leaving two unconstrained SOA factors was found to be the solution that exhibited higher relevance while also being robust and close to previous knowledge related to OA in the GAA. A BBOA fac- tor could not be identified during the warm periods, as the contribution of the marker fragments for biomass burning, m/z = 60 and m/z = 73, are almost absent in these periods' dataset. The COA factor is present in all of the studied periods, validated following the approach of (Mohr et al.,

2012)) (**Fig. 10.9**), and emerged in all of the steps (unconstrained and constrained runs) of the strategy implemented (**Figs. 10.5–10.8** and related discussion in **Sect. 10.4**).

4.3 Results and Discussion

4.3.1 Comparison of ACSM data with ancillary measurements

As an initial quality control/quality assurance of the ACSM data, the ammonium concentrations are compared to the respective values derived from the PILS, on an hourly basis for winter 2016–2017. A good agreement is found (r^2 = 0.80 and slope of 0.82). The sulfate and nitrate concentrations for the winter 2016–2017 period are compared to the respective values from the ion chromatography analysis ($PM_{2.5}$ filters) on a daily basis (r^2 = 0.75 and slope of 0.81 and r^2 = 0.78 and slope of 0.95, respectively). The concentrations of organics are compared to the OC concentrations of the $PM_{2.5}$ filters. An excellent agreement is found (r^2 = 0.93, slope of 1.59) with the slope being close to values reported for urban areas (Petit et al., 2015) and OM : OC calculations from AMS measurements in polluted environments (Saarikoski et al., 2012). The results from the aforementioned comparisons are provided in the Supplement (**Sect. 10.3**).

During the intensive winter 2015–2016 campaign, the concentrations of the ACSM components are compared to those determined from ion chromatography, based on con- current filter samples collected at the same site, twice per day, (06:00–18:00 and 18:00–06:00 LT – local time). Results indicate an excellent agreement for sulfate (r^2 = 0.88, slope of 1.0), ammonium (r^2 = 0.82, slope of 1.06), and nitrate (r^2 = 0.88, slope of 1.12) (**Fig. 10.4**). During the intensive winter 2013–2014 campaign, the ammonium concentrations from the ACSM showed significant correlation with the respective concentrations from the PILS instrument (r^2 = 0.80, slope of 0.81).

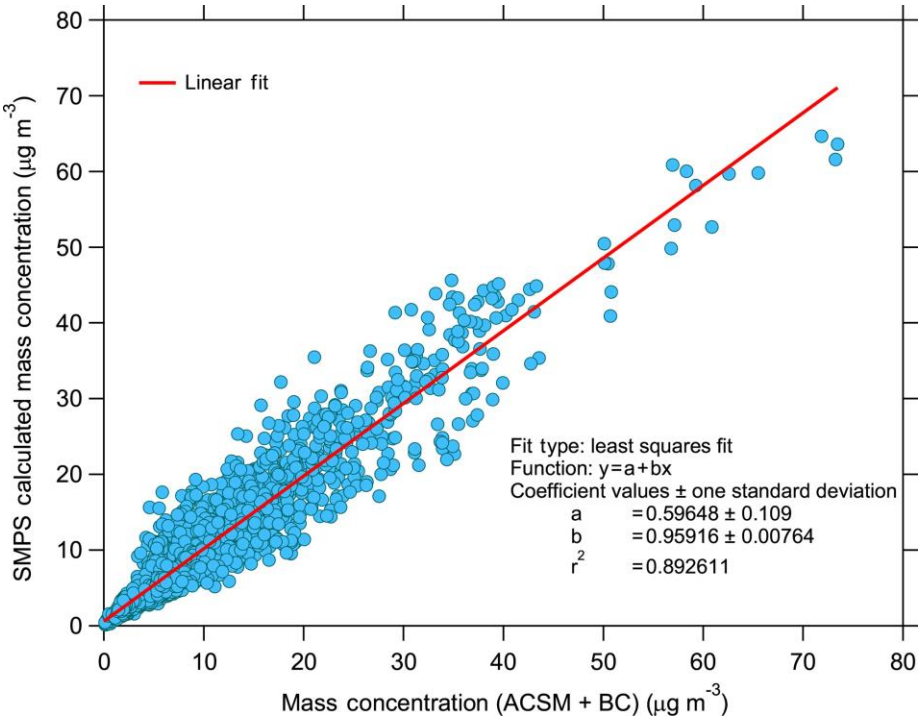

Figure 4.1. Correlation between ACSM + BC vs. SMPS-derived 1 h averaged mass concentrations for the 2016–2017 measurement period.

Finally, the sum of the ACSM component concentrations plus BC, measured using the 7-wavelength Aethalometer, was compared with the mass concentrations determined by the SMPS since February 2017 at Thissio. The density used to convert volume distributions, and consequently the volume concentrations of spherical particles to mass concentrations, was obtained by applying the methodology of (Bougiatioti et al., 2014) assuming that the aerosol PM_1 population was dominated by ammonium sulfate and organics and calculating the respective mass fractions time series based on the ACSM measurements. A density of 1.77 g cm^{-3} was used for ammonium sulfate, and a value of 1.3 g cm^{-3} was utilized for organics (Florou et al., 2017). The results obtained using a chemical dependent collection efficiency to deter- mine the ACSM derived mass concentrations are portrayed in **Fig. 4.1** and indicate excellent correlation (r^2 = 0.89), a slope of 0.96, and an intercept of 0.60.

4.3.2 PM_1 average chemical composition and temporal variability

4.3.2.1 Chemical composition and characteristics

The time series of the main submicron aerosol components measured using the ACSM and the black carbon concentrations are presented in **Fig. 4.2a** (one complete year period). The period average cumulative concentration of the ACSM components and BC was 12.4 ± 12.5 μg m^{-3}. The highest concentrations were measured during winter (average 16.1 ± 19.5 μg m^{-3}) and the lowest during spring (average 7.9 ± 5.7 μg m^{-3}). On an annual basis, the most abundant component was OA, followed by sulfate, which contributed 44.5 % and 27.8 % to the total submicron mass, respectively, while the BC contribution was calculated at 15.1 %, ammonium at 7.9 %, and nitrate at 4.3 %. In **Fig. 4.2b** and c the respective time series of the main submicron aerosol components during the two intensive 2-month winter campaigns are presented. During winter 2013–2014 the average mass concentration of the ACSM components (plus BC concentrations) was 27.8 ± 28.3 μg m^{-3}, with organics and BC contributing 55.6 % and 14.6 % to the total submicron mass, respectively, followed by sulfate (13.6 %). During winter 2015–2016 the average concentration was 20.8 ± 27.5 μg m^{-3}, with organics and BC contributing 51.6 % and 15.2 % to the total sub-micron mass, respectively, followed by sulfate (14.8 %), nitrate (6.5 %), and ammonium (6.7 %). It is clearly deduced that during wintertime, organics constitute half or even more of the total PM1 mass, sulfate around 20 %, and BC around 14 %.

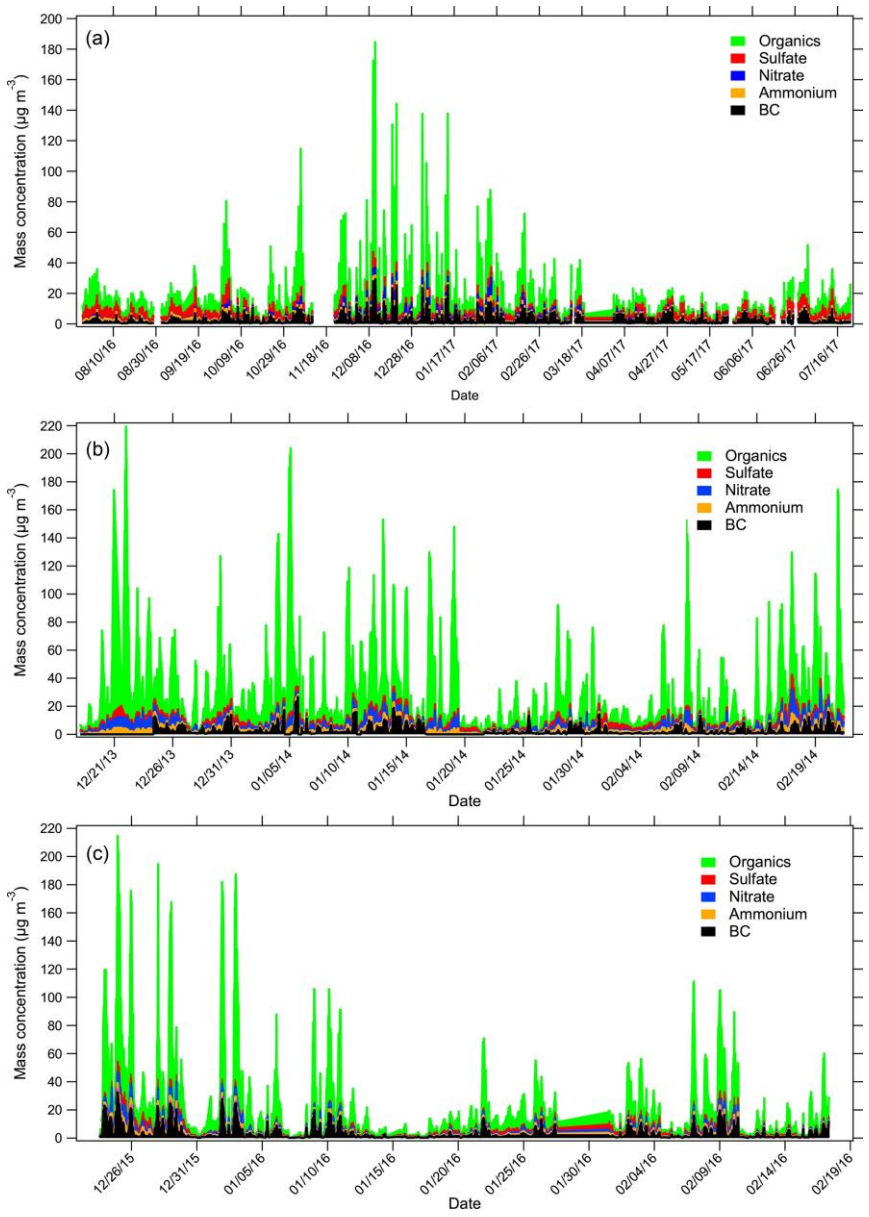

Figure 4.2. Time series of the main submicron aerosol components. (a) The 1-year period starting on 26 July 2016 and ending on 31 July 2017, (b) the 2013–2014 winter campaign (18 December–21 February), and (c) the 2015–2016 winter campaign (23 December–17 February).

The other striking feature is that during wintertime, PM_1 concentration spikes can reach up to 220 μg m^{-3} hourly values, with organics constituting most of the mass. Maxima are recorded during nighttime and mostly during meteorological conditions that favor pollutant emission and accumulation, such as low wind speed and low temperature (Fourtziou et al., 2017). On average, 8 such incidents occur each winter (10 in 2013–2014, 7 in 2015–2016, and 7 in 2016–2017), with

recorded organic levels higher than 100 µg m−3. To our knowledge, such levels are the highest reported for Europe during wintertime and highlight the strong impact of local emissions – especially those related to heating/wood burning (see below) – on the levels of organics and consequently PM1. Similar maxima to those observed in this study are also reported by Florou et al. (2017; at the same site from 10 January until 9 February 2013), where organics concentration alone reached up to 125 µg m^{-3} and maxima of 8 µg m^{-3} for BC and up to 5 µg m−3 for nitrate were recorded. Similarly, wintertime pollution events with an increased local character and elevated concentrations of organics (up to around 100 µg m^{-3}, average of 22.6 µg m^{-3}) were reported at a regional background site, just outside of Paris, during February 2012 (Petit et al., 2015).

4.3.2.2 Seasonal variability

The seasonal variability of the main measured species, along with the average PM_1 concentration (µg m^{-3}), as calculated from the ACSM + BC measurements is shown in **Fig. 4.3** and the basic statistics are included in Table 1. Organics contribute 46 % to the total submicron aerosol mass in summer, followed by sulfate (30.5 %), BC (12.6 %), ammonium (8.3 %), and nitrate (2.6 %), while in winter, organics and sulfate contribute 48.1 % and 23.2 %, respectively, followed by BC (14.7 %), ammonium (6.9 %), and nitrate (6.3 %).

Table 4.1. Seasonal average concentrations ± standard deviation (range) and total mass of the main submicron aerosol components for the 1-year study period and the two winter campaigns.

	March–April–May 2017	July–August 2016 & June–July 2017	September–October–November 2016	December–January–February 2016–2017	December–January–February 2013–2014	December–January–February 2015–2016
Organics	3.3 ± 3.0 (0.3–31.3)	5.4 ± 3.4 (0.3–41.9)	6.1 ± 7.5 (0.1–98.2)	9.0 ± 13.4 (0.2–153.9)	18 ± 24.4 (0.4–212.2)	12.4 ± 19.9 (0.7–160.6)
Ammonium	0.6 ± 0.5 (0.4–3.1)	1.0 ± 0.6 (0.2–4.1)	1.0 ± 0.7 (0.4–5.7)	0.9 ± 0.7 (0.2–5.7)	1.8 ± 1.2 (0.2–9.1)	1.1 ± 1 (0.3–6.7)
Sulfate	2.1 ± 1.5 (0.2–10.1)	3.6 ± 2.1 (0.3–14.9)	3.5 ± 2.3 (0.1–17.1)	2.5 ± 1.5 (0.1–11.7)	2.6 ± 1.4 (0.4–13.9)	2.2 ± 1.7 (0.4–10.3)
Nitrate	0.4 ± 0.5 (0.05–5.4)	0.3 ± 0.2 (0.01–1.5)	0.5 ± 0.7 (0.1–6.9)	1.2 ± 1.5 (0.05–12.1)	2.6 ± 2.4 (0.09–18.3)	1.5 ± 1.4 (0.07–16)
Chloride	0.02 ± 0.05 (0–0.8)	0.02 ± 0.02 (0.04–0.2)	0.04 ± 0.09 (0.07–2.0)	0.15 ± 0.3 (0–3.5)	0.16 ± 0.24 (0.09–8.1)	0.12 ± 0.24 (0–2.6)
BC	1.5 ± 1.4 (0.1–14.6)	1.2 ± 0.8 (0.2–10.5)	1.7 ± 1.6 (0.1–12.4)	2.4 ± 3.4 (0.1–29.6)	2.7 ± 3.2 (0.2–26.8)	3.4 ± 4.6 (0.2–32.3)
PM_1	7.9 ± 5.7 (0.6–42.4)	11.5 ± 6.2 (0.5–52.2)	12.8 ± 10.9 (0.9–115.5)	16.1 ± 19.5 (0.8–185.8)	27.8 ± 28.3 (1.4–227.2)	20.8 ± 27.5 (1.7–215.3)

The mass concentrations of organics, nitrate, chloride, and BC exhibit a clear annual cycle, with a minimum during summer and a maximum in winter. This pattern seems to be due to a combination of three simultaneous processes. Firstly, the additional primary emissions from domestic heating play an important role, as is evident from the largely elevated concentrations of organics and BC, which are emitted by central heating systems and fireplaces during winter. Secondly, the decreased planetary boundary layer (PBL) depth during winter may influence observed pollutant patterns: according to (Kassomenos et al., 1995) and (Alexiou et al., 2018), the daytime PBL depth shows a clear annual cycle, with maxima during the warm months (June to September) and a 2-fold decrease during wintertime. Finally, the effect of temperature on the partitioning of semi-volatile inorganics and organics can also contribute to the processes leading to the observed pattern. In support of the above, a larger standard deviation is found in winter, which demonstrates the

frequency and magnitude of the pollution events observed due to the increased need for heating (Fourtziou et al., 2017). Independently of the year, it can be seen that winter concentrations of organics, nitrate, chloride, and BC are very similar and are more than twice the respective values of these species during the other seasons (**Table 4.1**).

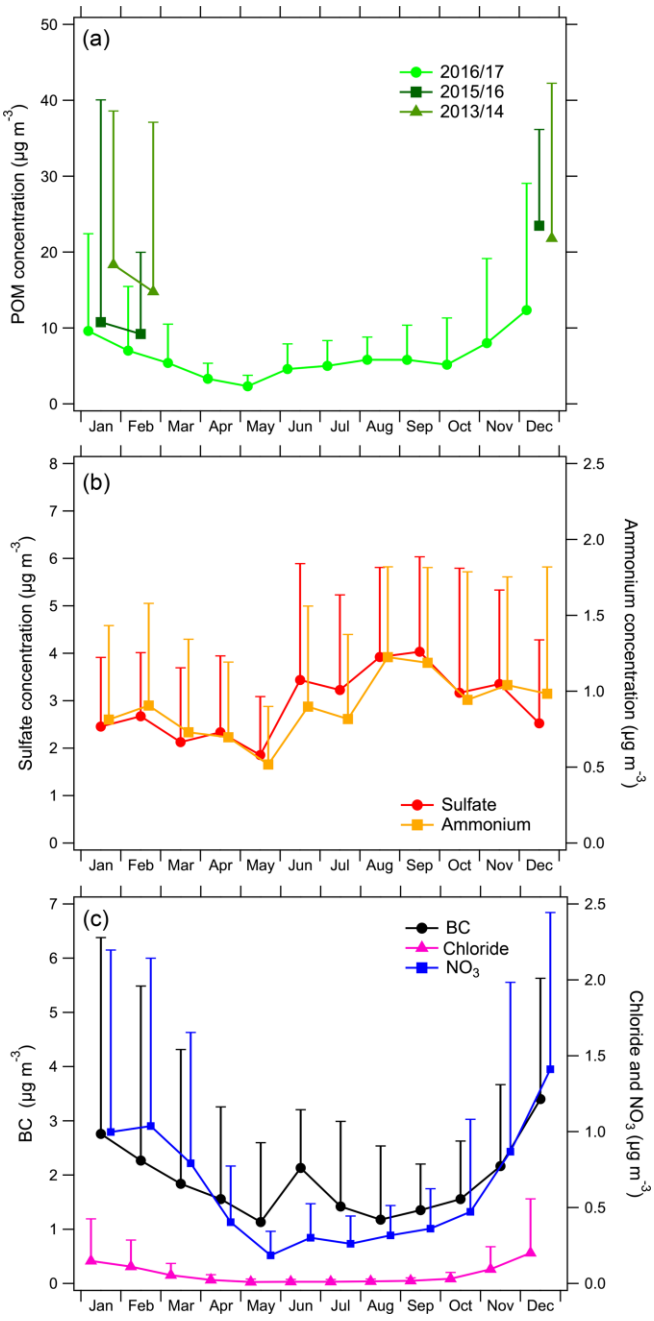

Figure 4.3. Monthly average concentrations of the main aerosol constituents. Organics are shown in (a) for the 2016–2017 period as well as the 2013–2014 and 2015–2016 winter periods, while

sulfate and ammonium are shown in (b) and BC, nitrate, and chloride are shown in (c) for the 2016–2017 period. The standard deviation is also depicted (error bars; only the positive part is shown for the sake of clarity).

The concentrations of organics are consistently high during all of the winters studied (from December to February), while the higher nitrate values, which exhibit a similar trend to organics and BC, can be attributed to the combination of lower temperatures during nighttime and the increase of combustion sources; this leads to reduced acidity and results in the favorable partitioning of nitrate in the aerosol phase (Guo et al., 2016; Mariani and de Mello, 2007; Park et al., 2005). Ammonium and sulfate exhibit the opposite seasonal cycle, with maximum values in summer and minimum values during winter and spring. The higher summer sulfate levels are the result of enhanced photochemistry associated with more intense insolation, combined with less precipitation, favoring the regional transport of polluted air masses (Cusack et al., 2012). The seasonal variation of concentrations is in agreement with observations from Athens made during prior long-term measurement campaigns based on the analysis of daily filter samples (Paraskevopoulou et al., 2015, 2014; Theodosi et al., 2011).

4.3.2.3 Diurnal variability

When investigating the diurnal patterns of the measured species (**Fig. 4.4**), it was observed that ammonium and sulfate did not exhibit significant variability during wintertime, which was due to the regional character of ammonium sulfate. In order to quantify the extent of this variability we calculated the normalized diurnal pattern by dividing each hourly value by the respective species' daily mean concentration. More specifically, sulfate varies by 13 % around the mean value while ammonium varies by 40 %. Conversely, organics, BC, and nitrate vary significantly during the day (183 %, 79.8 %, and 110 %, respectively). These species clearly double their concentrations during nighttime, due to the additional primary emissions. Furthermore, BC also exhibits a second maximum during the early morning hours, which can be attributed to the primary emissions during the morning traffic rush hours.

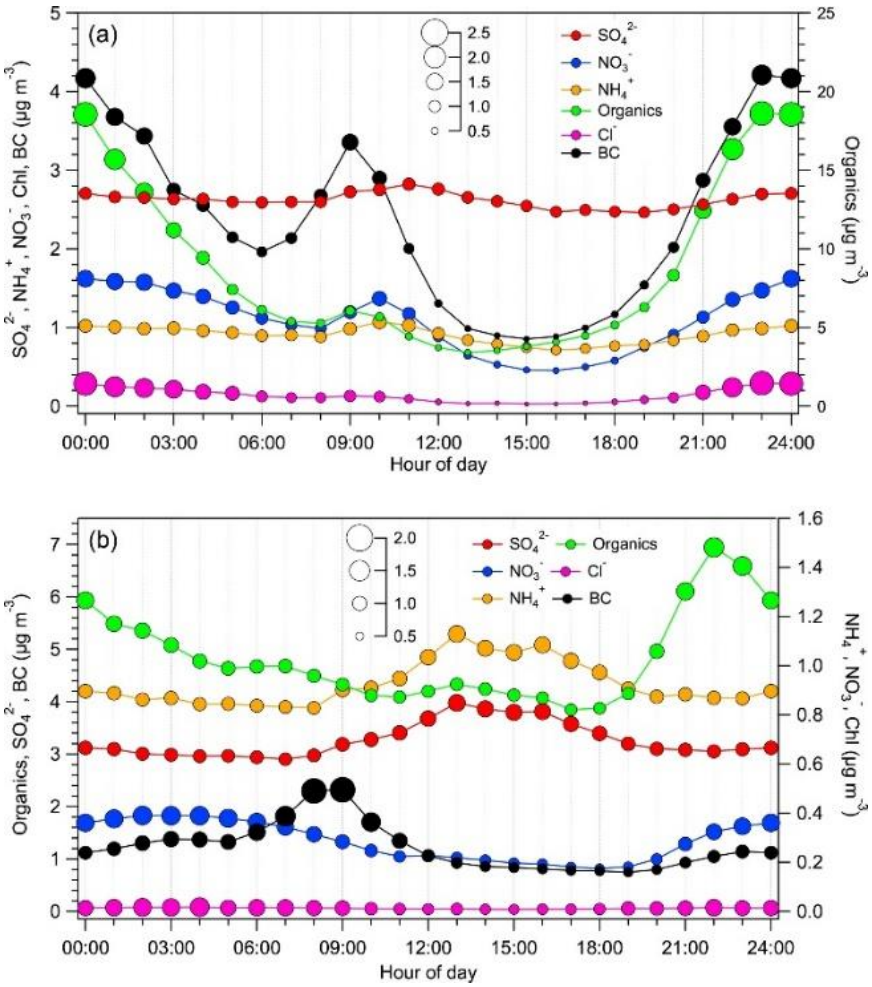

Figure 4.4. Average daily cycle of the main submicron aerosol constituents for the cold period 2016–2017 (a) and the warm period of 2017 (b). The size of the markers indicates the normalized values relative to each species' daily mean value.

During summer, all concentrations are significantly lower, especially organics (note the scale change in **Fig. 4.4**) which exhibit a 5-fold decrease of their mean maximum concentration during nighttime. Normalizing the diurnal cycles, as mentioned above, reveals a much less pronounced variability for organics (65 %), implying a more regional character, while BC and nitrate exhibit the highest variability (67.7 % and 77 %, respectively) in accordance with their local nature. The nighttime maxima of BC vanish, while nitrate shows much lower concentrations, due to nitrate partitioning be- tween the gas and aerosol phase, favoring the vaporization of ammonium nitrate. BC still only exhibits one maximum during the early morning hours owing to traffic emissions. The ammonium and sulfate diurnal profile follows expected photochemistry patterns, with peaking

concentrations around 14:00 LT (UTC + 02:00); this is consistent with secondary aerosol formation and increased vertical mixing with regional aerosol from aloft due to the evolution of the convective boundary layer which exhibits a bell shaped diurnal structure ranging from a few hundred meters to above one kilometer, with maximum heights during early afternoon (Asimakopoulos et al., 2004; Tombrou et al., 2007). Finally, the concentrations of organics are somewhat higher during the early nighttime which could possibly be associated with either local or regional biogenic/vegetation sources that pro- duce volatile compounds and condense on the particulate phase during nighttime when temperatures are lower, as is further elaborated on during the source apportionment results discussion in **Sect. 4.3.3**. Furthermore, the variation of organics also follows the late afternoon peak observed for ammonium and sulfate. Condensation of the particulate phase could apply for nitrate as well, as this species also exhibits higher concentrations during nighttime (almost double).

4.3.3 Source apportionment of organic aerosol

The warm period: in this period, the selected solution stems from a two-factor constrained run (HOA using $\alpha = 0.05$ and COA using $\alpha = 0.1$) and consists of four factors: HOA, COA, SV-OOA, and LV-OOA. As previously mentioned, the two summer periods were treated separately, but the spectra derived were almost identical (r^2 ranging from 0.98 to 0.99). The time series of the four identified sources during summer 2017 is shown in **Fig. 4.5** along with their diurnal variability and the respective average hourly contribution. The mass spectra of the selected solution are also provided in the Supplement (**Fig. 10.12**). No primary biomass burning aerosol could be identified, which is justified by the absence of fresh emissions over the city center during the warm period. In the summer periods HOA makes up 4.3 % of the total organic fraction, while COA comprises around 10 % on aver- age (7.3 % and 11.3 % for 2016 and 2017, respectively). In summer 2016 SV-OOA made up 32 %, while the remaining 56 % was LV-OOA. In summer 2017, SV-OOA contributed 34.6 % to the total organic fraction, while LV-OOA made up 49.7 %. The dominance of the secondary influence (SV- OOA and LV-OOA) is apparent and accounts for the majority of the OA. This finding is in accordance with Kostenidou et al. (2015), who reported that 65 % of the sampled aerosol during summer could be attributed to SOA (SV-OOA and LV- OOA) at a suburban site in Athens.

A comparison of the derived FPs against mass spectra from the literature is shown in **Figs. 10.15–10.19** in the Supplement. COA FP exhibits excellent correlation with spectra obtained during previous studies in the city (Florou et al., 2017; Kostenidou et al., 2015) as well as with spectra obtained in laboratory experiments investigating fresh OA emissions from meat charbroiling (Kaltsonoudis et al., 2017). When calculating the O:C ratio in COA following the study of (Canagaratna et al., 2015) we find a ratio of 0.19, which is comparable with the value of 0.24 obtained for COA during summer at a suburban site in Athens (Kostenidou et al., 2015).

The HOA FP exhibits excellent correlation with spectra from the literature measured in cities located within the Mediterranean environment (Florou et al., 2017; Kostenidou et al., 2015; Gilardoni et al., 2016) as well as in other environmental and socioeconomic settings (Crippa et al., 2013; Lanz et al., 2007). According to **Fig. 10.18**, where the affinity of SV-OOA with literature spectra is assessed, some assumptions could be made regarding the origin of this factor: its similarity to isoprene-epoxydiol organic aerosol (IEPOX–OA), which is the oxidation product of isoprene, could denote a possible link between SV-OOA and biogenic aerosol. This association is further strengthened by considering the excel- lent correlation with SOA from biogenic precursors, such as α- and β-pinene reported by Bahreini et al. (2005) (r^2 of 0.86 and 0.89, respectively). These precursors are found to exhibit maxima during nighttime (Harrison et al., 2001; Hatch et al., 2011; Li et al., 2018) which coincides with the diurnal behavior of SV-OOA in this study. Conversely, a comparison of the derived SV-OOA with SOA from diesel exhaust after 4 h of photochemical ageing (Sage et al., 2008) yields an r^2 of 0.89. Finally, SV-OOA exhibits the lowest correlations with the mass spectrum from aged OA emissions from meat charbroiling (Kaltsonoudis et al., 2017). The abovementioned comparisons with literature FPs provide some indication that SV-OOA could be linked to SOA formation from the oxidation of volatile organic compounds (VOCs) from both biogenic and traffic sources during summer, and is not linked to the oxidation of primary COA. The low volatility component derived exhibits an excellent correlation with the very oxidized regional OOA found in the area (Bougiatioti et al., 2014) and a good correlation with deconvolved OOA factors from previous studies in Athens (Florou et al., 2017; Kostenidou et al., 2015). When calculating the elemental ratios based on the study of (Canagaratna et al., 2015), the O:C ratio for LV-OOA is 1.2, which is identical to the value of OOA obtained at Finokalia (Bougiatioti et al., 2014).

In terms of comparison with independent measurements, HOA exhibits good correlation with nitrate (r^2 = 0.62) as well as with BC_{ff} (r^2 = 0.63), while COA, as expected, shows poor correlation with CO (r^2 = 0.33) and nitrate (r^2 = 0.36). SV-OOA is highly correlated with nitrate (r^2 = 0.86), implying common mechanisms in their variability, which is possibly linked with the partitioning between the gas and particulate phases. The poor correlation with CO (r^2 = 0.4) and BC (r^2 = 0.35) implies that SV-OOA may, to some ex- tent, partially originate from a combustion source. LV-OOA shows good correlation with sulfate (r^2 = 0.62) and ammonium (r^2 = 0.63), which is consistent with the regional character of this factor. Results from the trajectory cluster analysis (**Fig. 10.21**) show that enhanced LV-OOA levels are related to air masses originating from eastern Europe and the Black Sea region, which have both been identified as the main areas of influence for secondary aerosols that are regionally processed and transported to Athens (Gerasopoulos et al., 2011; Grivas et al., 2018). The regional character of LV-OOA is confirmed by high concentrations associated with increased wind speeds (**Fig. 10.20**), especially those that originate from the northern sector. These results (presented in the **Fig. 10.20** for the full dataset) are in contrast to HOA which displays a much less diffuse spread, due to the intensity of local emissions (mainly traffic in the center of Athens). The distant signal of LV-OOA in the southeast direction could possibly be associated with processed aerosol derived from shipping activity (Petit et al., 2014) in the Aegean Sea.

Primary fossil fuel emissions (HOA) are very low during summer exhibiting a 5-fold decrease compared to the cold season; this is due to the fact that in July and August most of Athenians leave for their summer vacations, which reduces local traffic. Concentrations peak at around 07:00 and after 19:00 LT which corresponds to the early morning and evening rush hours in downtown Athens. COA exhibits a slight hump during the lunchtime hours (13:00–15:00 LT) when concentrations rise to 65 % of the daily COA average after the morning minimum of around 50 % (also seen in the relative contribution of the factor), while a large nighttime peak is present at around 22:00 LT. This late peak, which is three times higher than the daily average value, is consistent with the late dinner hours and the operation of grill houses and restaurants in central Athens. SV-OOA exhibits 40 % higher concentrations during nighttime compared with the SV-OOA daily average, which apart from boundary layer dynamics may also be attributed to the condensation of semi volatile compounds, as also implied by the excellent correlation of the factor with nitrate. During daytime, following the sharp decrease from the nighttime maxima,

concentrations remain close to 80 % of the daily average for some hours (10:00 to 14:00) before declining further in the afternoon. Finally, LV-OOA exhibits a peak during midday that is consistent with increased photochemical processes during the peak of solar radiation intensity (**Fig. 10.2**) which lead to further OA oxidation.

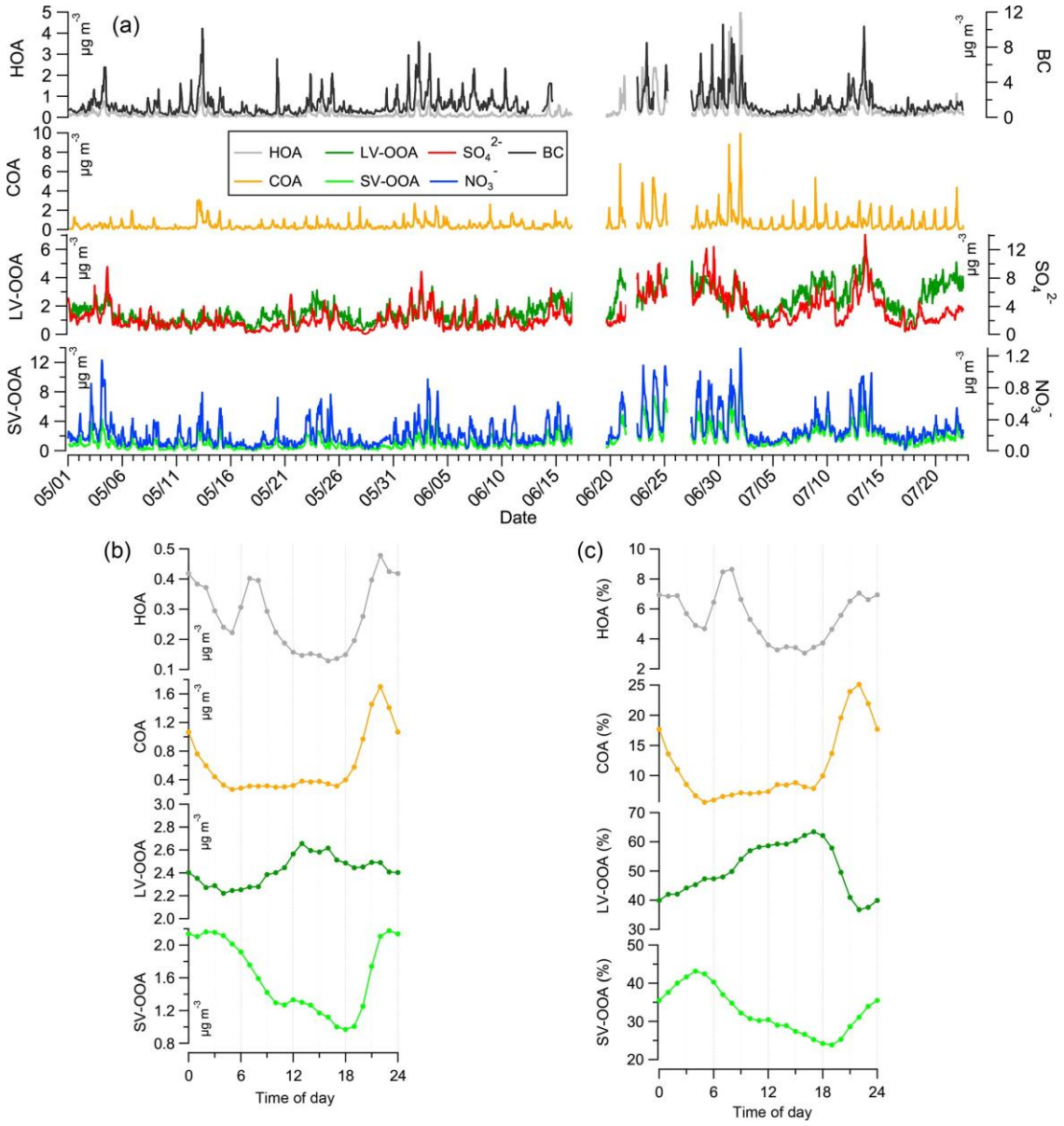

Figure 4.5. Time series of the contribution of the different factors identified by PMF between 1 May and 31 July 2017 (a) along with their average diurnal cycles (b) and the respective hourly average contributions (c).

In summary, during the warm period, the vast majority (more than 80 %) of OA in the area is linked to SOA formation. The semi-volatile product is of mixed origin and is linked to quick atmospheric processes (within a few hours), such as photochemistry of primary sources, like biogenic emissions from vegetation, traffic emissions, or probably to a lesser extent regional biomass burning. This last assumption could be supported by the fact that OOA linked to aged BBOA has been reported at regional background sites in Greece (Bougiatioti et al., 2014) and elsewhere (Minguillón et al., 2015), as well as by the fact that during the warm season, air masses which mostly originate from the north or northeastern sector, carry pollutants from the Balkans and around the Black Sea, which are areas that are heavily impacted by wildfires from July to September ((Sciare et al., 2008); **Fig. 10.21**). On the contrary, the low-volatility product is the result of more extensive oxidation of OA in the area, within a few days, and thus exhibits a more regional character.

The cold period: in this period, the selected solution stems from a three-factor constrained run (HOA using $\alpha = 0.1$, COA using $\alpha = 0.2$, and BBOA using $\alpha = 0.4$) and consists of five factors: BBOA, HOA, COA, SV-OOA, and LV-OOA. The solution for winter 2016–2017 is presented (**Fig. 4.6**), while the respective solutions for winter 2013–2014 and 2015–2016 are provided in the Supplement (**Fig. 10.13**). The time series of the five PMF factors for winter 2016–2017 are shown in **Fig. 4.6** along with their diurnal variability and the hourly contribution of each factor.

In terms of its affinity with RFPs found in the literature, HOA for the cold season in this study is found to exhibit excellent correlations with spectra obtained during the same season in earlier studies in Athens as well as other Greek cities (e.g., Patras; (Florou et al., 2017)) and also with HOA factors obtained in different environments, a fact also observed for the spectrum obtained in the warm season (**Fig. 10.15**). COA is excellently correlated with COA from (Florou et al., 2017) in both Athens and Patras as well as with COA measured by (Kaltsonoudis et al., 2017) (**Fig. 10.16**).

When calculating the elemental ratios based on the study of Canagaratna et al. (2015) the O:C ratio for COA is 0.18, which is in accordance with the value of 0.11 derived for COA at the same site by (Florou et al., 2017). BBOA exhibits a high correlation with factors from Zurich, Paris, and Finokalia as summarized in **Fig. 10.17**, while an excellent correlation is found when it is compared to BBOA found in Bologna, and earlier studies in Athens and Patras (Florou et al., 2017; Gilardoni

et al., 2016). Once more, the calculated O:C ratio for BBOA is 0.25, which is in accordance with the value of 0.27 derived for BBOA at the same site by (Florou et al., 2017). The SV-OOA spectrum exhibits a high correlation with the average SV-OOA from (Ng et al., 2011a), as well as with the IEPOX-OA from (Budisulistiorini et al., 2013) (r^2 = 0.80 in both cases), as isoprene's main oxidation products such as methyl vinyl ketone and methacrolein are often used as biomass burning tracers (Santos et al., 2018). A similar correlation is also found with IEPOX-OA and SV-OOA during the winter 2015–2016 campaign. The factor exhibits a high correlation with SV-OOA from wintertime in Paris (Crippa et al., 2013) and SV-OOA from Hyytiälä (Äijälä et al., 2017) (**Fig. 10.18**). Finally, LV-OOA records an excel- lent correlation with the LV-OOA from (Crippa et al., 2014), the average LV-OOA from (Ng et al., 2011a), LV-OOA from Zurich during winter (Lanz et al., 2007), and with the oxidized OOA found in the region (Finokalia) ((Bougiatioti et al., 2014); **Fig. 10.19**).

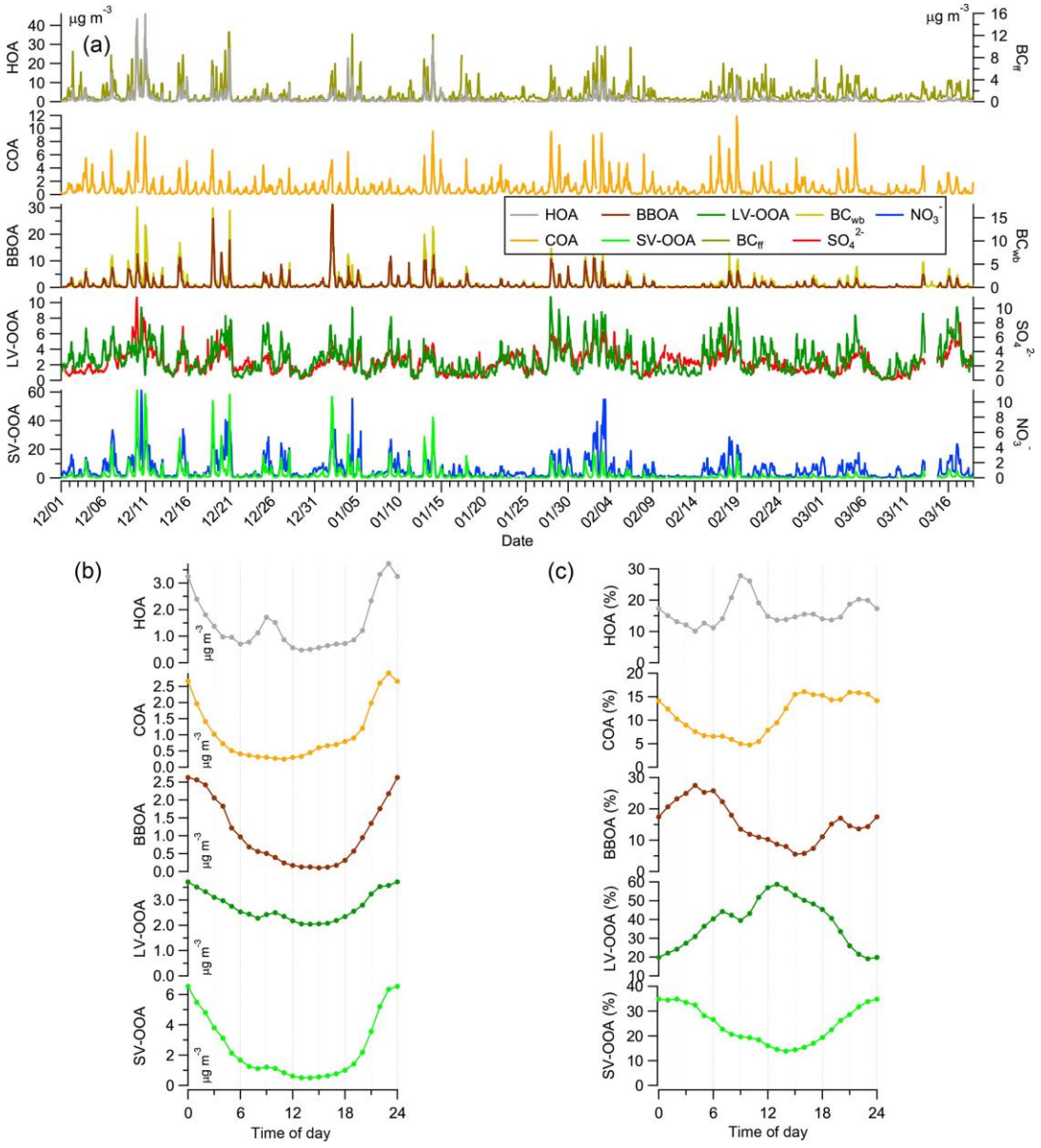

Figure 4.6. Time series of the contribution of the different factors identified by PMF between 21 November 2016 and 1 March 2017 (a) along with their average diurnal cycle (b) and respective hourly contribution (c).

The identification of BBOA is mainly based on the two fragments of m/z 60 and 73, considered as the "fingerprint" fragments of levoglucosan and biomass burning tracers. In- deed, BBOA exhibits an excellent correlation with these two fragments (r^2 = 0.94 and 0.9, respectively). Nss-K^+ is also proposed as a very good tracer for biomass burning and, as reported by Fourtziou et al. (2017), it shows a significant correlation with BC from wood burning (BC_{wb}), during wintertime

in Athens. Consequently, the time series of nss-K^+ provided by the PILS-IC and m/z 60 are studied together.

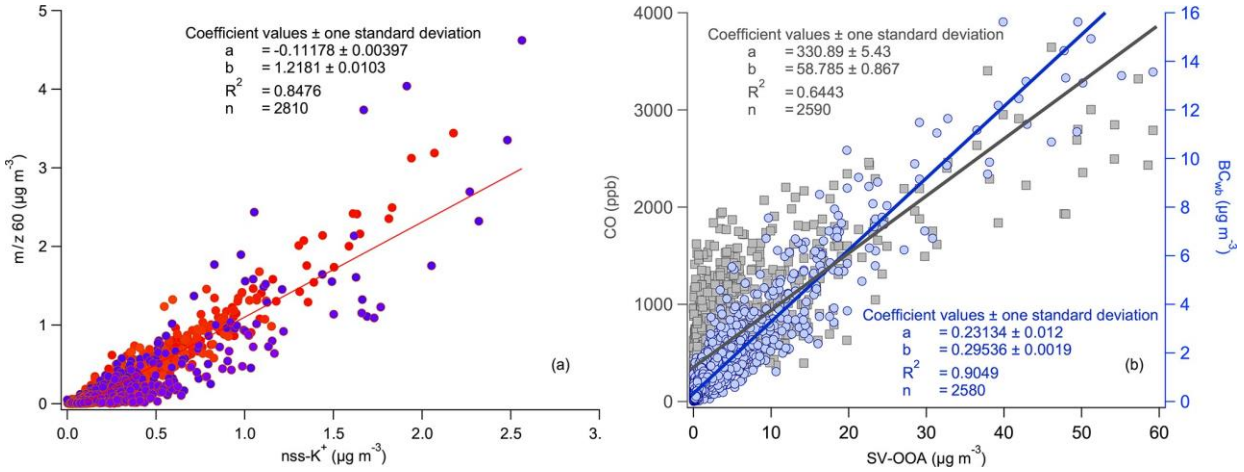

Figure 4.7. (a) The correlation of m/z 60 with nss-K^+ for 2013–2014 (red) and 2016–2017 (blue), and (b) the correlation of SV-OOA with CO (grey) and BC (blue) for 2016–2017.

It appears that during both winters (2013–2014 and 2016– 2017) for which nss-K^+ data is available, m/z 60 is in very good agreement with nss-K^+ (r^2 = 0.85; **Fig. 4.7a**). Furthermore, BBOA is highly correlated with BC_{wb} (r^2 = 0.77), and exhibits a good correlation with nss-K^+ (r^2 = 0.55) and CO (r^2 = 0.51). SV-OOA correlates excellently with both wood burning "fingerprint" fragments of m/z 60 and 73 (r^2 = 0.99 for both), highly with BC_{wb} (r^2 = 0.90) and CO (r^2 = 0.73) (**Fig. 4.7b**), and it exhibits a good correlation with nss-K^+ (r^2 = 0.55); this demonstrates the direct link between SV-OOA and primary combustion sources (mainly biomass burning; **Table 10.2**). It can be seen in **Fig. 10.21** that increased concentrations of both BBOA and SV-OOA are linked to air masses originating from northern and eastern Europe. During wintertime, these flow categories are associated with the prevalence of synoptic-scale northern winds and a decline in temperature in the area, leading to the appearance of PM episodes due to local combustion for residential heating (Paschalidou et al., 2015). The input of local sources confined in the Athens basin and in the vicinity of the sampling site is indicated by results of the wind analysis presented in **Fig. 10.20**. Markedly enhanced levels are associated with weak or stagnant conditions. These results are in contrast with those of Grivas et al. (2018) from a moderately populated area in the eastern part of the basin. They found that local biomass burning emissions played a less important role than advections from the northern part of the area. In the present case, in the densely populated center

of Athens this effect is less apparent. The local character of wood burning aerosols in dense residential areas in Athens has also been indicated by (Argyropoulos et al., 2017).

Comparison of the HOA time series with BC and CO yields good correlations (r^2 = 0.65 and r^2 = 0.65, respectively). The factor is consistently more well correlated with BC_{ff} than with BC_{wb} (e.g., for the 2016–2017 r^2 is 0.60 vs. 0.52, respectively). Correlation of COA with nss-K^+ and chloride ($0.3 < r^2 < 0.4$) could indicate a minor influence from emissions derived from biomass burning in meat cooking (Akagi et al., 2011; Kaltsonoudis et al., 2017). Finally, LV-OOA showed a good correlation with ammonium (r^2 = 0.58), nitrate (r^2 = 0.61), nss-K^+ (r^2 = 0.4), and m/z 73 (r^2 = 0.51), demonstrating that part of the very oxidized OA during wintertime may also originate from combustion sources.

Therefore, during the cold period, the OA in the area linked to SOA formation contributes around 65 % of the total organic fraction. In contrast to summer, the semi-volatile products seem to be linked to the fast oxidation of primary combustion emissions (e.g., BBOA), which is also reflected on its diurnal variability (**Fig. 4.6**) and in the strong correlations with external tracers of primary combustion (see **Table 10.2**). Affinity with biomass burning tracers highlights that the largest part of SV-OOA originates from the fast oxidation of BBOA. The low-volatility product is, in this case, likely of a more local than long-range transport nature, as also emphasized by the almost 2-fold higher values during nighttime.

The diurnal cycles of the five factors are shown in **Fig. 4.6**. HOA, originating from fossil fuel combustion, exhibits maximum values during nighttime, associated with combustion from central heating, and presents a secondary peak at 09:00 coinciding with the early morning traffic rush hour. The as- sociation of the factor with local primary emissions is also corroborated by the wind analysis plots (**Fig. 10.20**). The dependence of HOA on wind speed and direction is simi- lar between cold and warm seasons. The concentration vs. wind speed distribution displays a wind dilution effect and is characteristic for traffic-related fine particles in Athens (Chaloulakou et al., 2003; Kassomenos et al., 2012).

COA has similar winter and summer diurnal profiles that display a moderate hump, with concentrations rising from 30 % (0.3 μg m^{-3}) to 60 % (0.6 μg m^{-3}) of the daily average (0.98 μg m^{-3}) during the lunchtime hours (12:00–15:00 LT) and a large nighttime peak (at approx. 22:00 LT); this is partly controlled by the decrease of the planetary boundary layer, but is also owing to

the expected increase in the activity of numerous restaurants in the area. A similar diurnal cycle for COA was reported by Florou et al. (2017). BBOA is characterized by a pronounced diurnal cycle with peaking values during nighttime, associated with the production of this component in the evening by combustion for heating purposes. SV-OOA exhibits the largest diurnal amplitude, with nighttime values that are almost 6-fold higher compared to daytime. A plateau, with concentrations of SV-OOA around 50 % of the daily average value, following the sharp decline after midnight, is observed during the morning traffic rush hour, before another decline occurs until the daily minimum is reached at 14:00; this demonstrates the possibility of the factor's provenance from the oxidation of freshly-emitted primary combustion OA. Finally, LV-OOA also exhibits 2- fold higher values during nighttime compared with daytime. It has similar behavior to the SV-OOA factor, with a secondary peak at 10:00, exhibiting a 1 h lag after the morning traffic rush hour; this once again shows that part of the low volatility OA may also originate from the fast oxidation of primary combustion emissions, as also implied by its correlation with combustion tracers.

Table 4.2. Contribution of the five organic aerosol components to the total organic fraction during the three individual winter campaigns.

	Winter 2013–2014 (18 Dec. 2013–21 Feb. 2014)	Winter 2015–2016 (23 Dec. 2015–17 Feb. 2016)	Cold 2016–2017 (1 Nov. 2016–18 Mar. 2017)
BBOA	12.4 %	8.9 %	11.9 %
HOA	12.2 %	9.7 %	16.4 %
COA	10.4 %	8.1 %	11.7 %
SV-OOA	19.8 %	17.7 %	28 %
LV-OOA	45.2 %	55.6 %	32 %

Table 4.2 sums up the contribution of each one of the five identified factors during the three winters studied. Overall, during wintertime BBOA constitutes around 10 % of the total organic fraction. Based on the diurnal variability of this factor, its contribution is more pronounced during nighttime, when concentrations are 4-fold or higher than the daytime values, matching emissions from fossil fuel combustion rep- resented by the HOA factor incorporating both traffic and heating oil combustion. Even though an exact mechanism is yet to be established, our assumption that the

larger part of the SV-OOA comes from the rapid oxidation of freshly emitted BBOA through processes which involve nitrate radicals and/or heterogeneous reactions, appears justified by the excellent correlations with biomass burning tracers as well as by considering similar assessments found in other studies (Bougiatioti et al., 2014; Cubison et al., 2011; Lathem et al., 2013). In this manner the overall contribution of biomass burning becomes even more significant. Given that SV-OOA contributes around 30 % to the organic mass, it is evident that during wintertime, biomass burning may contribute al- most half of the total OA, with this contribution reaching a maximum during nighttime. More specifically, for BBOA the lowest contribution during daytime is 5.5 %, whilst it reaches a maximum of 27.5 % during nighttime (**Fig. 4.6**). The same applies to SV-OOA with daytime minimum contribution of 13.8 % and a nighttime maximum of 34.9 %. It is also very important to note that even though the winter and summer mass spectra of SV-OOA have some similarities (r^2 = 0.83), there are also differences, especially in the origin of this com- ponent: during winter the majority of SV-OOA is linked to the oxidation of primary combustion sources, while during summer the absence of a significant correlation with BC or nss-K^+ implies the presence of different sources, both anthropogenic (but not biomass burning) and possibly biogenic.

4.4 Summary and conclusions

High temporal-resolution measurements were conducted for an entire year (plus two, 2-month, intensive measurement campaigns during wintertime) at an urban background site in Athens, using an ACSM, a PILS-IC system, and an Aethalometer, in addition to routine pollution measurements. During the 16-month measurement period, several pollution events with PM_1 concentrations reaching as high as 220 μg m−3 were recorded, all encountered during the night in wintertime. In these cases, organics contributed the largest fraction to the submicron particulate mass, with the overall contribution during wintertime reaching 50 %, followed by sulfate (∼ 20 %) and BC (∼ 14 %). On a typical winter day, organics, BC, and nitrate double their concentrations during nighttime. The increase of the first two can be attributed to emissions linked to domestic heating, while nitrate exhibits higher concentrations due to the combined effect of de- creased temperature and aerosol acidity, favoring partitioning in the aerosol phase. During summer, organics, BC, and nitrate concentrations are significantly lower, while sulfate and ammonium levels are increased. Organics are once more the main aerosol constituent contributing 46 %, followed by sulfate (30.5 %), ammonium (8.3 %), and BC (8 %). On a typical summer day, ammonium and sulfate

concentrations peak at about 14:00 LT (UTC + 2), which is consistent with secondary aerosol formation. Organics, nitrate, chloride, and BC exhibited a clear seasonal cycle with a maximum during winter and a minimum during summer. Sulfate and ammonium exhibited an opposite cycle as the result of enhanced photochemistry, limited precipitation, and higher regional transport.

Based on the source apportionment of the OA, four fac- tors were identified during summer, namely HOA, COA, SV-OOA, and LV-OOA, and five factors during winter, the same as in summer with the addition of primary biomass burning emissions (BBOA). During summer, HOA made up 4.3 % of the total organic fraction, COA comprised around 10 %, and the rest was linked to secondary organics (SV- OOA and LV-OOA). HOA had peak values during the morning traffic rush hour, and COA mainly peaked during night-time. SV-OOA exhibited 2-fold higher concentrations during nighttime while LV-OOA exhibited a peak during midday, which is consistent with photochemical processes. The semi volatile product was clearly of mixed origin, was linked to quick atmospheric processing (within a few hours) of VOCs emitted from primary sources like vegetation, traffic, and to some limited extent to processed regional biomass burning. The low-volatility product, in contrast, was the result of more excessive oxidation, in the order of several days, and thus has a more regional character.

Combining the results from the three different winter campaigns, HOA accounts for almost 13 % of the organic fraction, COA for around 10 %, BBOA for 10 %, SV-OOA for 22 %, and LV-OOA for 45 %. All constituents exhibit significantly higher concentrations during nighttime, with HOA also being linked to primary emissions by heating oil combustion from central heating units and presenting a secondary peak during the morning traffic rush hours. COA has a similar diurnal profile to that observed during summer. BBOA is also characterized by a pronounced diurnal cycle with peaking values during the night from combustion for heating. SV-OOA has almost 6-fold higher concentrations during nighttime, consistent with its link to the oxidation of primary combustion sources, while even LV-OOA exhibits almost 2- fold higher concentrations during nighttime. In contrast to summer, the semi-volatile product during winter has a very clear origin, which is linked to the fast oxidation of primary combustion sources (HOA and BBOA); BBOA is the major source, due to the affinity of SV-OOA with biomass burning tracers. Part of the LV-OOA could also originate from the extensive oxidation of the local primary combustion sources, which shows that LV-OOA is of more local than regional character during winter.

In summary, it is clear that OA constitutes a large fraction of submicron aerosol throughout the year in the urban environment of Athens. During wintertime, a large part of this OA, as high as 50 %, originates from combustion sources for heating purposes, such as biomass burning and diesel oil fueled central heating, causing significant air quality deterioration. The nighttime contribution of BBOA is 7-fold higher than that during the day, while the respective contribution of SV-OOA is increased by a factor of 2.6. Given that fine PM concentrations reach up to 220 μg m^{-3} during wintertime, the significance of the contribution of these sources to air quality degradation becomes even more striking, demonstrating the necessity for strategic, long-term mitigation actions.

5 Online Chemical Characterization and Sources of Submicron Aerosol in the Major Mediterranean Port City of Piraeus, Greece

Iasonas Stavroulas[1,2], Georgios Grivas[2], Eleni Liakakou[2], Panayiotis Kalkavouras[1,2], Aikaterini Bougiatioti[2], Dimitris G. Kaskaoutis[1,2], Maria Lianou[2], Kyriaki Papoutsidaki[1], Maria Tsagkaraki[1], Pavlos Zarmpas[1], Evangelos Gerasopoulos[2] and Nikolaos Mihalopoulos[1,2]

[1]Environmental Chemical Processes Laboratory, Department of Chemistry, 70013 Heraklion, Greece

[2]Institute for Environmental Research and Sustainable Development, National Observatory of Athens, 15236 Athens, Greece

Abstract

Port cities are affected by a wide array of emissions, including those from the shipping, road transport, and residential sectors; therefore, the characterization and apportionment of such sources in a high temporal resolution is crucial. This study presents measurements of fine aerosol chemical composition in Piraeus, one of the largest European ports, during two monthly periods (winter vs. summer) in 2018–2019, using online instrumentation (Aerosol Chemical Speciation Monitor—ACSM, 7-λ aethalometer). PMF source apportionment was performed on the ACSM mass spectra to quantify organic aerosol (OA) components, while equivalent black carbon (BC) was decomposed to its fossil fuel combustion and biomass burning (BB) fractions. The combined traffic, shipping and, especially, residential emissions led to considerably elevated submicron aerosol levels (22.8 μg m^{-3}) in winter, which frequently became episodic late at night under stagnant conditions. Carbonaceous compounds comprised the major portion of this submicron aerosol in winter, with mean OA and BC contributions of 61% (13.9 μg m^{-3}) and 16% (3.7 μg m^{-3}), respectively. The contribution of BB to BC concentrations was considerable and spatially uniform. OA related to BB emissions (fresh and processed) and hydrocarbon-like OA (from vehicular traffic and port-related fossil fuel emissions including shipping) accounted for 37% and

30% of OA, respectively. In summer, the average PM_1 concentration was significantly lower (14.8 μg m^{-3}) and less variable, especially for the components associated with secondary aerosols (such as OA and sulfate). The effect of the port sector was evident in summer and maintained BC concentrations at high levels (2.8 μg m^{-3}), despite the absence of BB and improved atmospheric dispersion. Oxygenated components yielded over 70% of OA in summer, with the more oxidized secondary component of regional origin being dominant (41%) despite the intensity of local sources, in the Piraeus environment. In general, with respect to local sources that can be the target of mitigation policies, this work highlights the importance of port-related activities but also reveals the extensive wintertime impact of residential wood burning. While a separation of the BB source is feasible, more research is needed on how to disentangle the short-term effects of different fossil-fuel combustion sources.

5.1 Introduction

Health studies in recent years definitively implicated fine aerosols in a causal relationship with mortality and cardiovascular effects, both for long-term and short-term exposures (Atkinson et al., 2014; Di et al., 2017). The EU addressed the long-term exposure concern in the 2008/50/EC EU directive on air quality and cleaner air for Europe, enforcing an annual $PM_{2.5}$ limit value. A decade later, while $PM_{2.5}$ is recognized as the regulatory pollutant with the strongest link to premature mortality (379,000 excess cases in EU-28 during 2018) (European Environmental Agency, 2020), its annual mean levels in Europe are on the decline due to wide-ranging legislative action to curb emissions of particulate matter (PM) and its precursors (Hammer et al., 2020). However, EU air quality standards do not consider the issue of short-term exposure to fine PM, thus they are not aligned with existing scientific knowledge, and hamper the ability of air quality management authorities to implement direct action plans targeted at local sources. In this framework, it is clear that reliable solutions are needed to monitor and characterize on a continuous short-term basis, not only the levels, but also the chemical composition and sources of fine aerosols. There is mounting evidence that their chemical components (e.g., black carbon—BC, organic aerosol—OA, and sulfate), as well as their sources, are explicitly linked to short-term effects (mortality, cardiovascular hospital admissions and emergency department visits) (Basagaña et al., 2015; Kim et al., 2015; Lippmann et al., 2013; Ostro et al., 2016). Therefore, information provided by online

instruments for the chemical characterization and source apportionment of fine aerosols, such as the Aerosol Chemical Speciation Monitor (ACSM), is invaluable.

Notwithstanding the aforesaid improvement in urban air quality in the EU, particle pollution remains a serious issue in areas that confront strong socio-economic challenges, being disproportionately burdened by local emissions (Kheirbek et al., 2013; Martenies et al., 2017). Port cities are a good example of this (Burwell-Naney et al., 2017; Rosenbaum et al., 2011), since they gather PM-emitting activities from diverse sectors (e.g., passenger and commercial shipping, the vehicular sector including goods transport, drayage and cargo handling, the residential and tourism sectors). Moreover, port areas frequently neighbor industrial zones, and also tend to be inhabited by lower-income citizens (Fredrickson, 2013; Houston et al., 2008).

Port-related sources, including shipping and the associated road and commercial activity, directly affect air quality in port cities (Donateo et al., 2014; Merico et al., 2020; Viana et al., 2014). The deterioration of air quality and effects on health and welfare are sustained in these areas and beyond, since operations of a large port can have an impact at a distance of many kilometers (Grivas et al., 2018). In recent years, there was targeted action by international organizations (IMO, USEPA, EU) to reduce maritime emissions and control air pollution in coastal areas. Coordinated EU policies, including the reduction in the sulfur content in marine fuels (Sulfur Directive 2012/33/EU) and the adoption of emission control zones (North and Baltic Sea, but not yet the Mediterranean), have led to reductions in SO_2 concentrations in European coastal cities (Merico et al., 2021; Sorte et al., 2020), and there are plans for expanding the strategy to also consider PM. In this context, port cities are focal points for the development of air quality management plans that require detailed knowledge on the variability, composition and sources of pollutants. According to the European Sea Ports Organization (ESPO), air quality is the top environmental priority in two thirds of 97 major EU ports (Darbra et al., 2020).

Piraeus, a port city in the Eastern Mediterranean, can be seen as a characteristic case where air quality is a pressing issue for the protection of residents, commuters and tourists (Tzannatos, 2010). Piraeus has been the busiest commercial port in Europe for over 10 years. Furthermore, during the last decade, Piraeus has evolved into the second busiest container port in the Mediterranean (Grivas et al., 2019). The central Piraeus area, where shipping and commercial activities are concentrated, is traversed by high-traffic roads (Kassomenos et al., 2014). Moreover,

the population density in Piraeus is one of the highest in the Greater Area of Athens (GAA), resulting in additional emissions from residential heating. More specifically, residential wood burning (RWB) has emerged as a major environmental pressure in the GAA during the last decade (Liakakou et al., 2020b; Theodosi et al., 2018) and Piraeus is not an exception, with recent research reporting excessive nighttime aerosol levels in winter (Grivas et al., 2019). Several studies examined the variability of regulatory pollutants in Piraeus over the years, recognizing the area as one of the most heavily impacted by particle pollution in the GAA (Grivas et al., 2008; Kassomenos et al., 2012, 2014). However, information on the chemical composition and aerosol sources in Piraeus is very limited and outdated (Siskos et al., 2001; Thomaidis et al., 2003).

In general, there are numerous studies on the chemical characterization and source apportionment of fine aerosols in port areas using offline filter sampling (Cesari et al., 2014; Pandolfi et al., 2011; Pérez et al., 2016). Their results are useful for determining aerosol types and source contributions on a long-term basis, but do not often provide detailed information on emission patterns of sources that induce short-term variations, and this limits their applicability in designing intervention policies. Online chemical composition measurements (coupled with source apportionment in high resolution) can address this need, but such results are not abundant in the case of port cities, especially in the Mediterranean (Chazeau et al., 2021; Mohr et al., 2012). Various studies using aerosol mass spectrometry near major ports noted the potential effect of shipping emissions. Lu et al. (2006) used an aerosol mass spectrometer (AMS) in the port of Vancouver to identify and characterize the effect of ship plumes, indicating similarities between mass spectra recorded inland and reference ship stack-exhaust spectra. On the contrary, the source apportionment study of Dall'Osto et al. (2013), near the shipping berths of the port of Cork, Ireland, by combining data from aerosol time-of-flight mass spectrometry and high-resolution AMS, reported shipping emissions to be associated with a processed OA component. Schulze et al. (2018) likewise showed that offshore shipping emissions were sensed as oxidized OA at a receptor site in the Texas Gulf Coast Area near Houston. However, Al-Naiema et al. (2018), with the use of high-resolution measurements at the Houston Ship Channel and various receptor modelling methods, highlighted the diversity of local sources that contributed to fine aerosols in a major port city, with shipping emissions ac-counting for a relatively small OA fraction. In order to discern between fine aerosol im-pacts from various activities in a port city, Shah et al. (2018) performed mobile AMS measurements in Oakland, verifying significant source-related diurnal and spatial patterns and

highlighting the impact of port-related vehicle emissions. Overall, it appears that unravelling the contributions of shipping emissions from those of general fossil-fuel combustion sources is a strenuous task, and more data from field studies are needed in order to better understand these constraints.

The present study attempts to address the identified knowledge gaps and provides insights in the temporal variability—at various scales—of major fine aerosol components and contributions of carbonaceous aerosol sources. Online instrumentation (ACSM and 7-λ aethalometer) was installed at a central site, close to the passenger–port terminals, monitoring during two distinct sampling periods in 2018–2019 (winter—strong residential heating emissions; summer—increased passenger–port activity). The temporal variability of the major aerosol components was statistically assessed, also against external tracers and meteorological parameters. PMF source apportionment was performed on the ACSM organic spectra to quantify OA components (primary and oxidized). Their temporal patterns along with those of source-specific BC components were examined and supplemented with wind and air-mass back-trajectory analysis for the identification of source areas. This is one of the first studies utilizing aerosol mass spectrometry data for source apportionment in a major Mediterranean port city. Apart from the results that can guide air quality management and mitigation scenarios in Piraeus and other port cities in the Mediterranean, the analysis reveals the complexity and challenges of aerosol chemical characterization and source apportionment in port areas, and advocates for specialized research on the topic.

5.2 Study Area and Methods

5.2.1 Study Area and Measurement Site

The port area of Piraeus (**Figure 5.1a**) is found in the southwestern part of the GAA, on the shore of the Saronic Gulf (Aegean Sea in the Eastern Mediterranean). The area is bounded to the northwest by Mt. Aegaleo, which separates the Attica basin from the Thriassion plain. The municipality of Piraeus has a population of 164,000 (~15,000 per km^2), while the Regional Unit of Piraeus, which includes 4 surrounding municipalities, hosts 450,000 inhabitants (~9000 km^{-2}).

The central Piraeus area is developed around the passenger port that serves over 12 million people per annum travelling on coastal and cruise liners. The commercial port activities are concentrated

to the west, mostly around three large container terminals in the area of Keratsini. A large part of the HDV (heavy-duty vehicles) traffic, carrying freight between the port and the E75 international roadway that reaches Piraeus to the east, traverses the city center, and aggravates the already heavy local traffic. Several dockyards are located further to the west in the area of Perama, while oil tanker traffic is mostly routed to the Gulf of Eleusis to the northwest, where two large refineries operate. There are no major industries in the area of Piraeus but a few secondary industrial installations across the coast (mainly tank farms) and to the northwest (industrial area of Rentis) (Siskos et al., 2001). On the contrary, most of the industrial activity in the GAA is concentrated in the Thriassion Plain, 10–20 km to the northwest of Piraeus (Manalis et al., 2005).

The area is characterized by a typical Mediterranean climate (mild winters, warm dry summers), moderated by the coastal environment. The effect of the sea/land breeze system from the Saronic Gulf cell is present throughout the year, but is far more prevalent in the summer, with strong onshore flows observed during the day (typically exceeding 6 m s^{-1} around noon), also exhibiting a large vertical extent. This daytime pattern is typically combined with weak northerlies or calms during the night (Kallos et al., 1993; Kassomenos et al., 1998). Strong synoptic-scale N-NE advections are most frequent during winter over the GAA and blow over day and night, while in summer, the northern Etesian wind regime often prevails in the daytime. These northern winds usually contribute to atmospheric clearance and the improvement of air quality (Pateraki et al., 2010), but it is possible that they also transport pollutants to Piraeus from in-land (Attica Basin).

Measurements at the central site in Piraeus (P1, **Figure 5.1b**) were conducted during two season-specific monthly periods: winter (10 December 2018–16 January 2019) and summer (11 June 2019–9 July 2019). The average temperatures during the two periods were 9.8 and 28.6 °C, respectively, indicating characteristic winter and summer conditions in the GAA. Online instruments (ACSM and 7-λ aethalometer) were placed at the building (1st floor) of the Athens Metro (Urban Rail Transport S.A., Athens, Greece) terminal station (**Figure 5.1b**; 37.9479 °N, 23.6429 °E, 10 m a.s.l.).

Figure 5.1. Overview of the Greater Area of Athens (GAA), highlighting the Piraeus port area and also the ancillary background measurement sites P2 (yellow circle) and THI (green circle) (a); measurement locations (P1—main site, PEI-1—roadside traffic site) in the center of Piraeus, near the passenger port (b). Source: Google Earth, 6 October 2021.

The sampling height was approximately 9 m above ground and the sampling manifold was at a distance of 1 m from the building façade. A sampler used for collection of 24 h filters was placed on the rooftop of the building (~20 m above ground). The site was expected to be influenced by traffic emissions, being at a distance of 70 m from the coastal avenue, which is adjacent to the ferry berths. Moreover, due to its central placement at a shipping and rail transportation hub, the site is also characterized by intense human and commercial activity.

5.2.2 Online Measurements

An aerosol chemical speciation monitor (ACSM, Aerodyne Inc., Billerica, MA, USA) was used to obtain near-real time (30 min resolution) data on the chemical composition of non-refractory submicron aerosols (NR-PM_1). The instrument sampled at a flow rate of 3.0 L min−1, through a PM_1 sharp-cut cyclone (SCC 1.109, BGI Inc., Waltham, MA, USA). The incoming air flow was dried using a Nafion membrane dryer placed upstream. The dryer was operated in purge vacuum mode, where the space between the outer wall of the Nafion membrane and the dryer enclosure was kept at a pressure below 0.4 atm using a vacuum pump, drawing already dried air from the ACSM's auxiliary flow exhaust. The ACSM measures concentrations of OA, sulfate, ammonium, nitrate, and chloride, by obtaining aerosol mass spectra with a quadrupole mass spectrometer,

following flash vaporization and electron impact ionization of aerosol sampled through an aerodynamic focusing lens (effective particle size range: 40–700 nm) (Liu et al., 2007). Concentrations were determined using a collection efficiency dependent on chemical composition but independent of RH as the inflow was dried to <60% (Middlebrook et al., 2012). The mean CE (dry) was 0.604 ± 0.150% and 0.499 ± 0.102% in winter and summer, respectively. Since the CE correction in a dried air-stream depends on the ammonium nitrate fraction, the observed seasonal contrast is reasonable in view of the very low ammonium nitrate levels in summer due to volatilization. The instrument participated successfully in the second ACTRIS inter-comparison campaign and was found well within the threshold for satisfactory performance (Freney et al., 2019). Further details on the methodology, operating procedures, maintenance, calibration and data validation can be found in (Ng et al., 2011b) and (Stavroulas et al., 2019), the latter specifically for ACSM measurements in the GAA during 2013–2017. ACSM concentration outputs were averaged on an hourly basis (866 hourly values in winter and 484 hourly values in summer, respectively; a lower data capture rate in summer was due to some interruptions in the power supply of the instrument).

Black carbon (BC) concentrations were measured at a 1 min resolution using a 7-λ aethalometer (AE33, Magee Scientific, Berkeley, CA, USA) that sampled at an airflow of 5 L min^{-1}. The AE33 records light absorption coefficients at seven wavelengths in 370–950 nm, by measuring the light attenuation through particles deposited on a PTFE-coated glass-fiber filter tape (Part No. 8060). BC concentrations are calculated at each wavelength (including at 880 nm for the equivalent concentration referred to as BC) using reference mass absorption efficiencies (MAE). A dual-spot measurement approach is followed by the AE33 to compensate internally for the "filter loading" effect (Drinovec et al., 2015), while a correction for multiple scattering, specific for the filter tape material, is also applied (Weingartner et al., 2003). The aethalometer inflow was not dried, but due to the short tubing used (<1 m indoors) and the PTFE-coated glass-fiber filter tape that has a low affinity for water vapor, relative humidity (**Figure 11.1**) artifacts were expected to be insignificant (Laing et al., 2020). Absorption Ångström Exponents (AAE) were calculated in the 370–950 nm range ($AAE_{370–950}$). Furthermore, through the implementation of the "Aethalometer model", the source-specific BC fractions at-tributed to fossil fuel combustion (BC_{ff}) and biomass burning (BC_{bb}) were calculated automatically by the instrument, under the assumptions of constant AAE values for aerosols from fossil fuel combustion (AAE_{ff} = 1) and biomass burning (AAE_{bb} = 2)

(Sandradewi et al., 2008). Data records with $AAE_{470–950}$ outside the 1-2 range were automatically truncated by the AE33 to 1 and 2, respectively. However, such data were very limited in our dataset (4 hourly values, 0.3% of BC data at P1 for the two periods combined). There are some uncertainties in considering spectrally independent AAE_{ff} and AAE_{bb} of 1 and 2. While pure black carbon is considered to be approximated by $AAE_{BC} = 1$, aging processes involving BC internal mixing (e.g., lensing effects in core–shell mixing) can lead to increased AAE_{ff} (Lack and Cappa, 2010), while such an increase is also possible due to the presence of brown carbon particles from fossil fuel combustion (Yuan et al., 2020). There are also studies examining the stability of the $AAE_{bb} = 2$ assumptions, with varying results (Rajesh et al., 2021). While it is fairly common to present the AE33 BB% estimates "as is", these uncertainties should be kept in mind (a detailed discussion can be found in (Kaskaoutis et al., 2021a)). All data deriving from aethalometer measurements were subsequently averaged hourly (887 and 652 values in winter and summer, respectively).

5.2.3 Offline Measurements and Auxiliary Data

Chemical composition measurements were performed, in parallel with online measurements, on $PM_{2.5}$ quartz-fiber filters collected every day (midnight-to-midnight), using a reference-equivalent low-volume sampler (Derenda LVS-PNS-15; Comde-Derenda, Stahnsdorf, DE, USA). Organic and elemental carbon (OC and EC) were quantified from filter punches using a thermal/optical Sunset carbon analyzer (Sunset Laboratories Inc., Portland, OR, USA), according to the EUSAAR-II protocol (Cavalli et al., 2010). Nanopure water extracts were analyzed using an ion chromatography system (Dionex DX-500, Thermo Fisher Scientific Inc., Waltham, MA, USA) for major cations and anions, including sulfate, nitrate, ammonium, and chloride (Paraskevopoulou et al., 2014). The results from filter-based analyses were used to assess the quality of ACSM measurements for OA and major ions. The covariance between EC and BC was also explored.

Additional data on hourly concentrations of regulatory pollutants (nitrogen oxides, sulfur dioxide, benzene, ozone, $PM_{2.5}$, as well as CO that was available only in the summer period) were obtained from a monitoring site (PEI-1) of the National Air Pollution Monitoring Network, 400 m to the southeast (37.9447 °N, 23.6452 °E, 4 m a.s.l.). This roadside traffic site is known to have recorded some of the highest levels of traffic-related pollutants in the GAA over the years (Grivas et al.,

2008). Meteorological data (temperature, relative humidity, wind speed-direction) were also monitored at a nearby station (2 km to the south) in central Piraeus.

AE33 measurements (including BC_{ff}, BC_{bb} estimates) were also available for the same periods at the National Observatory of Athens (NOA) Thissio urban background monitoring site (THI, green marker in **Figure 5.1a**) in central Athens (37.9732 °N, 23.7180 °E, 105 m a.s.l.), and were used to assess the spatial homogeneity of levels. Details on AE33 long-term measurements at THI can be found elsewhere (Kaskaoutis et al., 2021a; Liakakou et al., 2020b). Moreover, BC concentrations were measured at a secondary background location in the area of Piraeus (P2, yellow marker in Figure 1a) using a Multi-Angle Absorption Photometer (MAAP, Thermo Fisher Scientific Inc., Waltham, MA, USA), installed in the NOA mobile air quality monitoring station. The station's location was 2.1 km to the west of P1 (37.9461 °N, 23.6191 °E, 21 m a.s.l.) and can be considered representative of background conditions in the port area, as it is at least 200 m away from major roads and residential blocks, and also upwind of passenger-port emissions. The MAAP sampled at 16.7 L min^{-1} through a $PM_{2.5}$ inlet (at a sampling height of 5 m), determining equivalent BC concentrations at 637 nm. The agreement of MAAP measurements (637 nm) with those of a collocated AE33 (at the nearest wavelength: 660 nm) was demonstrated previously at THI, with r^2 > 0.75 and slope close to unity (1.15) (Liakakou et al., 2020b). Such differences in BC estimates from the MAAP and multi-wavelength aethalometers were occasionally reported (Chow et al., 2009), mainly due to the different way of multiple scattering compensation (by measurement in the MAAP and using a C coefficient in aethalometers) and also because there is no correction for filter loading in MAAP data. These differences tend to become significant for high BC concentrations (e.g., > 9 μg m^{-3}) where the MAAP response is no longer linear (Hyvärinen et al., 2013). In view of this, we excluded MAAP values higher than 9 μg m^{-3} from our analysis (36 hourly values in total, observed only in winter). The MAAP measurements at P2 were compared with those at P1 (BC_{660nm}) to establish the "urban" enhancement of BC concentrations in Piraeus (ΔBCu). It should be noted that in case of an AE33/MAAP slope of 1.15 as mentioned above, mean ΔBCu calculations could have an uncertainty in the area of 20% in both winter and summer periods.

The impact of wind circulation and transport from sources at the local/medium spatial scale was assessed using bivariate polar and annular (assessment of the diurnal variability) wind plots, as

well as wind plots for the conditional probability function (CPF) that a fractional source contribution associated with specific wind vectors would exceed a predefined percentile threshold (Petit et al., 2015; Uria-Tellaetxe and Carslaw, 2014). To assess the impact of remote sources and long-range transport, five-day air mass back-trajectories, arriving in Piraeus at 750 m every one hour, were computed using the Hybrid Single Particle Lagrangian Integrated Trajectory (HYSPLIT) model (Stein et al., 2015) and GDAS (Global Data Assimilation System) meteorological data fields at a 1° resolution. The PSCF (Potential Source Contribution Function) (Dimitriou and Kassomenos, 2017) technique was implemented to assess the origins of chemical components and source contributions for which a regional influence was expected, using the Zefir software (Petit et al., 2017) developed for the Igor Pro data analysis suite (Wavemetrics Inc, Portland, OR, USA).

5.2.4 Source Apportionment of Organic Aerosol

The mass spectra acquired by the ACSM for the organic fraction of submicron aerosol were analyzed in order to distinguish between different OA sources and formation processes, using Positive Matrix Factorization (PMF). In this context, the multilinear engine algorithm (ME-2) (Paatero, 1999) was used, as implemented in the SoFi 6.1 (Datalystica Ltd., Villigen, Switzerland) package (Canonaco et al., 2013) that runs within Igor Pro. The PMF bilinear model is a factor-analytic, data reduction approach that also includes non-negativity constrains in its matrices and utilizes measurement uncertainties in its solution. Through PMF, the measured OA time series can be represented as a linear combination of static mass spectra (factor profiles—FPs) and time series of respective factor contributions. A more detailed theoretical overview of the PMF model can be found in **Section 11.1.1** in the Supplementary Materials. Variables up to m/z = 125 were retained in the PMF analysis. Variables with a low signal-to-noise ratio or duplicates due to the fragmentation table settings (Allan et al., 2004) and their respective errors were treated to downweigh their contribution to the PMF solutions (Ulbrich et al., 2009).

In this study, an OA source apportionment strategy similar to the one described by (Stavroulas et al., 2019) was adopted, based on the guidelines proposed in previous studies (Crippa et al., 2014) and adapted accordingly to the specifics of the examined site. In brief, PMF was initially performed for a range of 3 to 8 factors without any constrains to the factor profiles (FP), thus acquiring a first estimate on the number of primary and secondary factors potentially present in the dataset.

Subsequently, constrains were introduced, implementing the a-value approach (Canonaco et al., 2013) to the primary organic aerosol (POA) factors. A detailed de-scription of the applied PMF strategy can be found in **Section 11.1.2** (**Figures 11.2–11.5, Table 11.1**) in the Supplementary Materials. In brief, first the traffic-related hydrocarbon-like organic aerosol (HOA) factor was constrained tightly ($0.02 < a < 0.2$). Since no evidence of a cooking organic aerosol (COA) factor could be identified (see scatterplot of f55 vs. f57 and discussion in **Figure 11.3**), only a biomass-burning organic aerosol (BBOA) factor was con-strained as a next step for the winter dataset, applying less strict a-values ($0.2 < a < 0.6$). For the summer dataset, a constrain was applied only for the HOA factor. No BBOA factor was identified in summer since the f_{60} contribution was mostly below 0.3% (Cubison et al., 2011), with the few points above this threshold mostly associated with signal-to-noise ratios below 2. The rest of resulting factors in both seasons, including secondary organic aerosol (SOA), were left unconstrained. All abbreviations used in the text are gathered in **Table 11.2** at the end of the Supplementary Materials.

The quality of model outputs (FPs and respective time series) was assessed by exploring performance metrics, e.g., solutions minimizing the Q/Q_{exp} ratio while limiting the magnitude and/or temporal structures in model residuals. Environmentally sound model solutions were determined by comparing resulting FPs to spectra found in the literature (Crippa et al., 2014, 2013; Florou et al., 2017; Ng et al., 2011a). The optimum combination of a-values applied, was determined by investigating the correlation between factor contributions and other source-specific tracers (Fröhlich et al., 2015).

5.3 Results and Discussion

5.3.1 Comparison of ACSM Data with Filter-Based Analyses

Scatterplots between daily-averaged online and offline measurements (and also the respective daily time series), for the two campaigns combined, are presented in **Figure 11.6**. The results displayed a very good agreement for sulfate and nitrate (r^2: 0.84 and 0.80, respectively) between the two methods (this was also valid for ammonium ions, but not for chloride due to the differences between the very fine non-refractory ammonium chloride measured by the ACSM and the coarser sodium chloride that participated in the $PM_{2.5}$ fraction). A very good correlation ($r^2 = 0.80$) was also found between OA and OC, with a slope of 1.63. It is expected that the actual OA concentrations in $PM_{2.5}$ would be slightly higher than those measured by the ACSM due to the

small amount of organic particles concentrated in the intermodal range (Pateraki et al., 2012). However, the obtained slope is rather indicative for OA/OC ratios (1.4–1.8), being reported for traffic-impacted urban sites (Chow et al., 2015). Black and elemental carbon daily average concentrations at P1 also correlated strongly (r^2 = 0.79), although BC recorded higher concentrations, possibly due to a contribution of non-EC light-absorbing particles, inadequate compensation for multi-scattering effects and a somewhat different mass absorption cross-section for aerosols in Piraeus compared to the default value used by the aethalometer (Liakakou et al., 2020b; Zanatta et al., 2016).

5.3.2 Composition of Submicron Aerosol and Black Carbon

5.3.2.1 Winter Period

Descriptive statistics for the main species are presented in Table 1. Mean diurnal cycles and time series of hourly concentration values are shown in **Figures 5.2** and **5.3**, respectively. The mean wintertime PM_1 concentration, calculated as the sum of ACSM components plus BC (Sun et al., 2014), was 22.8 μg m^{-3}. These concentrations were comparable and well-correlated with $PM_{2.5}$ measured concurrently at the PEI-1 traffic site (21.6 μg m^{-3}, r^2 = 0.88), indicating that local anthropogenic sources drove a substantial part of the variability at P1. Daily mean concentrations exceeded 25 μg m^{-3} (the WHO short-term guideline for fine particles) on 39% of the days in winter, with a maximum of 47 μg m^{-3} (including a nighttime 130 μg m^{-3} hourly value), highlighting the severity of short-term exposure in the center of Piraeus.

OA was the dominant component in wintertime, averaging 13.9 μg m^{-3} and contributing 61% to the estimated PM_1 mass. The mean contribution was comparable to those reported for successive winter periods during 2013–2017 at the urban background THI site (from 65% in winter 2013–2014 to 56% in winter 2016–2017) (Stavroulas et al., 2019), implying that it is not only vehicular traffic and port activity that regulates the excessive wintertime OA concentrations in Piraeus (reaching 90 μg m^{-3} on an hourly basis).

It is evident from the diurnal cycle of OA (**Figure 5.2a**) that its nocturnal levels were greatly enhanced, with peak hourly mean values recorded in the 23:00–3:00 timeframe. This is attributed to residential heating emissions coupled with the shallow wintertime boundary layer and low-wind conditions. The high wintertime levels of OA in Piraeus definitely exceed those reported at European and North American urban sites (e.g., Helsinki and Atlanta) (Barreira et al., 2021; Xu et

al., 2015), even where biomass burning was recognized as a major source (Zhang et al., 2019). Although period mean concentrations are lower compared to Chinese megacities such as Beijing and Nanjing (Sun et al., 2013; Zhang et al., 2015), their observed peaks during extreme haze episodes are in the same order of magnitude as the maxima in Piraeus.

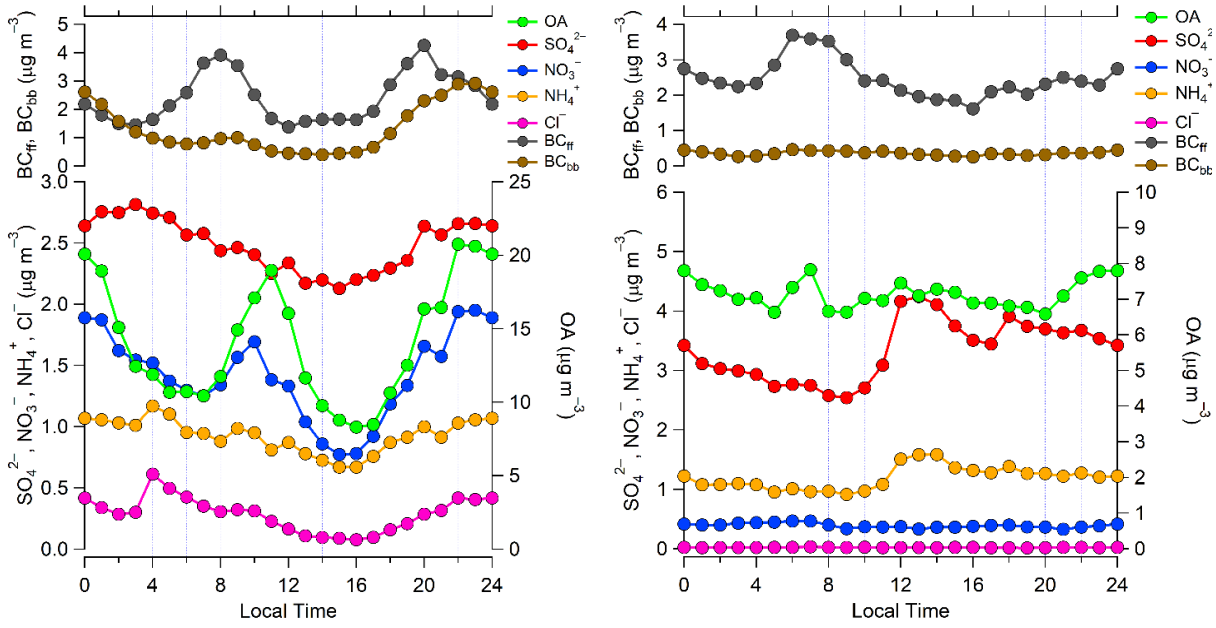

Figure 5.2. Mean diurnal cycles of the major submicron aerosol components (OA and ions from the ACSM, BC_{ff} and BC_{bb} from the aethalometer) for the winter (a) and summer (b) measurement periods.

Table 5.1. Descriptive statistics (arithmetic mean and min.-max. range in parentheses) for concentrations of ACSM non-refractory species, BC and its source-specific components, and PM1, in Piraeus. All values in μg m^{-3}. Day and night periods were defined as 06:00–18:00 and 18:00–06:00, respectively. The winter and summer measurement periods were 10 December 2018–16 January 2019 and 11 June–9 July 2019, respectively.

	Total	**Day**	**Night**	**Weekday**	**Weekend**
Winter					
OM	13.88 (0.41–89.56)	12.21 (1.10–58.90)	15.57 (0.41–89.56)	14.30 (0.41–89.56)	12.80 (1.10–88.03)
SO_4^{2-}	2.48 (0.01–9.19)	2.33 (0.01–7.14)	2.63 (0.11–9.19)	2.51 (0.01–9.19)	2.40 (0.01–7.60)
NO_3^-	1.40 (0.01–7.97)	1.19 (0.01–5.92)	1.62 (0.01–7.97)	1.44 (0.01–7.97)	1.31 (0.05–7.00)
NH_4^+	0.92 (0.14–4.56)	0.83 (0.14–3.74)	1.02 (0.14–4.56)	0.94 (0.14–4.46)	0.88 (0.14–4.56)
Cl^-	0.28 (0.01–6.13)	0.21 (0.01–4.07)	0.35 (0.01–6.13)	0.29 (0.01–6.13)	0.26 (0.01–4.49)
BC	3.72 (0.17–28.52)	2.96 (0.32–17.24)	4.47 (0.17–28.52)	3.73 (0.17–28.47)	3.66 (0.34–28.52)
BC_{ff}	2.43 (0.01–18.63)	2.31 (0.22–13.92)	2.56 (0.01–18.63)	2.48 (0.16–18.63)	2.30 (0.01–15.49)
BC_{bb}	1.28 (0.01–13.65)	0.65 (0.04–3.56)	1.91 (0.01–13.65)	1.25 (0.01–13.38)	1.36 (0.01–13.65)
PM_1	22.75 (1.11–130.69)	19.76 (2.28–78.51)	25.76 (1.11–130.69)	23.29 (1.11–126.19)	21.33 (2.28–130.69)
Summer					
OM	7.14 (1.70–15.94)	7.11 (1.70–15.94)	7.16 (1.71–15.25)	7.63 (1.70–15.94)	6.15 (1.74–14.67)
SO_4^{2-}	3.32 (0.13–10.91)	3.29 (0.13–10.91)	3.35 (0.68–8.50)	3.47 (0.13–10.91)	2.95 (0.68–9.75)
NO_3^-	0.46 (0.04–1.69)	0.52 (0.04–1.69)	0.41 (0.05–1.32)	0.51 (0.04–1.69)	0.33 (0.05–1.22)
NH_4^+	1.20 (0.14–3.82)	1.22 (0.14–3.82)	1.18 (0.14–3.29)	1.26 (0.14–3.82)	1.04 (0.14–3.14)
Cl^-	0.03 (0.01–0.21)	0.04 (0.01–0.21)	0.02 (0.01–0.10)	0.03 (0.01–0.21)	0.02 (0.01–0.06)
BC	2.81 (0.28–11.82)	2.88 (0.39–11.82)	2.74 (0.28–11.71)	3.10 (0.37–11.82)	2.05 (0.28–11.71)
BC_{ff}	2.45 (0.04–10.39)	2.51 (0.04–10.39)	2.39 (0.14–10.36)	2.71 (0.04–10.39)	1.79 (0.23–10.36)
BC_{bb}	0.36 (0.01–1.90)	0.37 (0.01–1.90)	0.35 (0.01–1.86)	0.40 (0.01–1.90)	0.26 (0.03–1.35)
PM_1	14.78 (3.37–34.11)	14.69 (3.37–34.11)	14.84 (3.62–29.33)	16.02 (3.72–34.11)	12.26 (3.37–29.33

The diurnal cycle of OA was bimodal, which is not commonly observed even at urban sites, and differed from the unimodal cycle (nighttime maxima) recorded at the urban background THI site in past winters (Stavroulas et al., 2019). However, a similar bimodal cycle was observed for online OC measurements during the cold period at a traffic site in central Athens (Grivas et al., 2012). Comparing the OA diurnal profile to those of source-specific BC components (**Figure 5.2a**), it can be seen that BC_{bb} also reached a maximum in the same evening timeframe, highlighting the impact

of RWB emissions on OA levels. For the verification, OA was excellently correlated (correlation matrices provided in **Figures 11.7–11.9**) with BC_{bb} (r^2 = 0.91, slope: 6.20) during the night hours (18:00–6:00). It is noteworthy that very increased short-term OA levels with peak concentrations exceeding 50 μg m^{-3} were seen on six occasions, all nighttime episodes characterized by high BC_{bb} contributions (**Figure 5.3a**).

Conversely, BC_{ff} presented a typical traffic-related bimodal cycle, with levels peaking during morning and evening rush-hours. The latter peak was observed at 20:00, with concentrations decreasing afterwards (Mousavi et al., 2019), probably negating a significant impact from the residential use of heating oil. The BC_{ff} morning traffic peak was registered at 8:00, with levels starting to escalate from 5:00, indicative of commercial HDV traffic activity (Kimbrough et al., 2018) in the port area. While OA also presented a daytime maximum, its time of appearance was less consistent on a day-to-day basis, depending on the intensity of local sources (Minguillón et al., 2016) and suggested that the daytime OA source attribution should be more complex.

BC was a significant contributor to PM_1 mass in winter (16%) as it originated from a combination of car traffic, port-related and RWB sources, with its levels largely enhanced (51%) during the night hours (18:00–6:00). The wintertime BC contribution to fine aerosol was higher than that observed at THI in Athens (11%) (Liakakou et al., 2020b) and comparable to values re-ported for polluted Asian megacities, such as Delhi (15% for $BC/PM_{2.5}$) (Dumka et al., 2019). The observed levels, with a mean of 3.7 μg m^{-3} and hourly maxima approaching 30 μg m^{-3} were among the highest observed in European cities (Costabile et al., 2017; Crilley et al., 2015). The mean concentration was significantly higher (33%, $p < 0.01$) than at THI (2.8 μg m^{-3}). The average BB% fraction (BC_{bb}/BC) was 34% and comparable with findings at other urban sites affected by RWB (Briggs and Long, 2016). Most of the peak BC hourly values exceeding 15 μg m^{-3} were associated with high BC_{bb} (**Figure 5.3a**). The average BC fractionation presented similarities with results from AE33 measurements (mean BB%: 32%) in successive winters at THI (Liakakou et al., 2020b), although nighttime mean BB% contributions were relatively lower at P1. Despite being comparable to the THI BC_{bb} levels, the points in the diurnal cycle of the BB% fraction at P1 did not exceed 45% at nighttime, in contrast to Athens, thus denoting a substantial BC_{ff} contribution throughout the day in Piraeus.

The effect of different BC sources was reflected by the diurnal cycles of the source-specific BC components but also by their wind-dependence (polar and annular plots in **Figures 11.10** and **11.11**). BC_{bb} concentrations maximized during the night, under stagnant conditions or low winds (Grivas et al., 2018; Stavroulas et al., 2019; Theodosi et al., 2018) from the urban area inland, indicating the impact of local nighttime emissions. While this pattern was repeated to a certain extent for BC_{ff}, there was also an enhancement for winds from the port sector, related to vehicular and shipping emissions. This pattern can be more readily understood by the comparison with wind plots of NO_x (enhancement for low winds of the northeast sector, twice a day) and SO_2 (an indicator of shipping emissions, presenting large enhancements for flows from the port sector to the west, which intensify around midday (Progiou et al., 2021)). The patterns observed for BC_{ff} and NO_x, with wind-dependence indicative of traffic, port activity and residential heating, were reproduced also by OA (Chazeau et al., 2021).

BC concentrations at P1 were compared to those concurrently measured at the back-ground location P2 to provide an estimate of the urban enhancement in Piraeus (ΔBCu), which was expected to be mainly related with traffic and emissions around the passenger port (Lin et al., 2020). Indeed, the calculated ΔBCu parameter (BC_{660nm} at P1 minus BC_{637nm} at P2) was strongly correlated with BC_{ff} at P1 ($r^2 = 0.77$), which in turn was directly associated with NO_x ($r^2 = 0.74$). The average ΔBCu enhancement was substantial (1.7 μg m^{-3}, 45% of mean BC at P1) but, at the same time, indicative of a strong BC background, most likely driven by residential and shipping emissions in the wider area of Piraeus, including the commercial port sector. The BC_{bb} component was less strongly correlated with ΔBCu ($r^2 = 0.50$), but, on the contrary, presented a high correlation ($r^2 = 0.79$) and similar mean levels (~1.3 μg m^{-3}) with BC_{bb} recorded concurrently at THI in central Athens. This result is markedly different from the findings of studies in Europe and North America, which, when assessing the spatial variability of BC_{bb}, tended to report much higher BC_{bb} concentrations at background sites, as opposed to downtown urban locations (Healy et al., 2017; Titos et al., 2017). This spatial uniformity observed between different parts of the GAA indicates the magnitude of the wintertime RWB issue and carries important implications for population exposure (Tsiodra et al., 2021). Moreover, these intense residential emissions enhance the importance of BC as a parameter of climatic relevance due to atmospheric heating (Athanasopoulou et al., 2017). The mean winter $AAE_{370–950}$ at P1 was 1.43 (ranging in 0.85–2.08) with a characteristic day/night pattern, as it increased from 1.35 in daytime to 1.52 in nighttime

due to the abundance of aerosols produced by biomass burning (black and brown carbon), which absorb strongly at shorter wavelengths (Kaskaoutis et al., 2021a).

Regarding the major inorganic species, SO_4^{2-} contributed 11% to PM1, NO_3^- 6%, NH_4^+ 4% and Cl^- also had a minor contribution (1%). The diurnal cycle of sulfate displayed minimal variability (2.1–2.9 μg m^{-3}), in agreement with its regional character, which was extensively documented in the GAA (Grivas et al., 2018; Pateraki et al., 2012; Theodosi et al., 2011). The mean sulfate concentration at P1 (2.5 μg m^{-3}) was similar to mean values recorded in previous winters at THI (2.2–2.6 μg m^{-3}) (Stavroulas et al., 2019). Apart from the expected association with the ammonium ion (r^2 = 0.72), its correlation with other aerosols and gaseous parameters was moderate-to-low, irrespective of source-related wind sectors, indicating a minor impact from local sources. Sulfate concentrations were unrelated to SO_2 measured at PEI-1, and while the NO_x/SO_2 ratio at PEI-1 decreased significantly when examining data for winds of the S-W sector (port), a fact indicative of shipping emissions of sulfur oxides, sulfate levels did not present an analogous increase but instead decreased by 24%, respective to the mean. Moreover, there were no correlation patterns with relative humidity, which have been reported as indicative of the local-scale formation of sulfate in port-industrial areas through short-term heterogeneous processes (S. Zhang et al., 2021). Overall, the present observations are indicative of sulfate in the cold period of the year being mainly associated with northern synoptic scale winds that transport aerosols from continental Greece, the Balkans and Eastern Europe (Theodosi et al., 2011), as can be observed in the PSCF plot of **Figure 11.12a**. Accordingly, the wind plots of **Figures 11.10** and **11.11** show a dispersal of mid-to-high levels of sulfate for winds from the northern sector. A characteristic buildup of sulfate levels can be seen during 19–21 December (80% higher compared to the winter mean), a period when moderate, constant winds from N-NE directions were observed (**Figure 5.3a**). As SO_2 levels did not record any increase during this time, this pattern can indicate the transport of rather processed aerosols.

In contrast to sulfate, nitrate produced a bimodal diurnal cycle in winter (Budisulistiorini et al., 2016; Zhang et al., 2015). While the nighttime peak is known to be related to the fast processing of BB emissions (Stavroulas et al., 2019; Theodosi et al., 2018), the morning peak trailed that of BC_{ff} by two hours and was much more distinct than the small morning hump observed at THI in the past (Stavroulas et al., 2019). This provides an indication of local nitrate production through

the fast atmospheric conversion of NO_x emissions, most likely co-emitted with ammonia by vehicles (Chazeau et al., 2021), in the cool winter conditions that prevent evaporative losses (Sun et al., 2012). Nitrate was correlated well with the ammonium ion ($r^2 = 0.62$), with BC_{bb} especially in nighttime ($r^2 = 0.69$; **Figure 11.8b**) and more modestly with BC_{ff} and NO_x during the daytime (r^2: 0.36, 0.37, respectively; **Figure 11.8a**). In contrast to what was observed for OA and sulfate, nitrate mean levels in Piraeus were similar or lower compared to urban sites in Central/Northern Europe, probably due to the lower temperatures and the more abundant ammonia emissions facilitating the neutralization of nitric acid, in the latter case (Bressi et al., 2021). Chloride levels were low in terms of median value (0.1 μg m^{-3}), but were inflated as an average (0.2 μg m^{-3}) by the presence of some conspicuous nocturnal events, associated with intense BB and stagnant conditions or weak winds from NE directions. Hence, chloride presented a substantial correlation ($r^2 = 0.43$) with BC_{bb}. The correlation with ammonium ($r^2 = 0.51$), mostly driven by late-night to early-morning peaks for both species, as also indicated by the maxima in their diurnal variation (**Figure 5.2a**), points to NH_4Cl condensing to the particulate phase (Han et al., 2021), favored by elevated RH and decreased acidity during the night (Bougiatioti et al., 2017). As can be seen in **Figure 5.3a**, all of these high ammonium and chloride values (observed mainly on 24 and 29 December, and 9 January) were present in the context of nighttime BB episodes that were prolonged for several hours until the early morning.

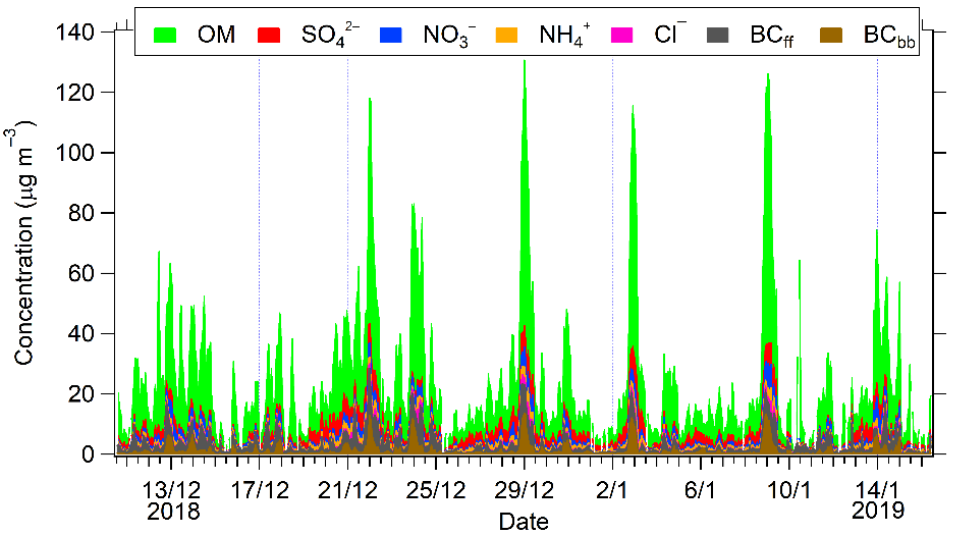

(**a**)

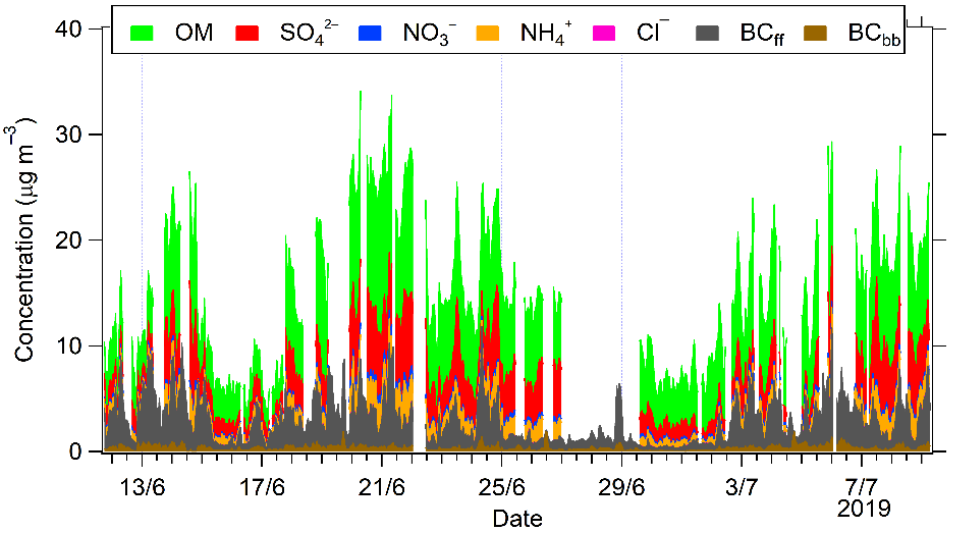

(**b**)

Figure 5.3. Time series of hourly ACSM (non-refractory OA and major inorganic ions) and AE-33 (BC components) measurements for the winter (**a**) and summer (**b**) periods.

5.3.2.2 Summer Period

The estimated mean PM1 concentration in summer (14.8 μg m^{-3}) was significantly reduced compared to winter (35% reduction, $p < 0.01$), with daily and hourly maxima of 26 and 34 μg m^{-3}, respectively. These levels indicate an absence of important air quality events and generally improved conditions compared to winter, linked to the deactivation of the residential heating source and the enhanced summertime aerosol dispersion (Kassomenos et al., 1995). PM_1 levels at

P1 were significantly ($p < 0.01$) lower compared to $PM_{2.5}$ at the PEI-1 roadside traffic site, where a mean of 17.4 μg m^{-3} was recorded.

OA remained the dominant PM_1 component (48% on average), but was likewise characterized by a lower mean concentration compared to winter (7.1 μg m^{-3}, 49% reduction) and limited short-term variability (with an hourly maximum of 16 μg m^{-3}). However, these levels were substantially higher than those reported at the urban background THI site in Athens during past summers (5.4 μg m^{-3}) (Stavroulas et al., 2019), justifying a measurable input from local sources. The summertime diurnal cycle of OA (**Figure 5.2b**) was mostly flat (Chazeau et al., 2021; Xu et al., 2015), with hourly means varying between 6–8 μg m^{-3} and only a minor hump around the morning rush hour (this was also present in the mean weekday cycle, but not at week-ends). This variability pattern is attributed to the combination of local sources with photochemically formed and regionally transported organic particles, since the summertime levels of the latter in the GAA are known to peak during midday and afternoon (Kostenidou et al., 2015). As a result, the OA correlation with BC_{ff} was weaker than in winter ($r^2 = 0.17$, improving to 0.38 for daytime-only data; **Figure 11.9a**). A similar seasonal pattern between organic aerosols and primary elemental or black carbon is often observed due to the photochemical formation of secondary organics (Na et al., 2004; Plaza et al., 2006). However, weekday OA levels here were still higher than at weekends (24%, $p < 0.01$), indicating the substantial effect of primary sources. On the other hand, OA was more closely associated with sulfate ($r^2 = 0.58$), which supports the elevated baseline and limited variation in its diurnal cycle. The OA wind plots (**Figures 11.13** and **11.14**) were markedly different compared to winter, with enhanced concentrations linked to S-SW flows throughout the day, suggesting the influence of sea breeze circulation (Rivellini et al., 2020).

Mean BC levels, while contributing 19% to PM_1, were reduced compared to winter (2.8 against 3.7 μg m^{-3}, $p < 0.01$, 19% of PM_1); however, this is attributed to the large decline in the BC_{bb} component (72%, $p < 0.01$), which, in the absence of local RWB, registered an average of 0.4 μg m^{-3}. Such low BC_{bb} levels are comparable with regional background levels in the Eastern Mediterranean that are mostly related with long-range transported smoke from agricultural burning and wildfires (Bougiatioti et al., 2014). Conversely, summertime BC_{ff} levels matched those in winter (2.4 μg m^{-3}), in spite of improved dispersion conditions, highlighting the enhancement of port-related BC emissions (traffic and shipping). This comes in contrast to the seasonal pattern at

THI, where BC_{ff} levels declined significantly (20%, $p < 0.01$). Such seasonal homogeneity is not frequently observed for BC_{ff} in European cities (Becerril-Valle et al., 2017), but can be occasionally seen at traffic sites (Helin et al., 2018) and sites in port areas (Chazeau et al., 2021).

While the mean diurnal BC_{ff} cycle was unimodal, with a prominent morning traffic peak (a pattern present mostly during weekdays, when BC_{ff} increased by 51% on average), the baseline remained high during midday (2.1 μg m^{-3} in 10:00–18:00 against 1.9 μg m^{-3} in winter), notwithstanding the large development of the mixing layer in this timeframe. It is indicative that the mean BC_{ff} concentration was largely enhanced (4.0 μg m^{-3}) for data corresponding to S–W wind directions (port sector). The wind plots (**Figures 11.13 and 11.14**) for BC_{ff} in summer show a much more distinct impact from the port area compared to winter, that intensified in the morning rush hour and persisted throughout the day. It can be argued that the activity in the port (including both shipping and vehicular emissions) is more important for defining BC_{ff} levels in summer, judging from the clear S–SW effect to SO_2 (shipping emission indicator) and NO_x (general combustion indicator, strongly related to diesel emissions), against the local roadside influence observed for CO (indicator mostly of gasoline vehicle emissions in summer; Fameli and Assimakopoulos, 2015). A very similar BC wind-dependence, indicative of emissions from the port sector, was observed in Civitavecchia, Italy, another major passenger port in the Mediterranean (Gobbi et al., 2020). On the contrary, a period of low BC_{ff} concentrations can be observed during 25 June–1 July (**Figure 11.3b**), when the Etesian wind regime prevailed, with strong (53% enhanced compared to the period mean) winds of the northern sector blowing throughout the day and sweeping port emissions away from the measurement site.

The inter-site BC correlation between the P1 (BC_{660nm}) and the P2 background site in Piraeus (BC_{637nm}) was greatly reduced ($r^2 = 0.29$) compared to winter ($r^2 = 0.78$) when RWB leveraged the spatial uniformity. Similarly, there was a decrease in the correlation of BC between P1 and THI ($r^2 = 0.30$ vs. 0.63 in winter), reflecting the effect of local emissions around the port. The average enhancement at P1 compared to P2 (ΔBCu) was slightly lower in summer and correlated less strongly with BC_{ff} ($r^2 = 0.61$), also suggesting the substantial impact of port activities at the background site. The absence of RWB emissions also led to lower mean $AAE_{370–950}$ values in summer (1.22, ranging from 0.86 to 2.46) than in winter, with limited diurnal and weekend–weekday variability (Sun et al., 2020).

Sulfate doubled its average contribution to PM_1 in summer (3.3 μg m^{-3}, 22%). It correlated excellently with ammonium (r^2 = 0.93), with a mean sulfate/ammonium ratio of 2.81, which suggested a high degree of neutralization similar to ammonium sulfate and, most likely, less acidic aerosol compared to winter (as indicated by the ACSM ion balance when examining NH_4^+ neutralization) (Siskos et al., 2001; Zhang et al., 2007). The diurnal variation of sulfate presented the typical post-noon enhancement that extended to a plateau until the evening. While this pattern has been linked to the vertical mixing of regionally transported ammonium sulfate in parallel with the evolution of the mixing layer (this regional influence for the upper 25th percentile of concentrations can be seen in the PSCF plot of **Figure 11.12b**), the wind plots also displayed an increase for stronger winds from the SE-SW and NW sectors (**Figures 11.13** and **11.14**). This might provide an indication of converted primary SO_2 from ship-ping emissions in the Saronic and Eleusis Gulfs. When calculating the particulate S to the total S ratio (S_p/S: sulfate to the sum of sulfate and SO_2; concentrations in μgS m^{-3}), a large increment compared to winter was observed (0.26 vs. 0.09), which can be thought of as indicative of the gas-to-particle conversion of SO_x originating from heavy oil combustion (Siskos et al., 2001; Zhang et al., 2019). The ratio increased for higher relative humidity values (0.35 for RH > 70%) and its diurnal cycle showed an enhancement in the afternoon to evening hours (16:00–20:00), which, compared to time of the wind-related enhancement of SO_2 around noon, allows for several hours to facilitate the conversion. A period with elevated sulfate concentrations (by 61% compared to the summer mean) can be seen on 19–22 June (**Figure 11.3b**), with an in-creased S_p/S ratio of 0.37, under very low winds (mean speed < 1 m s^{-1}), mainly from the SE-SW.

Concentrations of nitrate and chloride were very low (averages of 0.46 and 0.03 μg m^{-3}, respectively), consistent with their depletion under warm conditions (Jiang et al., 2019). Therefore, both ions recorded their highest levels in post-midnight and early morning hours. Nitrate levels showed an increase in 18–22 June (**Figure 11.3b**), a period when increased sulfate from local processing was also suspected, and may be related with oxidative conditions favorable for the production of secondary ions. This is also indicative of O_3 concentrations at PEI-1 in this period that were elevated by 13% against the period mean, which, considering the type of the measurement site (roadside traffic), is substantial.

5.3.3 Sources of Organic Aerosol

5.3.3.1 Winter Period

A five factor solution was extracted from the PMF analysis on winter data. The five OA components were characterized as hydrocarbon-like OA (two components: HOA-1 and HOA-2), biomass-burning OA (BBOA), less-oxidized oxygenated OA (LO-OOA) and more-oxidized oxygenated OA (MO-OAA). The solution was repeatable, with a limited variability of factor profiles between different runs, while modeled OA (i.e., the sum of all deconvolved factors) correlated excellently with measured OA (**Table 11.1**). HOA-1 and BBOA were constrained factors while the remaining three emerged from the solution, presenting distinct spectral characteristics, degrees of oxidation and temporal patterns. The source profiles for winter are presented in **Figure 5.4a** (**Figure 5.4b** shows the source profiles for summer; see Section 5.3.3.2). Furthermore, diurnal cycles of OA components are shown in **Figure 5.5**, average contributions in **Figure 5.6** and time series of contributions in **Figure 11.15**.

HOA-1: The source profile of HOA-1 was constrained according to the HOA profile determined by measurements and PMF analysis in Paris (Crippa et al., 2013) and was dominated by fragments related to the non-oxygenated alkane/alkene series (m/z: 27, 29, 41, 43, 55, 57, ….). The HOA-1 profile was excellently correlated with traffic-related HOA factors found previously in studies in the GAA and other cities (**Figure 11.16a**). The concentrations of HOA-1 correlated highly with BC_{ff} at P1 ($r^2 = 0.63$) and also substantially with NO_x ($r^2 = 0.43$) (**Figure 11.7a**) and benzene ($r^2 = 0.42$) at the PEI-1 roadside station, indicating its association with vehicular traffic. The absence of a significant weekday/weekend pattern is interesting (mean concentration higher by 4% on weekdays, $p > 0.05$) and possibly suggests the impact of local emissions in the vicinity of the site, which, being downtown, experiences substantial traffic even at weekends, and especially during the nights of the late-December holiday period. When examining this contrast separately for daytime/nighttime, it appears that in the daytime (06:00–18:00) HOA-1 concentrations were indeed higher during weekdays (36%, $p < 0.01$), while for nighttime data (18:00–6:00), HOA-1 weekend concentrations were higher (24%) but not significant ($p > 0.05$). This combined weekday/weekend and day/night variability pattern for HOA was also observed at an urban site in Beijing during winter (Sun et al., 2013). The overall diurnal cycle of HOA-1 concentrations was bimodal (Figure 5a), with a morning rush hour peak at 10:00, similar to the one of BC_{ff}, and a

nighttime plateau (21:00–02:00), the latter characteristic of evening traffic emissions in the stable nocturnal boundary layer. The CPF polar plot (**Figure 11.18**) for fractional contributions of HOA-1 (75th percentile) indicates a large enhancement for weak-to-moderate winds from the S–SW sector, representing the impact of traffic in the Piraeus central and coastal roads, as well as a possible input of shipping emissions at the passenger port. The factor contributed 12% (1.7 μg m^{-3}) of the total OA in winter (**Figure 5.6a**), with a daily maximum of 4.6 μg m^{-3}.

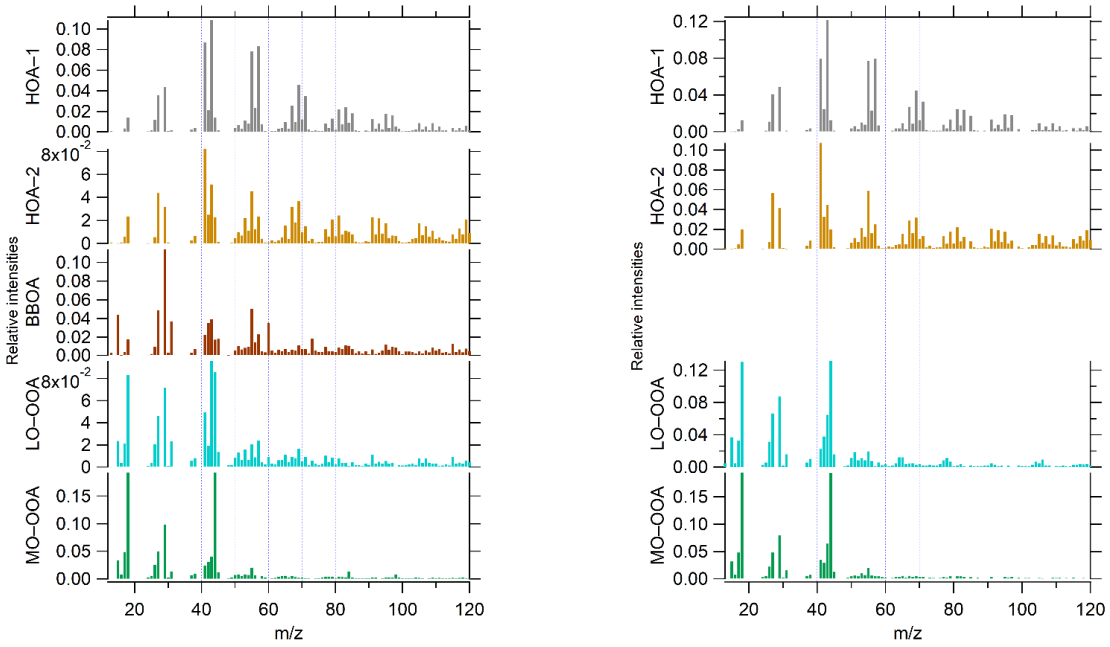

Figure 5.4. Mass spectra of PMF factors (FP: factor profiles) resolved from (a) winter (December-January) and (b) summer (June-July) OA measurements in Piraeus.

HOA-2: While the profiles of HOA-2 and HOA-1 had similar main features (i.e., primary hydrocarbon fragments), the former appears to be slightly more oxidized, with relatively enhanced contributions at m/z 44 and 18, most likely suggesting a longer atmospheric residence time compared to the more local HOA-1. Moreover, the contributions at m/z 55, 57, with respect to m/z 41, 43, were lower when compared to the HOA-1 profile, a feature that was related to container ship exhaust plumes (Murphy et al., 2009). Correlations with BC_{ff} and other primary gases for HOA-2 were lower than for HOA-1. However, HOA-2 was better correlated than HOA-1 with LO-OOA (r^2: 0.64 vs. 0.46) during daytime, supporting a certain degree of processing. Its concentrations were significantly higher during daytime (110%, $p < 0.01$) and weekdays (43%, p

< 0.01), still indicative of anthropogenic activity in the medium spatial scale. The morning maximum of HOA-2 concentrations trailed the respective cycle of HOA-1 by 2 h; however, there was no nighttime peak. It can be argued that this pattern is linked to local atmospheric circulation that transports aerosols from the wider port area to the center or Piraeus, as western onshore flows intensify at midday. Examining the CPF plot (**Figure 11.18**) of fractional HOA-2 contributions, the highest prob-abilities of exceeding the 75% percentile were associated with relatively strong winds from W-NW directions, implying an impact from the commercial sector of the port, as well as from shipping/industrial activity in the Gulf of Eleusis and the Thriassion Plain (**Figure 5.1a**) (Kanellopoulos et al., 2021; Kassomenos et al., 2014). The mean contribution of HOA-2 to OA was 18% (2.5 μg m^{-3}), with a daily peak concentration of 5.4 μg m^{-3}, while its mean contribution was the highest among components for winds of the SW-NW sector (28%). The combined fraction of the two HOA components was 30% (**Figure 5.6a**), which is a large fossil fuel combustion contribution compared to other urban locations (Aurela et al., 2015; Guo et al., 2020; Rattanavaraha et al., 2017; Salcedo et al., 2018), but nevertheless reasonable, considering the central placement of the site in a particle pollution hotspot.

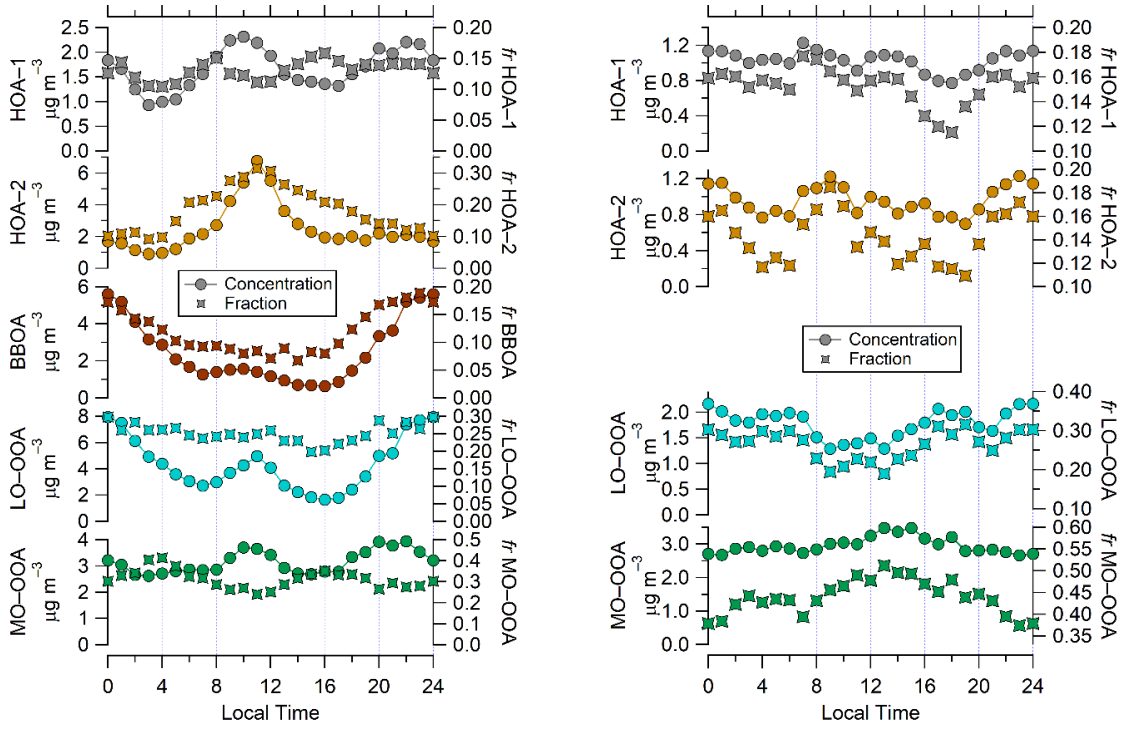

Figure 5.5. Average diurnal cycles and respective hourly average fractional contributions, identified by PMF analysis for OA components in Piraeus in the winter (a) and summer (b) periods.

BBOA: The characterization of the BBOA component, that was constrained based on the respective profile from the meta-analysis of (Ng et al., 2011a), was straightforward, with the mass spectrum being characterized by the presence of the fingerprint ions at m/z 60 and 73, which derive from the fragmentation of pyrolytical products of cellulose (Alfarra et al., 2007). The factor profile of BBOA was quite similar to factors obtained for OA in the GAA in previous studies and elsewhere (**Figure 11.16b**), although not at the level observed for HOA-1, as expected by the differences in burning conditions, atmospheric residence time and proximity to the source. BBOA concentrations were excellently correlated with BC_{bb} ($r^2 = 0.88$); therefore, a similar diurnal cycle was presented, with a nocturnal enhancement of concentrations in 23:00–2:00 (Canonaco et al., 2013). This factor was also correlated with nitrate ($r^2 = 0.69$) and chloride ($r^2 = 0.57$) (**Figure 11.7a**). Fresh BB smoke is known to produce compounds such as KCl and KNO_3 (Aurela et al., 2015) that can also interact with co-emitted ammonia to form the ammonium compounds detected by the ACSM (Zhou et al., 2015). Nighttime mean concentrations were more than three times higher (3.7 vs. 1.2 μg m^{-3}) but the weekday–weekend variability was not significant (mean concentrations higher by 6% at weekends, $p > 0.05$), This most likely verifies the constant use of biomass for space heating, and not recreational purposes, at weekends, as reported in other cases (Rattanavaraha et al., 2017; Zhang et al., 2019). The CPF plot in **Figure 11.18** validates the association of the BB source with stagnant conditions or low-to-moderate N–NE winds that prevail during winter nights and promote either the accumulation of emissions produced locally or the local transport from residential areas upwind in the GAA (Grivas et al., 2018; Theodosi et al., 2018). BBOA ac-counted on average for 17% of OA (2.4 μg m^{-3}) in Piraeus during winter (**Figure 5.6a**). Compared to the BBOA mean winter fractions estimated in past winters (2013–2017) at THI in central Athens (9–12%) (Stavroulas et al., 2019), the mean contribution in Piraeus appeared enhanced. Again, this contrasts with other European metropolitan areas, where BBOA from residential heating is reportedly higher for urban and suburban background sites rather than for downtown locations (Aurela et al., 2015). Unlike HOA-1 and HOA-2, BBOA was more episodic in nature, registering daily and hourly maximum concentrations of 8.0 and 30.4 μg m^{-3}, respectively. These values were recorded on 9 January 2019 (**Figure 11.15a**), with the hourly peak observed in the early hours of the day, under calm conditions and near-zero temperatures (~2–2.5 °C), in the aftermath of an uncommon snowstorm impacting the GAA and amplifying space heating demands.

LO-OOA: The profile of the processed LO-OOA component was characterized by enhancements in characteristic m/z fragments at 44 and 18, related with decarboxylation and dehydration of oxygenated ambient aerosols, respectively, while retaining the hydro-carbon peaks (Ng et al., 2011a). The source profile presented similarities with those reported for winter periods in central Athens for semi-volatile OOA linked to oxidized RWB emissions (Florou et al., 2017; Stavroulas et al., 2019). In fact, the LO-OOA factor correlated (r^2 = 0.82) with an SV-OOA (semi-volatile OOA) factor identified for the winter period of 2016-17 at THI, and even more with the SV-OOA factor identified for the winter of 2015-16 (r^2 = 0.94) (Stavroulas et al., 2019). The spectral characteristics and temporal variability of the component suggest that it was associated with rapid atmospheric formation processes. LO-OOA correlated with BC_{bb} (r^2: 0.77 for the full winter dataset, 0.82 for nighttime only) while traces of m/z 60, 73 were present in its spectrum, suggesting that the processing of fresh BB emissions leads to LO-OOA formation in winter (Crippa et al., 2013; Kodros et al., 2020; Zhang et al., 2019). The diurnal cycle starts escalating in the evening (18:00) and maximizes (0:00) concurrently with BBOA, likely indicating a very fast oxidation rate (Jorga et al., 2021). This process was also favored by the lower nighttime temperatures (**Figure 11.1**) that prevent the loss of semi-volatile compounds constituting LO-OOA (Zhang et al., 2015). Similar to BBOA, LO-OOA was well-correlated with nitrate and chloride (r^2: 0.69 and 0.51, respectively). However, in contrast to BBOA, the diurnal cycle of LO-OOA also presented a notable midday peak (Xu et al., 2015), that was mostly due to data corresponding to weekdays and could be related with the conversion of fresh traffic- and port-related emissions. This dual character of LO-OOA could be traced in its CPF plot (**Figure 11.18**), with enhancements for calm and low winds from the NE and to a lesser extent for stronger winds from the W-NW. In fact, during day-time, LO-OOA recorded the highest correlation with HOA-2 among components (r^2 = 0.64). The mean LO-OOA fraction (**Figure 5.6a**) was estimated at 30% (4.3 μg m^{-3}), with daily and hourly maxima of 13.8 and 53.2 μg m^{-3}, respectively, that were observed simultaneously with BBOA maxima on January 9. Under the hypothesis that all nighttime LO-OOA is attributed to processed BB emissions, it can be reasoned that the combined contribution of biomass burning, both directly (BBOA) and indirectly (nighttime LO-OOA), would rise to 37% of OA (up to 50% in winter nights), highlighting that, even in the port-city of Piraeus, RWB is the major source of organics in winter.

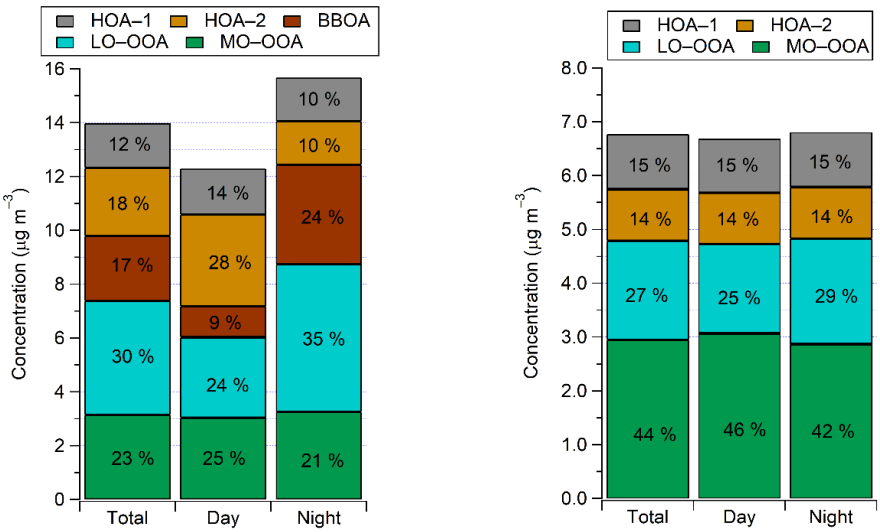

Figure 5.6. PMF-resolved mass concentrations and fractions for the OA components during the winter (a) and summer (b) periods in Piraeus.

MO-OOA: The mass spectrum of the MO-OOA component, which corresponds to aged aerosols, was distinguished by the stronger fraction at m/z 44 and 18 and the near absence of the hydrocarbon series (m/z 41, 43…) yielding a high f44 to f43 ratio (4.8), com-pared to the one calculated for LO-OOA (0.89). The MO-OOA FP correlated excellently with FPs for OOA and LV-OOA (low-volatility OOA) factors from earlier studies in the GAA and elsewhere (**Figure 11.17**). Values ranging from 0.90 to 0.99 were found for r^2 com-pared to the LV-OOA spectra for the winter seasons at THI (Stavroulas et al., 2019), while r^2 was 0.93 when compared to OOA at a regional background site in the Eastern Mediterranean (Bougiatioti et al., 2014). An excellent correlation (r^2 = 0.97) was also found when comparing with the average spectrum of LV-OOA factors derived from various sites across Europe (Crippa et al., 2014), as well as the average profile of LV-OOA (r^2 = 0.96) from an ensemble of sites in North America, Asia and Europe (Ng et al., 2011a). Consistent with a more regional origin, MO-OOA was the component most correlated with sulfate and ammonium, especially during the daytime (r^2: 0.39 and 0.49, respectively). Compared to the other components, the diurnal variability of MO-OOA seems relatively flat (Guo et al., 2020; Sun et al., 2016), with mean hourly concentrations ranging from 2.7 to 4.0 μg m^{-3}. Considering the nighttime boundary layer effect for the appearance of enhanced levels, it should be expected that MO-OOA inputs from regional transport intensified in the 10:00–14:00 timeframe, in spite of strong atmospheric mixing (Kaskaoutis et al., 2021b). Supporting the

hypothesis that MO-OOA represents a background aerosol category that is spatiotemporally uniform and mostly extraneous to local anthropogenic activity, the weekend/weekday and daytime/nighttime contrasts were not statistically significant at the 0.05 level (Rattanavaraha et al., 2017; Sun et al., 2013). The regional transport of aerosol in the GAA was consistently linked to advections from the northern sector under synoptic-scale circulation (Grivas et al., 2018; Stavroulas et al., 2019), and this was repeated in the CPF plot for MO-OOA (**Figure 11.18**), showing high probabilities of increased contributions for strong northern winds. This was also verified by the PSCF plot in (**Figure 11.12c**), which showed the spatial extent of transport to be confined within the Balkan Peninsula. The mean contribution (**Figure 5.6a**) of MO-OOA (23%, 3.2 μg m^{-3}), combined with the concentration of ammonium sulfate, constitutes a substantial baseline of regional aerosol in PM_1.

5.3.3.2 Summer Period

Four OA components (**Figure 5.4b**) were identified by PMF analysis in the summer dataset. Their source profiles presented similarities with those determined in winter; there-fore, the components were named accordingly. The exception was BBOA, which could not be identified in the summer period, due to the absence of local biomass burning (**Section 11.1**).

HOA-1: HOA-1 in the summer dataset was constrained using the same anchor profile as in winter, albeit with a higher a-value (0.1 vs. 0.02 for winter), and the two resulting spectral profiles were very similar (r^2 = 0.99). The component was again correlated with BC_{ff} (r^2 = 0.34), but to a smaller degree than in winter, with correlations slightly enhanced for daytime data (r^2 = 0.49; **Figure 11.9a**). This winter–summer correlation pattern can be supported when comparing it with cases where primary sources dominated (strong correlations) at urban sites, such as in Delhi (Patel et al., 2021), and where secondary sources became more important (weaker correlations), such as at an urban background site in Paris (Srivastava et al., 2019). The diurnal cycle displayed a peak area between 07:00–10:00 that was consistent with morning traffic, but, in a fashion similar to BC_{ff}, HOA concentrations remained elevated until the afternoon, again signifying the importance of emissions from the passenger port and the city center under the influence of the sea breeze. Such persistence of HOA levels was mostly observed at urban sites that were affected by heavy traffic during the whole daytime (Barreira et al., 2021; Sun et al., 2016). The influence of the passenger port sector is clear in the CPF polar plot (**Figure 11.19**). The mean HOA-1 concentration in

summer was significantly lower than in winter (38%, p <0.01); nevertheless, its mean contribution to OA increased to 15% (**Figure 5.6b**).

HOA-2: The HOA-2 factor was constrained based on the profile of the respective fac-tor in winter (a-value = 0.2). The two HOA-2 profiles were strongly correlated (r^2 = 0.95). In summer, the HOA-2 time series was better correlated with HOA-1 (r^2 = 0.67 vs. 0.36 in winter), a pattern created mostly by concurrent high concentration data pairs during winds from the passenger port sector. Excluding the impact of these data by examining the CPF wind plot for percentiles between 50–95°, a similar wind-dependence pattern as the one observed for HOA-2 in winter (**Figure 11.18**) could be revealed, indicating again an impact from the western sector (**Figure 11.19**). As in the winter period, the morning peak of HOA-2 trailed that of HOA-1 by two hours. While shipping and vehicular traffic data were not available in this study, it was reported in Oakland that HOA related to commercial port emissions tended to increase its concentrations and contributions in the late morning hours and beyond, partially due to a reported increase in drayage activity (Shah et al., 2018). The mean contribution of HOA-2 to OA was 14% (**Figure 5.6b**). Therefore, the combined HOA components also retained a large contribution to OA (29%) in summer, in spite of improved atmospheric dispersion and the enhanced photochemical processing of primary hydrocarbons. While contributions of HOA in the order of 30% are in the upper echelon of values reported at urban sites in Europe and North America (Crippa et al., 2014; Mallet et al., 2019), they are comparable with the enhanced HOA contribution of 37% reported at the Houston Ship Channel, under the joint impact of vehicular and shipping emissions (Al-Naiema et al., 2018).

LO-OOA and MO-OOA: Both OOA components were obtained as unconstrained fac-tors. The LO-OOA source profile in summer had some differences compared to the winter one (r^2 = 0.83), specifically a higher degree of oxidation (higher m/z 44 compared to m/z 43) and the absence of BB-related fragments (m/z: 60, 73). The f_{44} to f_{43} ratio was higher in comparison to winter (2.0 vs. 0.9), reflecting a higher degree of oxidation. The retrieved LO-OOA profile showed similarities to the average SV-OOA profile (r^2 = 0.9) from 25 European sites (Crippa et al., 2014), as well as the mass spectrum of laboratory-simulated, photochemically oxidized diesel exhaust plumes (Sage et al., 2008). While the diurnal cycle of LO-OOA presented a minor hump around noon that could be related to the photo-oxidation of HOA, its highest levels were observed in nighttime under lower temperatures (**Figure 11.1**), indicating that its variability could depend on the temperature-

driven, gas-to-particle partitioning of oxidized species. Therefore, it is reasonable that LO-OOA presented its highest correlation among PM_1 species with nitrate (r^2 = 0.40). It is noted that the nighttime enhancement of LO-OOA was much less pronounced compared to that at THI in summer, even though the mean period levels were similar (1.8–1.9 μg m^{-3}) (Stavroulas et al., 2019).

In contrast to LO-OOA, the more oxidized MO-OOA component produced a profile highly comparable to the one in winter (r^2 = 0.98). Its concentrations and especially its fractional contributions maximized during the post-noon hours, suggesting an input from photochemically oxidized organics (Carbone et al., 2013), in a similar way to the results reported for the urban background THI site (Stavroulas et al., 2019) and a suburban background site in the northeastern part of the Attica basin (Kostenidou et al., 2015). MO-OOA was not particularly well-correlated with sulfate (r^2 = 0.24) or other ACSM compounds, recording its highest correlation with OA (r^2 = 0.36) to which it was the most major contributor during summer. Sulfate was not outright correlated with either of the OOA components in summer, but, given its dual character discussed in **Section 5.3.2.2** (regional transport and local conversion), it had a substantial correlation with the sum of the OOA components (r^2 = 0.49). Both OOA components showed higher fractional contributions for moderate-to-strong winds from the north sector (**Figure 11.19**), although this was more apparent for MO-OOA. However, this regional impact (**Figure 11.12d**) during the study month did not appear related to the usually reported source origins in the Black Sea region (Tsiodra et al., 2021) but rather to the western Balkans and the polluted Po Valley (Gerasopoulos et al., 2011). LO-OOA recorded significantly lower concentrations at weekends (20%, $p < 0.01$), similarly to the HOA components (42% and 36% reductions for HOA-1 and HOA-2, respectively). However, MO-OOA, consistent with its regional profile, did not display significant weekday–weekend variability (1% higher in weekends, $p > 0.05$).

The LO-OOA mean contribution to OA was comparable to the one in winter (27% vs. 30%), and in the absence of BB emissions for processing, showed a more subtle nighttime enhancement (Figure 6b). On the other hand, MO-OOA, that preserved its mean levels in summer (6% lower compared to winter, $p > 0.05$), almost doubled its mean contribution (44%). The combined fraction of OOA components (71%) reveals the importance of SOA during summer, even in the polluted environment of a port city like Piraeus.

5.4 Conclusions

The study analyzed seasonal measurements (monthly periods in winter and summer) from online instruments (ACSM and multi-wavelength aethalometer) for submicron aerosol speciation in Piraeus, a large Greek city in the Greater Area of Athens and a major European port.

In general, the concentrations of ACSM components were notably higher than those observed at urban sites in other Mediterranean cities (Chazeau et al., 2021; Struckmeier et al., 2016; Via et al., 2021), especially during win-ter. For OA, BC, nitrate and even submicron chloride, this difference in wintertime levels was mainly driven by residential wood burning (RWB). Although RWB emissions are a cause of concern all over Europe, Greek cities face a particularly serious problem, since wood-burning as a source escalated rapidly in the setting of the Greek recession and has been unregulated for almost a decade, despite the established scientific knowledge about its public health impacts (Paraskevopoulou et al., 2019; Tsiodra et al., 2021). Organic aerosol from biomass burning and the fast processing of its emissions can account for more than 35% of OA in winter and, consequently, more than 20% of non-refractory PM_1. These can be considered substantial contributions, given the number and diversity of local sources, and point to an additional air pollution mitigation opportunity, in excess of cutbacks in port emissions (e.g., traffic routing, regulation of marine fuels, cold ironing, etc.). Considering the different diurnal pattern of biomass burning and fossil fuel combustion sources in winter (and also the fact that residential burning in stoves and fireplaces also aggravates indoor exposure), combined with the limited weekday-weekend variability, the respiratory function of residents in the entire area of Piraeus may come under constant pressure. This is highly important, taking into account the potential of pyrogenic species (e.g., water-soluble organics, polyaromatic compounds) to promote inflammation in the respiratory tract and induce short- and long-term toxicity. In view of these, and given the proof provided in this study that the biomass burning issue permeates the entire area of the Athens basin, measures for the regulation of biomass-burning fuel and emissions at the local scale appear imperative.

The impacts from overall port activities were clearly illustrated by the results, which showed a significant enhancement of carbonaceous aerosol concentrations related to fossil fuel combustion (mainly traffic and shipping), as compared to background sites in the GAA. This enhancement persists during the warm period of the year, in spite of improved atmospheric dispersion, as it

coincides with increased activity in the passenger port and daytime onshore flows that transport aerosols from the passenger and commercial port areas. This leads again to constant exposure above an elevated baseline, which is propagated by the increased time spent outdoors in summer and the enhanced infiltration of aerosol in residences. The combined contributions of HOA factors to OA was approximately 30%, demonstrating a substantial year-round impact that should be addressed. While large-scale works to improve public transportation in Piraeus are expected to alleviate the pressure from traffic emissions in the future, elucidating the contribution of shipping, and if possible, its various sectors, should be a necessary step before considering measures at the local scale for the mitigation of shipping emissions. Although a first quantification attempt was made in this study, it was found that the distinction between traffic and shipping short-term contributions using only aerosol mass spectrometry could be very difficult. Additional advanced instrumentation, including online trace metal analyzers, VOC monitors and particle sizers, combined with actual information on shipping traffic, would enable a better characterization of marine combustion and ship plumes. In this context, the comparative evaluation of findings from both online and offline source apportionment (filter-based analyses with shipping tracers) could also be valuable.

Processed aerosols were recognized as an important factor in the area, especially in summer when they comprised over 70% of OA. Less-oxidized organics appeared to be associated with the conversion of local emissions from traffic and port activities and also from RWB in winter. Additional measurements of gas-phase condensable organics would be needed in order to further characterize the transformation processes at the local scale and the atmospheric properties that promote them. Furthermore, there was a substantial fraction of more-oxidized OA, unrelated to local emissions and with large contributions, especially in summer (over 40% of total OA). Sulfate was also considered to be mainly of regional origin, even though there were some indications of the rapid gas-to-particle con-version of shipping emissions. The contrast in sulfate levels between Piraeus and cities in the Western Mediterranean is remarkable and was documented also at the regional back-ground site of Finokalia (Crete) against other coastal/rural background sites in the Western Mediterranean basin (Fröhlich et al., 2015; Minguillón et al., 2015). This pattern can be attributed to the reduction in emissions from coal- and oil-fired power plants in Western Europe as a result of European legislation (Pandolfi et al., 2016; Querol et al., 2009), while in the Eastern Mediterranean, regionally transported air masses are still impacted by emissions in the Balkans,

Eastern Europe and the Middle East, where the use of sulfur-rich fuels in stationary combustion remains common. In this framework, it is a concern that the ammonium sulfate contribution, combined with that of highly oxidized OA, form a solid background amounting to more than 5 μg m^{-3} of fine aerosols, which, due to their mostly transboundary character, will be hard to tackle in order to achieve compliance with the new WHO air quality guidelines and the foreseen revision of the EU air quality directive.

6 Field Evaluation of Low-Cost PM Sensors (Purple Air PA-II) Under Variable Urban Air Quality Conditions, in Greece

Iasonas Stavroulas[1,2], Georgios Grivas[1], Panagiotis Michalopoulos[1], Eleni Liakakou[1], Aikaterini Bougiatioti[1], Panayiotis Kalkavouras[1], Kyriaki Maria Fameli[1], Nikolaos Hatzianastassiou[3], Nikolaos Mihalopoulos[1,2], and Evangelos Gerasopoulos[1]

[1]Institute for Environmental Research and Sustainable Development, National Observatory of Athens, 15236 Athens, Greece

[2]Environmental Chemical Processes Laboratory, Department of Chemistry, University of Crete, 70013 Heraklion, Greece

[3]Laboratory of Meteorology, Department of Physics, University of Ioannina, 45110 Ioannina, Greece

Abstract

Recent advances in particle sensor technologies have led to an increased development and utilization of low-cost, compact, particulate matter (PM) monitors. These devices can be deployed in dense monitoring networks, enabling an improved characterization of the spatiotemporal variability in ambient levels and exposure. However, the reliability of their measurements is an important prerequisite, necessitating rigorous performance evaluation and calibration in comparison to reference-grade instrumentation. In this study, field evaluation of Purple Air PA-II devices (low-cost PM sensors) is performed in two urban environments and across three seasons in Greece, in comparison to different types of reference instruments. Measurements were conducted in Athens (the largest city in Greece with nearly four-million inhabitants) for five months spanning over the summer of 2019 and winter/spring of 2020 and in Ioannina, a medium-sized city in northwestern Greece (100,000 inhabitants) during winter/spring 2019–2020. The $PM_{2.5}$ sensor output correlates strongly with reference measurements (R^2 = 0.87 against a beta attenuation monitor and R^2 = 0.98 against an optical reference-grade monitor). Deviations in the sensor-reference agreement are identified as mainly related to elevated coarse particle concentrations and high ambient relative humidity. Simple and multiple regression models are tested to compensate for these biases, drastically improving the sensor's response. Large decreases

in sensor error are observed after implementation of models, leading to mean absolute percentage errors of 0.18 and 0.12 for the Athens and Ioannina datasets, respectively. Overall, a quality-controlled and robustly evaluated low-cost network can be an integral component for air quality monitoring in a smart city. Case studies are presented along this line, where a network of PA-II devices is used to monitor the air quality deterioration during a peri-urban forest fire event affecting the area of Athens and during extreme wintertime smog events in Ioannina, related to wood burning for residential heating.

6.1 Introduction

Exposure to airborne particulate matter (PM) has been documented, over the last three decades, as being related to a wide range of human health impacts, including respiratory and cardiovascular disease (Brook et al., 2010; Olstrup et al., 2019), increased mortality, and loss of life expectancy (Lelieveld et al., 2020; Liu et al., 2019). Fine particulate matter ($PM_{2.5}$) has been recognized as a leading factor in human disease and premature mortality among air pollutants (EEA, 2019) and a causal relationship has been identified between long-term exposure to $PM_{2.5}$ and cardiovascular effects and mortality (Lipsett et al., 2011; Shi et al., 2016). In this context, annual $PM_{2.5}$ standards have been established in international environmental legislation. In the European Union, the standing annual limit value is 25 μg m^{-3}, as set by the 2008/50/EC air quality directive, with a provision for its future revision, given that significant effects can be associated with long-term exposure to much lower levels (Cesaroni et al., 2014; Di et al., 2017). The World Health Organization, which has issued a 10 μg m^{-3} guideline value (World Health Organization. Regional Office for Europe, 2006), is prompting more representative ambient exposure assessment by filling gaps in existing ambient air pollution monitoring infrastructures (World Health Organization, 2016). Causal relationships for cardiovascular effects and mortality have also been recognized for short-term exposure to $PM_{2.5}$ (Atkinson et al., 2014; Zhang et al., 2009). Therefore, there exists an unambiguous need for reliable, representative, and timely monitoring of $PM_{2.5}$, in order to inform the general population and especially sensitive population subgroups how to avoid unhealthy outdoor exposure and support informed decision making with respect to mitigation measures. This need becomes more imminent during pollution events of episodic nature, such as urban smog

events (Weichenthal et al., 2017) or urban/peri-urban wildfire plumes impacting populated areas (Delfino et al., 2009).

The small-scale variability of air pollution within large urban agglomerations, where local sources can contribute to varying degrees, is an issue pointing towards the need for densification of air quality monitoring networks in order to improve the spatial representation of ambient exposure. However, to accomplish this by using reference-grade instrumentation would require significant investment (Kumar et al., 2015). Low-cost PM monitors, which are based on optical particle counting technology, have emerged as a cost-efficient solution where indicative yet dense monitoring is required in order to provide real-time information to citizens and stakeholders. Around the world, state and local authorities are moving towards the deployment of such devices in dense networks for urban particle pollution monitoring (Gao et al., 2015; Jiao et al., 2016; Park et al., 2020). At the same time, low-cost monitoring technologies are proving useful in studies involving citizen science or for the evaluation of AQ models, in order to derive particle pollution predictive tools at an urban scale (Bi et al., 2020).

While measurements from low-cost PM devices cannot be used for the assessment of regulatory compliance with air quality standards, it has been demonstrated that they can track reasonably well the variability of concentrations (on various time-scales) and therefore can be subject to calibration based on reference-monitor data, in order to provide realistic ambient concentration levels (Feenstra et al., 2019). In this respect, low-cost PM sensors have been recently evaluated by laboratory and field studies (Borrego et al., 2016; Tagle et al., 2020), and are also proposed as tools for both long-term as well as event-based monitoring—for instance when dealing with forest fires (Kelleher et al., 2018). The digital transition promoted through the Urban Agenda for the EU and the rising of smart city approaches, point towards the integration of IoT (Internet of Things) technologies and other ICT (Information and Communication Technologies) into policy making, with sustainable development and urban resilience being the overarching goals. Along these lines, the utility of low-cost AQ cross-cuts many different sectors (e.g., health, transport, carbon neutral cities, climate change), which makes them, under proper treatment, an important component of a smart and resilient city.

The Plantower PMS sensor is one of the most widely used for low-cost PM measurements and it forms the basis of the PurpleAir monitor, a compact low-cost platform with advanced online data

reporting capabilities (Kelly et al., 2017). Several field studies have been recently performed for the evaluation of Plantower PMS sensors (models 1003 through 7003), in different environments and conditions (Feenstra et al., 2019; He et al., 2020; Levy Zamora et al., 2019; Zheng et al., 2018). These studies, while finding good correlations with reference monitors, have also pointed out biases related to relative humidity and high ambient PM levels, and have suggested various approaches in order to correct the sensor's concentration outputs. Laboratory and chamber tests have corroborated the above findings (Wang et al., 2015) and have revealed further issues, such as the sensor's poor size selectivity and their performance dependence on ambient particle size distributions (Kuula et al., 2020), as well as their non-linear response to elevated PM concentrations (Sayahi et al., 2019b). A thorough understanding of the factors controlling the performance of the sensor is critical in order to perform reliable calibration and apply specific corrections to obtain realistic outputs.

Particle size distribution and chemical composition have been considered as important error-inducing factors in PA-II devices. The majority of studies on PA-II validation has indicated that relative humidity variations can alter the aerosols size distribution and scattering properties, biasing the sensor's response (Kim et al., 2019; Levy Zamora et al., 2019; Mehadi et al., 2020). Therefore, relative humidity was considered in this study as well, as a parameter for adjustment of the PA-II output. Moreover, because aerosol chemical composition drives the optical and hygroscopic properties (Crilley et al., 2018; Wang et al., 2015), we made a fist attempt to examine the associations of errors with concentrations of major aerosol components. The second key issue in PA-II calibration is related to the sensor's geometry that restricts its ability to accurately track supermicron particles (Karagulian et al., 2019; Sahu et al., 2020), which, under special conditions, can amount to a significant fraction of actual $PM_{2.5}$. Here, we propose a novel approach using external size fractionation data (such as $PM_{2.5}$ and PM_{10} from a reference station), that can be applied in urban PA-II networks, especially in cases of regional dust events, which are frequent in Southern European countries. In this framework, we have developed calibration models which have been tested at the operational scale of locally developed low-cost networks for an extended period, highlighting the monitor's capabilities in ambient conditions, including air quality episodic events. Such large-scale implementation of calibrated low-cost devices can lead to integrated solutions for effective and hi-resolution spatiotemporal monitoring and prediction centered on ground-based measurements (Bi et al., 2020).

In this study, the performance of the Purple Air PA-II low-cost PM monitor was evaluated during several ambient intercomparison campaigns in Greece. The study is focused on the $PM_{2.5}$ fraction, since the response of the sensor to PM_{10} has been deemed much less reliable (Park et al., 2020; SCAQMD, 2017), while PM_1 monitoring is not yet foreseen by existing EU air quality standards. Measurement campaigns were held in different cities and seasons, covering a wide range of ambient $PM_{2.5}$ concentrations (up to several hundred μg m^{-3} on an hourly basis), in environments influenced by diverse particle sources and meteorological conditions. Furthermore, the sensor's performance under elevated coarse-mode PM concentrations related to regional dust transport was assessed, while ways to mitigate the sensor's bias through multiple regression models, incorporating reference PM ratios, was investigated. Moreover, the effectiveness of the Purple Air PA-II monitor as component of a low-cost monitoring network was explored, by assessing the inter-site correlations and intra-urban homogeneity of $PM_{2.5}$ concentrations at urban/suburban background locations. Finally, the utility and operational capabilities of the network were evaluated during large urban air pollution episodes that were caused by intense residential wood burning and forest fires.

6.2 Study Area and Methods

6.2.1 Sites and Measurement Periods

Field evaluation tests were held in two Greek cities, Athens and Ioannina, during 2019–2020. In Athens, the Greek capital and largest city with approximately four million inhabitants, measurements were performed at the Thissio urban background monitoring station (37.97326° N, 23.71836° E, 105 m ASL), operated by the National Observatory of Athens (NOA). The site is not directly affected by particle emissions, is located in an area of moderate population density, close to a large pedestrian zone and away from major roads. Therefore, it can be considered to be representative of background pollution in central Athens (Athanasopoulou et al., 2017; Grivas et al., 2019; Theodosi et al., 2018). Initially, eight PA-II monitors were installed at Thissio for a nearly one-month period (8 March 2019–2 April 2019) during spring 2019. In a second phase, five PA-IIs were in operation at Thissio during summertime, from 3 July 2019 to 3 September 2019. In the third phase, during late winter and spring of 2020 (26 February 2020–18 May 2020), a single PA-II monitor (continuously operating since 7 July 2019 at the site, thus covering both calibration periods) was used. **Table 12.1** summarizes information regarding each intercomparison campaign.

Ioannina is a medium-sized city in northwestern Greece with a population of approximately 100,000 inhabitants, located on a plateau in the foothills of the Pindus Mountain range. Measurements in Ioannina were performed at the Vilara Air Quality Monitoring Station (39.67102° N, 20.84648° E, 484 m a.s.l.), operated by the Regional Authority of Epirus, in collaboration with the University of Ioannina. The station is located in the city center and is close to a road with moderate traffic. The intercomparison in Ioannina took place from 15 December 2019 until 31 May 2020, covering the spring period but also most of the winter period, when the city is heavily impacted by residential wood burning emissions, leading to persistent wintertime smog episodes (Kaskaoutis et al., 2020).

Furthermore, several PA-II devices have been deployed at background locations within the larger urban zones of the two cities, with the objective to gradually form dense monitoring networks. In this study, we present results from nine such nodes in Athens and three in Ioannina. The network configuration, as well as the locations of the sites hosting reference instruments, can be seen in **Figure 6.1**, while details on the site characteristics are presented in **Table 12.2** and **Figure 12.1**.

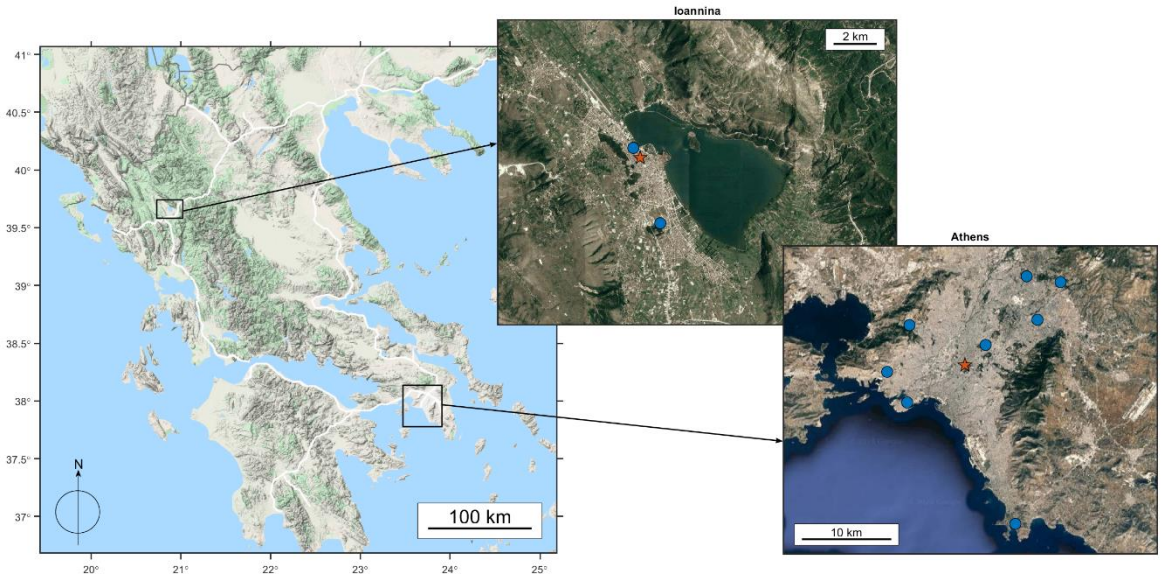

Figure 6.1. Map of mainland Greece (left) and overviews of the Athens (bottom right) and Ioannina (top right) basins. Measurement sites hosting both reference and low-cost instrumentation are denoted with red stars, while the other sites of the low-cost PA-II networks are denoted with blue dots.

6.2.2 Instrumentation

6.2.2.1 The Purple Air PA-II Low-Cost PM Monitor

The PA-II monitor and its PA-II-SD version (PurpleAir LLC, Draper, UT, USA) incorporate a pair of PMS5003 (Plantower Ltd., Beijing, China) laser optical particle counter (OPC) sensors, along with a temperature, relative humidity, and barometric pressure sensor (BME 280, Bosch Sensortec GmbH, Reutlingen, Germany), both connected to a microcontroller equipped with a wireless network communication module. The device records and transmits data over Wi-Fi to a cloud-based platform, from where they can be downloaded at a 2 min. resolution. Pictures of the PA-II monitor and the PMS5003 sensor are provided in **Figure 12.2**. A side view with the twin-sensor design can be seen (**Figure 12.2b**), with air entering from four small holes in the bottom of the sensor and exiting from the fan at the same side. The sample flow is guided to the laser detector after two 90° turns. Drawn schematics on the internal sensor geometry and sample flow path can be found in (Sayahi et al., 2019a) and Ardon-Dryer et al. (2020).

The PMS5003 sensor provides digital outputs for 12 data fields. The first three correspond to the mass concentrations of PM_1, $PM_{2.5}$, and PM_{10} fractions, without applying any correction, and they are labeled CF = 1. The next three, labeled CF = atm, correspond to adjusted mass concentrations derived after applying a proprietary algorithm developed by Plantower Ltd. The next six data fields contain the cumulative particle size distribution in six size ranges (>0.3 μm, >0.5 μm, >1 μm, >2.5 μm, >5 μm, and >10 μm). In addition to these parameters, from each of the two PM5003 sensors, the PA-II also reports data for temperature, relative humidity, and barometric pressure.

6.2.2.2 Reference Instrumentation

At Thissio, reference $PM_{2.5}$ concentration measurements were conducted using a reference-grade beta attenuation monitor (PX-375, Horiba Ltd., Kyoto, Japan), providing data that were averaged on a 3 h basis. The instrument was sampling through a PM_{10} size-selective inlet upstream of a $PM_{2.5}$ sharp cut cyclone (VSCC 2.251, BGI Inc., Butler, NJ, USA) and was equipped with a sample heating system to avoid measurement bias due to variations in atmospheric moisture. In addition, a research-grade 31-channel optical particle counter (Model 11-D, Grimm Aerosol Technik, Ainring, Germany) was in operation at Thissio, sampling through a TSP sampling head, providing particle size distributions in the 0.2 μm to 35 μm range and mass concentrations for PM_1, $PM_{2.5}$, and PM_{10}, at a 1 min resolution. Measurement data for meteorological parameters (ambient

temperature—T, relative humidity—RH) were obtained from the adjacent NOA meteorological station, on an hourly basis.

In Ioannina a 32-channel optical particle counter (APDA-372, Horiba Ltd., Kyoto, Japan) was used as reference. The instrument is reference-equivalent for $PM_{2.5}$ and PM_{10} measurement according to the EN 14907 and EN 12341 standards, respectively. It was sampling through a TSP sampling head with a vertical sampling line that was equipped with a particle drying system, providing mass concentrations of PM_1, $PM_{2.5}$ and PM_{10} fractions on hourly intervals. Hourly average values of meteorological parameters (T, RH) were obtained using a, collocated, automated weather station.

6.2.2.3 Ancillary Measurements

Chemical composition of submicron aerosol at Thissio was monitored using an Aerosol Chemical Speciation Monitor (ACSM, Aerodyne Inc., Billerica, MA, USA) providing concentrations of the non-refractory (NR-PM_1) aerosol components (namely organic aerosol—OA, sulfate, nitrate, ammonium, and chloride) at a 30 min. resolution, complemented by Black Carbon (BC) measurements performed by a 7-λ aethalometer (AE-33, Magee Scientific, Berkeley, CA, USA) operating at a 1 min. resolution. Details on the operation and quality assurance regarding the ACSM can be found in (Stavroulas et al., 2019). BC was also measured in Ioannina using again an AE-33 aethalometer at a 1 min. resolution. Furthermore, the aethalometer model (Drinovec et al., 2015; Sandradewi et al., 2008) was used to calculate the fossil fuel (BC_{ff}) and biomass burning (BC_{bb}) fractions of black carbon, at both sites.

In order to support the identification of dust transport events, 120 h backward trajectories arriving at the two reference sites were calculated for selected periods, every 6 h at a height of 1000 m, using the HYSPLIT trajectory model (Stein et al., 2015), while PSCF (Potential Source Contribution Function) calculations were performed with the ZeFir toolkit developed for the Igor Pro software package (Petit et al., 2017).

6.2.3 Data Treatment

For the comparative evaluation and calibration of PA-II monitors, raw data from the two PMS5003 sensors in each monitor were averaged on 1 h time intervals. For the Athens datasets, in addition to 1 h average values for all of the examined parameters, 3 h averages were also calculated for

comparisons with $PM_{2.5}$ reference concentrations from the beta-attenuation monitor. The agreement between the two individual sensors of each PA-II device was checked for hourly-averaged values and obvious outliers were excluded (Bi et al., 2020), however their frequency was negligible (< 0.05%).

Data capture (recovery) from the PA-II devices was very high (exceeding 99% for hourly average values at all sites, during all study periods), considerably exceeding the 90% threshold (that we indicatively mention as the minimum data capture rate required in reporting of continuous measurement data according to the EU air quality directive). Therefore, no imputation for missing values was performed. Data capture rates exceeding 99% have also been reported for the PA-II monitor by other studies (Feenstra et al., 2019), attesting to the device's durability and consistent operation in field conditions.

The squared Pearson correlation coefficient (R^2) is used throughout the manuscript as a correlation metric. PA-II $PM_{2.5(CF = 1)}$ measurement biases in comparison to reference $PM_{2.5}$ are assessed through the mean bias error (MBE), the mean absolute error (MAE), and the normalized Root Mean Squared Error (nRMSE). These metrics are also used for analyzing the performance of the proposed calibration models. Bias errors correspond to the difference of the PA-II concentration minus the reference concentration. All related equations can be found in **Section 12.1** of the supplement.

6.3 Results and Discussion

6.3.1 Field Evaluation and Device Calibration

6.3.1.1 $PM_{2.5}$ Data Output of the PA-II device

One of the main issues that need to be accounted for is which of the data fields (CF = 1, CF = atm), provided by the PMS5003 and, consequently, the PA-II monitor, should be considered when performing $PM_{2.5}$ field calibration, since the two outputs deviate notably in certain concentration ranges (Kelly et al., 2017). Examining the CF = 1 versus CF = atm scatterplots, a linear 1:1 relationship is observed for low concentrations. Then, a non-linear adjustment appears to be applied in mid-range CF = 1 values to derive CF = atm. Finally, another linear correction is applied for higher concentrations, with a coefficient that is smaller than one. Based on repeated

observations on all datasets, the different $PM_{2.5(CF = 1)}$ ranges (in μg m^{-3}) where the three different corrections are applied to obtain $PM_{2.5(CF = atm)}$, are approximately the following:

- Low Range: $PM_{2.5(CF = 1)} < 20$, where $PM_{2.5(CF = atm)} = PM_{2.5(CF = 1)}$.
- Mid-Range: $20 < PM_{2.5(CF = 1)} < 110$, where an unknown correction is applied by the sensor manufacturer.
- High Range: $PM_{2.5(CF = 1)} > 110$ where $PM_{2.5(CF = atm)} \approx 0.66\ PM_{2.5(CF = 1)}$.

To illustrate this, three scatterplots corresponding to the above concentration ranges, along with the linear regression equations for the first and third range are depicted in **Figure 6.2a–c**. The winter-time measurements in Ioannina were utilized for the visualization, as the dataset is characterized by a wide concentration range (hourly concentrations from as low as a few μg m^{-3} up to several hundreds of μg m^{-3}). Splitting the reference dataset into 35 equidistant concentration bins that cover the entire ambient concentration range, calculating each bin's $PM_{2.5(CF = 1)}$ and $PM_{2.5(CF = atm)}$ average, and finally plotting those values against the reference $PM_{2.5}$ values, leads to the plot of **Figure 6.2d**. It can be seen that for both data fields, while, at low concentrations binned averages follow a 2:1 line, they gradually deviate from it with increasing ambient concentrations.

A similar pattern has been reported for the PA-II monitor when comparing its outputs to a reference (TEOM) instrument (Tryner et al., 2020), while non-linear fits with a similar curvature, as in Figure 2d, have been documented to better describe the sensor to reference relationship (Sayahi et al., 2019b). In **Figure 6.2d**, the pattern seems to be more pronounced for the CF = atm output, which, while falling on the 2:1 line for low concentrations, it tends towards the 1:1 line for higher ambient $PM_{2.5}$ levels. While this non-linear behavior of CF = atm should be addressed by any proposed calibration scheme, the use of the CF = 1 field may provide a more straightforward approach, also allowing for a more direct assessment of the effects that are related to aerosol physical properties, since there seems to be a more direct linkage between $PM_{2.5(CF = 1)}$ and measured particle number concentrations. Thus, the CF = 1 field was utilized in the subsequent analysis. It is noted that the proprietary algorithm used for the correction of CF = 1 to CF = atm (Sayahi et al., 2019b), to the best of our knowledge, has not been yet documented in the literature,

is not available in the sensor manual or any relevant documentation, while it is also not known to the manufacturer of the PA-II monitor either (personal communication with Purple Air LLC).

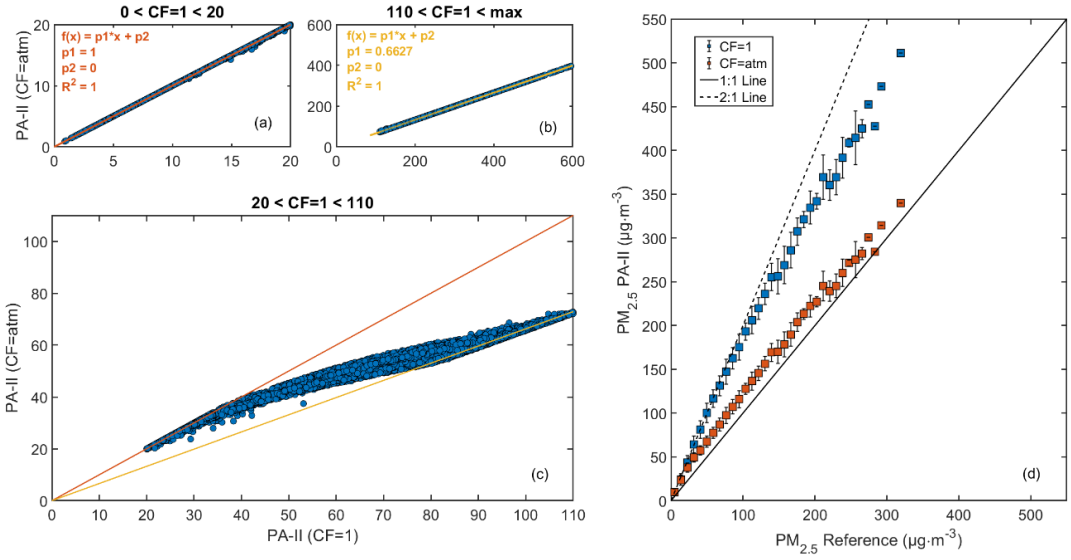

Figure 6.2. Breakdown of the CF = atm versus CF = 1 data channel responses during the Ioannina intercomparison campaign ($PM_{2.5}$ concentrations), when stratified by the relevant CF = 1 data ranges (<20, >110, 20–110 μg m^{-3}), on panels (a–c), respectively. On panel (d), the binned average output of the two channels plotted against the reference instrument is illustrated.

6.3.1.2 Repeatability of $PM_{2.5}$ and T-RH Measurements

Eight devices—which subsequently were deployed at the various sites—were installed at the Thissio site during the 1st intercomparison period of 2019 in order to assess the repeatability of the PA-II monitor in ambient conditions. The results from pairwise comparisons of the $PM_{2.5(CF = 1)}$ output of the devices are presented in **Figure 12.3** and **Table 12.3**. The inter-device repeatability was high, with slopes and R^2 values very close to unity (0.98 < slope < 1.02, 0.997 <R^2 <1). Similar results supporting the high precision of the Purple Air PA-II monitor have been also documented by Feenstra et al. (2019), using a triplet of PA-II devices. These results support the utilization of the device in low-cost PA-II networks, since they indicate the comparability of different monitors after their field deployment, and can facilitate different approaches for batch calibration.

A similar evaluation was performed for the temperature and relative humidity measurements by the BME280 sensors included in the PA-II devices. Precision is important in this case, since several calibration approaches utilize T and RH as inputs in order to minimize PA-II biases. For

temperature, slopes varied in the range 0.82–1.10 and R^2 between 0.989 and 1, while, for relative humidity, ranges were 0.90 < slope < 1.07 and 0.996 < R^2 < 1, respectively. Detailed results regarding the pairwise comparisons of T-RH sensors can be found in **Tables 12.4** through **12.7**. When compared to reference T and RH measurements, the devices exhibit excellent linearity (**Figure 12.4**) but tend to overestimate temperature and underestimate relative humidity, probably owing to the BME sensor's proximity to the electronics board inside the sensors' housing (Malings et al., 2020).

6.3.1.3 Coarse Particle and Relative humidity Effects on Sensor Bias

During the intercomparison campaigns in Athens and Ioannina, the PA-II devices operated under a wide range of ambient conditions, regarding the meteorology, aerosol sources, and chemical composition. Furthermore, several dust episodes were observed, linked principally to air masses originating from northern Africa. Scatterplots of reference measurements conducted in Ioannina versus the PA-II $PM_{2.5(CF = 1)}$ measurements can be seen in **Figure 6.3a,b**, providing an indication of coarse particle effects. Respectively, data from the 2nd Athens intercomparison campaign (the Grimm 11D OPC that provided the particle fraction ratios was not available during the 3rd intercomparison campaign) are depicted in **Figure 6.3c,d**.

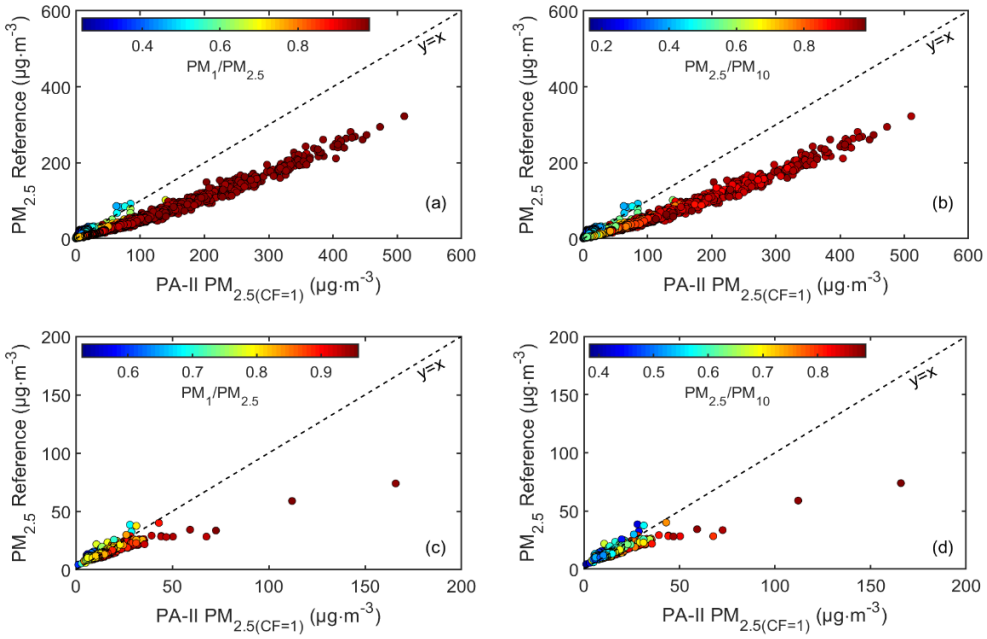

Figure 6.3. Scatter plots of the reference versus PA-II $PM_{2.5}$ concentrations, color-coded according to the $PM_1/PM_{2.5}$ ratio for Ioannina (a) and Athens (c) and the $PM_{2.5}/PM_{10}$ ratio for Ioannina (b) and Athens (d), with the ratios calculated by the HORIBA APDA-372 and Grimm 11-D instruments for Ioannina and Athens respectively.

The PMS5003 sensor has been documented to have poor size selectivity for coarse particles (Kuula et al., 2020), while the design of the flow path—from inlet to optical cavity—forces the sample flow along two consecutive 90^o angles, favoring the deposition of larger particles before reaching the optical detector (Sayahi et al., 2019b). Therefore, the response is susceptible to error when aerosol is dominated by coarse particles, which in Southern European areas is typically observed during Saharan dust transport episodes (Gerasopoulos et al., 2006).

In the present case, when color-coding data-points in the scatterplots according to their corresponding $PM_1/PM_{2.5}$ and $PM_{2.5}/PM_{10}$ ratios (calculated from measurements of the multi-channel OPC instruments), it is evident (**Figure 6.3**) that the data-points deviate from the general pattern for increasing coarse PM fractions (lower ratios). Points corresponding to lower ratios follow a steeper, almost 1:1 line, as compared to points corresponding to higher ratios, for which a clear overestimation by the PA-II is observed. Because these deviations become clearer when using $PM_1/PM_{2.5}$, this ratio will be henceforth used as a proxy in the related graphs.

On the other hand, important sensor biases can be expected in elevated ambient RH, since no conditioning of the sample takes place in the PMS5003 sensor. When evaluating the PA-II monitor, Magi et al. (2020) reported linearly increasing MAE and RMSE errors with increasing RH, while a positive relationship between RH and MBE was documented by Feenstra et al. (2019).

For the investigation of these effects, the absolute error of the PA-II $PM_{2.5(CF = 1)}$ relative to the reference values in both datasets was first calculated. Given the fact that wintertime mean $PM_{2.5}$ concentrations in Ioannina were high (57.2 μg m^{-3}), the analysis was initially focused on the springtime measurements (mean 13.4 μg m^{-3}), in order to achieve comparability with the Athens dataset where the mean $PM_{2.5}$ concentration for the 2nd and 3rd campaigns combined was 15.2 μg m^{-3}. Plotting the absolute error against the $PM_{2.5}$ reference concentrations, steeper slopes in the relationships with ambient concentrations were observed for higher RH values (**Figure 12.5**). This was more obvious in Ioannina, while, in Athens, this pattern was much less pronounced, probably due to the drier ambient conditions (RH: 49% in Athens versus 64% in Ioannina, on average, for the respective periods).

Data were divided in 20 equidistant bins according to RH, and the corresponding Mean Absolute Error (MAE) values was plotted, in order to examine the humidity effect. The results are shown in **Figure 12.6**, where an evident dependence of MAE on RH can be observed. The effect is more evident in the Ioannina dataset, with MAE rising from 8.5 μg m^{-3} to 35.7 μg m^{-3} when RH increases from 30% to 90%. This behavior could be linked to the frequent lake-effect fog events during wintertime in Ioannina (Houssos et al., 2012), with the error being possibly related to water droplets that are introduced in the sample stream and counted in the $PM_{2.5}$ size range. A similar observation, with fog events inducing a positive bias in $PM_{2.5}$ measurements performed with the PMS1003 sensor—a previous version of PMS5003—has been also reported in Brisbane, Australia (Jayaratne et al., 2018). A positive but nevertheless more modest relationship can be observed in the Athens dataset, with MAE rising from 4.3 μg m^{-3} to 9.3 μg m^{-3} along the 30% to 90% RH increment.

It should be noted that higher concentration levels in Ioannina were mostly observed during the evening, coinciding with elevated RH levels. This means that part of the bias could be due to an additive effect of high concentration and RH, given the positive relationship between absolute error and ambient $PM_{2.5}$ levels (**Figure 12.5**). Other than that, the observations noted earlier,

regarding the sensor behavior under elevated coarse mode concentrations (when the PA-II underestimates real $PM_{2.5}$ concentrations), implies that, in this case, the examination of the absolute error hinders the correct attribution of the actual measurement bias. Thus, it is necessary to isolate the influence of different effects and then examine their corresponding errors.

Because the RH and coarse particle effects tend to bias the performance in opposite directions, the bias error was examined as a metric of the sensor's performance, for both Ioannina springtime and Athens datasets (**Figure 12.7**). The effect of coarse mode particles can be now observed clearly (**Figure 12.7**), with the majority of negative errors being calculated for low $PM_1/PM_{2.5}$ ratios, while a linear relationship with increasing concentration can be suggested for any $PM_1/PM_{2.5}$ ratio, starting with apparently negative slopes for low ratios and gradually moving towards positive slopes for higher ratios. A positive relationship with RH, even at mid-range concentrations is again suggested (**Figure 12.6**), while negative errors seem to be linked to lower RH, possibly related to drier and dust-laden southern air masses affecting continental Greece (Dimitriou and Kassomenos, 2019). A boxplot of MBEs in 10% RH bins is also presented (**Figure 12.7**), where the RH dependence is obvious.

It is necessary to exclude that this increase was introduced by the positive error-concentration relationship to examine whether the increased bias linked to RH can be actually attributed to rising RH values. In this scope, the ratio of PA-II $PM_{2.5(CF = 1)}$ to $PM_{2.5}$ reference concentrations (PA-II/Ref) was calculated and its association with the observed reference concentration was explored (**Figure 6.4**). In **Figure 6.4a,b**, data-points are color-coded by the $PM_1/PM_{2.5}$ ratio and RH respectively, and it is indicated that lower $PM_1/PM_{2.5}$ ratios correspond to low PA-II/Ref ratios (ranging from zero to roughly 1.5). We used the $PM_{2.5}/PM_{10}$ ratio (according to the analysis in **Figure 12.8**) in order to remove the points affected by the elevated coarse mode concentrations and consequently focus on the RH effect, given that, as an external parameter, it should be more readily available by regulatory monitoring stations, where, in most cases, PM_1 will not be routinely monitored. The colored scatterplot in **Figure 6.4c**, were coarse-related data-points ($PM_{2.5}/PM_{10}$ ratios less than 0.5) have been removed, clearly illustrates the RH effect on the sensor data deviation from reference dried measurements, while the resulting boxplot of **Figure 6.4e** points towards a linear pattern with the lower bin median PA-II/Ref at 1.41 and the higher at 2.10. A line

was fitted to the calculated medians of each bin versus RH yielding an excellent correlation (R^2 = 0.96).

Through the error analysis, it is suggested that, in order to correct the PA-II $PM_{2.5}$ values, a multivariable approach should be followed, incorporating both humidity and coarse particle effects. The PA-II devices include a RH sensor, characterized by high repeatability (**Section 6.3.1.2**), which can be calibrated ahead of field deployment (**Figure 12.4**). However, the representative PM ratios required for corrections related to the presence of coarse mode particles should be externally provided. Such a solution could lie in the integration of $PM_{2.5}$, PM_{10} data from a central or the nearest available regulatory air quality station (AQS), and it should be necessary when coarse-particle episodes are frequent and effective over wide urban areas. Similar calibration approaches have been already documented (Becnel et al., 2019; Bi et al., 2020), albeit directly using reference $PM_{2.5}$ measurements coming from nearby regulatory AQS. Nevertheless, because lower PM ratios are not only related to regional phenomena, such as Saharan dust events in Southern Europe, this approach could face limitations regarding locally re-suspended dust. Therefore, its use in traffic sites, for example, where traffic induced resuspension can be substantial (Grivas et al., 2018), may result in unsolicited errors.

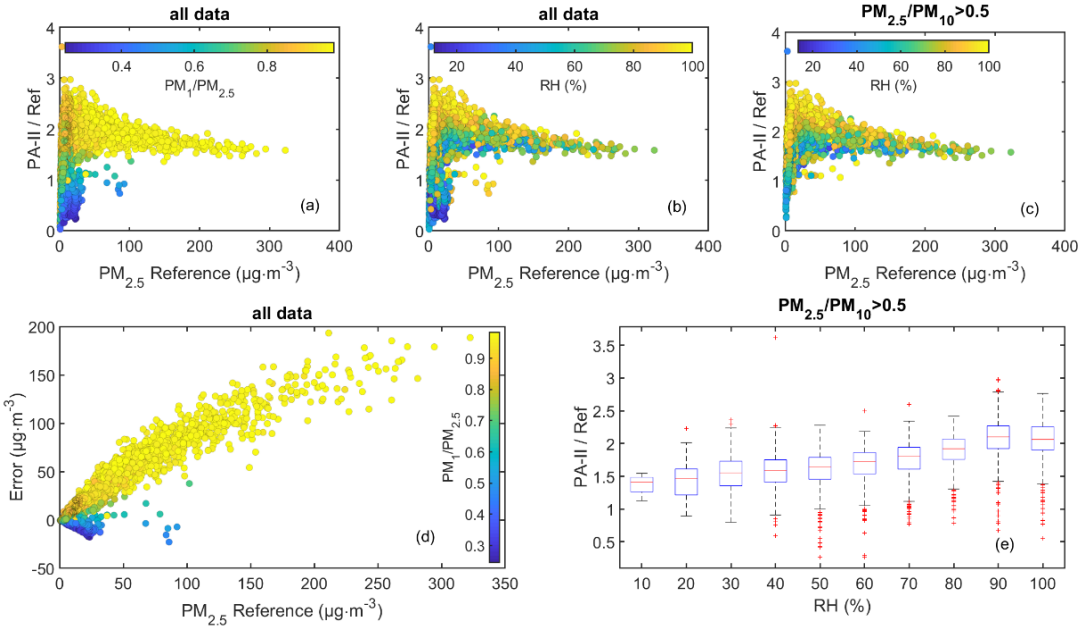

Figure 6.4. Behavior of the error (PA-II—Reference) and PA-II/Reference ratio for the PA-II monitor in the Ioannina intercomparison during the entire deployment period. Panels (a,b) show

scatterplots of the PA-II/Ref ratio versus reference concentrations color-coded by $PM_1/PM_{2.5}$ and RH, respectively. In panel (c) RH color-coded data are presented, excluding points where $PM_{2.5}/PM_{10}$ ratios were less than 0.5. In (d) the error is plotted against reference measurements color-coded by $PM_1/PM_{2.5}$ while a boxplot of PA-II/Ref ratios versus binned RH is also presented (e).

6.3.1.4 Models for Correction of PA-II $PM_{2.5}$ Measurements

Models for Ioannina: The Ioannina dataset was randomly divided in two subsets, selecting 60% as the base dataset (n = 2556 hourly observations) and the remaining 40% as the evaluation dataset (n = 1706) (**Figure 12.9**). The base dataset was used to fit different regression models. Reference $PM_{2.5}$ concentration was used as the dependent variable and PA-II $PM_{2.5(CF=1)}$ concentration, ratios related to the presence of coarse particles ($PM_1/PM_{2.5}$ or $PM_{2.5}/PM_{10}$) and RH, were used as predictors. In total, ten different models were fitted, using all or a combination of the aforementioned predictors, starting with simple linear and quadratic regression models involving only the sensor and reference $PM_{2.5}$ data (iModel 1, iModel 2), then incorporating the PM ratios (iModel 3 to iModel6), and finally RH (iModel 7 to iModel 10). Motivation for including the PA-II $PM_{2.5\ (CF=1)}$ as a squared term comes from the convex patterns observed in **Figure 6.3**, as well as the PA-II versus reference relationships documented in other studies (Feenstra et al., 2019; Sayahi et al., 2019b; Zheng et al., 2018). A detailed description of the developed models can be found in **Table 12.7**. Generally, the larger part of the variability in the models can be explained by the PA-II $PM_{2.5}$ concentration variable. Positive increments with added predictors were somewhat small in terms of adjusted R^2, however coefficients of all added predictors were statistically significant at the 0.05 level, for all the models.

The obtained equations were then applied in the evaluation dataset and the model-corrected PA-II $PM_{2.5cor}$ concentrations were compared to the reference measurements, calculating R^2, MAE, and normalized RMSE (nRMSE) as performance metrics. **Table 6.1** summarizes the results of the evaluation. The fitting ability of the models increased by progressively adding as predictors the variables that have been shown to directly influence the sensor's measurement. Specifically, the nRMSE decreased by approximately 17% when the PM ratios were incorporated (iModel 3 and iModel 5) and approximately 21% when the polynomial model included also RH (iModel 7 and iModel 9), in comparison to the simple linear model (iModel 1). An important decrease (19%) in

nRMSE, was also found by the simple quadratic models (iModel2), with no other external predictors. The model with the best descriptive power was the one incorporating $PM_1/PM_{2.5}$, RH, and a PA-II $PM_{2.5(CF = 1)}$ quadratic term (iModel 8), yielding a 40% improvement in nRMSE, relative to the simple linear model. It is noted here that the $PM_{2.5(CF = 1)}$ MAE, calculated for the evaluation dataset (before application of a correction model), was 25.4 μg m^{-3}, much higher than the MAE of models, for which the lowest value was for iModel 8 (MAE = 2.2 μg m^{-3}, 41% lower as compared to the simple linear iModel 1). Including PM ratios in the PA-II $PM_{2.5}$ calibration scheme appeared to drastically improve the behavior of the post-processed sensor signal during dust events.

Table 6.1. Performance metrics for the ten models tested in Ioannina (reference $PM_{2.5}$ versus the modeled PA-II $PM_{2.5cor}$) as calculated for the evaluation dataset.

Ioannina	R^2	Slope	Intercept	nRMSE	MAE (μg m^{-3})
iModel 1	0.975	1.005	0.044	0.200	3.7
iModel 2	0.984	1.008	−0.012	0.162	2.9
iModel 3	0.983	1.007	−0.062	0.165	3.3
iModel 4	0.989	1.010	−0.112	0.135	2.7
iModel 5	0.983	1.006	0.034	0.168	3.4
iModel 6	0.987	1.008	−0.008	0.145	2.9
iModel 7	0.985	1.001	−0.044	0.158	2.9
iModel 8	0.992	1.004	−0.184	0.119	2.1
iModel 9	0.984	1.002	−0.091	0.166	3.2
iModel 10	0.988	1.005	−0.229	0.142	2.6

Trying to discern which model incorporating the two coarse-related ratios (iModel 8 or iModel 10) performs better during a dust event, we focused on a severe dust episode recorded during 20–22 December 2019 and a milder event during 11–21 May 2020 in Ioannina. During these periods, air masses mostly originated from the southern sectors, with PSCF analysis indicating dust transport from north Africa (**Figure 12.11**), in agreement with the low $PM_{2.5}/PM_{10}$ ratios calculated. In Figure 5, the time-series of coarse PM as measured by the reference instrument is depicted, with the shaded areas corresponding to the respective dust events.

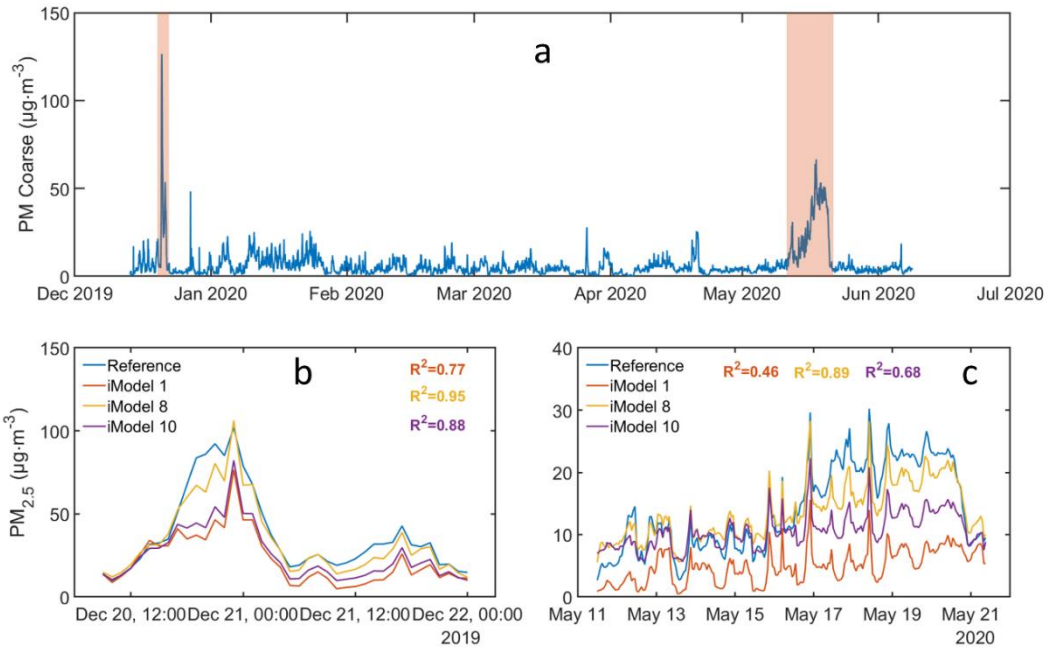

Figure 6.5. The time-series of $PM_{10\text{-}2.5}$ concentrations in Ioannina, highlighting two distinct dust events, is illustrated in the top panel (a). The behavior of different modeled PA-II $PM_{2.5cor}$ measurements is shown in the bottom panels, for the December (b) and May (c) events.

The mean $PM_{10\text{-}2.5}$ concentration was 38.7 μg m^{-3} during the December and 27.3 μg m^{-3} during the May event, in contrast to the 6.7 μg m^{-3} average that was registered for the entire period. In the bottom panels of Figure 5 the behavior of the two examined models along with the linear model (iModel 1) is shown. iModel 8 seems to generally perform better (**Tables 12.10** and **12.11**), yielding average $PM_{2.5}$ values that were closer to the recorded for each period (34.0 μg m^{-3} for December and 13.6 μg m^{-3} for May, against 37.7 and 14.2 μg m^{-3} that were measured by the reference instrument, respectively).

Models for Athens: The same approach was followed for the investigation of the best corrections applicable to the Athens intercomparison campaigns, using the beta attenuation monitor measurements as reference. As opposed to Ioannina, in Athens the models were not found to benefit from the inclusion of PA-II $PM_{2.5(CF = 1)}$ as a quadratic term, since maximum ambient concentrations were relatively low (below 80 μg m^{-3} throughout the entire period; **Figure 6.3**). Because the $PM_1/PM_{2.5}$ and $PM_{2.5}/PM_{10}$ ratios data availability was limited to the 2nd Athens intercomparison campaign, multiple linear regression models incorporating those ratios were

tested only for this period. Additionally, in Athens, models using only PA-II $PM_{2.5(CF = 1)}$ and RH as predictors were tested, with data spanning both the 2nd and 3rd campaigns, after excluding data-points evidently affected by dust events. As criteria for this exclusion, we used: (i) a threshold of 0.5 for the $PM_{2.5}/PM_{10}$ ratio for the 2nd campaign (considering the analysis presented in **Figure 12.8**) and (ii) inspection of backward air mass trajectories when the $PM_{2.5}/PM_{10}$ ratio was not available.

The corresponding datasets were again randomly divided in base and evaluation subsets (60% and 40% respectively), creating in total four subsets (**Figure 12.10**). Six different regression models were tested and they are summarized in **Table 12.12** (configuration) and **12.13** (performance). The results for the evaluation datasets are summarized in **Table 6.2**. Once more, the models incorporating the coarse-related PM ratios (aModel 2 through aModel 5), exhibited the lowest nRMSE (0.133–0.147) and MAE (1.8 μg m^{-3}) values and they were better correlated with the reference $PM_{2.5}$ measurements. Overall, the implementation of multiple regression models, resulted in an improvement of performance metrics, with aModel 4—the model incorporating the $PM_1/PM_{2.}5$ ratio and RH—corresponding to the smallest nRMSE (0.142) and MAE (1.8 μg m^{-3}) values.

Table 6.2. Performance metrics for the various models tested in Ioannina (reference PM2.5 versus the modeled PA-II PM2.5cor) as calculated for the evaluation dataset.

Athens	R^2	Slope	Intercept	nRMSE	MAE (μg m^{-3})
aModel 1*	0.822	1.004	−0.273	0.198	2.2
aModel 2	0.838	1.326	−5.147	0.133	1.8
aModel 3	0.824	1.307	−4.950	0.139	1.9
aModel 4	0.817	1.269	−4.208	0.142	1.8
aModel 5	0.802	1.242	−3.870	0.147	1.8
aModel 6*	0.844	1.015	−0.439	0.186	2.0

* Data for both intercomparison campaigns (2nd and 3rd) at Thissio are used for aModel 1 and aModel 6.

It is evident that correcting the raw sensor signal drastically improved the PA-II performance metrics for both the Ioannina and Athens datasets, effectively reducing MAE from 25.4 μg m^{-3} to below 3.7 μg m^{-3} and from 3.1 μg m^{-3} to below 2.2 μg m^{-3}, respectively. Similar improvements have been observed by the majority of studies applying statistical models for correction. For

example, Magi et al. (2020) reported a 45% improvement in MAE after implementing a multilinear regression correction scheme, incorporating RH and reference $PM_{2.5}$ measurements as predictors, while Malings et al., (2020), using more complex corrections by calculating an RH-related hygroscopic growth factor, documented a reduced MAE by 40%. Pawar and Sinha (2020) applied a particle density adjustment followed by growth factor and aspiration efficiency corrections, reporting a 10–15% improvement in RMSE. Tryner et al. (2020) reported that their correction (taking RH into account in a simple regression approach) reduced the absolute value of the mean bias from 2.1 to 0.6 μg m^{-3}. Significant improvements in PA-II signal corrections have also been shown by the application of non-linear supervised machine learning approaches, such as artificial neural networks (Mahajan and Kumar, 2020; Si et al., 2020).

6.3.1.5 Comparison to Reference Instrumentation in Different Seasons

The corrected (aModel 6) PA-II output was examined against reference measurements at Thissio, in three different seasons during the 2nd and 3rd intercomparison campaigns, in order to assess the potential influence of seasonal factors on the performance of the PA-II monitor (that could be for example related to the seasonally variable chemical composition of urban aerosols).

The model choice was mainly dictated by the fact that the base dataset used in model aModel 6 was more representative, spanning all seasons in Athens, with the model displaying an overall good performance. The results are presented in **Figure 6.6**. Temperature and relative humidity diurnal patterns and basic statistics during those three seasons are presented in **Table 12.14** and **Figure 12.12**. For the warm season (3 July 2019–3 September 2019, **Figure 6.6a**), the averaged PA-II $PM_{2.5cor}$ and $PM_{2.5(CF = 1)}$ data from the five installed PA-II devices at Thissio were used as independent variables in the displayed linear regressions. For the other two seasons, the cold (26 February 2020–7 April 2020) and intermediate (8 April 2020–19 May 2020), data from one PA-II deployed at Thissio were used as the independent variable. The cold and intermediate seasons were categorized according to long-term climatology studies for Southern Greece (Argiriou et al., 2004). It is noted that, for the warm season data-points affected by coarse particles, according to criterion (i) described previously, were excluded, while for the intermediate and cold seasons, where no concurrent PM_1 or PM_{10} measurements were available at Thissio, the affected data were excluded according to criterion (ii).

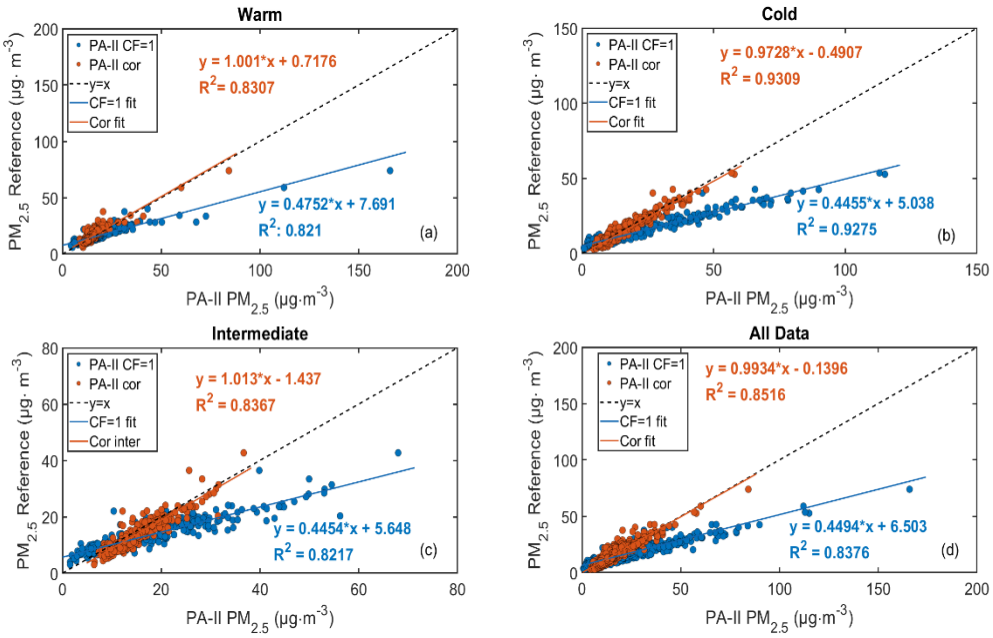

Figure 6.6. Linear regression of reference versus PA-II$_{CF\ =\ 1}$ PM2.5 data during the two intercomparison periods (2nd and 3rd) at Thissio, Athens. On panel (a), data obtained during the warm period are shown, with data for the cold and intermediate periods on panels (b,c), respectively. In panel (d), all data are included.

The comparisons indicate a relatively uniform response of the PA-II monitor, regardless of the measurement season in Athens, which is characteristic of consistent behavior for monitoring short-term $PM_{2.5}$ concentrations in the absence of elevated coarse mode concentrations. Furthermore, it is indicative that no significant drift in the sensor's response was observed in the span of almost one year. The slopes of the linear regression of $PM_{2.5}$ reference versus $PM_{2.5(CF\ =\ 1)}$, range between 0.44 and 0.48, while the correlations remain excellent with R^2 varying in the range of 0.86 to 0.93. It must be noted that a statistically significant intercept was observed for the Thissio dataset, probably owing to the different operation principle of the compared instruments, with PMS5003 being limited to the direct detection of particles only larger than 0.3 μm (Kuula et al., 2020).

On the other hand, the performance of selected models is considered to be satisfactory and consistent, yielding, in all seasons, small intercepts, slopes very close to unity, and excellent correlations to reference measurements, despite changes in chemical composition and aerosol source intensity year-round. The chemical composition and sources of aerosols have been

extensively studied in the area of Athens. The main characteristics in urban/suburban background areas (such as those where devices were installed in the local network) are dominated by secondary aerosol throughout the year (Grivas et al., 2018; Paraskevopoulou et al., 2014; Theodosi et al., 2018). Ammonium sulfate is more abundant during summer, while secondary organics (especially the less oxidized fraction) are enhanced in the cold period (Stavroulas et al., 2019). Moreover, levels of primary organics and black carbon are largely enhanced during winter, mainly due to residential wood-burning emissions, while they diminish in summer, also due to decreased traffic (Kaskaoutis et al., 2020; Liakakou et al., 2020b; Stavroulas et al., 2019; Theodosi et al., 2018). The contribution of larger mineral dust particles in $PM_{2.5}$ is generally limited in the long-term (typically less than 10%). At background sites, where road-dust resuspension is limited, mineral dust is expected to contribute to $PM_{2.5}$ mostly during regional dust transport events (Grivas et al., 2018).

It is possible that the content in primary organics and black carbon, which are typically emitted in the ultrafine range, is an additional error-inducing factor in the PA-II output, since particles with nominal diameters lower than 0.3 μm are not directly counted by the sensor. Actually, the mass fraction gathered in this size-range can be substantial. For example, Pennanen et al. (2007) in central Athens has found 26% of $PM_{2.5}$ mass to be concentrated in sizes below 0.2 μm. These size ranges are dominated by organic and elemental carbon particles, while upper ranges (0.3–0.5 μm, 0.5–1 μm) are characterized by the increased presence of nitrate and sulfate particles (Brown et al., 2000; Chow et al., 2008; Pennanen et al., 2007). However, aerosol ions are susceptible to water uptake which alters the scattering characteristics of sampled particles. Moreover, differences on apparent densities and shape factors of particles are related to their chemical characterization (Pitz et al., 2008) and they can indirectly bias the sensor's estimation algorithm that assumes fixed values (Bulot et al., 2020).

The association between measurement error and concentrations of source-specific aerosol components was examined in order to assess the potential effects of the seasonal variability of sources and chemical composition on the monitor's performance. Small differences in error indicators have been found when evaluating the PA-II device in laboratory conditions for specific polydisperse particle sources with largely variable density and size distribution characteristics (Kelly et al., 2017; Levy Zamora et al., 2019). However, for ambient aerosols, where particle

density is less variable and submicron aerosol dominates the $PM_{2.5}$ fraction (Theodosi et al., 2011), there is not much evidence on the chemical composition effects.

In the present case, the absolute error of PA-II $PM_{2.5cor}$ (corrected with aModel6) relative to reference measurements was correlated against components that function as tracers of specific sources and atmospheric processes. The two aethalometer BC components (BC_{ff} and BC_{bb}) were used as indicators of traffic-related and biomass burning emissions (residential wood burning during the cold period and regional forest and agricultural fires during the warm) (Liakakou et al., 2020a; Sciare et al., 2008). The sulfate concentrations that were determined using the ACSM were used to represent regional transported and processed secondary aerosol (Stavroulas et al., 2019). Comparisons were performed for the 2nd and 3rd Athens intercomparison campaigns; therefore, covering all three examined seasons (cold, warm, intermediate). **Figure 12.13** shows the season-specific fine aerosol chemical composition measured by on-line instruments and **Figure 12.14** the results of the comparison.

The results provide a first indication that the PA-II corrected signal is not directly affected by changes in chemical composition and intensity of examined sources. Correlations with aerosol type indicators in all cases were very weak ($R^2 < 0.15$). Additionally, the performance of the monitor remained stable when shifting from the warm to the cold period, which are characterized by distinct fine aerosol speciation. However, more work is needed in order to find an optimal way of investigating and addressing chemical composition effects and, furthermore, to explore links between the chemical composition and aerosol hygroscopic properties affecting the sensor's performance in ambient conditions (Malings et al., 2020).

6.3.2 Monitoring $PM_{2.5}$ using the PA-II in Greece

6.3.2.1 Athens

The performance of the PA-II network in Athens was evaluated during August 2019, when a large-scale wildfire event took place in a forested mountainous area in Euboea, approximately 70 km to the N-NW of Athens, in an effort to assess the effectiveness of low-cost PM monitors, such as the PA-II, in providing alerts and real-time input to competent stakeholders, health experts and to the general public. The fire started in the late evening of August 12 and was active for almost three days. The transport of dense smoke plumes towards Athens was favored by the seasonally prevailing Etesian NW wind regime (Kalkavouras et al., 2020) and impacted on the Athens basin

on August 13 and, to a lesser extent, during the following day. This can be also seen by satellite imagery (**Figure 12.15**) for the morning of August 13, when maximum hourly concentrations of 75–80 μg m^{-3} were recorded across the Athens basin at stations of the National Air Pollution Monitoring Network.

During this period, the PA-II monitoring network that was installed in the framework of the PANACEA project in Greece was operational, comprising of nine active devices, as presented in **Figure 6.1**. All PA-II data were corrected according to aModel 6 (using the PA-II RH corrected outputs). **Figure 6.7** illustrates the August 13 time-series of the hourly corrected $PM_{2.5}$ concentrations, for all nine sensors. The first sites to be affected by the fire plume, were those on the western and northern parts of the Athens basin (HAI, PEF and CHA, see map in Figure S1), with concentration levels rising after 04:00 (local time), peaking at HAI at 07:00, while PEF and CHA, followed by the third northern site (MEL), reached maximum values at 08:00. The sites in the city center were affected after 06:00 with concentrations at THI (the Thissio central site) and GYZ reaching their maximum at 09:00, followed by a gradual decline till late afternoon. The two sites in the southern zone around the port of Piraeus (KER and PIR) were the last to be affected, mainly after 08:00, exhibiting maxima at 10:00–11:00 along with a new maximum at the nearby western HAI site. Performing a simple nearest neighbor interpolation (Wong et al., 2004) on a 0.01° grid (**Figure 12.16**), for every hourly averaged set of measurements, the evolution of the plume's influence on the basin can be illustrated, with some generalization of the effect to areas that surround each site.

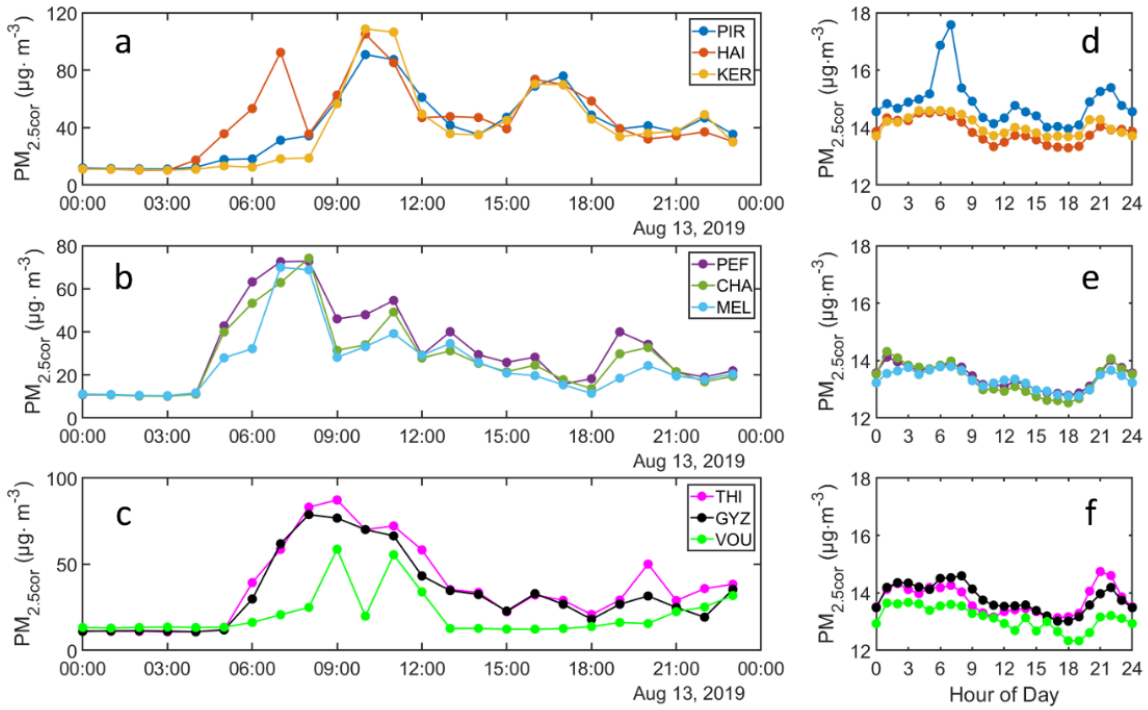

Figure 6.7. Hourly corrected PA-II $PM_{2.5cor}$ measurements in Athens, impacted by a forest-fire in 13 August 2019 (a–c). Average diurnal PM2.5cor variability in August 2019, excluding data impacted by the fire plume (d–f).

The degree of spatial homogeneity between the hourly $PM_{2.5}$ measurements in the nine urban/suburban background sites was also assessed during the entire month of August. The coefficient of divergence (CoD, **Section 12.1**) and squared correlation coefficient (R^2) were calculated for each site-pair, after excluding the wildfire event, and the results are presented in **Table 6.3** and **Section 12.14**. In general, values of CoD that are closer to zero are related to higher spatial homogeneity (Pinto et al., 2004). A high degree of spatial homogeneity for $PM_{2.5}$ can be seen across sites, as the CoD values were found below 0.2, which is considered as a threshold value (Wilson et al. (2005) and references therein). The mean CoD value was 0.10 (ranging between 0.05–0.16), very similar to the mean CoD value of 0.09 found by Lianou et al. (2007) for $PM_{2.5}$ measurements at 35 residential sites in the greater area of Athens. Generally, inter-site distance appears to be inversely related with CoD, with lower values between sites in the same sectors of the basin, as, for example, can be observed by the very low values (0.05–0.06) between the three sites in the north sector (CHA, MEL, PEF).

Table 6.3. Coefficient of divergence (CoD) values for each pair of monitoring sites in Athens during August 2019, excluding the days that the basin was impacted by the Euboea wildfire plume.

	THI	GYZ	PEF	PIR	MEL	CHA	VOU	KER
GYZ	0.07							
PEF	0.08	0.06						
PIR	0.11	0.12	0.13					
MEL	0.09	0.08	0.05	0.14				
CHA	0.08	0.07	0.05	0.14	0.06			
VOU	0.13	0.12	0.12	0.19	0.12	0.11		
KER	0.09	0.09	0.09	0.09	0.11	0.10	0.16	
HAI	0.08	0.09	0.09	0.10	0.10	0.10	0.15	0.05

The low CoD results are mainly due to the similar characterization of sites (urban background or suburban background), which are not directly affected by local emissions. They also extend past results for CoD values regarding PM_{10} measured at numerous locations in the Athens basin, which, in the case of background site-pairs, ranged between 0.17–0.21 (Grivas et al., 2008). The exclusion of the coarse fraction is expected to lead to smaller CoD (Massoud et al., 2011), especially in the present case, where dust-related $PM_{2.5}$ are not effectively measured. On the contrary, higher than 0.2 CoD values have been documented in Athens for fine and coarse particles in traffic vs. urban background site-pairs (Grivas et al., 2018). At background locations within the Athens basin, several source apportionment studies have identified secondary species as the main component of background fine aerosols (Grivas et al., 2018; Paraskevopoulou et al., 2015; Theodosi et al., 2018). Due to the regional scale of processing and transport of secondary aerosol, its levels are spatially uniform over the entire area (Grivas et al., 2018), leading to a higher degree of uniformity for $PM_{2.5}$ particles as well. It should be also noted that the impact of traffic sources, that is already limited in background locations, is further decreased during the August vacation period in Athens (Liakakou et al., 2020b).

Two sites that present different characteristics in **Figure 6.7** are PIR and VOU, which were associated with CoD values almost consistently larger than 0.10. Concentrations at VOU, a suburban background site at a relatively large distance from the city center (18.5 km from Thissio), were lower than in the other sites (mean concentration of 13.1 μg m^{-3}). Meanwhile, $PM_{2.5}$

concentrations in PIR (Piraeus), an area where the largest European passenger port is located—at the peak of its capacity during summer (Tzannatos, 2010)—appear to be affected by the activity related to the port, with a primary maximum in early morning (07:00 LT) linked to the traffic rush hour and secondary maxima during the evening related to passenger ship departures and arrivals (Kassomenos et al., 2014).

6.3.2.2 Ioannina

Studies in Ioannina have revealed the important effect of residential wood burning in elevated fine aerosol concentrations during wintertime (Kaskaoutis et al., 2020; Sindosi et al., 2019). Three PA-II devices were deployed (**Figure 6.1**, **Figure 12.1**), specifically at two urban background (VIL, GIR) and one suburban background (ANA) site, in order to monitor the spatial variability of $PM_{2.5}$ concentrations in the city. During the 13 December 2019–13 January 2020 period, pollution in Ioannina was dominated by residential wood burning, as inferred by concurrent aethalometer (AE-33, Magee Scientific) measurements at the city center. During this period an average BC concentration of 5.02 μg m^{-3} was measured, with hourly maxima up to 31 μg m^{-3} and a very high contribution of BC_{bb} (75% on average). In fact, during the night hours (18:00–6:00 local time), BC concentrations were almost completely attributed to biomass burning, with the BC_{bb} contribution rising to 88%.

In this context, PA-II $PM_{2.5cor}$ concentrations, corrected according to iModel 8, were calculated for the three sites. The selection of the model is primarily dictated by the need to compensate for the intense regional dust event observed during December 20 to December 22 (**Figure 12.11**), but it is also based on the fact that all of the stations are relatively close to the regulatory AQS site (VIL), 3.1 and 0.5 km, respectively, for ANA and GIR (in contrast to an average inter-site distance of 9 km for Athens), thus allowing for uniform use of the AQS (VIL site) measured $PM_1/PM_{2.5}$ ratio. Very high $PM_{2.5cor}$ levels (**Figure 6.8a**) were determined at all sites, with average concentrations for the monthly period ranging between 62.8–74.8 μg m^{-3}. Higher concentrations were measured at the GIR site, located in a street-canyon of a densely populated neighborhood in the city center. However, the high-concentration event appeared to be effective over the larger urban zone of Ioannina, with comparable levels also recorded at the suburban background ANA site. Hourly maxima reached 350 μg m^{-3} at all sites, while the frequency of hourly measurements above 100

μg m^{-3} was 29%, 27%, and 24% at GIR, ANA, and VIL, respectively, with the vast majority of these observations recorded during nighttime.

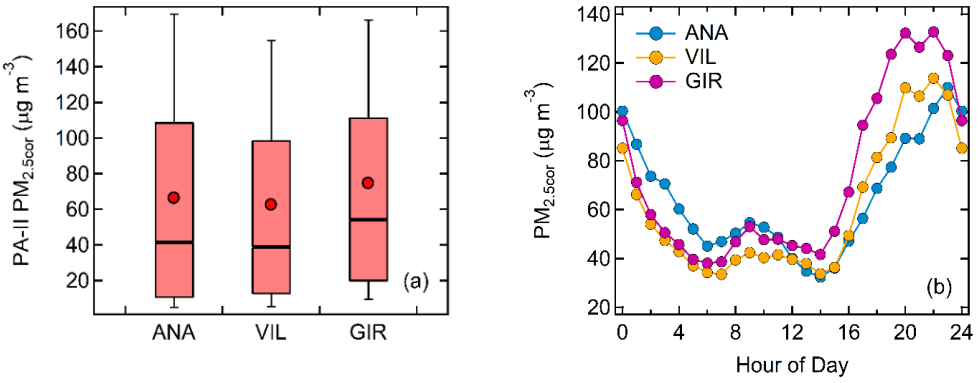

Figure 6.8. (a)Boxplots (25th, 50th and 75th percentiles) of hourly corrected PM2.5cor concentrations at the three sites in Ioannina, with whiskers extending to the 10th and 90th percentiles. Average values depicted with red dots; (b) Diurnal variability of PM2.5cor observed at ANA, VIL, and GIR during the 13 December 2019–13 January 2020 period.

Focusing on the diurnal variability during the examined one-month period (**Figure 6.8b**), it appears that, for all sites, maximum concentrations were recorded during nighttime, capturing the important role of wood combustion for residential heating, with GIR—representing a typical residential area—exhibiting the highest night-time peak. Secondary maxima were observed during the morning traffic rush hour at all sites, with the central VIL site being the least affected. The ANA site, although located in a suburban area, is close to the major international motorway connecting the city, which is burdened with heavy traffic (Tsogas et al., 2009), while GIR is located close to the main road traversing the Ioannina Lake shore and leading to the city airport. These differences in the monitoring sites characteristics were also reflected on the moderate spatial heterogeneity inferred by the pairwise CoD calculation. The GIR-ANA sites exhibited the highest differences with CoD = 0.33, while levels at the central VIL site were fairly uniform with the other two sites (CoD: 0.23–0.24), indicating its suitability as a representative background location for $PM_{2.5}$ measurements in the city (**Tables 12.16 and 12.17**).

6.4 Conclusions

In recent years, low-cost PM monitors, which are based on optical particle counting/sizing technology, are widely used to monitor PM levels, providing a cost-effective and practical solution. As their performance is strongly dependent on environmental factors, including humidity and abundance of coarse particles, which vary seasonally, but also spatially, extensive work is required to better understand their response and propose suitable calibration procedures. This task was addressed in the present study, by examining the performance of the Purple Air PA-II sensor, on both seasonal and spatial scales, and in two contrasting environments in Greece: Athens, the capital of Greece with more than four-million inhabitants and Ioannina, a medium-sized city in northwestern Greece, affected by residential wood burning emissions in winter, rendering it one of the most polluted cities of Greece, during that season. The main results of this study are summarized below:

- The CF = 1 data field provided by the PMS5003 sensor was considered more appropriate to calibrate the PA-II device, as it displayed better linear behavior against reference measurements and without the necessity to interpret the sensor's black-box data processing.

- The PA-II temperature and relative humidity sensor proved to be robust, linear, and easy to calibrate, allowing for temperature and relative humidity data use in correction approaches.

- The presence of—mainly dust related—coarse particles, along with elevated ambient relative humidity conditions, have been identified as important sources of measurement bias and a limiting factor for a uniform correction, due to area and site specificities.

- Polynomial multiple regression models can improve the PA-II performance and minimize biases that are related to relative humidity levels and coarse-to-fine particle fractionation. However, such corrections should be applied locally and additional work is needed to check their applicability at a regional scale. In this sense and given that the gains in performance, although indicative of the effects, were not very pronounced, it has to be weighted whether they justify the additional required work and dataflow as compared to simple calibration using only reference PM measurements.

- The correlations found between the PA-II monitor and reference $PM_{2.5}$ were notably higher in the case of the reference optical monitor than for the beta-gauge monitor, mainly attributed to

the similar operating principle. Intercomparison experiments for PA-II against different collocated reference instruments, and also comparisons with the same reference instrument at multiple locations, will substantially broaden the scope of research.

The PA-II performance appears to remain rather stable in the mid-to-long term, regardless of seasonal fluctuations in ambient conditions and aerosol chemical composition; however, more detailed work is required in order to assess the latter. Overall, the installation of dense PA-II networks, complementing regulatory AQS networks, can improve our knowledge on the spatial variability of PM concentrations and population exposure, in general and especially during local or regional pollution events affecting the urban landscape. The potential availability of concentration data from tens of measurement locations in a large city can prove rather useful for health studies in order to develop more representative spatial models for population exposure and minimize exposure misclassification errors due to within-area variability of concentrations. Moreover, as most low-cost networks operate frequently according to open-data principles, they can provide useful data to the research community and broaden the scope of air quality research.

Sensor-based monitoring and citizen networks are emerging solutions as it becomes clear that future urban air quality management should be integrated in a smart city framework. In this sense, a diffuse utilization of air quality sensor-based monitors, while it can provide a wealth of real-time data with high spatial resolution, can also lead to inaccurate estimations of the air quality status or misuse by third parties, if proper calibration is not applied. Direct comparison of uncorrected measurements with air quality standards should be avoided and this should be emphasized as much as possible. Therefore, more research and strategic planning is necessary regarding the optimal incorporation of low-cost devices in operational monitoring networks, with focus on their reliable calibration and the possibility for automation in calibration procedures. Furthermore, more work is needed in order to link caveats in the performance of the PA-II monitor to physical and chemical properties of sampled aerosol. Future research should include testing of the device in controlled laboratory conditions by chamber experiments, also evaluating solutions for the mitigation of the identified humidity and particle size distribution effects.

7 Cooking as an Organic Aerosol source leading to urban Air Quality degradation

I. Stavroulas[1,2,3*], A. Bougiatioti[1*], G. Grivas[1], E. Liakakou[1], K. Petrinoli[1], K. Kourtidis[4], E. Gerasopoulos[1] and N. Mihalopoulos[1,2,3]

[1]Institute for Environmental Research and Sustainable Development, National Observatory of Athens, 15236, Palea Penteli, Greece

[2]Climate and Atmosphere Research Center, The Cyprus Institute, Nicosia, 2121, Cyprus

[3]Environmental Chemical Processes Laboratory, Department of Chemistry, University of Crete, 71003, Heraklion, Greece

[4]Department Of Environmental Engineering, Democritus University of Thrace, 67100, Xanthi, Greece

Abstract

Air quality degradation events in the urban environment are often attributed to anthropogenic aerosol sources related to combustion of liquid or solid fuels in various activities. In this study, the effects of massive cooking activities during nationwide traditional festivities in Greece were investigated by a combined characterization of particulate matter (PM) levels and sources of organic aerosol (OA). Focus was centered on periods around two major festivities, namely "Fat Thursday" and Easter Sunday along six different years. OA sources were apportioned through Positive Matrix Factorization (PMF) on Aerosol Chemical Speciation Monitor (ACSM) mass spectra, while the spatial characteristics of the episodes were assessed through a low-cost, sensor-based PM2.5 monitoring network operating in Athens and other Greek cities. Contrasts were examined by considering a 15-day period around each event, while the effect of the 2020-2021 mobility restrictions, related to COVID-19, was also assessed. An episode-specific cooking OA (COA) mass spectral profile was delineated, and can be considered as a reference for ambient COA from meat grilling. Severe pollution episodes that affected the entire Athens basin were recorded, with $PM_{2.5}$ concentrations exceeding 300 μg m^{-3}. COA contributions dominated primary OA (POA) and made up almost half of OA concentrations. During "Fat Thursday" COA concentrations and contributions peaked during night-time (23.2 μg m^{-3} and 46%, respectively)

while for Easter Sunday COA maxima were recorded in the early afternoon (27.4 μg m^{-3} and 39%). Analyzing a full-year OA source dataset, revealed a pronounced recreational cooking pattern in central Athens, with COA concentrations rising towards the weekend, reflecting the impact of the food service sector. In view of the upcoming review of the EU air quality directive, foreseeing stricter annual $PM_{2.5}$ limits as well as 24-h limit values and related alerts, controlling cooking emissions appears as a potent instrument for achieving tangible air quality benefits.

7.1 Introduction

Organic aerosol (OA) represents a major mass fraction (20-90%) of submicron particles (Kanakidou et al., 2005) and is the most complex aerosol component in terms of chemical composition and physicochemical processing. The development of aerosol mass spectrometry (AMS) technologies has offered the possibility to gain insights into the OA chemical composition in high temporal resolution. Moreover, the source apportionment methods that have been developed to utilize organic mass spectra obtained by AMS, provided a major breakthrough in differentiating between primary and secondary OA components (Jimenez et al., 2009).

During the last decade, several AMS studies have identified a factor representative of cooking organic aerosol (COA; (Allan et al., 2010; Mohr et al., 2012; Sun et al., 2011). Emissions from cooking activities had been recognized as a potentially important source of particulate matter (PM) much earlier (Gray, 1986; Rogge et al., 1991), however, little was known about their contribution to organic aerosol, especially on a short-term basis. It is now understood that cooking sources may account for 10-35% of ambient OA mass in urban areas (Crippa et al., 2013; Ge et al., 2012; Lee et al., 2015; Stavroulas et al., 2019), while co-emitted semi-volatile and intermediate volatility compounds such as non-methane organic gases (NMOGs), can act as precursors for secondary organic aerosol (SOA) formation (Z. Zhang et al., 2021; Zhou et al., 2021). Cooking related SOA may also form through primary COA photooxidation as well as aqueous-phase processing (Liang et al., 2023), while SOA production can be quite significant, even compared to primary COA (Liu et al., 2018a).

Indicative spectra of specific cooking processes for various types of food have so far been derived mostly from AMS measurements, in chambers simulations (Kaltsonoudis et al., 2017; Z. Zhang et al., 2021), as well as in various indoor settings and other controlled experiments (Abdullahi et al.,

2013; Katz et al., 2021; Mohr et al., 2009). A key characteristic of COA mass spectra is on one hand it's similarity to hydrocarbon-like OA associated to combustion in vehicles, with prominent signals at m/z = 41, 43, 55 and 57, linked to the fragmentation of alkyls and specifically the C_nH_{2n+1} and C_nH_{2n-1} ion series. Hence, the isolation of representative ambient cooking spectra in urban areas can be rather challenging, since the cooking signal is often masked by other POA sources with similar spectra and temporal variability. On the other hand, cooking-related OA spectra either extracted through PMF analysis or directly measured in single-source characterization studies, share the common feature of an m/z=55 over m/z=57 contribution ratio (i.e. f_{55}/f_{57}) well above unity (He et al., 2019; Liu et al., 2018b). This characteristic can facilitate robust COA factor separation in environments where the source has an adequate presence.

In the United States, OA emissions from meat charbroiling (grilling) or frying have been known for decades to exert a measurable effect on ambient air quality (Rogge et al., 1991). In Pittsburgh, PA the cooking-related source reportedly contributed 20% to the annual mean organic carbon concentration (Shrivastava et al., 2007), in Queens, NY COA accounted for 16% of total OA mass (Sun et al., 2011), while model results have shown that cooking emissions contributed up to 35% of SOA in downtown Los Angeles (Hayes et al., 2015). Individual restaurant plumes may result in sporadic yet significant enhancements of OA concentrations (by tens to hundreds of μg m^{-3}) at the neighborhood scale (Robinson et al., 2018). Cooking emissions can also factor in environmental inequality, since it has been suggested that certain racial-ethnic and socio-economic groups living closer to restaurants in the United States are exposed to higher PM concentrations (Shah et al., 2020). Furthermore, a recent study (Saha et al., 2022) combining AMS measurements, land use regression and chemical transport model simulations, has pointed out higher contributions of cooking organic $PM_{2.5}$ nationwide compared to primary traffic-related organic $PM_{2.5}$ aerosol.

In European cities, the estimated contribution of COA to OA during winter was 23-30% in Manchester (Allan et al., 2010), 17% in Barcelona (Mohr et al., 2015, 2012), and 15-20% in Paris (Crippa et al., 2014, 2013). Chen et al. (2022) identified COA in five out of twelve examined urban sites across Europe, which accounted on average for 15% of OA on an annual basis. Moreover, at an urban background site in Marseille COA was found to contribute 12% on average over a fourteen-month period. The modeled annual contribution of COA to atmospheric particulate matter in central London was estimated at around 20% of total OA (Ots et al., 2016).

OA source apportionment studies in Greek cities based on aerosol mass spectrometry measurements, have also pointed out the significance of cooking aerosol. (Stavroulas et al., 2019), based on ACSM measurements at an urban background site in central Athens found an annual COA contribution of 12% to OA. At the same site, (Florou et al., 2017) reported a 16% COA contribution during a monthly wintertime campaign, while in Patras, Greece they found a COA share of 11% to OA. Moving to the Athens suburban background, (Zografou et al., 2022), resolved a COA factor as well, contributing 18% to total OA. Modeled contributions of COA attributed to meat grilling have also been reported as significant (20-33% of OA) in Patras during summer (Siouti et al., 2021).

Apart from the long-term impact of cooking on ambient organic aerosol, several studies have reported on the episodic nature of cooking events, which can aggravate short-term human exposure. For example, in Santiago, Chile, short-term episodes linked with $PM_{2.5}$ concentrations exceeding 400 μg m^{-3} have been reported during evening football games of the national team, caused by massive barbecue cooking (*asados*) (Lapere et al., 2020). COA was found to dominate OA concentrations in a football stadium before and during a football match in Mainz, Germany (Faber et al., 2013).

While such events are often localized, there are circumstances of collective festivities when the spatial extent of cooking emissions becomes substantial. A prime example is the traditional feast of "*Fat Thursday*" in Greece (or "*Tsiknopempti*[2] as it is known in the vernacular), which marks the last Thursday before Lent and the culmination of Carnival festivities. While it is mostly observed in the Eastern Orthodox Church, there are similar festivities in Western European countries as well (e.g., *Giovedì grasso* in Italy). In Greece, it is customary for the vast majority of the population to eat grilled meat on "*Fat Thursday*" – especially for dinner – either preparing it at home or visiting restaurants and grill houses. Another occasion of massive meat grilling in Greece is on *Easter Sunday*, when it is a national tradition to eat lamb spit-roasted over charcoals. While it is typical for the urban population to celebrate *Easter Sunday* in the countryside, during 2020 and 2021, due to the enforcement of strict COVID-19 lockdowns, most people remained in their cities for Easter. As a result, severe urban air quality events were recorded on *Easter Sunday* for the first time in recent history. While these two festivities take place nationwide, there are also

[2] From the Greek words "*tsikna*" which is the smell of grilled meat and "*Pempti*", the day Thursday

various local cooking events (such as in Xanthi, Northern Greece) that can occasionally aggravate local air quality.

To study fine particles and cooking aerosol in the duration of such meat-grilling events, this study bridges ACSM submicron aerosol speciation and OA source apportionment in high temporal resolution, with spatial variability characteristics provided by a novel low-cost $PM_{2.5}$ monitoring network (Gupta et al., 2018; Kelly et al., 2021). The manuscript initially examines the effect of cooking events on air quality, in terms of $PM_{2.5}$ concentration enhancement on a temporal and spatial basis, in different urban environments, using a sensor-based monitoring network in Greece (Dimitriou et al., 2023). Consequently, the association of the documented air quality degradation with COA (resolved by PMF source apportionment on ACSM measurements in Athens), as well as the characterization of the COA source is assessed, focusing specifically on "*Fat Thursday*" and *Easter Sunday* days in consecutive years (2014, 2017-2021) along with comparisons against control periods. This effort also attempts to produce a "realistic" ambient COA source profile related to meat grilling. Finally, the temporal variability of COA time-series in Athens is examined at seasonal, weekly and diurnal scales, searching for associations with recreational and cooking habits of the urban population and indicating its potential to impact short- and long-term exposure to ambient OA. The produced results have important implications in view of the impeding update of EU air quality legislation that will lay out ambitious ambient $PM_{2.5}$ standards, for the attainment of which it will be necessary to curb until now unregulated emission sources, including cooking and meat grilling in both households and the food service sector.

7.2 Materials and Methods

7.2.1 Online aerosol measurements

To characterize the short-term variability of fine aerosol concentrations at an extended spatial scale, measurements from a sensor-based $PM_{2.5}$ monitoring network were utilized. The network, operating in the framework of the national Research Infrastructure PANACEA since 2019, numbers over 100 sampling locations in Greece and uses reference-calibrated PurpleAir PA-II devices. Details on the calibration procedure and the field evaluation of the device are provided in Stavroulas et al. (2020). In the greater area of Athens (GAA), the network is administered by the

National Observatory of Athens (NOA) and by 2021 it included 19 residential monitoring locations (urban background and suburban background; **Figure 13.1**).

In Athens, aerosol chemical composition measurements were conducted at the NOA Thissio monitoring supersite (37.9732° N, 23.7180° E, 105 m a.s.l.). The site lies far from major roads in a moderately-populated residential area and is considered representative of urban background conditions in central Athens (Athanasopoulou et al., 2017; Grivas et al., 2019). High-temporal resolution measurements of non-refractory submicron aerosol chemical composition were performed with a quadrupole Aerosol Chemical Speciation Monitor (ACSM; Aerodyne Research Inc.; (Ng et al., 2011b) operated at a 30-minute temporal resolution. Details on sampling and calibration of the instrument can be found in (Stavroulas et al., 2021, 2019) and in **Table 13.1** in the supplement. For quality assurance purposes, ACSM concentrations of major species were compared to concurrent filter measurements at Thissio (Paraskevopoulou et al., 2014; Theodosi et al., 2018), with the results provided in **Figure 13.2**. Black carbon (BC) monitoring was conducted using a 7-wavelength AE-33 aethalometer (Magee Scientific; Drinovec et al., 2015) at a 1-min resolution. Source specific components of BC, namely BC_{ff} related to fossil fuel combustion and BC_{bb} attributed to biomass burning, were calculated internally by the AE33 implementing the aethalometer model (Sandradewi et al., 2008), with the instrument-default Absorption Ångström Exponents ($a_{ff} = 1$ and $a_{bb} = 2$; Liakakou et al., 2020).

ACSM aerosol composition monitoring is carried out continuously at Thissio since December 2016, with additional campaigns having been performed also during previous winters (including the winter of 2013-2014). Based on available data, it was possible to analyze measurements during "*Fat Thursday*" (henceforth FT) events – occurring mostly in the month of February – in 6 different years (2014 and 2017- 2021). The analysis was focused on a 15-day period around each FT, with 1-week periods before and after FT combined, in order to provide an adequate reference period, that is seasonally representative of emissions and atmospheric conditions. Similarly, 15-day periods around *Easter Sunday* (henceforth ES) for the years 2017 through 2021 were also investigated. Different restrictions on citizen mobility were imposed due to the COVID-19 pandemic in recent years, notably affecting FT and ES activities. No lockdown was imposed during 2020 FT, but in 2021 FT stay-at-home regulation was in effect with restaurants and grill houses only serving through home delivery. In both 2020 and 2021 ES periods, a lockdown was

imposed and traveling outside the city was not allowed, thus the population of Athens celebrated Easter at home, and not in the countryside according to the custom. Consequently, a contrast in prevailing sources for the ES periods for years 2017 – 2019 as opposed to 2020 and 2021 can be expected. Furthermore, the festivities in Xanthi (OTF) were also canceled in 2020 and 2021. Details on the exact dates used for each case study can be found in **Table 13.2**. An FT day is defined here as the 24-h period starting on FT noon (12:00 – 12:00 LST) to fully capture the event that usually begins in the early afternoon and lasts several hours past midnight. On the other hand, the standard calendar day is used for ES, since the meat-grilling period is mostly during midday.

Moreover, data from calibrated PA-II devices in Xanthi, a medium-sized (ca. 70,000) city in Northeastern Greece (region of Thrace) were analyzed for the years 2019, 2020 and 2021, focusing on the "Old Town Festival" (henceforth OTF) held over 8 consecutive days in early September, when local cultural associations organize concerts with live music, food and drink. $PM_{2.5}$ was monitored at the city center, close to the actual venue (Old Town site; **Fig. 13.3**), while rural background $PM_{2.5}$ was also recorded outside the city, in the campus of the Democritus University of Thrace (DUTh site; **Fig. 13.3**). These events are characterized by strong meat charbroiling emissions. A time-series of reconstructed $PM_{2.5}$ concentrations in Xanthi were also available for the year 2018, when measurements were conducted with a Radiance Research M903 nephelometer (Radiance Research, Seattle, USA) operating at 530 nm. The formula

$$PM_{2.5}(\mu g\ m^{-3}) = 5.33 \cdot 10^{-6} \times \sigma_{sp} - 1.13 \qquad 7.1$$

that was deduced through comparisons with concurrent gravimetric sampling using a TE-6001-2.5-I $PM_{2.5}$ sampler (Tisch Environmental Inc., Village of Cleves, OH, USA) was used to convert the scattering coefficient σ_{sp} to $PM_{2.5}$ concentrations (Karali et al., 2018).

7.2.2 Organic aerosol Source Apportionment

Positive Matrix Factorization (PMF; (Paatero and Tapper, 1994) was applied for source apportionment on organic mass spectra obtained by the ACSM, using the SoFi program (Source Finder; (Canonaco et al., 2013) that implements the multilinear engine algorithm ME-2 (Paatero and Hopke, 2003). The input organic signal and error matrices was automatically produced by the ACSM data analysis software, while variables with low signal to noise ratios were down-weighed according to Ulbrich et al. (2009). For the FT analysis, with the event temporally situated within

the heating season (February or early March), the α-value approach was followed (Canonaco et al., 2015) to constrain three factors, namely HOA, BBOA and COA, generally following the methodology proposed in (Crippa et al., 2014). Part of the chosen configuration and the selected optimal solution (along with the selection strategy) has already been published in (Stavroulas et al., 2019) for the years 2014 and 2017, and the same solution selection criteria were applied for the remaining years (2018-2021).

A COA factor was anticipated in all FT studied periods, since when following the approach of (Mohr et al., 2012), i.e. plotting the OA fragment contributions f_{55} vs f_{57} and coloring the data according to the respective hour of the day, a distinct pattern was visible. It can be observed in **Figure 13.4** that most of the data-points corresponding to typical lunch and dinner times in the city (early afternoon and late evening) lie on the left side of the reference triangular space, while those corresponding to the morning traffic rush hour fall closer to the right side. A COA factor emerged in the PMF analysis for both unconstrained and constrained runs. The resulting solutions also included two oxidized factors, one less oxidized (LO-OOA) and one more oxidized (MO-OOA).

In an effort to estimate a more specific COA profile for "*Fat Thursday*" that is related with ambient OA produced during meat grilling, PMF also was carried out specifically for the FT days (288 acquired 30-min spectra over 6 years of measurement). In this case, while the HOA and BBOA factors were constrained as above, the COA factor was left unconstrained.

Easter periods were treated separately, since by then the heating season was over and therefore no significant contribution by a BBOA factor was expected. In fact, the f_{60} fragment contribution averaged 0.33±0.16% throughout the 15-day ES periods combined, close to the value considered indicative of clean regional background contributions (Cubison et al., 2011). During the Easter periods, the HOA and COA factors were constrained, while two secondary factors were again resolved exhibiting different levels of oxidation (LO-OOA and MO-OOA).

7.3 Results and Discussion

7.3.1 Large-scale air quality degradation during cooking events

As mentioned in the introduction, other than the nationwide festivities during *"Fat Thursday"* and *Easter Sunday*, several other local celebrations and festivals, associated with strong cooking emissions, take place around the country. A characteristic case study where the link between meat charbroiling and poor air quality is particularly obvious is the *"Old Town Festival"* in Xanthi, a medium-sized city in Northern Greece. **Figure 7.1a** shows the $PM_{2.5}$ time-series for 2019, indicating a steep enhancement during the afternoon and evening hours when the OTF takes place (17:00 – 23:00 LST) in the Old Town, as opposed to the DUTh site where levels remained invariably low. Concentrations in Xanthi receded to rural background levels in the morning, noon and early afternoon, with their variability and levels being almost identical to those recorded at the DUTh site. During the festival period in 2019, the average $PM_{2.5}$ concentrations in the rural background site was 14 μg m^{-3} when concurrently, concentrations averaged 23.9 μg m^{-3} in the Old Town site (an 170% increment).

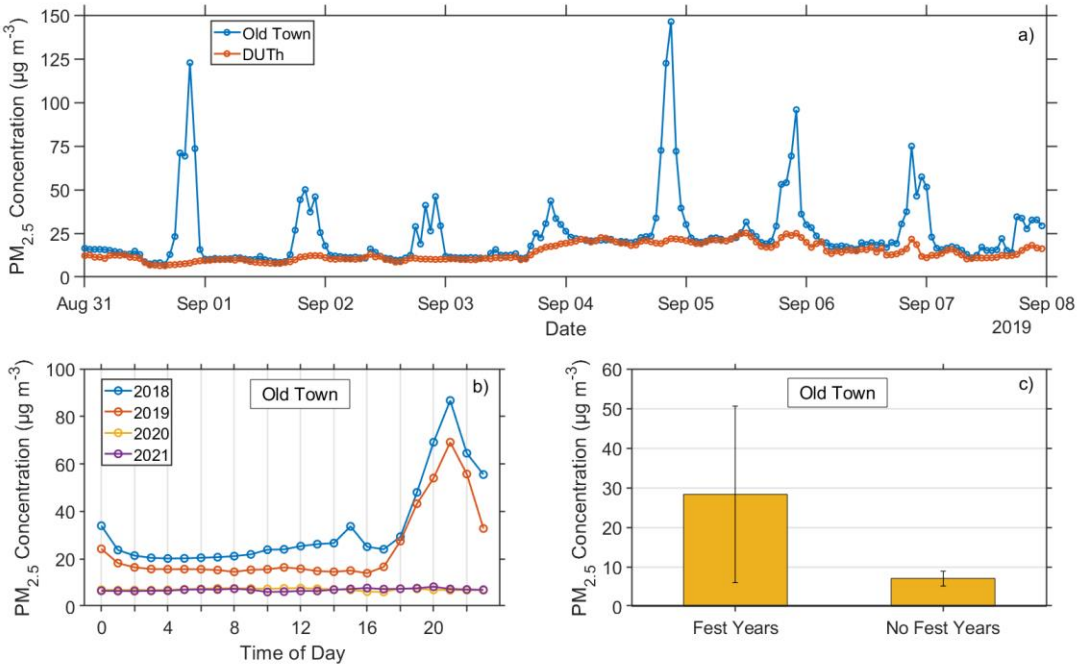

Figure 7.1: $PM_{2.5}$ measurements in Xanthi during the "Old Town Festival" (OTF) celebrations (a) during 2019 in both urban central and rural background (DUTh) sites, (b) on a diurnal basis at the urban site for all reported years and (c) on average at the urban site during years when OTF took

place (2018-2019) vs years that got canceled or were under restrictions due to the COVID-19 pandemic (2020-2021).

In 2018 and 2019, increased $PM_{2.5}$ concentrations were measured during OTF (**Figure 7.1b**), with maximum concentrations observed during nighttime, peaking at 21:00 LST when street barbeques were operated at full capacity throughout the city center. The fact that OTF-related cooking activities control air quality over the city in the beginning of September, can be clearly seen when examining the following years (2020 and 2021). The festival was canceled due to COVID-19 restrictions in 2020 and 2021. As a result, OTF levels in those years were close to the background values and almost 4 times lower on average than those measured in 2018 and 2019 (**Fig. 7.1c**). Moreover, while there was no inter-site correlation of $PM_{2.5}$ between the Old Town and DUTh monitoring locations in 2019 (r^2 = 0.13), in the absence of the OTF-related intense grilling emissions, the correlation rose significantly (r^2 = 0.67) in 2021.

Regarding the analysis of spatial effects of "*Fat Thursday*" and *Easter Sunday* cooking events in the Greater Area of Athens, measurements from the dense local $PM_{2.5}$ sensor network were utilized. As shown in **Figure 7.2**, during both the FT and ES episodes, elevated $PM_{2.5}$ concentrations were recorded at the majority of monitoring locations. The $PM_{2.5}$ hourly time-series in selected sites of the GAA can be seen in **Figure 13.5**. Six-hour averages were calculated to track the evolution of the events and provide emphasis on the segments of the day when cooking emissions are at their peak. As can be observed for FT in 2021, extreme concentrations were recorded, exceeding 100 μg m^{-3} on a 6-hour basis at several locations within the GAA (**Figure 7.2d**).

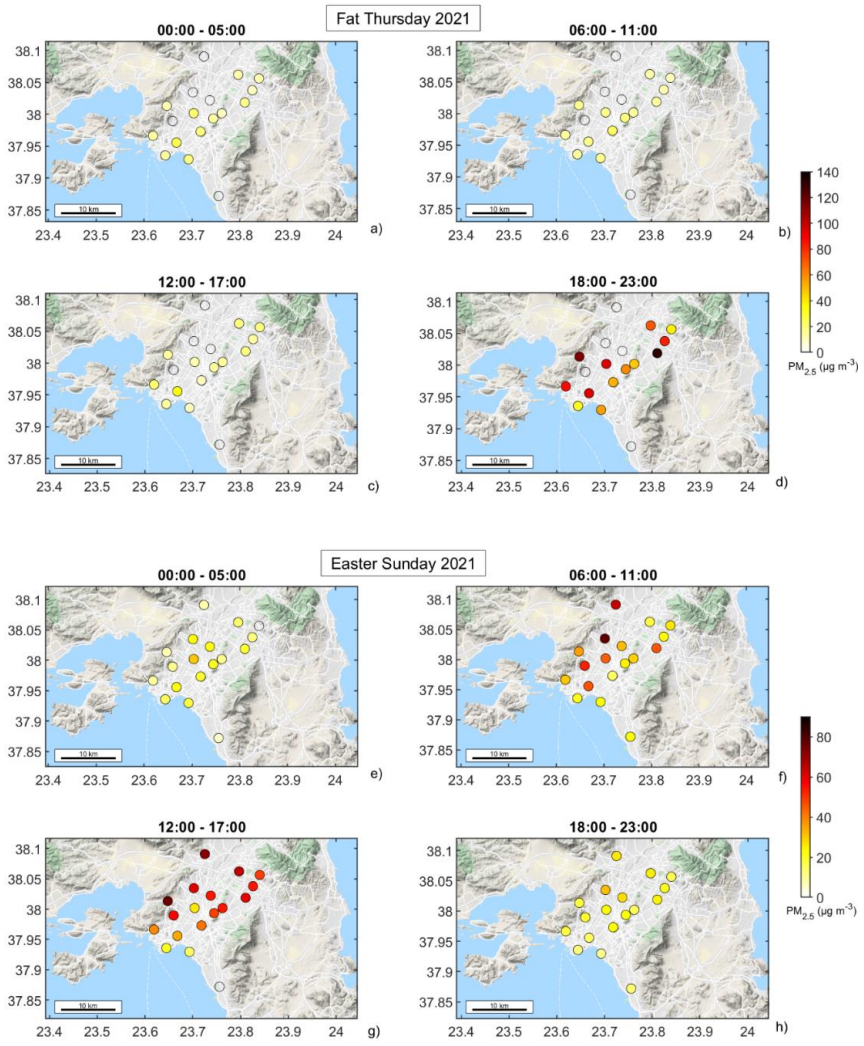

Figure 7.2. Spatial distribution of $PM_{2.5}$ concentrations recorded by the PANACEA low-cost sensor network in the GAA, in 6-hour average intervals during *"Fat Thursday"* 2021 (a, b, c, d) and *Easter Sunday* 2021 (e, f, g, h).

With 13 network sites active for the 2021 FT event, recorded concentrations clearly increased in the 18:00 – 23:00 interval, with average $PM_{2.5}$ concentrations being above 30 μg m^{-3} at all sites. This result points to the large spatial extent of air quality degradation during such events. When calculating a single average concentration for each 6-hour segment throughout the basin, the one calculated for the 18:00 – 23:00 interval (74.1 μg m^{-3}) was 4.6, 4.9 and 4.8 times higher compared to the 12:00 – 17:00, 06:00 – 11:00 and 00:00 – 05:00 segments respectively. While $PM_{2.5}$ hourly levels at Thissio (THI; **Figure 13.1**) reached a maximum of 97.6 μg m^{-3} at 23:00 LST (**Figure 13.5**), maxima more than three times higher were recorded (314.1 μg m^{-3} at 22:00 LST) in the

north of the GAA. As FT measurements were conducted during the winter season, such increased levels could be to a lesser extent influenced by the residential wood burning source (Theodosi et al., 2018). Nevertheless, the significant impact of FT events can be verified by contrasting FT-day average concentrations to the respective control periods. $PM_{2.5}$ averages for selected sites around the GAA, before, after and during FT, can be found in **Figure 13.6**. A clear pattern of elevated $PM_{2.5}$ concentrations was observed, being in most cases close to double and in specific sites up to more than triple during FT with respect to the control period.

During the 2021 ES day, with the network numbering 19 sites, concentrations started to rise early in the morning, with the stations at the Northwestern part of the basin recording 77.6 μg m^{-3} and 63.7 μg m^{-3} 6-hour averages, respectively, reflecting the early onset of grilling activities in the feast day. Most sites recorded maximum levels in the afternoon (12:00 – 17:00), when, as illustrated in **Figure 7.2g**, in 16 out of 19 sites within the GAA, 6-hour average concentrations exceeded 30 μg m^{-3}. In the afternoon, similar concentration levels were recorded in the central, western and northern parts of the basin, implying enhanced homogeneity of the source and significant air quality deterioration during the event. In fact when calculating the coefficient of divergence (CoD; Pinto et al., 2004) values below 0.2 were calculated for site pairs clustered to the center and north as well as towards the west of the basin, as depicted in **Figure 13.7**. In contrast to the FT events, $PM_{2.5}$ enhancement recorded during ES, occurred during the early afternoon and in springtime conditions. At this time of the day and year, wood combustion for space heating is scarce, leaving the cooking source as the sole contributor to the observed air quality degradation. Regarding the spatial distribution of $PM_{2.5}$ maxima in the afternoon, a south-east to north-west enhancement gradient could be observed. In fact, on an hourly basis, higher concentrations were recorded at sites in northwest of the basin (with peak concentrations exceeding 150μg m^{-3}). A similar spatial and temporal evolution of $PM_{2.5}$ concentrations were observed for ES day in 2021, with the respective maps depicted in **Figure 13.8**.

7.3.2 Cooking organic aerosol during "*Fat Thursday*" and *Easter Sunday* events

7.3.2.1 Ambient COA concentrations and contributions to OA during cooking events

The average diurnal variability of the resolved COA factor during all the FT and lockdown-impacted ES periods is presented in **Figure 7.3**, along with the respective COA contributions to

OA. An outright enhancement of COA levels can be seen for both FT and ES days, compared to concentrations recorded during the respective control periods. During FT (**Figure 7.3a**), COA average concentrations started rising after 19:00 LST and reached a maximum of 23.3 μg m^{-3} at 22:00 LST. Elevated concentrations, above 10 μg m^{-3} on average, were retained until midnight. Control-period average concentrations extended to a 1-h maximum of 4.0 μg m^{-3}, being less than 20% of the maximum recorded for FT, at 23:00 LST. In terms of fractional contributions to total OA (**Figure 7.3c**), the FT day again stands out with a diurnal cycle displaying high values after midday up to late night (peaking at 46% at 20:00 LST). During the FT control period, a clear pattern impacted by typical lunch and dinner times can be observed, with contributions after midday (13:00 – 23:00 LST) being almost half on average (20 vs 38%) compared to FT.

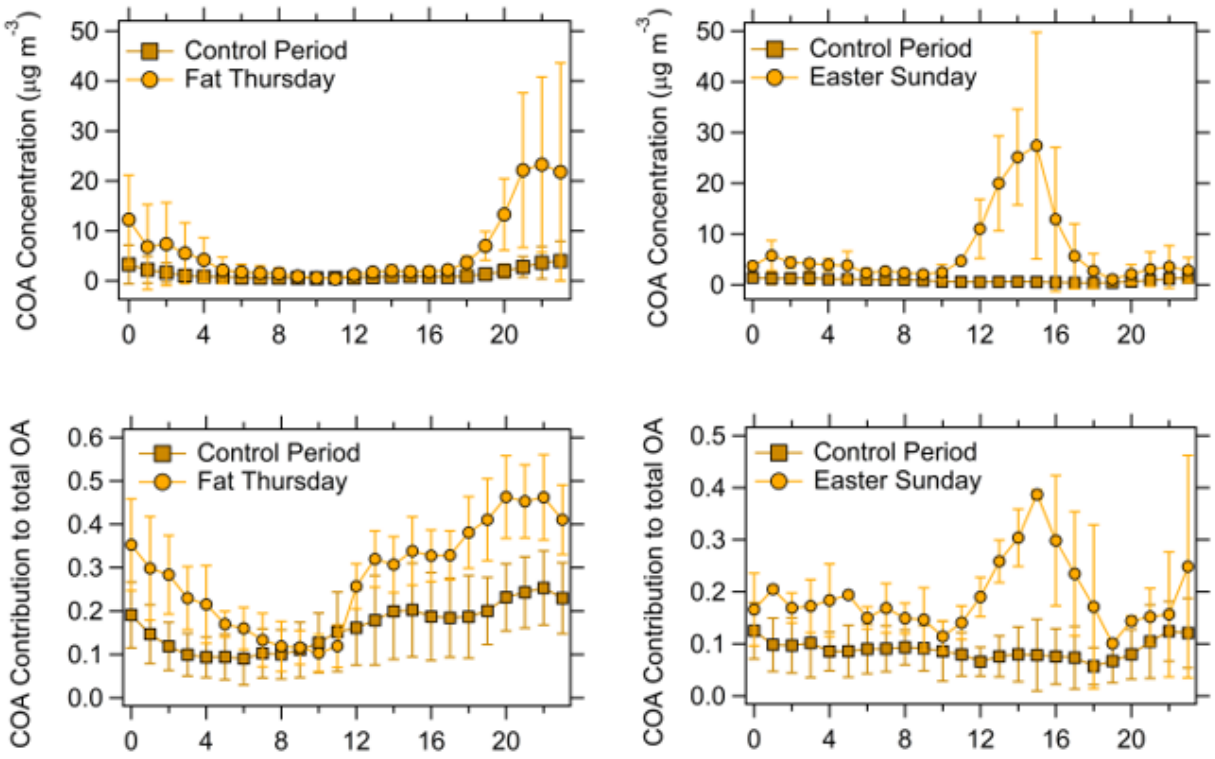

Figure 7.3. Diurnal variability during "*Fat Thursday*" (2014, 2017-2021) and *Easter Sunday* (2020-2021) and the corresponding control periods, for COA concentrations (upper panels) and COA contributions to OA (lower panels).

The diurnal variability during ES days (**Figure 7.3**) is even more pronounced compared to its control period as well as compared to the FT periods. On ES days, the peaks were characteristically shifted to the early afternoon, and COA concentrations exhibited an extreme average value of 27.4

μg m^{-3} at 15:00 LST corresponding to a staggering 50-fold increase compared to the average COA concentration of 0.5 μg m^{-3} for the same hour in the control period. When assessing the magnitude of the ES COA events, the fact that they occurred during midday, in a well-developed boundary layer that favors pollutant dispersion, needs to be emphasized as it illustrates the extreme intensity of meat roasting emissions. A 4-fold increase was documented in terms of fractional contribution to total OA (**Figure 7.3d**), with a maximum of 39% at 15:00 LST during ES, as opposed to 8% during the control period. The higher ES midday increase rate of COA concentrations compared to COA contributions to OA, reflects the significant rise in other OA components as well (**Section 7.3.2.2** below).

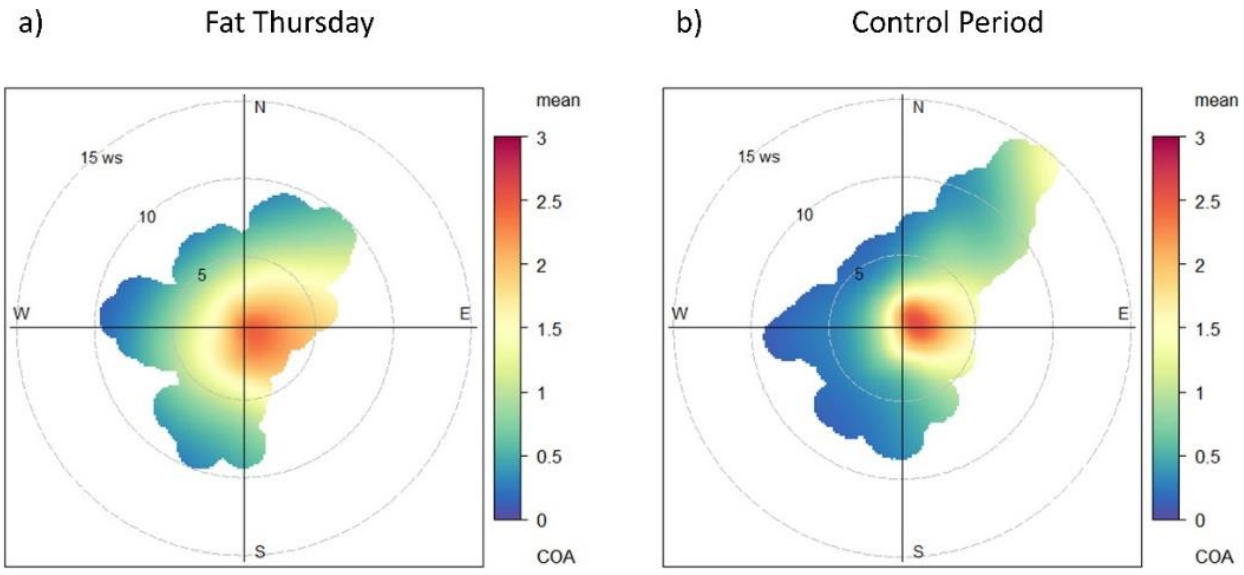

Figure 7.4. Polar plots showing the wind-dependence of COA concentrations (μg m^{-3}) at the Thissio supersite, central Athens (a) on FT days in 2014, 2017-2021 and (b) during respective control periods. Wind speed (m s^{-1}) shown on the radial axis.

The association of wind speed and direction with the estimated COA concentrations is presented in the polar plots of **Figure 7.4**, designed using the Openair package in R© (Uria-Tellaetxe and Carslaw, 2014). Examining separate plots for the FT days and FT control periods (for the six years of measurements combined), a patent contrast is observed. During the control period, there was a COA concentration enhancement area that corresponds to low-wind to stagnant conditions, indicating the impact of local cooking emissions at short distances to the N-NE of the site. This impact appears reasonable when paralleled with the spatial distribution of commercial cooking sources in the area (**Section 7.3.3** below), and might back the assumption that in normal conditions,

emissions from restaurants tend to prevail. However, during FT days, COA enhancements could be observed also under moderate-strong winds, signifying the intra-city transport of cooking emissions. This can be seen as evidence of widespread grilling also at the residential level during the event days. The contrast is also observed in conditional probability function (CPF; Kim et al., 2003) plots (**Figure 13.9**), where while the wide enhancement area during FT events is still seen when moving to higher CPF percentiles (75^{o} to 95^{o}), the control-period COA hotspot progressively becomes more focused locally.

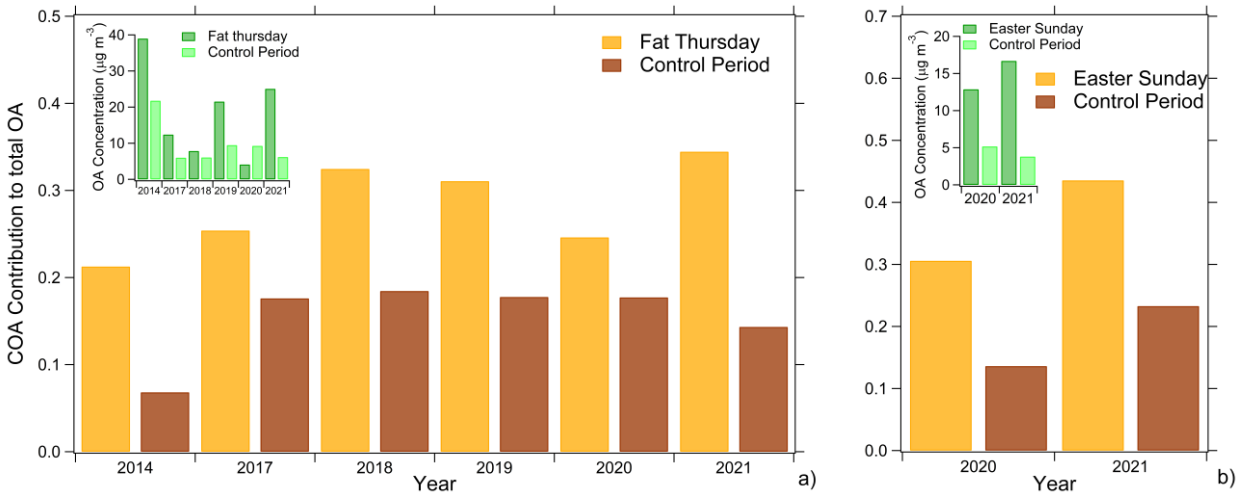

Figure 7.5: Contribution of COA to total OA during the (a) "*Fat Thursday*" for all examined years and (b) *Easter Sunday* for 2020 and 2021. Respective absolute OA concentrations are displayed in the insert figures.

Figure 7.5 shows COA contributions to total OA (and OA concentrations in the inserts) during FT, ES and respective control periods, on a year-to-year basis. The average 24-hour OA concentration during FT was up to 2 times higher compared to the control period for the majority of reported years. The COA contribution to OA during FT was again almost twice on average compared to the control period (28% vs 16%), reaching 35% in 2021. It is noteworthy that COA contributions remained high even for low OA levels, as for instance during 2018, or even when the OA concentration on an FT day was lower than the OA average of its control period, e.g. in 2020 when night hours of FT were characterized by strong Northern winds (~ 4 m s^{-1}) leading to atmospheric clearance in the basin and preventing the accumulation of atmospheric aerosol within the boundary layer.

7.3.2.2 Cooking events influence on PM_1 and OA sources. Insights into the COVID-19 effect

It becomes clear that during cooking events, PM concentration levels increased considerably, even though in a short-term, episodic manner. Specifically, for PM_1 – as a sum of BC and ACSM derived species (Poulain et al., 2020) – a 57% increase compared to the control period was documented for the FT periods. The significant enhancement of OA seems to be controlling such increases in both case studies. The OA to PM_1 contribution rises when comparing the FT control period to the corresponding FT day from 53% to 70% (**Figure 7.6**) and the respective increase was from 47% to 62% for the ES periods (**Figure 13.10**). In the case of ES events, a steep increase in average PM_1 concentrations was documented, being 145% higher than the control period (**Figure 13.11**) and reflecting the absence of the residential biomass burning source during the spring period.

It is also evident that the properties of organic aerosol changed during the cooking events, since primary sources dominated over secondary OA which contrasts the typical pattern observed in urban background sites in Athens and other European cities (Chen et al., 2022; Stavroulas et al., 2019), as well as at traffic locations (Aurela et al., 2015) or at sites impacted by intense anthropogenic activity (Stavroulas et al., 2021), where SOA typically prevail. In **Figure 7.6c-d** the average contribution of the different PMF OA factors is presented during the FT days and their respective control periods. During the control period (**Fig. 7.6d**) COA had a contribution of 16%, lower than that of primary BBOA (22%), while the processed MO-OOA component had the highest share (35%). Although the majority of OA was secondary aerosol (LO-OOA + MO-OOA: 53%) during the control period, the OA composition clearly shifted towards primary organic aerosol (POA) during FT days. The largest fraction during FT days was attributed to COA (34%), effectively doubling its OA contribution (**Fig. 7.6c**). The total POA contribution also increased to 60%. HOA contributed more during FT days than in the control period (14% vs. 9%), probably reflecting enhanced mobility within the city during the feast, with people driving to join the celebrations in restaurants, grill houses or homes.

The LO-OOA fraction was also higher on FT days than during the control period (25% vs. 18%) but the MO-OOA contribution decreased markedly (15% vs 35% in the control period) resulting in LO-OOA dominating the secondary OA fraction. Such a feature could indicate a link between secondary OA and the immense cooking activities recorded, with the fast atmospheric processing

of various co-emitted organics contributing to the LO-OOA factor (Huang et al., 2021) or even through night-time oxidation of primary cooking related emitted aerosol, through a mechanism that could be similar to the one documented for BBOA (Jorga et al., 2021; Kodros et al., 2020; Stavroulas et al., 2019). Further corroborating the above, correlations between the COA and LO-OOA factors timeseries increased significantly when moving from the control period (r^2 = 0.65) to the FT days (r^2 = 0.92). On the contrary, the correlation between BBOA and LO-OOA was comparable between FT days and the control period (r^2: 0.81 and 0.77, respectively).

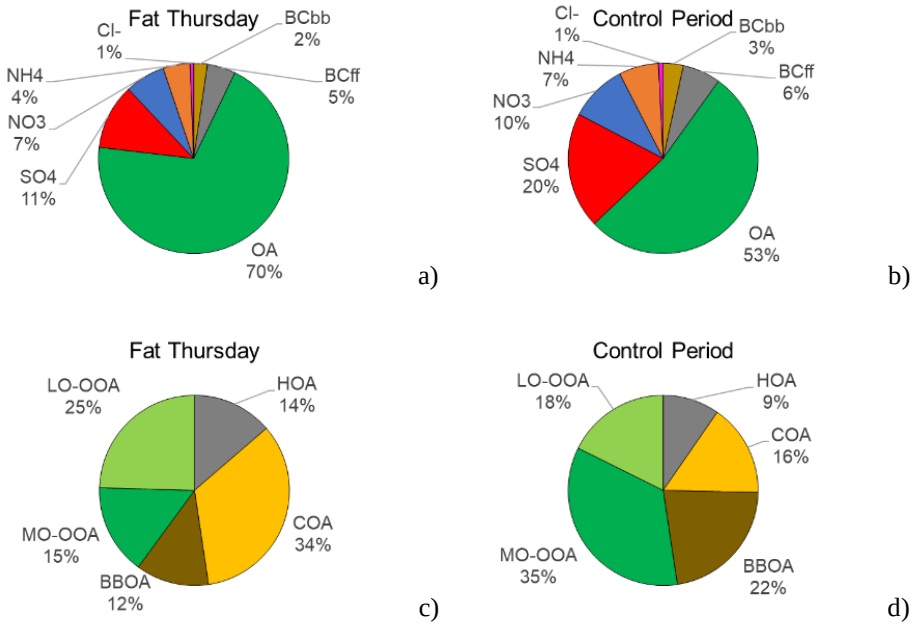

Figure 7.6: Average contributions of ACSM-derived chemical components and apportioned BC to total $PM_{1,}$ and PMF-derived OA factor contributions to OA, during "*Fat Thursday*" (a, c) and the respective control period (b, d).

Similar enhancements of OA contributions to PM_1 and POA contributions to OA were recorded during the 2020-2021 ES events (**Figure 13.10**), with OA contribution to PM_1 (ACSM+BC) being more pronounced during ES days (62%). OA was dominated by primary components during these events, since 45% was attributed to COA and 14% to HOA, unlike in the control period when the primary OA fraction ascended to 27% (18% COA and 9% HOA). For the ES periods in 2020-2021 examined in **Figure 13.10** the MO-OOA factor retained its significant contribution to total OA during ES days (28%), that even though being less compared to the control period (MO-OOA at 45%), points to the persistence of the factor during the event.

Noteworthy contrasts are seen by comparing the diurnal variability of OA factors – especially COA – during the ES periods of 2017-2019, prior to the COVID-19 pandemic and in the absence of mobility restrictions, when a large portion of the population of Athens travelled outside the city (especially during Holy Saturday and ES). The midday enhancement of COA concentrations during ES day was still present, albeit much less pronounced. COA showed a midday peak at 14:00 LST for the ES days in 2017-2019 (5.9 μg m^{-3}), which is roughly three times above the daily average (**Figure 7.7a**), but at the same time being 21% of the maximum COA concentration value recorded during the early afternoon for the 2020-2021 ES day events. In **Fig. 7.7b**, the differences in the COA diurnal variability between the pre-COVID-19 *Easter Sunday* control periods versus the COVID-19 impacted years are examined, highlighting the effects of the lockdown on the COA factor levels and variability. COA, during the COVID-19 impacted years, while keeping its midday enhancement in similar levels, registered a notable decrease during night-time (2.16 μg m^{-3} vs 1.1 μg m^{-3} on average in the 20:00-24:00 LST timeframe), reflecting the reduction in the food service sector activity, especially since a lockdown was in place in 2020 while for 2021 a nighttime curfew after 21:00 was imposed, effectively limiting the contribution of the food service sector in the COA levels recorded in the urban background.

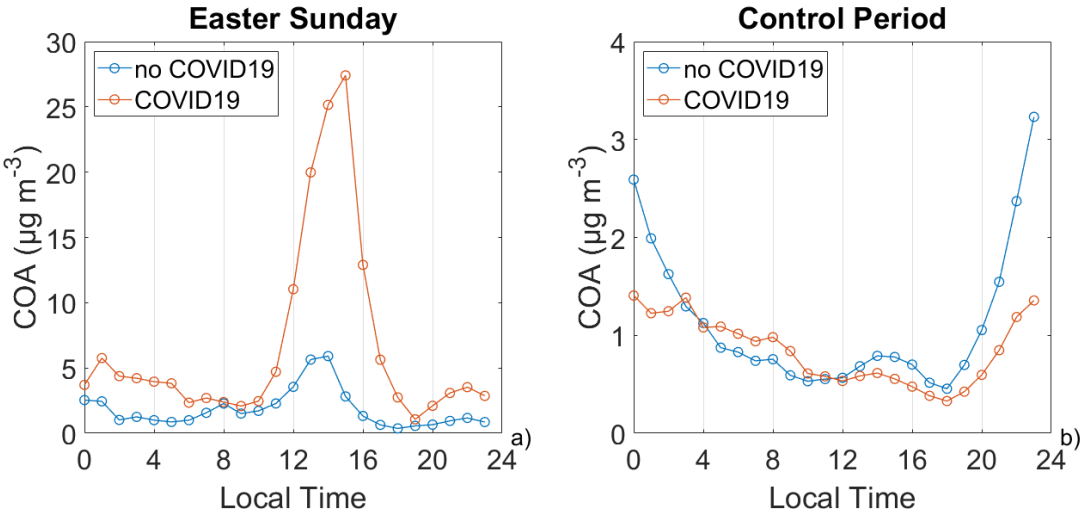

Figure 7.7. Diurnal variability of COA during *Easter Sunday* (a) and the respective control period (b) for both the COVID-19 impacted years (2020-2021) as well as the years before the global pandemic (2017-2019).

7.3.2.3 Profile of ambient COA associated with meat grilling during FT days

Regarding the source-specific mass spectra produced by the PMF analysis, noteworthy observations can be made when focusing on the OA factor profiles resolved by running the model only for FT days (288 acquired OA spectra), and how they relate to those obtained for the 2016-2017 cold period (Stavroulas et al., 2019). The FT-day COA factor (COA_{FT}; **Fig. 7.8**), which was left unconstrained in the PMF analysis, showed many similarities to the COA factor resolved for the entire 2016 – 17 cold period (r^2 = 0.96). The observed association might suggest that the COA factor identified at the central Athens site throughout the year might be linked more with meat-grilling emissions (both domestically and from the food service sector) than with emissions from general household cooking activities. The f_{55}/f_{57} ratio was found to be enhanced for the COA_{FT} factor (3.8 vs 3.2 for the 2016 – 17 cold period), highlighting larger f_{55} contributions in line with the general behavior observed for ambient resolved or laboratory COA (Mohr et al., 2012, 2009). Furthermore, the f_{44}/f_{43} ratio, characteristic of the level of oxidation of a resolved factor, was lower for the COA_{FT} factor (0.11), reflecting the dominance of freshly emitted aerosol sampled at the site during the intense FT-day events, compared to the 2016 – 17 entire cold period (COA f_{44}/f_{43}: 0.33).

In terms of its affinity with literature factor profiles (**Figure 13.12**), COA_{FT} showed many similarities (r^2 = 0.93) with wintertime COA in Athens (Florou et al., 2017), as well as with wintertime COA in Paris (r^2 = 0.96) (Crippa et al., 2013). Again, a distinctive difference was the quite lower f_{44}/f_{43} ratio observed for the COA_{FT} compared to the ones calculated for Patras (0.48) and Paris (0.35) respectively. Furthermore, an association (r^2 = 0.92) was found with the fresh COA factor identified for meat charbroiling in a chamber experiment in Patras, Greece, with a cooking setup typical of Greek cuisine (Kaltsonoudis et al., 2017), while the two factors showed similar f_{44}/f_{43} ratios (0.11 for COA_{FT} vs 0.14), further corroborating the dominance of freshly emitted COA during the FT days. The FT-specific factor presented also common characteristics with the factor profiles reported by a laboratory experiment involving grilling of chicken and burgers (Mohr et al., 2009).

Important differences were observed for the LO-OOA_{FT} factor when comparing to the 2016-2017 cold period SV-OOA resolved factor (r^2 = 0.56). The main differences are related to the contribution of the *m/z* 44 fragment, which was enhanced during FT days and also corresponded

to a higher f_{44}/f_{43} ratio (2.1 vs. 0.5 in the cold period) as well as with a higher contribution of signal in the characteristic fragments related to COA, namely m/z 55 and 57. The findings support the potential of cooking emissions for producing oxidized secondary aerosol, compared to other primary OA emission sources that normally dominate in the cold period (traffic and biomass burning). Supporting its link with COA, the LO-OOA$_{FT}$ spectrum had contributions at *m/z* 55 and 57 markedly enhanced compared to the 2016 – 2017 cold period (**Fig. 7.8**). The LO-OOA$_{FT}$ signal at *m/z* 60 and 73 still indicate a link to BBOA, however, the respective contributions were markedly lower compared to the 2016 – 2017 cold period SV-OOA spectrum implying the potential shift, with cooking activities directly influencing the less oxidized OA component. On the other hand, the processed MO-OOA factor resolved for the FT days had many similarities to the one for the 2016-2017 cold period (r^2 = 0.94), although it presented a larger contribution at *m/z* 44 and a higher f_{44}/f_{43} ratio. HOA$_{FT}$ showed an excellent match with the 2016-17 cold period HOA (r^2 = 0.99) while similarities were observed between the two respective BBOA factors (r^2 = 0.91).

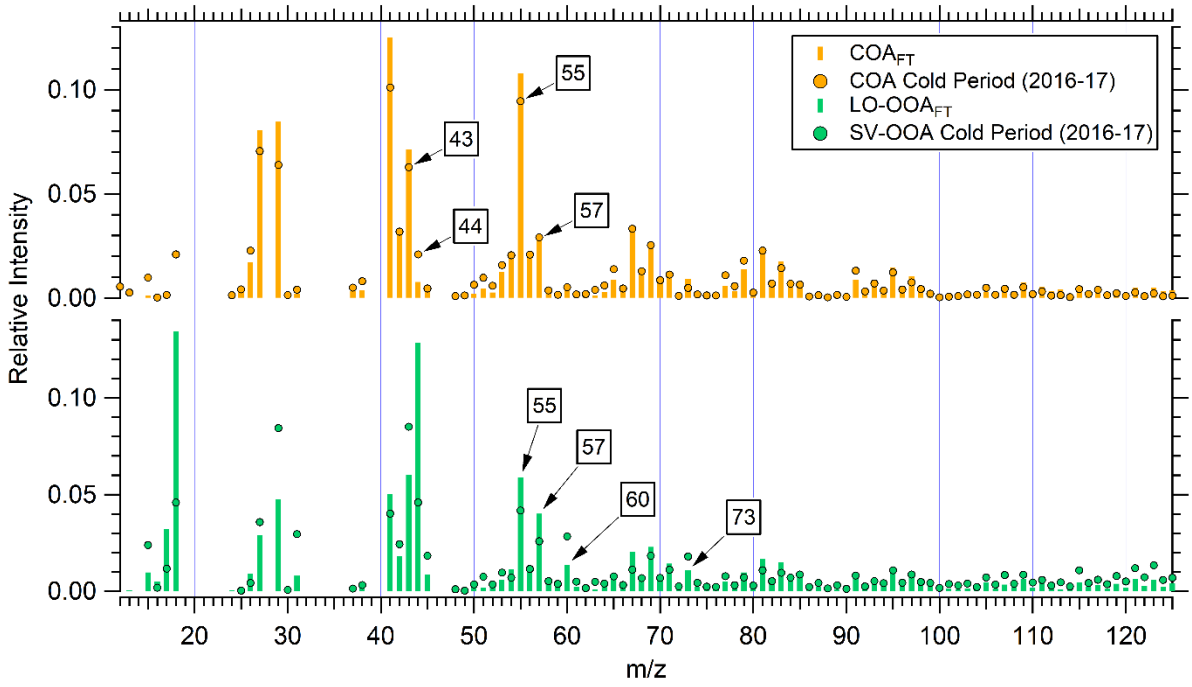

Figure 7.8: Mass spectra (bars) of the COA and LO-OOA factors resolved for "*Fat Thursday*" days only and spectra of the factors resolved (markers) for the 2016-2017 period (COA and SV-OOA; Stavroulas et al., 2019).

When comparing OA factors resolved for the entire FT period, i.e., running the model for all the days including the FT control period, to those derived only for FT days, significant correlations were found, with r^2 values higher than 0.90. Furthermore, notable similarities were observed between ES period and spectra for the warm period in 2016-2017 (**Figure 13.12**). On the other hand, the f_{44}/f_{43} ratio of the ES period COA was found to be higher than that of the COA_{FT} mass spectrum (0.23 *vs* 0.10), implying a higher degree of oxidation, given the occurrence of the ES events during midday, favoring atmospheric processing. The link between meat grilling and COA during the ES period can be also assumed given the significant similarities to both the FT-day spectra as well as with the spectra obtained for meat charbroiling in (Kaltsonoudis et al., 2017).

7.3.3 Temporal variability of cooking organic aerosol in central Athens on an annual basis

Apart from the cooking events, COA has been identified as an important OA and PM_1 source in Athens year-round (Stavroulas et al., 2019). This section provides a more in-depth analysis of the longer-term variability of COA concentrations and contribution, using the high-resolution PMF results obtained at Thissio supersite. Thissio can be considered as a receptor site of emissions in Athens and mostly in the central part of the Athens basin, which is occupied by the densely-populated municipality of Athens (17,000 residents km^{-2}). This indicates a large potential for emissions from residential cooking. Moreover, restaurants, fast food outlets and grill houses are a central part of economic activity in downtown Athens. The city-center is a leisure area for inhabitants of the entire Greater Athens Area (GAA) and visitors alike throughout the year. The map in **Figure 7.9a** (produced using data from the Open Street Map GIS database) shows the spatial distribution of commercial cooking locations in the GAA (restaurants, fast foods, grill houses etc.) and reveals a notably elevated density in the city center. The location of the Thissio monitoring site lies downwind of this high-density area, especially during night hours when northeastern flows prevail almost throughout the year (Kassomenos et al., 1998).

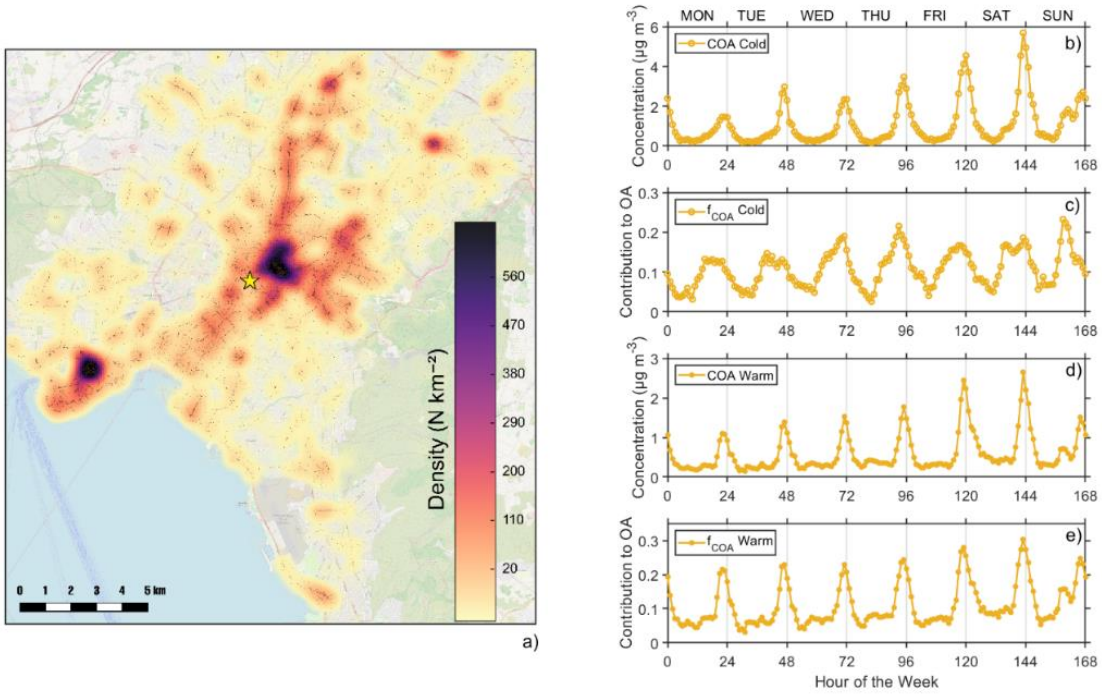

Figure 7.9. Map of restaurant and grill house density within the GAA (a) using data acquired by the Open Street Map database and mean weekly variability (1-h step) of COA concentrations along with fractional contribution (f_{COA}) to total OA averaged over the cold (a, b) and warm periods (c, d) for 2016-17.

Stavroulas et al. (2019) identified a COA factor, for both the cold and warm periods, in a full-year PMF analysis for Thissio during 2016-2017. COA accounted for 12% of total OA on average. The mean diurnal variability of COA showed elevated concentrations during nighttime with contributions reaching 25% during warm period evenings, implying a significant contribution of local restaurants to the source. Revisiting this dataset, the weekly variation of the COA factor was calculated and is depicted in **Figure 7.9(b-e)**, along with its contribution to total OA (for cold and warm periods as defined in Stavroulas et al. (2019), while the respective plots for the other OA factors are shown in **Figure 13.13**. A clear upward trend in COA concentrations can be observed when moving from Monday towards the weekend. Concentrations peaked on Saturday evening in both the cold and warm periods, in line with the expected peak of leisure activity and late dinner hours of the city's population. A different diurnal pattern can be seen on Sundays compared to the rest of the days. Specifically, besides the nighttime peak, a significant afternoon peak was also

recorded, consistent with the local recreational habit of having lunch outside on Sunday. During the cold period, Monday and Wednesday evenings were less impacted compared to the other weekdays. This observation also stands for evening HOA (**Fig. 13.13**), mirroring the fact that commercial stores on Monday and Wednesday are closed in the afternoon, as opposed to Tuesday, Thursday and Friday. This means that commercial workers return home earlier and also less people drive to stores and visit restaurants afterwards.

COA concentrations were higher in the cold period, even though the factor contributed less during nighttime compared to the warm period. The lower cold-period contribution should be mostly attributed to the presence of the BBOA component (absent in the warm period), as wood burning for residential heating in winter overshadows the other OA sources. It is indicative that BBOA and its fast oxidation secondary product SV-OOA, registered conspicuous peaks in late evening hours (**Fig. 13.13**). As a result, broader maximum contribution plateaus for COA in the cold period can be observed in **Figure 7.9c**, which incorporate the COA factor's important presence in the early afternoon (after 14:00 LST) nevertheless not advancing into any further increase later in the evening, due to the onset of the biomass burning source that significantly contributes from 18:00 LST onwards. On Sunday, an afternoon peak in COA contribution was observed (15:00 LST), most probably corresponding to the peak of the food service sector activity in central Athens, considering also that factors related with biomass burning (BBOA and SV-OOA) presented their weekly maxima on late Sunday evening.

In the warm period, COA concentrations were somewhat lower throughout the week, which is attributed to enhanced atmospheric dynamics with pollutants dispersed in a more developed mixing layer. However, the factor still contributed significantly during the evening hours (18:00 – 24:00 LST). In fact, evening maximum contributions in **Figure 7.9e** were consistently above 20% throughout the week, reaching 30% on Saturday. Given that tourism and the related leisure industry is at its maximum activity during the summer months in Athens, the observed pattern in COA contributions clearly indicates a shift of nighttime anthropogenic emissions toward cooking and traffic, in contrast to the prevalence of biomass burning during the cold period. When focusing on primary OA the cold vs warm period contrast becomes even clearer. COA contribution to POA close to or exceeding 80% consistently from 21:00 to 24:00 LST in the evenings of the warm period. On the other hand, during the cold period a maximum contribution of 56% was recorded

on Sunday afternoon, with most of the evening maximum contributions being below 20% during the remaining days of the week.

7.4 Conclusions

Several studies have been conducted in Greece concerning air quality throughout the years, especially during the last decade that was characterized by an economic recession that led to the alteration of emission intensities and profiles. However, none of those studies has described the cooking-related episodic events that are observed in the two major feast days before and after the Lent period ("*Fat Thursday*" and *Easter Sunday*), even though their impact to air quality may be substantial. Such an assessment was pursued in the current study, examining PM characteristics and their spatial variability during the events, through bridging aerosol mass spectrometry measurements, OA source apportionment and $PM_{2.5}$ levels from a dense, calibrated low-cost monitoring network. Apart from characterizing the significance of the COA source in an episodic manner, and in view of the successful mitigation of pollution owing to vehicular traffic, through ever stricter emission legislation, focus was also placed on organic aerosol related to cooking throughout the year.

Episodes of extreme concentrations were recorded during cooking-related events. In Xanthi, celebrations during the Old Town Festival were found to severely contribute to air quality aggravation in the center of the city. In Athens, especially at sites lying to the North of the basin, $PM_{2.5}$ concentrations during "*Fat Thursday*" were as high as 315 μg m^{-3}, with cooking related aerosol adding to the already important contribution of residential wood burning during night-time at this time of the year. During *Easter Sunday*, $PM_{2.5}$ concentrations were as high as 153 μg m^{-3} in the middle of the day, driven by massive meat grilling throughout the basin.

Based on ACSM measurements, OA tends to dominate PM_1 during these events, with contributions reaching 70% of PM_1 in contrast to contributions around 50% during the respective control periods. PM_1 levels were also significantly affected, with average concentrations of 26 μg m^{-3} during "*Fat Thursday*" and 24 μg m^{-3} during *Easter Sunday*, while PM_1 was found to average 16.5 and 9.8 μg m^{-3} during the control periods, respectively. Primary OA, contributed the majority of OA (~ 60%), diverging from the SOA-dominant setting under normal conditions. Through PMF on OA mass spectra, COA was found to drive such events. COA effectively doubled its

contribution to total OA during the events, while its correlation with secondary components (LO-OOA during "*Fat Thursday*" and MO-OOA during *Easter Sunday*) may imply a significant link between cooking activities and SOA production in the urban environment. While no significant effect of the COVID-19 pandemic related restrictive policies was documented for the "*Fat Thursday*" case studies, limitations on citizen mobility during *Easter Sunday*, effectively altering standard habits, were found to greatly enhance concentrations of COA and OA in the Athens basin, with total OA rising from 5.7 μg m^{-3} during the years 2017-2019, to 14.7 μg m^{-3} during 2020-2021 with COA enhancing their contribution from 29% to 34% respectively. Furthermore, analyzing wind patterns, during these events, emissions were associated with wider geographical areas, as opposed to normal conditions where cooking aerosol was also linked to local sources related to the food service sector. An increased stability in the spectral footprint of the COA factor was documented, with similar profiles emerging in both constrained and unconstrained PMF configurations, and moving from long-term to event-specific datasets. Finally, as the stability of the factor during the studied years was very high, and its affinity to specific profiles representative of meat charbroiling/meat cooking excellent, the factor can be used in future studies as representative of ambient COA in the urban setting.

Moreover, by analyzing yearlong OA source apportionment data, a clear recreational pattern was observed in the weekly variability of primary OA sources in the urban background at Thissio. COA concentrations were higher during the cold (1.1 μg m^{-3}) compared to the warm period (0.6 μg m^{-3}). COA aerosol load was found to be affected by the food industry (restaurants, fast-food and grill houses) and leisure habits of the city's residents and visitors alike, recording a clearly increasing pattern moving towards the weekend. Elevated COA concentrations and contribution to total OA were observed on Friday and the weekends for both the cold and warm seasons, in line with the above. Cooking-related peaks followed the usual eating habits, occurring either during early afternoon or in the nighttime on a working day or at lunchtime during the weekend.

8 Concluding Remarks

In the current thesis, long-term aerosol chemical composition measurements at high temporal resolution were collected for the first time in regional and urban background locations in Greece, allowing for a comprehensive characterization of the sources and processes controlling submicron aerosol concentrations.

In the urban environment in Athens, OA contributed the largest fraction to the submicron particulate mass, with the overall contribution during wintertime reaching 50 %, followed by sulfate (~ 20 %) and BC (~ 14 %). During summer, organics, BC, and nitrate concentrations are significantly lower, while sulfate and ammonium levels are increased, pointing to the suppression of local attributed pollution and a rise in concentrations of long range advected aerosol. During wintertime, most of OA, with contributions reaching 50 %, is related to space heating activities, either through residential wood burning or diesel oil fueled central heating systems. The nighttime contribution of primary biomass burning related OA is 7-fold higher than that during the day, while the respective contribution of the secondary component was increased by a factor of 2.6. It would feel like stating the obvious, but this study proves in a both quantitative and qualitative manner, that biomass burning as a popular means of space heating in a metropolitan area hosting close to 3.5 million inhabitants, being located in a poorly ventilated basin, results in a dramatic deterioration of air quality, with several days recording extraordinarily elevated PM levels. Such a deterioration is expected to exert adverse effects in public health and needs to be drastically addressed.

During two intensive measurement campaigns in Piraeus, covering winter and summer time conditions, similar conclusions regarding biomass burning related submicron aerosol could be reached. During wintertime BB related particles contributed up to 20 % on NR-PM_1 and up to 35% of total OA. Contrary to the urban background in Athens, an important enhancement of carbonaceous components related to fossil fuel combustion that persisted regardless of the measuring season was recorded, mirroring the significant impact from the overall port activity. OA source apportionment identified an HOA factor related specifically to shipping during both seasons, that when being summed with the traffic related HOA, results in a 30% contribution to total OA during both seasons. Processed OA attributed to long range transport were found to be

significant contributing up to 40%, which together with recorded sulfate concentrations form a background exceeding 5 μg m^{-3}, i.e., being higher than the updated WHO guidelines for fine particulate matter.

A diffuse utilization of air quality sensor-based monitors, while it can provide a wealth of real-time data with high spatial resolution, can also lead to inaccurate estimations of the air quality status, if proper calibration is not applied. As low-cost instrumentation performance is strongly dependent on environmental factors, including humidity and abundance of coarse particles, which vary seasonally, but also spatially, extensive work is required to better understand their response and propose suitable calibration procedures. The PA-II performance appears to remain rather stable in the mid-to-long term, regardless of seasonal fluctuations in ambient conditions and aerosol chemical composition. Furthermore, their response is linear under most pollution scenarios, allowing for effective bias correction. However, more detailed work is required in order to assess the latter. Overall, the installation of dense PA-II networks, complementing regulatory AQS networks, can improve our knowledge on the spatial variability of PM concentrations and population exposure in general and especially during local or regional pollution events affecting the urban landscape.

The importance of cooking as a source of organic aerosol was assessed through the study of OA source apportionment during extraordinary events as well as a full year period. Popular celebrations, like Fat Thursday and Easter Sunday, were found to produce air quality degradation events, affecting the entire basin of Athens. Interestingly, festivities involving meat grilling were found to be related to extraordinary $PM_{2.5}$ concentrations in the province as well. In Athens, COA was found to play a driving role during such events. For instance, during Easter Sunday in 2021, OA concentrations nearly tripled, compared to the business-as-usual scenario, with COA contributing nearly half of that increase. Synergy between high end instrumentation at an urban background representative monitoring location and a dense low-cost PM monitoring network, essentially allowed for the spatial characterization of these events, resulting in a more detailed assessment of population exposure. In the long-term, COA variability, other than representing the day-to-day cooking habits of the population, was also found to be affected by the local food industry (restaurants, fast-food, grill houses) and leisure habits of the city's residents and visitors alike, recording a clear increasing pattern moving towards the weekend.

The human health effects of exposure, together with wider climate impacts, have highlighted particulate matter as a high priority pollutant at a European level and especially for South East Europe. Overall, the Greater Area of Athens seems to face a particularly serious air quality problem, associated with residential wood burning. Even though scientific knowledge on its diverse health impacts is established, emissions from RWB in Greece remain widely unregulated. From a policy making standpoint, appropriate mitigation measures to reduce emissions of particulate matter and air pollutants from residential wood burning need to be urgently introduced, in both EU and national legislation. Attention should also be given to sources of rising importance. For instance, the renewed port activity and its development prospects tend to highlight Piraeus as a source of pollution with an impact on the wider region. In this sense long-term characterization of submicron aerosol in this major port city seems imperative. Finally, with industrial activity within the basin being largely limited and with European legislation effectively reducing vehicle emissions and fuel quality, the composition of the mix of primary sources as well as their spatial distribution has significantly changed. Taking into account the elevated growth rate of the leisure and tourism industry in the GAA, other sources, such as cooking, may rise to significant importance, calling for effective moderation.

Some ideas on future work, stemming from this thesis, are listed below:

* Since the ACSM is now measuring for seven straight years in the urban background in Athens, long-term source apportionment of OA through PMF comes as an obvious next step forward. Trend analysis can be performed to concentrations of PM_1 chemical constituents and OA source intensities, allowing for the identification of impactful factors, either naturally occurring (e.g. changes in atmospheric circulation patterns or weather extremes) or being interwoven with various socioeconomic variables or political circumstances (e.g., tourism, the pandemic lockdowns, the recent energy crisis or changes in emission restriction legislation).
* Building on this large dataset, in combination with the concurrent multiple wavelength absorption coefficient data collected at Thissio, valuable work can be performed addressing the field of aerosol radiative forcing. The ability of particles to behave as quasi-greenhouse “gases” is largely determined by their content of BC particles, which absorb radiation. An important parameter for enhancing the greenhouse potential of BC particles is their internal mixing with radiative scattering particles, which can direct and focus even more

radiation for absorption onto the BC core. Consequently, long-term measurement of the main radiation-scattering particulate components (primary and secondary organic compounds, ammonium sulfate and nitrate) can be exploited to estimate the direct and indirect absorption of BC by calculating the absorption enhancement parameter (E_{abs}), as well as to investigate the degree to which each component drives these processes.

* A key piece of information missing in high temporal resolution chemical composition measurements with an ACSM and in absorption coefficient monitoring through filter-based photometers, is the level of dependence of the measured quantities to particle size. It is after all a well-documented fact that adverse health outcomes related to PM exposure and aerosol relevant climate effects alike, are highly corelated to particle size. Novel instrumentation allowing particle sizing with minimum losses can be coupled to a suite of instruments including the ACSM and AE33 aethalometer. Online size segregated chemical composition and OA sources in near – real time, coupled with size resolved absorption by ambient aerosol would be adding one more dimension to the information available. Such a research direction could be sought and expanded to numerous open questions varying from aerosol toxicity and oxidative potential to the sources and absorption of Brown Carbon aerosol.

* The extensive OA mass spectra dataset obtained both in Finokalia and Athens, in combination with existing long-term datasets from other European cities or rural areas, can provide a unique testbed for applying novel approaches in OA source apportionment, involving machine learning techniques. With such a large and diverse ensemble of data, machine learning systems can learn to recognize patterns, identify relationships between variables and make predictions. In particular, machine learning classification algorithms can be trained on source specific literature mass spectra obtained either by laboratory or field studies and consequently attempt to separate the contributions of different sources, estimating their relative importance, on a real-world dataset. Comparison of the output with traditional PMF approaches and against independent source tracers, can provide the means for assessing the accuracy and efficiency of such an approach and can help improve our understanding on caveats or biases introduced by either of the techniques.

9 Appendix A. Supplement to the manuscript: *Long term chemical composition, based on near-real time measurements, at a regional background site over the Eastern Mediterranean.*

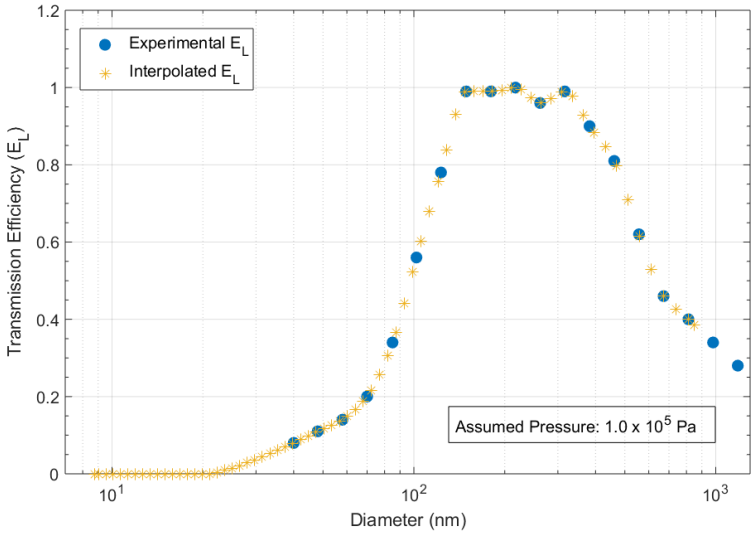

Figure 9.1. Interpolated transmission efficiency applied to SMPS particle volume distributions allowing for the direct comparison of SMPS derived mass concentration to ACSM measurements

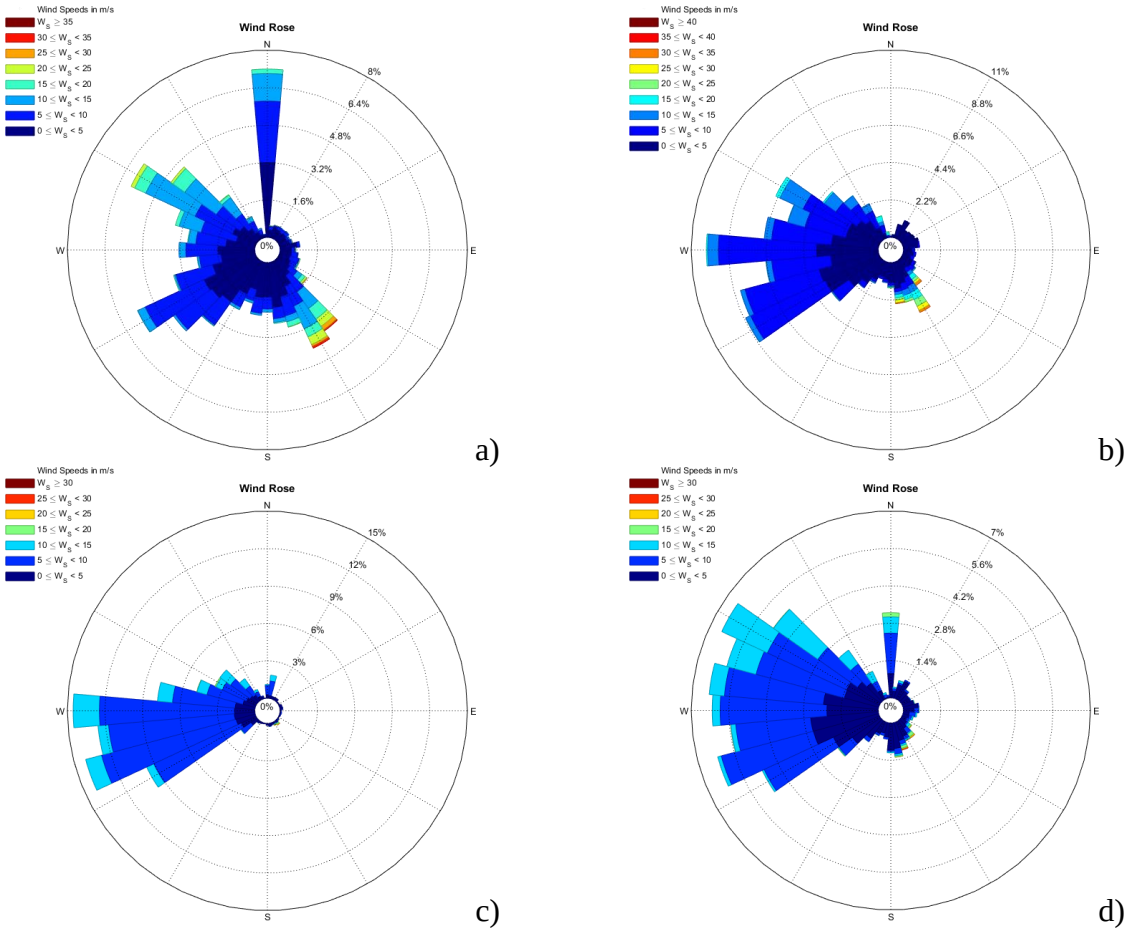

Figure 9.2. Wind roses at Finokalia for (a) winter, (b) spring, (c) summer and (d) autumn over the 2012 – 2015 period.

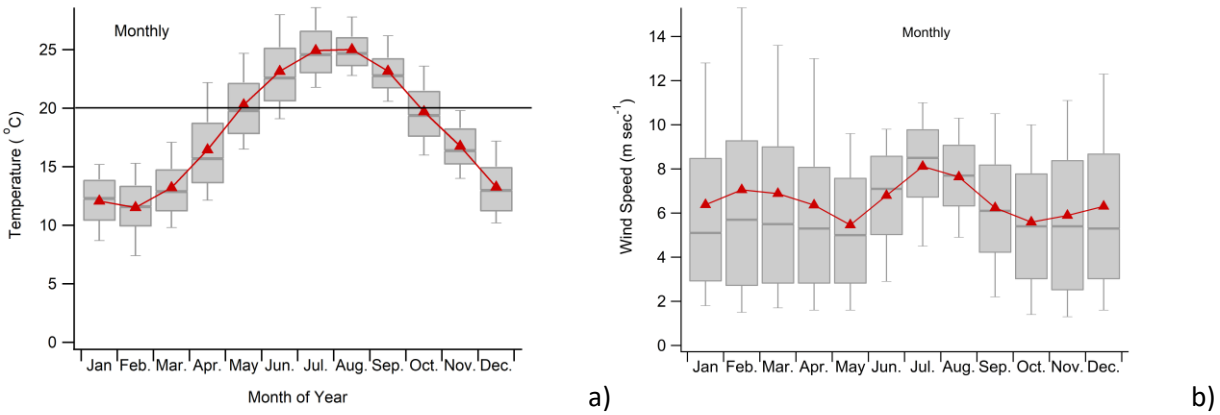

Figure 9.3. Monthly (a) ambient temperature and (b) wind speed statistics at Finokalia. Markers are averages, horizontal lines represent median values, boxes are the 25th and 75th percentiles while whiskers extend to the 10th and 90th percentiles.

10 Appendix B. Supplement to the manuscript: *Sources and processes that control the submicron organic aerosol composition in an urban Mediterranean environment (Athens): a high temporal-resolution chemical composition measurement study.*

10.1 ACSM Calibration

Table 10.1. Response factor and relative ionization efficiencies determined for the different measuring periods

Measuring Period	RF NO_3^-	RIE NH_4^+	RIE $SO_4^=$
Winter 2013-2014	$5.91e^{-11}$	4.5	0.6
Winter 2015-2016	$5.63e^{-11}$	5.15	0.48
2016-2017	$4.61e^{-11}$	4.8	0.58

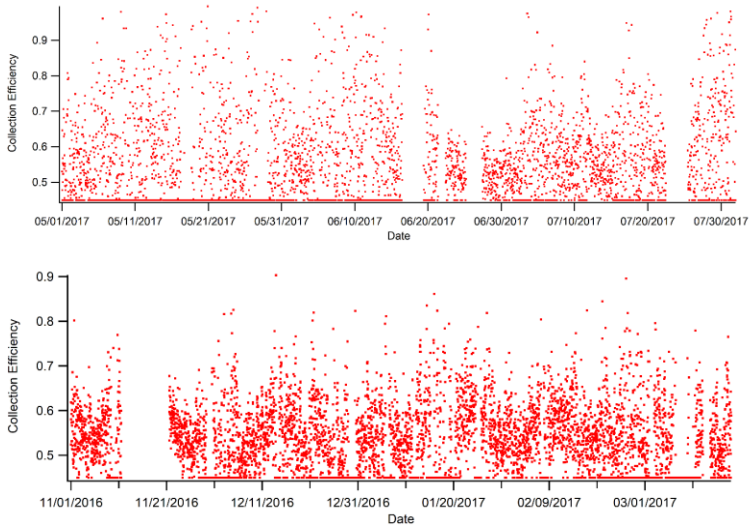

Figure 10.1. Collection efficiencies applied to the ACSM datasets indicativelly for the warm period of 2017 and the cold period of 2016 – 17 according to Middlebrook et al. (2012)

10.2 Meteorological Parameters

An overview of the prevailing meteorological conditions, regarding the yearlong period of measurements 2016 – 2017 is presented in terms of diurnal variability below.

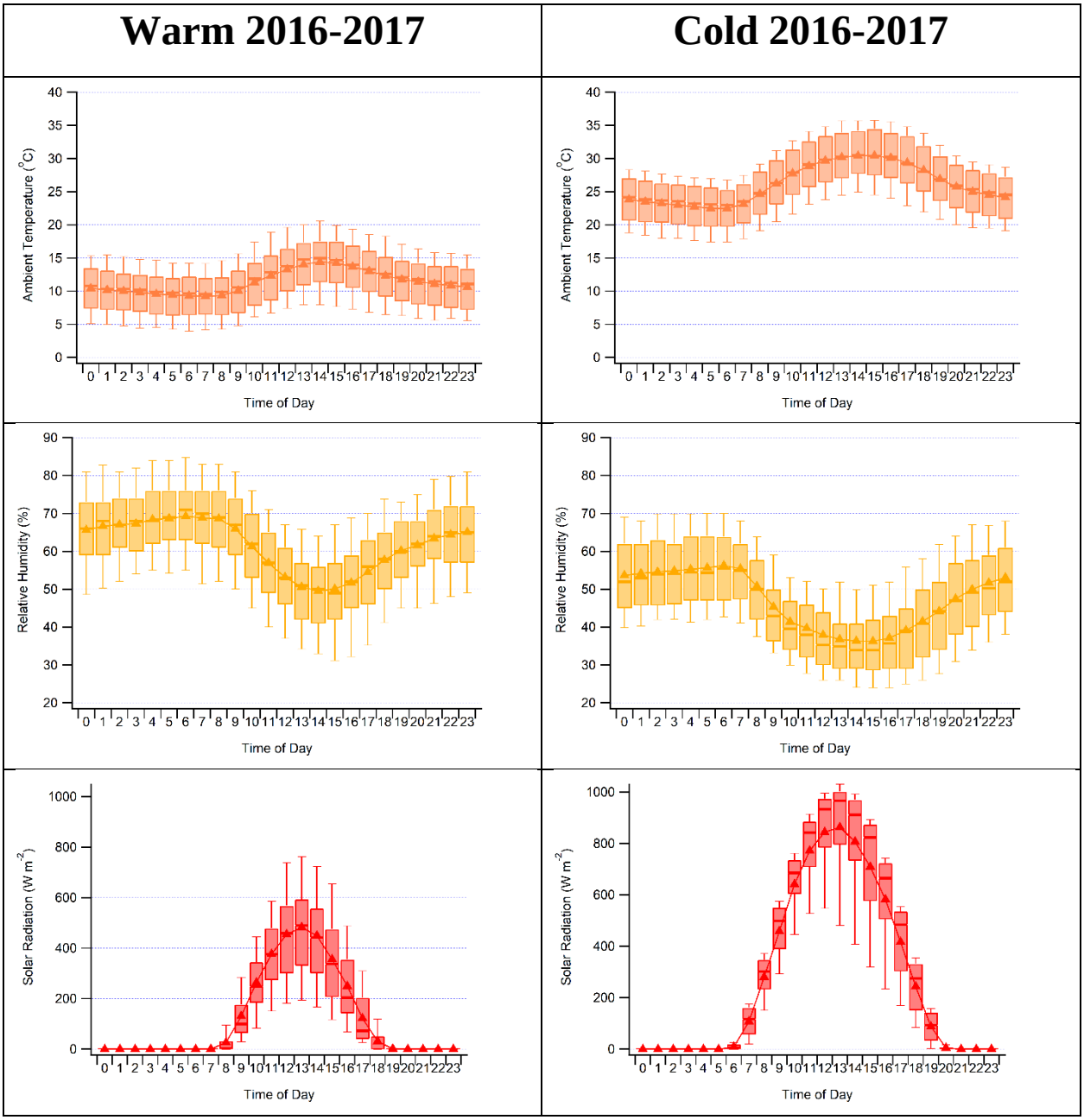

Figure 10.2. Diurnal variability during the cold versus warm season for ambient temperature (top), relative humidity (middle) and solar irradiance (bottom).

10.3 ACSM Quality Assurance/ Quality Control

As a first quality control/quality assurance of the obtained data, ammonium concentrations obtained by the ACSM are compared to the respective ammonium concentrations derived from the PILS, both for winter 2016-17 as well as winter 2013-2014. Both measurements are averaged hourly for synchronization reasons. The respective graphs are given in the following figures (Figure SI.1.1, SI.1.2). Furthermore, ACSM concentrations are daily-averaged and the derived averages are compared to the respective concentrations obtained by ion chromatography analysis and thermal-optical analysis of the respective daily $PM_{2.5}$ filters for all the winter periods (Figure SI.1.1, SI.1.2).

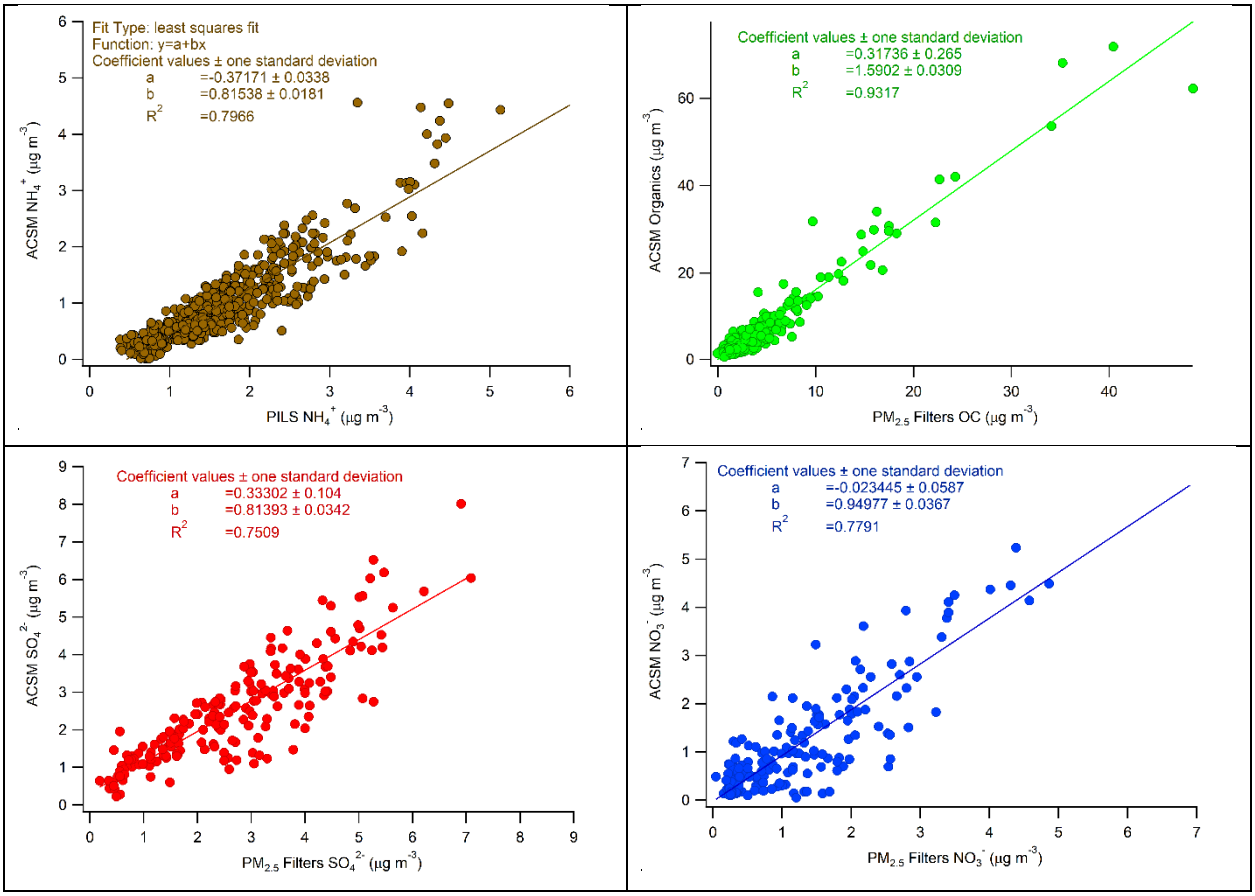

Figure 10.3. Correlations of the non-refractory PM_1 constituents as measured by the ACMS versus external measurements for the year-long period 2016-2017. Top left ammonium from ACSM vs PILS measurements, top right ACSM Organics vs OC measured on filters using a thermal optical method, bottom left ACSM sulfate vs IC sulfate and bottom left ACSM nitrate vs IC nitrate.

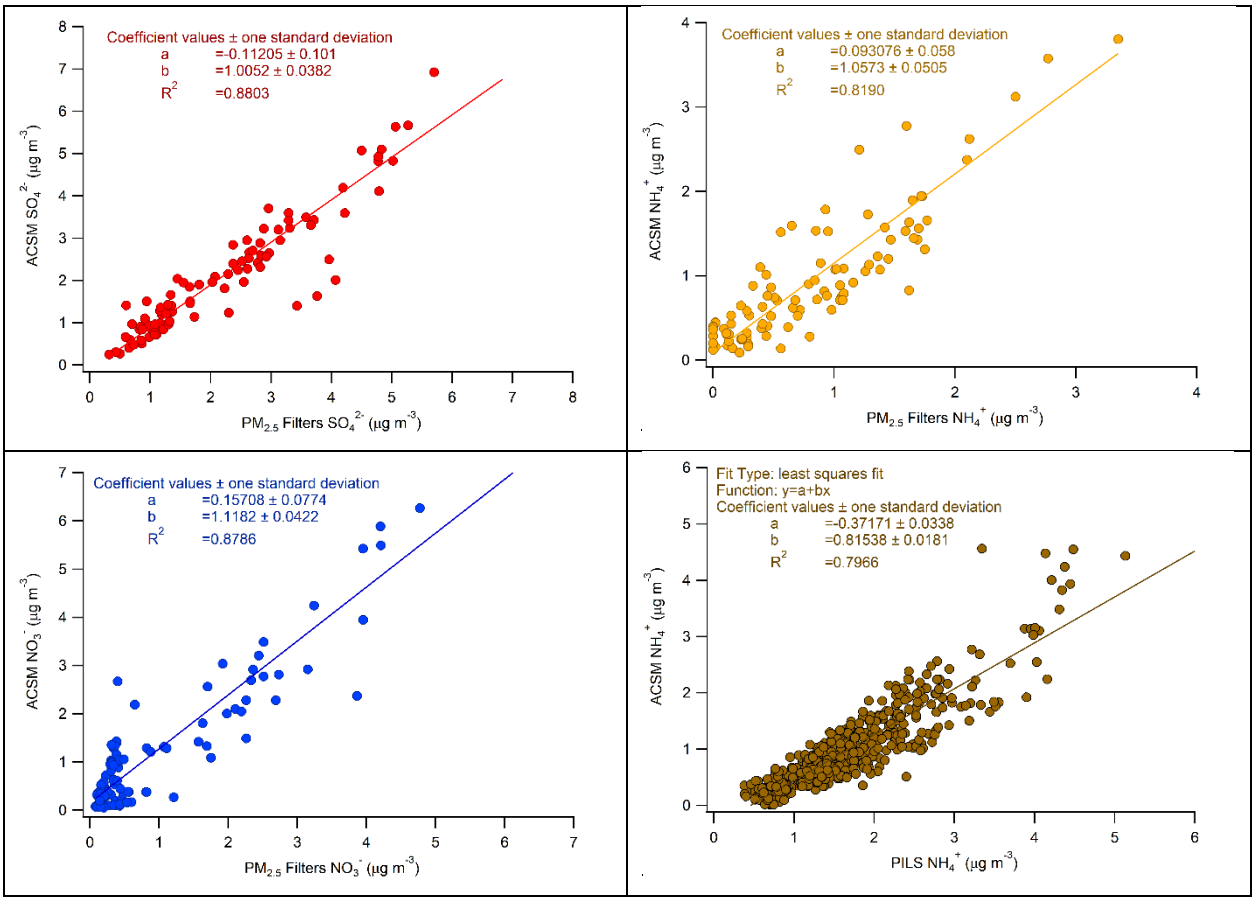

Figure 10.4. Correlations of the non-refractory PM_1 constituents as measured by the ACMS versus external measurements for the wintertime intensive campaigns of 2013-2014 and 2015-2016. Top left ACSM sulfate vs IC sulfate (2015-2016), top right ACSM ammonium vs IC ammonium (2015-2016), bottom left ACSM nitrate vs IC nitrate (2015-2016) and bottom right ACSM ammonium vs PILS ammonium (2013-2014)

The instrument has participated in an intercomparison study of 15 Q-ACSM instruments organized by the European Center for Aerosol Calibration (ECAC) at the Aerosol Chemical Monitor Calibration Center (ACMCC) at Site Instrumental de Recherche par Télédétection Atmosphérique (SIRTA, Paris) during March 2016 (www.actris-ecac.eu/acsm-2016-1.html). It showed excellent agreement (well below ±20%) with the ACMCC's reference instrument, in both pre- and post-calibration periods of the intercomparison study, while the relative ionization efficiencies (RIE) for ammonium and sulfate, obtained by the on-site calibration, were very close to the ones previously used, indicating a stable performance of the instrument.

10.4 Source Apportionment of OA

The source apportionment procedure is presented for the cold season of 2016 – 2017 and for the warm season of 2017, which are discussed in the manuscript.

10.4.1 Anchor profiles

The spectra used as RFPs are ambient deconvolved mass spectra found in the AMS spectral database (Ulbrich et al., 2009; Ulbrich et al., 2013). Specifically, the HOA and BBOA factors were constrained using the RFPs derived from multiple datasets in the study of (Ng et al., 2011a), while the anchor FP used for the COA factor was deconvolved during a study in Paris by (Crippa et al., 2013). Representativeness of the selected RFPs is assessed by comparison to factors reported in earlier studies in the region and the relevant coefficients of determination can be seen in figures SF.15 through SF.17. For the HOA RFP, values for r^2>0.95 were calculated when comparing to HOA factors from Athens, Patras and Bologna (Florou et al., 2017; Kostenidou et al., 2015; Gilardoni et al., 2016), COA RFP exhibited excellent correlation with spectra for Athens and Patras (r^2>0.9) (Florou et al., 2017), while BBOA showed excellent correlation (r^2*>0.87)* with spectra obtained earlier in urban areas in the region (Florou et al., 2017; Gilardoni et al., 2016) as well as in the regional background site at Finokalia (Bougiatioti et al., 2014) (r^2=0.79).

10.4.2 Unconstrained runs

As stated in step 1 of the SA methodology proposed by Crippa et al. (2014), an unconstrained run (PMF) was first performed in the split data sets. A discussion of the PMF findings for each period follows.

Cold Period 2016-2017: The 4 and 5 factor solution PMF (unconcstrained) runs for this period are displayed in Figure SF.5. For the 4 solution PMF runs we can distinguish an HOA-like factor at position 1, a BBOA-like factor in position 3, an OOA like factor in position 2, and what could be a COA-like factor in position 4. Small seed variability was observed for the four factor solution. Nevertheless, the model produced residuals exhibiting a clear diurnal structure for several variables (e.g. m/z 43, 51, 53, 55, 57) with a maximum during the morning traffic rush hour, as can be seen indicatively in the lower panel of Figure SF.5 for m/z=55. This fact led us to the exploration of the 5 factor PMF solution which is presented in the top left panel of Figure SF.5. The issue in the residual structure is mitigated when going through the 5 factor solution, where the model seems to be able to predict the OA behavior during the traffic rush hour, exhibiting no

residual structure in the fragments associated with primary HOA. Nevertheless, FPs vary considerably for different seed runs leading to the exploration of a constrained five factor run in the next step of the SA procedure.

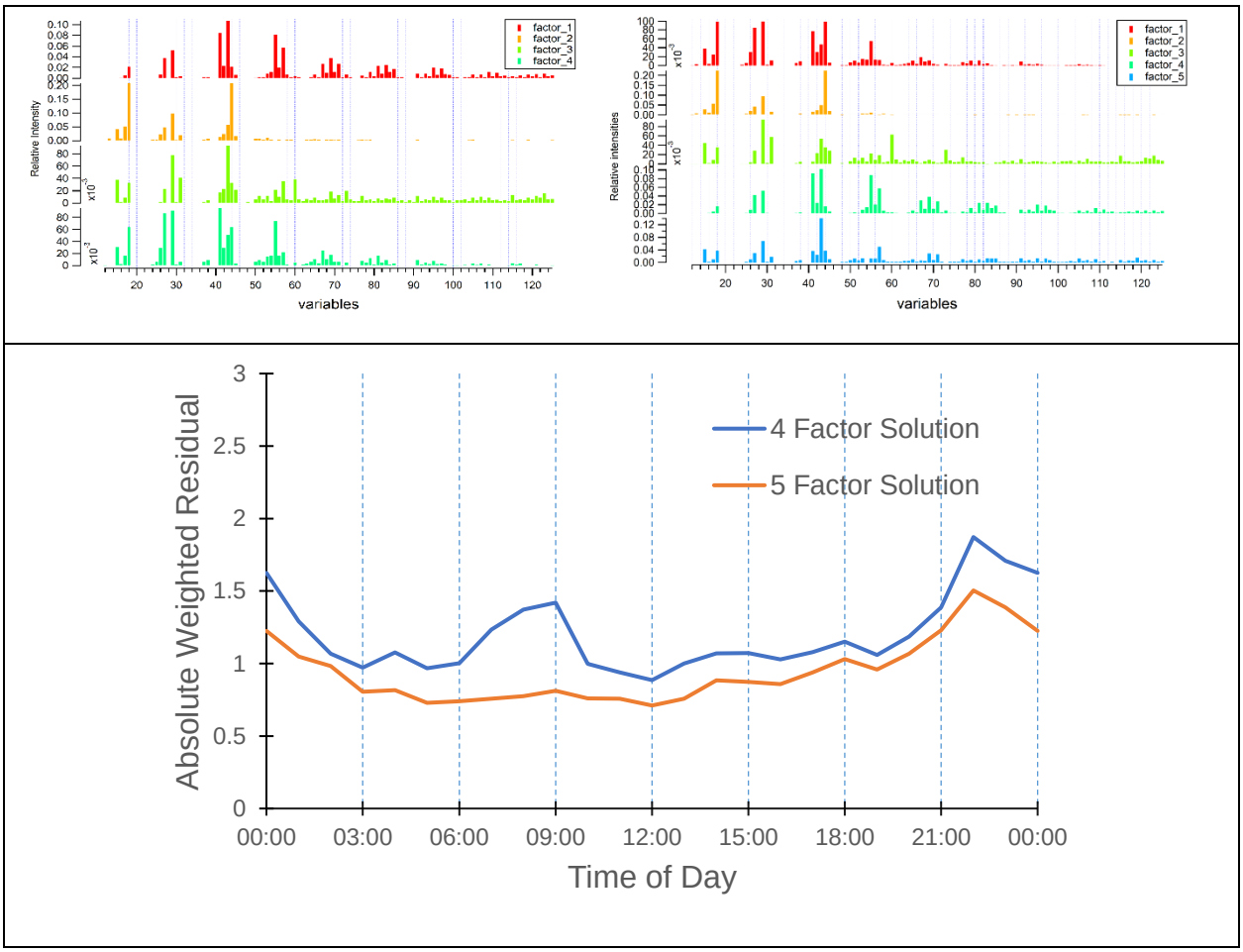

Figure 10.5. Four factor unconstrained PMF run for the cold season of 2016 – 2017 is shown in the upper left panel. The five factor PMF solution is presented in the upper right panel. Diurnal variability of the Absolute Residual weighted over uncertainty for both solutions m/z=55 fragment is presented in the lower panel.

2017 Warm period: For the warm period, given the absence of significant signal at the two key biomass burning fragments at m/z=60 and m/z=73, a five-factor solution containing a biomass burning factor was not anticipated. Nevertheless, four and five factor solutions were examined and resulting FPs are presented in figure SF.6. As can be seen the four-factor solution is able to predict what could be an HOA – like factor in position two, heavily impacted though by the fragment of

CO_2^+ at m/z=44, a COA – like factor in position 1, exhibiting the expected difference in relative intensities between m/z=55 and m/z=57, plus two SOA factors, one resembling a highly oxygenated product at position 4 and an SV-OOA like spectrum at position 3. When going through the five-factor run some splitting behavior can be observed. An environmentally irrelevant factor immerges at position 4, while no satisfactory profile can be seen for any primary factor, either HOA or COA. Consequently, the four-factor solution will be explored on the next step of the SA procedure.

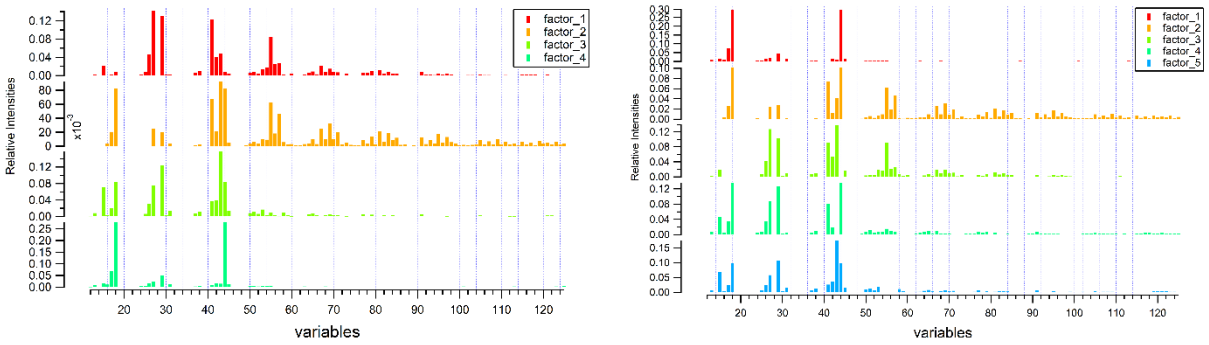

Figure 10.6. Factor profiles for the four (left) and five (right) factor unconstrained runs for the 2017 warm period dataset.

10.4.3 HOA constrained runs

Proceeding to the second step of the SA method, a constrain is introduced for one of the factors, using as an RFP the average HOA profile obtained by (Ng et al., 2011a).

Cold Period 2016-2017: In the left panel of Figure SF.7 the obtained FPs are presented. As can be seen, a BBOA – like factor with contributions from m/z=60 and m/z=73 emerges in position 3. A COA – like factor can be seen in position 5. Two SOA factors, with a contribution at m/z=44 seem to also appear in positions 2 and 4.

2017 Warm period: The solution obtained when constraining the HOA factor at position 1 is presented in the right panel of Figure SF.7. It is apparent that this model configuration leads to a COA – like factor in position 2 and two SOA factors exhibiting different levels of oxidation. In the next step the optimum solution is obtained by constraining the COA factor as well.

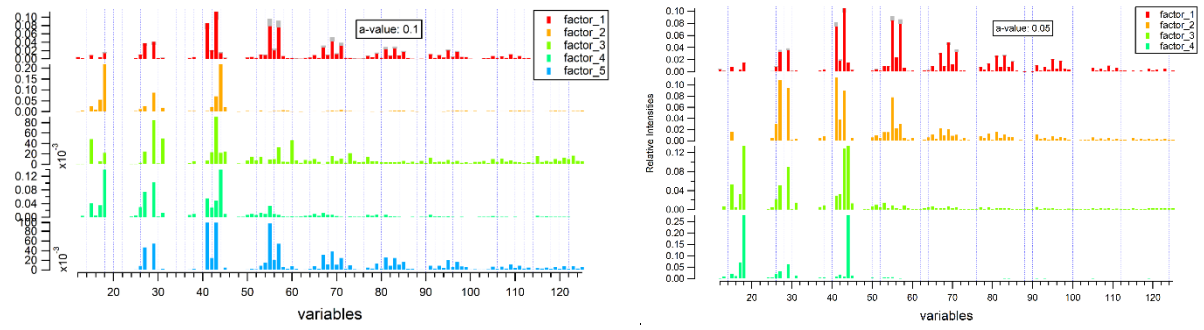

Figure 10.7. Five factor run with HOA constrained (a=0.1) at position 1 for the cold period of 2016 – 2017 depicted on the left panel. On the right panel, the HOA constrained solution for the warm 2017 period.

10.4.4 HOA – BBOA constrained runs

This step is performed for the winter – time datasets. When constraining two factors, one using the average HOA spectrum from (Ng et al., 2011a) and the second using the BBOA spectrum obtained in the same study, the five factor solution indicatively for the 2016 – 17 cold period, is presented in Figure SF.8. This step has been implemented for all winter – time datasets, with similar results. As is evident in position three a primary factor resembling COA emerges once more. The model exhibits low seed variability while an oxidized factor with considerable contribution at m/z 60 and 73 emerges in position 5.

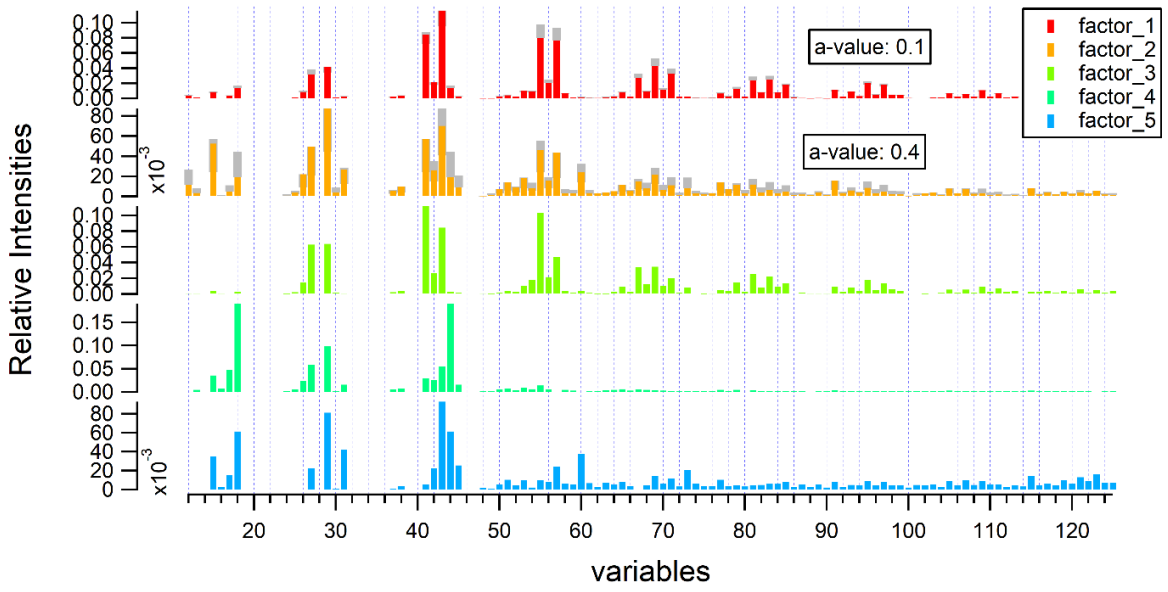

Figure 10.8. Five factor solution constraining HOA and BBOA for the cold period of 2016 – 2017.

When replicating the methodology of (Mohr et al., 2012) (Figure SF.9) for the same period, data points corresponding to early afternoon (~16:00) and the evening lie closer to the linear fit slopes representing COA factors indicating the presence of cooking – like aerosol affecting the measuring site. On the other hand, data obtained during the time frame of the morning rush hour border on the reference line of HOA.

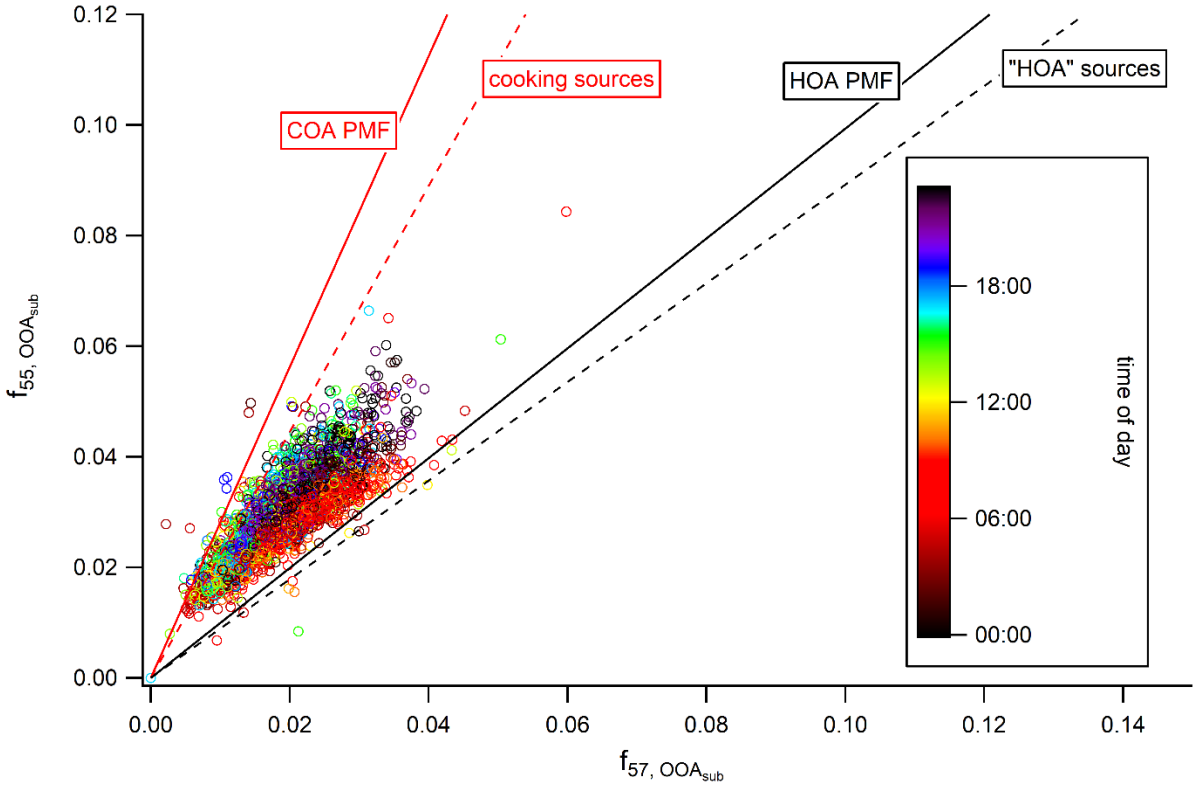

Figure 10.9. $f_{55,\ OOAsub}$ plotted against $f_{57,\ OOAsub}$ indicatively for the 2016 – 2017 cold period. Data points are colored according to time of day. Lines correspond to linear fit results conducted using COA and HOA results both from PMF and laboratory standards studies (Mohr et al., 2012).

10.4.5 Sensitivity analysis on the α value

When proceeding to the final step of the SA procedure, three constrains are implemented for the cold period datasets (HOA, BBOA, COA) and two (HOA, COA) for the warm period datasets. Three scenarios of different levels of constrains applied to the primary OA factors and the respective impact on the relative contribution of each factor have been tested in an effort to minimize subjectivity introduced by the degree of freedom left for the model to vary around the RFP used. The α values ranged from 0.05 to 0.1 with an increment of 0.025 for the HOA factor (Crippa et al., 2014), from 0.1 to 0.2 (Canonaco et al., 2015) with an increment of 0.05 for COA

for all the datasets handled. For BBOA the examined range was for α values varying from 0.3 to 0.5 with an increment of 0.1 and was tested for the cold season datasets. As indicatively exhibited in Figures 10.10 and 10.11 no considerable variability was observed for both the cold and warm period datasets, where maximum fractional difference of contributions was found to be less than 5%.

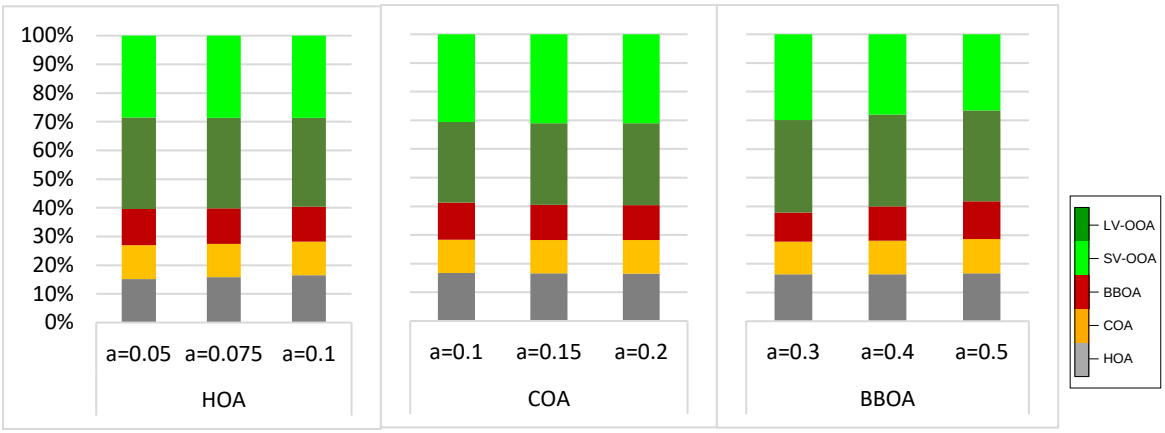

Figure 10.10. Relative contribution of each deconvolved factor for varying α values regarding HOA, COA and BBOA for the winter 2016 – 17 dataset.

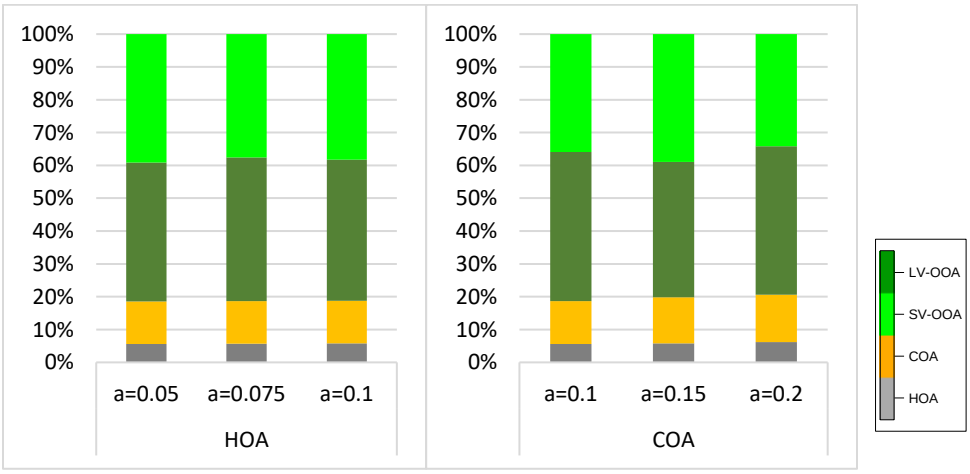

Figure 10.11. Relative contribution of each deconvolved factor for varying α values regarding HOA and COA for the warm period of 2017.

10.4.6 Mass spectra of the selected solutions

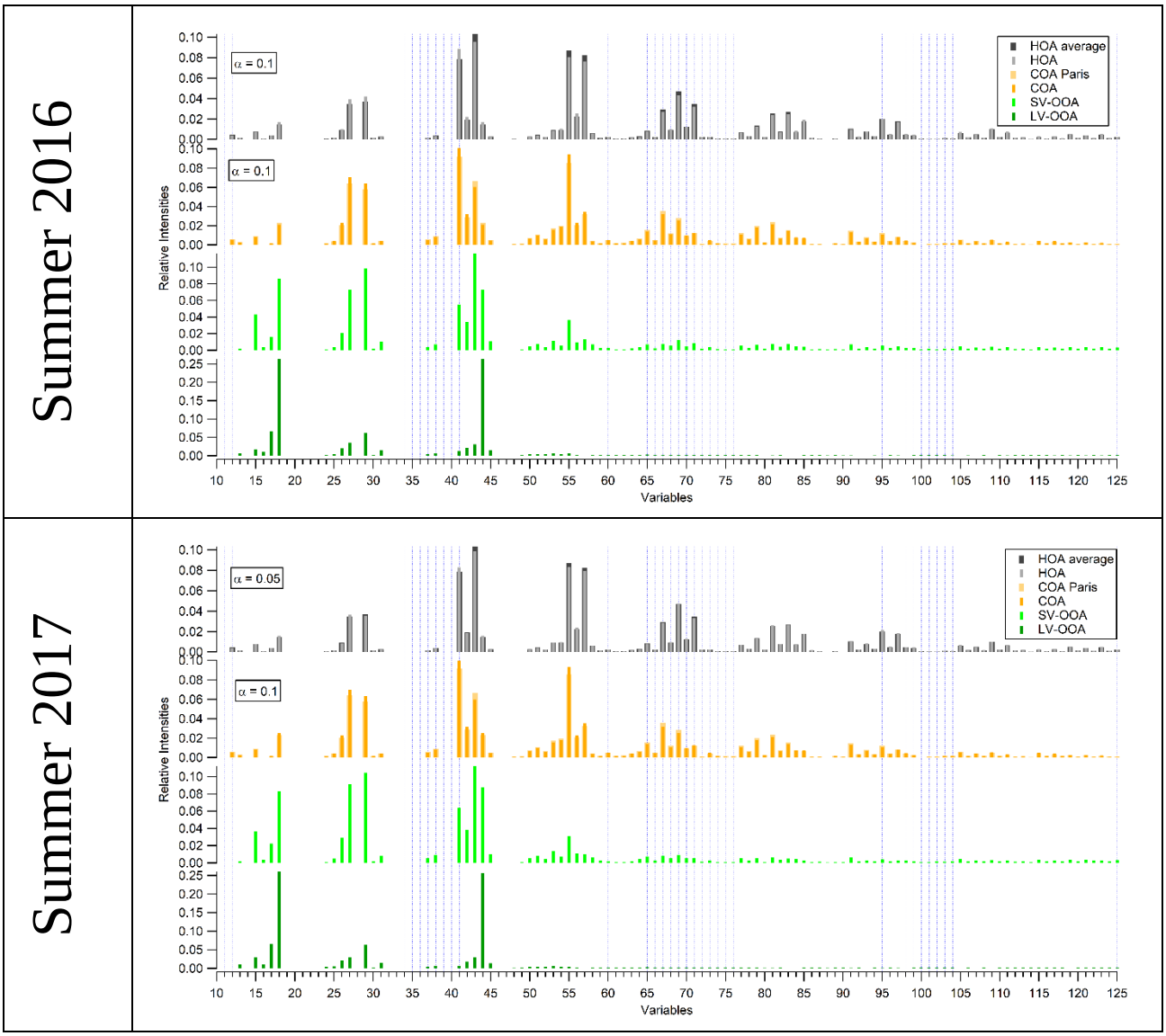

Figure 10.12. Mass spectra of the derived PMF Factors and reference spectra used, together with the corresponding α-values for the two studied summer periods.

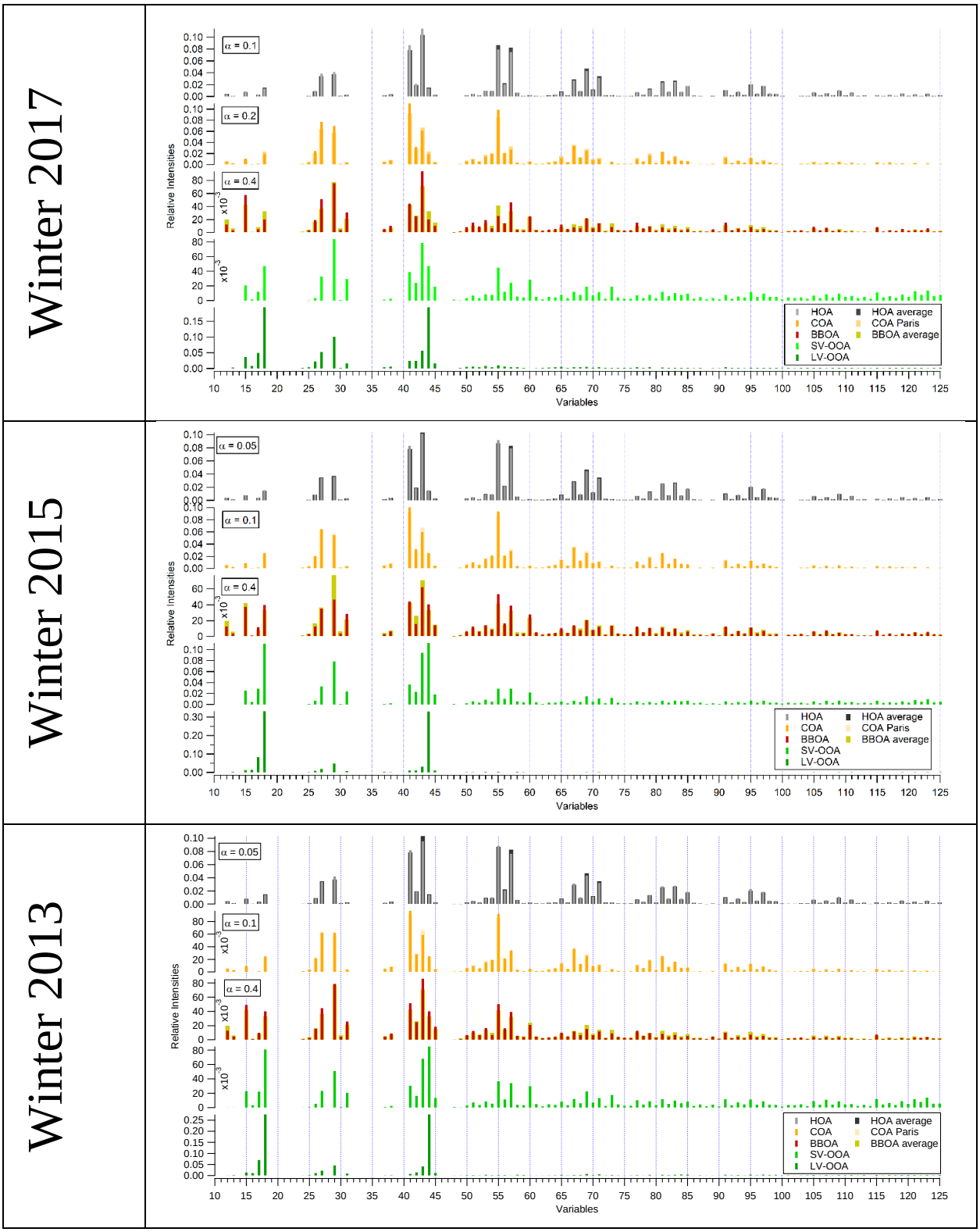

Figure 10.13. Mass spectra of the derived PMF Factors and reference spectra used, together with the corresponding α-values for the three studied winters.

10.4.7 Model residuals for the selected solutions

For the selected solutions, residuals weighted over uncertainty analysis and Organics concentration reconstruction, as resulting from the sum of the different PMF Factors is provided in the following figure.

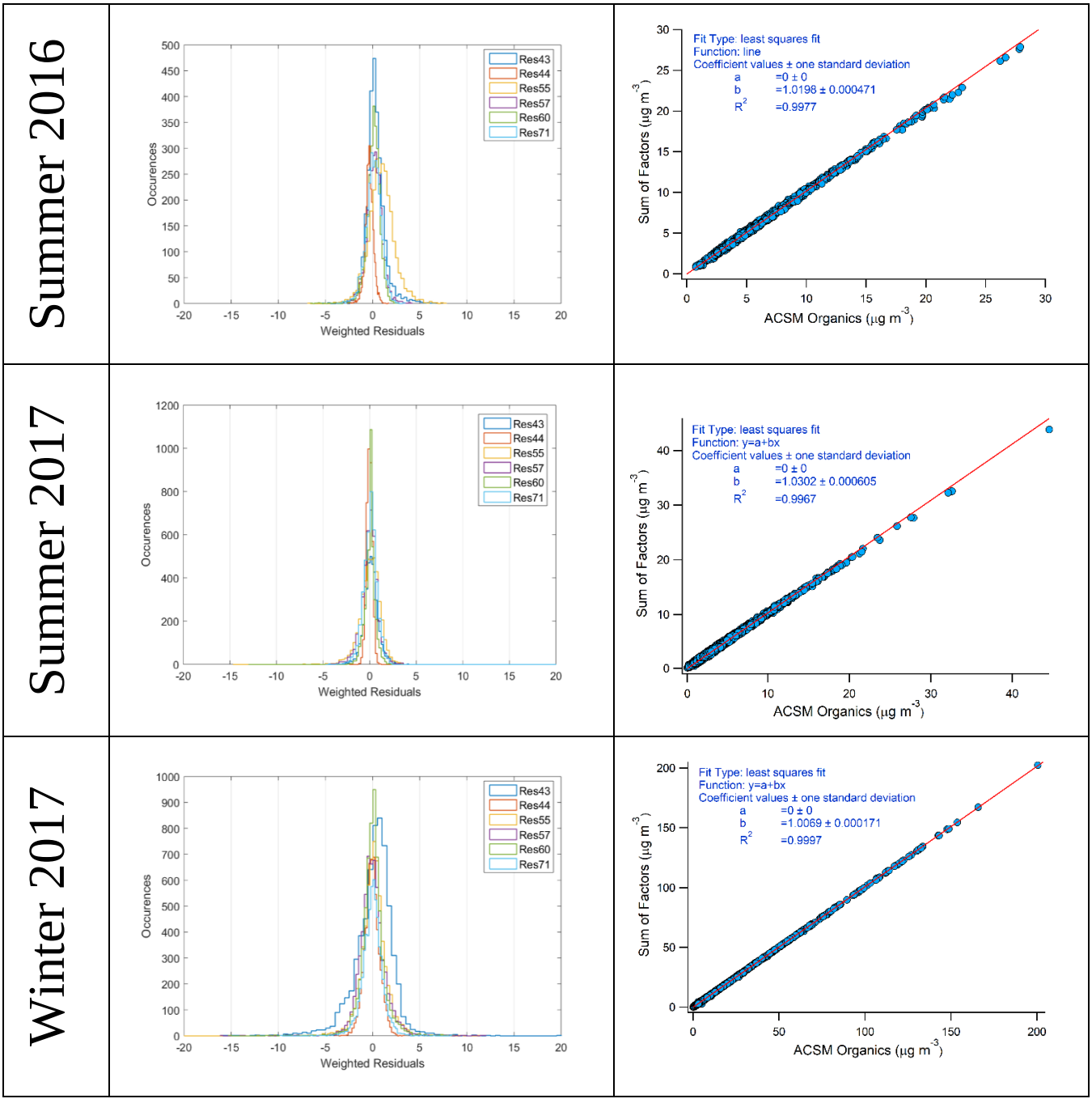

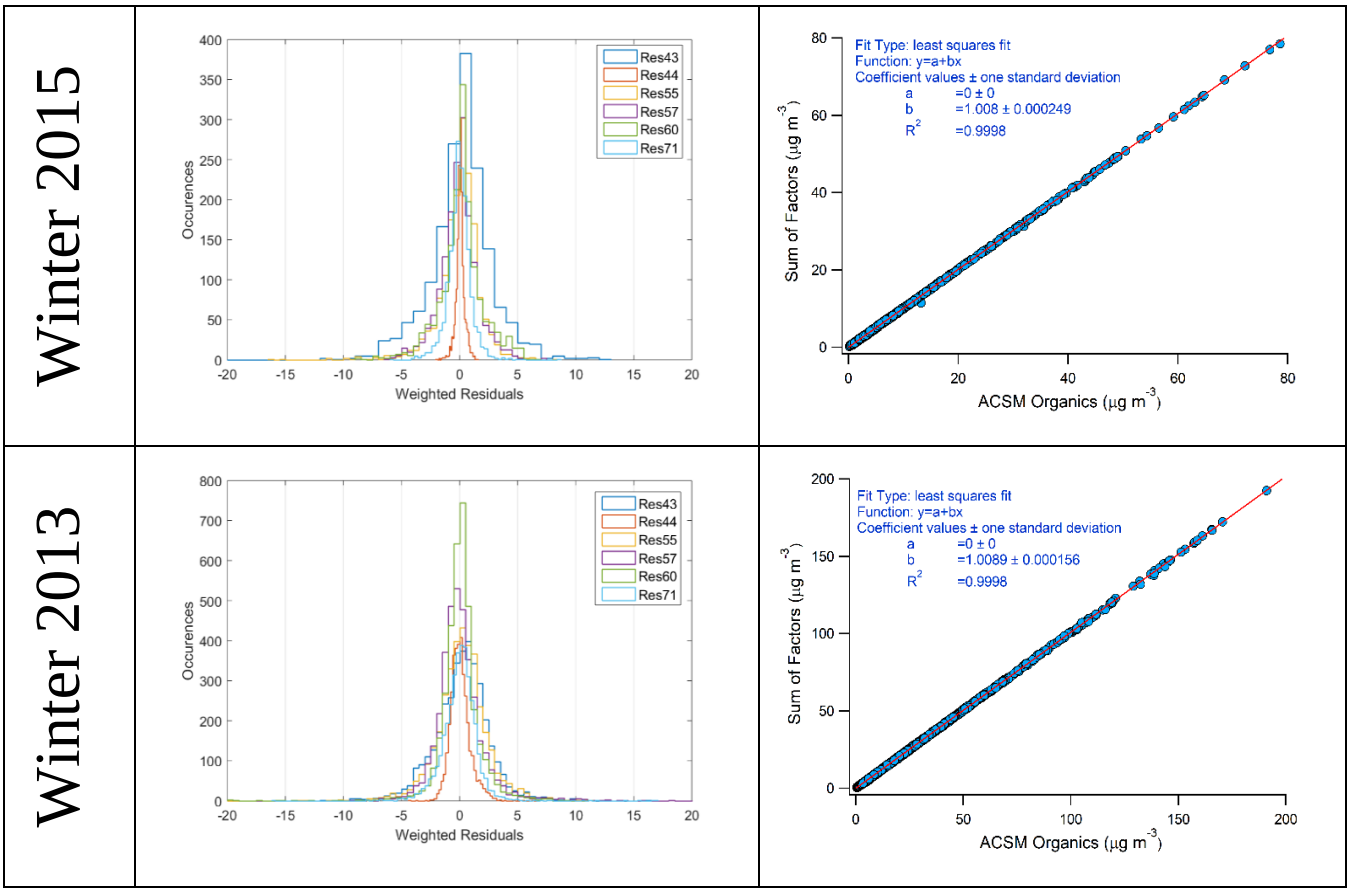

Figure 10.14. Histograms of weighted residuals for variables m/z 43, 44, 55, 57, 60, 71 of the selected solutions and comparison of the sum of the PMF Factors with the Organics measured by the ACSM.

10.4.8 Affinity of obtained spectra with literature mass spectra

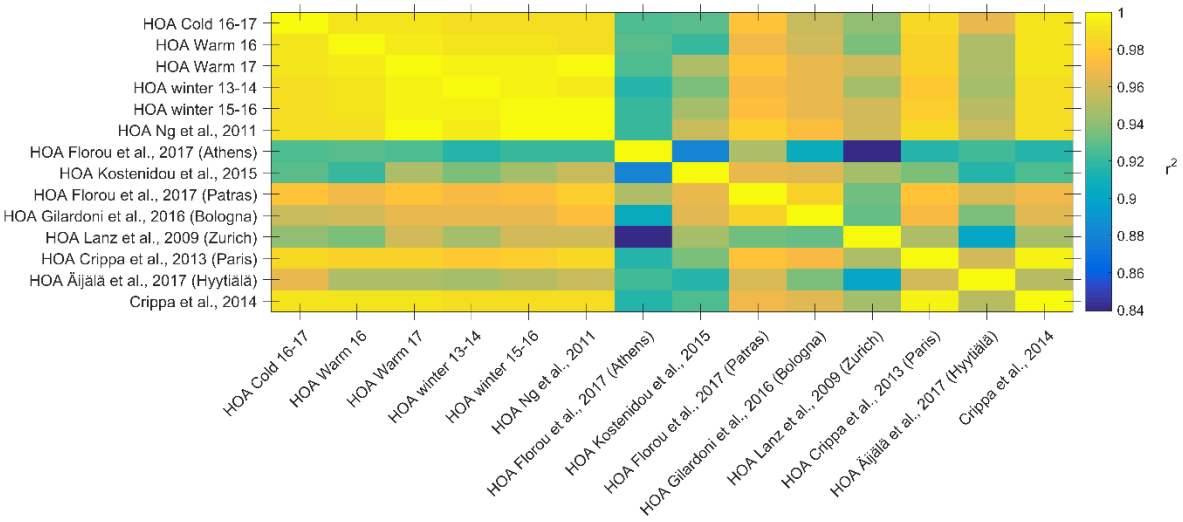

Figure 10.15. Coefficient of determination for linear regression (r^2) of deconvolved HOA profiles from this study versus literature spectra. Note range of color scale.

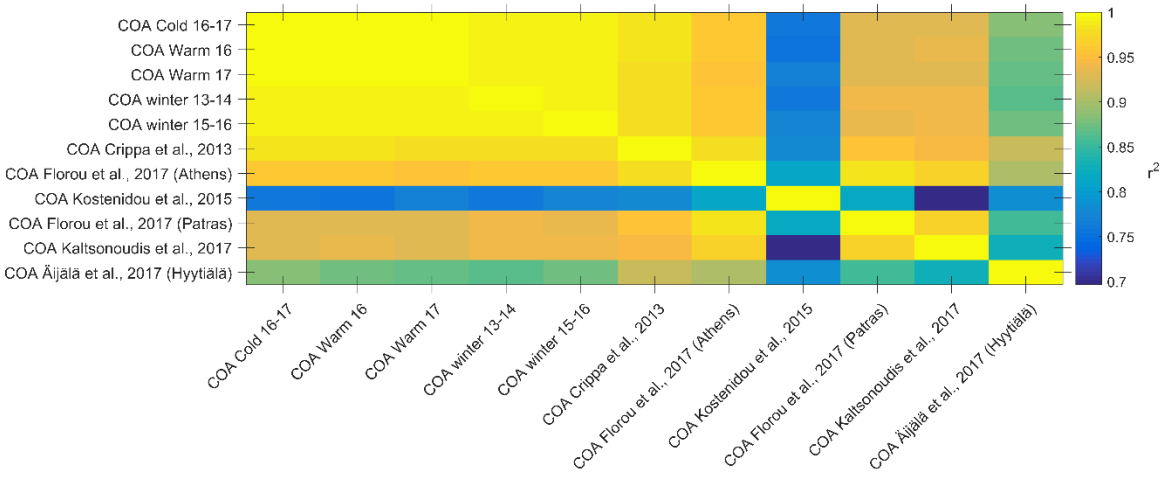

Figure 10.16. Coefficient of determination for linear regression (r^2) of deconvolved COA profiles from this study versus literature spectra. Note range of color scale.

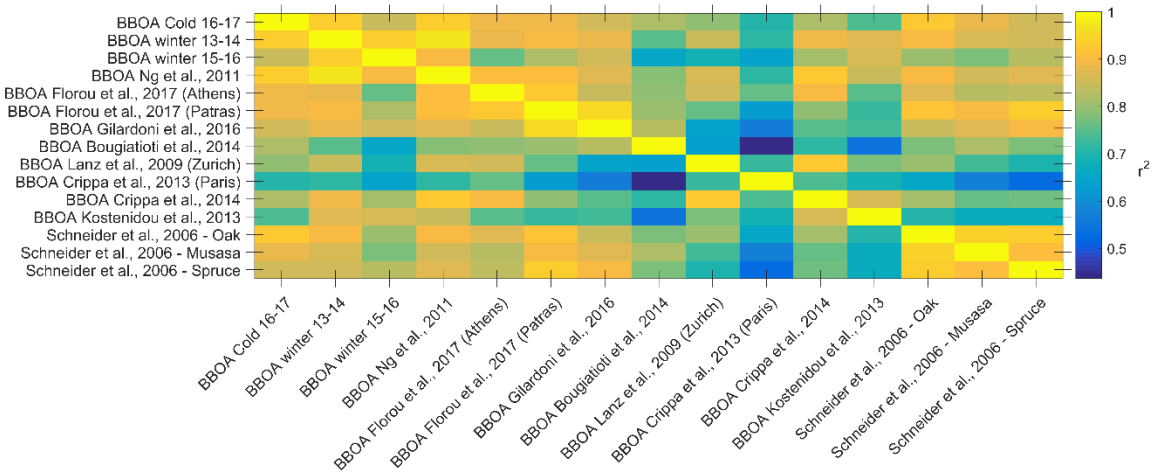

Figure 10.17. Coefficient of determination for linear regression (r^2) of deconvolved BBOA profiles from this study versus literature spectra. Note range of color scale.

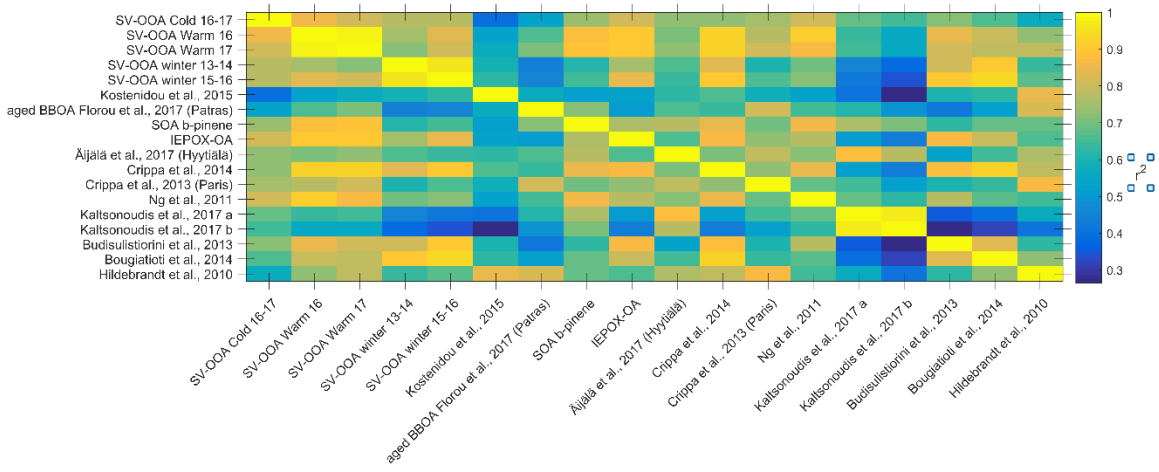

Figure 10.18. Coefficient of determination for linear regression (r^2) of deconvolved SV-OOA profiles from this study versus literature spectra. Note range of color scale.

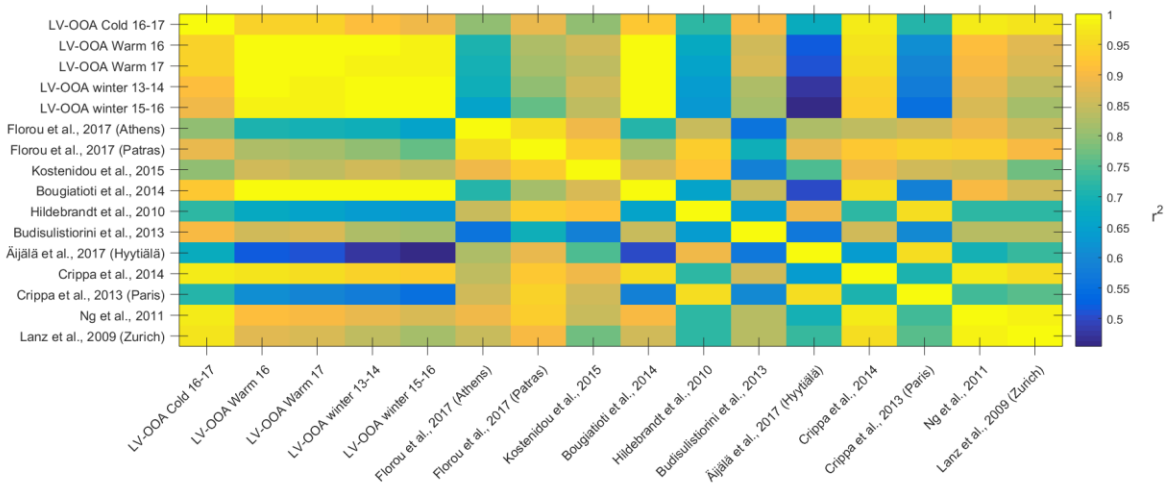

Figure 10.19. Coefficient of determination for linear regression (r^2) of deconvolved LV-OOA profiles from this study versus literature spectra. Note range of color scale.

10.4.9 Correlation of obtained factor timeseries with independent measurements

Table 10.2. Coefficients of determination r^2 of the factor timeseries obtained against independent measurements for the cold period of 2016 – 2017.

r^2	BC	BC_{wb}	BC_{ff}	CO	nss-K^+	SO_4^{2-}	NO_3^-	NH_4^+	Cl
HOA	0.65	0.52	0.60	0.65	0.32	0.22	0.30	0.26	0.54
COA	0.39	0.36	0.32	0.33	0.34	0.11	0.22	0.15	0.35
BBOA	0.56	0.77	0.24	0.51	0.55	0.12	0.35	0.19	0.61
SV-OOA	0.77	0.90	0.44	0.73	0.55	0.21	0.38	0.26	0.80
LV-OOA	0.26	0.18	0.27	0.21	0.40	0.36	0.61	0.58	0.27

Table 10.3. Coefficients of determination r^2 of the factor timeseries obtained against independent measurements for the 2017 warm period

r^2	CO	BC_{wb}	BC_{ff}	BC	NO	NO_2	SO_4^{2-}	NO_3^-	NH_4^+
HOA	0.44	0.50	0.63	0.64	0.47	0.13	0.02	0.62	0.02
COA	0.33	0.19	0.12	0.13	0.08	0.24	0.05	0.36	0.05
SV-OOA	0.40	0.37	0.34	0.35	0.19	0.26	0.22	0.86	0.24
LV-OOA	0.04	0.08	0.06	0.07	0.01	0.02	0.62	0.34	0.63

10.5 Influence of wind speed/direction and of air masses origin

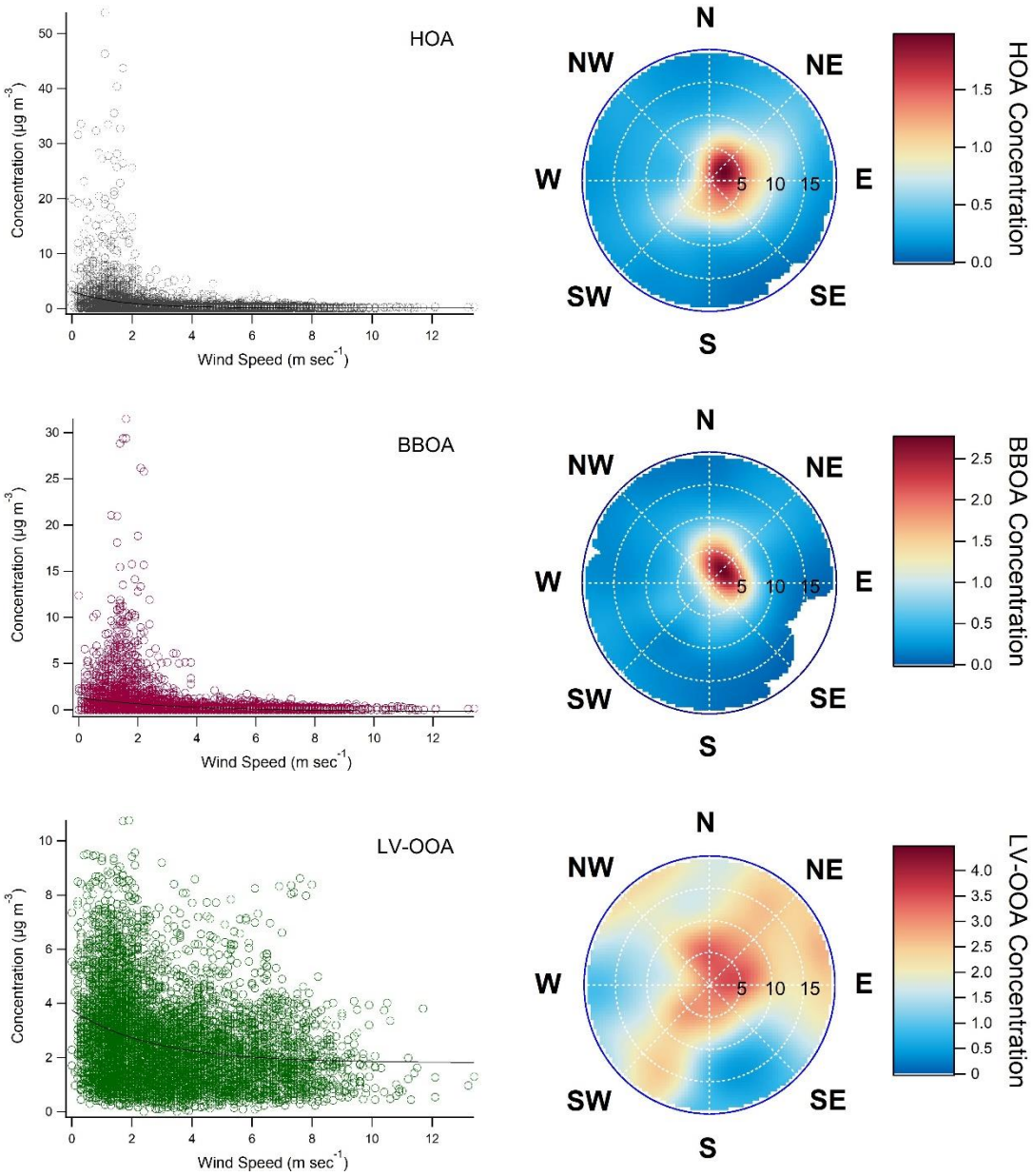

Figure 10.20. Indicative wind analysis results for organic aerosol components in Athens. On the left, hourly averaged concentration vs. wind speed scatterplots. On the right, respective bivariate (wind speed-direction) polar plots for hourly averaged concentrations. The radial axis (wind speed) in km h^{-1}.

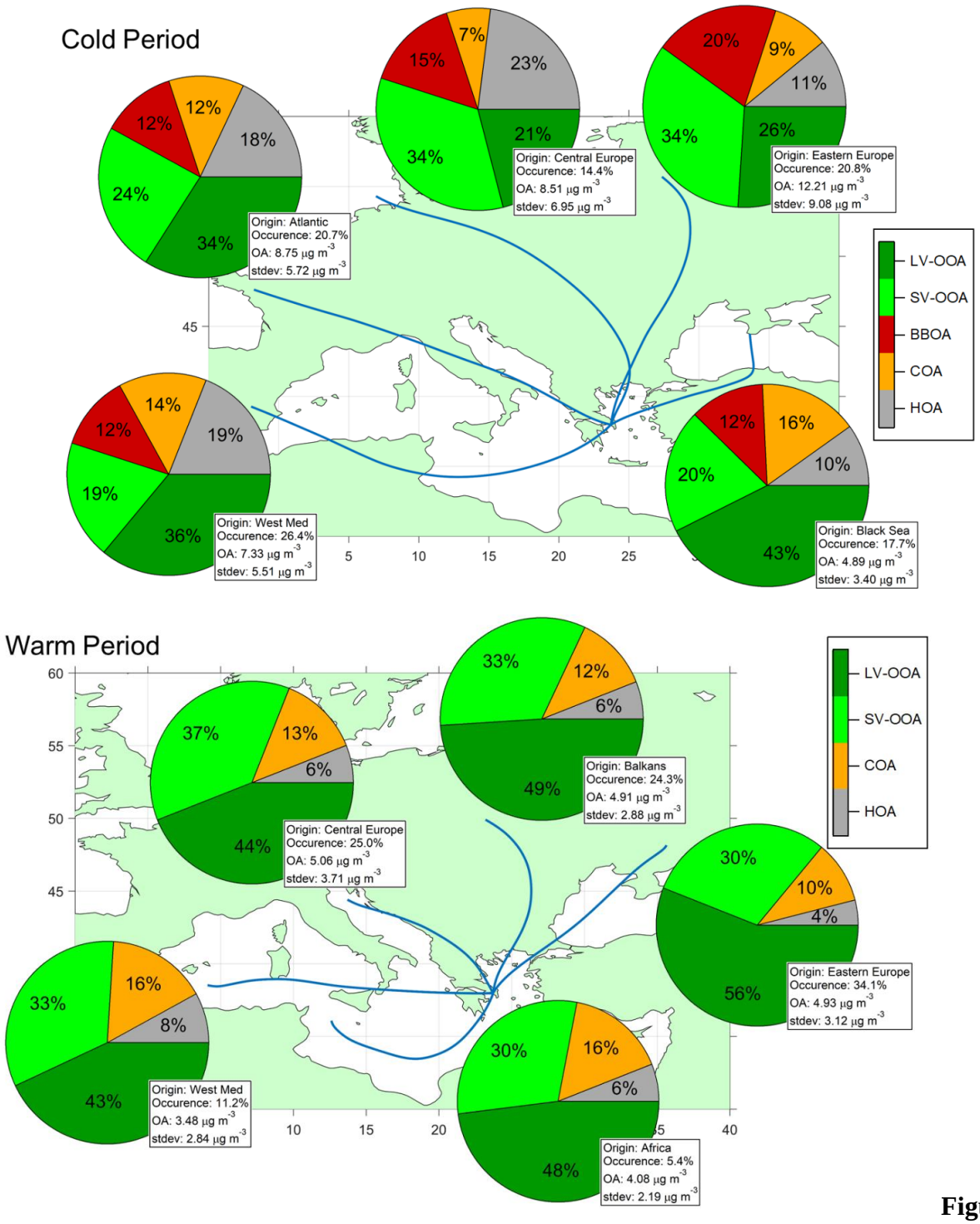

Figure 10.21. Average compositional pie-charts of OA fractions for each trajectory cluster, separately for cold (November 2016 – March 2017) and warm (Aug-Sep 2016 and May-Jul 2017) periods on the top and bottom panel respectively. Displaying also frequency of occurrence and average OA concentrations for each cluster.

11 Appendix C. Supplement to the manuscript: *Online Chemical Characterization and Sources of Submicron Aerosol in the Major Mediterranean Port City of Piraeus, Greece*

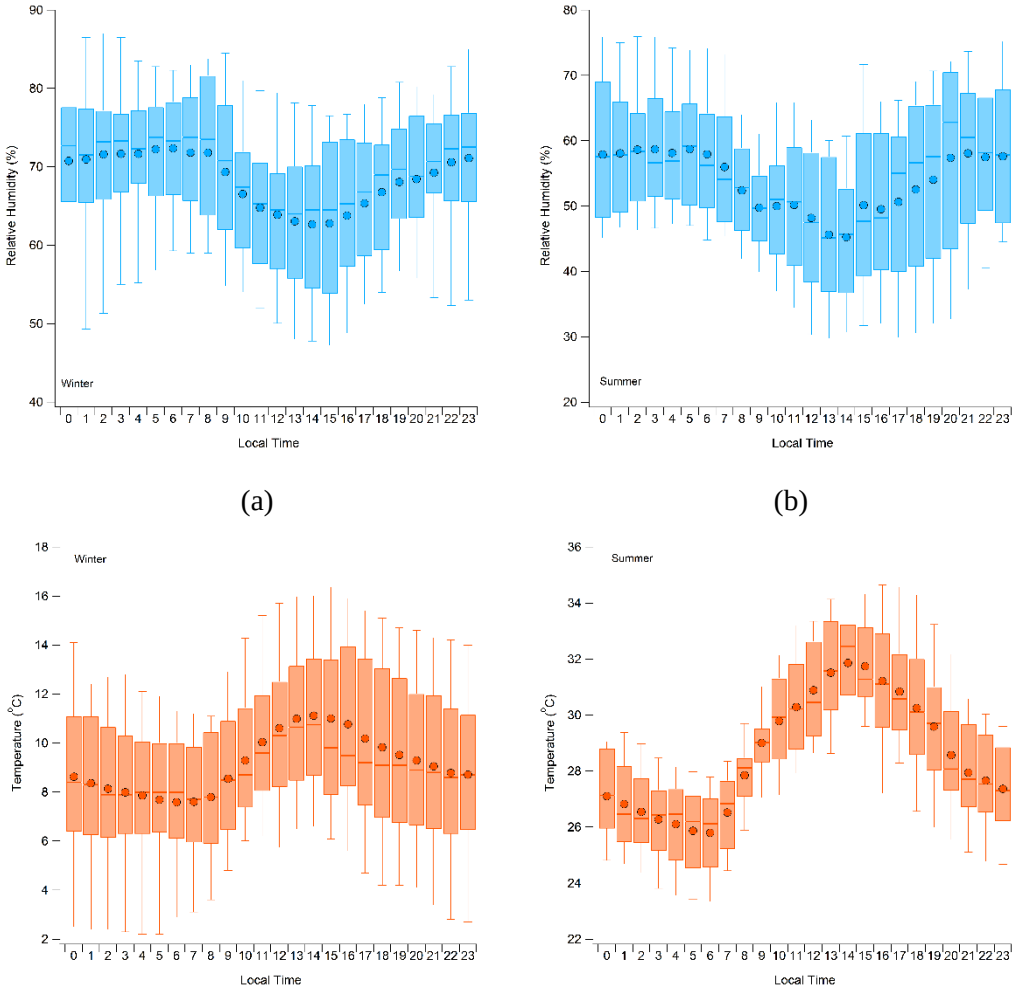

Figure 11.1. Diurnal box-whisker plots of relative humidity (a, b), and temperature (c, d) for the winter and summer periods, respectively. Boxes are the 25th, 50th and 75th percentiles, whiskers are the 10th and 90th percentiles, while dot markers are average values.

11.1 PMF Overview

11.1.1 Theory

Source apportionment of the obtained mass spectra makes use of a bi-linear model, representing the obtained OA mass spectra matrix *X*, in which data in each column *j* are measured intensities for a given *m/z*, and data in each row *i* represent a single mass spectrum obtained at a given time. The bi-linear model analyses the matrix *X* to the linear combination of two static matrices *G* and *F*:

$$X = GF + E$$

where E is the model residual matrix. In this case PMF was applied (Paatero and Tapper, 1994), meaning that the resulting matrices are required to include non-negative values only, which makes sense when dealing with concentrations in the atmosphere. The number (*p*) of columns in *G*, or for that matter, the number of rows in *F*, represent the predefined number of factors, while each column in G represents the time-series of a factor and each row in F is the factor's profile, effectively the factor's mass spectrum.

A least squares algorithm is implemented, which minimizes the quantity *Q*:

$$Q^m = \sum_{i=1}^{m}\sum_{j=1}^{n}\left(\frac{e_{ij}}{\sigma_{ij}}\right)^2$$

where e_{ij} are the model residuals and σ_{ij} are the corresponding measurement uncertainties of the model input matrix X of size $m \times n$. When assessing model performance, the relative change in the normalized *Q* over its expected value Q_{exp} is monitored, where:

$$Q_{exp} = n \cdot m - p \cdot (m + n)$$

Given that model solutions exhibit rotational ambiguity (Paatero et al., 2002), the ME-2 solver, as implemented in the SoFi software package (Canonaco et al., 2013) provides tools to address the issue. Introducing a priori information, e.g. predefined factor profiles, or predefined factor time-series, significantly reduces this rotational ambiguity (Paatero and Hopke, 2009). In this study we are using the a-value approach to introduce these a priori information, thus constraining the resulting matrices *F* and/or *G*. The a-value is a measure of the extent to which the resulting profile

or time series is allowed to vary from the ones introduced as parts of the constrained matrices *G* or *F*:

$$g_{i,solution} = g_i \pm a \cdot g_i$$

$$f_{j,solution} = f_j \pm a \cdot f_j$$

where *g* and *f* are a column of *G* or a row of *F* respectively. The a-value can vary between 0 and 1 representing a fully constrained and a fully unconstrained result respectively.

11.1.2 Applied Strategy

For both seasons, PMF was initialized with no factor profile constrains, exploring solutions ranging from 3 to 8 factors. For the winter dataset, the 3-factor unconstrained PMF revealed 2 primary factors– one associated with fossil fuel combustion, the other with biomass burning – and a secondary OA factor (Figure S1a). The OOA factor showed significant diurnal variability peaking in the evening, thus exhibiting important influence from RWB emissions. While the BBOA factor had high correlations with BC_{bb} (r^2 above 0.8), the HOA factor's correlation to BC_{ff} was rather low with r^2 values around 0.3. The later led to the exploration of the 4-factor solution. The 4-factor solution revealed another HOA-like factor, with limited variability between seeds and runs, consistently exhibiting highly similar relative intensity patterns in the mass spectra, with pronounced contributions to *m/z* 41 and 43 and lower peaks at the rest of the alkane and alkene related fragments (e.g. 55, 57 etc.) as illustrated in the spectrum of factor four in Figure S2. This factor appeared as slightly more oxidized, with higher contributions at *m/z* 44 implying atmospheric processing and was also present in runs within the 5 and 6 factor solutions.

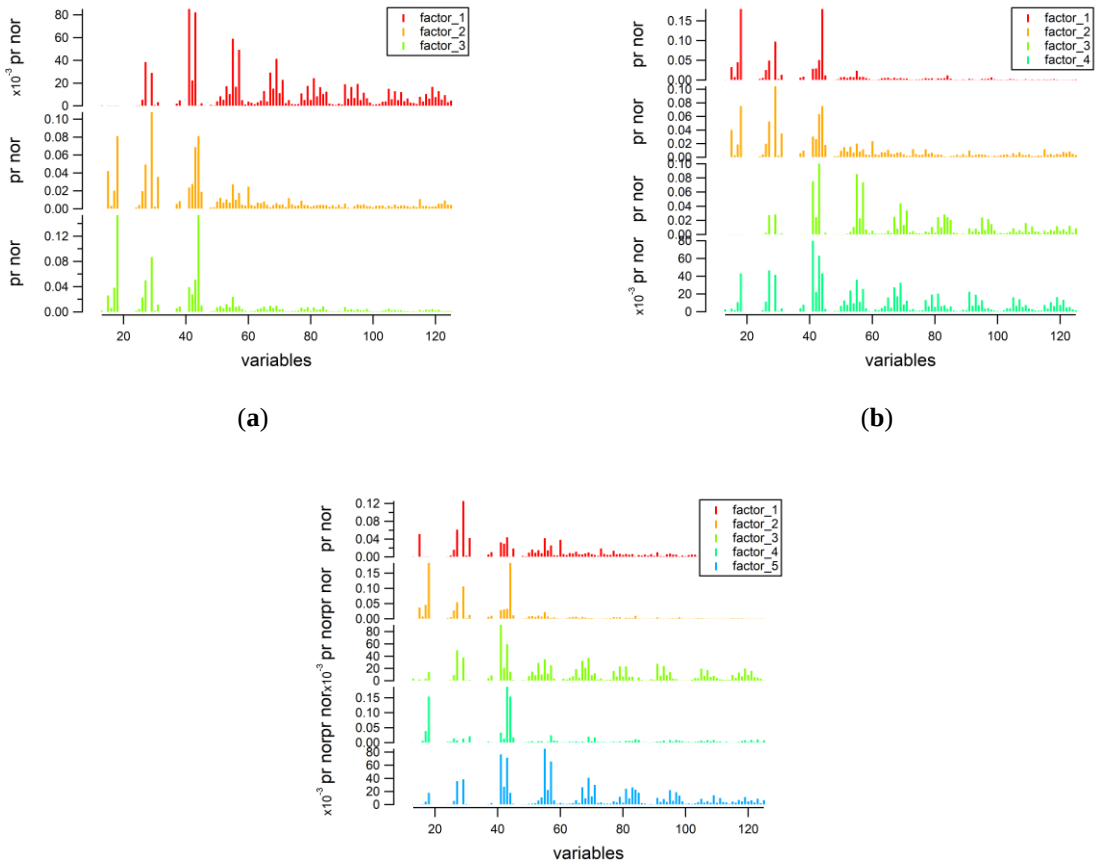

Figure 11.2. Factor profiles of wintertime unconstrained PMF solutions for (a) 3, (b) 4, (c) and 5 factors respectively.

Inspecting factors 3 and 4 in Figures S2c and S2b, respectively, the factor's small difference in intensities between the *m/z* 55 and 57 ions, points away from a cooking source, a conclusion further corroborated by plotting the measured f_{55} over f_{57} scatter plot (Mohr et al., 2012) . When coloring the data points according to the time of day there is no evident shift of data points towards the COA PMF and "cooking source" lines during typical meal hours (Figure S3). This observation, also present in summertime data, lead to the adjustment of the implemented PMF strategy, thus not applying any COA factor constrains in subsequent analysis.

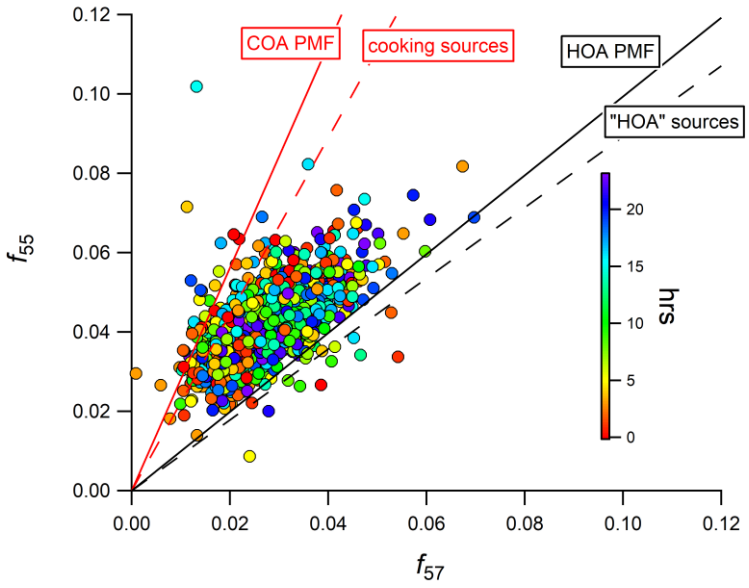

Figure 11.3. Scatter plot of f_{55} vs f_{57} for wintertime data in Piraeus according to (Mohr et al., 2012). Data points are color coded according to time of day. Red and black lines correspond to linear fits of f_{55} and f_{57} extracted from HOA COA factors as well as spectra from cooking and traffic emission studies grouped accordingly.

Furthermore, in winter, while exploring the unconstrained runs and moving to more than 5 factors, factor splitting behavior started to emerge, while the stability of the solutions was hindered with large variability observed for resulting profiles between different seed runs.

As a next step, constrains were introduced to the primary OA factors by implementing the a-value approach (Crippa et al., 2014). Initially, only the HOA traffic-related factor was constrained using the factor profile acquired by Crippa et al. during wintertime in Paris (Crippa et al., 2013). The a-values applied ranged from 0.02 to 0.2. The applied constrain improved substantially the observed correlation of the HOA traffic-related factor to BC_{ff}, bringing r^2 values close to 0.5 while all 4 and 5 factor runs incorporated the second HOA-like factor, which retained its distinct profile among different seed runs. It should be mentioned here that the 3-factor solution, while constraining the HOA traffic factor, other than exhibiting larger Q/Qexp values, showed a clear structure in the diurnal variation of both the Q value as well as the residuals of key variables (e.g. *m/z* 44 or *m/z* 60) indicating an inferior performance of the PMF model (Figure S4a and S4b). When exploring the diurnal variability of residuals for the summer dataset, a similar behavior was observed (Fig.

S4c and S4d). Consequently, we placed the focus on solutions with at least 4 factors for both measuring periods.

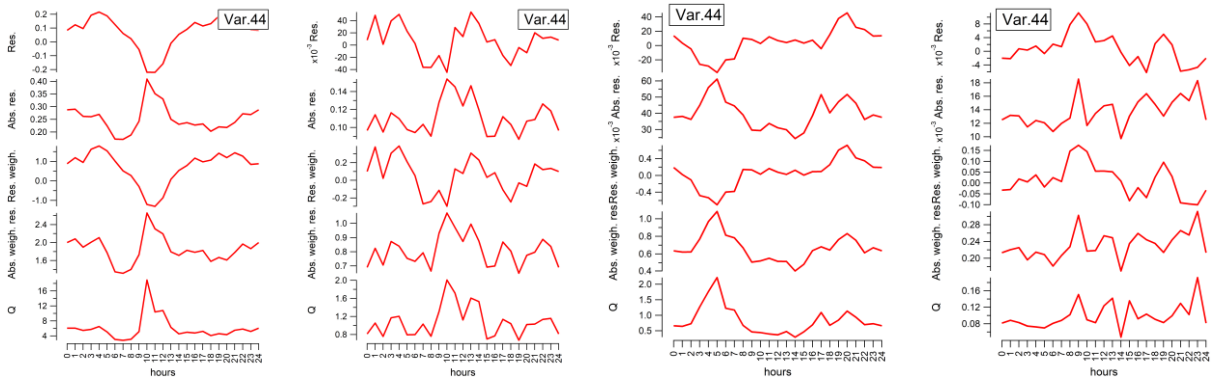

(**a**) (**b**) (c) (d)

Figure 11.4. Diurnal variability of the PMF model residuals and the value Q for the variable *m/z* 44 in the case of (a) a 3-factor solution and (b) a 4-factor solution when constraining an HOA factor for wintertime and in the case of 3- factor (c) and 4-factor (d) solution for summertime respectively.

In winter, given the fact that when constraining the HOA factor only, the resulting unconstrained BBOA factor was lacking stability among different seeds runs, we introduced constrains using the BBOA factor profile derived in (Ng et al., 2011a). The a-values used, ranged from 0.2 to 0.6. Different combinations of a-values for the HOA and BBOA factors were tested and the resulting HOA and BBOA time-series were assessed in terms of their correlation with BC_{ff} and BC_{bb}, respectively. Exploring 4-factor solutions with both BBOA and HOA constrained, while the second HOA-like factor persisted, appearing in most of the examined seed runs, the remaining factor, largely resembling an OOA factor in terms of mass spectra, seemed to be highly affected by primary sources, exhibiting large peaks during evening hours and tracking the BBOA factor's nighttime variability related to residential heating. In order to tackle this behavior, 5-factor solutions were consequently explored. While keeping the two aforementioned constrains, in the majority of the 5-factor runs, together with than the second HOA-like factor and a highly oxygenated OOA factor, a seemingly less oxygenated factor was revealed, with considerable contributions at the *m/z* 60 fragment. Most of the nighttime elevated concentrations were attributed to this less oxidized OOA factor. Other than the Q/Qexp values, behavior of the residual diurnal cycles improved, while the 3 unconstrained factors of the 5-factor solution showed low variability

among different seed runs, supporting the choice of the 5-factor solution in winter. Eventually, the selected final wintertime 5-factor solution includes two HOA factors (HOA-1 & HOA-2) a BBOA, a less oxidized and a more oxidized (LO-OOA and a MO-OOA) factor.

In summer, after constraining the traffic-related HOA factor with the same anchor profile and going through the 4-factor solutions, a HOA-like factor similar to the one found in the winter dataset (Fig S4), could be observed in the majority of the different seed runs. This HOA-like factor was characterized by limited stability, mostly in terms of the *m/z* 44 contribution to its profile, which for some of the runs was as high as the respective contributions of *m/z* 43 and 41. When *m/z* 44 contributions were rather low, the factor showed similarities with the HOA-2 factor obtained for wintertime (r^2~0.8). In order to extract this HOA-like factor more effectively, we used the wintertime HOA-2 factor profile as an anchor, applying rather loose a-values (0.1 – 0.3). No BBOA-resembling factor could be identified for the summer season, since no substantial contribution from the *m/z* 60 and *m/z* 73 fragments was observed. In fact, an average f_{60} value of 0.27% was recorded for the summer data, in contrast to the 0.7% average f_{60} measured in winter. Therefore, a 4-factor solution was chosen, incorporating two HOA factors, a less oxidized and a more oxidized OOA factor

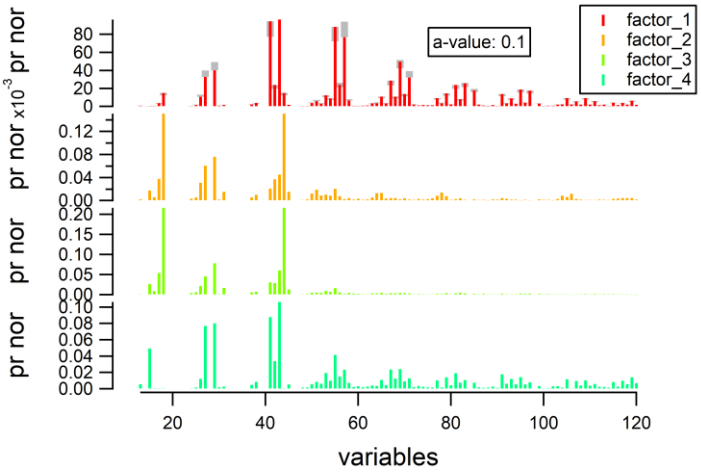

Figure 11.5. PMF run constraining an HOA factor (a-value=0.1) for the summertime period. A second HOA like factor with major contributions at *m/z* 41 and 43, can be spotted in position 4.

Table 11.1. Brief overview of the constrains and model performance for the selected PMF solutions in the two measurement periods.

	Winter	**Summer**
Number of Factors	5	4
Modeled vs. Measured OA r^2	0.99	0.99
Modeled vs. Measured OA Slope	0.99	1.03
HOA-1 Anchor Profile	Crippa et al., 2013	Crippa et al., 2013
HOA-1 a-value	0.02	0.1
HOA-2 Anchor Profile	-	This Study
HOA-2 a-value	-	0.2
BBOA Anchor Profile	(Ng et al., 2011a)	-
BBOA a-value	0.6	-

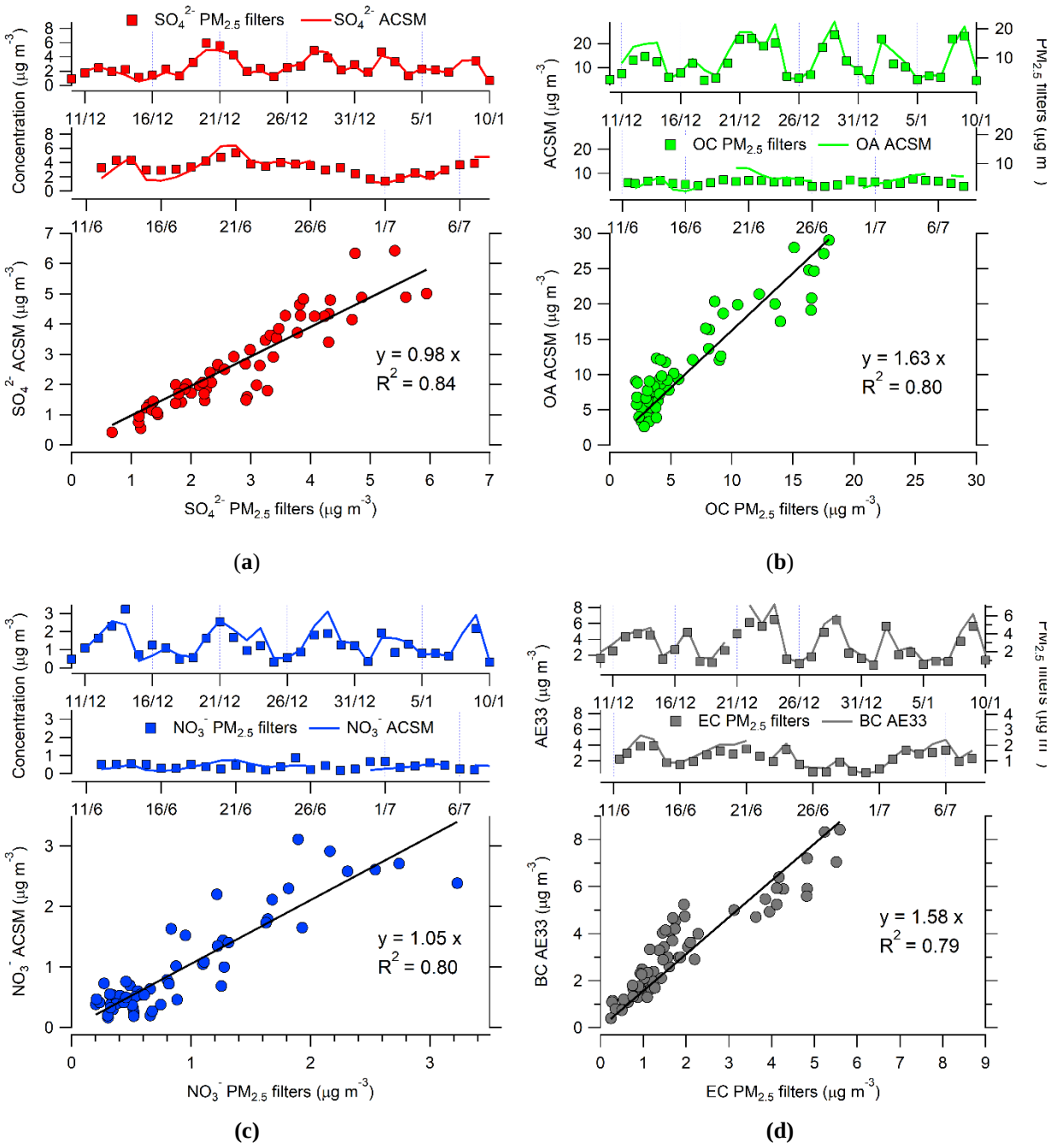

Figure 11.6. Comparison of 24 h averaged concentrations determined with the on-line instruments and from filter-based analyses, for major fine aerosol species in Piraeus, for the two campaigns combined. Daily averaged time-series for both seasons are also included.

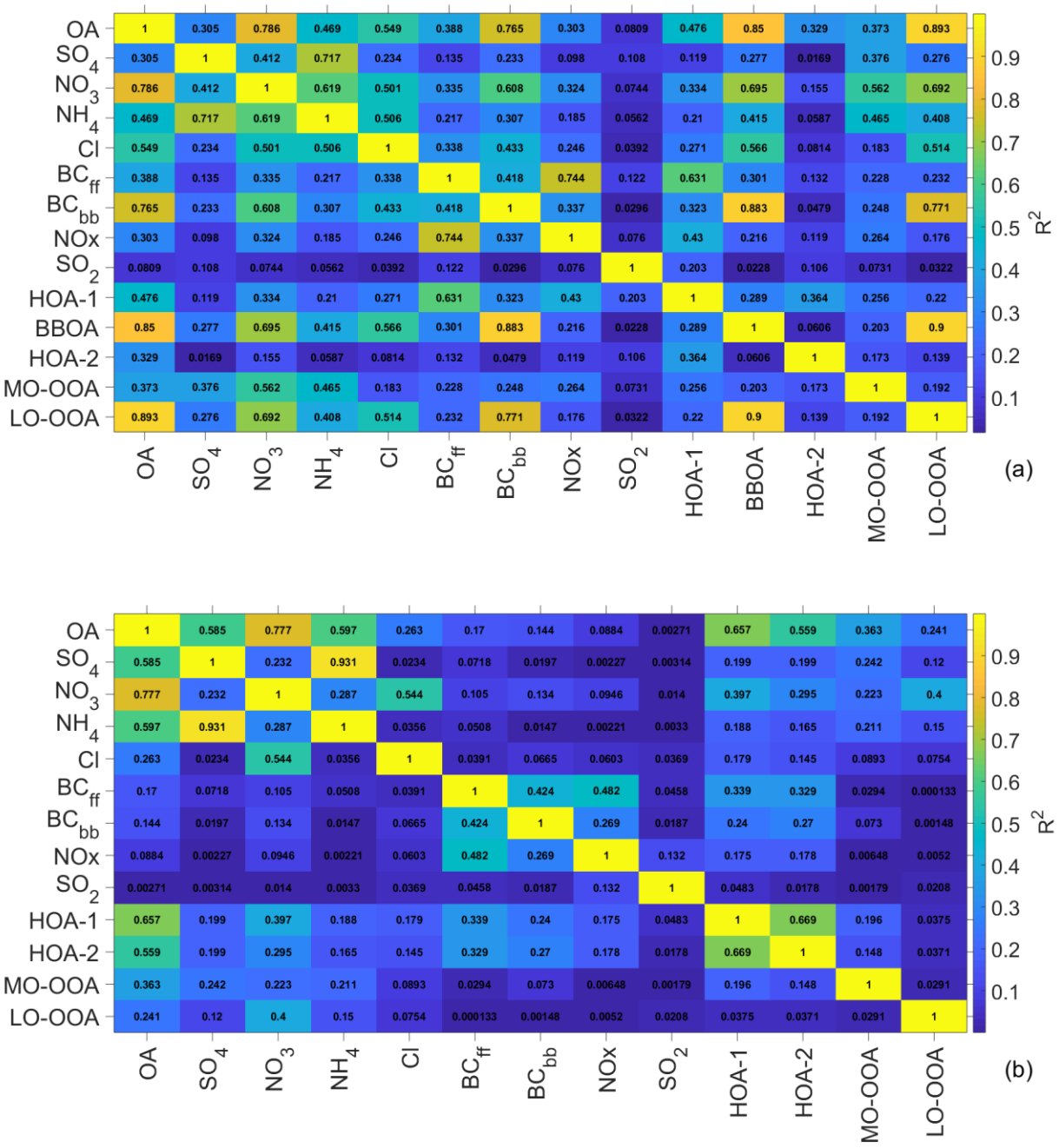

Figure 11.7. Correlation plot for major species, source factors, BC constituents, NO_x and SO_2 for wintertime (a) and summertime (b) measurements.

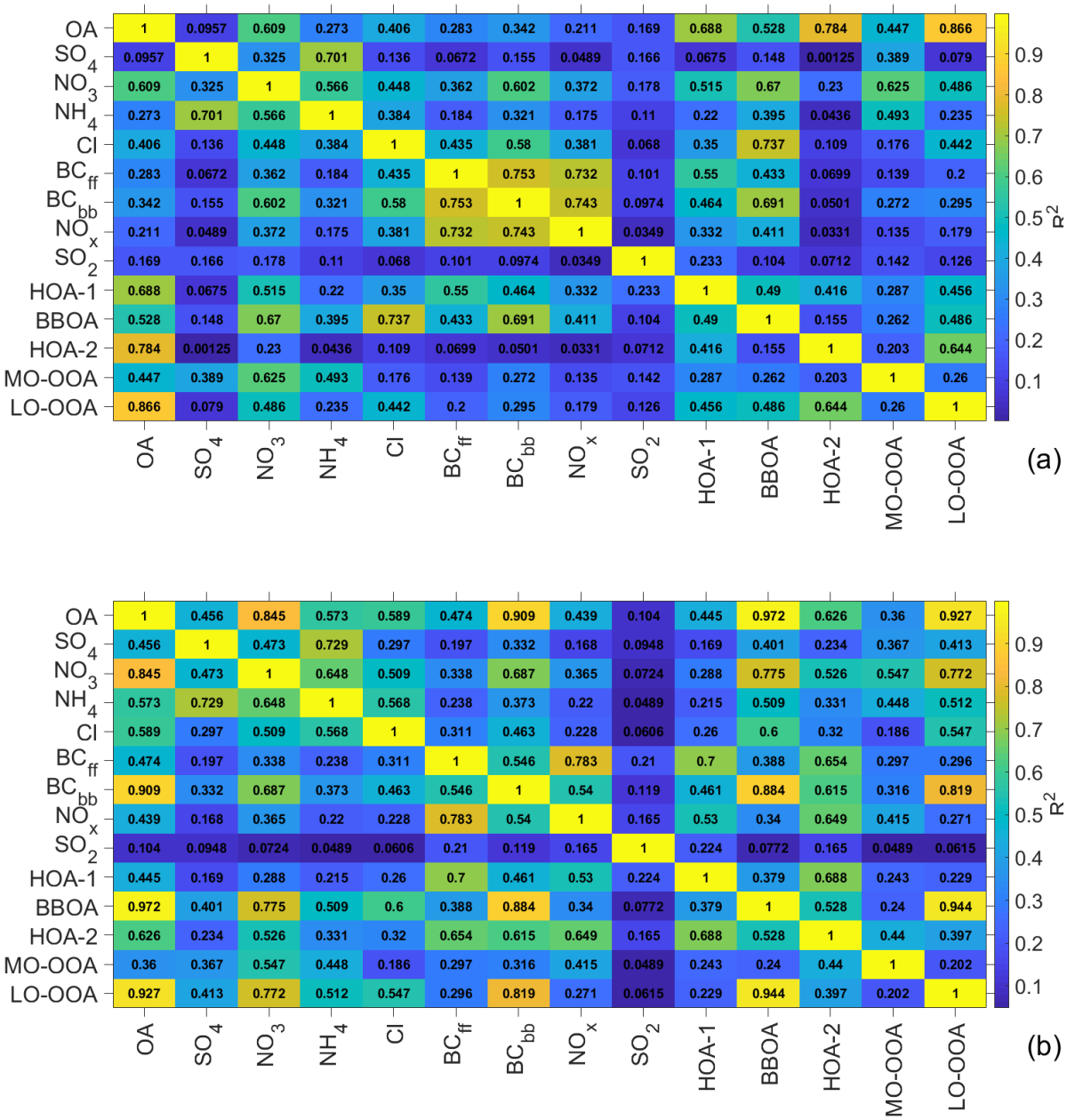

Figure 11.8. Correlation plot for major species, source factors, BC constituents, NO_x and SO_2 during the winter period for daytime (a) and nighttime data (b).

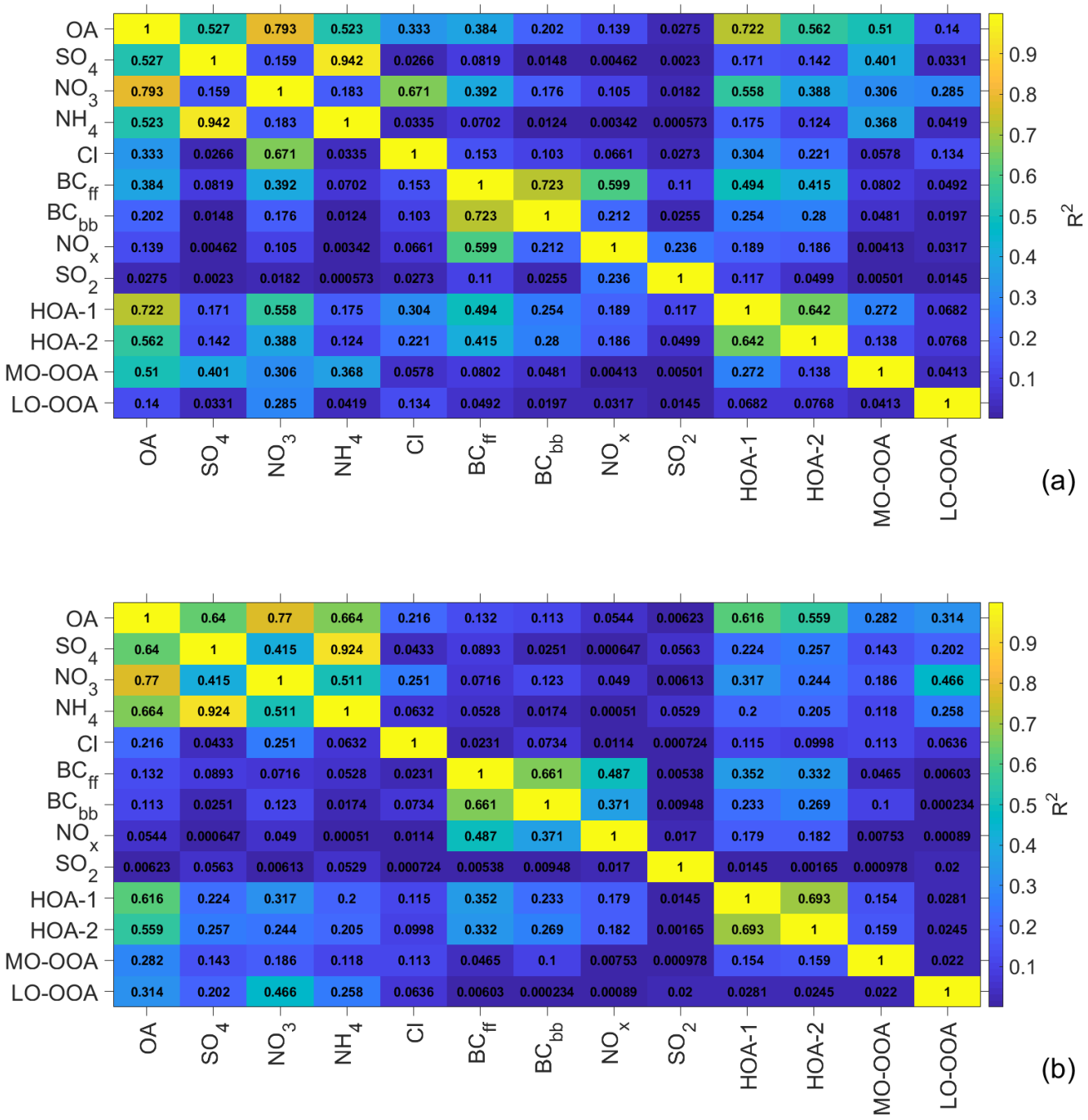

Figure 11.9. Correlation plot for major species, source factors, BC constituents, NO_x and SO_2 during the summer period for daytime (a) and nighttime data (b).

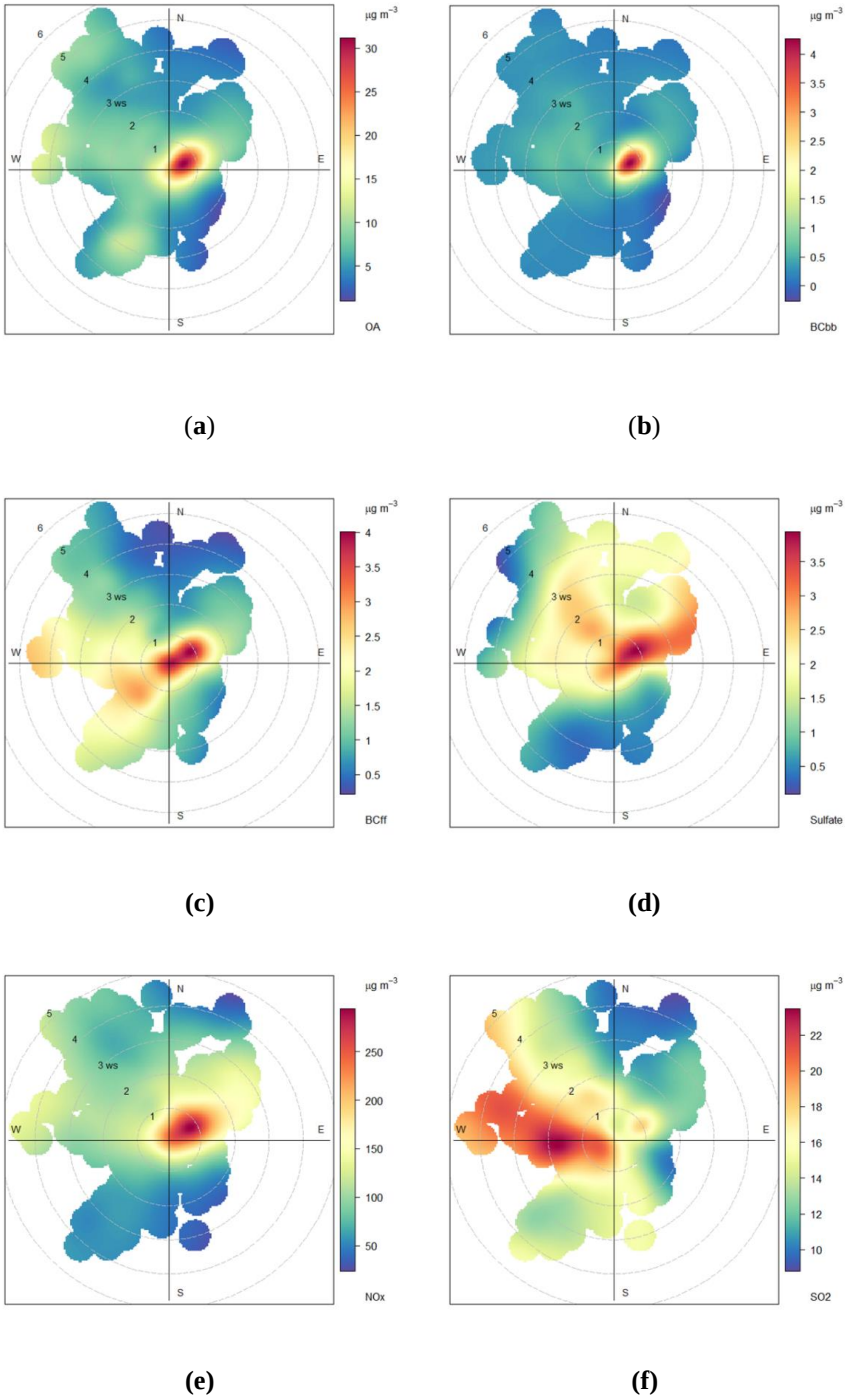

(**a**) (**b**)

(**c**) (**d**)

(**e**) (**f**)

Figure 10.10. Bivariate polar wind plots for the effects of wind direction and wind speed (radial axis in m s^{-1}) to concentrations of OA, (a), BC_{bb} (b), BC_{ff} (c), sulfate (d) as measured at P1 and NO_x (e) and SO_2 (f) as measured at PEI-1, during the winter period.

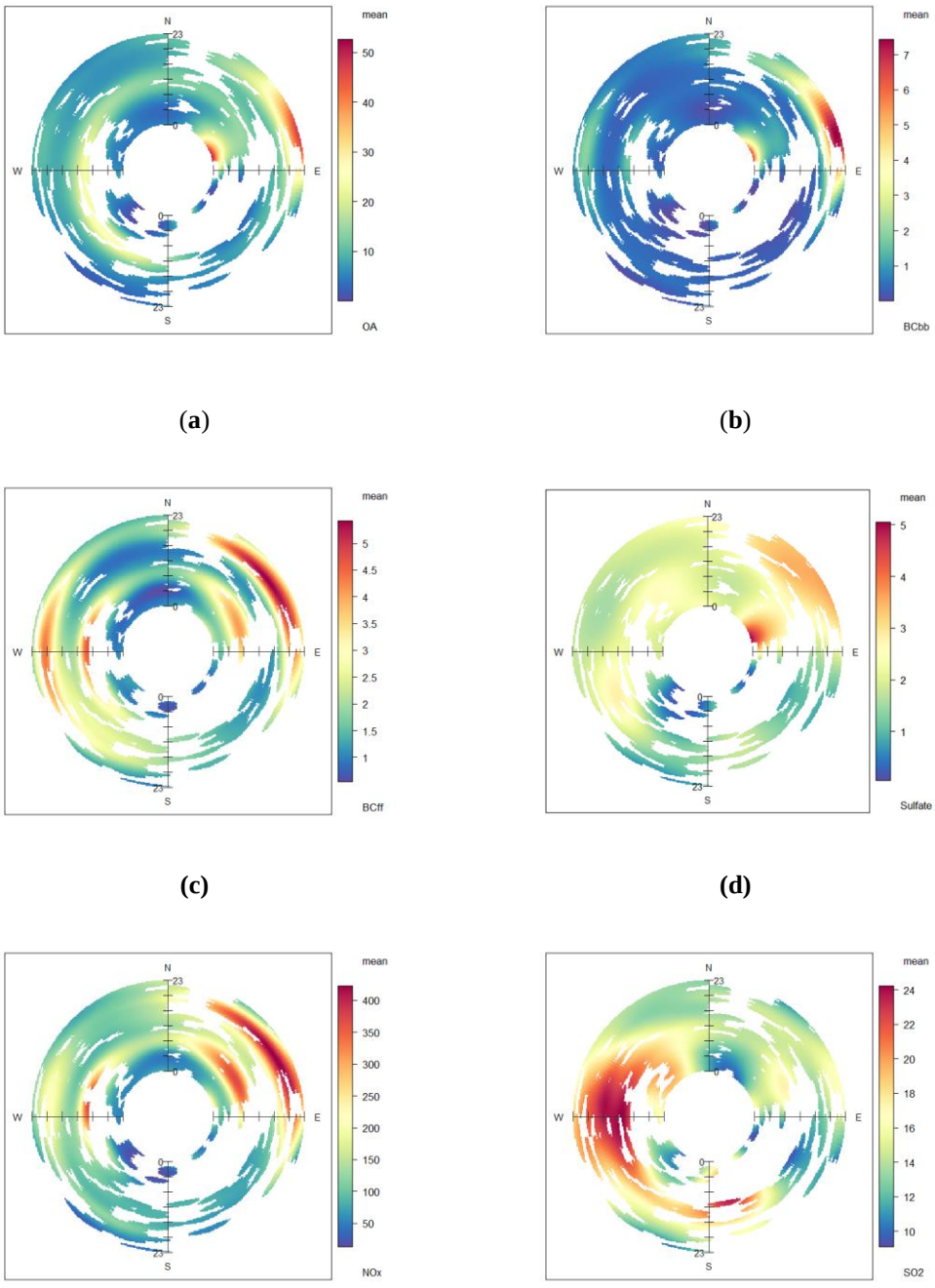

(a) **(b)**

(c) **(d)**

(e) **(f)**

Figure 11.11. Annular wind plots for the effects of wind direction per hour of the day (radial axis, increments by 4 hr) to concentrations of OA, (a), BC_{bb} (b), BC_{ff} (c), sulfate (d) as measured at P1 and NO_x (e) and SO_2 (f) as measured at PEI-1, during the winter period

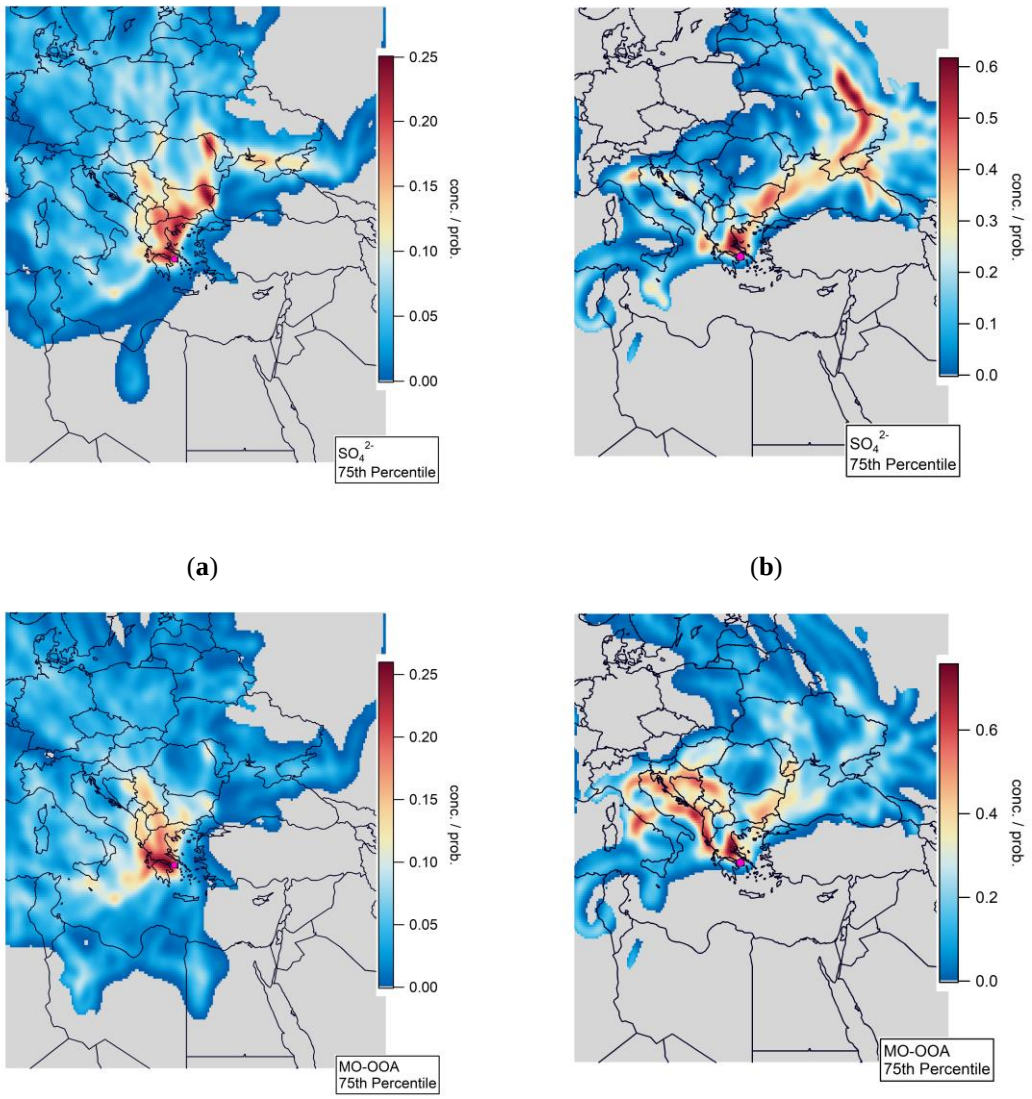

Figure 11.12. Potential Source Contribution Function calculations for sulfate during winter (a) and summer (b) as well as MO-OOA for winter (c) and summer (d), respectively.

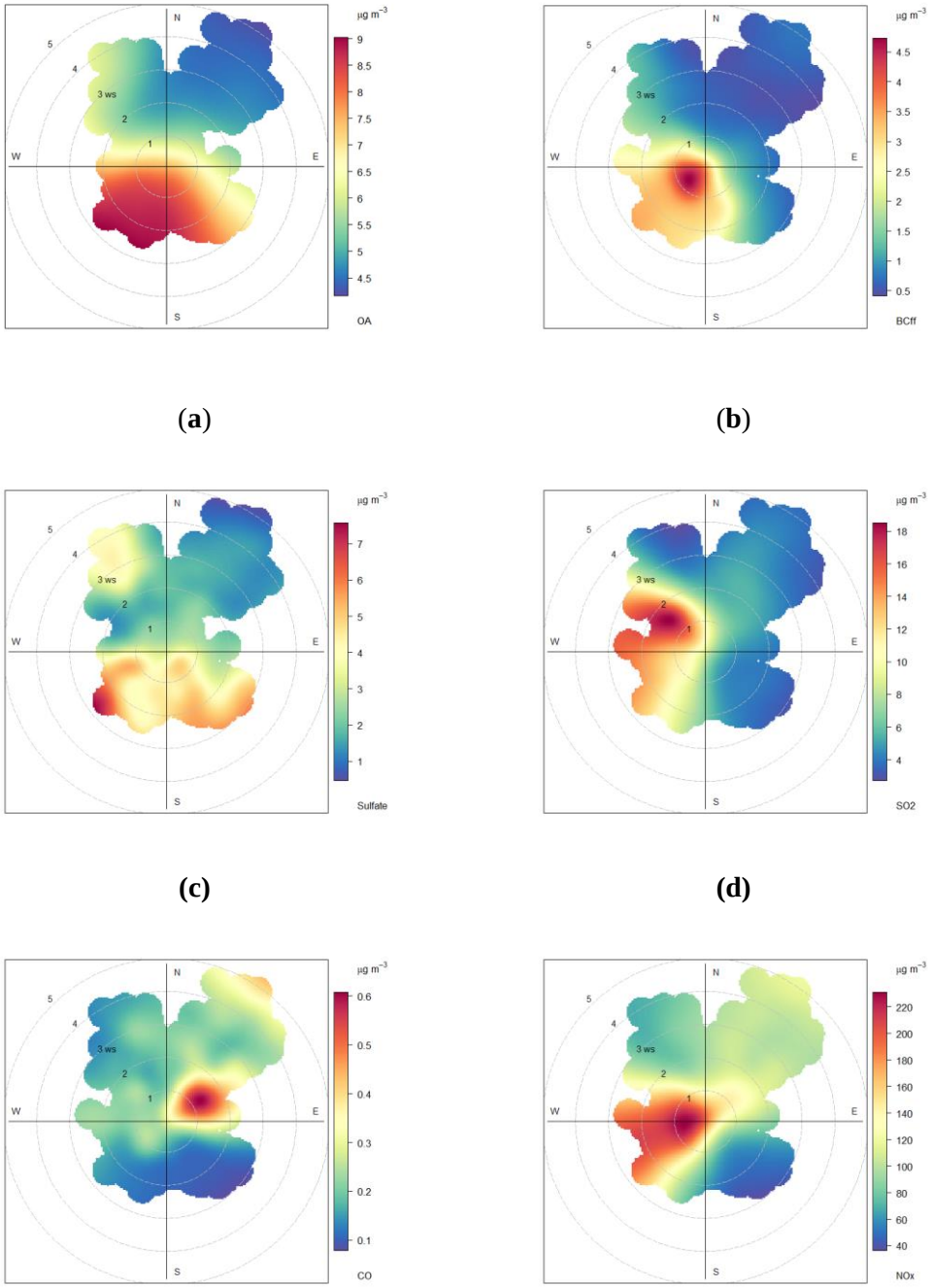

(a) **(b)**

(c) **(d)**

(e) **(f)**

Figure 11.13. Bivariate polar wind plots for the effects of wind direction and wind speed (radial axis in m s^{-1}) to concentrations of OA, (a), BC_{ff} (b), sulfate (c) as measured at P1 and SO_2 (d), CO (e), NO_x (f) as measured at PEI-1, during the summer period.

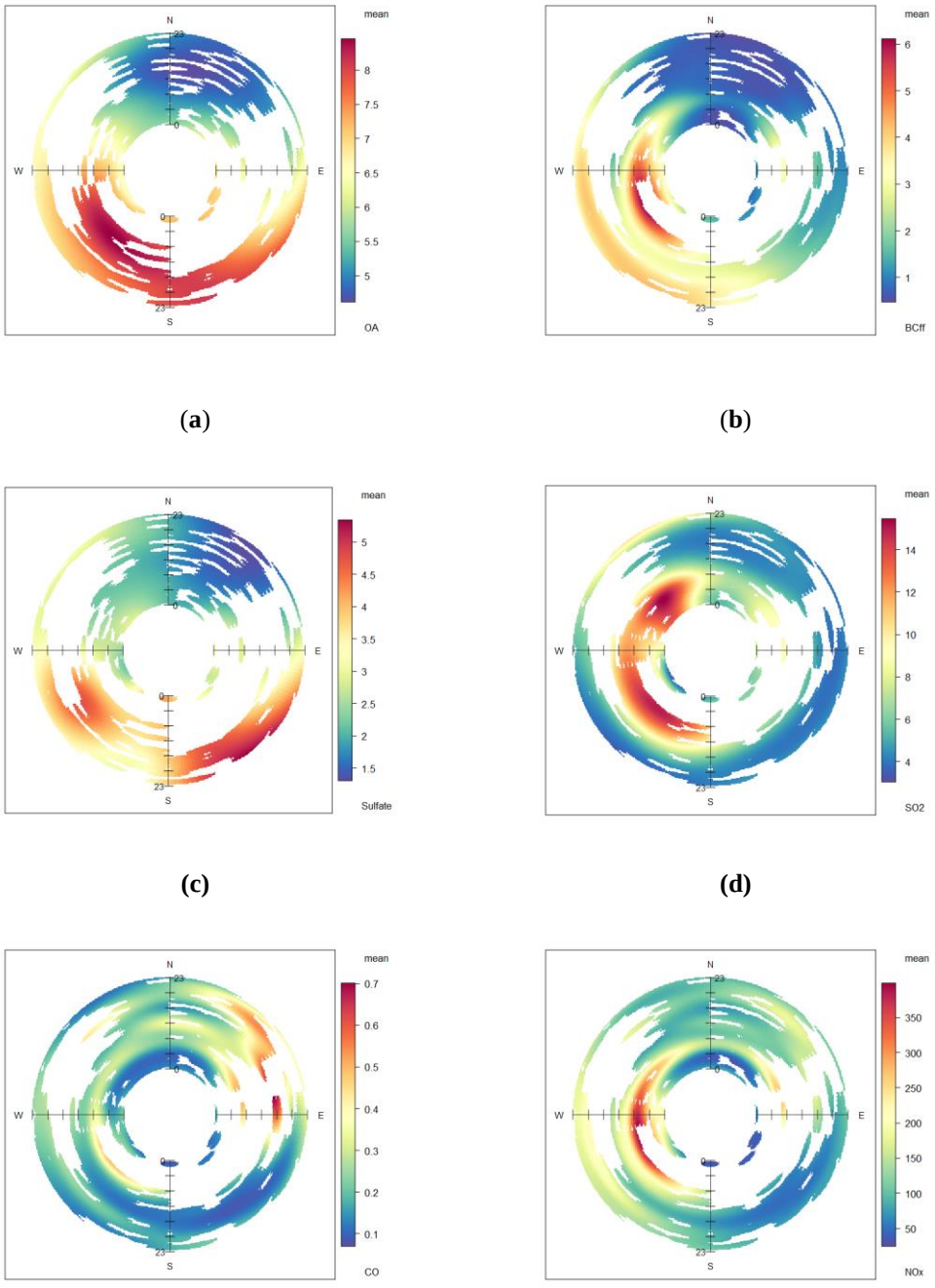

(**a**) (**b**)

(**c**) (**d**)

(**e**) (**f**)

Figure 11.14. Annular wind plots for the effects of wind direction per hour of the day (radial axis, increments by 4 hr) to concentrations of OA, (a), BC_{ff} (b), sulfate (c) as measured at P1 and SO_2 (d), CO (e), NO_x (f) as measured at PEI-1, during the summer period.

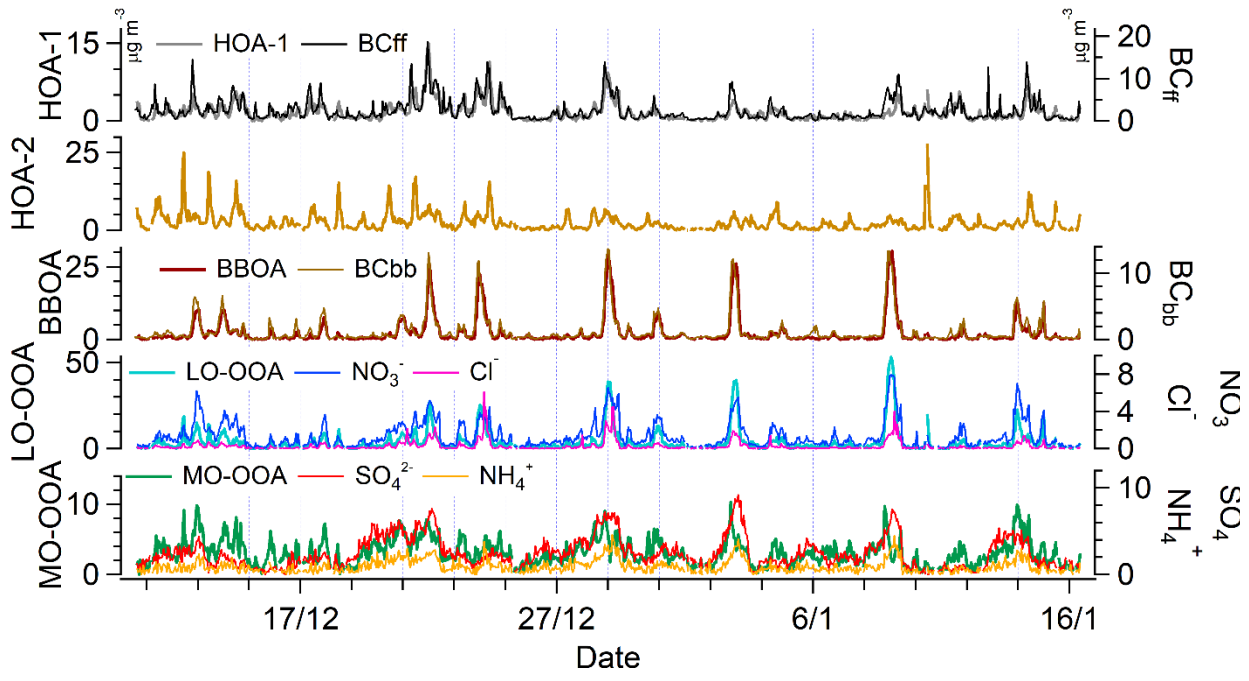

(**a**)

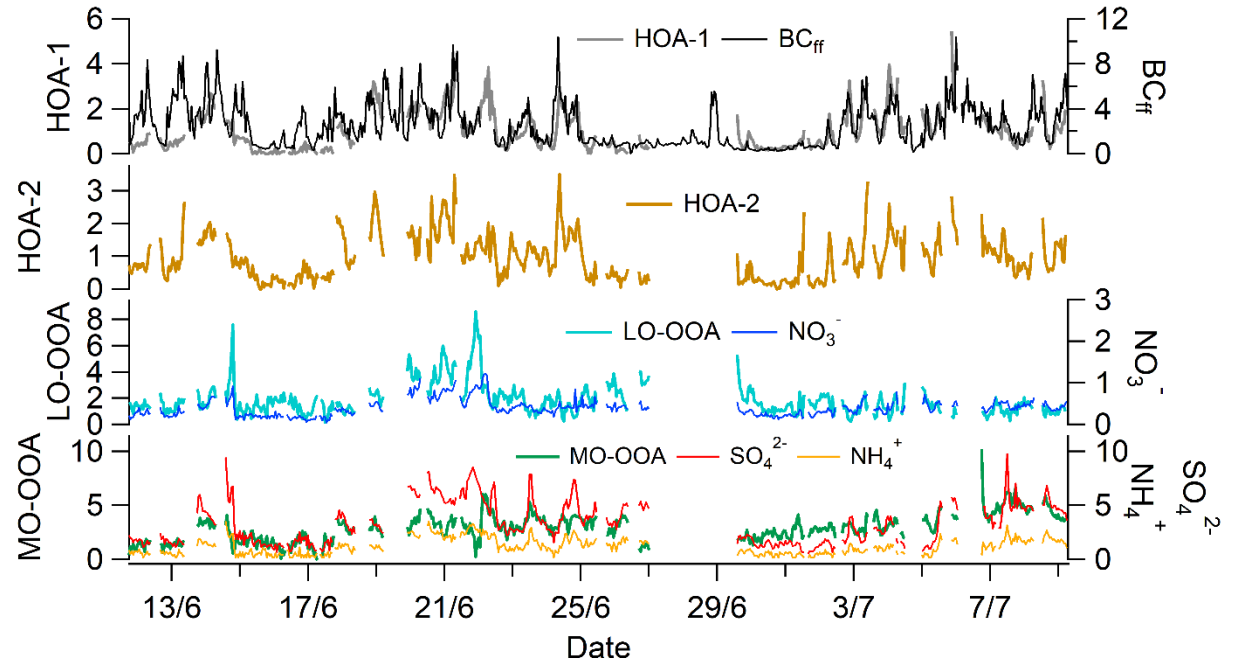

(b)

Figure 11.15. Time series of the PMF factors, along with key ACSM and aethalometer measurements for winter (a) and summer (b) campaigns.

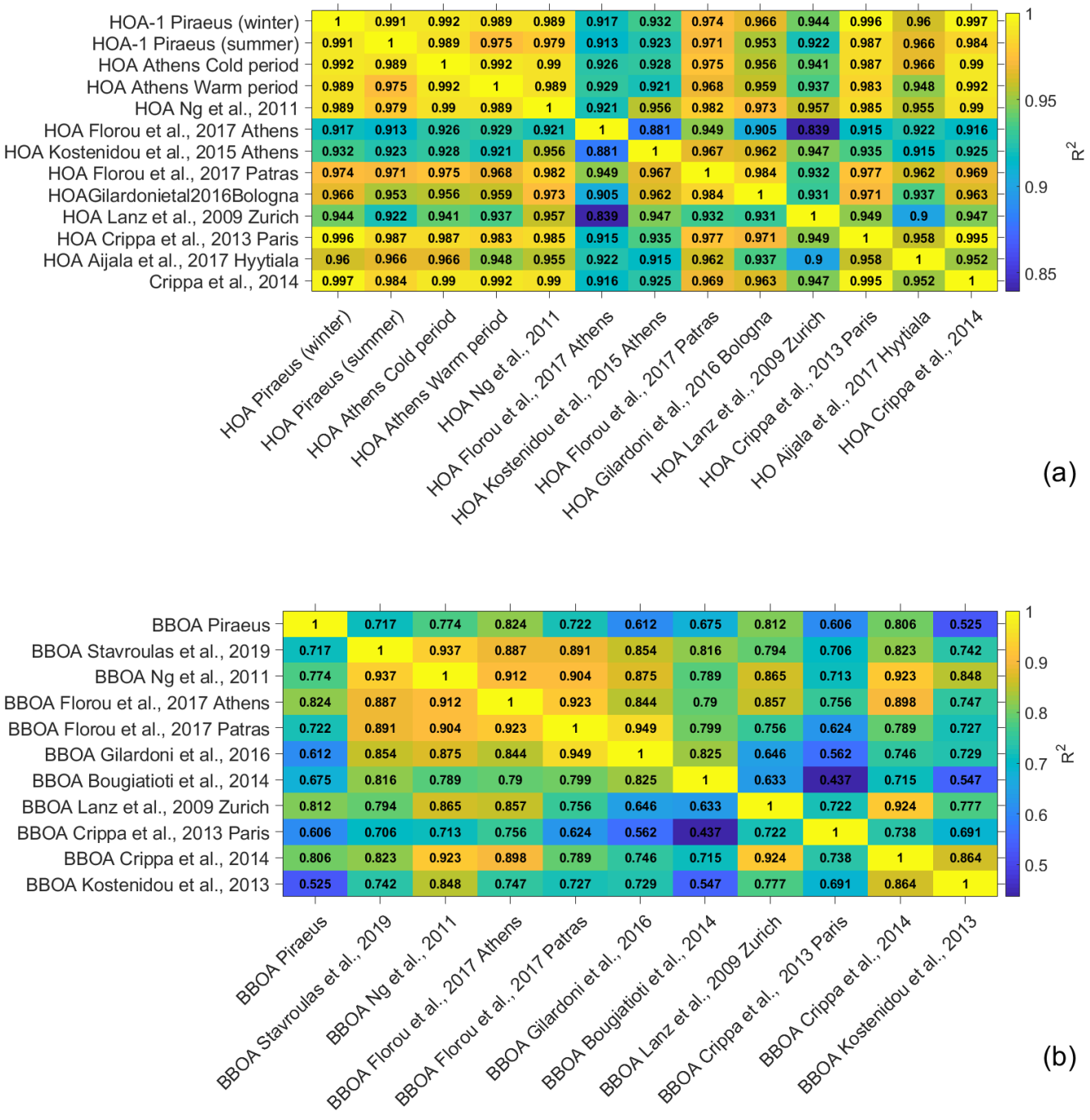

Figure 11.16. Correlation plots for the two primary factor mass spectra obtained at Piraeus vs. a selection of published mass spectra in Greece and elsewhere (Äijälä et al., 2017; Bougiatioti et al., 2014; Florou et al., 2017; Gilardoni et al., 2016; Kostenidou et al., 2013; Ng et al., 2011a; Stavroulas et al., 2019).

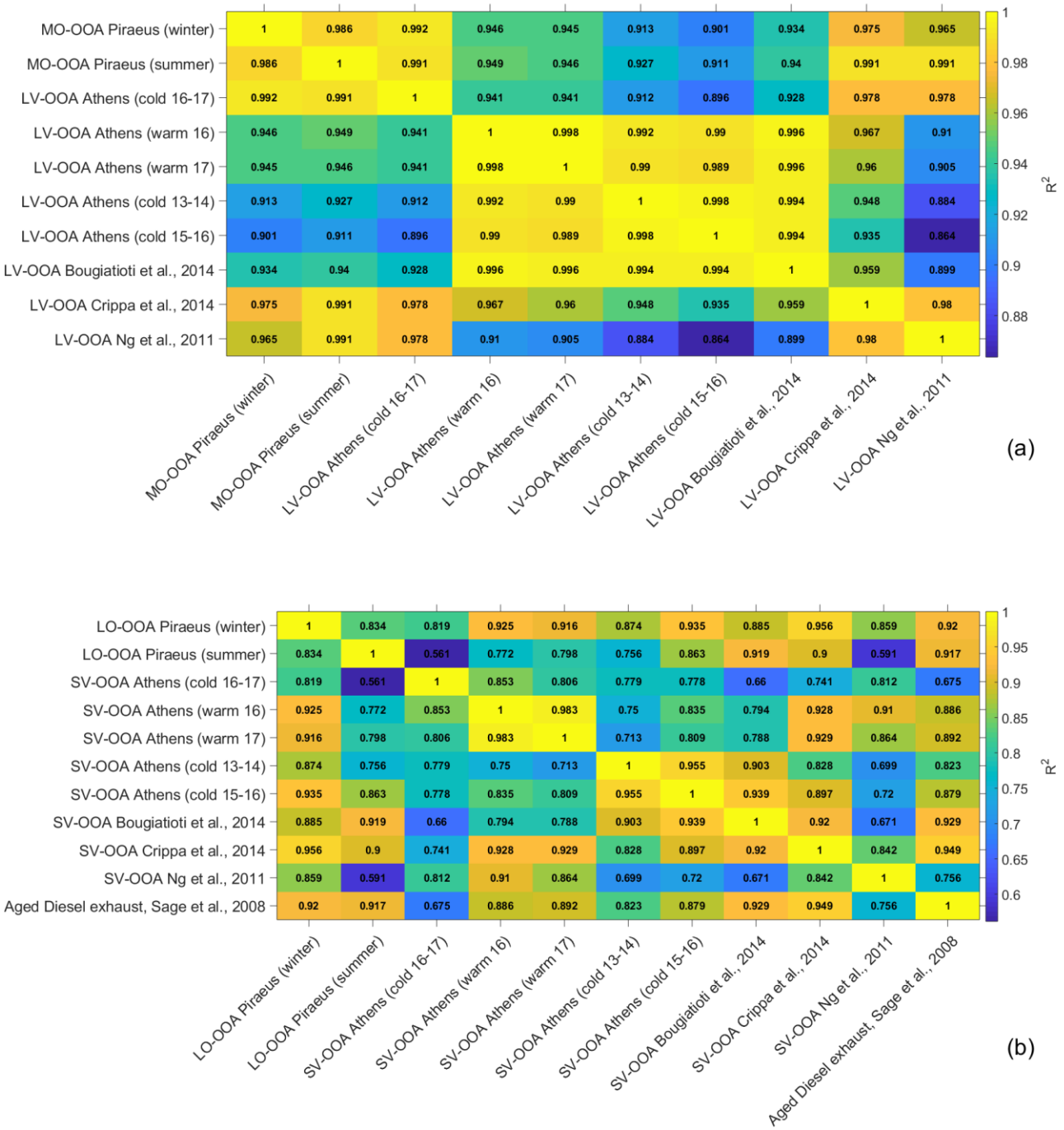

Figure 11.17. Correlation plots for the two secondary factor mass spectra obtained at Piraeus vs. a selection of published mass spectra in Greece and elsewhere (Äijälä et al., 2017; Bougiatioti et al., 2014; Florou et al., 2017; Gilardoni et al., 2016; Kostenidou et al., 2013; Ng et al., 2011a; Sage et al., 2008; Stavroulas et al., 2019).

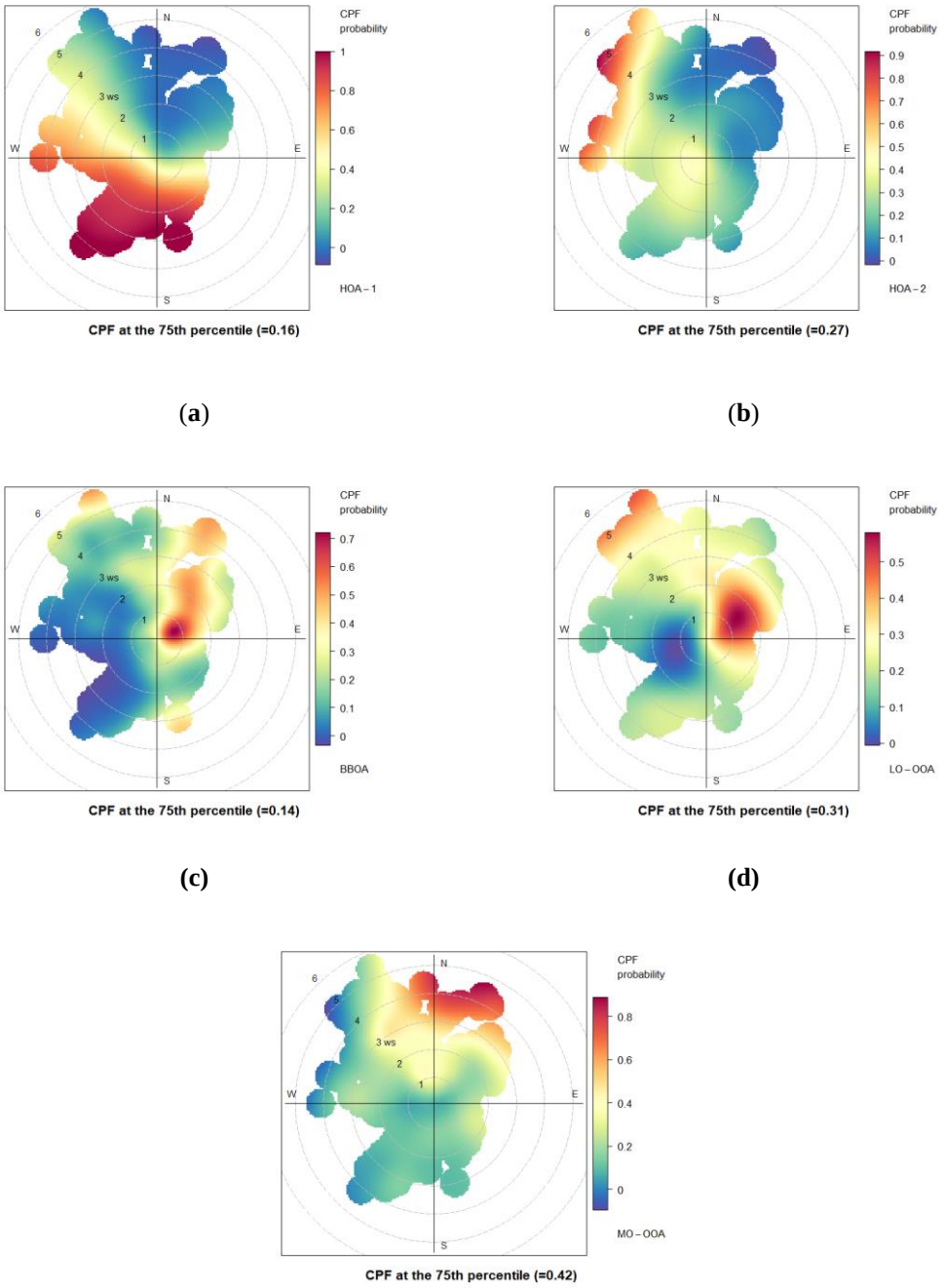

Figure 11.18. Bivariate polar plots for conditional probabilities of threshold exceedance (75th percentile), for fractional contributions of OA component in Piraeus, during the winter period.

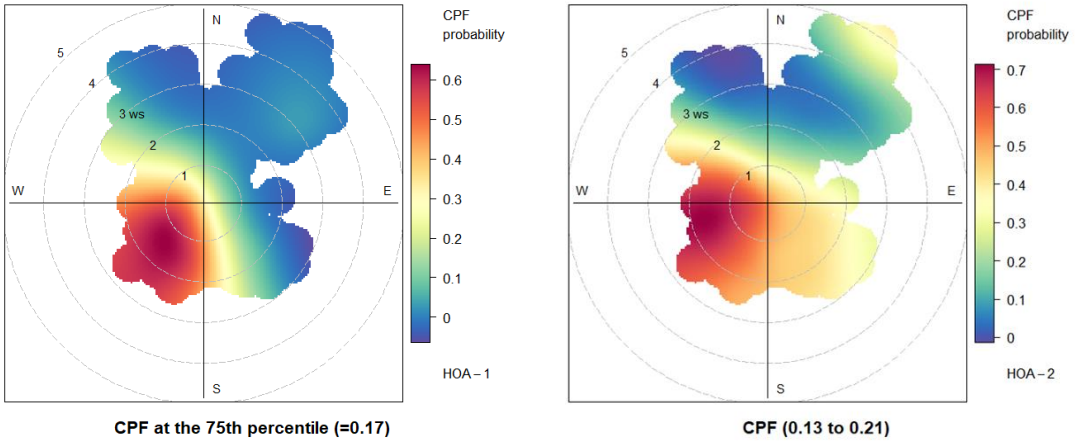

(**a**) (**b**)

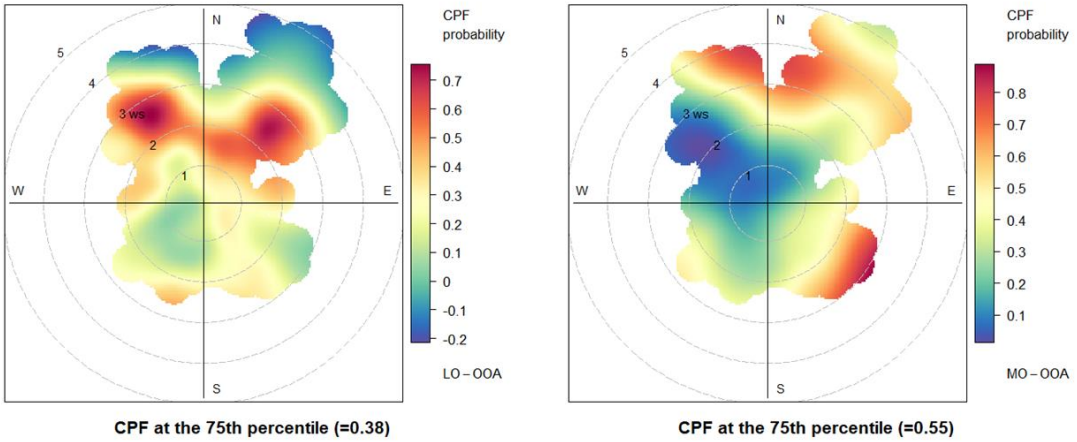

(c) **(d)**

Figure 11.19. Bivariate polar plots for conditional probabilities of threshold exceedance (75th percentile), for fractional contributions of OA component in Piraeus, during the summer period. Displaying the 50th – 95th percentile range for HOA-2

Table 11.2. Abbreviation Table

Abbreviation	Meaning
AAE	Absorption Ångström Exponent
ACSM	Aerosol Chemical Speciation Monitor
BB	Biomass Burning
BBOA	Biomass Burning Organic Aerosol
BC	Black Carbon
BC_{bb}	Biomass Burning BC
BC_{ff}	Fossil Fuel Combustion BC
COA	Cooking Organic Aerosol
CPF	Conditional Probability Function
EC	Elemental Carbon
FP	Factor Profile
GAA	Greater Area of Athens
HDV	Heavy-Duty Vehicles
HOA	Hydrocarbon-like Organic Aerosol
LO-OOA	Less Oxidized Oxygenated Organic Aerosol
LV-OOA	Low-Volatility Oxygenated organic Aerosol
MAAP	Multi-Angle Absorption Photometer
MO-OOA	More Oxidized Oxygenated Organic Aerosol
OA	Organic Aerosol
OC	Organic Carbon
PMF	Positive Matrix Factorization

POA	Primary Organic Aerosol
PSCF	Potential Source Contribution Function
RWB	Residential Wood Burning
SOA	Secondary Organic Aerosol
SV-OOA	Semi-Volatile Oxygenated Organic Aerosol
WHO	World Health Organization
ΔBC_u	"Urban" Enhancement of BC ($BC_{660nm,P1} - BC_{637nm,P2}$)

12 Appendix D. Supplement to the manuscript: *Field Evaluation of Low-Cost PM Sensors (Purple Air PA-II) Under Variable Urban Air Quality Conditions, in Greece.*

12.1 Equations for performance assessment metrics and coefficient of divergence

$$RMSE\ (Root\ Mean\ Square\ Error) = \sqrt{\frac{\sum_{i=1}^{n}(y_i - \hat{y})^2}{n}}$$

where y_i is the ith reference observation and $\hat{y}$ is the predicted value produced by the model

$$nRMSE = \frac{RMSE}{\bar{y}}$$

where $\bar{y}$ is the mean value of reference observations for the given dataset

$$MAE\ (Mean\ Absolute\ Error) = \frac{\sum_{i=1}^{n}|x_i - y_i|}{n}$$

where x_i is the ith PA-II measured or modeled value and y_i the corresponding reference measurement

$$MBE\ (Mean\ Bias\ Error) = \frac{\sum_{i=1}^{n}(x_i - y_i)}{n}$$

where x_i is the ith PA-II or modeled value and y_i the corresponding reference measurement

$$CoD\ (Coefficient\ of\ Divergence = \sqrt{\frac{1}{n}\sum_{i=1}^{n}\left[\frac{(x_{ij}-x_{ik})}{(x_{ij}+x_{ik})}\right]^2}$$

where x_{ij} and x_{ik} are concentrations at sites j and k respectively at time i and n is the total number of measurements.

12.2 Field Intercomparison Campaigns

Table 12.1: Duration, reference site and number of participating PA-II devices at each intercomparison campaign held in Athens and Ioannina

	Campaign Start	Campaign End	Reference Site	PA-II devices	PA-II data completeness
1st Athens Campaign	08/Mar/2019	02/Apr/2019	Thissio (THI)	8	>99%
2nd Athens Campaign	03/Jul/2019	03/Sep/2019	Thissio (THI)	5	>99%
3rd Athens Campaign	26/Feb/2020	18/May/2020	Thissio (THI)	1	>99%
Ioannina Campaign	15/Dec/2019	31/May/2020	Vilara (VIL)	1	>99%

12.3 Description of the PA-II network in Athens and Ioannina

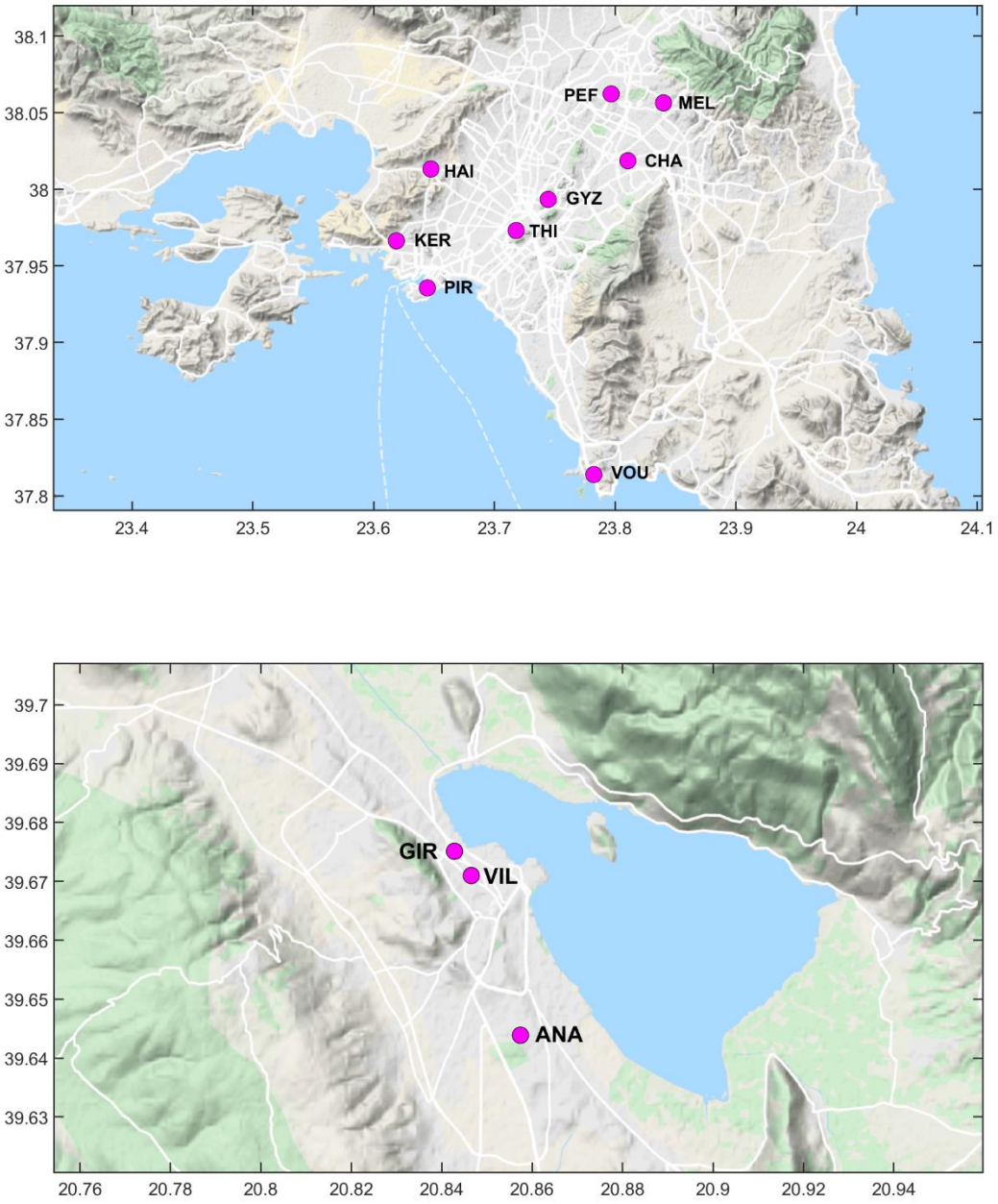

Figure 12.1: Maps of the PA-II network in Athens and Ioannina, displaying monitoring sites.

Table 12.2: Characteristics of the measurement locations in Athens and Ioannina during the two examined periods

Site Name	Abbreviation	Device	Start Date	End date	Site Type *	Data completeness
Athens						
Thissio	THI	PA-000	01 Aug 19	31 Aug 19	UB	>99%
Gyzi	GYZ	PA-001	01 Aug 19	31 Aug 19	UB	>99%
Pefki	PEF	PA-002	01 Aug 19	31 Aug 19	SB	>99%
Piraeus	PIR	PA-003	01 Aug 19	31 Aug 19	UB	>99%
Melissia	MEL	PA-004	01 Aug 19	31 Aug 19	SB	>99%
Chalandri	CHA	PA-005	01 Aug 19	31 Aug 19	SB	>99%
Vouliagmeni	VOU	PA-006	01 Aug 19	31 Aug 19	SB	>99%
Keratsini	KER	PA-007	01 Aug 19	31 Aug 19	UB	>99%
Haidari	HAI	PA-014	01 Aug 19	31 Aug 19	SB	>99%
Ioannina						
Anatoli	ANA	PA-013	15 Dec 19	15 Jan 20	SB	>99%
Girokomio	GIR	PA-016	15 Dec 19	15 Jan 20	UB	>99%
Vilara	VIL	PA-015	15 Dec 19	15 Jan 20	UB	>99%

* UB: Urban Background, SB: Suburban Background

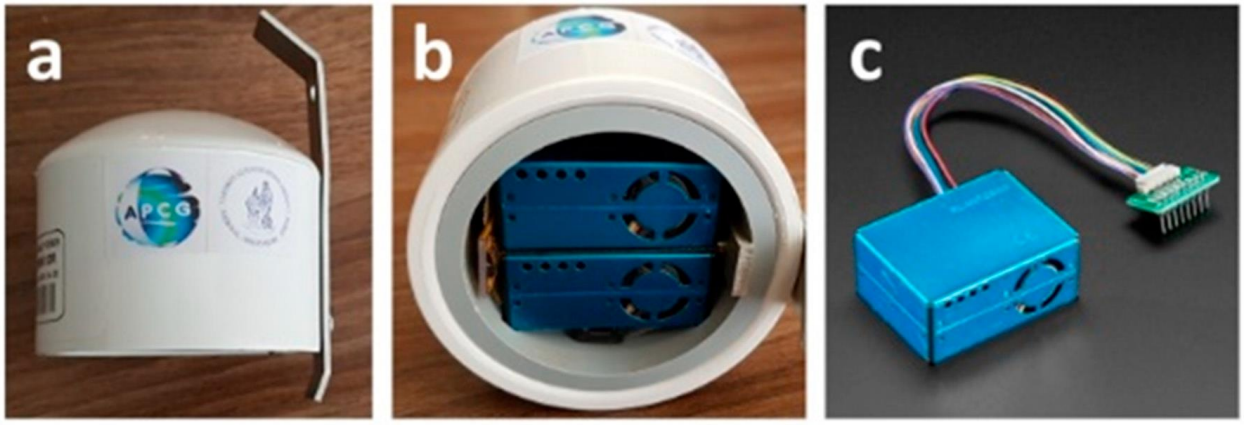

Figure 12.2. External view of the Purple Air PA-II air monitor (a); upward view with the two Plantower PMS5003 sensors showing (b); the PMS5003 sensor with a breadboard adapter (c).

12.4 Repeatability of PA-II $PM_{2.5(CF=1)}$, Temperature and Relative Humidity measurements

12.4.1 $PM_{2.5(CF=1)}$

Table 12.3: Pairwise correlations $PM_{2.5(CF=1)}$ measurements from the eight PA-II devices deployed at Thissio during the 1st intercomparison campaign in Athens

R^2	PA_000	PA_001	PA_002	PA_003	PA_004	PA_005	PA_007	PA_008
PA_000	1.000							
PA_001	0.996	1.000						
PA_002	0.998	0.996	1.000					
PA_003	0.995	0.997	0.995	1.000				
PA_004	0.999	0.996	0.998	0.995	1.000			
PA_005	0.998	0.995	0.997	0.994	0.998	1.000		
PA_007	0.999	0.998	0.998	0.997	0.998	0.997	1.000	
PA_008	0.996	0.994	0.997	0.993	0.998	0.997	0.997	1.000

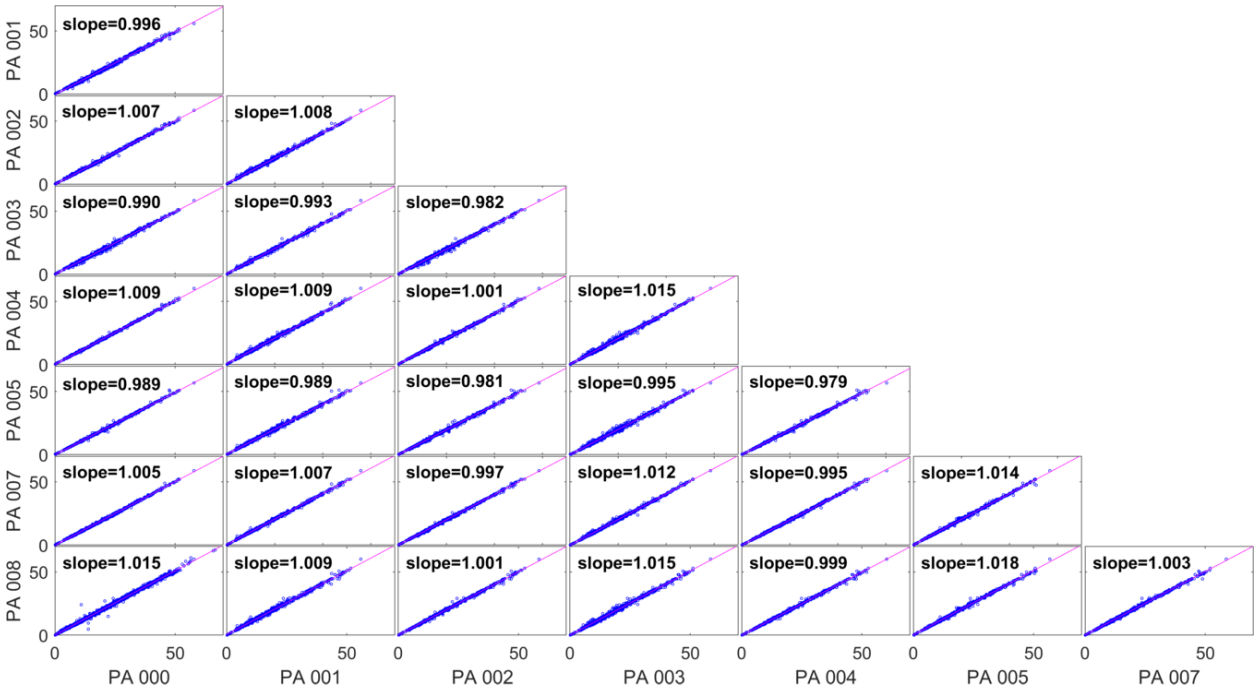

Figure 12.2: Scatterplots for pairwise comparisons of the eight collocated devices operating at Thissio, Athens, for a one-month period during the 1st intercomparison campaign. Displaying slopes for the ordinary least-squares fit.

12.4.2 Temperature

Table 12.4: Pairwise correlations of temperature measurements from the eight PA-II devices deployed at Thissio during the 1st intercomparison campaign in Athens

R^2	PA_000	PA_001	PA_002	PA_003	PA_004	PA_005	PA_007	PA_008
PA_000	1.000							
PA_001	0.987	1.000						
PA_002	0.980	0.979	1.000					
PA_003	0.984	0.990	0.989	1.000				
PA_004	0.996	0.992	0.982	0.987	1.000			
PA_005	0.997	0.980	0.982	0.980	0.992	1.000		
PA_007	0.983	0.983	0.994	0.989	0.990	0.985	1.000	
PA_008	0.989	0.983	0.995	0.989	0.988	0.990	0.992	1.000

Table 12.5: Linear regression slopes for pairwise comparisons of temperature measurements between eight devices deployed at Thissio during the 1st intercomparison campaign in Athens

Slope	PA_000	PA_001	PA_002	PA_003	PA_004	PA_005	PA_007	PA_008
PA_000	1.000							
PA_001	1.095	1.000						
PA_002	0.913	0.828	1.000					
PA_003	1.021	0.930	1.110	1.000				
PA_004	0.980	0.887	1.055	0.948	1.000			
PA_005	0.948	0.853	1.020	0.913	0.963	1.000		
PA_007	0.911	0.825	0.994	0.887	0.930	0.960	1.000	
PA_008	0.955	0.823	0.989	0.883	0.926	0.959	0.991	1.000

12.4.3 Relative Humidity

Table 12.6: Pairwise correlations of RH measurements from the eight PA-II devices deployed at Thissio during the 1st intercomparison campaign in Athens

R^2	PA_000	PA_001	PA_002	PA_003	PA_004	PA_005	PA_007	PA_008
PA_000	1.000							
PA_001	0.996	1.000						
PA_002	0.998	0.996	1.000					
PA_003	0.995	0.997	0.995	1.000				
PA_004	0.999	0.996	0.998	0.995	1.000			
PA_005	0.998	0.995	0.997	0.994	0.998	1.000		
PA_007	0.999	0.998	0.998	0.997	0.998	0.997	1.000	
PA_008	0.996	0.994	0.997	0.993	0.998	0.997	0.997	1.000

Table 12.7: Linear regression slopes for pairwise comparisons of RH measurements between eight devices deployed at Thissio during the 1st intercomparison campaign in Athens

Slope	PA_000	PA_001	PA_002	PA_003	PA_004	PA_005	PA_007	PA_008
PA_000	1.000							
PA_001	1.074	1.000						
PA_002	1.009	0.931	1.000					
PA_003	1.021	0.948	1.008	1.000				
PA_004	1.021	0.942	1.005	0.991	1.000			
PA_005	1.030	0.946	1.013	0.997	1.006	1.000		
PA_007	0.976	0.899	0.966	0.949	0.956	0.947	1.000	
PA_008	1.011	0.922	0.990	0.972	0.979	0.972	1.023	1.000

12.4.4 Temperature and Relative humidity sensor calibration

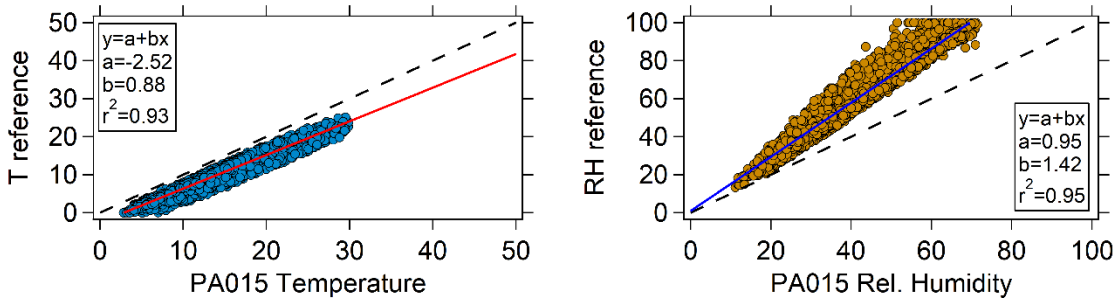

Figure 12.3: Linear regression of reference T (left) and RH (right) versus T and RH measured by the BME80 sensor of the PA-II device.

12.5 PA-II $PM_{2.5(CF=1)}$ measurement error

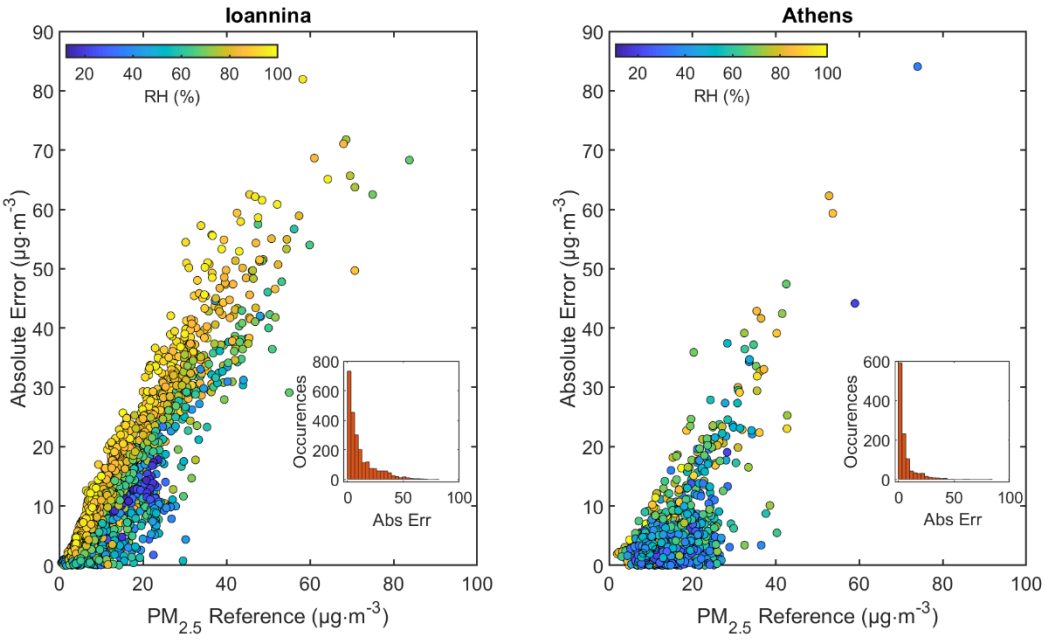

Figure 12.4: Scatterplots of the PA-ii $PM_{2.5(CF=1)}$ absolute error versus reference $PM_{2.5}$ measurements in Ioannina (left) and Athens (right). Plots are color-coded according to ambient relative humidity.

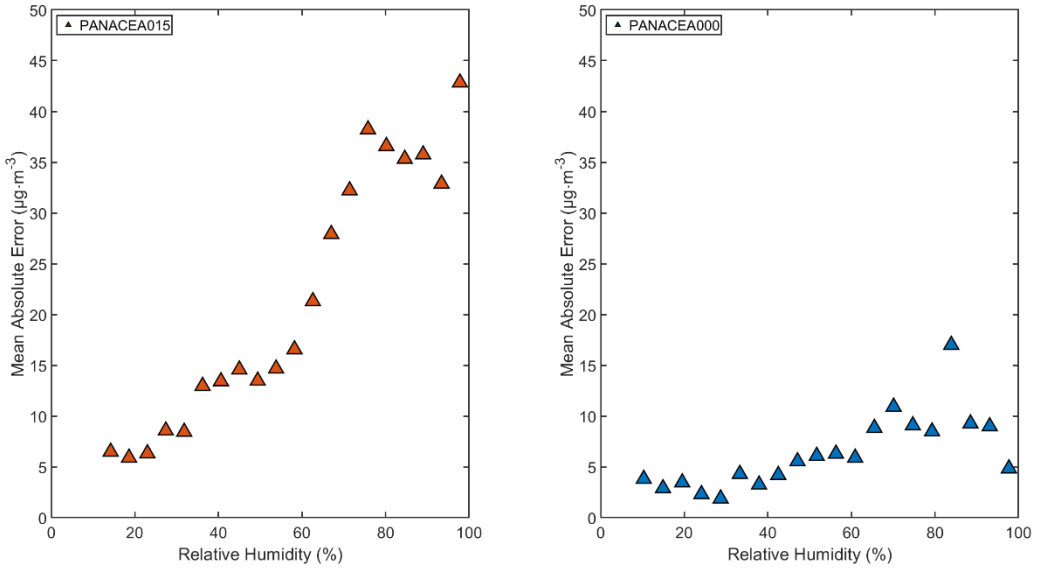

Figure 12.5: PA-II $PM_{2.5(CF=1)}$ MAE as a function of binned RH measurements at Thissio (left) and Ioannina (right).

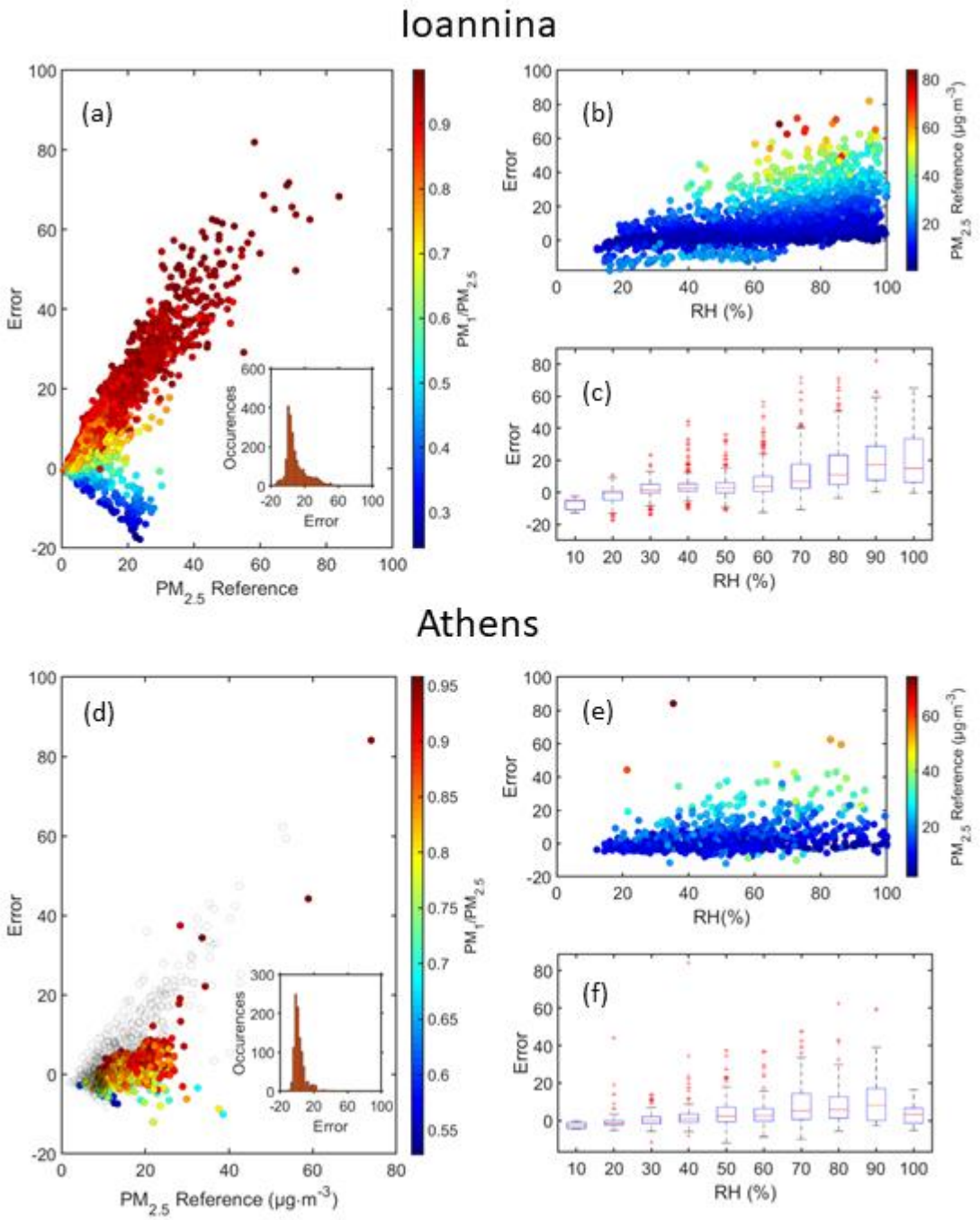

Figure 12.6: Bias error examination for Ioannina (a, b, c) and Athens (d, e, f). The bias error ($PM_{2.5(CF=1)}$ - Ref) versus reference $PM_{2.5}$ are depicted in (a) and (d) color-coded by the $PM_1/PM_{2.5}$ ratio. The bias error versus RH, color-coded by the reference $PM_{2.5}$ can be seen in (b) and (e), while boxplots of mean bias error for 10% RH increments are depicted in (c) and (f)

12.6 Coarse mode affected data according to the $PM_{2.5}/PM_{10}$ ratio

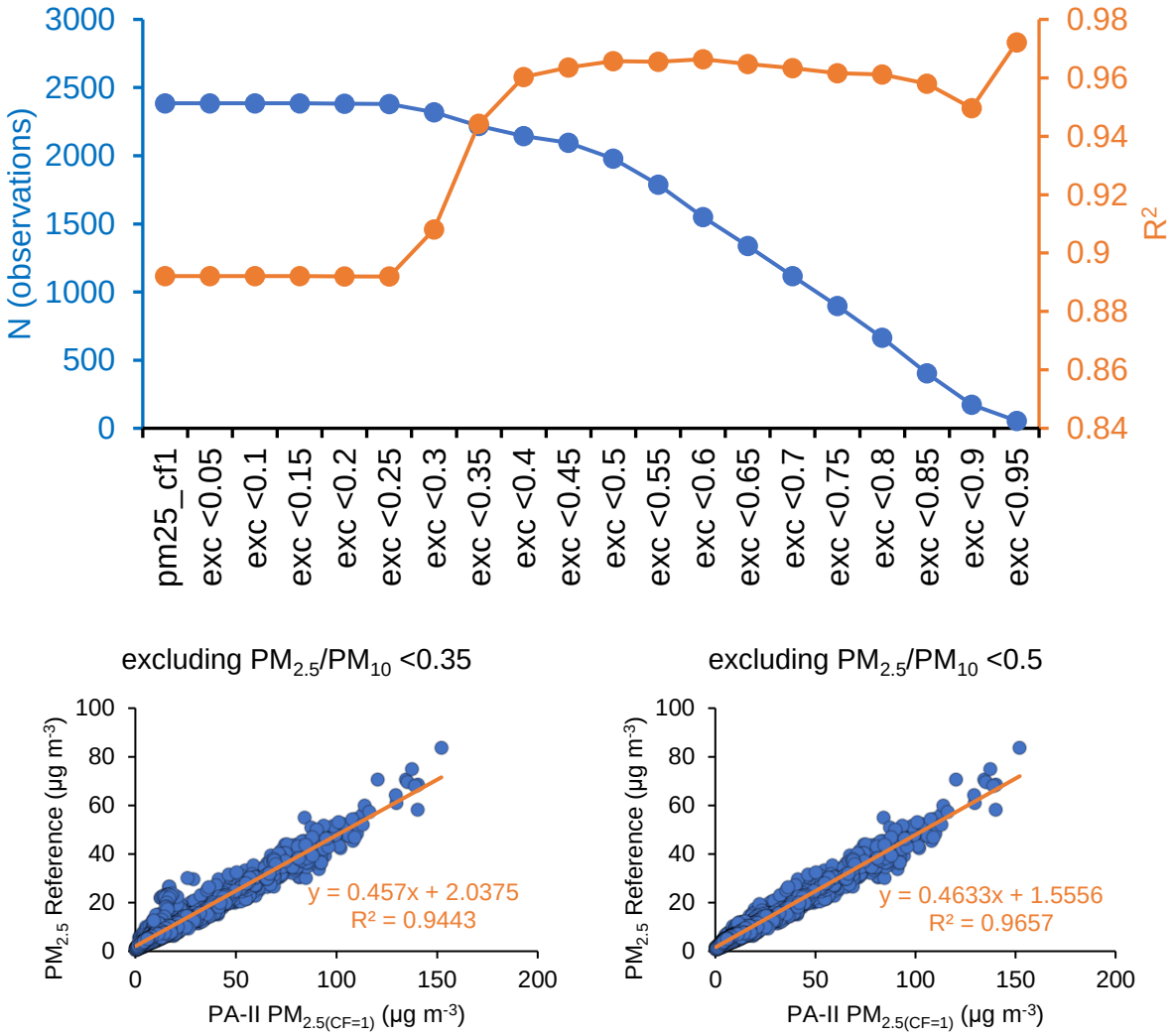

Figure 12.7: In order to determine and fine-tune a threshold, useful in excluding data affected by the presence of coarse mode particles, we use the $PM_{2.5}/PM_{10}$ ratio, given that these two fractions are more frequently part of routine measurements at regulatory AQS. We analyze the springtime Ioannina dataset for calculations. Initially all data points are used to perform linear regression to reference measurements, followed by the gradual exclusion of data points with ratios lower than 0.05. Each time, this number is increased by 0.05 and linear regression is performed with the remaining data. The top panel illustrates the linear regression R^2, as well as the number of remaining data-points, as a function of the data exclusion $PM_{2.5}/PM_{10}$ threshold. Finally, a $PM_{2.5}/PM_{10}$ ratio of 0.5 is selected as the exclusion threshold, as a trade-off between high R^2 without excluding much of the initial dataset.

12.7 Base and Evaluation Data split

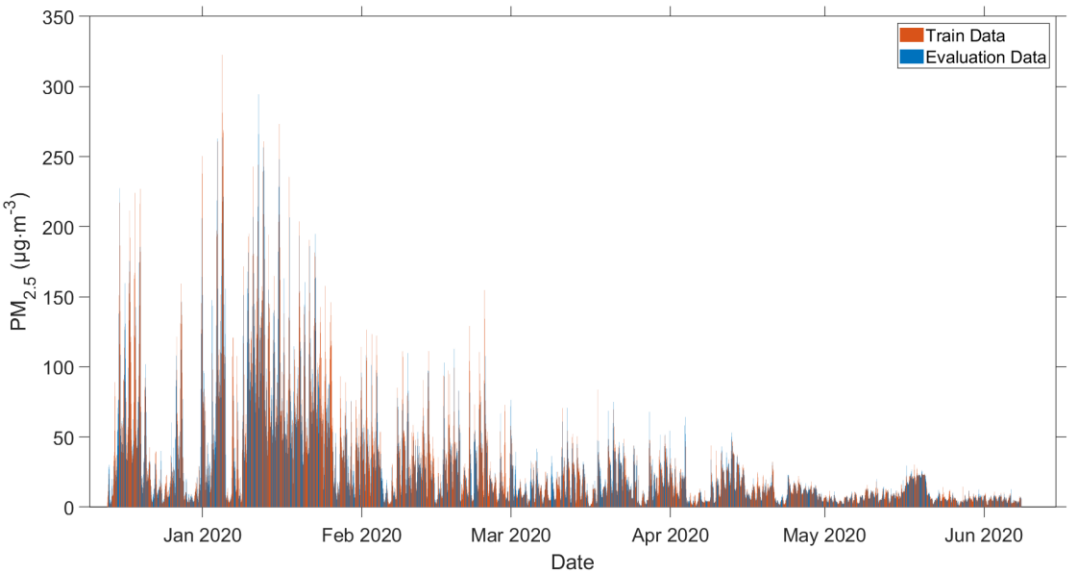

Figure 12.8: Bar plot of the ambient $PM_{2.5}$ time-series recorded in Ioannina. Orange bars represent data selected for the base dataset while blue represent evaluation data.

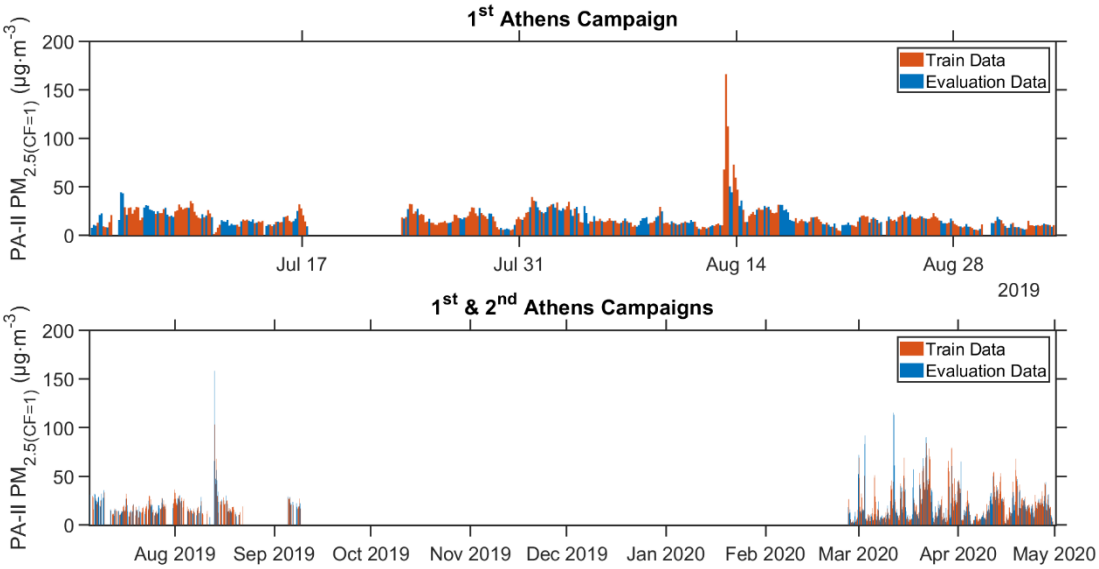

Figure 12.9: Bar plots of the PA-II $PM_{2.5(CF=1)}$ time-series recorded in Athens during the 1st and 2nd intercomparison campaigns. Orange bars represent data selected for the base dataset while blue represent evaluation data.

12.8 Calibration Models for the Ioannina dataset

Table 12.8: Configuration of the PA-II $PM_{2.5\ (CF=1)}$ correction models tested for the Ioannina dataset. The numbers represent the polynomial degree assigned to the corresponding predictor.

Ioannina	iModel 1	iModel 2	iModel 3	iModel 4	iModel 5	iModel 6	iModel 7	iModel 8	iModel 9	iModel 10
$PM_{2.5(CF=1)}$	1	2	1	2	1	2	1	2	1	2
$PM_1/PM_{2.5}$	-	-	1	1	-	-	1	1	-	-
$PM_{2.5}/PM_{10}$	-	-	-	-	1	1	-	-	1	1
RH	-	-	-	-	-	-	1	1	1	1

- **iModel 1:** $PM_{2.5cor} = 0.550 \times PM_{2.5(CF=1)} - 0.244$
- **iModel 2:** $PM_{2.5cor} = 0.000387 \times PM_{2.5(CF=1)}{}^2 + 0.443 \times PM_{2.5(CF=1)} + 2.60$
- **iModel 3:** $PM_{2.5cor} = 22.2 + 0.570 \times PM_{2.5(CF=1)} - 27.1 \times \frac{PM_1}{PM_{2.5}}$
- **iModel 4:** $PM_{2.5cor} = 11.7 + 1.13 \times PM_{2.5(CF=1)} - 12.8 \times \frac{PM_1}{PM_{2.5}} + 0.000348 \times PM_{2.5(CF=1)}{}^2 - 0.683 \times PM_{2.5(CF=1)} \times \frac{PM_1}{PM_{2.5}}$
- **iModel 5:** $PM_{2.5cor} = 14.5 + 0.579 \times PM_{2.5(CF=1)} - 21.9 \times \frac{PM_{2.5}}{PM_{10}}$
- **iModel 6:** $PM_{2.5cor} = 8.49 + 0.7301 \times PM_{2.5(CF=1)} - 10.8 \times \frac{PM_{2.5}}{PM_{10}} + 0.000334 \times PM_{2.5(CF=1)}{}^2 - 0.276 \times PM_{2.5(CF=1)} \times \frac{PM_{2.5}}{PM_{10}}$
- **iModel 7:** $PM_{2.5cor} = 25.9 + 0.578 \times PM_{2.5(CF=1)} - 0.09245 \times RH - 24.6 \times \frac{PM_1}{PM_{2.5}}$
- **iModel 8:** $PM_{2.5cor} = -10.0 \times \frac{PM_1}{PM_{2.5}} - 0.0386 \times RH + 0.00466 \times RH \times \frac{PM_1}{PM_{2.5}} + 1.483 \times PM_{2.5(CF=1)} - 0.940 \times PM_{2.5(CF=1)} \times \frac{PM_1}{PM_{2.5}} - 0.00131 \times PM_{2.5(CF=1)} \times RH + 10.9 + 0.000339 \times PM_{2.5(CF=1)}{}^2$
- **iModel 9:** $PM_{2.5cor} = 16.8 + 0.581 \times PM_{2.5(CF=1)} - 0.0720 \times RH - 18.5 \times \frac{PM_{2.5}}{PM_{10}}$

- **iModel 10:** $PM_{2.5cor} = -9.055 \times \frac{PM_{2.5}}{PM_{10}} + 0.00267 \times RH - 0.02528 \times RH \times \frac{PM_{2.5}}{PM_{10}} + 0.745 \times PM_{2.5(CF=1)} - 0.203 \times PM_{2.5(CF=1)} \times \frac{PM_{2.5}}{PM_{10}} - 0.000961 \times PM_{2.5(CF=1)} \times RH + 8.34 + 0.000310 \times PM_{2.5(CF=1)}{}^{2}$

Table 12.9: Goodness-of-fit metrics for all tested models in the base dataset for the Ioannina intercomparison campaign.

Ioannina	iModel 1	iModel 2	iModel 3	iModel 4	iModel 5	iModel 6	iModel 7	iModel 8	iModel 9	iModel 10
R^2	0.976	0.983	0.983	0.987	0.982	0.986	0.985	0.991	0.984	0.988
nRMSE	0.198	0.166	0.169	0.144	0.170	0.153	0.154	0.118	0.161	0.139
MAE ($\mu g\ m^{-3}$)	3.8	3.1	3.5	2.8	3.6	3.0	3.0	2.3	3.4	2.8

12.9 Dust events identified at Ioannina and model response

12.9.1 PSCF analysis

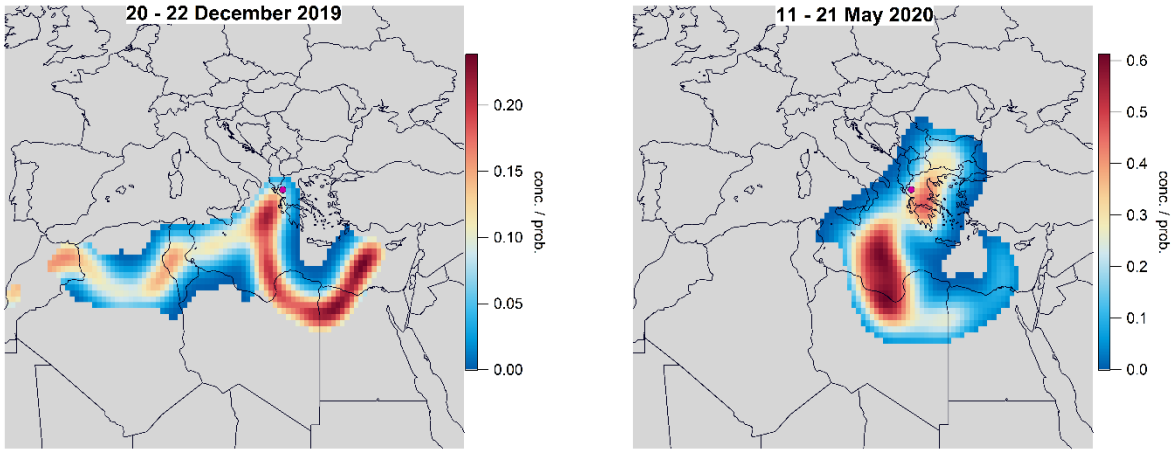

Figure 12.10: PSCF analysis (75th percentile of concentrations) performed using 120-hour back trajectories arriving at a height of 1000 m every 6 hours and $PM_{10-2.5}$ reference concentrations during December 20-22 2019 (left) and May 11-21 2020 (right).

12.9.2 December 20-22 2019 dust-transport event

Table 12.10: Model performance metrics along with basic $PM_{2.5cor}$ statistics (model corrected concentrations) for the December dust event.

	R^2	Slope	Intercept	Mean	St Dev	MAE
iModel1	0.774	1.424	6.057	22.2	15.3	15.8
iModel2	0.772	1.597	3.206	21.6	13.6	16.2
iModel3	0.904	1.542	-7.361	29.3	15.2	8.8
iModel4	0.940	1.188	-2.026	33.5	20.2	5.3
iModel5	0.875	1.451	-0.520	26.4	16.0	11.5
iModel6	0.877	1.347	1.200	27.1	17.2	10.9
iModel7	0.905	1.541	-2.846	26.4	15.3	11.4
iModel8	0.954	1.094	0.507	34.0	22.1	4.7
iModel9	0.869	1.454	2.817	24.0	15.9	13.3
iModel10	0.876	1.448	0.960	25.4	16.0	12.4

12.9.3 May 11-21 2020 dust-transport event

12.10 Calibration Models for the Athens dataset

Table 12.12: Configuration of the PA-II $PM_{2.5\ (CF=1)}$ correction models tested for the Athens dataset. The numbers represent the polynomial degree assigned to the corresponding predictor.

Athens	aModel 1*	aModel 2	aModel 3	aModel 4	aModel 5	aModel 6*
$PM_{2.5(CF=1)}$	1	1	1	1	1	1
$PM_1/PM_{2.5}$	-	1	-	1	-	-
$PM_{2.5}/PM_{10}$	-	-	1	-	1	-
RH	-	-	-	1	1	1

* Data for both intercomparison campaigns are used for aModel 1 and aModel 6

- **aModel 1:** $PM_{2.5cor} = 0.449 \times PM_{2.5(CF=1)} + 6.72$
- **aModel 2:** $PM_{2.5cor} = 22.5 + 0.491 \times PM_{2.5(CF=1)} - 17.5 \times \frac{PM_1}{PM_{2.5}}$

- **aModel 3:** $PM_{2.5cor} = 14.1 + 0.492 \times PM_{2.5(CF=1)} - 9.76 \times \frac{PM_{2.5}}{PM_{10}}$
- **aModel 4:** $PM_{2.5cor} = 20.3 + 0.485 \times PM_{2.5(CF=1)} + 0.0481 \times RH - 17.5 \times \frac{PM_1}{PM_{2.5}}$
- **aModel 5:** $PM_{2.5cor} = 11.8 + 0.487 \times PM_{2.5(CF=1)} + 0.0675 \times RH - 10.9 \times \frac{PM_{2.5}}{PM_{10}}$
- **aModel 6:** $PM_{2.5cor} = 9.32 + 0.464 \times PM_{2.5(CF=1)} - 0.0574 \times RH$

Table 12.13: Goodness of fit metrics for all tested models on the base dataset for the Athens intercomparison campaigns.

Athens	aModel 1*	aModel 2	aModel 3	aModel 4	aModel 5	aModel 6*
R^2	0.831	0.841	0.834	0.846	0.843	0.852
nRMSE	0.197	0.172	0.176	0.170	0.171	0.185
MAE ($\mu g\ m^{-3}$)	2.4	1.9	2.0	1.9	2.0	2.1

* Data for both intercomparison campaigns are used for aModel 1 and aModel 6

12.11 Temperature and Relative Humidity during the Athens intercomparison campaigns

Table 12.14: Mean and Standard Deviation of Temperature and Relative Humidity in Thissio during the Athens intercomparison campaigns

	Temperature (°=C)		Relative Humidity (%)	
	mean	stdev	Mean	Stdev
Warm	29.0	3.6	46.7	11.0
Cold	13.2	3.2	60.6	14.6
Intermediate	19.5	4.9	47.6	13.4

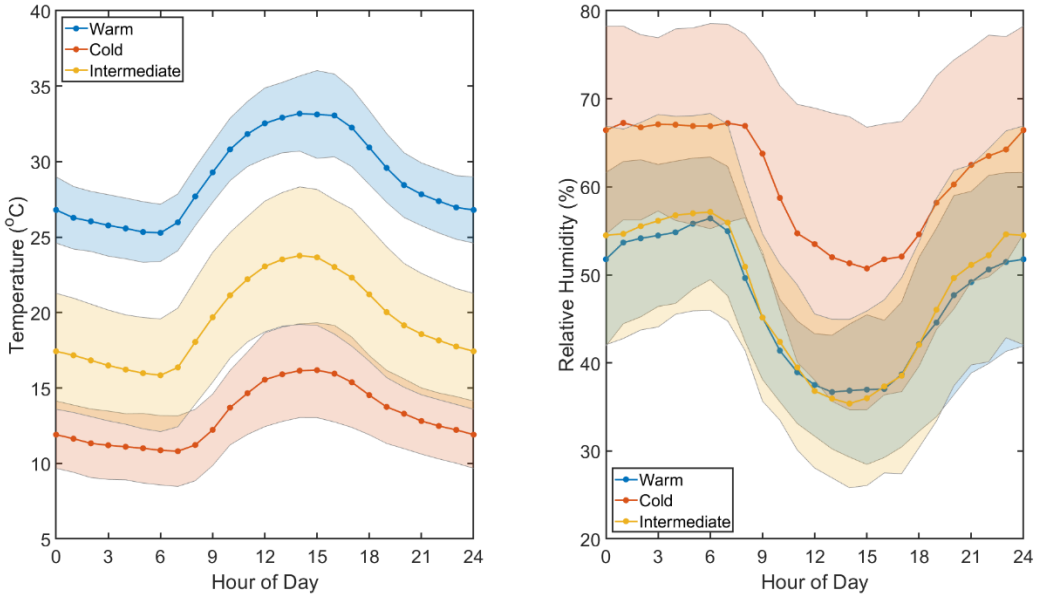

Figure 12.11: Diurnal variability of Temperature and Relative Humidity at Thissio during the Warm, Cold and Intermediated identified periods of the 2nd and 3rd Athens intercomparison campaigns.

12.12 Chemical Composition of Submicron Aerosols during the Athens intercomparison campaigns

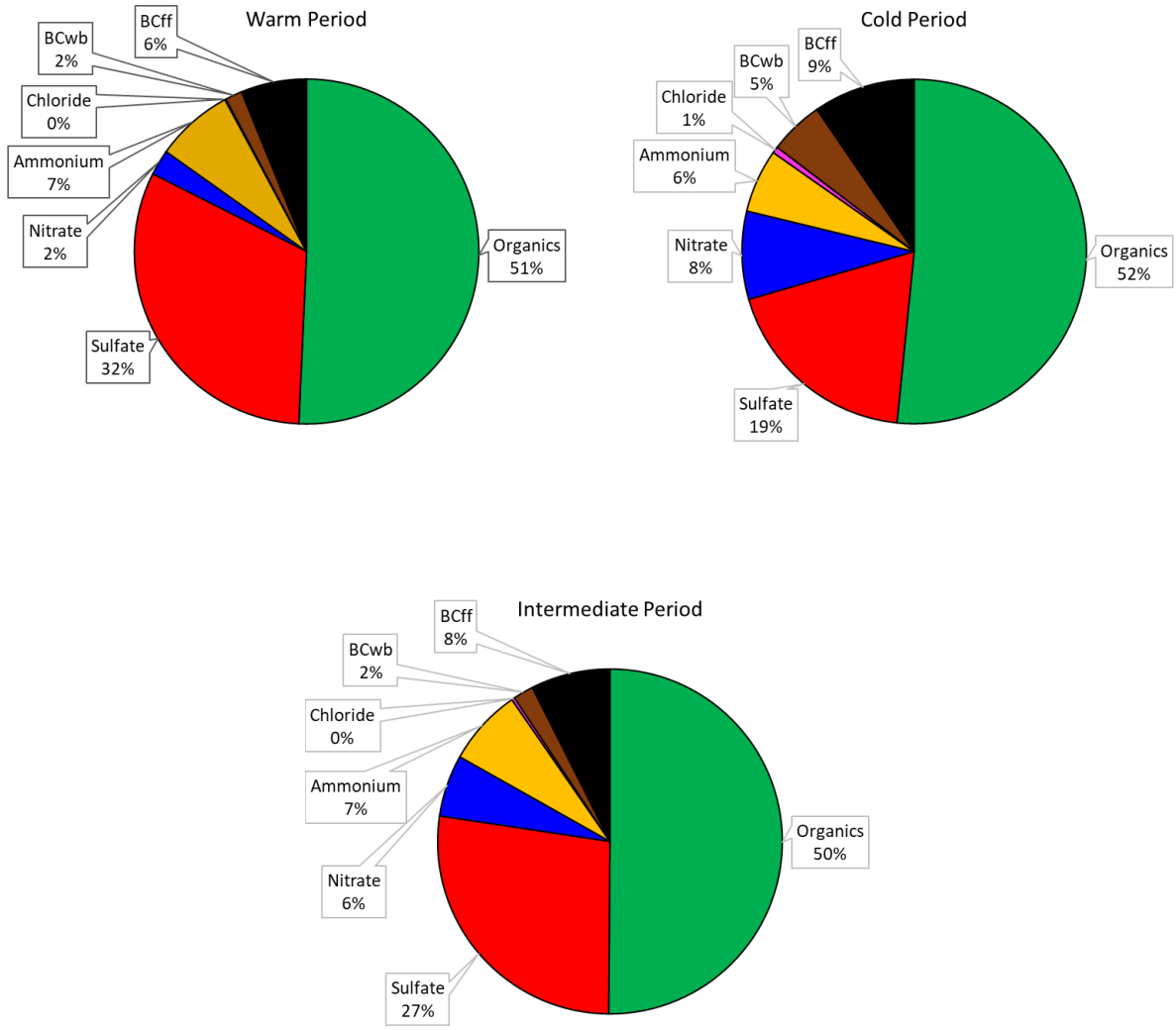

Figure 12.12: Chemical composition of PM_1 aerosol in Athens during the different periods 2nd and 3rd intercomparison campaigns. Non-Refractory PM_1 species were quantified using an Aerodyne ACSM operated at Thissio while BC components were apportioned using the Aethalometer Model on measurements conducted with an AE-33 aethalometer.

12.13 The August 2019 Euboea Forest Fire

Figure 12.13: Satellite image (MODIS) of Greece on 13 August 2019 (top), with the active forest fire region and the plume over the Athens basin (https://go.nasa.gov/2YIHqlv). On the bottom an image during the following day, when fire activity has declined (https://go.nasa.gov/31qOEMX).

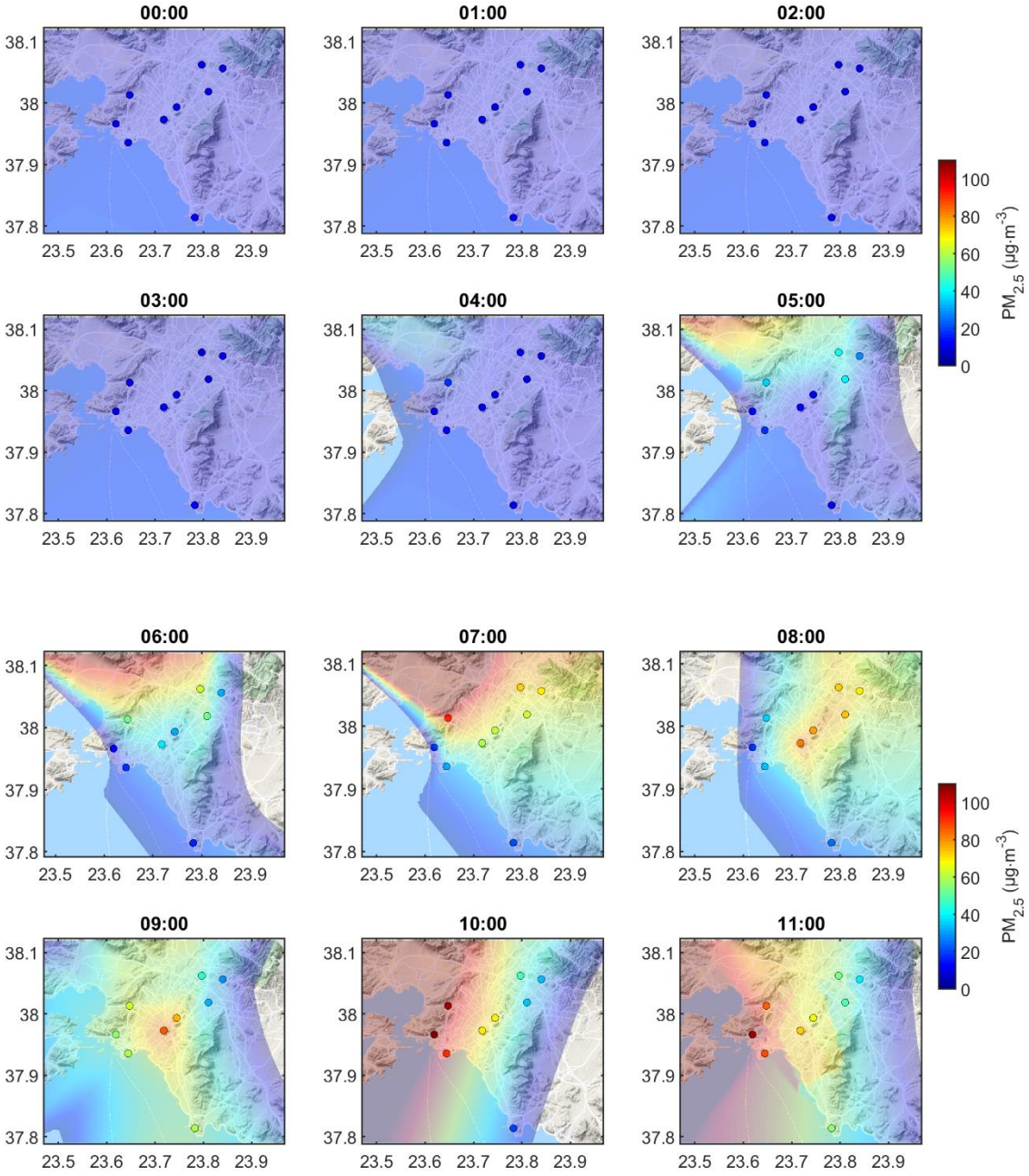
00:00
01:00
02:00
03:00
04:00
05:00
06:00
07:00
08:00
09:00
10:00
11:00
38.1
38
37.9
37.8
23.5 23.6 23.7 23.8 23.9
100
80
60
40
20
0
PM2.5 (µg·m-3)

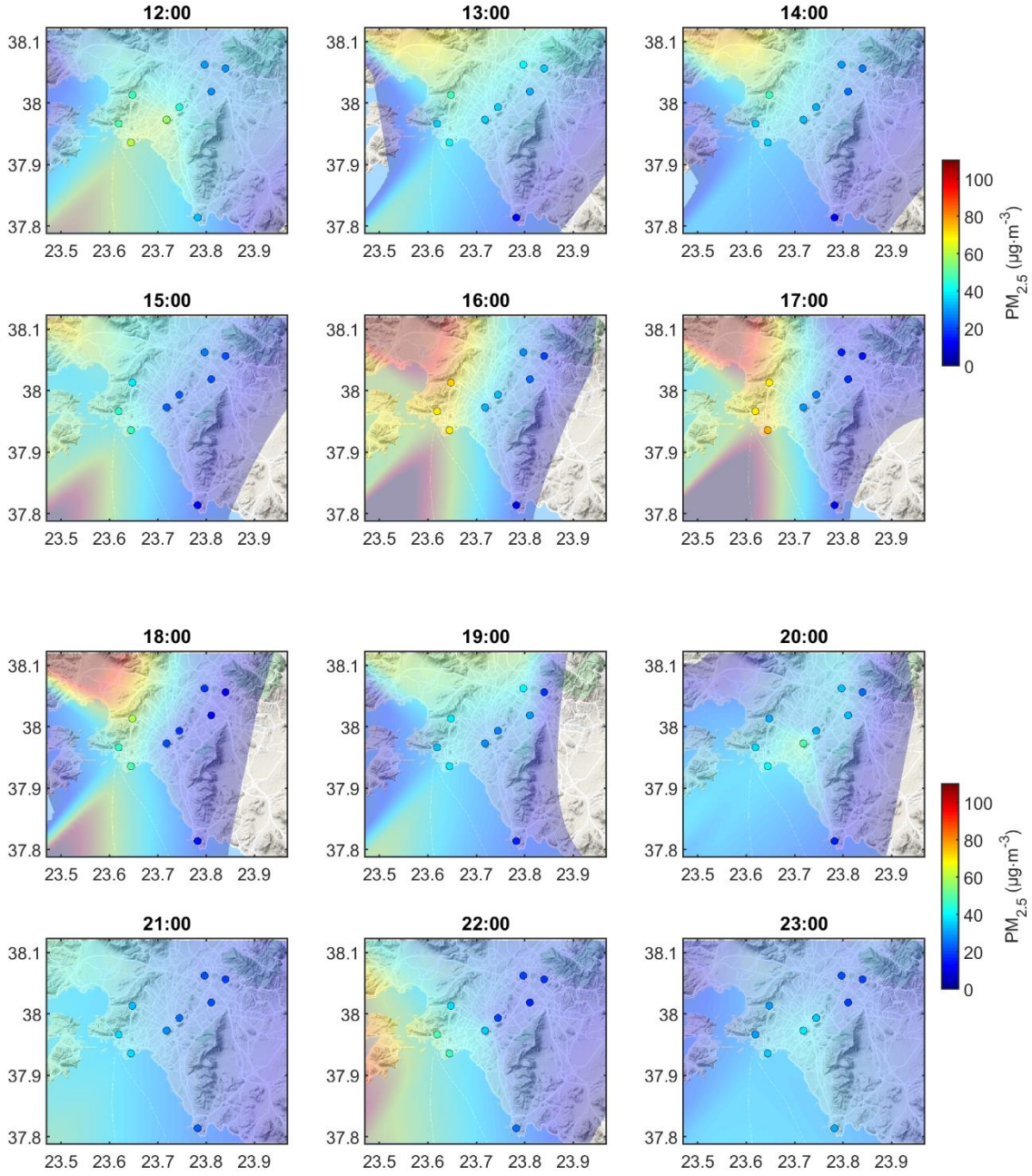

Figure 12.14: Spatial evolution of the Euboea Forest fire's impact on $PM_{2.5}$ concentrations over the Athens basin, as estimated by nearest neighbor interpolation on a 0.01° resolution grid (August 13th, 2019).

12.14 Spatial Variability in Athens and Ioannina

Table 12.15: Pairwise correlations of $PM_{2.5cor}$ measurements at sites in Athens during August 2019.

R^2		THI	GYZ	PEF	PIR	MEL	HAL	VOU	KER
		PA_000	PA_001	PA_002	PA_003	PA_004	PA_005	PA_006	PA_007
GYZ	PA_001	0.91							
PEF	PA_002	0.80	0.89						
PIR	PA_003	0.82	0.78	0.74					
MEL	PA_004	0.80	0.86	0.94	0.72				
HAL	PA_005	0.86	0.89	0.92	0.74	0.88			
VOU	PA_006	0.73	0.85	0.79	0.71	0.78	0.82		
KER	PA_007	0.84	0.81	0.80	0.87	0.77	0.76	0.72	
HAI	PA_014	0.84	0.81	0.801	0.83	0.77	0.77	0.69	0.94

Table 12.16: Coefficient of Divergence (CoD) values for each pair of monitoring sites in Ioannina during the 1-month wintertime campaign

CoD		ANA	VIL
		PA_013	PA_015
VIL	PA_015	0.24	
GIR	PA_016	0.33	0.23

Table 12.17: Pairwise correlations of $PM_{2.5cor}$ measurements at sites in Ioannina during the 1-month wintertime campaign

R^2		ANA	VIL
		PA_013	PA_015
VIL	PA_015	0.73	
GIR	PA_016	0.66	0.92

13 Appendix E. Supplement to the manuscript: Cooking as an Organic Aerosol source leading to urban Air Quality degradation

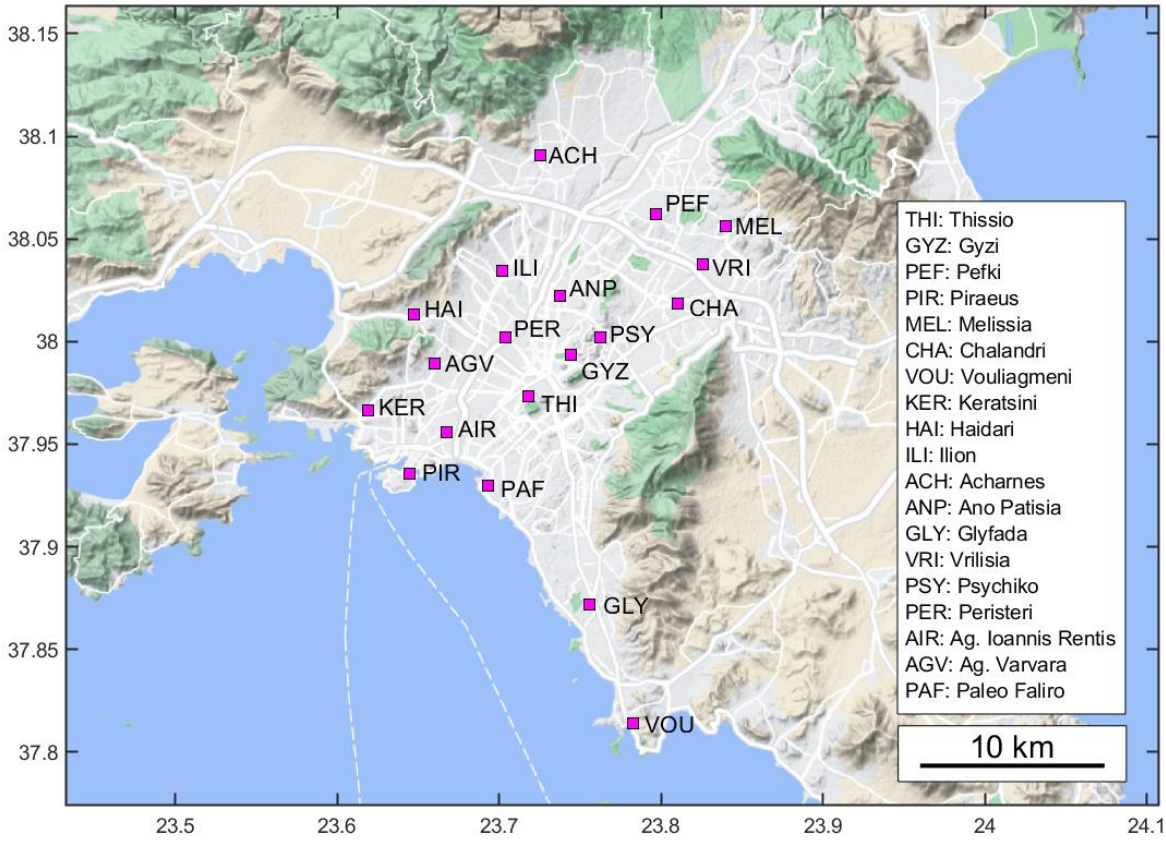

Figure 13.1. Map of the Greater Athens Area depicting the sites of the $PM_{2.5}$ monitoring network.

Table 13.1. Response factors and relative ionization efficiencies (RIEs) for SO_4^{2-} and NH_4^+

Activity Year	Response Factor	RIE SO_4^{2-}	RIE NH_4^+
FT* 2014	$5.91e^{-11}$	0.6	4.5
FT 2017	$4.61e^{-11}$	0.58	4.8
FT 2018	$3.1e^{-11}$	0.6	4.8
FT 2019 **	$3.1e^{-11}$ ($4.6e^{-11}$)	0.85 (0.6)	4.8 (3.7)
FT 2020	$3.7e^{-11}$	0.8	4.6
FT 2021	$4.1e^{-11}$	0.7	4.4
ES*** 2017	$4.61e^{-11}$	0.58	4.8
ES 2018	$3.1e^{-11}$	0.6	4.8
ES 2019	4.6e-11	0.6	3.7
ES 2020	4.6	0.67	4.6
ES 2021	4.1e-11	0.7	4.4

*FT: Fat Thursday

**numbers in parentheses represent values after 28/Feb/2019,

***ES: Easter Sunday

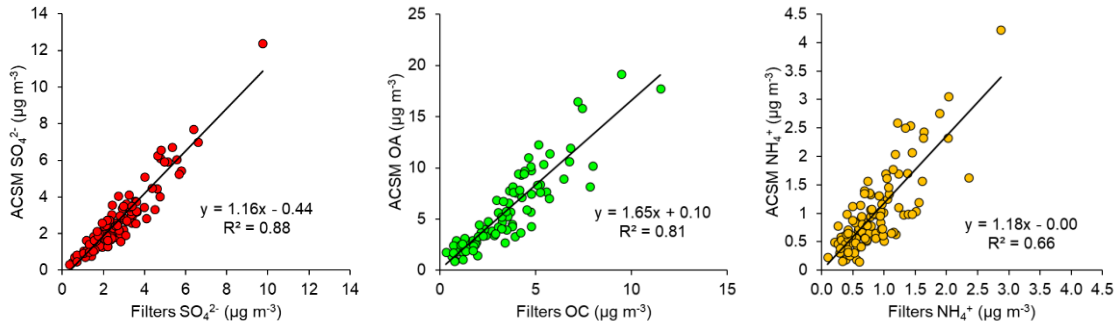

Figure 13.2. Comparison of ACSM derived species to with measurements from daily $PM_{2.5}$ filter sampling at Thissio during the periods under investigation.

Table 13.2. Dates of the festivities under investigation, and the corresponding control periods

year	Festivity	city	Fest date	Control period	COVID-19 Restrictions
2014	FT*	Athens	20 Feb 2014	13 Feb 2014 – 21 Feb 2014	None
2017	FT	Athens	16 Feb 2017	09 Feb 2017 – 23 Feb 2017	None
2017	ES**	Athens	16 Apr 2017	09 Apr 2017 – 23 Apr 2017	None
2018	FT	Athens	08 Feb 2018	01 Feb 2018 – 15 Feb 2018	None
2018	OTF***	Xanthi	01 Sep 2018 – 08 Sep 2018	–	None
2018	ES	Athens	08 Apr 2018	01 Apr 2018 – 15 Apr 2018	None
2019	FT	Athens	28 Feb 2019	21 Feb 2019 – 07 Mar 2019	None
2019	OTF	Xanthi	31 Aug 2019 – 07 Sep 2019	–	None
2019	ES	Athens	28 Apr 2019	21 Apr 2019 – 05 May 2019	None
2020	FT	Athens	20 Feb 2020	13 Feb 2020 – 27 Feb 2020	None
2020	OTF	Xanthi	–	–	Festival canceled
2020	ES	Athens	19 Apr 2020	12 Apr 2020 – 25 Apr 2020	Intra- and inter-city mobility restrictions
2021	FT	Athens	04 Mar 2021	25 Feb 2021 – 11 Mar 2021	Intra-city mobility Restrictions. Maximum number of people allowed per household imposed. Restaurants operating through home delivery
2021	OTF	Xanthi	04 Sep 2021 – 11 Sep 2021	–	Small scale concerts. No street vendors allowed
2021	ES	Athens	02 May 2021	25 Apr 2021 – 07 May 2021	Inter-city mobility restrictions. Maximum number of people allowed per household imposed.

*FT: Fat Thursday

**ES: Easter Sunday

***OTF: Old Town Festival

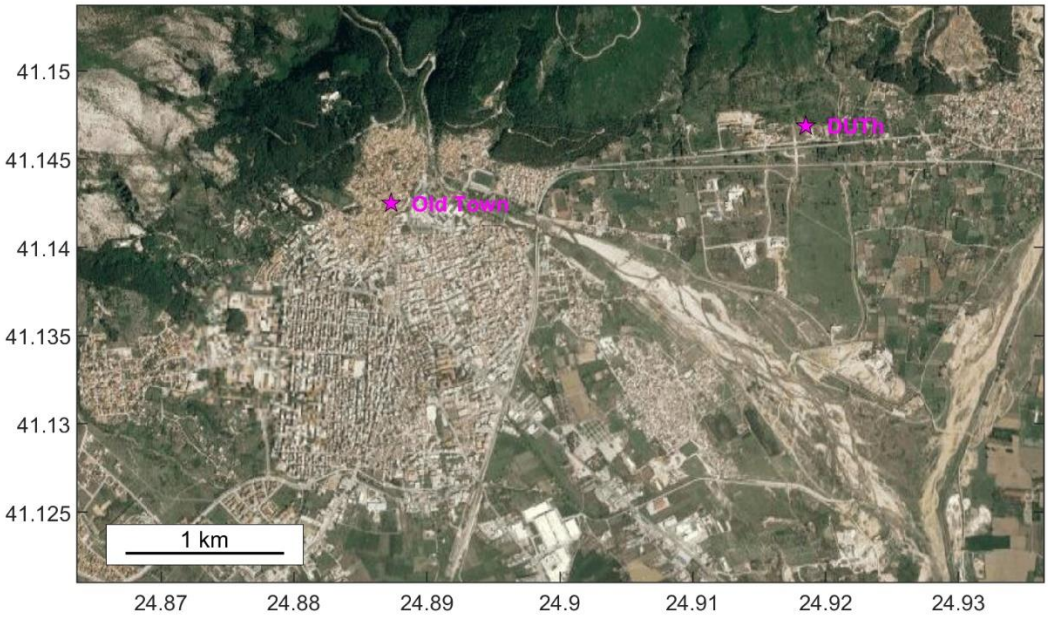

Figure 13.3. Measuring sites in Xanthi during the OTF festivities. Old Town positioned in the city's late 19th century-built part and DUTh positioned at the premises of the Democritus University of Thrace, in the rural Kimeria region.

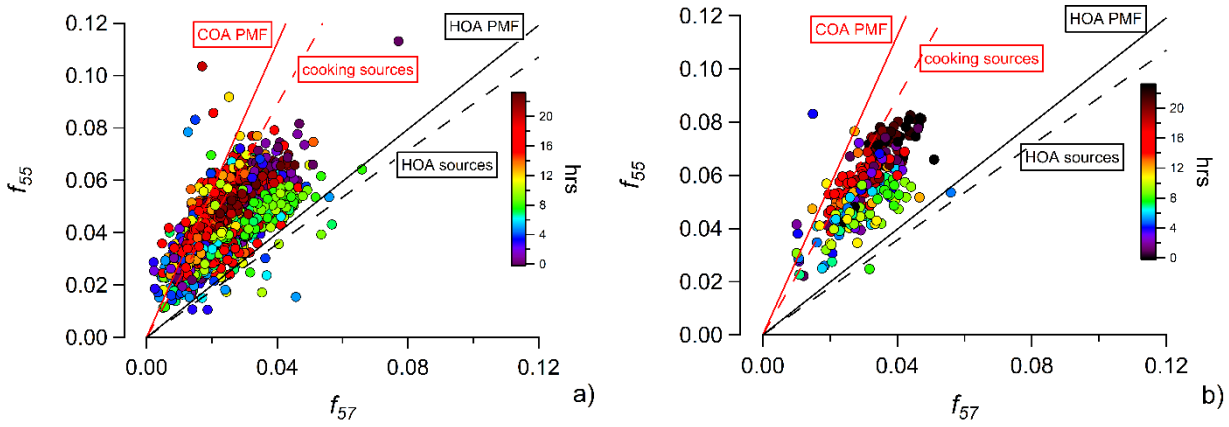

Figure 13.4. f_{55} vs f_{57} triangle plots during the (a) control period and (b) Fat Thursday for the years under investigation.

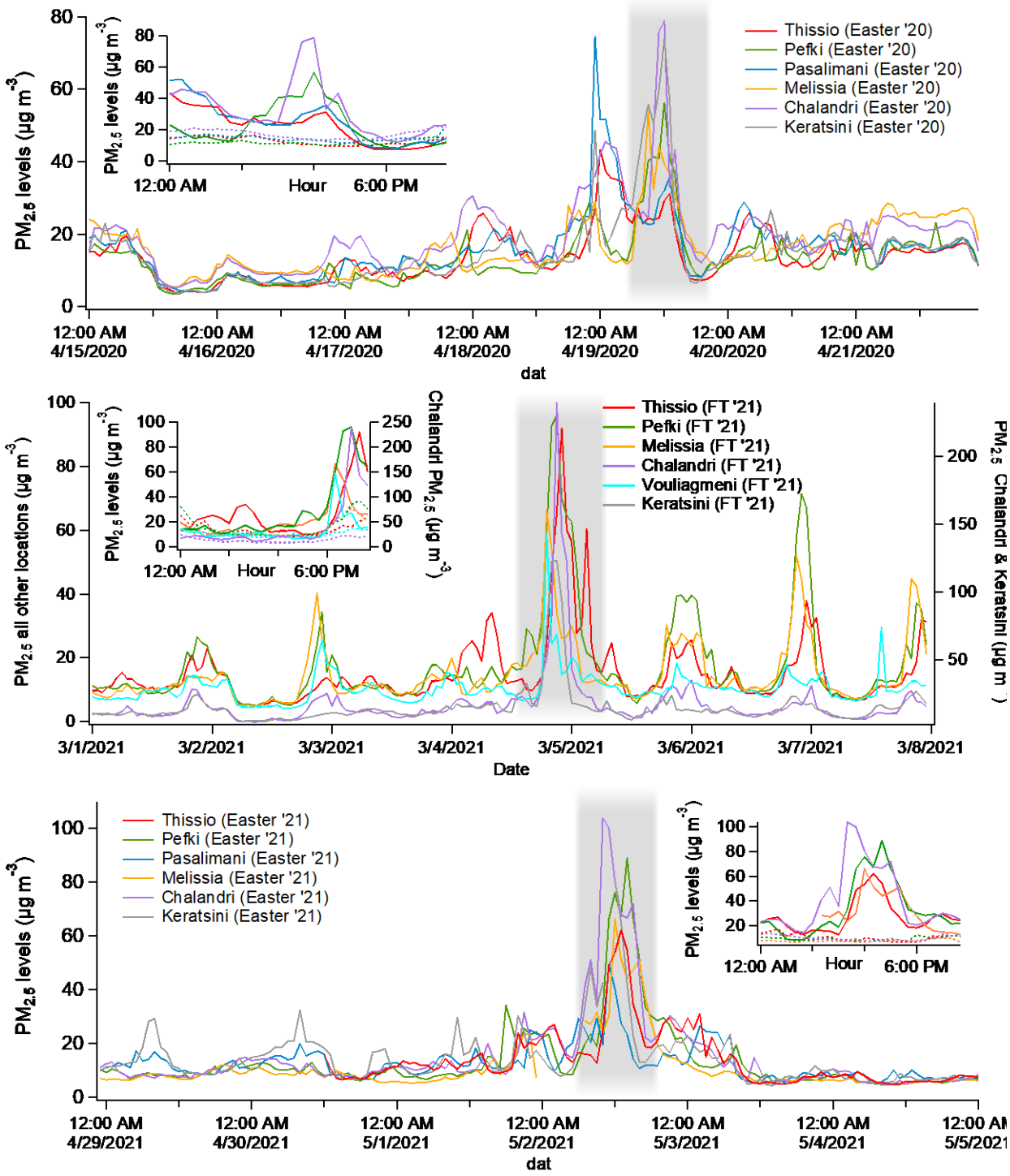

Figure 13.5: Hourly $PM_{2.5}$ levels in different locations within the Greater Athens Area, during Easter festivities (a,c) and "Fat Thursday" (b) as captured by the low-cost PM sensor network.

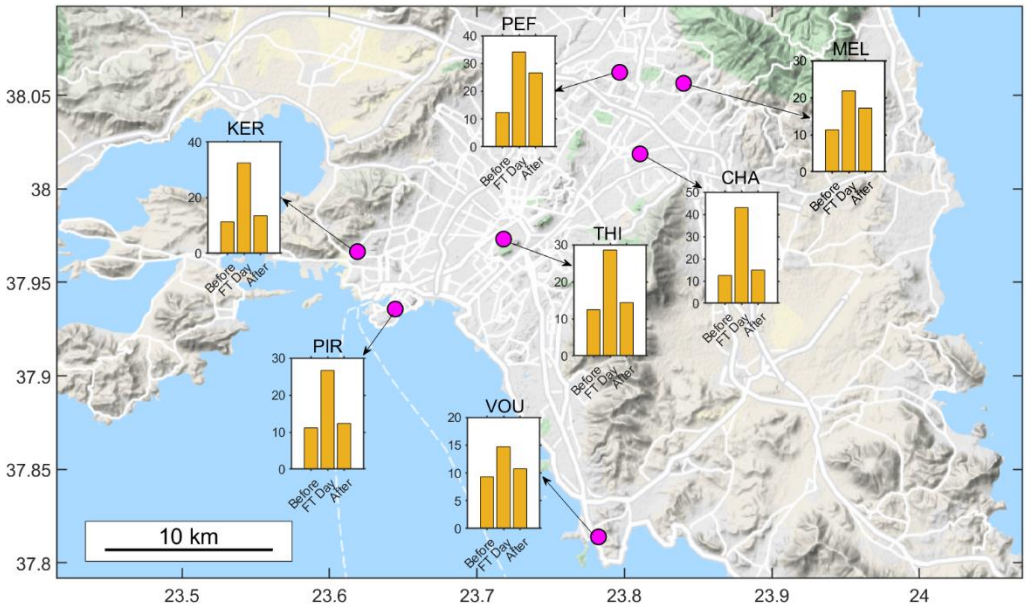

Figure 13.6. Average $PM_{2.5}$ concentrations of the control period before FT, during FT day and after FT in selected sites across the GAA, highlighting the events impact on air quality.

CoD	THI	GYZ	PEF	PIR	MEL	CHA	VOU	KER	HAI	ILI	ACH	ANP	GLY	VRI	PSY	PER	AIR	AGV	PAF
THI		0.151	0.218	0.299	0.285	0.257	0.536	0.282	0.329	0.373	0.387	0.206	0.419	0.250	0.303	0.287	0.313	0.337	0.343
GYZ	0.151		0.210	0.311	0.261	0.173	0.566	0.263	0.285	0.310	0.336	0.137	0.397	0.224	0.258	0.253	0.280	0.279	0.357
PEF	0.218	0.210		0.365	0.218	0.239	0.545	0.283	0.250	0.374	0.315	0.253	0.346	0.145	0.208	0.375	0.376	0.317	0.426
PIR	0.299	0.311	0.365		0.310	0.376	0.409	0.249	0.383	0.448	0.435	0.364	0.314	0.299	0.326	0.324	0.240	0.351	0.163
MEL	0.285	0.261	0.218	0.310		0.310	0.502	0.277	0.294	0.440	0.363	0.329	0.211	0.134	0.170	0.338	0.328	0.360	0.368
CHA	0.257	0.173	0.239	0.376	0.310		0.619	0.284	0.269	0.244	0.261	0.164	0.430	0.243	0.267	0.266	0.286	0.239	0.412
VOU	0.536	0.566	0.545	0.409	0.502	0.619		0.455	0.528	0.676	0.601	0.610	0.255	0.517	0.496	0.606	0.538	0.548	0.394
KER	0.282	0.263	0.283	0.249	0.277	0.284	0.455		0.240	0.350	0.287	0.277	0.250	0.223	0.218	0.333	0.243	0.182	0.306
HAI	0.329	0.285	0.250	0.383	0.294	0.269	0.528	0.240		0.357	0.232	0.295	0.239	0.237	0.226	0.411	0.369	0.198	0.436
ILI	0.373	0.310	0.374	0.448	0.440	0.244	0.676	0.350	0.357		0.265	0.267	0.518	0.365	0.377	0.301	0.341	0.272	0.491
ACH	0.387	0.336	0.315	0.435	0.363	0.261	0.601	0.287	0.232	0.265		0.311	0.356	0.290	0.296	0.386	0.377	0.206	0.492
ANP	0.206	0.137	0.253	0.364	0.329	0.164	0.610	0.277	0.295	0.267	0.311		0.449	0.269	0.299	0.245	0.305	0.271	0.405
GLY	0.419	0.397	0.346	0.314	0.211	0.430	0.255	0.250	0.239	0.518	0.356	0.449		0.291	0.258	0.500	0.409	0.309	0.351
VRI	0.250	0.224	0.145	0.299	0.134	0.243	0.517	0.223	0.237	0.365	0.290	0.269	0.291		0.142	0.350	0.318	0.272	0.370
PSY	0.303	0.258	0.208	0.326	0.170	0.267	0.496	0.218	0.226	0.377	0.296	0.299	0.258	0.142		0.376	0.317	0.251	0.384
PER	0.287	0.253	0.375	0.324	0.338	0.266	0.606	0.333	0.411	0.301	0.386	0.245	0.500	0.350	0.376		0.231	0.353	0.331
AIR	0.313	0.280	0.376	0.240	0.328	0.286	0.538	0.243	0.369	0.341	0.377	0.305	0.409	0.318	0.317	0.231		0.284	0.262
AGV	0.337	0.279	0.317	0.351	0.360	0.239	0.548	0.182	0.198	0.272	0.206	0.271	0.309	0.272	0.251	0.353	0.284		0.411
PAF	0.343	0.357	0.426	0.163	0.368	0.412	0.394	0.306	0.436	0.491	0.492	0.405	0.351	0.370	0.384	0.331	0.262	0.411	

Figure 13.7. Coefficient of Divergence (CoD) for $PM_{2.5}$ concentrations during Easter Sunday 2021, between the monitoring sites in the Greater Athens Area. Each site location is depicted in **Figure 13.1**.

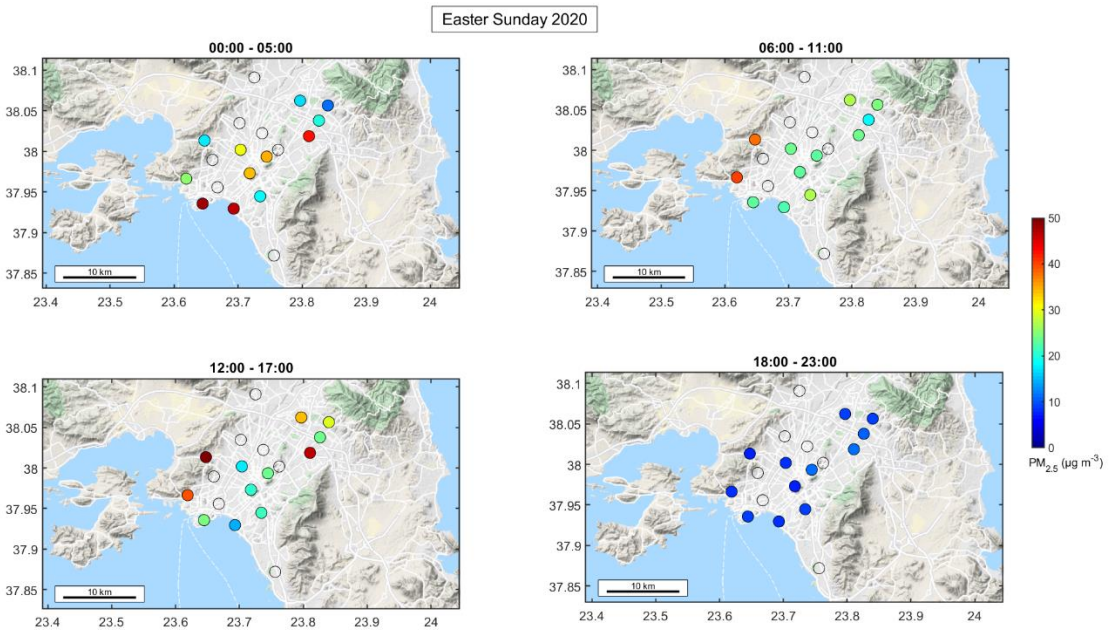

Figure 13.8. Snapshots of 6-hour average $PM_{2.5}$ concentrations during Easter Sunday 2020, recorded by the PANACEA low-cost $PM_{2.5}$ monitoring network in the GAA.

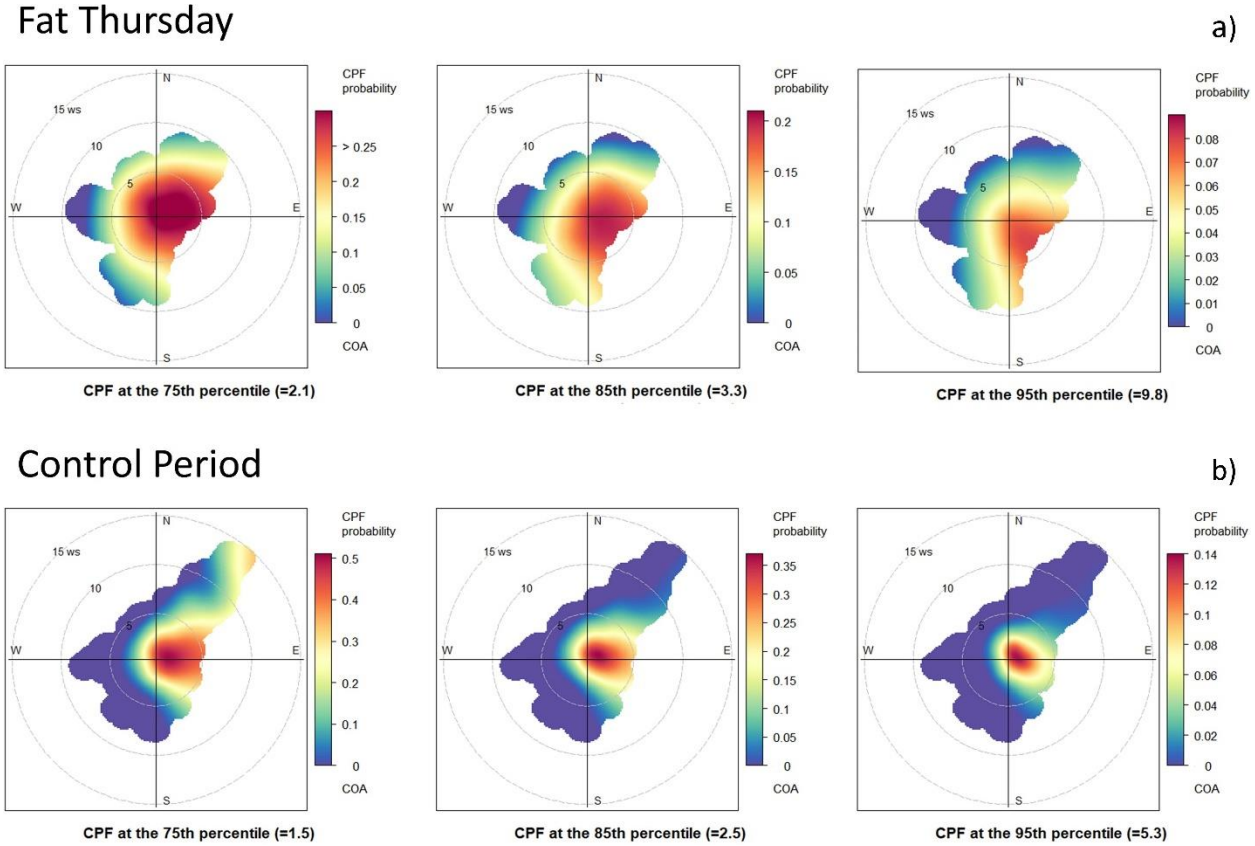

Figure 13.9. Bivariate polar plots for conditional probabilities (CPF) of threshold exceedance (various upper percentiles), for COA concentrations during FT days in 2014, 2017-2021 (a) and during the respective control periods (b). Wind speed (m s^{-1}) shown on the radial axis, CPF probabilities on the color scale.

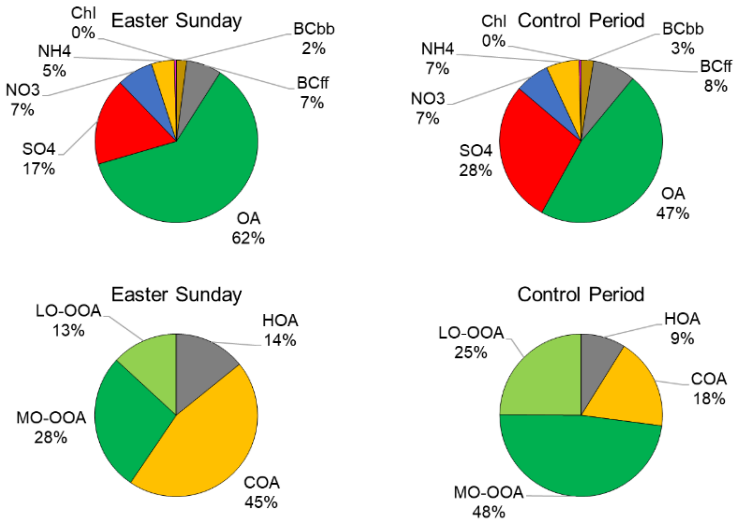

Figure 13.10. Average contribution of ACSM derived chemical components and apportioned BC to total PM_1 during (a) Easter Sunday and (b) the respective control period followed by the contribution of PMF derived OA factors to total OA during (c) "Fat Thursday" and (d) the respective control period.

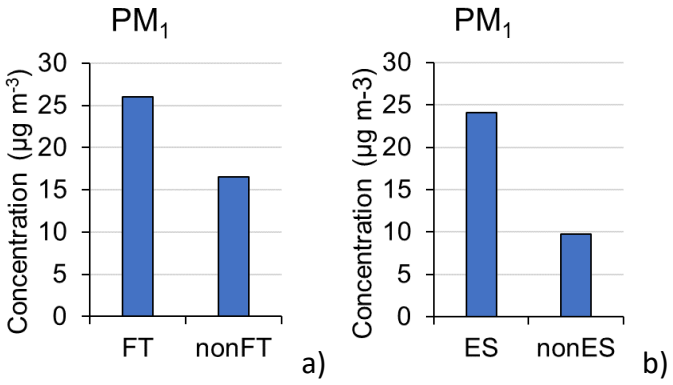

Figure 13.11. Average PM_1 concentrations during "Fat Thursday" (a) and Easter Sunday (b) case studies. The respective event day is compared to its corresponding control period.

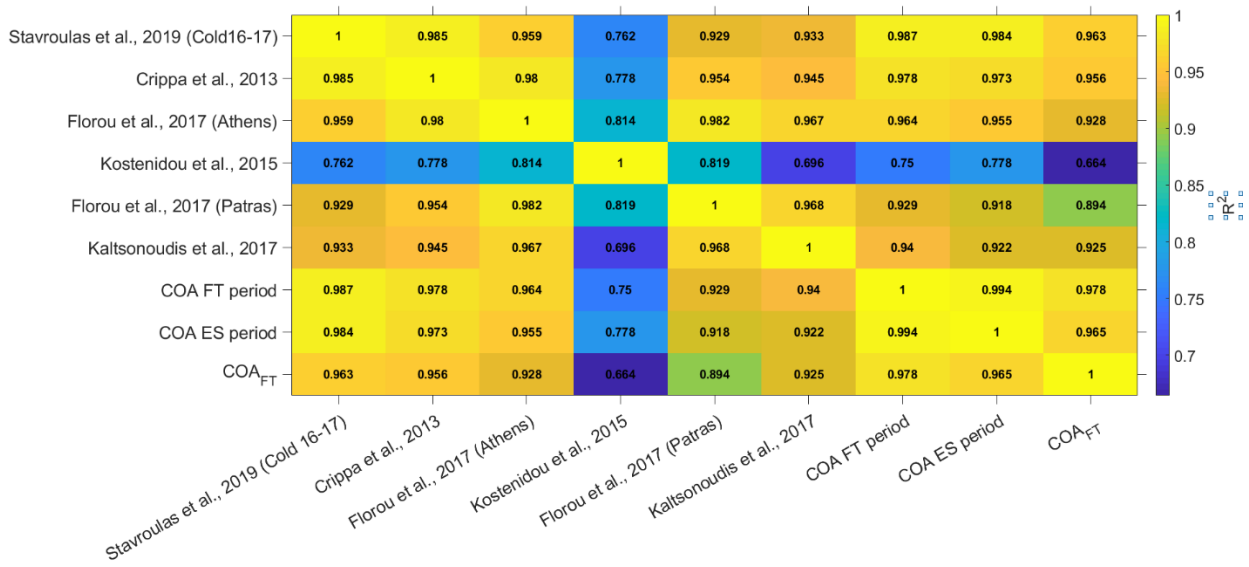

Figure 13.12. Correlation plot for COA obtained in this study vs selected spectra resolved in studies within Greece and elsewhere.

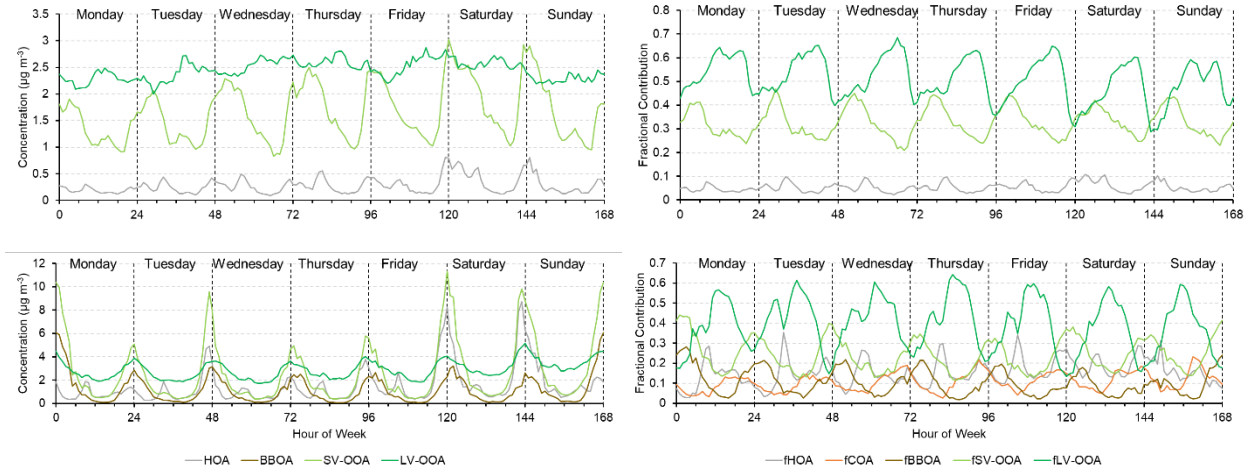

Figure 13.13. Weekly variability of PMF resolved OA factor concentrations along with their fractional contribution to total OA, excluding COA, for the warm (top row) and cold (bottom row) season.

14 References

Abdullahi, K.L., Delgado-Saborit, J.M., Harrison, R.M., 2013. Emissions and indoor concentrations of particulate matter and its specific chemical components from cooking: A review. Atmospheric Environment 71, 260–294. https://doi.org/10.1016/j.atmosenv.2013.01.061

Äijälä, M., Heikkinen, L., Fröhlich, R., Canonaco, F., Prévôt, A.S.H., Junninen, H., Petäjä, T., Kulmala, M., Worsnop, D., Ehn, M., 2017. Resolving anthropogenic aerosol pollution types - Deconvolution and exploratory classification of pollution events. Atmospheric Chemistry and Physics 17, 3165–3197. https://doi.org/10.5194/acp-17-3165-2017

Akagi, S.K., Yokelson, R.J., Wiedinmyer, C., Alvarado, M.J., Reid, J.S., Karl, T., Crounse, J.D., Wennberg, P.O., 2011. Emission factors for open and domestic biomass burning for use in atmospheric models. Atmospheric Chemistry and Physics 11, 4039–4072. https://doi.org/10.5194/acp-11-4039-2011

Alexiou, D., Kokkalis, P., Papayannis, A., Rocadenbosch, F., Argyrouli, A., Tsaknakis, G., Tzanis, C.G., 2018. Planetary boundary layer height variability over athens, greece, based on the synergy of raman lidar and radiosonde data: Application of the kalman filter and other techniques (2011-2016). EPJ Web Conf. 176, 06007. https://doi.org/10.1051/epjconf/201817606007

Alfarra, M.R., Prevot, A.S.H., Szidat, S., Sandradewi, J., Weimer, S., Lanz, V.A., Schreiber, D., Mohr, M., Baltensperger, U., 2007. Identification of the Mass Spectral Signature of Organic Aerosols from Wood Burning Emissions. Environ. Sci. Technol. 41, 5770–5777. https://doi.org/10.1021/es062289b

Allan, J.D., Delia, A.E., Coe, H., Bower, K.N., Alfarra, M.R., Jimenez, J.L., Middlebrook, A.M., Drewnick, F., Onasch, T.B., Canagaratna, M.R., Jayne, J.T., Worsnop, D.R., 2004. A generalised method for the extraction of chemically resolved mass spectra from Aerodyne aerosol mass spectrometer data. Journal of Aerosol Science 35, 909–922. https://doi.org/10.1016/j.jaerosci.2004.02.007

Allan, J.D., Williams, P.I., Morgan, W.T., Martin, C.L., Flynn, M.J., Lee, J., Nemitz, E., Phillips, G.J., Gallagher, M.W., Coe, H., 2010. Contributions from transport, solid fuel burning and cooking to primary organic aerosols in two UK cities. Atmospheric Chemistry and Physics 10, 647–668. https://doi.org/10.5194/acp-10-647-2010

Al-Naiema, I.M., Hettiyadura, A.P.S., Wallace, H.W., Sanchez, N.P., Madler, C.J., Cevik, B.K., Bui, A.A.T., Kettler, J., Griffin, R.J., Stone, E.A., 2018. Source apportionment of fine particulate matter in Houston, Texas: insights to secondary organic aerosols. Atmospheric Chemistry and Physics 18, 15601–15622. https://doi.org/10.5194/acp-18-15601-2018

Apte, J.S., Marshall, J.D., Cohen, A.J., Brauer, M., 2015. Addressing Global Mortality from Ambient PM2.5. Environ. Sci. Technol. 49, 8057–8066. https://doi.org/10.1021/acs.est.5b01236

Ardon-Dryer, K., Dryer, Y., Williams, J.N., Moghimi, N., 2020. Measurements of $PM_{2.5}$ with PurpleAir under atmospheric conditions. Atmospheric Measurement Techniques 13, 5441–5458. https://doi.org/10.5194/amt-13-5441-2020

Argiriou, A.A., Kassomenos, P.A., Lykoudis, S.P., 2004. On the Methods for the Delimitation of Seasons. Water, Air, & Soil Pollution: Focus 4, 65–74. https://doi.org/10.1023/B:WAFO.0000044787.71076.38

Argyropoulos, G., Samara, C., Diapouli, E., Eleftheriadis, K., Papaoikonomou, K., Kungolos, A., 2017. Source apportionment of PM10 and PM2.5 in major urban Greek agglomerations using a hybrid source-receptor modeling process. Science of The Total Environment 601–602, 906–917. https://doi.org/10.1016/j.scitotenv.2017.05.088

Ashbaugh, L.L., Malm, W.C., Sadeh, W.Z., 1985. A residence time probability analysis of sulfur concentrations at grand Canyon National Park. Atmospheric Environment (1967) 19, 1263–1270. https://doi.org/10.1016/0004-6981(85)90256-2

Asimakopoulos, D.N., Helmis, C.G., Michopoulos, J., 2004. Evaluation of Sodar methods for the determination of the atmospheric boundary layer mixing height. Meteorol Atmos Phys 85, 85–92. https://doi.org/10.1007/s00703-003-0036-9

Athanasopoulou, E., Speyer, O., Brunner, D., Vogel, H., Vogel, B., Mihalopoulos, N., Gerasopoulos, E., 2017. Changes in domestic heating fuel use in Greece: effects on atmospheric chemistry and radiation. Atmospheric Chemistry and Physics 17, 10597–10618. https://doi.org/10.5194/acp-17-10597-2017

Atkinson, R.W., Kang, S., Anderson, H.R., Mills, I.C., Walton, H.A., 2014. Epidemiological time series studies of PM2.5 and daily mortality and hospital admissions: a systematic review and meta-analysis. Thorax 69, 660–665. https://doi.org/10.1136/thoraxjnl-2013-204492

Aurela, M., Saarikoski, S., Niemi, J.V., Canonaco, F., Prevot, A.S.H., Frey, A., Carbone, S., Kousa, A., Hillamo, R., 2015. Chemical and Source Characterization of Submicron Particles at Residential and Traffic Sites in the Helsinki Metropolitan Area, Finland. Aerosol Air Qual. Res. 15, 1213–1226. https://doi.org/10.4209/aaqr.2014.11.0279

Bailey, J., Gerasopoulos, E., Rojas-Rueda, D., Benmarhnia, T., 2019. Potential health and equity co-benefits related to the mitigation policies reducing air pollution from residential wood burning in Athens, Greece. Journal of Environmental Science and Health, Part A 54, 1144–1151. https://doi.org/10.1080/10934529.2019.1629211

Barkjohn, K.K., Gantt, B., Clements, A.L., 2021. Development and application of a United States-wide correction for $PM_{2.5}$ data collected with the PurpleAir sensor. Atmospheric Measurement Techniques 14, 4617–4637. https://doi.org/10.5194/amt-14-4617-2021

Barreira, L.M.F., Helin, A., Aurela, M., Teinilä, K., Friman, M., Kangas, L., Niemi, J.V., Portin, H., Kousa, A., Pirjola, L., Rönkkö, T., Saarikoski, S., Timonen, H., 2021. In-depth characterization of submicron particulate matter inter-annual variations at a street canyon site in northern Europe. Atmospheric Chemistry and Physics 21, 6297–6314. https://doi.org/10.5194/acp-21-6297-2021

Basagaña, X., Jacquemin, B., Karanasiou, A., Ostro, B., Querol, X., Agis, D., Alessandrini, E., Alguacil, J., Artiñano, B., Catrambone, M., de la Rosa, J.D., Díaz, J., Faustini, A., Ferrari, S., Forastiere, F., Katsouyanni, K., Linares, C., Perrino, C., Ranzi, A., Ricciardelli, I., Samoli, E., Zauli-Sajani, S., Sunyer, J., Stafoggia, M., 2015. Short-term effects of particulate matter constituents on daily hospitalizations and mortality in five South-European cities: Results from the MED-PARTICLES project. Environment International 75, 151–158. https://doi.org/10.1016/j.envint.2014.11.011

Becerril-Valle, M., Coz, E., Prévôt, A.S.H., Močnik, G., Pandis, S.N., Sánchez de la Campa, A.M., Alastuey, A., Díaz, E., Pérez, R.M., Artíñano, B., 2017. Characterization of atmospheric black carbon and co-pollutants in urban and rural areas of Spain. Atmospheric Environment 169, 36–53. https://doi.org/10.1016/j.atmosenv.2017.09.014

Becnel, T., Sayahi, T., Kelly, K., Gaillardon, P.-E., 2019. A Recursive Approach to Partially Blind Calibration of a Pollution Sensor Network, in: 2019 IEEE International Conference on Embedded Software and Systems (ICESS). Presented at the 2019 IEEE International Conference on Embedded Software and Systems (ICESS), IEEE, Las Vegas, NV, USA, pp. 1–8. https://doi.org/10.1109/ICESS.2019.8782523

Beelen, R., Raaschou-Nielsen, O., Stafoggia, M., Andersen, Z.J., Weinmayr, G., Hoffmann, B., Wolf, K., Samoli, E., Fischer, P., Nieuwenhuijsen, M., Vineis, P., Xun, W.W., Katsouyanni, K., Dimakopoulou, K., Oudin, A., Forsberg, B., Modig, L., Havulinna, A.S., Lanki, T., Turunen, A., Oftedal, B., Nystad, W., Nafstad, P., De Faire, U., Pedersen, N.L., Östenson, C.-G., Fratiglioni, L., Penell, J., Korek, M., Pershagen, G., Eriksen, K.T., Overvad, K., Ellermann, T., Eeftens, M., Peeters, P.H., Meliefste, K., Wang, M., Bueno-de-Mesquita, B., Sugiri, D., Krämer, U., Heinrich, J., de Hoogh, K., Key, T., Peters, A., Hampel, R., Concin, H., Nagel, G., Ineichen, A., Schaffner, E., Probst-Hensch, N., Künzli, N., Schindler, C., Schikowski, T., Adam, M., Phuleria, H., Vilier, A., Clavel-

Chapelon, F., Declercq, C., Grioni, S., Krogh, V., Tsai, M.-Y., Ricceri, F., Sacerdote, C., Galassi, C., Migliore, E., Ranzi, A., Cesaroni, G., Badaloni, C., Forastiere, F., Tamayo, I., Amiano, P., Dorronsoro, M., Katsoulis, M., Trichopoulou, A., Brunekreef, B., Hoek, G., 2014a. Effects of long-term exposure to air pollution on natural-cause mortality: an analysis of 22 European cohorts within the multicentre ESCAPE project. The Lancet 383, 785–795. https://doi.org/10.1016/S0140-6736(13)62158-3

Beelen, R., Stafoggia, M., Raaschou-Nielsen, O., Andersen, Z.J., Xun, W.W., Katsouyanni, K., Dimakopoulou, K., Brunekreef, B., Weinmayr, G., Hoffmann, B., Wolf, K., Samoli, E., Houthuijs, D., Nieuwenhuijsen, M., Oudin, A., Forsberg, B., Olsson, D., Salomaa, V., Lanki, T., Yli-Tuomi, T., Oftedal, B., Aamodt, G., Nafstad, P., De Faire, U., Pedersen, N.L., Östenson, C.-G., Fratiglioni, L., Penell, J., Korek, M., Pyko, A., Eriksen, K.T., Tjønneland, A., Becker, T., Eeftens, M., Bots, M., Meliefste, K., Wang, M., Bueno-de-Mesquita, B., Sugiri, D., Krämer, U., Heinrich, J., de Hoogh, K., Key, T., Peters, A., Cyrys, J., Concin, H., Nagel, G., Ineichen, A., Schaffner, E., Probst-Hensch, N., Dratva, J., Ducret-Stich, R., Vilier, A., Clavel-Chapelon, F., Stempfelet, M., Grioni, S., Krogh, V., Tsai, M.-Y., Marcon, A., Ricceri, F., Sacerdote, C., Galassi, C., Migliore, E., Ranzi, A., Cesaroni, G., Badaloni, C., Forastiere, F., Tamayo, I., Amiano, P., Dorronsoro, M., Katsoulis, M., Trichopoulou, A., Vineis, P., Hoek, G., 2014b. Long-term Exposure to Air Pollution and Cardiovascular Mortality: An Analysis of 22 European Cohorts. Epidemiology 25, 368–378.

Bell, M.L., Davis, D.L., 2001. Reassessment of the lethal London fog of 1952: novel indicators of acute and chronic consequences of acute exposure to air pollution. Environmental Health Perspectives 109, 389–394. https://doi.org/10.1289/ehp.01109s3389

Bi, J., Wildani, A., Chang, H.H., Liu, Y., 2020. Incorporating Low-Cost Sensor Measurements into High-Resolution PM $_{2.5}$ Modeling at a Large Spatial Scale. Environ. Sci. Technol. 54, 2152–2162. https://doi.org/10.1021/acs.est.9b06046

Bond, T.C., Anderson, T.L., Campbell, D., 1999. Calibration and Intercomparison of Filter-Based Measurements of Visible Light Absorption by Aerosols. Aerosol Science and Technology 30, 582–600. https://doi.org/10.1080/027868299304435

Bond, T.C., Bergstrom, R.W., 2006. Light Absorption by Carbonaceous Particles: An Investigative Review. Aerosol Science and Technology 40, 27–67. https://doi.org/10.1080/02786820500421521

Borrego, C., Costa, A.M., Ginja, J., Amorim, M., Coutinho, M., Karatzas, K., Sioumis, Th., Katsifarakis, N., Konstantinidis, K., De Vito, S., Esposito, E., Smith, P., André, N., Gérard, P., Francis, L.A., Castell, N., Schneider, P., Viana, M., Minguillón, M.C., Reimringer, W., Otjes, R.P., von Sicard, O., Pohle, R., Elen, B., Suriano, D., Pfister, V., Prato, M., Dipinto, S., Penza, M., 2016. Assessment of air quality microsensors versus reference methods: The EuNetAir joint exercise. Atmospheric Environment 147, 246–263. https://doi.org/10.1016/j.atmosenv.2016.09.050

Bougiatioti, A., Paraskevopoulou, D., Stavroulas, I., Weber, R., Nenes, A., Kanakidou, M., Mihalopoulos, N., 2017. The effects of biomass burning on fine aerosol acidity, liquid water content and nitrogen partitioning. Presented at the European Aerosol Conference, Zurich, Switzerland.

Bougiatioti, A., Stavroulas, I., Kostenidou, E., Zarmpas, P., Theodosi, C., Kouvarakis, G., Canonaco, F., Prévôt, A.S.H., Nenes, A., Pandis, S.N., Mihalopoulos, N., 2014. Processing of biomass-burning aerosol in the eastern Mediterranean during summertime. Atmos. Chem. Phys. 14, 4793–4807. https://doi.org/10.5194/acp-14-4793-2014

Bressi, M., Cavalli, F., Putaud, J.P., Fröhlich, R., Petit, J.-E., Aas, W., Äijälä, M., Alastuey, A., Allan, J.D., Aurela, M., Berico, M., Bougiatioti, A., Bukowiecki, N., Canonaco, F., Crenn, V., Dusanter, S., Ehn, M., Elsasser, M., Flentje, H., Graf, P., Green, D.C., Heikkinen, L., Hermann, H., Holzinger, R., Hueglin, C., Keernik, H., Kiendler-Scharr, A., Kubelová, L., Lunder, C., Maasikmets, M., Makeš, O., Malaguti, A., Mihalopoulos, N., Nicolas, J.B., O'Dowd, C., Ovadnevaite, J., Petralia, E., Poulain, L., Priestman, M., Riffault, V., Ripoll, A., Schlag, P., Schwarz, J., Sciare, J., Slowik, J., Sosedova, Y.,

Stavroulas, I., Teinemaa, E., Via, M., Vodička, P., Williams, P.I., Wiedensohler, A., Young, D.E., Zhang, S., Favez, O., Minguillón, M.C., Prevot, A.S.H., 2021. A European aerosol phenomenology - 7: High-time resolution chemical characteristics of submicron particulate matter across Europe. Atmospheric Environment: X 10, 100108. https://doi.org/10.1016/j.aeaoa.2021.100108

Briggs, N.L., Long, C.M., 2016. Critical review of black carbon and elemental carbon source apportionment in Europe and the United States. Atmospheric Environment 144, 409–427. https://doi.org/10.1016/j.atmosenv.2016.09.002

Brook, R.D., Rajagopalan, S., Pope, C.A., Brook, J.R., Bhatnagar, A., Diez-Roux, A.V., Holguin, F., Hong, Y., Luepker, R.V., Mittleman, M.A., Peters, A., Siscovick, D., Smith, S.C., Whitsel, L., Kaufman, J.D., 2010. Particulate Matter Air Pollution and Cardiovascular Disease. Circulation 121, 2331–2378. https://doi.org/10.1161/CIR.0b013e3181dbece1

Brown, L.M., Collings, N., Harrison, R.M., Maynard, A.D., Maynard, R.L., Cass, G.R., Hughes, L.A., Bhave, P., Kleeman, M.J., Allen, J.O., Salmon, L.G., 2000. The chemical composition of atmospheric ultrafine particles. Philosophical Transactions of the Royal Society of London. Series A: Mathematical, Physical and Engineering Sciences 358, 2581–2592. https://doi.org/10.1098/rsta.2000.0670

Budisulistiorini, S.H., Baumann, K., Edgerton, E.S., Bairai, S.T., Mueller, S., Shaw, S.L., Knipping, E.M., Gold, A., Surratt, J.D., 2016. Seasonal characterization of submicron aerosol chemical composition and organic aerosol sources in the southeastern United States: Atlanta, Georgia,and Look Rock, Tennessee. Atmos. Chem. Phys. 16, 5171–5189. https://doi.org/10.5194/acp-16-5171-2016

Budisulistiorini, S.H., Canagaratna, M.R., Croteau, P.L., Baumann, K., Edgerton, E.S., Kollman, M.S., Ng, N.L., Verma, V., Shaw, S.L., Knipping, E.M., Worsnop, D.R., Jayne, J.T., Weber, R.J., Surratt, J.D., 2014. Intercomparison of an Aerosol Chemical Speciation Monitor (ACSM) with ambient fine aerosol measurements in downtown Atlanta, Georgia. Atmospheric Measurement Techniques 7, 1929–1941. https://doi.org/10.5194/amt-7-1929-2014

Budisulistiorini, S.H., Canagaratna, M.R., Croteau, P.L., Marth, W.J., Baumann, K., Edgerton, E.S., Shaw, S.L., Knipping, E.M., Worsnop, D.R., Jayne, J.T., Gold, A., Surratt, J.D., 2013. Real-Time Continuous Characterization of Secondary Organic Aerosol Derived from Isoprene Epoxydiols in Downtown Atlanta, Georgia, Using the Aerodyne Aerosol Chemical Speciation Monitor. Environ. Sci. Technol. 47, 5686–5694. https://doi.org/10.1021/es400023n

Bulot, F.M.J., Russell, H.S., Rezaei, M., Johnson, M.S., Ossont, S.J.J., Morris, A.K.R., Basford, P.J., Easton, N.H.C., Foster, G.L., Loxham, M., Cox, S.J., 2020. Laboratory Comparison of Low-Cost Particulate Matter Sensors to Measure Transient Events of Pollution. Sensors 20, 2219. https://doi.org/10.3390/s20082219

Burwell-Naney, K., Wilson, S.M., Tarver, S.L., Svendsen, E., Jiang, C., Ogunsakin, O.A., Zhang, H., Campbell, D., Fraser-Rahim, H., 2017. Baseline Air Quality Assessment of Goods Movement Activities before the Port of Charleston Expansion: A Community–University Collaborative. Environmental Justice 10, 1–10. https://doi.org/10.1089/env.2016.0018

Canagaratna, M. r., Jayne, J. t., Jimenez, J. l., Allan, J. d., Alfarra, M. r., Zhang, Q., Onasch, T. b., Drewnick, F., Coe, H., Middlebrook, A., Delia, A., Williams, L. r., Trimborn, A. m., Northway, M. j., DeCarlo, P. f., Kolb, C. e., Davidovits, P., Worsnop, D. r., 2007. Chemical and microphysical characterization of ambient aerosols with the aerodyne aerosol mass spectrometer. Mass Spectrometry Reviews 26, 185–222. https://doi.org/10.1002/mas.20115

Canagaratna, M.R., Jimenez, J.L., Kroll, J.H., Chen, Q., Kessler, S.H., Massoli, P., Hildebrandt Ruiz, L., Fortner, E., Williams, L.R., Wilson, K.R., Surratt, J.D., Donahue, N.M., Jayne, J.T., Worsnop, D.R., 2015. Elemental ratio measurements of organic compounds using aerosol mass spectrometry:

characterization, improved calibration, and implications. Atmospheric Chemistry and Physics 15, 253–272. https://doi.org/10.5194/acp-15-253-2015

Canonaco, F., Crippa, M., Slowik, J.G., Baltensperger, U., Prévôt, A.S.H., 2013. SoFi, an IGOR-based interface for the efficient use of the generalized multilinear engine (ME-2) for the source apportionment: ME-2 application to aerosol mass spectrometer data. Atmos. Meas. Tech. 6, 3649–3661. https://doi.org/10.5194/amt-6-3649-2013

Canonaco, F., Slowik, J.G., Baltensperger, U., Prévôt, A.S.H., 2015. Seasonal differences in oxygenated organic aerosol composition: implications for emissions sources and factor analysis. Atmos. Chem. Phys. 15, 6993–7002. https://doi.org/10.5194/acp-15-6993-2015

Carbone, S., Saarikoski, S., Frey, A., Reyes, F., Reyes, P., Castillo, M., Gramsch, E., Oyola, P., Jayne, J., Worsnop, D.R., Hillamo, R., 2013. Chemical Characterization of Submicron Aerosol Particles in Santiago de Chile. Aerosol Air Qual. Res. 13, 462–473. https://doi.org/10.4209/aaqr.2012.10.0261

Carslaw, D.C., Ropkins, K., 2012. openair — An R package for air quality data analysis. Environmental Modelling & Software 27–28, 52–61. https://doi.org/10.1016/j.envsoft.2011.09.008

Cavalli, F., Viana, M., Yttri, K.E., Genberg, J., Putaud, J.-P., 2010. Toward a standardised thermal-optical protocol for measuring atmospheric organic and elemental carbon: the EUSAAR protocol. Atmospheric Measurement Techniques 3, 79–89. https://doi.org/10.5194/amt-3-79-2010

Cesari, D., Genga, A., Ielpo, P., Siciliano, M., Mascolo, G., Grasso, F.M., Contini, D., 2014. Source apportionment of PM2.5 in the harbour–industrial area of Brindisi (Italy): Identification and estimation of the contribution of in-port ship emissions. Science of The Total Environment 497–498, 392–400. https://doi.org/10.1016/j.scitotenv.2014.08.007

Cesaroni, G., Forastiere, F., Stafoggia, M., Andersen, Z.J., Badaloni, C., Beelen, R., Caracciolo, B., Faire, U. de, Erbel, R., Eriksen, K.T., Fratiglioni, L., Galassi, C., Hampel, R., Heier, M., Hennig, F., Hilding, A., Hoffmann, B., Houthuijs, D., Jöckel, K.-H., Korek, M., Lanki, T., Leander, K., Magnusson, P.K.E., Migliore, E., Ostenson, C.-G., Overvad, K., Pedersen, N.L., J, J.P., Penell, J., Pershagen, G., Pyko, A., Raaschou-Nielsen, O., Ranzi, A., Ricceri, F., Sacerdote, C., Salomaa, V., Swart, W., Turunen, A.W., Vineis, P., Weinmayr, G., Wolf, K., Hoogh, K. de, Hoek, G., Brunekreef, B., Peters, A., 2014. Long term exposure to ambient air pollution and incidence of acute coronary events: prospective cohort study and meta-analysis in 11 European cohorts from the ESCAPE Project. BMJ 348, f7412. https://doi.org/10.1136/bmj.f7412

Chaloulakou, A., Kassomenos, P., Spyrellis, N., Demokritou, P., Koutrakis, P., 2003. Measurements of PM10 and PM2.5 particle concentrations in Athens, Greece. Atmospheric Environment 37, 649–660. https://doi.org/10.1016/S1352-2310(02)00898-1

Chazeau, B., Temime-Roussel, B., Gille, G., Mesbah, B., D'Anna, B., Wortham, H., Marchand, N., 2021. Measurement report: Fourteen months of real-time characterisation of the submicronic aerosol and its atmospheric dynamics at the Marseille–Longchamp supersite. Atmospheric Chemistry and Physics 21, 7293–7319. https://doi.org/10.5194/acp-21-7293-2021

Chen, G., Canonaco, F., Tobler, A., Aas, W., Alastuey, A., Allan, J., Atabakhsh, S., Aurela, M., Baltensperger, U., Bougiatioti, A., De Brito, J.F., Ceburnis, D., Chazeau, B., Chebaicheb, H., Daellenbach, K.R., Ehn, M., El Haddad, I., Eleftheriadis, K., Favez, O., Flentje, H., Font, A., Fossum, K., Freney, E., Gini, M., Green, D.C., Heikkinen, L., Herrmann, H., Kalogridis, A.-C., Keernik, H., Lhotka, R., Lin, C., Lunder, C., Maasikmets, M., Manousakas, M.I., Marchand, N., Marin, C., Marmureanu, L., Mihalopoulos, N., Močnik, G., Nęcki, J., O'Dowd, C., Ovadnevaite, J., Peter, T., Petit, J.-E., Pikridas, M., Matthew Platt, S., Pokorná, P., Poulain, L., Priestman, M., Riffault, V., Rinaldi, M., Różański, K., Schwarz, J., Sciare, J., Simon, L., Skiba, A., Slowik, J.G., Sosedova, Y., Stavroulas, I., Styszko, K., Teinemaa, E., Timonen, H., Tremper, A., Vasilescu, J., Via, M., Vodička, P., Wiedensohler, A., Zografou, O., Cruz Minguillón, M., Prévôt, A.S.H., 2022. European aerosol

phenomenology − 8: Harmonised source apportionment of organic aerosol using 22 Year-long ACSM/AMS datasets. Environment International 166, 107325. https://doi.org/10.1016/j.envint.2022.107325

Chow, J.C., Lowenthal, D.H., Chen, L.-W.A., Wang, X., Watson, J.G., 2015. Mass reconstruction methods for PM2.5: a review. Air Qual Atmos Health 8, 243–263. https://doi.org/10.1007/s11869-015-0338-3

Chow, J.C., Watson, J.G., Doraiswamy, P., Chen, L.-W.A., Sodeman, D.A., Lowenthal, D.H., Park, K., Arnott, W.P., Motallebi, N., 2009. Aerosol light absorption, black carbon, and elemental carbon at the Fresno Supersite, California. Atmospheric Research 93, 874–887. https://doi.org/10.1016/j.atmosres.2009.04.010

Chow, J.C., Watson, J.G., Lowenthal, D.H., Magliano, K.L., 2008. Size-resolved aerosol chemical concentrations at rural and urban sites in Central California, USA. Atmospheric Research, 17th International Conference on Nucleation and Atmospheric Aerosols 90, 243–252. https://doi.org/10.1016/j.atmosres.2008.03.017

Christodoulou, A., Stavroulas, I., Vrekoussis, M., Desservettaz, M., Pikridas, M., Bimenyimana, E., Kushta, J., Ivančič, M., Rigler, M., Goloub, P., Oikonomou, K., Sarda-Estève, R., Savvides, C., Afif, C., Mihalopoulos, N., Sauvage, S., Sciare, J., 2023. Ambient carbonaceous aerosol levels in Cyprus and the role of pollution transport from the Middle East. Atmospheric Chemistry and Physics 23, 6431–6456. https://doi.org/10.5194/acp-23-6431-2023

Cohen, A.J., Brauer, M., Burnett, R., Anderson, H.R., Frostad, J., Estep, K., Balakrishnan, K., Brunekreef, B., Dandona, L., Dandona, R., Feigin, V., Freedman, G., Hubbell, B., Jobling, A., Kan, H., Knibbs, L., Liu, Y., Martin, R., Morawska, L., Pope, C.A., Shin, H., Straif, K., Shaddick, G., Thomas, M., Dingenen, R. van, Donkelaar, A. van, Vos, T., Murray, C.J.L., Forouzanfar, M.H., 2017. Estimates and 25-year trends of the global burden of disease attributable to ambient air pollution: an analysis of data from the Global Burden of Diseases Study 2015. The Lancet 389, 1907–1918. https://doi.org/10.1016/S0140-6736(17)30505-6

Costabile, F., Alas, H., Aufderheide, M., Avino, P., Amato, F., Argentini, S., Barnaba, F., Berico, M., Bernardoni, V., Biondi, R., Casasanta, G., Ciampichetti, S., Calzolai, G., Canepari, S., Conidi, A., Cordelli, E., Di Ianni, A., Di Liberto, L., Facchini, M.C., Facci, A., Frasca, D., Gilardoni, S., Grollino, M.G., Gualtieri, M., Lucarelli, F., Malaguti, A., Manigrasso, M., Montagnoli, M., Nava, S., Perrino, C., Padoan, E., Petenko, I., Querol, X., Simonetti, G., Tranfo, G., Ubertini, S., Valli, G., Valentini, S., Vecchi, R., Volpi, F., Weinhold, K., Wiedensohler, A., Zanini, G., Gobbi, G.P., Petralia, E., 2017. First Results of the "Carbonaceous Aerosol in Rome and Environs (CARE)" Experiment: Beyond Current Standards for PM10. Atmosphere 8, 249. https://doi.org/10.3390/atmos8120249

Crilley, L.R., Bloss, W.J., Yin, J., Beddows, D.C.S., Harrison, R.M., Allan, J.D., Young, D.E., Flynn, M., Williams, P., Zotter, P., Prevot, A.S.H., Heal, M.R., Barlow, J.F., Halios, C.H., Lee, J.D., Szidat, S., Mohr, C., 2015. Sources and contributions of wood smoke during winter in London: assessing local and regional influences. Atmospheric Chemistry and Physics 15, 3149–3171. https://doi.org/10.5194/acp-15-3149-2015

Crilley, L.R., Shaw, M., Pound, R., Kramer, L.J., Price, R., Young, S., Lewis, A.C., Pope, F.D., 2018. Evaluation of a low-cost optical particle counter (Alphasense OPC-N2) for ambient air monitoring. Atmos. Meas. Tech. 11, 709–720. https://doi.org/10.5194/amt-11-709-2018

Crippa, M., Canonaco, F., Lanz, V.A., Äijälä, M., Allan, J.D., Carbone, S., Capes, G., Ceburnis, D., Dall'Osto, M., Day, D.A., DeCarlo, P.F., Ehn, M., Eriksson, A., Freney, E., Hildebrandt Ruiz, L., Hillamo, R., Jimenez, J.L., Junninen, H., Kiendler-Scharr, A., Kortelainen, A.-M., Kulmala, M., Laaksonen, A., Mensah, A.A., Mohr, C., Nemitz, E., O'Dowd, C., Ovadnevaite, J., Pandis, S.N., Petäjä, T., Poulain, L., Saarikoski, S., Sellegri, K., Swietlicki, E., Tiitta, P., Worsnop, D.R., Baltensperger, U., Prévôt, A.S.H., 2014. Organic aerosol components derived from 25 AMS data sets across Europe using a

consistent ME-2 based source apportionment approach. Atmos. Chem. Phys. 14, 6159–6176. https://doi.org/10.5194/acp-14-6159-2014

Crippa, M., El Haddad, I., Slowik, J.G., DeCarlo, P.F., Mohr, C., Heringa, M.F., Chirico, R., Marchand, N., Sciare, J., Baltensperger, U., Prévôt, A.S.H., 2013. Identification of marine and continental aerosol sources in Paris using high resolution aerosol mass spectrometry: AEROSOL SOURCES IN PARIS USING HR-TOF-MS. J. Geophys. Res. Atmos. 118, 1950–1963. https://doi.org/10.1002/jgrd.50151

Cubison, M.J., Ortega, A.M., Hayes, P.L., Farmer, D.K., Day, D., Lechner, M.J., Brune, W.H., Apel, E., Diskin, G.S., Fisher, J.A., Fuelberg, H.E., Hecobian, A., Knapp, D.J., Mikoviny, T., Riemer, D., Sachse, G.W., Sessions, W., Weber, R.J., Weinheimer, A.J., Wisthaler, A., Jimenez, J.L., 2011. Effects of aging on organic aerosol from open biomass burning smoke in aircraft and laboratory studies. Atmospheric Chemistry and Physics 11, 12049–12064. https://doi.org/10.5194/acp-11-12049-2011

Cuesta-Mosquera, A., Močnik, G., Drinovec, L., Müller, T., Pfeifer, S., Minguillón, M.C., Briel, B., Buckley, P., Dudoitis, V., Fernández-García, J., Fernández-Amado, M., Ferreira De Brito, J., Riffault, V., Flentje, H., Heffernan, E., Kalivitis, N., Kalogridis, A.-C., Keernik, H., Marmureanu, L., Luoma, K., Marinoni, A., Pikridas, M., Schauer, G., Serfozo, N., Servomaa, H., Titos, G., Yus-Díez, J., Zioła, N., Wiedensohler, A., 2021. Intercomparison and characterization of 23 Aethalometers under laboratory and ambient air conditions: procedures and unit-to-unit variabilities. Atmospheric Measurement Techniques 14, 3195–3216. https://doi.org/10.5194/amt-14-3195-2021

Cusack, M., Alastuey, A., Pérez, N., Pey, J., Querol, X., 2012. Trends of particulate matter ($PM_{2.5}$) and chemical composition at a regional background site in the Western Mediterranean over the last nine years (2002–2010). Atmospheric Chemistry and Physics 12, 8341–8357. https://doi.org/10.5194/acp-12-8341-2012

Daellenbach, K.R., Uzu, G., Jiang, J., Cassagnes, L.-E., Leni, Z., Vlachou, A., Stefenelli, G., Canonaco, F., Weber, S., Segers, A., Kuenen, J.J.P., Schaap, M., Favez, O., Albinet, A., Aksoyoglu, S., Dommen, J., Baltensperger, U., Geiser, M., El Haddad, I., Jaffrezo, J.-L., Prévôt, A.S.H., 2020. Sources of particulate-matter air pollution and its oxidative potential in Europe. Nature 587, 414–419. https://doi.org/10.1038/s41586-020-2902-8

Dall'Osto, M., Ovadnevaite, J., Ceburnis, D., Martin, D., Healy, R.M., O'Connor, I.P., Kourtchev, I., Sodeau, J.R., Wenger, J.C., O'Dowd, C., 2013. Characterization of urban aerosol in Cork city (Ireland) using aerosol mass spectrometry. Atmos. Chem. Phys. 13, 4997–5015. https://doi.org/10.5194/acp-13-4997-2013

Darbra, R.M., Wooldridge, C., Puig, M., 2020. ESPO Environmental Report 2020 EcoPortsinSights 2020. European Sea Ports Organisation: Brussels, Belgium 30.

DeCarlo, P.F., Slowik, J.G., Worsnop, D.R., Davidovits, P., Jimenez, J.L., 2004. Particle Morphology and Density Characterization by Combined Mobility and Aerodynamic Diameter Measurements. Part 1: Theory. Aerosol Science and Technology 38, 1185–1205. https://doi.org/10.1080/027868290903907

Delfino, R.J., Brummel, S., Wu, J., Stern, H., Ostro, B., Lipsett, M., Winer, A., Street, D.H., Zhang, L., Tjoa, T., Gillen, D.L., 2009. The relationship of respiratory and cardiovascular hospital admissions to the southern California wildfires of 2003. Occupational and Environmental Medicine 66, 189–197. https://doi.org/10.1136/oem.2008.041376

Di, Q., Wang, Yan, Zanobetti, A., Wang, Yun, Koutrakis, P., Choirat, C., Dominici, F., Schwartz, J.D., 2017. Air Pollution and Mortality in the Medicare Population. New England Journal of Medicine 376, 2513–2522. https://doi.org/10.1056/NEJMoa1702747

Dimitriou, K., Kassomenos, P., 2019. Estimation of North African dust contribution on PM10 episodes at four continental Greek cities. Ecological Indicators 106, 105530. https://doi.org/10.1016/j.ecolind.2019.105530

Dimitriou, K., Kassomenos, P., 2017. Aerosol contributions at an urban background site in Eastern Mediterranean – Potential source regions of PAHs in PM10 mass. Science of The Total Environment 598, 563–571. https://doi.org/10.1016/j.scitotenv.2017.04.164

Dimitriou, K., Stavroulas, I., Grivas, G., Chatzidiakos, C., Kosmopoulos, G., Kazantzidis, A., Kourtidis, K., Karagioras, A., Hatzianastassiou, N., Pandis, S.N., Mihalopoulos, N., Gerasopoulos, E., 2023. Intra- and inter-city variability of PM2.5 concentrations in Greece as determined with a low-cost sensor network. Atmospheric Environment 301, 119713. https://doi.org/10.1016/j.atmosenv.2023.119713

Donateo, A., Gregoris, E., Gambaro, A., Merico, E., Giua, R., Nocioni, A., Contini, D., 2014. Contribution of harbour activities and ship traffic to PM2.5, particle number concentrations and PAHs in a port city of the Mediterranean Sea (Italy). Environ Sci Pollut Res 21, 9415–9429. https://doi.org/10.1007/s11356-014-2849-0

Draxler, R.R., Hess, G.D., 1998. An Overview of the HYSPLIT_4 Modelling System for Trajectories, Dispersion, and Deposition. Aust. Meteorol. Mag. 47, 295–308.

Drinovec, L., Močnik, G., Zotter, P., Prévôt, A.S.H., Ruckstuhl, C., Coz, E., Rupakheti, M., Sciare, J., Müller, T., Wiedensohler, A., Hansen, A.D.A., 2015. The "dual-spot" Aethalometer: an improved measurement of aerosol black carbon with real-time loading compensation. Atmospheric Measurement Techniques 8, 1965–1979. https://doi.org/10.5194/amt-8-1965-2015

Dumka, U.C., Tiwari, S., Kaskaoutis, D.G., Soni, V.K., Safai, P.D., Attri, S.D., 2019. Aerosol and pollutant characteristics in Delhi during a winter research campaign. Environ Sci Pollut Res 26, 3771–3794. https://doi.org/10.1007/s11356-018-3885-y

El Haddad, I., D'Anna, B., Temime-Roussel, B., Nicolas, M., Boreave, A., Favez, O., Voisin, D., Sciare, J., George, C., Jaffrezo, J.-L., Wortham, H., Marchand, N., 2013. Towards a better understanding of the origins, chemical composition and aging of oxygenated organic aerosols: case study of a Mediterranean industrialized environment, Marseille. Atmospheric Chemistry and Physics 13, 7875–7894. https://doi.org/10.5194/acp-13-7875-2013

European Environmental Agency, 2020. Air quality in Europe 2020. Publications Office of the European Union, Luxembourg.

Ezzati, M., 2005. Indoor air pollution and health in developing countries. The Lancet 366, 104–106. https://doi.org/10.1016/S0140-6736(05)66845-6

Faber, P., Drewnick, F., Veres, P.R., Williams, J., Borrmann, S., 2013. Anthropogenic sources of aerosol particles in a football stadium: Real-time characterization of emissions from cigarette smoking, cooking, hand flares, and color smoke bombs by high-resolution aerosol mass spectrometry. Atmospheric Environment 77, 1043–1051. https://doi.org/10.1016/j.atmosenv.2013.05.072

Fameli, K.M., Assimakopoulos, V.D., 2015. Development of a road transport emission inventory for Greece and the Greater Athens Area: Effects of important parameters. Science of The Total Environment 505, 770–786. https://doi.org/10.1016/j.scitotenv.2014.10.015

Feenstra, B., Papapostolou, V., Hasheminassab, S., Zhang, H., Boghossian, B.D., Cocker, D., Polidori, A., 2019. Performance evaluation of twelve low-cost PM2.5 sensors at an ambient air monitoring site. Atmospheric Environment 216, 116946. https://doi.org/10.1016/j.atmosenv.2019.116946

Fleming, Z.L., Monks, P.S., Manning, A.J., 2012. Review: Untangling the influence of air-mass history in interpreting observed atmospheric composition. Atmospheric Research 104–105, 1–39. https://doi.org/10.1016/j.atmosres.2011.09.009

Florou, K., Papanastasiou, D.K., Pikridas, M., Kaltsonoudis, C., Louvaris, E., Gkatzelis, G.I., Patoulias, D., Mihalopoulos, N., Pandis, S.N., 2017. The contribution of wood burning and other pollution sources to wintertime organic aerosol levels in two Greek cities. Atmos. Chem. Phys. 17, 3145–3163. https://doi.org/10.5194/acp-17-3145-2017

Fourtziou, L., Liakakou, E., Stavroulas, I., Theodosi, C., Zarmpas, P., Psiloglou, B., Sciare, J., Maggos, T., Bairachtari, K., Bougiatioti, A., Gerasopoulos, E., Sarda-Estève, R., Bonnaire, N., Mihalopoulos, N., 2017. Multi-tracer approach to characterize domestic wood burning in Athens (Greece) during wintertime. Atmospheric Environment 148, 89–101. https://doi.org/10.1016/j.atmosenv.2016.10.011

Fredrickson, A., 2013. The California Coastal Act and Ports: The Unintended Environmental Justice Implications of Preserving California's Coastline. Coastal Management 41, 258–271. https://doi.org/10.1080/08920753.2013.784888

Freney, E., Zhang, Y., Croteau, P., Amodeo, T., Williams, L., Truong, F., Petit, J.-E., Sciare, J., Sarda-Esteve, R., Bonnaire, N., Arumae, T., Aurela, M., Bougiatioti, A., Mihalopoulos, N., Coz, E., Artinano, B., Crenn, V., Elste, T., Heikkinen, L., Poulain, L., Wiedensohler, A., Herrmann, H., Priestman, M., Alastuey, A., Stavroulas, I., Tobler, A., Vasilescu, J., Zanca, N., Canagaratna, M., Carbone, C., Flentje, H., Green, D., Maasikmets, M., Marmureanu, L., Minguillon, M.C., Prevot, A.S.H., Gros, V., Jayne, J., Favez, O., 2019. The second ACTRIS inter-comparison (2016) for Aerosol Chemical Speciation Monitors (ACSM): Calibration protocols and instrument performance evaluations. Aerosol Science and Technology 53, 830–842. https://doi.org/10.1080/02786826.2019.1608901

Fröhlich, R., Crenn, V., Setyan, A., Belis, C.A., Canonaco, F., Favez, O., Riffault, V., Slowik, J.G., Aas, W., Aijälä, M., Alastuey, A., Artiñano, B., Bonnaire, N., Bozzetti, C., Bressi, M., Carbone, C., Coz, E., Croteau, P.L., Cubison, M.J., Esser-Gietl, J.K., Green, D.C., Gros, V., Heikkinen, L., Herrmann, H., Jayne, J.T., Lunder, C.R., Minguillón, M.C., Močnik, G., O'Dowd, C.D., Ovadnevaite, J., Petralia, E., Poulain, L., Priestman, M., Ripoll, A., Sarda-Estève, R., Wiedensohler, A., Baltensperger, U., Sciare, J., Prévôt, A.S.H., 2015. ACTRIS ACSM intercomparison – Part 2: Intercomparison of ME-2 organic source apportionment results from 15 individual, co-located aerosol mass spectrometers. Atmos. Meas. Tech. 8, 2555–2576. https://doi.org/10.5194/amt-8-2555-2015

Gao, M., Cao, J., Seto, E., 2015. A distributed network of low-cost continuous reading sensors to measure spatiotemporal variations of PM2.5 in Xi'an, China. Environmental Pollution 199, 56–65. https://doi.org/10.1016/j.envpol.2015.01.013

Ge, X., Setyan, A., Sun, Y., Zhang, Q., 2012. Primary and secondary organic aerosols in Fresno, California during wintertime: Results from high resolution aerosol mass spectrometry: POA AND SOA IN FRESNO IN WINTER. J. Geophys. Res. 117, n/a-n/a. https://doi.org/10.1029/2012JD018026

Gerasopoulos, E., Amiridis, V., Kazadzis, S., Kokkalis, P., Eleftheratos, K., Andreae, M.O., Andreae, T.W., El-Askary, H., Zerefos, C.S., 2011. Three-year ground based measurements of aerosol optical depth over the Eastern Mediterranean: the urban environment of Athens. Atmospheric Chemistry and Physics 11, 2145–2159. https://doi.org/10.5194/acp-11-2145-2011

Gerasopoulos, E., Kouvarakis, G., Babasakalis, P., Vrekoussis, M., Putaud, J.-P., Mihalopoulos, N., 2006. Origin and variability of particulate matter (PM10) mass concentrations over the Eastern Mediterranean. Atmospheric Environment 40, 4679–4690. https://doi.org/10.1016/j.atmosenv.2006.04.020

Gilardoni, S., Massoli, P., Paglione, M., Giulianelli, L., Carbone, C., Rinaldi, M., Decesari, S., Sandrini, S., Costabile, F., Gobbi, G.P., Pietrogrande, M.C., Visentin, M., Scotto, F., Fuzzi, S., Facchini, M.C., 2016. Direct observation of aqueous secondary organic aerosol from biomass-burning emissions. Proceedings of the National Academy of Sciences 113, 10013–10018. https://doi.org/10.1073/PNAS.1602212113

Gobbi, G.P., Di Liberto, L., Barnaba, F., 2020. Impact of port emissions on EU-regulated and non-regulated air quality indicators: The case of Civitavecchia (Italy). Science of The Total Environment 719, 134984. https://doi.org/10.1016/j.scitotenv.2019.134984

Gratsea, M., Liakakou, E., Mihalopoulos, N., Adamopoulos, A., Tsilibari, E., Gerasopoulos, E., 2017. The combined effect of reduced fossil fuel consumption and increasing biomass combustion on

Athens' air quality, as inferred from long term CO measurements. Science of The Total Environment 592, 115–123. https://doi.org/10.1016/j.scitotenv.2017.03.045
Gray, H.A., 1986. Control of Atmospheric Fine Primary Carbon Particle Concentrations. California Institute of Technology. https://doi.org/10.7907/Z9WM1BBG
Grivas, G., Chaloulakou, A., Kassomenos, P., 2008. An overview of the PM10 pollution problem, in the Metropolitan Area of Athens, Greece. Assessment of controlling factors and potential impact of long range transport. Science of The Total Environment 389, 165–177. https://doi.org/10.1016/j.scitotenv.2007.08.048
Grivas, G., Cheristanidis, S., Chaloulakou, A., 2012. Elemental and organic carbon in the urban environment of Athens. Seasonal and diurnal variations and estimates of secondary organic carbon. Science of The Total Environment 414, 535–545. https://doi.org/10.1016/j.scitotenv.2011.10.058
Grivas, G., Cheristanidis, S., Chaloulakou, A., Koutrakis, P., Mihalopoulos, N., 2018. Elemental Composition and Source Apportionment of Fine and Coarse Particles at Traffic and Urban Background Locations in Athens, Greece. Aerosol Air Qual. Res. 18, 1642–1659. https://doi.org/10.4209/aaqr.2017.12.0567
Grivas, G., Stavroulas, I., Liakakou, E., Kaskaoutis, D.G., Bougiatioti, A., Paraskevopoulou, D., Gerasopoulos, E., Mihalopoulos, N., 2019. Measuring the spatial variability of black carbon in Athens during wintertime. Air Qual Atmos Health 12, 1405–1417. https://doi.org/10.1007/s11869-019-00756-y
Guo, H., Sullivan, A.P., Campuzano-Jost, P., Schroder, J.C., Lopez-Hilfiker, F.D., Dibb, J.E., Jimenez, J.L., Thornton, J.A., Brown, S.S., Nenes, A., Weber, R.J., 2016. Fine particle pH and the partitioning of nitric acid during winter in the northeastern United States. Journal of Geophysical Research: Atmospheres 121, 10,355-10,376. https://doi.org/10.1002/2016JD025311
Guo, J., Zhou, S., Cai, M., Zhao, J., Song, W., Zhao, W., Hu, W., Sun, Y., He, Y., Yang, C., Xu, X., Zhang, Z., Cheng, P., Fan, Q., Hang, J., Fan, S., Wang, Xinming, Wang, Xuemei, 2020. Characterization of submicron particles by time-of-flight aerosol chemical speciation monitor (ToF-ACSM) during wintertime: aerosol composition, sources, and chemical processes in Guangzhou, China. Atmos. Chem. Phys. 20, 7595–7615. https://doi.org/10.5194/acp-20-7595-2020
Gupta, P., Doraiswamy, P., Levy, R., Pikelnaya, O., Maibach, J., Feenstra, B., Polidori, A., Kiros, F., Mills, K.C., 2018. Impact of California Fires on Local and Regional Air Quality: The Role of a Low-Cost Sensor Network and Satellite Observations. GeoHealth 2, 172–181. https://doi.org/10.1029/2018GH000136
Gustafsson, Ö., Ramanathan, V., 2016. Convergence on climate warming by black carbon aerosols. Proceedings of the National Academy of Sciences 113, 4243–4245. https://doi.org/10.1073/pnas.1603570113
Hallquist, M., Wenger, J.C., Baltensperger, U., Rudich, Y., Simpson, D., Claeys, M., Dommen, J., Donahue, N.M., George, C., Goldstein, A.H., Hamilton, J.F., Herrmann, H., Hoffmann, T., Iinuma, Y., Jang, M., Jenkin, M.E., Jimenez, J.L., Kiendler-Scharr, A., Maenhaut, W., McFiggans, G., Mentel, T.F., Monod, A., Prevot, A.S.H., Seinfeld, J.H., Surratt, J.D., Szmigielski, R., Wildt, J., 2009. The formation, properties and impact of secondary organic aerosol: current and emerging issues. Atmos. Chem. Phys. 82.
Hammer, M.S., van Donkelaar, A., Li, C., Lyapustin, A., Sayer, A.M., Hsu, N.C., Levy, R.C., Garay, M.J., Kalashnikova, O.V., Kahn, R.A., Brauer, M., Apte, J.S., Henze, D.K., Zhang, L., Zhang, Q., Ford, B., Pierce, J.R., Martin, R.V., 2020. Global Estimates and Long-Term Trends of Fine Particulate Matter Concentrations (1998–2018). Environ. Sci. Technol. 54, 7879–7890. https://doi.org/10.1021/acs.est.0c01764

Han, L., Yan, H., Xiang, X., Liu, X., Shi, R., Wang, Haibin, Cheng, S., Wang, Haiyan, 2021. Characteristics, evolution, and potential source regions of submicron aerosol in Beijing, China. Atmospheric Environment 246, 118061. https://doi.org/10.1016/j.atmosenv.2020.118061

Hansen, A.D.A., Rosen, H., Novakov, T., 1984. The aethalometer — An instrument for the real-time measurement of optical absorption by aerosol particles. Science of The Total Environment, Carbonaceous Particles in the Atmosphere 1983 36, 191–196. https://doi.org/10.1016/0048-9697(84)90265-1

Hansen, A.D.A., Rosen, H., Novakov, T., 1982. Real-time measurement of the absorption coefficient of aerosol particles. Appl. Opt., AO 21, 3060–3062. https://doi.org/10.1364/AO.21.003060

Harrison, D., Hunter, M.C., Lewis, A.C., Seakins, P.W., Bonsang, B., Gros, V., Kanakidou, M., Touaty, M., Kavouras, I., Mihalopoulos, N., Stephanou, E., Alves, C., Nunes, T., Pio, C., 2001. Ambient isoprene and monoterpene concentrations in a Greek fir (Abies Borisii-regis) forest. Reconciliation with emissions measurements and effects on measured OH concentrations. Atmospheric Environment 35, 4699–4711. https://doi.org/10.1016/S1352-2310(01)00091-7

Hatch, L.E., Creamean, J.M., Ault, A.P., Surratt, J.D., Chan, M.N., Seinfeld, J.H., Edgerton, E.S., Su, Y., Prather, K.A., 2011. Measurements of Isoprene-Derived Organosulfates in Ambient Aerosols by Aerosol Time-of-Flight Mass Spectrometry—Part 2: Temporal Variability and Formation Mechanisms. Environ. Sci. Technol. 45, 8648–8655. https://doi.org/10.1021/es2011836

Hayes, P.L., Carlton, A.G., Baker, K.R., Ahmadov, R., Washenfelder, R.A., Alvarez, S., Rappenglück, B., Gilman, J.B., Kuster, W.C., de Gouw, J.A., Zotter, P., Prévôt, A.S.H., Szidat, S., Kleindienst, T.E., Offenberg, J.H., Ma, P.K., Jimenez, J.L., 2015. Modeling the formation and aging of secondary organic aerosols in Los Angeles during CalNex 2010. Atmospheric Chemistry and Physics 15, 5773–5801. https://doi.org/10.5194/acp-15-5773-2015

He, M., Kuerbanjiang, N., Dhaniyala, S., 2020. Performance characteristics of the low-cost Plantower PMS optical sensor. Aerosol Science and Technology 54, 232–241. https://doi.org/10.1080/02786826.2019.1696015

He, Y., Sun, Y., Wang, Q., Zhou, W., Xu, W., Zhang, Y., Xie, C., Zhao, J., Du, W., Qiu, Y., Lei, L., Fu, P., Wang, Z., Worsnop, D.R., 2019. A Black Carbon-Tracer Method for Estimating Cooking Organic Aerosol From Aerosol Mass Spectrometer Measurements. Geophysical Research Letters 46, 8474–8483. https://doi.org/10.1029/2019GL084092

Healy, R.M., Sofowote, U., Su, Y., Debosz, J., Noble, M., Jeong, C.-H., Wang, J.M., Hilker, N., Evans, G.J., Doerksen, G., Jones, K., Munoz, A., 2017. Ambient measurements and source apportionment of fossil fuel and biomass burning black carbon in Ontario. Atmospheric Environment 161, 34–47. https://doi.org/10.1016/j.atmosenv.2017.04.034

Helin, A., Niemi, J.V., Virkkula, A., Pirjola, L., Teinilä, K., Backman, J., Aurela, M., Saarikoski, S., Rönkkö, T., Asmi, E., Timonen, H., 2018. Characteristics and source apportionment of black carbon in the Helsinki metropolitan area, Finland. Atmospheric Environment 190, 87–98. https://doi.org/10.1016/j.atmosenv.2018.07.022

Hildebrandt, L., Engelhart, G.J., Mohr, C., Kostenidou, E., Lanz, V.A., Bougiatioti, A., DeCarlo, P.F., Prevot, A.S.H., Baltensperger, U., Mihalopoulos, N., Donahue, N.M., Pandis, S.N., 2010. Aged organic aerosol in the Eastern Mediterranean: the Finokalia Aerosol Measurement Experiment – 2008. Atmospheric Chemistry and Physics 10, 4167–4186. https://doi.org/10.5194/acp-10-4167-2010

Houssos, E.E., Lolis, C.J., Gkikas, A., Hatzianastassiou, N., Bartzokas, A., 2012. On the atmospheric circulation characteristics associated with fog in Ioannina, north-western Greece. International Journal of Climatology 32, 1847–1862. https://doi.org/10.1002/joc.2399

Houston, D., Krudysz, M., Winer, A., 2008. Diesel Truck Traffic in Low-Income and Minority Communities Adjacent to Ports: Environmental Justice Implications of Near-Roadway Land Use Conflicts. Transportation Research Record 2067, 38–46. https://doi.org/10.3141/2067-05

Hu, W., Campuzano-Jost, P., Day, D.A., Croteau, P., Canagaratna, M.R., Jayne, J.T., Worsnop, D.R., Jimenez, J.L., 2017. Evaluation of the new capture vapourizer for aerosol mass spectrometers (AMS) through laboratory studies of inorganic species. Atmospheric Measurement Techniques 10, 2897–2921. https://doi.org/10.5194/amt-10-2897-2017

Huang, D.D., Zhu, S., An, J., Wang, Q., Qiao, L., Zhou, M., He, X., Ma, Y., Sun, Y., Huang, C., Yu, J.Z., Zhang, Q., 2021. Comparative Assessment of Cooking Emission Contributions to Urban Organic Aerosol Using Online Molecular Tracers and Aerosol Mass Spectrometry Measurements. Environ. Sci. Technol. 55, 14526–14535. https://doi.org/10.1021/acs.est.1c03280

Hyvärinen, A.-P., Vakkari, V., Laakso, L., Hooda, R.K., Sharma, V.P., Panwar, T.S., Beukes, J.P., van Zyl, P.G., Josipovic, M., Garland, R.M., Andreae, M.O., Pöschl, U., Petzold, A., 2013. Correction for a measurement artifact of the Multi-Angle Absorption Photometer (MAAP) at high black carbon mass concentration levels. Atmospheric Measurement Techniques 6, 81–90. https://doi.org/10.5194/amt-6-81-2013

Intergovernmental Panel On Climate Change, 2023. Climate Change 2021 – The Physical Science Basis: Working Group I Contribution to the Sixth Assessment Report of the Intergovernmental Panel on Climate Change, 1st ed. Cambridge University Press. https://doi.org/10.1017/9781009157896

Ito, K., Mathes, R., Ross, Z., N, ádas A., Thurston, G., Matte, T., 2011. Fine Particulate Matter Constituents Associated with Cardiovascular Hospitalizations and Mortality in New York City. Environmental Health Perspectives 119, 467–473. https://doi.org/10.1289/ehp.1002667

Jayaratne, R., Liu, X., Thai, P., Dunbabin, M., Morawska, L., 2018. The influence of humidity on the performance of a low-cost air particle mass sensor and the effect of atmospheric fog. Atmospheric Measurement Techniques 11, 4883–4890. https://doi.org/10.5194/amt-11-4883-2018

Jayne, J.T., Leard, D.C., Zhang, X., Davidovits, P., Smith, K.A., Kolb, C.E., Worsnop, D.R., 2000. Development of an Aerosol Mass Spectrometer for Size and Composition Analysis of Submicron Particles. Aerosol Science and Technology 33, 49–70. https://doi.org/10.1080/027868200410840

Jiang, Q., Wang, F., Sun, Y., 2019. Analysis of Chemical Composition, Source and Processing Characteristics of Submicron Aerosol during the Summer in Beijing, China. Aerosol Air Qual. Res. 19, 1450–1462. https://doi.org/10.4209/aaqr.2018.12.0480

Jiao, W., Hagler, G., Williams, R., Sharpe, R., Brown, R., Garver, D., Judge, R., Caudill, M., Rickard, J., Davis, M., Weinstock, L., Zimmer-Dauphinee, S., Buckley, K., 2016. Community Air Sensor Network (CAIRSENSE) project: evaluation of low-costsensor performance in a suburban environment in the southeastern UnitedStates. Atmos. Meas. Tech. 9, 5281–5292. https://doi.org/10.5194/amt-9-5281-2016

Jimenez, J.L., Canagaratna, M.R., Donahue, N.M., Prevot, A.S.H., Zhang, Q., Kroll, J.H., DeCarlo, P.F., Allan, J.D., Coe, H., Ng, N.L., Aiken, A.C., Docherty, K.S., Ulbrich, I.M., Grieshop, A.P., Robinson, A.L., Duplissy, J., Smith, J.D., Wilson, K.R., Lanz, V.A., Hueglin, C., Sun, Y.L., Tian, J., Laaksonen, A., Raatikainen, T., Rautiainen, J., Vaattovaara, P., Ehn, M., Kulmala, M., Tomlinson, J.M., Collins, D.R., Cubison, M.J., E., Dunlea, J., Huffman, J.A., Onasch, T.B., Alfarra, M.R., Williams, P.I., Bower, K., Kondo, Y., Schneider, J., Drewnick, F., Borrmann, S., Weimer, S., Demerjian, K., Salcedo, D., Cottrell, L., Griffin, R., Takami, A., Miyoshi, T., Hatakeyama, S., Shimono, A., Sun, J.Y., Zhang, Y.M., Dzepina, K., Kimmel, J.R., Sueper, D., Jayne, J.T., Herndon, S.C., Trimborn, A.M., Williams, L.R., Wood, E.C., Middlebrook, A.M., Kolb, C.E., Baltensperger, U., Worsnop, D.R., 2009. Evolution of Organic Aerosols in the Atmosphere. Science 326, 1525–1529. https://doi.org/10.1126/science.1180353

Jimenez, J.L., Canagaratna, M.R., Drewnick, F., Allan, J.D., Alfarra, M.R., Middlebrook, A.M., Slowik, J.G., Zhang, Q., Coe, H., Jayne, J.T., Worsnop, D.R., 2016. Comment on "The effects of molecular weight and thermal decomposition on the sensitivity of a thermal desorption aerosol mass

spectrometer." Aerosol Science and Technology 50, i–xv. https://doi.org/10.1080/02786826.2016.1205728
Jimenez, J.L., Jayne, J.T., Shi, Q., Kolb, C.E., Worsnop, D.R., Yourshaw, I., Seinfeld, J.H., Flagan, R.C., Zhang, X., Smith, K.A., Morris, J.W., Davidovits, P., 2003. Ambient aerosol sampling using the Aerodyne Aerosol Mass Spectrometer. Journal of Geophysical Research: Atmospheres 108. https://doi.org/10.1029/2001JD001213
Jorga, S.D., Florou, K., Kaltsonoudis, C., Kodros, J.K., Vasilakopoulou, C., Cirtog, M., Fouqueau, A., Picquet-Varrault, B., Nenes, A., Pandis, S.N., 2021. Nighttime chemistry of biomass burning emissions in urban areas: A dual mobile chamber study. Atmospheric Chemistry and Physics 21, 15337–15349. https://doi.org/10.5194/acp-21-15337-2021
Kalivitis, N., Birmili, W., Stock, M., Wehner, B., Massling, A., Wiedensohler, A., Gerasopoulos, E., Mihalopoulos, N., 2008. Particle size distributions in the Eastern Mediterranean troposphere. Atmos. Chem. Phys. 10.
Kalivitis, N., Gerasopoulos, E., Vrekoussis, M., Kouvarakis, G., Kubilay, N., Hatzianastassiou, N., Vardavas, I., Mihalopoulos, N., 2007. Dust transport over the eastern Mediterranean derived from Total Ozone Mapping Spectrometer, Aerosol Robotic Network, and surface measurements. Journal of Geophysical Research: Atmospheres 112. https://doi.org/10.1029/2006JD007510
Kalivitis, N., Kerminen, V.-M., Kouvarakis, G., Stavroulas, I., Tzitzikalaki, E., Kalkavouras, P., Daskalakis, N., Myriokefalitakis, S., Bougiatioti, A., Manninen, H.E., Roldin, P., Petäjä, T., Boy, M., Kulmala, M., Kanakidou, M., Mihalopoulos, N., 2019. Formation and growth of atmospheric nanoparticles in the eastern Mediterranean: results from long-term measurements and process simulations. Atmospheric Chemistry and Physics 19, 2671–2686. https://doi.org/10.5194/acp-19-2671-2019
Kalkavouras, P., Bossioli, E., Bezantakos, S., Bougiatioti, A., Kalivitis, N., Stavroulas, I., Kouvarakis, G., Protonotariou, A.P., Dandou, A., Biskos, G., Mihalopoulos, N., Nenes, A., Tombrou, M., 2017. New particle formation in the southern Aegean Sea during the Etesians: importance for CCN production and cloud droplet number. Atmospheric Chemistry and Physics 17, 175–192. https://doi.org/10.5194/acp-17-175-2017
Kalkavouras, P., Bougiatioti, A., Grivas, G., Stavroulas, I., Kalivitis, N., Liakakou, E., Gerasopoulos, E., Pilinis, C., Mihalopoulos, N., 2020. On the regional aspects of new particle formation in the Eastern Mediterranean: A comparative study between a background and an urban site based on long term observations. Atmospheric Research 239, 104911. https://doi.org/10.1016/j.atmosres.2020.104911
Kallos, G., Kassomenos, P., Pielke, R.A., 1993. Synoptic and mesoscale weather conditions during air pollution episodes in Athens, Greece. Boundary-Layer Meteorol 62, 163–184. https://doi.org/10.1007/BF00705553
Kalogridis, A.-C., Vratolis, S., Liakakou, E., Gerasopoulos, E., Mihalopoulos, N., Eleftheriadis, K., 2018. Assessment of wood burning versus fossil fuel contribution to wintertime black carbon and carbon monoxide concentrations in Athens, Greece. Atmospheric Chemistry and Physics 18, 10219–10236. https://doi.org/10.5194/acp-18-10219-2018
Kaltsonoudis, C., Kostenidou, E., Louvaris, E., Psichoudaki, M., Tsiligiannis, E., Florou, K., Liangou, A., Pandis, S.N., 2017. Characterization of fresh and aged organic aerosol emissions from meat charbroiling. Atmos. Chem. Phys. 17, 7143–7155. https://doi.org/10.5194/acp-17-7143-2017
Kanakidou, M., Mihalopoulos, N., Kindap, T., Im, U., Vrekoussis, M., Gerasopoulos, E., Dermitzaki, E., Unal, A., Koçak, M., Markakis, K., Melas, D., Kouvarakis, G., Youssef, A.F., Richter, A., Hatzianastassiou, N., Hilboll, A., Ebojie, F., Wittrock, F., von Savigny, C., Burrows, J.P., Ladstaetter-Weissenmayer, A., Moubasher, H., 2011. Megacities as hot spots of air pollution in the East Mediterranean. Atmospheric Environment 45, 1223–1235. https://doi.org/10.1016/j.atmosenv.2010.11.048

Kanakidou, M., Seinfeld, J.H., Pandis, S.N., Barnes, I., Dentener, F.J., Facchini, M.C., Van Dingenen, R., Ervens, B., Nenes, A., Nielsen, C.J., Swietlicki, E., Putaud, J.P., Balkanski, Y., Fuzzi, S., Horth, J., Moortgat, G.K., Winterhalter, R., Myhre, C.E.L., Tsigaridis, K., Vignati, E., Stephanou, E.G., Wilson, J., 2005. Organic aerosol and global climate modelling: a review. Atmospheric Chemistry and Physics 5, 1053–1123. https://doi.org/10.5194/acp-5-1053-2005

Kanellopoulos, P.G., Verouti, E., Chrysochou, E., Koukoulakis, K., Bakeas, E., 2021. Primary and secondary organic aerosol in an urban/industrial site: Sources, health implications and the role of plastic enriched waste burning. Journal of Environmental Sciences 99, 222–238. https://doi.org/10.1016/j.jes.2020.06.012

Karagulian, F., Barbiere, M., Kotsev, A., Spinelle, L., Gerboles, M., Lagler, F., Redon, N., Crunaire, S., Borowiak, A., 2019. Review of the Performance of Low-Cost Sensors for Air Quality Monitoring. Atmosphere 10, 506. https://doi.org/10.3390/atmos10090506

Karali, D., Dalatsi, M., Varvatou, C., Spathara, M.E., Rapsomanikis, S., 2018. Fine particulate matter (PM2.5) in ambient air of Xanthi, Greece. Presented at the 18th International Conference on Meteorology, Climatology and Atmospheric Physics, Alexandoupolis, Greece.

Kaskaoutis, D.G., Grivas, G., Stavroulas, I., Bougiatioti, A., Liakakou, E., Dumka, U.C., Gerasopoulos, E., Mihalopoulos, N., 2021a. Apportionment of black and brown carbon spectral absorption sources in the urban environment of Athens, Greece, during winter. Science of The Total Environment 801, 149739. https://doi.org/10.1016/j.scitotenv.2021.149739

Kaskaoutis, D.G., Grivas, G., Stavroulas, I., Liakakou, E., Dumka, U.C., Dimitriou, K., Gerasopoulos, E., Mihalopoulos, N., 2021b. In situ identification of aerosol types in Athens, Greece, based on long-term optical and on online chemical characterization. Atmospheric Environment 246, 118070. https://doi.org/10.1016/j.atmosenv.2020.118070

Kaskaoutis, D.G., Grivas, G., Theodosi, C., Tsagkaraki, M., Paraskevopoulou, D., Stavroulas, I., Liakakou, E., Gkikas, A., Hatzianastassiou, N., Wu, C., Gerasopoulos, E., Mihalopoulos, N., 2020. Carbonaceous Aerosols in Contrasting Atmospheric Environments in Greek Cities: Evaluation of the EC-tracer Methods for Secondary Organic Carbon Estimation. Atmosphere 11, 161. https://doi.org/10.3390/atmos11020161

Kassomenos, P., Flocas, H.A., Lykoudis, S., Petrakis, M., 1998. Analysis of Mesoscale Patterns in Relation to Synoptic Conditionsover an Urban Mediterranean Basin. Theoretical and Applied Climatology 59, 215–229. https://doi.org/10.1007/s007040050025

Kassomenos, P., Kotroni, V., Kallos, G., 1995. Analysis of climatological and air quality observations from Greater Athens Area. Atmospheric Environment 29, 3671–3688. https://doi.org/10.1016/1352-2310(94)00358-R

Kassomenos, P., Vardoulakis, S., Chaloulakou, A., Grivas, G., Borge, R., Lumbreras, J., 2012. Levels, sources and seasonality of coarse particles (PM10–PM2.5) in three European capitals – Implications for particulate pollution control. Atmospheric Environment 54, 337–347. https://doi.org/10.1016/j.atmosenv.2012.02.051

Kassomenos, P.A., Vardoulakis, S., Chaloulakou, A., Paschalidou, A.K., Grivas, G., Borge, R., Lumbreras, J., 2014. Study of PM10 and PM2.5 levels in three European cities: Analysis of intra and inter urban variations. Atmospheric Environment 87, 153–163. https://doi.org/10.1016/j.atmosenv.2014.01.004

Katz, E.F., Guo, H., Campuzano-Jost, P., Day, D.A., Brown, W.L., Boedicker, E., Pothier, M., Lunderberg, D.M., Patel, S., Patel, K., Hayes, P.L., Avery, A., Hildebrandt Ruiz, L., Goldstein, A.H., Vance, M.E., Farmer, D.K., Jimenez, J.L., DeCarlo, P.F., 2021. Quantification of cooking organic aerosol in the indoor environment using aerodyne aerosol mass spectrometers. Aerosol Science and Technology 55, 1099–1114. https://doi.org/10.1080/02786826.2021.1931013

Kazadzis, S., Founda, D., Psiloglou, B.E., Kambezidis, H., Mihalopoulos, N., Sanchez-Lorenzo, A., Meleti, C., Raptis, P.I., Pierros, F., Nabat, P., 2018. Long-term series and trends in surface solar radiation in Athens, Greece. Atmospheric Chemistry and Physics 18, 2395–2411. https://doi.org/10.5194/acp-18-2395-2018

Kelleher, S., Quinn, C., Miller-Lionberg, D., Volckens, J., 2018. A low-cost particulate matter ($PM_{2.5}$) monitor for wildland fire smoke. Atmospheric Measurement Techniques 11, 1087–1097. https://doi.org/10.5194/amt-11-1087-2018

Kelly, K.E., Whitaker, J., Petty, A., Widmer, C., Dybwad, A., Sleeth, D., Martin, R., Butterfield, A., 2017. Ambient and laboratory evaluation of a low-cost particulate matter sensor. Environmental Pollution 221, 491–500. https://doi.org/10.1016/j.envpol.2016.12.039

Kelly, K.E., Xing, W.W., Sayahi, T., Mitchell, L., Becnel, T., Gaillardon, P.-E., Meyer, M., Whitaker, R.T., 2021. Community-Based Measurements Reveal Unseen Differences during Air Pollution Episodes. Environ. Sci. Technol. 55, 120–128. https://doi.org/10.1021/acs.est.0c02341

Kheirbek, I., Wheeler, K., Walters, S., Kass, D., Matte, T., 2013. PM2.5 and ozone health impacts and disparities in New York City: sensitivity to spatial and temporal resolution. Air Qual Atmos Health 6, 473–486. https://doi.org/10.1007/s11869-012-0185-4

Kim, E., Hopke, P.K., Edgerton, E.S., 2003. Source Identification of Atlanta Aerosol by Positive Matrix Factorization. Journal of the Air & Waste Management Association 53, 731–739. https://doi.org/10.1080/10473289.2003.10466209

Kim, S., Park, S., Lee, J., 2019. Evaluation of Performance of Inexpensive Laser Based PM2.5 Sensor Monitors for Typical Indoor and Outdoor Hotspots of South Korea. Applied Sciences 9, 1947. https://doi.org/10.3390/app9091947

Kim, S.-Y., Dutton, S.J., Sheppard, L., Hannigan, M.P., Miller, S.L., Milford, J.B., Peel, J.L., Vedal, S., 2015. The short-term association of selected components of fine particulate matter and mortality in the Denver Aerosol Sources and Health (DASH) study. Environ Health 14, 49. https://doi.org/10.1186/s12940-015-0037-4

Kimbrough, S., Hanley, T., Hagler, G., Baldauf, R., Snyder, M., Brantley, H., 2018. Influential factors affecting black carbon trends at four sites of differing distance from a major highway in Las Vegas. Air Qual Atmos Health 11, 181–196. https://doi.org/10.1007/s11869-017-0519-3

Klemm, R.J., Thomas, E.L., Wyzga, R.E., 2011. The Impact of Frequency and Duration of Air Quality Monitoring: Atlanta, GA, Data Modeling of Air Pollution and Mortality. Journal of the Air & Waste Management Association 61, 1281–1291. https://doi.org/10.1080/10473289.2011.617648

Kodros, J.K., Papanastasiou, D.K., Paglione, M., Masiol, M., Squizzato, S., Florou, K., Skyllakou, K., Kaltsonoudis, C., Nenes, A., Pandis, S.N., 2020. Rapid dark aging of biomass burning as an overlooked source of oxidized organic aerosol. Proceedings of the National Academy of Sciences 117, 33028–33033. https://doi.org/10.1073/pnas.2010365117

Kostenidou, E., Florou, K., Kaltsonoudis, C., Tsiflikiotou, M., Vratolis, S., Eleftheriadis, K., Pandis, S.N., 2015. Sources and chemical characterization of organic aerosol during the summer in the eastern Mediterranean. Atmos. Chem. Phys. 15, 11355–11371. https://doi.org/10.5194/acp-15-11355-2015

Kostenidou, E., Kaltsonoudis, C., Tsiflikiotou, M., Louvaris, E., Russell, L.M., Pandis, S.N., 2013. Burning of olive tree branches: A major organic aerosol source in the Mediterranean. Atmospheric Chemistry and Physics 13, 8797–8811. https://doi.org/10.5194/acp-13-8797-2013

Koulouri, E., Saarikoski, S., Theodosi, C., Markaki, Z., Gerasopoulos, E., Kouvarakis, G., Mäkelä, T., Hillamo, R., Mihalopoulos, N., 2008. Chemical composition and sources of fine and coarse aerosol particles in the Eastern Mediterranean. Atmospheric Environment 42, 6542–6550. https://doi.org/10.1016/j.atmosenv.2008.04.010

Kouvarakis, G., Tsigaridis, K., Kanakidou, M., Mihalopoulos, N., 2000. Temporal variations of surface regional background ozone over Crete Island in the southeast Mediterranean. J. Geophys. Res. 105, 4399–4407. https://doi.org/10.1029/1999JD900984

Kreyling, W.G., Semmler, M., Erbe, F., Mayer, P., Takenaka, S., Schulz, H., Oberdörster, G., Ziesenis, A., 2002. Translocation of Ultrafine Insoluble Iridium Particles from Lung Epithelium to Extrapulmonary Organs Is Size Dependent but Very Low. Journal of Toxicology and Environmental Health, Part A 65, 1513–1530. https://doi.org/10.1080/00984100290071649

Kumar, P., Morawska, L., Martani, C., Biskos, G., Neophytou, M., Di Sabatino, S., Bell, M., Norford, L., Britter, R., 2015. The rise of low-cost sensing for managing air pollution in cities. Environment International 75, 199–205. https://doi.org/10.1016/j.envint.2014.11.019

Kuula, J., Mäkelä, T., Aurela, M., Teinilä, K., Varjonen, S., González, Ó., Timonen, H., 2020. Laboratory evaluation of particle-size selectivity of optical low-cost particulate matter sensors. Atmospheric Measurement Techniques 13, 2413–2423. https://doi.org/10.5194/amt-13-2413-2020

Lack, D.A., Cappa, C.D., 2010. Impact of brown and clear carbon on light absorption enhancement, single scatter albedo and absorption wavelength dependence of black carbon. Atmospheric Chemistry and Physics 10, 4207–4220. https://doi.org/10.5194/acp-10-4207-2010

Laing, J.R., Jaffe, D.A., Arthur J. Sedlacek, I.I.I., 2020. Comparison of Filter-based Absorption Measurements of Biomass Burning Aerosol and Background Aerosol at the Mt. Bachelor Observatory. Aerosol Air Qual. Res. 20, 663–678. https://doi.org/10.4209/aaqr.2019.06.0298

Lanz, V.A., Alfarra, M.R., Baltensperger, U., Buchmann, B., Hueglin, C., Szidat, S., Wehrli, M.N., Wacker, L., Weimer, S., Caseiro, A., Puxbaum, H., Prevot, A.S.H., 2007. Source Attribution of Submicron Organic Aerosols during Wintertime Inversions by Advanced Factor Analysis of Aerosol Mass Spectra [WWW Document]. ACS Publications. https://doi.org/10.1021/es0707207

Lapere, R., Menut, L., Mailler, S., Huneeus, N., 2020. Soccer games and record-breaking PM_{2.5} pollution events in Santiago, Chile. Atmospheric Chemistry and Physics 20, 4681–4694. https://doi.org/10.5194/acp-20-4681-2020

Lathem, T.L., Beyersdorf, A.J., Thornhill, K.L., Winstead, E.L., Cubison, M.J., Hecobian, A., Jimenez, J.L., Weber, R.J., Anderson, B.E., Nenes, A., 2013. Analysis of CCN activity of Arctic aerosol and Canadian biomass burning during summer 2008. Atmospheric Chemistry and Physics 13, 2735–2756. https://doi.org/10.5194/acp-13-2735-2013

Lee, B.P., Li, Y.J., Yu, J.Z., Louie, P.K.K., Chan, C.K., 2015. Characteristics of submicron particulate matter at the urban roadside in downtown Hong Kong—Overview of 4 months of continuous high-resolution aerosol mass spectrometer measurements. Journal of Geophysical Research: Atmospheres 120, 7040–7058. https://doi.org/10.1002/2015JD023311

Lelieveld, J., Berresheim, H., Borrmann, S., Crutzen, P.J., Dentener, F.J., Fischer, H., Feichter, J., Flatau, P.J., Heland, J., Holzinger, R., Korrmann, R., Lawrence, M.G., Levin, Z., Markowicz, K.M., Mihalopoulos, N., Minikin, A., Ramanathan, V., de Reus, M., Roelofs, G.J., Scheeren, H.A., Sciare, J., Schlager, H., Schultz, M., Siegmund, P., Steil, B., Stephanou, E.G., Stier, P., Traub, M., Warneke, C., Williams, J., Ziereis, H., 2002. Global Air Pollution Crossroads over the Mediterranean. Science 298, 794–799. https://doi.org/10.1126/science.1075457

Lelieveld, J., Evans, J.S., Fnais, M., Giannadaki, D., Pozzer, A., 2015. The contribution of outdoor air pollution sources to premature mortality on a global scale. Nature 525, 367–371. https://doi.org/10.1038/nature15371

Lelieveld, J., Hadjinicolaou, P., Kostopoulou, E., Chenoweth, J., El Maayar, M., Giannakopoulos, C., Hannides, C., Lange, M.A., Tanarhte, M., Tyrlis, E., Xoplaki, E., 2012. Climate change and impacts in the Eastern Mediterranean and the Middle East. Climatic Change 114, 667–687. https://doi.org/10.1007/s10584-012-0418-4

Lelieveld, J., Pozzer, A., Pöschl, U., Fnais, M., Haines, A., Münzel, T., 2020. Loss of life expectancy from air pollution compared to other risk factors: a worldwide perspective. Cardiovascular Research 116, 1910–1917. https://doi.org/10.1093/cvr/cvaa025

Levy, J.I., Diez, D., Dou, Y., Barr, C.D., Dominici, F., 2012. A Meta-Analysis and Multisite Time-Series Analysis of the Differential Toxicity of Major Fine Particulate Matter Constituents. American Journal of Epidemiology 175, 1091–1099. https://doi.org/10.1093/aje/kwr457

Levy Zamora, M., Xiong, F., Gentner, D., Kerkez, B., Kohrman-Glaser, J., Koehler, K., 2019. Field and Laboratory Evaluations of the Low-Cost Plantower Particulate Matter Sensor. Environ. Sci. Technol. 53, 838–849. https://doi.org/10.1021/acs.est.8b05174

Li, Jianjun, Wang, G., Wu, C., Cao, C., Ren, Y., Wang, J., Li, Jin, Cao, J., Zeng, L., Zhu, T., 2018. Characterization of isoprene-derived secondary organic aerosols at a rural site in North China Plain with implications for anthropogenic pollution effects. Sci Rep 8, 535. https://doi.org/10.1038/s41598-017-18983-7

Liakakou, E., Kaskaoutis, D.G., Grivas, G., Stavroulas, I., Tsagkaraki, M., Paraskevopoulou, D., Bougiatioti, A., Dumka, U.C., Gerasopoulos, E., Mihalopoulos, N., 2020a. Long-term brown carbon spectral characteristics in a Mediterranean city (Athens). Science of The Total Environment 708, 135019. https://doi.org/10.1016/j.scitotenv.2019.135019

Liakakou, E., Stavroulas, I., Kaskaoutis, D.G., Grivas, G., Paraskevopoulou, D., Dumka, U.C., Tsagkaraki, M., Bougiatioti, A., Oikonomou, K., Sciare, J., Gerasopoulos, E., Mihalopoulos, N., 2020b. Long-term variability, source apportionment and spectral properties of black carbon at an urban background site in Athens, Greece. Atmospheric Environment 222, 117137. https://doi.org/10.1016/j.atmosenv.2019.117137

Liang, C., Wang, S., Hu, R., Huang, G., Xie, J., Zhao, B., Li, Y., Zhu, W., Guo, S., Jiang, J., Hao, J., 2023. Molecular tracers, mass spectral tracers and oxidation of organic aerosols emitted from cooking and fossil fuel burning sources. Science of The Total Environment 868, 161635. https://doi.org/10.1016/j.scitotenv.2023.161635

Lianou, M., Chalbot, M.-C., Kotronarou, A., Kavouras, I.G., Karakatsani, A., Katsouyanni, K., Puustinnen, A., Hameri, K., Vallius, M., Pekkanen, J., Meddings, C., Harrison, R.M., Thomas, S., Ayres, J.G., Brink, H. ten, Kos, G., Meliefste, K., Hartog, J.J. de, Hoek, G., 2007. Dependence of Home Outdoor Particulate Mass and Number Concentrations on Residential and Traffic Features in Urban Areas. Journal of the Air & Waste Management Association 57, 1507–1517. https://doi.org/10.3155/1047-3289.57.12.1507

Lin, C., Ceburnis, D., Xu, W., Heffernan, E., Hellebust, S., Gallagher, J., Huang, R.-J., O'Dowd, C., Ovadnevaite, J., 2020. The impact of traffic on air quality in Ireland: insights from the simultaneous kerbside and suburban monitoring of submicron aerosols. Atmos. Chem. Phys. 20, 10513–10529. https://doi.org/10.5194/acp-20-10513-2020

Lippmann, M., Chen, L.-C., Gordon, T., Ito, K., Thurston, G.D., 2013. National Particle Component Toxicity (NPACT) Initiative: integrated epidemiologic and toxicologic studies of the health effects of particulate matter components. Res Rep Health Eff Inst 5–13.

Lipsett, M.J., Ostro, B.D., Reynolds, P., Goldberg, D., Hertz, A., Jerrett, M., Smith, D.F., Garcia, C., Chang, E.T., Bernstein, L., 2011. Long-Term Exposure to Air Pollution and Cardiorespiratory Disease in the California Teachers Study Cohort. Am J Respir Crit Care Med 184, 828–835. https://doi.org/10.1164/rccm.201012-2082OC

Liu, C., Chen, R., Sera, F., Vicedo-Cabrera, A.M., Guo, Y., Tong, S., Coelho, M.S.Z.S., Saldiva, P.H.N., Lavigne, E., Matus, P., Valdes Ortega, N., Osorio Garcia, S., Pascal, M., Stafoggia, M., Scortichini, M., Hashizume, M., Honda, Y., Hurtado-Díaz, M., Cruz, J., Nunes, B., Teixeira, J.P., Kim, H., Tobias, A., Íñiguez, C., Forsberg, B., Åström, C., Ragettli, M.S., Guo, Y.-L., Chen, B.-Y., Bell, M.L., Wright, C.Y., Scovronick, N., Garland, R.M., Milojevic, A., Kyselý, J., Urban, A., Orru, H., Indermitte, E.,

Jaakkola, J.J.K., Ryti, N.R.I., Katsouyanni, K., Analitis, A., Zanobetti, A., Schwartz, J., Chen, J., Wu, T., Cohen, A., Gasparrini, A., Kan, H., 2019. Ambient Particulate Air Pollution and Daily Mortality in 652 Cities. N Engl J Med 381, 705–715. https://doi.org/10.1056/NEJMoa1817364

Liu, P.S.K., Deng, R., Smith, K.A., Williams, L.R., Jayne, J.T., Canagaratna, M.R., Moore, K., Onasch, T.B., Worsnop, D.R., Deshler, T., 2007. Transmission Efficiency of an Aerodynamic Focusing Lens System: Comparison of Model Calculations and Laboratory Measurements for the Aerodyne Aerosol Mass Spectrometer. Aerosol Science and Technology 41, 721–733. https://doi.org/10.1080/02786820701422278

Liu, T., Wang, Z., Huang, D.D., Wang, X., Chan, C.K., 2018a. Significant Production of Secondary Organic Aerosol from Emissions of Heated Cooking Oils. Environ. Sci. Technol. Lett. 5, 32–37. https://doi.org/10.1021/acs.estlett.7b00530

Liu, T., Wang, Z., Wang, X., Chan, C.K., 2018b. Primary and secondary organic aerosol from heated cooking oil emissions. Atmos. Chem. Phys. 18, 11363–11374. https://doi.org/10.5194/acp-18-11363-2018

Lu, G., Brook, J.R., Rami Alfarra, M., Anlauf, K., Richard Leaitch, W., Sharma, S., Wang, D., Worsnop, D.R., Phinney, L., 2006. Identification and characterization of inland ship plumes over Vancouver, BC. Atmospheric Environment, The Pacific 2001 Air Quality Study II 40, 2767–2782. https://doi.org/10.1016/j.atmosenv.2005.12.054

Magi, B.I., Cupini, C., Francis, J., Green, M., Hauser, C., 2020. Evaluation of PM2.5 measured in an urban setting using a low-cost optical particle counter and a Federal Equivalent Method Beta Attenuation Monitor. Aerosol Science and Technology 54, 147–159. https://doi.org/10.1080/02786826.2019.1619915

Mahajan, S., Kumar, P., 2020. Evaluation of low-cost sensors for quantitative personal exposure monitoring. Sustainable Cities and Society 57, 102076. https://doi.org/10.1016/j.scs.2020.102076

Malings, C., Tanzer, R., Hauryliuk, A., Saha, P.K., Robinson, A.L., Presto, A.A., Subramanian, R., 2020. Fine particle mass monitoring with low-cost sensors: Corrections and long-term performance evaluation. Aerosol Science and Technology 54, 160–174. https://doi.org/10.1080/02786826.2019.1623863

Mallet, M.D., D'Anna, B., Même, A., Bove, M.C., Cassola, F., Pace, G., Desboeufs, K., Di Biagio, C., Doussin, J.-F., Maille, M., Massabò, D., Sciare, J., Zapf, P., di Sarra, A.G., Formenti, P., 2019. Summertime surface PM_1 aerosol composition and size by source region at the Lampedusa island in the central Mediterranean Sea. Atmospheric Chemistry and Physics 19, 11123–11142. https://doi.org/10.5194/acp-19-11123-2019

Manalis, N., Grivas, G., Protonotarios, V., Moutsatsou, A., Samara, C., Chaloulakou, A., 2005. Toxic metal content of particulate matter (PM10), within the Greater Area of Athens. Chemosphere 60, 557–566. https://doi.org/10.1016/j.chemosphere.2005.01.003

Mannucci, P.M., Franchini, M., 2017. Health Effects of Ambient Air Pollution in Developing Countries. International Journal of Environmental Research and Public Health 14, 1048. https://doi.org/10.3390/ijerph14091048

Mariani, R.L., de Mello, W.Z., 2007. PM2.5–10, PM2.5 and associated water-soluble inorganic species at a coastal urban site in the metropolitan region of Rio de Janeiro. Atmospheric Environment 41, 2887–2892. https://doi.org/10.1016/j.atmosenv.2006.12.009

Markou, M.T., Kassomenos, P., 2010. Cluster analysis of five years of back trajectories arriving in Athens, Greece. Atmospheric Research, International Conference on Nucleation and Atmospheric Aerosols (Part 1) 98, 438–457. https://doi.org/10.1016/j.atmosres.2010.08.006

Martenies, S.E., Milando, C.W., Williams, G.O., Batterman, S.A., 2017. Disease and Health Inequalities Attributable to Air Pollutant Exposure in Detroit, Michigan. International Journal of Environmental Research and Public Health 14, 1243. https://doi.org/10.3390/ijerph14101243

Massoud, R., Shihadeh, Alan.L., Roumié, M., Youness, M., Gerard, J., Saliba, N., Zaarour, R., Abboud, M., Farah, W., Saliba, N.A., 2011. Intraurban variability of PM10 and PM2.5 in an Eastern Mediterranean city. Atmospheric Research 101, 893–901. https://doi.org/10.1016/j.atmosres.2011.05.019

Maynard, A.D., Kuempel, E.D., 2005. Airborne Nanostructured Particles and Occupational Health. J Nanopart Res 7, 587–614. https://doi.org/10.1007/s11051-005-6770-9

Mehadi, A., Moosmüller, H., Campbell, D.E., Ham, W., Schweizer, D., Tarnay, L., Hunter, J., 2020. Laboratory and field evaluation of real-time and near real-time PM $_{2.5}$ smoke monitors. Journal of the Air & Waste Management Association 70, 158–179. https://doi.org/10.1080/10962247.2019.1654036

Merico, E., Cesari, D., Gregoris, E., Gambaro, A., Cordella, M., Contini, D., 2021. Shipping and Air Quality in Italian Port Cities: State-of-the-Art Analysis of Available Results of Estimated Impacts. Atmosphere 12, 536. https://doi.org/10.3390/atmos12050536

Merico, E., Conte, M., Grasso, F.M., Cesari, D., Gambaro, A., Morabito, E., Gregoris, E., Orlando, S., Alebić-Juretić, A., Zubak, V., Mifka, B., Contini, D., 2020. Comparison of the impact of ships to size-segregated particle concentrations in two harbour cities of northern Adriatic Sea. Environmental Pollution 266, 115175. https://doi.org/10.1016/j.envpol.2020.115175

Middlebrook, A.M., Bahreini, R., Jimenez, J.L., Canagaratna, M.R., 2012. Evaluation of Composition-Dependent Collection Efficiencies for the Aerodyne Aerosol Mass Spectrometer using Field Data. Aerosol Science and Technology 46, 258–271. https://doi.org/10.1080/02786826.2011.620041

Mihalopoulos, N., Stephanou, E., Kanakidou, M., Pilitsidis, S., Bousquet, P., 1997. Tropospheric aerosol ionic composition in the Eastern Mediterranean region. Tellus B 49, 314–326. https://doi.org/10.1034/j.1600-0889.49.issue3.7.x

Minguillón, M.C., Pérez, N., Marchand, N., Bertrand, A., Temime-Roussel, B., Agrios, K., Szidat, S., Drooge, B. van, Sylvestre, A., Alastuey, A., Reche, C., Ripoll, A., Marco, E., O. Grimalt, J., Querol, X., 2016. Secondary organic aerosol origin in an urban environment: influence of biogenic and fuel combustion precursors. Faraday Discussions 189, 337–359. https://doi.org/10.1039/C5FD00182J

Minguillón, M.C., Ripoll, A., Pérez, N., Prévôt, A.S.H., Canonaco, F., Querol, X., Alastuey, A., 2015. Chemical characterization of submicron regional background aerosols in the western Mediterranean using an Aerosol Chemical Speciation Monitor. Atmospheric Chemistry and Physics 15, 6379–6391. https://doi.org/10.5194/acp-15-6379-2015

Mohr, C., DeCarlo, P.F., Heringa, M.F., Chirico, R., Richter, R., Crippa, M., Querol, X., Baltensperger, U., Prévôt, A.S.H., 2015. Spatial Variation of Aerosol Chemical Composition and Organic Components Identified by Positive Matrix Factorization in the Barcelona Region. Environmental Science and Technology 49, 10421–10430. https://doi.org/10.1021/acs.est.5b02149

Mohr, C., DeCarlo, P.F., Heringa, M.F., Chirico, R., Slowik, J.G., Richter, R., Reche, C., Alastuey, A., Querol, X., Seco, R., Peñuelas, J., Jiménez, J.L., Crippa, M., Zimmermann, R., Baltensperger, U., Prévôt, A.S.H., 2012. Identification and quantification of organic aerosol from cooking and other sources in Barcelona using aerosol mass spectrometer data. Atmos. Chem. Phys. 12, 1649–1665. https://doi.org/10.5194/acp-12-1649-2012

Mohr, C., Huffman, J.A., Cubison, M.J., Aiken, A.C., Docherty, K.S., Kimmel, J.R., Ulbrich, I.M., Hannigan, M., Jimenez, J.L., 2009. Characterization of primary organic aerosol emissions from meat cooking, trash burning, and motor vehicles with high-resolution aerosol mass spectrometry and

comparison with ambient and chamber observations. Environmental Science and Technology 43, 2443–2449. https://doi.org/10.1021/es8011518

Mousavi, A., Sowlat, M.H., Lovett, C., Rauber, M., Szidat, S., Boffi, R., Borgini, A., De Marco, C., Ruprecht, A.A., Sioutas, C., 2019. Source apportionment of black carbon (BC) from fossil fuel and biomass burning in metropolitan Milan, Italy. Atmospheric Environment 203, 252–261. https://doi.org/10.1016/j.atmosenv.2019.02.009

Murphy, S.M., Agrawal, H., Sorooshian, A., Padró, L.T., Gates, H., Hersey, S., Welch, W.A., Jung, H., Miller, J.W., Cocker, D.R., Nenes, A., Jonsson, H.H., Flagan, R.C., Seinfeld, J.H., 2009. Comprehensive Simultaneous Shipboard and Airborne Characterization of Exhaust from a Modern Container Ship at Sea. Environ. Sci. Technol. 43, 4626–4640. https://doi.org/10.1021/es802413j

Na, K., Sawant, A.A., Song, C., Cocker, D.R., 2004. Primary and secondary carbonaceous species in the atmosphere of Western Riverside County, California. Atmospheric Environment 38, 1345–1355. https://doi.org/10.1016/j.atmosenv.2003.11.023

Ng, N.L., Canagaratna, M.R., Jimenez, J.L., Zhang, Q., Ulbrich, I.M., Worsnop, D.R., 2011a. Real-Time Methods for Estimating Organic Component Mass Concentrations from Aerosol Mass Spectrometer Data. Environ. Sci. Technol. 45, 910–916. https://doi.org/10.1021/es102951k

Ng, N.L., Herndon, S.C., Trimborn, A., Canagaratna, M.R., Croteau, P.L., Onasch, T.B., Sueper, D., Worsnop, D.R., Zhang, Q., Sun, Y.L., Jayne, J.T., 2011b. An Aerosol Chemical Speciation Monitor (ACSM) for Routine Monitoring of the Composition and Mass Concentrations of Ambient Aerosol. Aerosol Science and Technology 45, 780–794. https://doi.org/10.1080/02786826.2011.560211

Olstrup, H., Johansson, C., Forsberg, B., Tornevi, A., Ekebom, A., Meister, K., 2019. A Multi-Pollutant Air Quality Health Index (AQHI) Based on Short-Term Respiratory Effects in Stockholm, Sweden. International Journal of Environmental Research and Public Health 16, 105. https://doi.org/10.3390/ijerph16010105

Orsini, D.A., Ma, Y., Sullivan, A., Sierau, B., Baumann, K., Weber, R.J., 2003. Refinements to the particle-into-liquid sampler (PILS) for ground and airborne measurements of water soluble aerosol composition. Atmospheric Environment 37, 1243–1259. https://doi.org/10.1016/S1352-2310(02)01015-4

Ostro, B., Malig, B., Hasheminassab, S., Berger, K., Chang, E., Sioutas, C., 2016. Associations of Source-Specific Fine Particulate Matter With Emergency Department Visits in California. American Journal of Epidemiology 184, 450–459. https://doi.org/10.1093/aje/kwv343

Ots, R., Vieno, M., Allan, J.D., Reis, S., Nemitz, E., Young, D.E., Coe, H., Di Marco, C., Detournay, A., Mackenzie, I.A., Green, D.C., Heal, M.R., 2016. Model simulations of cooking organic aerosol (COA) over the UK using estimates of emissions based on measurements at two sites in London. Atmospheric Chemistry and Physics 16, 13773–13789. https://doi.org/10.5194/acp-16-13773-2016

Ouimette, J.R., Malm, W.C., Schichtel, B.A., Sheridan, P.J., Andrews, E., Ogren, J.A., Arnott, W.P., 2022. Evaluating the PurpleAir monitor as an aerosol light scattering instrument. Atmospheric Measurement Techniques 15, 655–676. https://doi.org/10.5194/amt-15-655-2022

Paatero, P., 1999. The Multilinear Engine—A Table-Driven, Least Squares Program for Solving Multilinear Problems, Including the *n* -Way Parallel Factor Analysis Model. Journal of Computational and Graphical Statistics 8, 854–888. https://doi.org/10.1080/10618600.1999.10474853

Paatero, P., Hopke, P.K., 2009. Rotational tools for factor analytic models. Journal of Chemometrics 23, 91–100. https://doi.org/10.1002/CEM.1197

Paatero, P., Hopke, P.K., 2003. Discarding or downweighting high-noise variables in factor analytic models. Analytica Chimica Acta 490, 277–289. https://doi.org/10.1016/S0003-2670(02)01643-4

Paatero, P., Hopke, P.K., Song, X.H., Ramadan, Z., 2002. Understanding and controlling rotations in factor analytic models. Chemometrics and Intelligent Laboratory Systems 60, 253–264. https://doi.org/10.1016/S0169-7439(01)00200-3

Paatero, P., Tapper, U., 1994. Positive matrix factorization: A non-negative factor model with optimal utilization of error estimates of data values. Environmetrics 5, 111–126. https://doi.org/10.1002/env.3170050203

Pandolfi, M., Alastuey, A., Pérez, N., Reche, C., Castro, I., Shatalov, V., Querol, X., 2016. Trends analysis of PM source contributions and chemical tracers in NE Spain during 2004–2014: a multi-exponential approach. Atmospheric Chemistry and Physics 16, 11787–11805. https://doi.org/10.5194/acp-16-11787-2016

Pandolfi, M., Gonzalez-Castanedo, Y., Alastuey, A., de la Rosa, J.D., Mantilla, E., de la Campa, A.S., Querol, X., Pey, J., Amato, F., Moreno, T., 2011. Source apportionment of PM10 and PM2.5 at multiple sites in the strait of Gibraltar by PMF: impact of shipping emissions. Environ Sci Pollut Res 18, 260–269. https://doi.org/10.1007/s11356-010-0373-4

Paraskevopoulou, D., Bougiatioti, A., Stavroulas, I., Fang, T., Lianou, M., Liakakou, E., Gerasopoulos, E., Weber, R., Nenes, A., Mihalopoulos, N., 2019. Yearlong variability of oxidative potential of particulate matter in an urban Mediterranean environment. Atmospheric Environment 206, 183–196. https://doi.org/10.1016/j.atmosenv.2019.02.027

Paraskevopoulou, D., Liakakou, E., Gerasopoulos, E., Mihalopoulos, N., 2015. Sources of atmospheric aerosol from long-term measurements (5years) of chemical composition in Athens, Greece. Science of The Total Environment 527–528, 165–178. https://doi.org/10.1016/j.scitotenv.2015.04.022

Paraskevopoulou, D., Liakakou, E., Gerasopoulos, E., Theodosi, C., Mihalopoulos, N., 2014. Long-term characterization of organic and elemental carbon in the $PM_{2.5}$ fraction: the case of Athens, Greece. Atmospheric Chemistry and Physics 14, 13313–13325. https://doi.org/10.5194/acp-14-13313-2014

Park, H.-S., Kim, R.-E., Park, Y.-M., Hwang, K.-C., Lee, S.-H., Kim, J.-J., Choi, J.-Y., Lee, D.-G., Chang, L.-S., Choi, W., 2020. The Potential of Commercial Sensors for Spatially Dense Short-term Air Quality Monitoring Based on Multiple Short-term Evaluations of 30 Sensor Nodes in Urban Areas in Korea. Aerosol Air Qual. Res. 20, 369–380. https://doi.org/10.4209/aaqr.2019.03.0143

Park, S.S., Ondov, J.M., Harrison, D., Nair, N.P., 2005. Seasonal and shorter-term variations in particulate atmospheric nitrate in Baltimore. Atmospheric Environment 39, 2011–2020. https://doi.org/10.1016/j.atmosenv.2004.12.032

Paschalidou, A.K., Kassomenos, P., Karanikola, P., 2015. Disaggregating the contribution of local dispersion and long-range transport to the high PM10 values measured in a Mediterranean urban environment. Science of The Total Environment 527–528, 119–125. https://doi.org/10.1016/j.scitotenv.2015.04.094

Patel, K., Bhandari, S., Gani, S., Campmier, M.J., Kumar, P., Habib, G., Apte, J., Hildebrandt Ruiz, L., 2021. Sources and Dynamics of Submicron Aerosol during the Autumn Onset of the Air Pollution Season in Delhi, India. ACS Earth Space Chem. 5, 118–128. https://doi.org/10.1021/acsearthspacechem.0c00340

Pateraki, St., Asimakopoulos, D.N., Bougiatioti, A., Maggos, Th., Vasilakos, Ch., Mihalopoulos, N., 2014. Assessment of PM2.5 and PM1 chemical profile in a multiple-impacted Mediterranean urban area: Origin, sources and meteorological dependence. Science of The Total Environment 479–480, 210–220. https://doi.org/10.1016/j.scitotenv.2014.02.008

Pateraki, St., Asimakopoulos, D.N., Maggos, Th., Vasilakos, Ch., 2010. Particulate matter levels in a suburban Mediterranean area: Analysis of a 53-month long experimental campaign. Journal of Hazardous Materials 182, 801–811. https://doi.org/10.1016/j.jhazmat.2010.06.108

Pateraki, St., Assimakopoulos, V.D., Bougiatioti, A., Kouvarakis, G., Mihalopoulos, N., Vasilakos, Ch., 2012. Carbonaceous and ionic compositional patterns of fine particles over an urban Mediterranean area. Science of The Total Environment 424, 251–263. https://doi.org/10.1016/j.scitotenv.2012.02.046

Pawar, H., Sinha, B., 2020. Humidity, density, and inlet aspiration efficiency correction improve accuracy of a low-cost sensor during field calibration at a suburban site in the North-Western Indo-Gangetic plain (NW-IGP). Aerosol Science and Technology 54, 685–703. https://doi.org/10.1080/02786826.2020.1719971

Pennanen, A.S., Sillanpää, M., Hillamo, R., Quass, U., John, A.C., Branis, M., Hůnová, I., Meliefste, K., Janssen, N.A.H., Koskentalo, T., Castaño-Vinyals, G., Bouso, L., Chalbot, M.-C., Kavouras, I.G., Salonen, R.O., 2007. Performance of a high-volume cascade impactor in six European urban environments: Mass measurement and chemical characterization of size-segregated particulate samples. Science of The Total Environment 374, 297–310. https://doi.org/10.1016/j.scitotenv.2007.01.002

Pérez, N., Pey, J., Reche, C., Cortés, J., Alastuey, A., Querol, X., 2016. Impact of harbour emissions on ambient PM10 and PM2.5 in Barcelona (Spain): Evidences of secondary aerosol formation within the urban area. Science of The Total Environment 571, 237–250. https://doi.org/10.1016/j.scitotenv.2016.07.025

Petit, J.-E., Favez, O., Albinet, A., Canonaco, F., 2017. A user-friendly tool for comprehensive evaluation of the geographical origins of atmospheric pollution: Wind and trajectory analyses. Environmental Modelling & Software 88, 183–187. https://doi.org/10.1016/j.envsoft.2016.11.022

Petit, J.-E., Favez, O., Sciare, J., Canonaco, F., Croteau, P., Močnik, G., Jayne, J., Worsnop, D., Leoz-Garziandia, E., 2014. Submicron aerosol source apportionment of wintertime pollution in Paris, France by double positive matrix factorization (PMF^2) using an aerosol chemical speciation monitor (ACSM) and a multi-wavelength Aethalometer. Atmospheric Chemistry and Physics 14, 13773–13787. https://doi.org/10.5194/acp-14-13773-2014

Petit, J.-E., Favez, O., Sciare, J., Crenn, V., Sarda-Estève, R., Bonnaire, N., Močnik, G., Dupont, J.-C., Haeffelin, M., Leoz-Garziandia, E., 2015. Two years of near real-time chemical composition of submicron aerosols in the region of Paris using an Aerosol Chemical Speciation Monitor (ACSM) and a multi-wavelength Aethalometer. Atmospheric Chemistry and Physics 15, 2985–3005. https://doi.org/10.5194/acp-15-2985-2015

Pikridas, M., Bougiatioti, A., Hildebrandt, L., Engelhart, G.J., Kostenidou, E., Mohr, C., Prévôt, A.S.H., Kouvarakis, G., Zarmpas, P., Burkhart, J.F., Lee, B.-H., Psichoudaki, M., Mihalopoulos, N., Pilinis, C., Stohl, A., Baltensperger, U., Kulmala, M., Pandis, S.N., 2010. The Finokalia Aerosol Measurement Experiment – 2008 (FAME-08): an overview. Atmos. Chem. Phys. 10, 6793–6806. https://doi.org/10.5194/acp-10-6793-2010

Pinto, J.P., Lefohn, A.S., Shadwick, D.S., 2004. Spatial Variability of PM2.5 in Urban Areas in the United States. Journal of the Air & Waste Management Association 54, 440–449. https://doi.org/10.1080/10473289.2004.10470919

Pitz, M., Schmid, O., Heinrich, J., Birmili, W., Maguhn, J., Zimmermann, R., Wichmann, H.-E., Peters, A., Cyrys, J., 2008. Seasonal and Diurnal Variation of PM2.5 Apparent Particle Density in Urban Air in Augsburg, Germany. Environ. Sci. Technol. 42, 5087–5093. https://doi.org/10.1021/es7028735

Plaza, J., Gómez-Moreno, F.J., Núñez, L., Pujadas, M., Artíñano, B., 2006. Estimation of secondary organic aerosol formation from semi-continuous OC–EC measurements in a Madrid suburban area. Atmospheric Environment 40, 1134–1147. https://doi.org/10.1016/j.atmosenv.2005.11.007

Pope, C.A., Dockery, D.W., 2006. Health Effects of Fine Particulate Air Pollution: Lines that Connect. Journal of the Air & Waste Management Association 56, 709–742. https://doi.org/10.1080/10473289.2006.10464485

Poulain, L., Spindler, G., Grüner, A., Tuch, T., Stieger, B., van Pinxteren, D., Petit, J.-E., Favez, O., Herrmann, H., Wiedensohler, A., 2020. Multi-year ACSM measurements at the central European research station Melpitz (Germany) – Part 1: Instrument robustness, quality assurance, and impact of upper size cutoff diameter. Atmospheric Measurement Techniques 13, 4973–4994. https://doi.org/10.5194/amt-13-4973-2020

Progiou, A.G., Bakeas, E., Evangelidou, E., Kontogiorgi, Ch., Lagkadinou, E., Sebos, I., 2021. Air pollutant emissions from Piraeus port: External costs and air quality levels. Transportation Research Part D: Transport and Environment 91, 102586. https://doi.org/10.1016/j.trd.2020.102586

Putaud, J.-P., Raes, F., Van Dingenen, R., Brüggemann, E., Facchini, M.-C., Decesari, S., Fuzzi, S., Gehrig, R., Hüglin, C., Laj, P., Lorbeer, G., Maenhaut, W., Mihalopoulos, N., Müller, K., Querol, X., Rodriguez, S., Schneider, J., Spindler, G., Brink, H. ten, Tørseth, K., Wiedensohler, A., 2004. A European aerosol phenomenology—2: chemical characteristics of particulate matter at kerbside, urban, rural and background sites in Europe. Atmospheric Environment 38, 2579–2595. https://doi.org/10.1016/j.atmosenv.2004.01.041

Querol, X., Alastuey, A., Pey, J., Cusack, M., Pérez, N., Mihalopoulos, N., Theodosi, C., Gerasopoulos, E., Kubilay, N., Koçak, M., 2009. Variability in regional background aerosols within the Mediterranean. Atmospheric Chemistry and Physics 9, 4575–4591. https://doi.org/10.5194/acp-9-4575-2009

Raaschou-Nielsen, O., Andersen, Z.J., Beelen, R., Samoli, E., Stafoggia, M., Weinmayr, G., Hoffmann, B., Fischer, P., Nieuwenhuijsen, M.J., Brunekreef, B., Xun, W.W., Katsouyanni, K., Dimakopoulou, K., Sommar, J., Forsberg, B., Modig, L., Oudin, A., Oftedal, B., Schwarze, P.E., Nafstad, P., De Faire, U., Pedersen, N.L., Östenson, C.-G., Fratiglioni, L., Penell, J., Korek, M., Pershagen, G., Eriksen, K.T., Sørensen, M., Tjønneland, A., Ellermann, T., Eeftens, M., Peeters, P.H., Meliefste, K., Wang, M., Bueno-de-Mesquita, B., Key, T.J., de Hoogh, K., Concin, H., Nagel, G., Vilier, A., Grioni, S., Krogh, V., Tsai, M.-Y., Ricceri, F., Sacerdote, C., Galassi, C., Migliore, E., Ranzi, A., Cesaroni, G., Badaloni, C., Forastiere, F., Tamayo, I., Amiano, P., Dorronsoro, M., Trichopoulou, A., Bamia, C., Vineis, P., Hoek, G., 2013. Air pollution and lung cancer incidence in 17 European cohorts: prospective analyses from the European Study of Cohorts for Air Pollution Effects (ESCAPE). The Lancet Oncology 14, 813–822. https://doi.org/10.1016/S1470-2045(13)70279-1

Rajesh, T.A., Ramachandran, S., Dhaker, V.K., 2021. Black carbon aerosols: Relative source strengths of vehicular emissions and residential/open wood burning over an urban and a semi-urban environment. Atmospheric Pollution Research 12, 101060. https://doi.org/10.1016/j.apr.2021.101060

Rattanavaraha, W., Canagaratna, M.R., Budisulistiorini, S.H., Croteau, P.L., Baumann, K., Canonaco, F., Prevot, A.S.H., Edgerton, E.S., Zhang, Z., Jayne, J.T., Worsnop, D.R., Gold, A., Shaw, S.L., Surratt, J.D., 2017. Source apportionment of submicron organic aerosol collected from Atlanta, Georgia, during 2014–2015 using the aerosol chemical speciation monitor (ACSM). Atmospheric Environment 167, 389–402. https://doi.org/10.1016/j.atmosenv.2017.07.055

Reyes-Villegas, E., Green, D.C., Priestman, M., Canonaco, F., Coe, H., Prévôt, A.S.H., Allan, J.D., 2016. Organic aerosol source apportionment in London 2013 with ME-2: exploring the solution space with annual and seasonal analysis. Atmos. Chem. Phys. 16, 15545–15559. https://doi.org/10.5194/acp-16-15545-2016

Rivellini, L.-H., Adam, M.G., Kasthuriarachchi, N., Lee, A.K.Y., 2020. Characterization of carbonaceous aerosols in Singapore: insight from black carbon fragments and trace metal ions detected by a

soot particle aerosol mass spectrometer. Atmospheric Chemistry and Physics 20, 5977–5993. https://doi.org/10.5194/acp-20-5977-2020

Robinson, E.S., Gu, P., Ye, Q., Li, H.Z., Shah, R.U., Apte, J.S., Robinson, A.L., Presto, A.A., 2018. Restaurant Impacts on Outdoor Air Quality: Elevated Organic Aerosol Mass from Restaurant Cooking with Neighborhood-Scale Plume Extents. Environmental Science and Technology 52, 9285–9294. https://doi.org/10.1021/acs.est.8b02654

Rogge, W.F., Hildemann, L.M., Mazurek, M.A., Cass, G.R., Simoneit, B.R.T., 1991. Sources of fine organic aerosol. 1. Charbroilers and meat cooking operations. Environ. Sci. Technol. 25, 1112–1125. https://doi.org/10.1021/es00018a015

Rosenbaum, A., Hartley, S., Holder, C., 2011. Analysis of Diesel Particulate Matter Health Risk Disparities in Selected US Harbor Areas. Am J Public Health 101, S217–S223. https://doi.org/10.2105/AJPH.2011.300190

Saarikoski, S., Carbone, S., Decesari, S., Giulianelli, L., Angelini, F., Canagaratna, M., Ng, N.L., Trimborn, A., Facchini, M.C., Fuzzi, S., Hillamo, R., Worsnop, D., 2012. Chemical characterization of springtime submicrometer aerosol in Po Valley, Italy. Atmospheric Chemistry and Physics 12, 8401–8421. https://doi.org/10.5194/acp-12-8401-2012

Saffari, A., Daher, N., Samara, C., Voutsa, D., Kouras, A., Manoli, E., Karagkiozidou, O., Vlachokostas, C., Moussiopoulos, N., Shafer, M.M., Schauer, J.J., Sioutas, C., 2013. Increased Biomass Burning Due to the Economic Crisis in Greece and Its Adverse Impact on Wintertime Air Quality in Thessaloniki. Environ. Sci. Technol. 47, 13313–13320. https://doi.org/10.1021/es403847h

Sage, A.M., Weitkamp, E.A., Robinson, A.L., Donahue, N.M., 2008. Evolving mass spectra of the oxidized component of organic aerosol: results from aerosol mass spectrometer analyses of aged diesel emissions. Atmospheric Chemistry and Physics 8, 1139–1152. https://doi.org/10.5194/acp-8-1139-2008

Saha, P.K., Presto, A.A., Hankey, S., Murphy, B.N., Allen, C., Zhang, W., Marshall, J.D., Robinson, A.L., 2022. National Exposure Models for Source-Specific Primary Particulate Matter Concentrations Using Aerosol Mass Spectrometry Data. Environ. Sci. Technol. 56, 14284–14295. https://doi.org/10.1021/acs.est.2c03398

Sahu, R., Dixit, K.K., Mishra, S., Kumar, P., Shukla, A.K., Sutaria, R., Tiwari, S., Tripathi, S.N., 2020. Validation of Low-Cost Sensors in Measuring Real-Time PM10 Concentrations at Two Sites in Delhi National Capital Region. Sensors 20, 1347. https://doi.org/10.3390/s20051347

Salcedo, D., Alvarez-Ospina, H., Peralta, O., Castro, T., 2018. PM1 Chemical Characterization during the ACU15 Campaign, South of Mexico City. Atmosphere 9, 232. https://doi.org/10.3390/atmos9060232

Sandradewi, J., Prévôt, A.S.H., Szidat, S., Perron, N., Alfarra, M.R., Lanz, V.A., Weingartner, E., Baltensperger, U., 2008. Using Aerosol Light Absorption Measurements for the Quantitative Determination of Wood Burning and Traffic Emission Contributions to Particulate Matter. Environ. Sci. Technol. 42, 3316–3323. https://doi.org/10.1021/es702253m

Santos, F., Longo, K., Guenther, A., Kim, S., Gu, D., Oram, D., Forster, G., Lee, J., Hopkins, J., Brito, J., Freitas, S., 2018. Biomass burning emission disturbances of isoprene oxidation in a tropical forest. Atmospheric Chemistry and Physics 18, 12715–12734. https://doi.org/10.5194/acp-18-12715-2018

Sayahi, T., Butterfield, A., Kelly, K.E., 2019a. Long-term field evaluation of the Plantower PMS low-cost particulate matter sensors. Environmental Pollution 245, 932–940. https://doi.org/10.1016/j.envpol.2018.11.065

Sayahi, T., Kaufman, D., Becnel, T., Kaur, K., Butterfield, A.E., Collingwood, S., Zhang, Y., Gaillardon, P.-E., Kelly, K.E., 2019b. Development of a calibration chamber to evaluate the performance of low-

cost particulate matter sensors. Environmental Pollution 255, 113131. https://doi.org/10.1016/j.envpol.2019.113131
Schulze, B.C., Wallace, H.W., Bui, A.T., Flynn, J.H., Erickson, M.H., Alvarez, S., Dai, Q., Usenko, S., Sheesley, R.J., Griffin, R.J., 2018. The impacts of regional shipping emissions on the chemical characteristics of coastal submicron aerosols near Houston, TX. Atmospheric Chemistry and Physics 18, 14217–14241. https://doi.org/10.5194/acp-18-14217-2018
Sciare, J., Bardouki, H., Moulin, C., Mihalopoulos, N., 2003a. Aerosol sources and their contribution to the chemical composition of aerosols in the Eastern Mediterranean Sea during summertime. Atmospheric Chemistry and Physics 3, 291–302. https://doi.org/10.5194/acp-3-291-2003
Sciare, J., Cachier, H., Oikonomou, K., Ausset, P., Sarda-Estève, R., Mihalopoulos, N., 2003b. Characterization of carbonaceous aerosols during the MINOS campaign in Crete, July–August 2001: a multi-analytical approach. Atmospheric Chemistry and Physics 3, 1743–1757. https://doi.org/10.5194/acp-3-1743-2003
Sciare, J., Oikonomou, K., Cachier, H., Mihalopoulos, N., Andreae, M.O., Maenhaut, W., Sarda-Estève, R., 2005. Aerosol mass closure and reconstruction of the light scattering coefficient over the Eastern Mediterranean Sea during the MINOS campaign. Atmospheric Chemistry and Physics 5, 2253–2265. https://doi.org/10.5194/acp-5-2253-2005
Sciare, J., Oikonomou, K., Favez, O., Liakakou, E., Markaki, Z., Cachier, H., Mihalopoulos, N., 2008. Long-term measurements of carbonaceous aerosols in the Eastern Mediterranean: evidence of long-range transport of biomass burning. Atmos. Chem. Phys. 13.
Seinfeld, J.H., Pandis, S.N., 2016. Atmospheric Chemistry and Physics: From Air Pollution to Climate Change. John Wiley & Sons.
Shah, R.U., Robinson, E.S., Gu, P., Apte, J.S., Marshall, J.D., Robinson, A.L., Presto, A.A., 2020. Socio-economic disparities in exposure to urban restaurant emissions are larger than for traffic. Environmental Research Letters 15. https://doi.org/10.1088/1748-9326/abbc92
Shah, R.U., Robinson, E.S., Gu, P., Robinson, A.L., Apte, J.S., Presto, A.A., 2018. High-spatial-resolution mapping and source apportionment of aerosol composition in Oakland, California, using mobile aerosol mass spectrometry. Atmos. Chem. Phys. 18, 16325–16344. https://doi.org/10.5194/acp-18-16325-2018
Shi, L., Zanobetti, A., Kloog, I., Coull, B.A., Koutrakis, P., Melly, S.J., Schwartz, J.D., 2016. Low-Concentration PM2.5 and Mortality: Estimating Acute and Chronic Effects in a Population-Based Study. Environmental Health Perspectives 124, 46–52. https://doi.org/10.1289/ehp.1409111
Shrivastava, M.K., Subramanian, R., Rogge, W.F., Robinson, A.L., 2007. Sources of organic aerosol: Positive matrix factorization of molecular marker data and comparison of results from different source apportionment models. Atmospheric Environment 41, 9353–9369. https://doi.org/10.1016/j.atmosenv.2007.09.016
Si, M., Xiong, Y., Du, S., Du, K., 2020. Evaluation and calibration of a low-cost particle sensor in ambient conditions using machine-learning methods. Atmospheric Measurement Techniques 13, 1693–1707. https://doi.org/10.5194/amt-13-1693-2020
Sindosi, O.A., Markozannes, G., Rizos, E., Ntzani, E., 2019. Effects of economic crisis on air quality in Ioannina, Greece. Journal of Environmental Science and Health, Part A 54, 768–781. https://doi.org/10.1080/10934529.2019.1592534
Siouti, E., Skyllakou, K., Kioutsioukis, I., Ciarelli, G., Pandis, S.N., 2021. Simulation of the cooking organic aerosol concentration variability in an urban area. Atmospheric Environment 265, 118710. https://doi.org/10.1016/j.atmosenv.2021.118710
Sirois, A., Bottenheim, J.W., 1995. Use of backward trajectories to interpret the 5-year record of PAN and O3 ambient air concentrations at Kejimkujik National Park, Nova Scotia. Journal of Geophysical Research: Atmospheres 100, 2867–2881. https://doi.org/10.1029/94JD02951

Siskos, P.A., Bakeas, E.B., Lioli, I., Smirnioudi, V.N., Koutrakis, P., 2001. Chemical Characterization of PM2.5 Aerosols in Athens-Greece. Environmental Technology 22, 687–695. https://doi.org/10.1080/09593332208618241

Sorte, S., Rodrigues, V., Borrego, C., Monteiro, A., 2020. Impact of harbour activities on local air quality: A review. Environmental Pollution 257, 113542. https://doi.org/10.1016/j.envpol.2019.113542

Srivastava, D., Favez, O., Petit, J.-E., Zhang, Y., Sofowote, U.M., Hopke, P.K., Bonnaire, N., Perraudin, E., Gros, V., Villenave, E., Albinet, A., 2019. Speciation of organic fractions does matter for aerosol source apportionment. Part 3: Combining off-line and on-line measurements. Science of The Total Environment 690, 944–955. https://doi.org/10.1016/j.scitotenv.2019.06.378

Stavroulas, I., Bougiatioti, A., Grivas, G., Paraskevopoulou, D., Tsagkaraki, M., Zarmpas, P., Liakakou, E., Gerasopoulos, E., Mihalopoulos, N., 2019. Sources and processes that control the submicron organic aerosol composition in an urban Mediterranean environment (Athens): a high temporal-resolution chemical composition measurement study. Atmospheric Chemistry and Physics 19, 901–919. https://doi.org/10.5194/acp-19-901-2019

Stavroulas, I., Grivas, G., Liakakou, E., Kalkavouras, P., Bougiatioti, A., Kaskaoutis, D.G., Lianou, M., Papoutsidaki, K., Tsagkaraki, M., Zarmpas, P., Gerasopoulos, E., Mihalopoulos, N., 2021. Online Chemical Characterization and Sources of Submicron Aerosol in the Major Mediterranean Port City of Piraeus, Greece. Atmosphere 12, 1686. https://doi.org/10.3390/atmos12121686

Stavroulas, I., Grivas, G., Michalopoulos, P., Liakakou, E., Bougiatioti, A., Kalkavouras, P., Fameli, K., Hatzianastassiou, N., Mihalopoulos, N., Gerasopoulos, E., 2020. Field Evaluation of Low-Cost PM Sensors (Purple Air PA-II) Under Variable Urban Air Quality Conditions, in Greece. Atmosphere 11, 926. https://doi.org/10.3390/atmos11090926

Stein, A.F., Draxler, R.R., Rolph, G.D., Stunder, B.J.B., Cohen, M.D., Ngan, F., 2015. NOAA's HYSPLIT Atmospheric Transport and Dispersion Modeling System. Bulletin of the American Meteorological Society 96, 2059–2077. https://doi.org/10.1175/BAMS-D-14-00110.1

Stocker, T., Qin, D. (Eds.), 2013. Climate change 2013: the physical science basis: summary for policymakers, a report of working group I of the IPCC: technical summary, a report accepted by working group I of the IPCC but not approved in detail: and frequently asked questions: part of the working group I contribution to the fifth assessment report of the intergovernmental panel on climate change. WMO, UNEP, s.l.

Strickland, M.J., Darrow, L.A., Klein, M., Flanders, W.D., Sarnat, J.A., Waller, L.A., Sarnat, S.E., Mulholland, J.A., Tolbert, P.E., 2010. Short-term Associations between Ambient Air Pollutants and Pediatric Asthma Emergency Department Visits. Am J Respir Crit Care Med 182, 307–316. https://doi.org/10.1164/rccm.200908-1201OC

Struckmeier, C., Drewnick, F., Fachinger, F., Gobbi, G.P., Borrmann, S., 2016. Atmospheric aerosols in Rome, Italy: sources, dynamics and spatial variations during two seasons. Atmos. Chem. Phys. 16, 15277–15299. https://doi.org/10.5194/acp-16-15277-2016

Sun, C., Lee, B.P., Huang, D., Jie Li, Y., Schurman, M.I., Louie, P.K.K., Luk, C., Chan, C.K., 2016. Continuous measurements at the urban roadside in an Asian megacity by Aerosol Chemical Speciation Monitor (ACSM): particulate matter characteristics during fall and winter seasons in Hong Kong. Atmos. Chem. Phys. 16, 1713–1728. https://doi.org/10.5194/acp-16-1713-2016

Sun, J.Y., Wu, C., Wu, D., Cheng, C., Li, M., Li, L., Deng, T., Yu, J.Z., Li, Y.J., Zhou, Q., Liang, Y., Sun, T., Song, L., Cheng, P., Yang, W., Pei, C., Chen, Y., Cen, Y., Nian, H., Zhou, Z., 2020. Amplification of black carbon light absorption induced by atmospheric aging: temporal variation at seasonal and diel scales in urban Guangzhou. Atmos. Chem. Phys. 20, 2445–2470. https://doi.org/10.5194/acp-20-2445-2020

Sun, Y., Jiang, Q., Wang, Z., Fu, P., Li, J., Yang, T., Yin, Y., 2014. Investigation of the sources and evolution processes of severe haze pollution in Beijing in January 2013. Journal of Geophysical Research: Atmospheres 119, 4380–4398. https://doi.org/10.1002/2014JD021641

Sun, Y., Wang, Z., Dong, H., Yang, T., Li, J., Pan, X., Chen, P., Jayne, J.T., 2012. Characterization of summer organic and inorganic aerosols in Beijing, China with an Aerosol Chemical Speciation Monitor. Atmospheric Environment 51, 250–259. https://doi.org/10.1016/j.atmosenv.2012.01.013

Sun, Y.L., Wang, Z.F., Fu, P.Q., Yang, T., Jiang, Q., Dong, H.B., Li, J., Jia, J.J., 2013. Aerosol composition, sources and processes during wintertime in Beijing, China. Atmos. Chem. Phys. 13, 4577–4592. https://doi.org/10.5194/acp-13-4577-2013

Sun, Y.-L., Zhang, Q., Schwab, J.J., Demerjian, K.L., Chen, W.-N., Bae, M.-S., Hung, H.-M., Hogrefe, O., Frank, B., Rattigan, O. V., Lin, Y.-C., 2011. Characterization of the sources and processes of organic and inorganic aerosols in New York city with a high-resolution time-of-flight aerosol mass apectrometer. Atmospheric Chemistry and Physics 11, 1581–1602. https://doi.org/10.5194/acp-11-1581-2011

Tagle, M., Rojas, F., Reyes, F., Vásquez, Y., Hallgren, F., Lindén, J., Kolev, D., Watne, Å.K., Oyola, P., 2020. Field performance of a low-cost sensor in the monitoring of particulate matter in Santiago, Chile. Environ Monit Assess 192, 171. https://doi.org/10.1007/s10661-020-8118-4

Theodosi, C., Grivas, G., Zarmpas, P., Chaloulakou, A., Mihalopoulos, N., 2011. Mass and chemical composition of size-segregated aerosols (PM_1, $PM_{2.5}$, PM_{10}) over Athens, Greece: local versus regional sources. Atmospheric Chemistry and Physics 11, 11895–11911. https://doi.org/10.5194/acp-11-11895-2011

Theodosi, C., Tsagkaraki, M., Zarmpas, P., Grivas, G., Liakakou, E., Paraskevopoulou, D., Lianou, M., Gerasopoulos, E., Mihalopoulos, N., 2018. Multi-year chemical composition of the fine-aerosol fraction in Athens, Greece, with emphasis on the contribution of residential heating in wintertime. Atmospheric Chemistry and Physics 18, 14371–14391. https://doi.org/10.5194/acp-18-14371-2018

Thomaidis, N.S., Bakeas, E.B., Siskos, P.A., 2003. Characterization of lead, cadmium, arsenic and nickel in PM2.5 particles in the Athens atmosphere, Greece. Chemosphere 52, 959–966. https://doi.org/10.1016/S0045-6535(03)00295-9

Titos, G., del Águila, A., Cazorla, A., Lyamani, H., Casquero-Vera, J.A., Colombi, C., Cuccia, E., Gianelle, V., Močnik, G., Alastuey, A., Olmo, F.J., Alados-Arboledas, L., 2017. Spatial and temporal variability of carbonaceous aerosols: Assessing the impact of biomass burning in the urban environment. Science of The Total Environment 578, 613–625. https://doi.org/10.1016/j.scitotenv.2016.11.007

Tomasi, C., Fuzzi, S., Kokhanovsky, A., 2017. Atmospheric Aerosols: Life Cycles and Effects on Air Quality and Climate. John Wiley & Sons.

Tombrou, M., Dandou, A., Helmis, C., Akylas, E., Angelopoulos, G., Flocas, H., Assimakopoulos, V., Soulakellis, N., 2007. Model evaluation of the atmospheric boundary layer and mixed-layer evolution. Boundary-Layer Meteorol 124, 61–79. https://doi.org/10.1007/s10546-006-9146-5

Tryner, J., L'Orange, C., Mehaffy, J., Miller-Lionberg, D., Hofstetter, J.C., Wilson, A., Volckens, J., 2020. Laboratory evaluation of low-cost PurpleAir PM monitors and in-field correction using co-located portable filter samplers. Atmospheric Environment 220, 117067. https://doi.org/10.1016/j.atmosenv.2019.117067

Tsiodra, I., Grivas, G., Tavernaraki, K., Bougiatioti, A., Apostolaki, M., Paraskevopoulou, D., Gogou, A., Parinos, C., Oikonomou, K., Tsagkaraki, M., Zarmpas, P., Nenes, A., Mihalopoulos, N., 2021. Annual exposure to polycyclic aromatic hydrocarbons in urban environments linked to wintertime wood-burning episodes. Atmospheric Chemistry and Physics 21, 17865–17883. https://doi.org/10.5194/acp-21-17865-2021

Tsogas, G.Z., Giokas, D.L., Vlessidis, A.G., Aloupi, M., Angelidis, M.O., 2009. Survey of the Distribution and Time-Dependent Increase of Platinum-Group Element Accumulation Along Urban Roads in Ioannina (NW Greece). Water Air Soil Pollut 201, 265–281. https://doi.org/10.1007/s11270-008-9943-1

Turpin, B.J., Huntzicker, J.J., 1995. Identification of secondary organic aerosol episodes and quantitation of primary and secondary organic aerosol concentrations during SCAQS. Atmospheric Environment 29, 3527–3544. https://doi.org/10.1016/1352-2310(94)00276-Q

Tyrlis, E., Lelieveld, J., 2013. Climatology and Dynamics of the Summer Etesian Winds over the Eastern Mediterranean. Journal of the Atmospheric Sciences 70, 3374–3396. https://doi.org/10.1175/JAS-D-13-035.1

Tzannatos, E., 2010. Ship emissions and their externalities for the port of Piraeus – Greece. Atmospheric Environment 44, 400–407. https://doi.org/10.1016/j.atmosenv.2009.10.024

Ulbrich, I.M., Canagaratna, M.R., Zhang, Q., Worsnop, D.R., Jimenez, J.L., 2009. Interpretation of organic components from Positive Matrix Factorization of aerosol mass spectrometric data. Atmospheric Chemistry and Physics 9, 2891–2918. https://doi.org/10.5194/acp-9-2891-2009

Uria-Tellaetxe, I., Carslaw, D.C., 2014. Conditional bivariate probability function for source identification. Environmental Modelling & Software 59, 1–9. https://doi.org/10.1016/j.envsoft.2014.05.002

Via, M., Minguillón, M.C., Reche, C., Querol, X., Alastuey, A., 2021. Increase in secondary organic aerosol in an urban environment. Atmos. Chem. Phys. 21, 8323–8339. https://doi.org/10.5194/acp-21-8323-2021

Viana, M., Hammingh, P., Colette, A., Querol, X., Degraeuwe, B., Vlieger, I. de, van Aardenne, J., 2014. Impact of maritime transport emissions on coastal air quality in Europe. Atmospheric Environment 90, 96–105. https://doi.org/10.1016/j.atmosenv.2014.03.046

Virkkula, A., 2010. Correction of the Calibration of the 3-wavelength Particle Soot Absorption Photometer (3λ PSAP). Aerosol Science and Technology 44, 706–712. https://doi.org/10.1080/02786826.2010.482110

Virkkula, A., Mäkelä, T., Hillamo, R., Yli-Tuomi, T., Hirsikko, A., Hämeri, K., Koponen, I.K., 2007. A Simple Procedure for Correcting Loading Effects of Aethalometer Data. Journal of the Air & Waste Management Association 57, 1214–1222. https://doi.org/10.3155/1047-3289.57.10.1214

Vrekoussis, M., Kanakidou, M., Mihalopoulos, N., Crutzen, P.J., Lelieveld, J., Perner, D., Berresheim, H., Baboukas, E., 2004. Role of the NO_3 radicals in oxidation processes in the eastern Mediterranean troposphere during the MINOS campaign. Atmospheric Chemistry and Physics 4, 169–182. https://doi.org/10.5194/acp-4-169-2004

Vrekoussis, M., Liakakou, E., Koçak, M., Kubilay, N., Oikonomou, K., Sciare, J., Mihalopoulos, N., 2005. Seasonal variability of optical properties of aerosols in the Eastern Mediterranean. Atmospheric Environment 39, 7083–7094. https://doi.org/10.1016/j.atmosenv.2005.08.011

Vu, T.V., Delgado-Saborit, J.M., Harrison, R.M., 2015. A review of hygroscopic growth factors of submicron aerosols from different sources and its implication for calculation of lung deposition efficiency of ambient aerosols. Air Qual Atmos Health 8, 429–440. https://doi.org/10.1007/s11869-015-0365-0

Wang, Y., Li, J., Jing, H., Zhang, Q., Jiang, J., Biswas, P., 2015. Laboratory Evaluation and Calibration of Three Low-Cost Particle Sensors for Particulate Matter Measurement. Aerosol Science and Technology 49, 1063–1077. https://doi.org/10.1080/02786826.2015.1100710

Wang, Y.Q., Zhang, X.Y., Draxler, R.R., 2009. TrajStat: GIS-based software that uses various trajectory statistical analysis methods to identify potential sources from long-term air pollution measurement data. Environmental Modelling & Software 24, 938–939. https://doi.org/10.1016/j.envsoft.2009.01.004

Weichenthal, S., Kulka, R., Lavigne, E., van Rijswijk, D., Brauer, M., Villeneuve, P.J., Stieb, D., Joseph, L., Burnett, R.T., 2017. Biomass Burning as a Source of Ambient Fine Particulate Air Pollution and Acute Myocardial Infarction. Epidemiology 28, 329–337. https://doi.org/10.1097/EDE.0000000000000636

Weingartner, E., Saathoff, H., Schnaiter, M., Streit, N., Bitnar, B., Baltensperger, U., 2003. Absorption of light by soot particles: determination of the absorption coefficient by means of aethalometers. Journal of Aerosol Science, Intercomparison of Soot Measurement Techniques 34, 1445–1463. https://doi.org/10.1016/S0021-8502(03)00359-8

Wilson, J.G., Kingham, S., Pearce, J., Sturman, A.P., 2005. A review of intraurban variations in particulate air pollution: Implications for epidemiological research. Atmospheric Environment 39, 6444–6462. https://doi.org/10.1016/j.atmosenv.2005.07.030

Wong, D.W., Yuan, L., Perlin, S.A., 2004. Comparison of spatial interpolation methods for the estimation of air quality data. J Expo Sci Environ Epidemiol 14, 404–415. https://doi.org/10.1038/sj.jea.7500338

World Health Organization, 2016. Ambient air pollution: a global assessment of exposure and burden of disease. World Health Organization.

World Health Organization. Regional Office for Europe, 2006. Air quality guidelines: global update 2005: particulate matter, ozone, nitrogen dioxide and sulfur dioxide. World Health Organization. Regional Office for Europe.

Xu, L., Suresh, S., Guo, H., Weber, R.J., Ng, N.L., 2015. Aerosol characterization over the southeastern United States using high-resolution aerosol mass spectrometry: spatial and seasonal variation of aerosol composition and sources with a focus on organic nitrates. Atmos. Chem. Phys. 15, 7307–7336. https://doi.org/10.5194/acp-15-7307-2015

Yuan, W., Huang, R.-J., Yang, L., Guo, J., Chen, Z., Duan, J., Wang, T., Ni, H., Han, Y., Li, Y., Chen, Q., Chen, Y., Hoffmann, T., O'Dowd, C., 2020. Characterization of the light-absorbing properties, chromophore composition and sources of brown carbon aerosol in Xi'an, northwestern China. Atmospheric Chemistry and Physics 20, 5129–5144. https://doi.org/10.5194/acp-20-5129-2020

Zanatta, M., Gysel, M., Bukowiecki, N., Müller, T., Weingartner, E., Areskoug, H., Fiebig, M., Yttri, K.E., Mihalopoulos, N., Kouvarakis, G., Beddows, D., Harrison, R.M., Cavalli, F., Putaud, J.P., Spindler, G., Wiedensohler, A., Alastuey, A., Pandolfi, M., Sellegri, K., Swietlicki, E., Jaffrezo, J.L., Baltensperger, U., Laj, P., 2016. A European aerosol phenomenology-5: Climatology of black carbon optical properties at 9 regional background sites across Europe. Atmospheric Environment 145, 346–364. https://doi.org/10.1016/j.atmosenv.2016.09.035

Zanobetti, A., Franklin, M., Koutrakis, P., Schwartz, J., 2009. Fine particulate air pollution and its components in association with cause-specific emergency admissions. Environmental Health 8, 58. https://doi.org/10.1186/1476-069X-8-58

Zhang, Q., Jimenez, J.L., Canagaratna, M.R., Ulbrich, I.M., Ng, N.L., Worsnop, D.R., Sun, Y., 2011. Understanding atmospheric organic aerosols via factor analysis of aerosol mass spectrometry: a review. Anal Bioanal Chem 401, 3045–3067. https://doi.org/10.1007/s00216-011-5355-y

Zhang, Q., Jimenez, J.L., Worsnop, D.R., Canagaratna, M., 2007. A Case Study of Urban Particle Acidity and Its Influence on Secondary Organic Aerosol. Environ. Sci. Technol. 41, 3213–3219. https://doi.org/10.1021/es061812j

Zhang, S., Tison, E., Dusanter, S., Beaugard, C., Gengembre, C., Augustin, P., Fourmentin, M., Delbarre, H., Riffault, V., 2021. Near real-time PM1 chemical composition measurements at a French urban background and coastal site under industrial influence over more than a year: Temporal variability and assessment of sulfur-containing emissions. Atmospheric Environment 244, 117960. https://doi.org/10.1016/j.atmosenv.2020.117960

Zhang, Y., Favez, O., Petit, J.-E., Canonaco, F., Truong, F., Bonnaire, N., Crenn, V., Amodeo, T., Prévôt, A.S.H., Sciare, J., Gros, V., Albinet, A., 2019. Six-year source apportionment of submicron organic aerosols from near-continuous highly time-resolved measurements at SIRTA (Paris area, France). Atmos. Chem. Phys. 19, 14755–14776. https://doi.org/10.5194/acp-19-14755-2019

Zhang, Y., Tang, L., Yu, H., Wang, Z., Sun, Y., Qin, W., Chen, W., Chen, Changhong, Ding, A., Wu, J., Ge, S., Chen, Cheng, Zhou, H., 2015. Chemical composition, sources and evolution processes of aerosol at an urban site in Yangtze River Delta, China during wintertime. Atmospheric Environment, PM2.5 Research in the Yangtze River Delta: Observations, processes, modeling and Health effects 123, 339–349. https://doi.org/10.1016/j.atmosenv.2015.08.017

Zhang, Z., Whitsel, E.A., Quibrera, P.M., Smith, R.L., Liao, D., Anderson, G.L., Prineas, R.J., 2009. Ambient Fine Particulate Matter Exposure and Myocardial Ischemia in the Environmental Epidemiology of Arrhythmogenesis in the Women's Health Initiative (EEAWHI) Study. Environmental Health Perspectives 117, 751–756. https://doi.org/10.1289/ehp.0800046

Zhang, Z., Zhu, W., Hu, M., Wang, H., Chen, Z., Shen, R., Yu, Y., Tan, R., Guo, S., 2021. Secondary Organic Aerosol from Typical Chinese Domestic Cooking Emissions. Environmental Science and Technology Letters 8, 24–31. https://doi.org/10.1021/acs.estlett.0c00754

Zheng, T., Bergin, M.H., Johnson, K.K., Tripathi, S.N., Shirodkar, S., Landis, M.S., Sutaria, R., Carlson, D.E., 2018. Field evaluation of low-cost particulate matter sensors in high- and low-concentration environments. Atmos. Meas. Tech. 11, 4823–4846. https://doi.org/10.5194/amt-11-4823-2018

Zhou, L., Liu, T., Yao, D., Guo, H., Cheng, C., Chan, C.K., 2021. Primary emissions and secondary production of organic aerosols from heated animal fats. Science of The Total Environment 794, 148638. https://doi.org/10.1016/j.scitotenv.2021.148638

Zhou, Y., Shuiyuan Cheng, Lang, J., Chen, D., Zhao, B., Liu, C., Xu, R., Li, T., 2015. A comprehensive ammonia emission inventory with high-resolution and its evaluation in the Beijing–Tianjin–Hebei (BTH) region, China. Atmospheric Environment 106, 305–317. https://doi.org/10.1016/j.atmosenv.2015.01.069

Zittis, G., Almazroui, M., Alpert, P., Ciais, P., Cramer, W., Dahdal, Y., Fnais, M., Francis, D., Hadjinicolaou, P., Howari, F., Jrrar, A., Kaskaoutis, D.G., Kulmala, M., Lazoglou, G., Mihalopoulos, N., Lin, X., Rudich, Y., Sciare, J., Stenchikov, G., Xoplaki, E., Lelieveld, J., 2022. Climate Change and Weather Extremes in the Eastern Mediterranean and Middle East. Reviews of Geophysics 60, e2021RG000762. https://doi.org/10.1029/2021RG000762

Zittis, G., Hadjinicolaou, P., Klangidou, M., Proestos, Y., Lelieveld, J., 2019. A multi-model, multi-scenario, and multi-domain analysis of regional climate projections for the Mediterranean. Reg Environ Change 19, 2621–2635. https://doi.org/10.1007/s10113-019-01565-w

Zografou, O., Gini, M., Manousakas, M.I., Chen, G., Kalogridis, A.C., Diapouli, E., Pappa, A., Eleftheriadis, K., 2022. Combined organic and inorganic source apportionment on yearlong ToF-ACSM dataset at a suburban station in Athens. Atmospheric Measurement Techniques 15, 4675–4692. https://doi.org/10.5194/amt-15-4675-2022